



High temperature resistivity, Hall effect, and Seebeck coefficient measurements

**And the extension of the van der Pauw technique
to anisotropic samples**

Department of Chemistry, Aarhus University

Ph.D. dissertation

Kasper Andersen Borup

July 28 2014



Preface

The work presented in this dissertation has been carried out under the supervision of Professor Bo Brummerstedt Iversen at Aarhus University. Dr. G. Jeffrey Snyder from Caltech has been an unofficial co-supervisor and most of this work has been carried out in a close collaboration with his group. The work has been carried out in the period from August 2010 to July 2014 at the Department of Chemistry and iNANO, Aarhus University. Some of the work is based on experiences from a previous visit to Dr. Snyder's group at Caltech from September 2009 to January 2010.

The dissertation is divided into several Chapters. Chapter 1 contains an introduction to thermoelectricity and a literature review of thermoelectric measurements. This serves as a foundation for the work in the rest of the dissertation. Chapter 2 contains some mathematical and physical techniques which are employed in the dissertation, particularly in Chapter 4, which is of a more theoretical nature. Chapter 3 presents two experimental setups which were constructed as part of this project. One measures the Seebeck coefficient while the other measures the resistivity and Hall effect. Both work at elevated temperatures. The main part of the construction was carried out during the first two years. Continuous improvements were made during the remainder of the project as problems and possible improvements presented themselves. Chapter 4 presents the theory for treating anisotropic samples using the van der Pauw method. This is a natural extension of the work in Chapter 3. This was motivated by the experience in the Aarhus group with growing single crystals. These are often anisotropic and a method for characterizing this proved useful. During the second half of the project, collaborating with fellow group members on characterizing their samples using these setups was also in focus. This resulted in a large number of publications. Some of these are discussed in Chapter 5 and included in Appendix C in this dissertation. The close collaboration with the Snyder group was also continued, mainly on a project concerned with Cu₂Se. This is not included in this dissertation since it is far from the main project.

Below follows a list of publications and manuscripts to which I have contributed. They appear in the order they were accepted for publication. Those included in this dissertation are marked with an asterisk. These are all discussed in this dissertation. The remainders are briefly summarized in section 5.4.

Published papers

1) "Enhanced thermoelectric properties of Mg₂Si by addition of TiO₂ nanoparticles", Journal of Applied Physics **111** (2011), 023701, 7 pages.

Daniel Cederkrantz, N. Farahi, Kasper Andersen Borup, Bo Brummerstedt Iversen, M. Nygren, A.E.C. Palmqvist.

DOI: 10.1063/1.3675512

*2) "Investigation of the correlation between stoichiometry and thermoelectric properties in a PtSb₂ single crystal", Dalton Transactions **41** (2012), 1278-1283.

Martin Søndergaard, Mogens Christensen, Lasse Bjerg, Kasper A. Borup, Peijie Sun, Frank Steglich, Bo B. Iversen.

DOI: 10.1039/C1DT11523E

*3) "Phase Separation and Bulk p-n Transition in Single Crystals of Bi₂Te₂Se Topological Insulator", Advanced Materials **25** (2012), 889-893.

Jian-Li Mi, Martin Bremholm, Marco Bianchi, Kasper A. Borup, Simon Johnsen, Martin Søndergaard, Dandan Guan, Richard Hatch, Philip Hofmann, Bo Brummerstedt Iversen

DOI: 10.1002/adma.201203542

*4) "Thermal stability and thermoelectric properties of Mg₂Si_{0.4}Sn_{0.6} and Mg₂Si_{0.6}Sn_{0.4}", Journal of Materials Science **48** (2012), 2002-2008.

Martin Søndergaard, Mogens Christensen, Kasper A. Borup, Hao Yin, Bo B. Iversen.

DOI: 10.1007/s10853-012-6967-0

5) "High-temperature thermoelectric properties of Ca_{0.9}Y_{0.1}Mn_{1-x}FexO₃(0 ≤ x ≤ 0.25)", Journal of Meterials Science **48** (2012), 2817-2822.

Le Thanh Hung, Ngo Van Nong, Li Han, Dang Le Minh, Kasper A. Borup, Bo B. Iversen, Nini Pryds, Søren Linderoth.

DOI: 10.1007/s10853-012-6834-z

*6) "Gravity-induced gradients in thermoelectric Mg₂Si_{0.9925-x}Sn_xSb_{0.0075}", Acta Materialia **60** (2012), 5745-5751.

Martin Søndergaard, Mogens Christensen, Kasper A. Borup, Hao Yin, Bo B. Iversen.

DOI: 10.1016/j.actamat.2012.06.050

*7) "Thermoelectric Properties of the Entire Composition Range in Mg₂Si_{0.9925-x}Sn_xSb_{0.0075}", Journal of Electronic Materials **42** (2012), 1417-1421.

Martin Søndergaard, Mogens Christensen, Kasper A. Borup, Hao Yin, Bo B. Iversen.

DOI: 10.1007/s11664-012-2282-4

*8) "Measurement of the electrical resistivity and Hall coefficient at high temperatures", Review of Scientific Instruments **83** (2012), 123902, 7 pages.

Kasper A. Borup, Eric S. Toberer, Leslie D. Zoltan, George Nakatsukasa, Michael Errico, Jean-Pierre Fleurial, Bo B. Iversen, G. Jeffrey Snyder.

DOI: 10.1063/1.4770124

9) "Sintering and annealing effects on ZnO microstructure and thermoelectric properties", Acta Materialia **61** (2013), 3314–3323.

Martin Søndergaard, Espen D. Bøjesen, Kasper A. Borup, Sebastian Christensen, Mogens Christensen, Bo B. Iversen

DOI: 10.1016/j.actamat.2013.02.021

10) "Highly enhanced thermal stability of Zn_4Sb_3 nanocomposites", Chemical Communications **49** (2013), 6540-6542.

Hao Yin, Simon Johnsen, Kasper Andersen Borup, Kenichi Kato, Masaki Takata , Bo Brummerstedt Iversen

DOI: 10.1039/c3cc42340a

11) "Phase Transition Enhanced Thermoelectric Figure-Of-Merit in Copper Chalcogenides", APL Materials **1** (2013), 052107, 10 pages.

David R. Brown, Tristan Day, Kasper A. Borup, Sebastian Christensen, Bo B. Iversen, G. Jeffrey Snyder

DOI: 10.1063/1.4827595

12) "Termoelektriske materialer", Aktuel Naturvidenskab (2014), 16-21. (Danish popular science journal, not peer-reviewed)

Bo B. Iversen, Jacob Becker, Kasper A. Borup

Link:http://aktuelnaturvidenskab.dk/fileadmin/Aktuel_Naturvidenskab/nr-1/AN1-2014termoel.pdf

13) "High Temperature Thermoelectric Properties of $Cu_{1.97}Ag_{0.03}Se_{1+y}$ ", Materials For Renewable and Sustainable Energy **3** (2014), 26, 7 pages

Tristan W. Day, Kasper A. Borup, Tiansong Zhang, Fivos Drymiotis, Xun Shi, Lidong Chen, Bo B. Iversen, G. Jeffrey Snyder

DOI: 10.1007/s40243-014-0026-5

Submitted manuscripts

*"Measuring Thermoelectric Transport Properties of Materials", invited review for Energy and Environmental Science

Kasper A. Borup, Johannes de Boor, Heng Wang, Franck Gascoin, Xun Shi, Lidong Chen, Mikhail I. Fedorov, Eckhard Müller, Bo B. Iversen, G. Jeffrey Snyder

* "Functionally graded Ge_{1-x}Six thermoelectrics by simultaneous band gap and carrier density engineering", submitted to Chemistry of Materials

Ellen M. J. Hedegaard, Simon Johnsen, Lasse Bjerg, Kasper A. Borup, Bo B. Iversen

In preparation

"Comparison of the phase transition thermoelectric properties of super-ionic Ag₂Se and Cu₂Se"

David R. Brown, Kasper A. Borup, Tristan W. Day, Bo B. Iversen and G. J. Snyder

*"Extracting Anisotropic Resistivity from van der Pauw Measurements"

Kasper A. Borup, David R. Brown, Karl F. F. Fischer, G. Jeffrey Snyder, Bo B. Iversen

Acknowledgements

I would like to sincerely acknowledge and thank my supervisor Bo Brummerstedt Iversen for granting me the opportunity to carry out this work and for allowing me the freedom I have experienced. This freedom has taught me much about scientific research, both through success and failure, which could only be blamed on me. A freedom I have been particularly happy with is to allow and support, both personally and financially, my many visits to Dr. G. Jeffrey Snyder's group at Caltech. Dr. Snyder has been as much of a supervisor as Professor Iversen. I am grateful for his help and advice. I am very thankful for this opportunity, which has provided a fantastic setting for carrying out my work.

I am also deeply indebted to the machine shop at Department of Chemistry. I would not have been able to construct the setups in just two years without their help. Specifically, Erik Ejler Pedersen and Eigil Hald have been a great help in the physical construction.

My colleagues are all thanked for helping to create a great working environment, both at Aarhus University and Caltech. Martin Søndergaard, Hao Yin, Jianli Mi, Ellen Marie Jensen Hedegaard, and Anders Bank Blichfeld from Aarhus University are thanked for the many interesting discussions over the years and for including me in their projects. Likewise, David Brown and Tristan Day from Caltech are thanked for a close and fruitful collaboration on an interesting project. Nicholas Heinz, Heng Wang, Fivos Drymiotis, and Hyun-Sik Kim are thanked for their great advice, help and interesting discussions.

I am very thankful to all my co-authors for their contributions or for including me in their research. This includes all the many users of my setups. Their continued feedback has helped improve the systems immensely and without this user base this would not have been a fruitful project.

Contents

Preface	ii
Published papers.....	iii
Submitted manuscripts	iv
In preparation.....	iv
Acknowledgements	vi
Abstract.....	xiv
Dansk resume	xvi
1 Introduction	2
1.1 Thermoelectrics.....	2
1.1.1 Thermoelectric transport	4
1.2 Thermoelectric measurements.....	13
1.2.1 zT calculation.....	14
1.2.2 Sample quality.....	15
1.2.3 Seebeck coefficient.....	16
1.2.3.1 Measurements and data extraction	16
1.2.3.2 Instrument geometries.....	17
1.2.3.3 Thermal and electrical contact.....	20
1.2.4 Electrical resistivity	21
1.2.4.1 Charge carrier concentration and mobility.....	23
1.2.5 Thermal conductivity.....	24
1.2.5.1 Direct measurements.....	25
1.2.5.2 Flash diffusivity.....	26
1.2.5.3 Heat capacity.....	27
1.2.5.4 Density and thermal expansion	28
2 Methods.....	30
2.1 Numerical methods.....	30
2.1.1 The Newton-Raphson method.....	30

2.1.2	Method of steepest descent (maxima and minima)	32
2.1.3	Newton's method (maxima and minima)	32
2.2	Physics.....	33
2.2.1	Image poles.....	33
3	Instrumentation.....	36
3.1	Resistivity and Hall effect.....	36
3.1.1	The van der Pauw method	37
3.1.2	Instrument setup.....	38
3.1.2.1	Sample and electrical contacts	38
3.1.2.2	Sample holder.....	42
3.1.3	Sample chamber and magnet.....	45
3.1.4	Electronics and wiring.....	48
3.1.5	Measurement procedure and data analysis	51
3.1.5.1	Raw resistance measurements and the Peltier effect	51
3.1.5.2	Lead resistance and current selection.....	56
3.1.5.3	Full measurements	58
3.1.5.4	Data analysis.....	59
3.1.6	Software	60
3.1.7	Comparison of results and conclusion.....	61
3.2	Seebeck.....	63
3.2.1	Instrument geometry	63
3.2.1.1	Heater design.....	65
3.2.1.2	Thermocouples.....	66
3.2.1.3	Thermal contact and cold finger effect	72
3.2.2	Measurement procedure	74
3.2.2.1	Data analysis.....	76
3.2.2.2	Dark voltage and dark temperature.....	78
3.2.3	Upgrade.....	80
3.2.3.1	Adaptation for thin films and bar shaped samples	81
3.2.4	Software	83

3.2.5 Conclusion	83
4 Anisotropic resistivity	86
4.1 Introduction.....	86
4.1.1 Coordinate transformations	87
4.2 Extension of the theory	88
4.2.1 Change of coordinates.....	88
4.2.2 Isotropic equivalent sample	90
4.2.2.1 Anisotropic rectangles.....	90
4.2.2.2 Anisotropic parallelograms	92
4.1.1 Conformal mapping from the complex half plane.....	93
4.2.2.3 Relating experiment to tensor elements	94
4.2.2.4 Anisotropic parallelogram	97
4.2.3 Known methods.....	97
4.2.3.1 5-point method	98
4.2.4 New methods.....	101
4.2.4.1 Principal axes in crystals.....	101
4.2.4.2 Changing tensor orientation.....	104
4.2.5 Verification.....	107
4.2.6 Numerical error analysis.....	107
4.2.7 Experimental tests.....	113
4.3 Conclusion	118
5 Studies utilizing the instruments (and other projects)....	120
5.1 Graded Ge _x Si _{1-x}	120
5.2 The Mg ₂ Si _{1-x} Sn _x system.....	124
5.2.1 Transport properties as function of composition.....	125
5.2.2 Effect of spark plasma sintering	126
5.2.3 Thermal stability.....	127
5.3 Bi ₂ Te ₂ Se topological insulators	130
5.4 Further projects not included in this thesis	133
6 Conclusion	138

7 References..... 140

8 Appendices..... 144

Appendix A Derivations from Chapter 4	144
Appendix A.1 Anisotropic parallelogram side lengths and angle	144
Appendix A.2 Resistivity tensor elements for an anisotropic rectangle.....	145
Appendix A.3 Resistivity tensor elements for the anisotropic parallelogram	146
Appendix A.4 Tensor orientation in parallelogram-shaped single crystals...	149
Appendix B MATLAB TM scripts from Chapter 4.....	150
Appendix B.1 setup.m: General settings and definitions	150
Appendix B.2 Error from χ	152
Appendix B.3 Error from contact placement.....	153
Appendix B.4 Errors from single crystal measurements.....	155
Appendix B.5 Errors in the method of changing tensor orientation.....	159
Appendix B.6 Error in 5-point method.....	164
Appendix B.7 getk.m: Extracting k from isotropic equivalent sample geometry	
167	
Appendix B.8 getm.m: Extracting m in the 5-point method from sample	
geometry.....	168
Appendix B.9 transf.m: Function to calculate the conformal mapping.....	169
Appendix B.10 SC_getalpha.m: Solve the single crystal equation.....	169
Appendix B.11 R_getalbe.m: Solve the rotating tensor equation.....	172
Appendix B.12 getalpha_5pt.m: Solves the equation for the 5 point method	175
Appendix C Attached papers	176
Appendix C.1 Measurement of the Electrical Resistivity and Hall Coefficient at	
High Temperatures	178
Appendix C.2 Review of Thermoelectric Measurement Techniques	188
Appendix C.3 Extracting Anisotropic Resistivity from van der Pauw Measurements	
204	
Appendix C.4 Functionally Graded Ge _{1-x} Si _x Thermoelectrics by Simultaneous	
Band Gap and Carrier Density Engineering	212
Appendix C.5 Investigation of the Correlation Between Stoichiometry and	
Thermoelectric Properties in a PtSb ₂ Single Crystal.....	222

Appendix C.6 Thermoelectric Properties of the Entire Composition Range in $Mg_2Si_{0.9925-x}Sn_xSb_{0.0075}$	230
Appendix C.7 Gravity-Induced Gradients in Thermoelectric $Mg_2Si_{0.9925-x}Sn_xSb_{0.0075}$	238
Appendix C.8 Thermal Stability and Thermoelectric Properties of $Mg_2Si_{0.4}Sn_{0.6}$ and $Mg_2Si_{0.6}Sn_{0.4}$	248
Appendix C.9 Phase Separation and Bulk p-n Transition in Single Crystals of Bi_2Te_2Se Topological Insulator	258

Abstract

Thermoelectric materials are able to interconvert heat and electricity through purely solid state processes. This can be applied in miniature coolers, *e.g.* for semiconductor chips etc., off-grid power supplies for wireless sensors, or for larger scale waste heat recovery. The latter has high potential for increasing the fuel efficiency of vehicles where much of the energy is lost as heat through the exhaust. The widespread utilization of thermoelectrics is limited by the poor efficiency of available materials. A particular problem slowing down material development is the large error bars on the transport property measurements used to estimate the efficiency of the material through the figure of merit, zT . These properties are the electrical resistivity, the thermal conductivity, and the Seebeck coefficient. The majority of the work in the dissertation focuses on the construction of two setups for measuring the electrical resistivity and Seebeck coefficient, respectively. The setup for resistivity measurements is also able to measure Hall effect data for calculating the charge carrier concentration and mobility. The two setups are described with the focus on the particular design specifics believed to increase the accuracy over other measurements. The main causes of error in the two setups are also discussed and possible future actions to remove or decrease these errors are suggested. As a natural extension of this work, the theoretical foundation for the van der Pauw method for resistivity measurements is extended to treat anisotropic samples. The resistivity and Hall effect setup utilizes this method. The theoretical foundation is extended and two methods for extracting the full in-plane resistivity tensor from standard van der Pauw measurements are presented. The allowed sample geometry is flat parallelograms which is a relaxation compared to the sparse previous literature. Previously, rectangles were required. This relaxation is also implemented in the most successful previously published method, which uses a modified van der Pauw method. In the end the use of the two setups is illustrated through three studies of thermoelectric materials and a topological insulator. Possible applications of the treatment of anisotropic samples are also pointed out.

Dansk resume

Termoelektriske materialer kan konvertere varme til elektricitet og elektricitet til varme udelukkende gennem faststofprocesser. Dette kan anvendes til miniature kølere, f.eks. til halvlederchips osv., strømforsyninger til trådløse sensorer, eller genindvinding af spildvarme på større skala. Det sidste har specielt gode anvendelsesmuligheder indenfor transportmidler, hvor termoelektrika kan reducere brandstofforbruget, da meget energi går tabt som varme i udstødningsgasserne. Bredere anvendelse af termoelektrika på stor skala er begrænset af materialernes ringe effektivitet. Et vigtigt problem, som sænker materialeudviklingen, er de store fejl på målinger af de transportegenskaber, som bruges til at estimere materialernes effektivitet gennem kvalitetsfaktoren, zT . Disse egenskaber er den elektriske resistivitet, den termiske ledningsevne og Seebeck koefficienten. Størstedelen af arbejdet i denne afhandling fokuserer på to opstillinger, som respectivt mäter den elektriske resistivitet of Seebeck koefficienten. Opstillingen til resistivitetsmålinger kan også måle Hall effekt data, som bruges til at beregne ladningsbærerkoncentrationen og -mobiliteten. Disse opstillinger beskrives med fokus på de specifikke designelementer, som menes at øge nøjagtigheden i forhold til andre målinger. Hovedfejlkilderne i de to opstillinger diskuteres ligeledes, og mulige fremtidige forbedringer foreslås. En naturlig fortsættelse af dette er et teoretisk arbejde, hvor teoreien bag van der Pauw resistivitetsmålinger udvides til at kunne behandle anisotrope prøver. Van der Pauw metoden anvendes i opstillingen til måling af resistivitet og Hall effekt. Udvidelsen af det teoretiske grundlag resulterer i to nye metoder til at ekstrahere den fulde resistivitetstensor i prøvens plan fra standard van der Pauw målinger. Den tilladte prøvegeometri er flade parallellogrammer, hvilket er et mildere krav end anvendt i den sparsomme litteratur. I literaturen forlanges prøven altid at være et rektangel. Dette mildere krav til geometri indføres også i den mest succesfulde tidligere publicerede metode, som anvender modificerede van der Pauw målinger. Til slut præsenteres en række eksempler på anvendelser af de to opstillinger. Der er henholdsvis tale om termoelektriske materialer og en topologisk isolator. Mulige anvendelsesområder af den udvidede van der Pauw metode pointeres også i disse eksempler.

1 Introduction

1.1 Thermoelectrics

The thermoelectric effect is the interconversion of gradients in the electrical field and temperature. If an electrical field gradient is applied, a temperature gradient will result and vice versa. It consists of three distinct but related effects: The Seebeck effect, which relates an applied temperature gradient to the resulting electrostatic field gradient; The Peltier effect which relates an electric current to heat transport; And the Thomson effect which balances the energy of the other two by absorbing or releasing heat internally in the material when the Seebeck coefficient depends on temperature. The Seebeck coefficient, S , is the ratio of the resulting electrostatic potential gradient to the applied temperature gradient. This is related to the Peltier coefficient, π , by $\pi = ST$, where T is the absolute temperature. The heat flux q from the Peltier effect when the current density j is applied is $q = \pi j$. The Seebeck effect is used for power generation while the Peltier effect is used for active cooling. The Thomson effect is mainly important to the thermodynamics of thermoelectric modules and will not be discussed further here. Devices are constructed by combining materials with opposite sign of the Seebeck coefficient in series electrically and parallel thermally. Both the active cooling and power generation modes of devices are sketched in Figure 1-1.

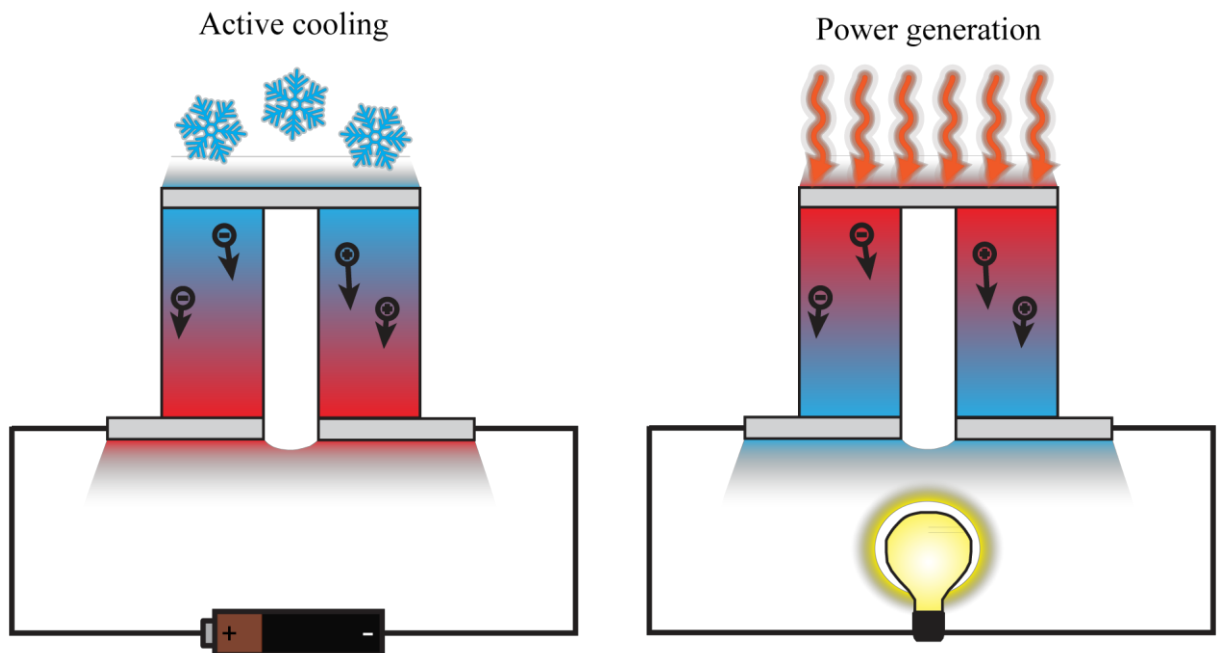


Figure 1-1: Schematics of thermoelectric modules used in the active cooling and power generation modes. For active cooling, a current is passed through the module which results in a temperature gradient across the module. For power generation, a temperature gradient is applied and the resulting Seebeck voltage is used to drive an electric current through an external circuit.

Thermoelectricity is a general material property and can be observed in any material. For the conversion to be efficient it requires the material to be electrical conductive, however the Seebeck effect can be observed even in insulating samples with resistances exceeding $10^{11}\Omega$,¹ which is the normal limit for voltage measurements. The reverse effect, the generation of temperature gradients when applying an electrical current, is not easily observed in an electrically insulating sample. In this case, the Peltier effect is completely outweighed by the Joule heating.

The cause of the thermoelectric effect is the temperature dependence of the Fermi-Dirac distribution. At the hot end the Fermi-Dirac distribution is slightly wider than at the cold end. This gives an increased density of high energy carriers at the hot end and low energy carriers at the cold end. These both tend to diffuse to the other end where their respective densities are lower. However, the momentum of the high energy carriers is higher than the low energy carriers, and the net diffusion of charge is hence toward the cold end. This accumulated charge generates an electric field which will change the electrochemical potential slightly and thus lower the excess concentration of high and low energy carriers. The diffusion thus proceeds until the system is balanced, that is when the electrochemical potential gradient balances the diffusion process. The difference in average momentum often leads to the description that carriers tend to ‘run away’ from the hot end. A slightly different explanation is that the density of states depends on electron energy. Hence in the hot end where the Fermi distribution is wider, there will be an excess of either high or low energy carriers compared to the cold end. If the low-energy carriers are in excess at the hot end the material is a p-type semiconductor, and if the high energy carriers are in excess it is n-type. This depends on the position of the Fermi energy relative to the valence and conduction band edges.

Thermoelectric materials can be used to construct thermoelectric modules by combining n- and p-type materials, as shown in Figure 1-1. These can either be used to generate electrical energy from heat,² or to move heat with electrical currents, i.e. cooling.³ Most work on thermoelectrics goes towards energy generation as this can be used to recover energy from waste heat and hence improve energy efficiency. This can be in factories producing large amounts of waste heat, in vehicles where much of the energy from the fuel is lost as heat in the exhaust,⁴ or any other place with a supply of waste heat. A niche application which is gaining more and more attention is power supplies for remote wireless sensors, such as in aircraft.^{5, 6} This can improve fuel efficiency by removing kilometers of heavy wires. One of the historically most important applications is in radioisotope thermoelectric generators used on deep space missions.⁴ These use a radioactive material (usually plutonium) that produces heat by radioactive decay. The radioactive core is encapsulated in a thermoelectric material that in turn is cooled on the other side by radiative heat loss to space. In both power generation and cooling applications, thermoelectric devices have the advantage that there are no moving parts and hence are more or less maintenance free.⁷ Additionally, traditional

cooling pumps are very inefficient for cooling small volumes whereas the efficiency of thermoelectric modules is approximately constant.

From a material point of view, the efficiency is governed by three properties: Its electrical resistivity, thermal conductivity, and Seebeck coefficient. The Seebeck coefficient represents the voltage generated when a temperature difference is applied. The electrical resistivity and thermal conductivity represent parasitic energy loss. The electrical resistivity is important because it measures how much of the energy is lost as Joule heating when a current passes through the material. If the thermal conductivity is high, much of the heat passes through the material without generating electricity or, when used for cooling, the heat from the hot side diffuses more easily to the cold side. The efficiency is estimated from the so-called thermoelectric figure of merit, zT , defined as

$$zT = \frac{S^2}{\rho\kappa} T \quad (1-1)$$

Here S is the Seebeck coefficient, κ the thermal conductivity, ρ the electrical resistivity, and T the temperature. Although the zT can be measured directly with the [Harman method](#)^{8, 9} it is customary to measure the individual properties as a function of temperature and then calculate zT . While zT is a good measure of the potential output of modules constructed using that material, it is not simply related to the final device efficiency. Generally, the efficiency of a module increases monotonously with the average zT of both the p- and n-type leg across the temperature interval employed (assuming the geometry is optimized). Many expressions of varying complexity exist which relates zT to device efficiency but these are all approximations ignoring parasitic losses to various extends. Nonetheless, zT is an excellent quantity to guide material research but should be used with care for anything but this.

1.1.1 Thermoelectric transport

In order to understand the transport properties, examining the Onsager equations is necessary. These relate fluxes to forces inside the material. A normal thermoelectric material transports charge and heat and the only forces present are from gradients in the electrostatic field and temperature. This gives the two Onsager equations

$$\mathbf{j}_e = -L_{ee}\nabla\mu_e - L_{eq}\nabla T \quad (1-2.a)$$

$$\mathbf{j}_h = -L_{he}\nabla\mu_e - L_{hh}\nabla T \quad (1-2.b)$$

In these equations \mathbf{j} is a flux, $\nabla\mu_e$ is the gradient in electrochemical potential, ∇T is the temperature gradient, and the L 's are the Onsager coefficients. The indices h and e are for heat and electricity, respectively. If the material is anisotropic the L 's turn into tensors. This will be ignored for now

but will be of importance in Chapter 4. The gradient in electrochemical potential is related to the electric field \mathbf{E} through $q\mathbf{E} = \nabla\mu_e$, where q is the charge of the charge carriers. In this formulation, the electrical conductivity is the ratio of the charge flux to the electric field measured at zero temperature gradient, $\nabla T = 0$. In other words, $\sigma \equiv \frac{qj_e}{\nabla\mu_e} = -qL_{ee}$. The thermal conductivity is equivalently the ratio of the heat flow to temperature gradient measured at zero current, $j_e = 0$. This gives $\kappa = L_{he}L_{ee}^{-1}L_{eh} - L_{hh}$. This is not dependent on just one Onsager coefficient since both electrons and phonons contribute to the thermal transport. Finally, the Seebeck coefficient is the ratio of the electric field to the temperature gradient measured in open circuit, $j_e = 0$. This gives $S = -\frac{L_{ee}}{qL_{eh}}$. This shows an important difference between electrical and thermal conductivity on one side and the Seebeck coefficient on the other: The expression for the Seebeck coefficient contains no fluxes but only two gradients. As such, it is not a transport property; Instead, it is thermodynamic quantity. This also implies that the Seebeck coefficient is independent on sample properties, such as density, shape, etc. that can affect fluxes but not gradients. If the material is also an ion conductor, an extra Onsager equation for the ion flux appears as well as its conjugate force, the ion concentration gradient. This further complicates the equations above. Ion concentrations may also be present in materials which are not ion conductors; however, including this complicates the expressions unnecessarily. Additional fluxes, such as entropy, may also be considered. This plays a role in some situations, such as phase transitions.^{10,11}

Many other approaches exist to analyzing thermoelectric transport and the Onsager approach is not necessarily the most transparent. The rest of this section deals with principles which are often used in explaining thermoelectric transport phenomena. The focus is on electrical transport since this is the focus of the rest of the dissertation. Naturally it starts with a discussion of zT and how to optimize thermoelectric materials.

From zT , Equation (1-1), it might seem simple to improve thermoelectric materials. You just need a high Seebeck coefficient and low electrical resistivity and thermal conductivity. Unfortunately, these properties are not independent but depend on other fundamental material properties¹², an important one of which being the charge carrier concentration. Rewriting zT using $\sigma = 1/\rho = ne\mu$, where n is the charge carrier concentration, e is the electronic charge and μ is the carrier mobility, yields

$$zT = (S^2 n) \left(\frac{\mu}{\kappa} \right) eT \quad (1-3)$$

To analyze this, it is first necessary to take a closer look at the Seebeck coefficient. From the Mott relation the Seebeck coefficient can be written in several ways¹³

$$S = \frac{\pi^2 k_B^2 T}{3 q} \left[\frac{d \ln \sigma(E)}{d E} \right]_{E=E_F} \quad (1-4.a)$$

$$S = \frac{\pi^2}{3} \frac{k_B^2 T}{q} \left[\frac{1}{n} \frac{dn(E)}{dE} + \frac{1}{\mu(E)} \frac{d\mu(E)}{dE} \right]_{E=E_F} \quad (1-4.b)$$

$$S = \frac{\pi^2}{3} \frac{k_B^2 T}{q} \left[\frac{g(E)}{n} + \frac{1}{\mu(E)} \frac{d\mu(E)}{dE} \right]_{E=E_F} \quad (1-4.c)$$

Here k_B is the Boltzmann constant, q is the carrier charge ($\pm e$), $g(E)$ is the density of states (DOS) at the carrier energy E and E_F is the Fermi energy. In Equation (1-4.b), $\sigma = ne\mu$ has been used in differentiating the conductivity and in Equation (1-4.c), $dn(E)/dE$ is recognized as the DOS at energy E . The number of carriers in the infinitesimal energy range between E and $E + dE$ is $n(E) = g(E)dE$, and hence differentiating the carrier density at energy E is simply $g(E)$. Equation (1-4.c) is a crude approximation (a more accurate treatment is given in reference 14) but it is sufficient for the discussion here (it neglects bipolar effects and the existence of a band edge, among other things).

The constants in front of (1-4.c) shows that the Seebeck coefficient has the same sign as the charge of the carriers, negative for n -type materials and positive for p -type materials. The first term in the parenthesis, $g(E)/n$, is related to the DOS. High DOS at the Fermi energy gives a high Seebeck coefficient. It also shows that the Seebeck coefficient decreases with the total carrier density. The second term takes into account the carrier scattering mechanisms. The mobility has to be low but increase strongly with carrier energy. The mobility is related to the relaxation time of the charge carriers, the average time a charge carrier moves freely before participating in a scattering event. This relaxation time, denoted τ , is often assumed to follow a power law,¹⁵

$$\tau = \tau_0 E^{\lambda-1/2}, \quad (1-5)$$

where λ is the scattering exponent and τ_0 is a proportionality constant. This is usually the case for a single band and only one scattering mechanism. For acoustic phonon scattering the scattering exponent is $\lambda = 0$, for scattering on neutral impurities (both macroscopic and atomic) and grain boundaries $\lambda = 1/2$ and for ionized impurity scattering $\lambda = 2$. Thus acoustic phonon scattering, which is normally dominant at high temperatures, decreases the Seebeck coefficient (τ decreases with E), whereas ionized impurity scattering increases the Seebeck coefficient, an effect often referred to as energy filtering since low energy carriers are preferentially scattered. The mobility is not a simple function of the relaxation time, but it is uniformly increasing with the relaxation time so the argument here is valid.

Equation (1-3) can now be analyzed. The first factor in parenthesis, $(S^2 n)$, is purely electronic. From the discussion above we know that the Seebeck coefficient is a decreasing function of n (when μ is constant, i.e. for a single, energy independent scattering mechanism), and hence there must be a maximum in $(S^2 n)$ at some n . The maximum can be increased by band structure engineering, such as band convergence,^{16, 17} alloying to create

maxima in the density of states at the Fermi level, or energy dependent scattering of the charge carriers. This can be done by micro structuring to create energy barriers that preferentially scatter the low energy carriers¹⁸ or by resonant scattering¹⁴ (from resonant impurity states). Making energy barriers is very hard in practice and requires the construction of superlattices of two or more materials, whereas resonant scattering is more easily achievable experimentally if a suitable dopant can be found. Resonant impurities are donor or acceptor levels inside the conduction or valence band, respectively. These increase the Seebeck coefficient by creating a maximum in the density of states and by preferentially scattering the low energy electrons, if the impurity levels are at the right energy with respect to the Fermi energy.

The second parenthesis, (μ/κ) , is a mixture of electronic and lattice properties. This term has the unfortunate property that improvements to one of κ or μ is often detrimental to the other. One way to improve the term is micro structuring to scatter long wavelength phonons but leave the short wavelength electrons relatively unaffected. This works best at low or intermediate temperatures where the phonon wavelength is much longer than the wavelength of the conducting electrons. Another approach is to use complex materials with large unit cells. These have a small Brillouin zone with flat phonon bands, and hence have a low thermal conductivity due to the low phonon group velocity ($d\omega(\mathbf{k})/d\mathbf{k}$) of the flat bands and umklapp scattering.¹⁹

The total thermal conductivity (κ_{tot}) has two contributions: The phonons in the crystal structure (κ_{ph}) and the electrically conducting electrons or holes (κ_e) and $\kappa_{tot} = \kappa_{ph} + \kappa_e$. The electronic thermal conductivity can be estimated by the Wiedemann-Franz law,²⁰

$$\kappa_e = L\sigma T \quad (1-6)$$

The proportionality constant L is called the Lorentz number, σ is the electrical conductivity, and T is the temperature. From the free electron model, the value of the Lorentz number is calculated as $L = \frac{\pi^2}{3} \left(\frac{k_B}{e} \right)^2 \cong 2.44 \cdot 10^{-8} \text{ W}\Omega\text{K}^{-2}$.²¹ This value is quite accurate for metals but for semiconductors, especially with low doping levels, the actual value can be much lower. This often leads to excessively low estimates of the lattice thermal conductivity (much lower than the amorphous limit and sometimes even negative altogether). Unfortunately the electronic or lattice thermal conductivity are hard to measure independently and so is the Lorentz number. The Lorentz number can, however, be extracted by modeling other transport property measurements, as will be discussed below.

In thermoelectrics, semi-classical approaches to model various transport properties have proved to be very successful.^{16, 22, 23} These are based on Boltzmann-type transport (classical) and terms and assumptions from modern quantum mechanical descriptions are added to this. This allows one to extract properties which are related to the microscopic band structure from measurements of macroscopic transport properties. The success relies largely on the fact that

most thermoelectric materials are heavily doped semiconductors and hence the electronic transport is dominated by properties of the minima and maxima in the conduction and valance bands, respectively. Hence the parts of the band structure contributing to electronic transport can often be modeled as parabolic. Usually it is assumed that there are one or two parabolic bands.

The expression for the Seebeck coefficient derived from the Mott relation in Equation (1-4.c) does not give much quantitative insight. Instead, within the single parabolic band model a relation valid for acoustic phonon ($\lambda = 0$) or ionized impurity ($\lambda = 2$) scattering is²⁴

$$S = \frac{k_B}{e} \left[\frac{(\lambda+2)F_{\lambda+1}(\eta)}{(\lambda+1)F_\lambda(\eta)} - \eta \right] \quad (1-7)$$

η is the reduced electrochemical potential related to the Fermi energy by $\eta = \frac{E_F}{k_B T}$ and $F_j(\eta)$ is the Fermi integral,

$$F_j(\eta) = \int_0^\infty \frac{\xi^j d\xi}{1 + \exp(\xi - \eta)} \quad (1-8)$$

The integration variable ξ is the energy. With $j = 0$ this is simply the integral of the Fermi distribution for energies above the band edge. The reduced electrochemical potential also occurs in relations for other transport coefficients but it can be extracted from Equation (1-7) when either acoustic phonon or ionized impurity scattering is assumed to dominate. One important property is the Lorentz number, which within the single parabolic band model is can be calculated from¹⁵

$$L = \frac{k_B^2}{e^2} \frac{(1+\lambda)(3+\lambda)F_\lambda(\eta)F_{\lambda+2}(\eta) - (2+\lambda)^2 F_{\lambda+1}(\eta)^2}{(1+\lambda)^2 F_\lambda(\eta)^2} \quad (1-9)$$

Again, either acoustic phonon or ionized impurity scattering needs to be assumed. This estimate is usually much more accurate than the metallic limit of $L = 2.44 \cdot 10^{-8} \text{ W}\Omega\text{K}^{-2}$ and yields physically meaningful values for the lattice thermal conductivity. The Equations (1-7) and (1-9) are only accurate for the two scattering mechanisms since the approximations used in the derivation do not hold for other mechanisms. It is, however, possible to derive equivalent formulae for two or more parabolic bands (by correct addition of the properties of the individual bands).^{24, 25}

It is also possible to model the Hall effect data in a similar way. Here it is important to distinguish between the true (or chemical) carrier concentration and the Hall carrier concentration. The equation for calculating the Hall carrier concentration from the Hall coefficient is derived using the free electron model. The measurements are sensitive to deviations from a parabolic shape or the presence of several bands and a correction is needed. In general this can be expressed as

$$n = n_H r_H \quad (1-10)$$

n_H is the Hall carrier concentration, n is the true carrier concentration, and r_H is the correction known as the Hall factor. The Hall factor rarely deviates much from unity^{15, 25} but it is temperature dependent since the widening of the Fermi distribution with temperature also increases the part of the band structure contributing to the measurement. Hence the Hall carrier concentration is often seen to change with temperature even in cases where the size of the band gap can rule out significant thermal excitation of carriers for the doping level in question. In a single parabolic band with only ionized impurity and acoustic phonon scattering the Hall factor can be calculated as¹⁵

$$r_H = \frac{3}{2} F_{1/2}(\eta) \frac{(\gamma_2 + \lambda) F_{2\lambda - \gamma_2}(\eta)}{(1 + \lambda)^2 F_\lambda^2(\eta)} \quad (1-11)$$

In deriving this it is also necessary to assume a spherical Fermi surface. Equations can also be derived for ellipsoidal surfaces or the generalized integrals can be evaluated for more complex shapes. In the single parabolic band model the carrier density can be calculated as¹⁵

$$n_H = n \cdot \frac{1}{r_H} = N_C F_{1/2}(\eta) \frac{1}{r_H} = 4\pi \left(\frac{2m^* k_B T}{h^2} \right)^{3/2} F_{1/2}(\eta) \frac{1}{r_H} \quad (1-12)$$

Here N_C is the density of states in a parabolic band, m^* is the effective mass of the band, and h is Planck's constant. Hence by using η extracted from the Seebeck coefficient measurement and fitting this expression to the measured Hall carrier concentration the effective mass of the band can be extracted. The approximations here are rather harsh and the method only works for highly parabolic bands.

The mobility is much more complicated to treat theoretically since it depends on the band structure, microstructure and defects, elastic properties of the lattice, and impurities. As above an expression for the cases of ionized impurity or acoustic phonon scattering can be derived¹⁵

$$\mu_H = \mu_0 \frac{(\gamma_2 + 2\lambda) F_{2\lambda - \gamma_2}(\eta)}{(1 + \lambda) F_\lambda(\eta)} \quad (1-13)$$

Here μ_0 depends on details of the material. In the case of acoustic phonon scattering, $\mu_0 \propto T^{-3/2} m^{*-5/2}$. In general $\mu_0 = e\tau_0/m^*$ where τ_0 is the relaxation time. As discussed previously, see Equation (1-5), the relaxation time for acoustic phonon scattering and ionized impurity scattering depends on the carrier energy. Therefore we get the Fermi integrals in Equation (1-13). The relaxation time for scattering by neutral impurities, macroscopic uncharged impurity inclusions and grain boundaries does not depend on the carrier energy. The presence of this can be allowed for by the addition rule for mobilities (known as Matthiessens's rule)²⁶, $1/\mu = 1/\mu_1 + 1/\mu_2 + \dots$.

Using these equations, plots of various transport properties have been generated in Figure 1-2 on page 12. The black curves have been calculated using properties close to those observed for $\text{Ba}_8\text{Ga}_x\text{Ge}_{46-x}$.²³ The other curves have been generated by changing different properties while keeping the others constant. A range of the reduced electrochemical potential η was selected to yield carrier concentrations between 10^{18} cm^{-3} and 10^{21} cm^{-3} . The input parameters are summarized in Table 1-1 below.

Table 1-1: Summary of parameters used to generate plots of transport properties in Figure 1-2. See the text for a discussion of the interpretation on the different changes.

Parent (black)	High temperature (red)	High mobility (green)	Low effective mass (blue)
$\lambda = 0$	$T = 600 \text{ K}$	$\mu_0 = 56 \text{ cm}^2/\text{V} \cdot \text{s}$	$m^* = 0.93 m_e$
$T = 300 \text{ K}$			
$m^* = 1.86 m_e$	μ_0 has been corrected plus the carrier concentration was recalculated.	No other corrections necessary.	μ_0 has been corrected plus the carrier concentration was recalculated.
$\mu_0 = 28 \text{ cm}^2/\text{V} \cdot \text{s}$			
$\kappa_L = 1 \text{ W/m} \cdot \text{s}$			

From the equations and the plot in Figure 1-2 some conclusions can be made about the transport properties. Increasing the temperature increases the Seebeck coefficient, resistivity, and electronic contribution to thermal conductivity, and the combined effect is to also increase the zT . This trend continues until the temperature is high enough to excite thermal carriers. In this case the single parabolic band model is no longer valid (a two-band model with holes and electrons is now necessary) and a decrease in zT is observed, which is not predicted by the model. Increasing the mobility but keeping the band structure and temperature constant is equivalent to changing the elastic properties of the lattice. This does not affect purely electronic properties such as the Seebeck coefficient, Hall factor and Lorentz number. As expected this increases the zT but these are intrinsic properties of the compound and are not readily tailored experimentally.

Lowering the density of states effective mass is equivalent to increasing the curvature of the band. This lowers the density of states at the Fermi energy, and in accordance with the Mott relation (Equation (1-4.c)) this also lowers the Seebeck coefficient. However, the increase in mobility more than offsets the decrease in Seebeck coefficient and a larger zT is obtained. Hence, we can see that increasing the DOS at the Fermi energy by flattening the electronic bands does not lead to higher zT . Instead, converging multiple low effective mass bands is a powerful approach.

Finally, a remark will be given on the Hall factor and Lorentz number. The fact that these depend on carrier concentration and temperature often leads to wrongful conclusions. The

Lorentz number can deviate strongly from the traditional value of $L = 2.44 \cdot 10^{-8} \text{ W}\Omega\text{K}^{-2}$ at low carrier densities and high temperatures. In the plots below the maximum in zT is at approximately 10^{20} cm^{-3} , and here the Lorentz number is significantly lower than the metallic limit. Hence, if the correct value is not used when subtracting the electronic thermal conductivity wrongful conclusions can result. The Hall factor increases with temperature, and hence the Hall carrier concentration will decrease with temperature if the chemical carrier concentration is constant, which is often the case. Therefor care should be taken when analyzing changes in Hall carrier concentration.

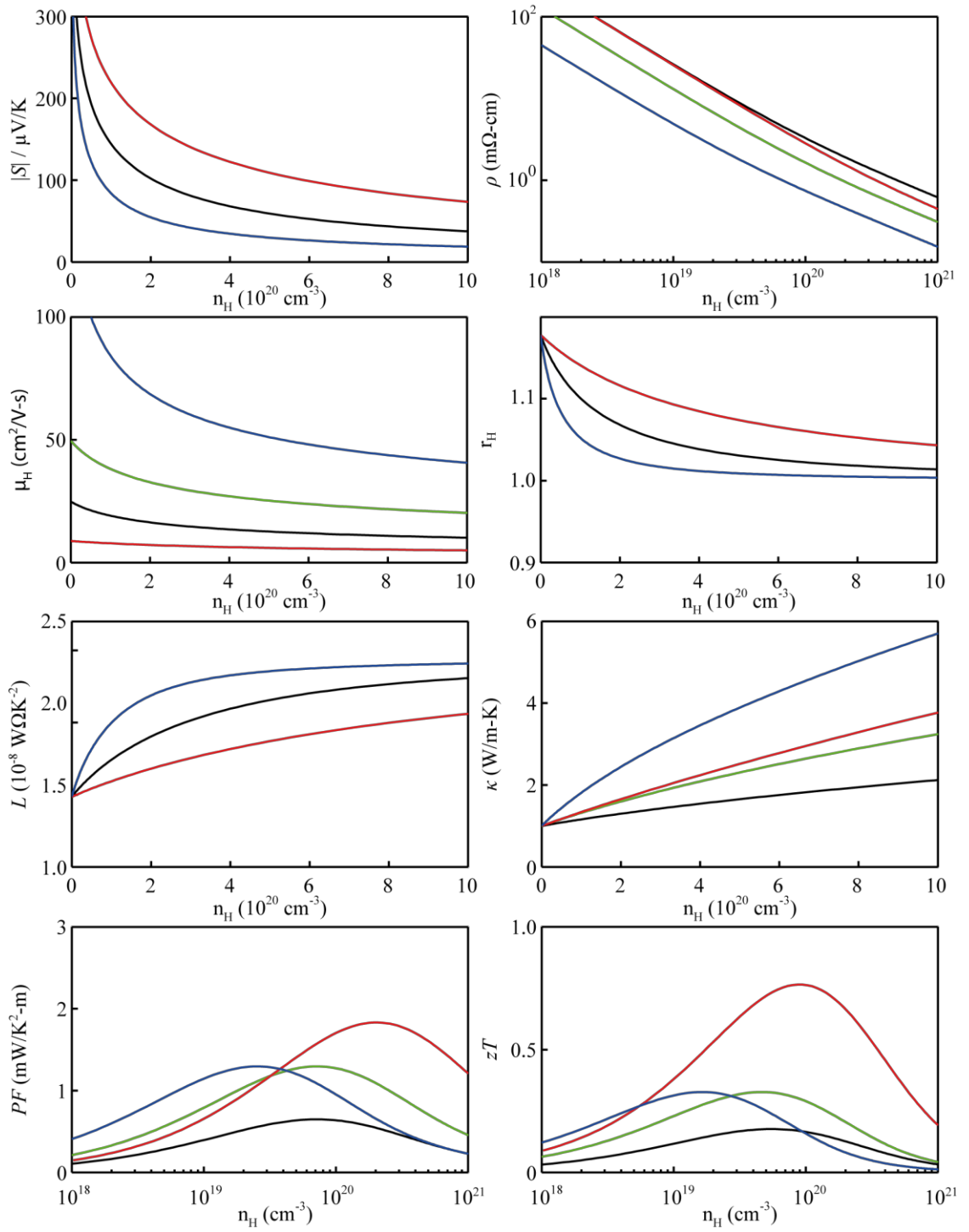


Figure 1-2: Plots of the transport properties in the single parabolic band model. Acoustic phonon scattering has been assumed ($\lambda=0$). The plots have been generated for different parameters which are summarized in Table 1-1. The parameters used for the black parent curve are close to those observed for $\text{Ba}_8\text{Ga}_x\text{Ge}_{46-x}$ ²³. The peak in the figure of merit is $zT = 0.18$, which is close to what is observed experimentally. Properties that are strongly varying with the carrier concentration have been shown on a logarithmic scale. The Seebeck coefficient is traditionally plotted with a linear scale (the Pisarenko plot) and resistivity is often plotted on a double logarithmic scale and this is also the case here.

1.2 Thermoelectric measurements

The main focus of this dissertation is on Seebeck coefficient, Hall effect, and resistivity measurements at high temperatures and treating anisotropy in the van der Pauw method. The higher goal, so to speak, is to improve the quality of measurements in thermoelectrics and hence help reduce the uncertainty and error in the final, calculated zT . The rest of this chapter is dedicated to a literature review on measurements in thermoelectrics. This will be published in part in a review paper. The manuscript has been through the first round of review in Energy and Environmental Science and is now being corrected. It can be found in Appendix C.2. The work in this dissertation as well as this review is motivated by a comprehensive Round-Robin by Hsin Wang et al.^{27, 28} published in 2013. They found a scatter in zT of 12% at 300 K and 21% at 475 K. The general trend was increasing with temperature and this is not expected to change at higher temperatures. The scatter was calculated as the maximum deviation from the mean represented by a fitted function. It is hence not an uncertainty but represents the variation that can be expected to occur in a measurement.

A scatter this high seems discouraging for thermoelectrics. An improvement in zT of 20% in state-of-the-art materials could potentially have large commercial impact. Hence improving measurement procedures is important for continued improvement in materials and should be addressed as thoroughly as materials research. As measurement accuracy improves it is necessary to reevaluate the properties of some materials; even properties of published standards needs to be periodically revisited. A good example is the lead chalcogenides. Their thermal conductivities were originally measured using the steady-state method which overestimated the thermal conductivity some 30%.^{29, 30} This is now one of the most heavily studied groups of high- zT materials.

An approach often used in materials science is to use standards; however, these are often not available with properties close to those of typical thermoelectric materials. Instead, it is recommended that laboratories develop internal standards. These can be materials the group has some experience working with and that are stable in the desired temperature range and with repeated thermal cycling. Elements with high vapor pressure, easily oxidized materials, or materials which can potentially react with thermocouples or contacts should be avoided. While such laboratory standards do not provide an estimate of apparatus accuracy, they are useful for identifying instrument drift and other errors. For example, thermocouple drift at elevated temperatures can be well in excess of 10 K due to thermocouple ageing or reactivity with samples or environment. This can potentially cause large systematic errors, particularly in Seebeck measurements.

The standards do not have to be high- zT materials. Instead, they need properties typical of thermoelectrics; this can be resistivity $\rho = 1 \text{ m}\Omega \cdot \text{cm}$, thermal conductivity $\kappa = 1 \text{ W/m} \cdot \text{K}$, and Seebeck coefficient $S = 100 \mu\text{V/K}$. It is not necessary to use the same sample, or even the same material, as a standard for all measurements. The highest priority is that it is stable,

both when stored and when heated in the instrument, and have one of its properties in the range of interest for thermoelectrics.

Even with apparently trivial measurements, skill and experience can be required to obtain high quality measurements. Hence, when training new researchers or students, having them repeatedly mount and measure an internal standard until consistent and accurate results are obtained ensures proper instrument use. Especially when both good electrical and thermal contact is required at multiple points, inexperience can lead to erroneous measurements. This may not always be obvious from the measurement itself, and hence using a standard is recommended.

1.2.1 zT calculation

zT is usually calculated from the Seebeck coefficient, electrical resistivity, and thermal conductivity which all have uncertainties provided by the instruments. These are often based on the statistical uncertainty, *i.e.* the noise in the raw data. This is not a true estimate of precision but rather an indication of the data quality and reproducibility. For instance, a resistivity measurement often has a statistical uncertainty of much less than 1% while the true uncertainty is more likely in the range of 2-5%. The statistical uncertainty in this case only accounts for the noise in the raw resistance measurements while errors from sample geometry, contact placements, temperature error etc. is not accounted for. Both error estimates are both important but serve different purposes.

The uncertainties from the individual measurements can be used to estimate the uncertainty on zT . From accumulation of errors this adds to zT according to

$$\left(\frac{\delta zT}{zT}\right)^n = \left(\frac{2\delta S}{S}\right)^n + \left(\frac{\delta \rho}{\rho}\right)^n + \left(\frac{\delta \kappa}{\kappa}\right)^n$$

S is Seebeck coefficient, ρ is resistivity, κ is thermal conductivity, δ is a small error (random or systematic), and n depends on the kind of error used. For random Gaussian errors $n = 2$. For small systematic errors $n = 1$ when only keeping first order term in the error in Seebeck. This is important since the error can easily be underestimated when using the wrong n . Propagating the statistical errors with $n = 2$ to zT does not provide an estimate of the accuracy but rather an indication of the overall quality of the data used to calculate zT . This can be important to identify bad data points. If, on the other hand, estimates of the maximum error in each measurement are given, an upper bound for the error in zT is calculated by $n = 1$. If 5% error in the individual measurements is assumed the maximum error in zT is 20% (12% when using the wrong $n = 2$). This is high, even for these low errors. The errors in most measurements are significantly larger than this, as will be discussed later. This is partially remedied by two facts: It is an estimate of the maximum error and it doesn't account for errors partially cancelling each other.

As the individual properties are often measured in different instruments in separate runs, they are also rarely measured at the same temperature. Even when the temperature is stabilized before each data point is measured errors from the thermocouple calibration still affect zT . When the temperature is not stabilized, interpolation of the data is necessary to calculate zT . This will usually not significantly affect the accuracy but makes it difficult to use the statistical error of each data point.

1.2.2 Sample quality

When discussing measurement accuracy, one source of error which is often overlooked or underestimated is the sample quality. The most important parameters are density and homogeneity. The theoretical density can be calculated from the unit cell size and contents, and from this the relative density can be calculated. This is usually greater than 98% for dense samples. The measured zT usually deviates from that of a dense sample when the relative density is less than 90% and suspect when less than 97%.³¹ The Seebeck coefficient is only weakly affected by density since it is not a true transport property and is independent of the sample geometry. For small volume fractions of evenly dispersed, equally sized, and approximately spherical voids the resistivity and thermal conductivity are changed by the same factor but in opposite directions. Hence, in this case also the $\rho\kappa$ product is unaffected.

There are two different types of inhomogeneity worth distinguishing for thermoelectrics: multi-phase inhomogeneity and charge carrier concentration (dopant) fluctuations. The first is normally detected by powder X-ray diffraction (PXRD) when large amounts ($> 2 - 5\%$) of impurities are present. Small amounts of impurities or amorphous phases are more easily detected by microscopy (*e.g.* SEM). The effect of secondary phases is strongly linked to the shape of inclusions. While a few volume percent of dispersed compact impurities normally do not affect the transport properties (especially Seebeck coefficient), insulating or metallic phases or cracks along grain boundaries may significantly influence the electrical and thermal conductivities. This is somewhat similar to the effect of voids. The presence of impurities may change the dopant content and hence charge carrier concentration of the main phase. For materials where the charge carrier concentration can be estimated from simple charge counting (*e.g.* using the Zintl principle)^{23, 32-35} comparison of stoichiometry (nominal and *e.g.* Electron Microprobe Analysis) with the measured Hall effect charge carrier concentration can be used to check for this. A sample falling outside the general trend calls for further examination. Both impurities and voids can cause significant errors in zT if the individual properties are measured along different directions or on different samples.

Post synthesis processing, *e.g.* ball milling, compaction, annealing, etc. may develop secondary phases or otherwise change the material, particularly in spark plasma sintering where large DC currents may drive mobile species.³⁶⁻⁴⁰ While scanning PXRD and SEM are powerful tools for investigating purity, they may completely miss dopant variations.⁴¹ Instead, spatially resolved scanning Seebeck coefficient measurements⁴¹⁻⁴⁴ (*e.g.* using PSM

from Panco Gmbh, Germany) can detect these variations and thus provide an important complementary technique for establishing homogeneity and quality control of bulk materials. The measurement geometry for this is shown in Figure 1-4 (d)

Even materials (both single crystals and polycrystalline materials) believed to melt congruently will in general produce doping inhomogeneity during solidification from the melt.⁴⁵ Figure 1-3 (a) shows a scanning Seebeck map of melt solidified Ba₈Ga₁₆Si₃₀ displaying a solidification microstructure not seen in PXRD or SEM. Such dopant gradients can also be observed and controlled in Bridgman grown single crystals of PtSb₂ (Figure 1-3 (b)) which clearly demonstrates that single crystals are not necessarily homogeneous.⁴⁶ Powdered, hot pressed, and solid-state annealed samples are typically better to ensure homogeneous charge carrier concentration on the macroscopic and microscopic level.⁴⁵

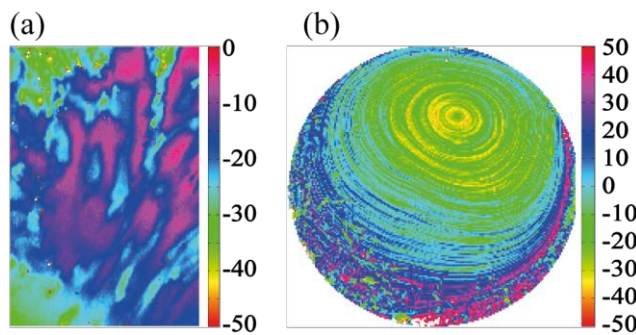


Figure 1-3: (a) Scanning Seebeck coefficient map of the same Ba₈Ga₁₆Si₃₀ surface; (b) Scanning Seebeck coefficient map of a Stockbarger grown PtSb₂ single crystal. This illustrates the complementarity of X-Ray diffraction and scanning Seebeck measurements.

1.2.3 Seebeck coefficient

A variation of about 6% in measured Seebeck coefficient at 500 K can generally be expected.²⁷ This will, however, also depend on the method employed.⁴⁷ The differences between the methods and possible ways to improve the results are discussed below. The absolute precision of Seebeck coefficient measurements is unknown due to the lack of exact value standards with appropriate properties.

1.2.3.1 Measurements and data extraction

The Seebeck coefficient is the ratio of a resulting electric field gradient to an applied temperature gradient. While the Seebeck coefficient is conceptually simple, in reality it can be difficult to measure accurately. A recent review addresses some of the instrument design challenges,⁴⁸ while another studies data analysis.⁴⁹ In a typical measurement, the temperature is varied around a constant average temperature and the slope of the voltage (V) vs. temperature difference (ΔT) curve gives the Seebeck coefficient (the slope method) or just $V/\Delta T$ is measured (single point measurement). Either a specific temperature difference is stabilized before each measurement (steady-state),⁵⁰⁻⁵² which takes longer, or measurements are conducted continuously while the temperature difference is varied slowly (quasi-steady-state).⁵²⁻⁵⁵ In a recent study,⁴⁷ little difference was found between steady-state and quasi-

steady-state measurements when good thermal and electrical contact is ensured. A modified version of the slope method was discussed by de Boor *et al.*⁴⁹ This method uses the slope of the voltage measured with one set of thermocouple leads vs. the voltage measured with the other set of leads. In the custom setup presented in Chapter 3 these are niobium and Chromel. This method suppresses some of the noise that enters the measurements when calculating the temperature difference (difference of two large numbers to give a small number) and reduces the number of necessary measurements from 3 to 2. This is further discussed in Section 3.2.2.1.

The employed temperature difference should be kept small, but a too small difference will lead to decreased accuracy. Usually $4 - 20\text{ K}$ (or $\pm 2 - \pm 10\text{ K}$) is appropriate for the full temperature span. This will be further discussed in section 3.2 on the Seebeck setup that has been constructed as part of this project. When using the quasi-steady-state method, all voltages and temperatures should ideally be measured simultaneously^{48, 52} or timed using the “delta measurement” technique (individual voltage measurements performed symmetrically in time) or with time stamps to compensate for a linear drift.^{49, 54}

In the slope method the measured raw data is corrected for constant offset voltages by using the slope of several ($\Delta T, V$) points for extracting the Seebeck coefficient.^{48, 49, 52, 54} The offset voltages can reach several hundred microvolts, increasing at elevated temperatures. The offset can be caused by several effects, including differences in thermocouple wires, reactive samples, and the cold finger effect (heat being drawn away from the sample through the thermocouple, causing a temperature drop between the sample and thermocouple tip due to the thermal contact resistance). It is an open circuit voltage and is not usable for power generation since a heat engine cannot output power without a heat flow. The single point method is unable to separate this from the actual thermopower (defined as the absolute value of Seebeck). The slope method, in contrary, is designed to extract only the usable part of the voltage, provided the offset is constant during one measurement. Most systems, both commercial and custom, including the one that will be described in Chapter 3 ,use the slope method to extract the Seebeck coefficient.

1.2.3.2 Instrument geometries

The contact arrangement is also of importance. Generally three different geometries exist:^{48, 54} 2-point (Figure 1-4 (a)), off-axis 4-point (Figure 1-4 (b)), and uniaxial 4-point (Figure 1-4 (c)). The geometry in Figure 1-4 (d) is an adapted 2-point geometry designed for scanning Seebeck measurements like the ones in Figure 1-3 (b) and (c). It is important to minimize electrical and thermal contact resistances and make sure the temperature and voltage are measured at the same point in space. This is not realized in the 2-point geometry, where thermocouple and voltage leads are generally imbedded in metallic contact pads in the heaters, however, the error may be small when good thermal and electrical contact is made to the sample (*e.g.* by soldering or using pads of high thermal conductivity metals such as

tungsten).⁴⁷ The 2-point geometry is also often used where other considerations than accuracy are important, such as in scanning systems.⁴² An embodiment of this is shown in Figure 1-4 (d).

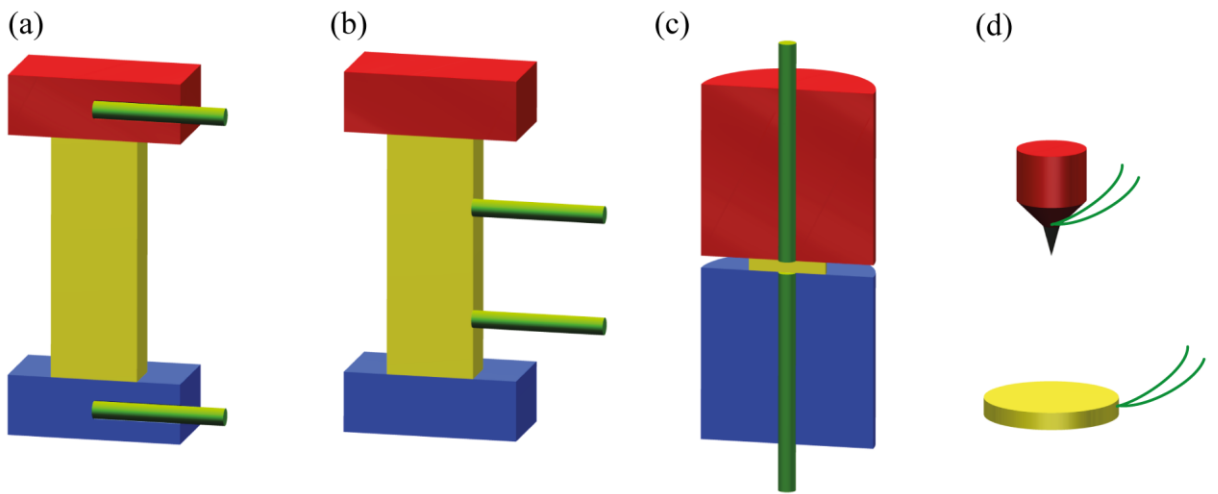


Figure 1-4: Different geometries often encountered in Seebeck coefficient measurements. (a) 2-point geometry; (b) Off-axis 4-point; (c) Uniaxial 4-point; (d) Geometry for scanning Seebeck measurements as adopted by Panco GmbH. In (a)-(c) the upper and lower heaters are shown in red and blue, the sample in between the two heaters in yellow, and the thin thermocouple rods in green. The thermal gradient can be applied in both directions. In (d) there is only one heater which is heated to slightly above room temperature. A tungsten needle is attached to the heater and this is pressed against points on the surface of the sample. Thermocouples, illustrated by small, green wires, are attached to the tungsten needle and sample holder (thus essentially making it a 2-point measurement) and the Seebeck coefficient is measured by the method described by de Boor *et al.*⁴⁹

In the off-axis 4-point geometry the thermocouples and voltage leads are pressed against the sides of the sample thus allowing simultaneous measurement of resistivity. This method is used in the most popular commercial instruments (*e.g.* by ULVAC-Rico or Linseis). Here, the thermocouples are in direct contact with the sample, reducing the distance between the electrical and thermal contacts. Since only low force can be used on the thermocouples to avoid bending (some materials may turn soft at high temperatures), breaking or shifting the sample, the thermal and electrical contact resistance may actually be large. High thermal conductivity alumina sheathed thermocouples extend to outside the heated zone to a chamber near room temperature. They may thus act as cold fingers and create a temperature gradient across the thermocouple tip-sample interface. The thermocouples would then underestimate each temperature and also the resulting ΔT , leading to an overestimated thermopower.^{47, 54} The analysis of the cold finger effect by Martin⁴⁷ further implies that the average temperature of the two thermocouples (which is used as the sample temperature) underestimates the true average temperature of the sample. This effect is expected to be a linear function of the temperature difference between the sample and surroundings and will compress the temperature interval of the measured Seebeck coefficient. If the Seebeck coefficient has strong temperature dependence this can affect the accuracy significantly. A large deviation between the temperatures of the gradient heaters in direct contact with the sample and

average sample temperature can be an indication that cold finger effects are affecting the measurement accuracy.

In a recent study by Martin⁴⁷ the results from the 2-point and off-axis 4-point geometries were compared. The off-axis 4-point geometry was observed to yield thermopower values higher than the 2-point geometry, with the difference being proportional to the temperature difference between the sample and surroundings. With a thorough analysis of the thermal resistances the study concludes that the cold finger effect is responsible for the higher thermopower values and that the 2-point geometry is preferable. While this is not a direct comparison to the ZEM systems, his custom setup was constructed to resemble this as much as possible. This is a strong indication that the ZEM measurements should be used with care. An analysis of the cold finger effect in both the off-axis and uniaxial 4-point geometries can be found in section 3.2.1.3 on page 72 . This comparison was not included by Martin.

The uniaxial 4-point geometry was developed to remedy these problems. The cold finger effect is reduced by inserting the thermocouples through the heaters, while the thermal contact resistance is kept low by having the thermocouples in direct contact with the sample with independent, constant pressure. The thermocouples may act as both cold and hot fingers in this geometry, depending on the strength of the thermal coupling to the heaters. Due to the heaters, the cold finger effect will be reduced compared to the 4-point off-axis geometry and since the temperature difference between the heater and sample is small, the hot finger effect is also believed to be small. With bad thermal contact in this setup, the thermocouples can both over- and underestimate the temperature and ΔT , depending on whether they act as cold or hot fingers; however, the error is believed to be smaller than for the 4-point off-axis geometry. The thin sample geometry with high cross sectional area leads to a high heat flux compared to the off-axis geometry and may increase the temperature drop across the heater-sample and thermocouple-sample interfaces. If each sample-heater and sample-thermocouple interface is not of approximately equal quality, it can be difficult to keep the average sample temperature constant during a ΔT sweep.

At low temperatures, the Quantum Design, Physical Property Measurement System (PPMS) has been extensively used. In the Thermal Transport Option (TTO), four copper leads are attached to a bar shaped sample with conductive adhesive and a heater, two resistance thermometers, and a heat sink are mechanically attached to these (corresponding to the off-axis 4-point geometry but without the thermocouples in direct contact with the sample). Hence, the temperature and voltage are measured far from each other and the cold-finger effect may be large. This geometry is further discussed in section 1.2.5.

1.2.3.3 Thermal and electrical contact

If possible, points should be measured for both increasing and decreasing ΔT and the data checked for hysteresis, such as in Figure 1-5 (b). Hysteresis can be an indication of poor thermal contact between sample and thermocouples or heaters. In Figure 1-5 (a) measurements with good and bad thermal contact are shown. Thermal voltages resulting from temperature changes in the wiring can also lead to hysteresis. The latter can be checked by heating local areas around the sample stage with a heat gun or soldering tip. Using higher pressure on the thermocouples or inserting a thin piece of graphite foil may help improving thermal contact. When combining resistivity and Seebeck measurements, the graphite may significantly increase the contact size and hence affect the resistivity measurement and should be used with care.

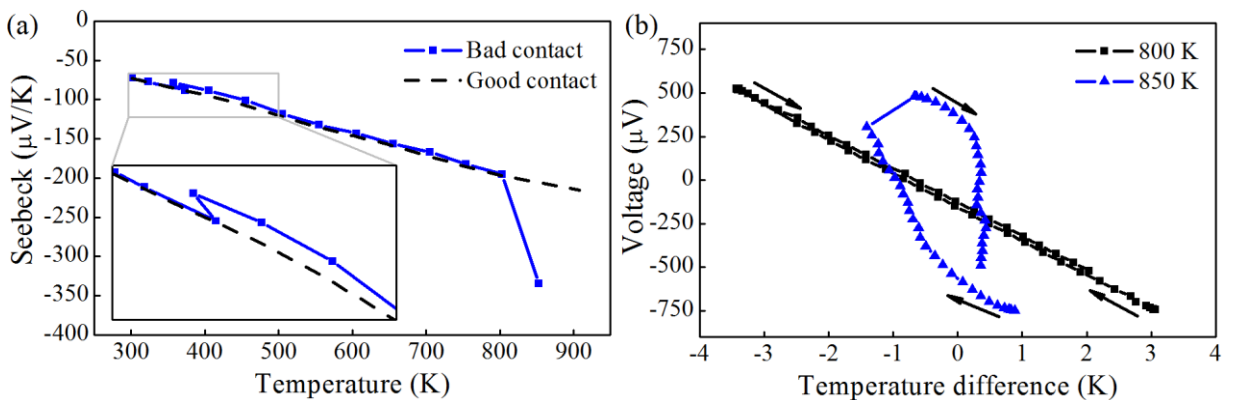


Figure 1-5: Example of the effect of bad thermal contact in Seebeck coefficient measurements. (a) A sample was measured from 300 K to 900 K both with good (dashed black line) and bad thermal contact between the sample and thermocouples (solid blue line and square symbols). (b) The raw voltage vs. temperature difference plots at 800 K (squares) and 850 K (triangles) for the measurement with bad thermal contact.

Since the thermocouples are exposed to many reactive materials, monitoring the ageing is important. This can be monitored by comparing the sample temperature to the furnace or gradient heater temperatures. After a number of measurement runs, the temperature difference will change indicating ageing of the thermocouples. Platinum, for example, is frequently used due to its high inertness to oxygen and many oxides but it reacts readily with Pb, Te, Sb, Si and other elements often found in thermoelectric materials. During a measurement run and sample mounting, poor electrical or thermal contact and other instrument errors can be identified by examining the voltage vs. temperature difference curves for hysteresis. For non-reactive and stable samples, the heating and cooling curves of the Seebeck coefficient should be identical, and the same is true for repeated measurement (if the first cooling and second heating curves agree but the rest do not, the sample properties are most likely changing). During sample mounting, 2-point I-V curves or resistances between two electrical contacts, including current contacts in combined Seebeck and resistivity systems, can help identify bad electrical contacts.

As with hysteresis, if the Seebeck coefficient depends on the heating rate and size or direction of the temperature difference employed there is likely bad thermal contact between the sample and thermocouples. When measuring in inert gas atmospheres (or air), the Seebeck coefficient should not depend on the gas pressure as this is an indication of bad thermal contact between the sample and thermocouples. This is also visible in Figure 1-5 (a) where data below 400 K are measured in air. For the measurement with bad thermal contact a change in the measurement is observed when the chamber is evacuated. In air the two measurements agree since the air improves the thermal contact. This is an early indication of bad thermal contact and the data quality is expected to be bad. In such cases using an inert gas can improve the data quality.

1.2.4 Electrical resistivity

Even though resistivity measurements are often regarded as routine, they are still prone to large errors. The most widely used method is the linear 4-point method with bar-shaped samples as shown in Figure 1-6 (a). Current (I) is passed from one end to the other while the voltage is being measured at two intermediate points (indicated by ρ). The voltage contacts should be placed sufficiently far from the ends to ensure a uniform current distribution in the bar at and between the contacts (usually placed at 1/3 and 2/3 of the sample length). The resistivity is $\rho = R \cdot A/l$ where R is the measured 4-point resistance, A is the cross sectional area, and l is the separation of the voltage contacts. The resistivity is therefore highly sensitive to errors in the geometric factor A/l which can easily be in excess of 5%. If the sample is not a parallelepiped, appropriate geometric factors need to be found, either analytically or numerically, e.g. from finite element methods. The voltage contacts should be narrow along the length of the sample to avoid uncertainty in l . This can be a problem when resistivity and Seebeck coefficient measurements are combined since the thermocouple tip often has a significant size.

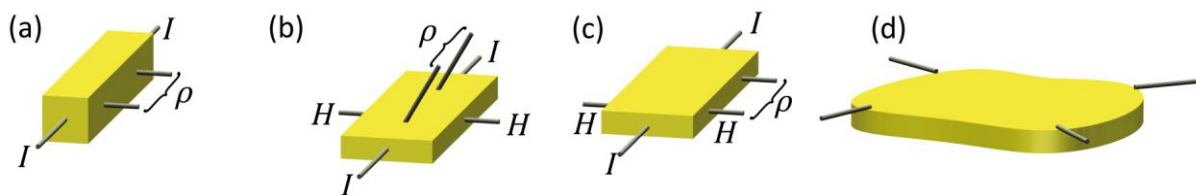


Figure 1-6: Four different samples and contact arrangements for resistivity and Hall effect measurements. (a) Contact arrangement and optimal sample geometry for only resistivity measurements on bar samples; (b) 6-point and (c) 5-point for combined resistivity and Hall effect measurements with sample geometry optimized for Hall effect measurements; (d) For combined resistivity and Hall effect measurement with the van der Pauw method. In (a)-(c), contacts for the applied current are marked with an I , contacts for resistivity measurements with ρ , and contacts for Hall effect with H . In (d), resistivity measurements are performed by applying current between adjacent contacts while Hall effect measurements are performed with current along a diagonal. This is further discussed in Reference 56 and in a later chapter in this dissertation.

Other techniques exist that may be less sensitive to errors in geometric factors. The most widely used of these in thermoelectrics is the van der Pauw technique, Figure 1-6 (d).^{57, 58} In this technique, the resistivity is obtained from a flat sample of arbitrary shape but uniform thickness with point contacts along its circumference. Since flat samples can be polished to have a uniform thickness (preferably with a variation of 0.005 mm or less, depending on thickness) that can be measured accurately using a micrometer, the error from the geometric factor may be reduced. Errors may arise if the sample sides are not perpendicular to the flat faces at all places, such as if the edge is chipped. In the van der Pauw method, the resistivity can be measured directly from hot pressed samples or slices of Bridgman, Stockbarger, or Czochralski grown ingots. The sample geometry is compatible with measurements of all thermoelectric transport properties, and zT can hence be obtained using only one sample.⁵⁶

The variation in electrical resistivity when using the 4-point bar method can be as high as 10% at 500 K,²⁷ twice that in Seebeck coefficient. The reason for the high scatter is mainly errors in determining the geometric factor,⁵⁹⁻⁶¹ indicating that this is indeed important in obtaining accurate resistivities. In the PPMS several options exist for measuring the electrical resistivity. Leads are attached with conducting adhesive, such as silver containing epoxy, which can lead to excessively large contact areas that reduce the accuracy.

In all resistivity measurements, a current sufficiently low to avoid significant Joule heating should be used. In thermoelectrics, there is a further complication due to the high Peltier effect.⁶² Heat is transported by the current from one contact to the other, creating a temperature gradient, which in turn leads to Seebeck voltages.⁶³ To reduce these errors either AC or pulsed (unipolar) DC measurements, where the voltage is measured immediately before and after turning the current on, are used. Carefully heat sinking the sample can further help reduce the errors from the Peltier effect. In DC measurements, switching the current direction can help minimizing the temperature gradient established. This pulsed bipolar measurement is in essence a square wave DC measurement but without lock-in data extraction. Any measurement circuit can schematically be described as a capacitor in parallel with a resistor. Hence, using too high frequency or low current in AC resistance measurements can lead to a lowered resistance due to current loss in the capacitor. A comparison and discussion of pulsed DC and AC is found in section 3.1.5.1 from page 51 and on.

A simple experimental criterion is that repeated raw resistance measurements should not show a systematic change, which is usually caused by the Peltier effect. Changes in resistivity in repeated full measurements are often due to Joule heating of the sample (or possibly the Peltier effect when using pulsed unipolar DC measurements). The quality of the contacts is best tested with 2-point I-V curves: Nonlinearity at low voltage indicates poor electrical contact while a curvature at higher currents is most likely caused by the Peltier effect or Joule heating. If I-V sweeps are not possible, 2-point resistance measurements can be used. If AC

measurements are used, the frequency should be chosen sufficiently high to suppress the Peltier effect, usually some tens of hertz. A thermal time constant can be estimated as $\tau = l^2/D_T$, where l is the distance between the voltage contacts and D_T is the thermal diffusivity. The error from the Peltier effect is low for frequencies significantly greater than τ^{-1} . Additionally, to avoid noise in frequency sensitive measurements, the base frequency should be chosen different from the power line frequency and integer multiples or fractions of this.

1.2.4.1 Charge carrier concentration and mobility

Even though the charge carrier concentration is not necessary for calculating zT , it is still very important since all transport properties depend strongly upon it. It provides an important reference frame for characterizing and identifying the cause of changes in transport properties.

In heavily doped semiconductors, such as thermoelectrics, the charge carrier concentration is usually calculated from the Hall coefficient measured on a flat sample in a magnetic field. The Hall voltage V_H is the voltage arising perpendicular to both the field and current direction. The Hall resistance is $R_\perp = V_H/I$ and Hall coefficient $R_H = R_\perp d/B$. d is the sample thickness and B is the perpendicular field strength. Since the current distribution does not have to be uniform, flat and wide samples are usually preferred to samples with square cross sectional area of the same size since these allow the same current and give a high R_\perp due to the low thickness.²⁵ The traditional 5 and 6-point measurement geometries for combined Hall effect and resistivity measurements are shown in Figure 1-6 (b) and (c). A flat sample is less appropriate for resistivity measurements than one with square cross section since the current distribution is less uniform. Combining Hall effect measurements with van der Pauw resistivity reduces this problem and allows a simpler setup with 4 contacts instead of the 5 and 6-point geometries.⁵⁶⁻⁵⁸

Inspired by the free electron model, the Hall carrier concentration is calculated as $n_H = 1/eR_H$ and will be positive for holes and negative for electrons.²⁵ e is the elementary charge. If the resistivity ρ is also known, the Hall mobility can be calculated as $\mu_H = R_H/\rho$. The Hall carrier concentration is related to the true carrier concentration n by $n = r_H n_H$. r_H is the Hall factor which is generally only equal or close to 1 in the free electron model and the limit of high doping levels in a single parabolic band.¹⁵ In other cases, either appropriate modelling using single or multi band models^{16, 23, 30, 64-66} or *ab initio* calculations are necessary for estimating the true carrier concentration.²⁰ In complex band structures or for bipolar samples, r_H can deviate strongly from 1. Despite the ambiguity, the Hall carrier concentration is an excellent way to compare relative carrier concentrations within the same materials system (with similar band structure).

The challenges associated with measuring the Hall coefficient are generally the same as for resistivity measurements. In addition, there is also a resistive offset when the voltage contacts are not placed directly across from each other but are displaced slightly along the current path. The Hall signal is usually very low ($R_{\perp} \approx 63 \mu\Omega$ for $n_H = 10^{20} \text{ cm}^{-3}$, $B = 1 \text{ T}$, and $d = 1 \text{ mm}$) and can be orders of magnitude lower than the voltage offset. For this reason at least two magnetic fields (e.g., on/off or with opposite directions) are necessary to remove all offsets. Especially for metals (or semiconductors with very high doping levels) and intrinsic or bipolar semiconductors the Hall signal can be very low. In intrinsic semiconductors, the resistivity changes rapidly with temperature and hence Joule heating can strongly affect the offset resistance, making Hall effect measurements difficult.

For high mobility samples there is also an offset from the magneto resistance; however, this does not depend on the field orientation and can be subtracted by reversing the field direction rather than switching it on and off.⁵⁶ Alternatively, several points on a $V(B)$ curve including both positive and negative B can be used. In such a curve, magneto resistance would lead to a parabolic curve shape while the Hall effect is linear, allowing separation of the two.

Due to the low signal level, accurate nanovoltmeters and shielded cables are necessary for measuring the Hall coefficient.⁵⁶ All measurement leads should be mechanically fixed to reduce errors from vibrating wires. In sensitive measurements, the signal can be overlaid by an induced voltage arising from leads vibrating in the magnetic field. If this coincides with the frequency in AC measurements, this voltage cannot be eliminated by lock-in techniques.

1.2.5 Thermal conductivity

Many methods exist for measuring thermal conductivity, κ . While the most frequently used method today is flash diffusivity,⁶⁷⁻⁶⁹ traditionally direct methods were employed. Since flash diffusivity also requires measurement of the heat capacity and density these are also covered in this section.

Other methods also exist. One example is the thermal van der Pauw method,⁷⁰ which illustrates the fundamental analogy between thermal and electrical conduction. The Harman method^{8, 9} for directly measuring zT is also frequently used. In this method, zT is calculated from the difference in resistance with very low frequency (with Peltier effect) and high frequency (only resistive part). Both methods fundamentally have the same difficulties as direct thermal conductivity measurements and are hence not discussed individually.

1.2.5.1 Direct measurements

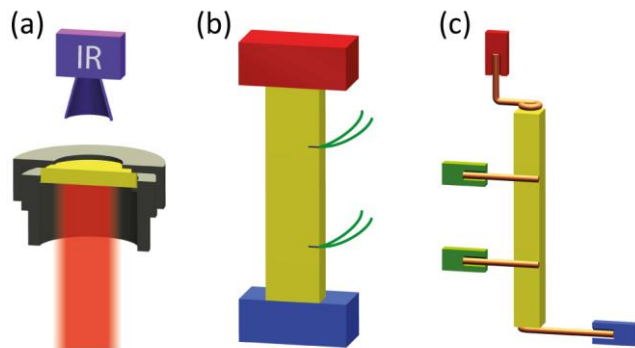


Figure 1-7: Cross sectional geometries for measurements of thermal conductivity and diffusivity. (a) Thermal diffusivity with the laser flash method; (b) thermal conductivity with the steady-state method; (c) thermal conductivity in the PPMS TTO; (d) a real sample used in the TTO option. In (a), a short laser pulse is applied to the bottom of a sample (shown in a sample holder) and the resulting temperature rise on the top is monitored with an IR camera. In (b), a constant power is applied to a heater at the top of a sample (red) while the temperature is monitored along its length with thermocouples inserted in small holes (green wires). The thermal conductivity is calculated when steady-state has been reached. In (c), a heat pulse is applied to a heater shoe (red) at the top of a sample while the temperature response is monitored with thermometers (green) along its length and the thermal conductivity is calculated from the transient. This sample and contact arrangement is also used for Seebeck and resistivity measurements. In (b) and (c) the sample is heat sunk at the bottom (blue). Samples are shown in yellow.

Before the development of the flash diffusivity method,⁶⁹ methods directly using the Fourier equation, $q = -\kappa A \nabla T$, were most common. Here q is the heat flow along the sample, A is the cross sectional area, and ∇T is the temperature gradient. The heat flow needs to be corrected for loss through heater and thermometer wires and radiation. While this works well at low temperatures (below approximately 200 K), the difficulty in accurately correcting for radiation loss limits the accuracy at higher temperatures.⁷¹ In these methods the sample needs to be in good thermal contact with the heater, heat sink, and thermocouples while being thermally insulated from the surroundings. For small temperature differences between the sample and surroundings, the heat loss due to radiation is $q_{rad} = \epsilon A \Delta T T^3$, where ϵ is the emissivity, A is the surface area, T is the temperature, and ΔT the temperature difference between sample and surroundings.⁷² Hence, accurate radiation correction becomes much more important at high temperatures, even for the same ΔT .

A steady-state setup described by Zaitsev *et al.*⁷³ uses a radiation shield thermally anchored to both the heater and heat sink to establish a temperature gradient similar to the gradient in the sample. The space between sample and heat shield is filled with thermally insulating powder to further reduce the radiation loss, whereas heat loss due to conduction through the powder was calibrated. Alekseeva *et al.*⁷⁴ reported thermal conductivity of n-type PbSe using this setup and the result is consistent with the laser flash method around room temperature. However, it is noticeably higher at high temperatures, as seen in Figure 1-8. Nonetheless, comparing an improved steady-state setup with the laser flash method, the results are fairly consistent up to 700 K for n-type PbSe, suggesting the steady-state method as implemented by the Ioffe Institute could be as accurate in this temperature range. This setup will be

described by the Ioffe Institute in a future publication. Figure 1-8 shows a comparison of results from the same PbSe samples including low temperature data obtained from a PPMS, together with Alekseeva's result from a sample with very similar electrical properties.

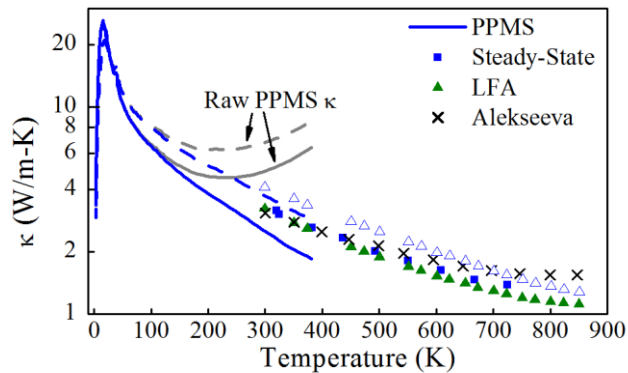


Figure 1-8: Comparison of thermal conductivity between the PPMS (lines), laser flash method (triangles), Ioffe Institute steady-state method (squares) and published data from Reference 74 (black crosses). Two PbSe samples were used for comparison, one $n_H = 2.0 \cdot 10^{19} \text{ cm}^{-3}$ (solid lines and symbols) and $n_H = 4.5 \cdot 10^{19} \text{ cm}^{-3}$ (dashed line and open symbols). The data represented with black crosses are measured on a sample similar to the solid symbols and line. The grey lines marked as “Raw PPMS κ ” are the measured thermal conductivity before correction for radiation loss.

In the PPMS the thermal conductivity is measured by a direct transient method where the increase and decrease in temperature difference between two thermometers is modeled when a square wave heat pulse is applied. The heat loss through the electrical wires is accounted for through the calibration, while the radiation loss is calculated from the sample surface area and emissivity and is subtracted from the measured thermal conductivity. The latter is difficult since the emissivity is usually not known and the surface area is difficult to calculate since leads are attached with thermally conductive adhesive to the surface of the sample, as shown in Figure 1-7 (c) (without the adhesive) and (d). This difficulty is clearly visible from Figure 1-8, where the radiation loss is clearly overestimated. The radiation correction is visible from about 100 K and becomes a significant fraction of the thermal conductivity at approximately 200 K. The emissivity was set to 1 (an overestimate) while the sample surface area without attached leads was used (an underestimate). These errors oppose each other and the resulting correction in this case is an overestimate resulting in an underestimated thermal conductivity.

1.2.5.2 Flash diffusivity

In the flash diffusivity method, the thermal conductivity is calculated as $\kappa = D_T d C_p$ where D_T is thermal diffusivity, d is density, and C_p is the constant pressure heat capacity. In this method, a short heat pulse (often by laser flash) is applied to one side of a thin sample, while the temperature of the other side is monitored continuously. The temperature will rise to a maximum, after which it will decay. In the original method, the time for the temperature to increase to half-maximum, $T_{1/2}$, is used to calculate the thermal diffusivity, $D_T = 1.38d^2/\pi T_{1/2}$ where d is the thickness.⁶⁹ This is derived assuming only axial flow of heat and

no heat loss, and hence the sample thickness should be much smaller than the diameter and $T_{1/2}$ should be kept in the range from a millisecond to no more than a few seconds, but always much larger than the pulse duration. This method is crude but makes for an excellent check for the data quality.

A correction was proposed by Cowan⁷⁵ to account for heat losses on the sample faces, still assuming axial flow. He used the temperature at $T_{1/2}$ and 5 or 10 times $T_{1/2}$ to also estimate the heat loss terms occurring in his revised expression for D_T . Alternatively, Clark and Taylor⁷⁶ proposed a method only using the heating section of the transient. This method also accounts for heat loss at the sides of the sample and finite heat pulse duration. These two methods are usually recommended²⁸ but another method by Cape and Lehman⁷⁷ is also frequently used. In the modern implementation of these methods, the expressions are fitted to the entire transient to obtain better estimates of the heat loss terms and corrections for the pulse width and shape can also be applied.

In the comparison to the steady-state method and PPMS data in Figure 1-8, the laser flash data is believed to be more accurate since it is less susceptible to errors from radiation loss when using these corrections. However, the Ioffe Institute steady-state method does seem to produce good results below 700 K (the highest reported temperature) and may provide a useful method for measuring thermal conductivity, especially when the heat capacity is not easily obtained, such as across phase transitions etc.^{10, 11}

The scatter in thermal diffusivity between different laboratories can be as high as 5% at room temperature and almost 10% at 500 K.²⁸ Much of this can be ascribed to variations in measured thickness. This indicates that a constant and accurately measured thickness is as important for diffusivity measurements as the geometric factor is for resistivity measurements. Another possible source of error is the graphite coating often employed in diffusivity measurements. While this ensures a high emissivity and hence good absorption of the laser pulse and maximum detector signal, too thick coatings or poor adhesion to the sample can cause significant errors, especially for thin samples.

1.2.5.3 Heat capacity

When using flash diffusivity, measurement of the heat capacity is also necessary to obtain thermal conductivity. While some commercial flash diffusivity systems can estimate the heat capacity relative to a standard, this is often inaccurate and can lead to underestimates of thermal conductivity. Instead, differential scanning calorimetry (DSC) is more frequently used. As an example, Toberer *et al.*³¹ measured a room temperature C_p on Ba₈Ga₁₆Ge₃₀ of 0.23 J/gK using a laser flash analysis (LFA) setup. This was later corrected by the same group to 0.30 J/gK using DSC, much closer to the Dulong-Petit value of 0.307 J/gK (see below).²³ In a DSC, the heat capacity is measured relative to a standard, usually sapphire. First a baseline is measured with empty sample holders, then the sample and reference is measured. Often, the baseline is measured again after measuring the sample to check for

changes in baseline during the measurement.²⁸ The reference should be chosen to give a signal close to the measured sample to reduce errors. In the PPMS heat capacity option the heat capacity is measured without a reference. First a baseline is measured with only thermal grease in the sample holder, then the sample is added and measured. The heat capacity is calculated from the heating and cooling transient when applying a heat pulse from the two-tau method.⁷⁸

A scatter in heat capacity of 15% has been observed.²⁸ The primary sources of error are operator error or inexperience, baseline shift and inappropriate reference sample. Heat capacity is the measurement most sensitive to operator error and inexperience.²⁸ Above the Debye temperature and in the absence of phase transitions, C_p normally increases slightly with temperature. The best data quality check is comparison to the Dulong-Petit law which states that the constant volume heat capacity above the Debye temperature is approximately $3k_B$ per atom, or $C_V^{DP} = 3ZN_Ak_B/M$. C_V^{DP} is the Dulong-Petit heat capacity, Z is the number of atoms in the formula unit, k_B the Boltzmann constant, N_A Avogadro's number, and M is the molar mass of one formula unit. C_V is related to C_p by $C_p = C_V^{DP} + 9\alpha^2T/\beta_TD$. α is the linear coefficient of thermal expansion, β_T isothermal compressibility, and D density. The measured C_p above the Debye temperature should be close to or slightly higher than the Dulong-Petit value and increase slowly with temperature. When the correction is applied, the measured and calculated heat capacities usually agree within 2%. When the values disagree more than about 5%, extra verification is recommended before using the measured values. If no DSC is available or measured values are unexplainable, it is recommended to use the Dulong-Petit value.

In the example with Ba₈Ga₁₆Ge₃₀, both LFA and DSC resulted in a heat capacity that was increasing linearly with temperature. However, the C_p estimated from LFA was lower than the $C_V^{DP} = 0.307\text{ J/gK}$ for all temperatures while the DSC values crossed C_V^{DP} slightly above the Debye temperature of approximately 300 K as expected. This is a clear indication that the LFA estimate was unreliable, which the authors also commented upon.

1.2.5.4 Density and thermal expansion

The last property necessary for calculating thermal conductivity is the density. The geometric density is measured by calculating the volume from the geometry and dimension of the sample which works well for regularly shaped samples. Density measured using Archimedes' principle (by immersion in a liquid) can overestimate the density relevant for $\kappa = D_T dC_p$ if the liquid is absorbed in the pores. This can be checked by measuring the weight in air both before and after the measurement in the liquid. These measurements are fairly accurate at room temperature and the density is usually assumed to be independent of temperature.²⁸

The density as well as resistivity, diffusivity, and thermal conductivity are dependent on the sample dimensions and hence thermal expansion. An analysis by Toberer et al.³¹ shows that while each property is affected by thermal expansion, both $\rho\kappa$, Seebeck and zT are unaffected by this. This was derived assuming a temperature independent coefficient of linear thermal expansion; however, it can be extended to any temperature dependence of thermal expansion. When a sample with length l and linear coefficient of thermal expansion α is subjected to a temperature change ΔT the new length is $l' = l(1 + \alpha\Delta T)$ assuming α to be constant in the temperature interval. Generally this can be write this as $l' = lf(T)$ where $f(T)$ is the expansion relative to some temperature, say room temperature, at which the length is l . Hence, when assuming isotropic thermal expansion, the area expands as $A' = A(f(T))^2$ (or $A' = A(1 + 2\alpha\Delta T)$ for constant α and keeping only first order) and the volume as $V' = V(f(T))^3$ (or $V' = V(1 + 3\alpha\Delta T)$ again only keeping the first order). Hence the resistivity $\rho = RA/l$ needs to be corrected as $\rho' = \rho f(T)$ (an analysis of the van der Pauw method gives the same result). Similarly for the thermal diffusivity $D'_T = D_T(f(T))^2$ (the corrections discussed above do not affect this) and density $D' = D(f(T))^{-3}$. Whether measuring thermal conductivity from diffusivity, density and gravimetric heat capacity (unaffected by thermal expansion) or direct methods gives $\kappa' = \kappa(f(T))^{-1}$. Since both $\rho\kappa$ and Seebeck are then unaffected by thermal expansion, so is zT . If the sample has anisotropic thermal expansion and all properties are not measured along the same direction, this is no longer true.

Some commercial LFA software (like that by Netzsch) has the capability to correct for thermal expansion. While this can increase the accuracy of the thermal diffusivity and conductivity, it can decrease the accuracy of zT unless the same expansion correction is applied to all the properties affected by thermal expansion. Since the software from different companies applies this differently, it is important to understand how this is done to avoid introducing errors from the correction. With the software by Netzsch, a file containing the thermal expansion coefficient can be provided to the software. This can be used to set the thermal expansion to 0 at all temperatures.

2 Methods

This chapter introduces the different methods used in this dissertation. The next chapter deals with equipment for Hall effect, resistivity, and Seebeck coefficient measurements and these are hence not introduced here.

2.1 Numerical methods

2.1.1 The Newton-Raphson method

The Newton-Raphson method is a powerful numerical method for solving equations of the form $f(x) = 0$. A reasonable starting guess x_1 for the solution x_0 is required and the method works best if the function is monotonously increasing or decreasing between x_1 and x_0 . The method works by taking a starting guess x_1 and approximating $f(x)$ with a straight line through $f(x_1)$ and slope $f'(x_1)$. The intersection of the straight line and the x-axis is used as the next guess. The distance between this intersection at x_2 and the initial guess is

$$\Delta x = -\frac{f(x)}{f'(x)}. \quad (2-1)$$

This change is added to x_1 to obtain the improved guess x_2 . This is continued to form $x_3, x_4, \dots, x_n, \dots$ and is eventually stopped when $f(x_n) < \delta$, where δ is some fixed threshold.

The method will in most cases not converge if a local minimum or maximum is located between x_0 and x_1 . Regions in $f(x)$ with very low gradient $f'(x)$ (saddle points, deflection tangents etc.) can also make the step size converge and hence cause the algorithm to not converge. If the solution corresponds to a minimum or maximum with a local approximate shape of $f(x_0 + \delta) \propto \pm \delta^2$ (or higher powers) the step size can also converge close to the solution. This is especially a problem if the floating point precision is lower than the desired accuracy of the solution or when this exceeds the accuracy of the calculation of $f(x)$ and $f'(x)$.

The method is best illustrated via an example. A good example is the van der Pauw equation since the solution to this is the basis for much of the dissertation. It will be rewritten in the form

$$f(\rho) = \exp\left(-\frac{\pi d R_A}{\rho}\right) + \exp\left(-\frac{\pi d R_B}{\rho}\right) - 1 = 0. \quad (2-2)$$

R_A and R_B are the two measured resistances, ρ is the resistivity, and d is the sample thickness. In the special case $R_A = R_B \equiv R$ the equation has the explicit solution $\rho = \pi d R / \ln 2$. When $R_A \neq R_B$ the solution hence has to be between $\pi d R_A / \ln 2$ and $\pi d R_B / \ln 2$, which provide good boundaries for the iterative procedure. To solve this equation in the general case, the derivative is needed,

$$f'(\rho) = \frac{\pi d R_A}{\rho^2} \exp\left(-\frac{\pi d R_A}{\rho}\right) + \frac{\pi d R_B}{\rho^2} \exp\left(-\frac{\pi d R_B}{\rho}\right). \quad (2-3)$$

Equation (2-2) is monotonously increasing since $f'(x) > 0$ for all $\rho > 0$ and considering the limits $\rho \rightarrow 0$ and $\rho \rightarrow \infty$ it is seen that $-1 < f(\rho) < 1$. These properties make it a perfect candidate for the Newton-Raphson method.

As an example $dR_A = 1 \text{ m}\Omega \cdot \text{cm}$ and $R_B = 2 \text{ m}\Omega \cdot \text{cm}$ is used. A starting guess of $\rho_1 = \pi d(R_A + R_B)/2\ln 2$ is used. This is the average of the two boundaries for the solution. The iterative procedure is illustrated in Figure 2-1 and follows the procedure

1. Calculate $\Delta\rho = -\frac{f(\rho_n)}{f'(\rho_n)}$.
2. Calculate $\rho_{n+1} = \rho_n + \Delta\rho$.
3. Check if ρ_{n+1} is within the boundaries. If not, set ρ_{n+1} to the average of ρ_n and the appropriate boundary.
4. If $|f(\rho_{n+1})| > \delta$ go to step one; otherwise stop.

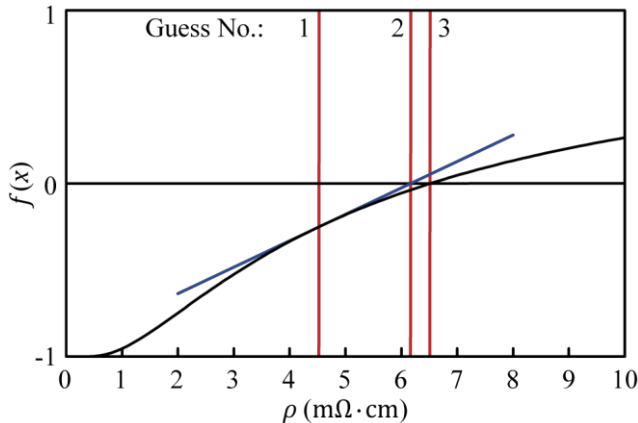


Figure 2-1: Iterative improvement of the starting guess for the solution to the van der Pauw equation. The black line represents $f(\rho)$, the blue line the straight line approximation to the first guess, and the red lines the iterative improvements. After three iterations the procedure converged to the desired accuracy.

The simple convergence criterion above only works since the scale for $f(\rho)$ is always the same. Other criteria can be used, such as $\Delta\rho/\rho < \delta$. This ensures the algorithm will continue until the solution is stable.

The boundary check above ensures the algorithm will almost always converge. Alternatively, the guess could just be reset to the boundary itself instead of the average of the previous guess and the boundary. Since $f'(0) = f'(\infty) = 0$ this can lead to the algorithm not converging when R_A and R_B are very far from each other. If the algorithm does not converge with either boundary checks it can always be made to converge with binary search. In this method, the n'th iteration takes the average of the upper and lower boundary as a guess, ρ_n . If $f(\rho_n) > 0$ the upper boundary is reset to ρ_n otherwise the lower boundary is reset. This can be continued until the boundaries are close enough to try the Newton-Raphson method. If it is

continued sufficiently long it will eventually also reach the right solution. Here, an appropriate criterion is on the distance between the upper and lower boundaries. When the desired accuracy has been reached the average of the two boundaries is the final guess. This has the advantage that it supplies a solution with both an upper and lower boundary. In the Newton-Raphson method the absolute precision is in principle not known unless a more elaborate convergence criterion is used. This could for instance be that $f(\rho \pm \delta)$ have opposite signs for some small δ .

2.1.2 Method of steepest descent (maxima and minima)

If an extremum is sought instead of a solution to $f(x) = 0$, the Newton-Raphson method cannot be used directly. A simple extension is to solve $f'(x) = 0$. This is frequently applied to functions of several variables which is slightly more complicated since $f'(\mathbf{x}) = \nabla f(\mathbf{x}) \equiv \mathbf{d}$ is now a vector. Instead, the method of steepest descent is a natural extension which is discussed briefly here. In this method Equation (2-1) is reformulated as

$$\Delta\mathbf{x} = \frac{k}{|\mathbf{d}|} \mathbf{d}. \quad (2-4)$$

k is some small step size. The sign of k depends on whether a maximum or minimum is sought; k is positive for maxima and negative for minima since \mathbf{d} points along the steepest ascent. When the extremum is approached, the step size needs to be lowered to avoid overshooting the extremum or oscillate about it. This can simply be checked; if $(f(\mathbf{x}_n) - f(\mathbf{x}_n + \Delta\mathbf{x})) / k > 0$ the extremum is overshot and k is lowered and $\Delta\mathbf{x}$ is recalculated. This works for both minima and maxima.

Like with the Newton-Raphson method different kinds of criteria for convergence can be used. The appropriate choice depends on the specific case.

2.1.3 Newton's method (maxima and minima)

While the method of steepest descent is simple and intuitive, it usually requires many iterations before it converges. To remedy this, the full extension of the Newton-Raphson method for $\nabla f(\mathbf{x})$ needs to be used. With one variable, the function $f(x)$ in Equation (2-1) is simply substituted by its slope $f'(x)$ and its slope by its curvature $f''(x)$. For several dimensions, the slope turns into a gradient vector $\nabla f(\mathbf{x})$ and the curvature becomes the Hessian matrix,

$$H = (\nabla \nabla^T) f(\mathbf{x}) = \begin{pmatrix} \frac{\partial^2}{\partial x_1^2} & \dots & \frac{\partial^2}{\partial x_1 \partial x_n} \\ \vdots & \ddots & \vdots \\ \frac{\partial^2}{\partial x_n \partial x_1} & \dots & \frac{\partial^2}{\partial x_n^2} \end{pmatrix} f(\mathbf{x}) \quad (2-5)$$

The improvement of the guess is now calculated as

$$\Delta \mathbf{x} = \gamma H^{-1} \mathbf{d} \quad (2-6)$$

γ determines whether the step is towards a minimum or maximum. If gamma is +1 the step moves towards a maximum, if it is -1 it moves towards a minimum. $|\gamma| = 1$ corresponds to using the full step size. If divergence is a problem, $|\gamma|$ is often lowered to only apply partial steps. If $f(\mathbf{x})$ is quadratic (the Hessian is independent of \mathbf{x}), the extremum is found in the first step. The further $f(\mathbf{x})$ deviates from a quadratic function the more steps are generally required. In such cases it may also be beneficial to lower $|\gamma|$ to avoid divergence or overshooting.

2.2 Physics

2.2.1 Image poles

The method of image poles is a simple and intuitive way to calculate the electrostatic potential using symmetry. The method relies on the uniqueness of a solution to the Laplace equation: If a solution is found which obeys the boundary conditions this is the only one. Hence in some cases the problem can be simplified by reproducing the boundary conditions by other means. For instance, if current is passed between two contacts in a semi-infinite plane, isotropic conductor, the appropriate boundary conditions are: 1) Current cannot flow across the sample edge; 2) the conductor is grounded at infinity. The second condition serves to fix the scale of the potential while the first is the condition that is troublesome. This condition can be reproduced first adding two more current contacts that are mirror images of the first two on the other side of the sample edge. These four contacts are then imagined to reside on an infinite conductor. In this case current will not flow across the line where the edge was before and the solution to the original problem is hence a subset of the solution to the new problem. By uniqueness, this is the only correct solution to the original problem.

The problem is now to find the electrostatic potential in an infinite conductor with four current contacts. The total electrostatic potential is the superposition of the potential from each contact. If a current I is passed into a contact, the current will flow away from this equally in all directions. Hence, at a distance r the current density \mathbf{j} is

$$\mathbf{j} = \frac{I}{2\pi r} \quad (2-7)$$

This relates to the electrostatic potential through

$$\mathbf{j} = -\sigma d\nabla\varphi = -\sigma d \frac{\partial}{\partial r} \varphi(r) \quad (2-8)$$

σ is the conductivity and d is the thickness of the conductor. For the current density in Equation (2-7) this has the solution (in polar coordinates without angular components the gradient operator is unaffected)

$$\varphi(r) = -\frac{I}{2\pi d\sigma} \ln(r) \quad (2-9)$$

Since polar coordinates have been used the Laplace operator is (without the angular dependence) $\nabla^2 = \frac{\partial}{\partial r} \left(r \frac{\partial}{\partial r} \right)$. Hence, Equation (2-9) is a solution to the Laplace equation, $\nabla^2 \varphi(r) = 0$, but does not obey the boundary condition $\varphi(\infty) = 0$. This is remedied when considering pairs of contacts with opposite polarity, which is necessary to pass a current. The positive and negative contacts are at distances r^+ and r^- , respectively. The total electrostatic potential is then the sum of the contributions from the individual contacts

$$\varphi(r^+, r^-) = \frac{I}{2\pi d\sigma} \ln \left(\frac{r^-}{r^+} \right) \quad (2-10)$$

Now, when moving to infinity, $r^+, r^- \rightarrow \infty$, φ approaches 0 and the Laplace equation is still obeyed. This equation is convenient when deriving the van der Pauw equation as well as the extension in Chapter 4.

The above was done for two dimensions but it can easily be extended to three. In that case, the current spreads out spherically and the current density becomes $\mathbf{j} = I/4\pi r^2$ and hence the electrostatic potential from one contact

$$\varphi = \frac{I}{4\pi\sigma r} \frac{1}{r} \quad (2-11)$$

In this case the radial part of the Laplace operator is $\nabla^2 = \frac{1}{r^2} \frac{\partial}{\partial r} \left(r^2 \frac{\partial}{\partial r} \right)$ and hence also Equation (2-11) fulfills the Laplace equation and has the correct limit for $r \rightarrow \infty$.

Using Equation (2-9) or (2-11) the electrostatic potential can be calculated in an infinite two or three dimensional conductor. In Figure 2-2 (a), two current contacts, represented by circles with a dot, are placed on an infinite two-dimensional conductor. In (b) a boundary is added such that the positive contact is on the boundary, represented by a dashed line. To reproduce the boundary condition, no current flowing across the line, an image of the negative pole needs to be added, represented by the circle with a dotted line. Current leaving the positive contact already obeys the boundary condition since it is on the line. However, current will flow equally to both the real and image contact and it is hence necessary to apply a current of $2I$ to keep a current of I running between the two real contacts. In (c) another line through the negative contact is added. Now also the positive contact needs an image and the negative contact a current of $2I$. One image for each contact is not enough to reproduce the boundary conditions. To prevent current from flowing across the boundaries the contact arrangement needs to be completely symmetric across the two boundaries. This is only achieved if an

infinite array of contacts is constructed. Two more boundaries can be added to get a rectangular sample. The same principles apply this time: The current has to be doubled to keep the current between the two real contacts at I and symmetry is needed across all boundaries. This results in an infinite lattice of contacts as depicted in (d). Extending this to three dimensions just follows the same principles again.

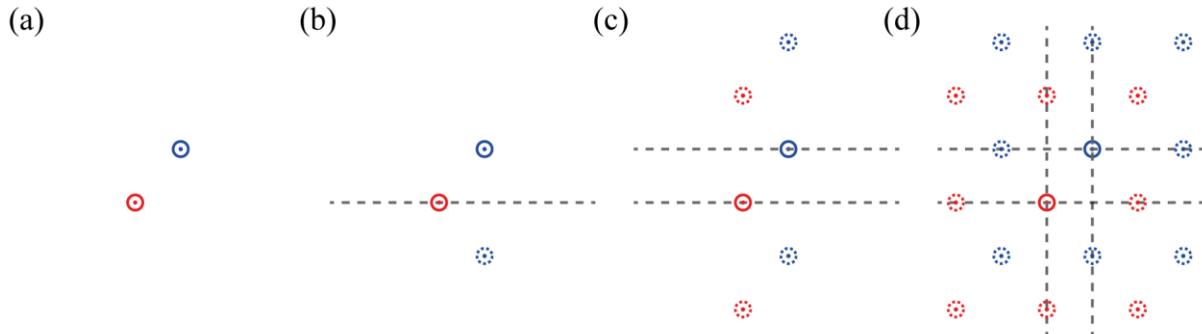


Figure 2-2: Illustration of the image pole method. Starting at (a), which represents two poles on an infinite conductor, one boundary (dashed gray line) is added in (b), two in (c) and all four boundaries of a rectangular sample in (d). Poles are represented with circles with a dot inside, red are positive and blue are negative. The circles of actual poles are full lines while those of image poles are dotted lines.

While this approach works well for rectangular samples, it cannot be used for general shapes: The mirror planes have to be compatible with a three-dimensional lattice. In two dimensions this requires rectangular lattice while in three an orthorhombic lattice is required.

3 Instrumentation

A large part of this project has been to construct two setups for measurement of the Seebeck coefficient, electrical resistivity and Hall effect at elevated temperatures. This chapter contains a description of the two setups constructed. The resistivity and Hall effect measurements have been combined in a single setup utilizing the van der Pauw method^{57, 58} while the Seebeck coefficient is measured in a dedicated setup using the uniaxial 4-point geometry developed by NASA-JPL⁵³ and adapted by Iwanaga *et al.*⁵⁴ This geometry has been further adapted to allow measurements on thin films and bar samples. The advantage of using the van der Pauw method and the uniaxial 4-point geometry is that they both accept flat, arbitrarily shaped discs as samples. Particularly, compacted discs can be measured directly without shaping the sample between measurements. These discs can furthermore be used directly in laser flash analysis⁶⁷⁻⁶⁹ (LFA) for thermal diffusivity measurements thus allowing full characterization on a single sample. Both the thermal diffusivity and Seebeck coefficient are measured cross-plane while the van der Pauw method inherently supplies the in-plane resistivity. When combining LFA with Seebeck and resistivity measurements on bars, the properties are also measured along different directions. However, in this case shaping the sample or using two different samples is necessary. When reshaping the sample, the diffusivity measurements cannot be repeated to check the data after the sample has been cut. When using two samples, there might be differences between the two which ultimately decreases the accuracy of zT . A disadvantage of the present combination of techniques is that an additional measurement run with associated thermal cycle is needed; however, if the sample is not thermally stable the measured zT is inaccurate in either case.

Section 1.2 in the introduction contains a literature review with a discussion of some of the main sources of error and common mistakes in measuring these properties. The two setups are described with this review in mind and the measures taken to avoid the errors are explained. Other difficulties encountered during the construction are also discussed.

3.1 Resistivity and Hall effect

In this section the combined resistivity and Hall effect setup is described. The first section gives the brief introduction to the van der Pauw method necessary to understand the setup. Then the hardware is discussed starting at the sample, moving outward to electrical contacts, sample stage, etc. and ending in a discussion of the electronics and finally measurement procedure. The last subsection contains a brief description of the software. Describing and discussing software in a useful manner is difficult; however, it is briefly included since making a program to automate the measurements is a rather comprehensive task.

Some of the details in this chapter have been published in reference 56. This publication included a description of three different setups: One at NASA-JPL, one at Caltech, and this one at Aarhus University. This paper is intended to be a general discussion of the different

ways setups can be constructed. At the same time it is a review of the sparse literature on setups for measuring the Hall coefficient of heavily doped semiconductors at high temperatures. The review part of the paper is partially included in the introduction and here only the setup at Aarhus University is discussed. Most of the setups in the literature are of little resemblance to this setup and they are not discussed further.

3.1.1 The van der Pauw method

In the van der Pauw method, the resistivity and Hall coefficient are measured on plate like samples⁵⁸, see Figure 3-1. The method differs from the traditional measurement techniques in three important ways: 1) Only one sample dimension is needed: the thickness; 2) Only four sample contacts are needed for measuring both the resistivity and Hall coefficient; 3) Knowledge of the current paths is not needed thus reducing the requirements for sample and contact geometry. Four contacts are made to the top of a thin sample of known thickness at the periphery as shown in the Figure. These have to be point contacts but the internal distances are principally unimportant. Alternatively, the contacts can be line contacts on the sides of the sample (extending between the top and bottom faces but not along the periphery). This increases the maximum acceptable sample thickness⁷⁹. Contacts not fulfilling these requirements are considered imperfect and lead to errors. A final requirement is that the sample may not have any holes.

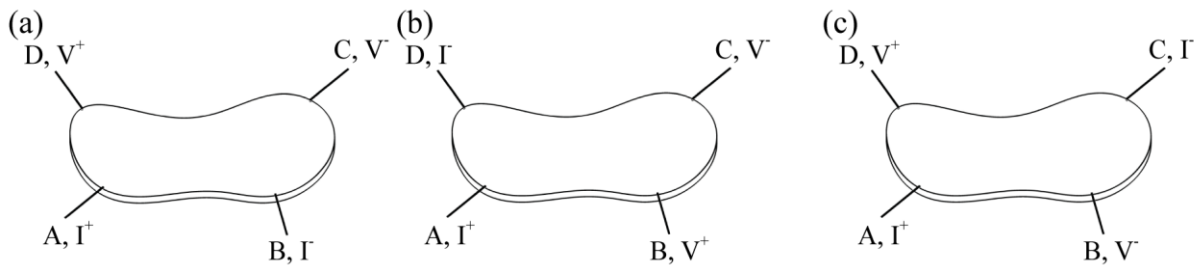


Figure 3-1: The three measurements necessary to perform a full van der Pauw measurement including Hall effect. In the resistivity part, current is applied between two adjacent contacts while the current is measured between the remaining two, (a) and (b). In Hall effect measurements the current is applied along one diagonal while the voltage is measured along the other, (c). For the contact assignment in (c) the positive direction of the magnetic field is upwards. + and – refers to whether the contact is connected to the positive or negative pole, respectively, on the current source (I) and voltmeter (V).

In a resistivity measurement, the current is passed between two adjacent contacts while the voltage is measured between the other two. Referring to Figure 3-1 (a), passing a current from A to B (I_{AB}) and measuring the voltage drop from D to C (V_{DC}) results in the resistance $R_{AB,DC}$. Reversing the polarity of both the current source and voltmeter yields the same resistance. Additionally, interchanging the voltmeter and current source gives the same result (this is due to the theorem of reciprocity of passive multipoles). This means that only two distinct resistances can be measured: $R_A \equiv R_{AB,DC} = R_{BA,CD} = R_{DC,AB} = R_{CD,BA}$ and $R_B \equiv R_{AD,BC} = R_{DA,CB} = R_{BC,AD} = R_{CB,DA}$. $R_{AB,DC}$ is shown in Figure 3-1 panel (a) and $R_{AD,BC}$ in panel (b) as examples. Only one resistance from each group is necessary but this setup measures all four in each group to provide a consistency check and uses the average to reduce

the effect of sample inhomogeneities. The two groups of resistances fulfill the van der Pauw relation⁵⁷

$$\exp\left(-\frac{\pi d R_A}{\rho}\right) + \exp\left(-\frac{\pi d R_B}{\rho}\right) = 1 \quad (3-1)$$

d is the sample thickness. This equation cannot be solved analytically except when $R_A = R_B$, and instead a numerical algorithm is needed. This was developed in section 2.1.1. No derivation of the relation is included for this even though it is straight forward. In Chapter 4 the method will be extended to anisotropic materials and the derivation of Equation (3-1) is included and extended as part of this.

The Hall effect measurement in the van der Pauw method is similar to the above. The geometry is shown in Figure 3-1 (c). Four measurements with current along a diagonal can be made: $R_{AC,DB}$ (shown in the figure), $R_{CA,BD}$, $R_{DB,CA}$, and $R_{BD,AC}$. Any of these can be used but only one is strictly needed. The first two and the last two are equivalent since they represent polarity inversion but the two groups are different. The setup constructed as part of this project measures all four for both positive and negative field directions. The Hall resistance is $R_\perp = \frac{1}{2}(R_{AC,DB}^+ - R_{AC,DB}^-)$ where + and - denotes the field direction. From this the Hall coefficient is calculated as $R_H = R_\perp d / B$ where d is thickness and B is the field strength. Inspired by the free electron model, the Hall carrier concentration is $n_H = 1/R_H e$ where e is the elementary charge. The Hall mobility can be calculated as $\mu_H = 1/nep = R_H/\rho$.

The Hall carrier concentration is only identical to the true carrier concentration n for a free electron gas. In general, the two are related through the Hall factor r_H as $n = r_H n_H$. r_H is a function of both band structure, doping level and scattering mechanism. Hence, carrier concentrations should only be compared between samples within the same material system and band structure. Nevertheless it is an excellent parameter for interpreting the other transport parameters. It is particularly far from the true carrier concentration in metals, intrinsic semiconductors and when bipolar conduction is important (e.g. at high temperatures).

3.1.2 Instrument setup

3.1.2.1 Sample and electrical contacts

The requirements for the sample are that it is thin, of uniform thickness, and without holes. The thickness has to be low since the van der Pauw equation was derived from two-dimensional principles. If the sample is not sufficiently thin to only consider the current distribution in two dimensions this assumption breaks down. By measuring round discs of graphite of varying thickness it has been found that round samples are ‘thin’ when the thickness is less than the radius.⁷⁹ This can be reproduced numerically using the image pole method with square or rectangular samples of varying thickness. This method was introduced in section 2.2.1. This has been done for a 1 by 1 and 1 by 2 sample for thicknesses from 0 to

1. The units are arbitrary. The two resistances measured in the van der Pauw method were calculated this way with the contacts placed on the top face at the corners. This was then used to extract the resistivity from Equation (3-1). The calculated resistivity was then divided by the input resistivity to provide a relative resistivity. This is plotted in Figure 3-1. As can be seen from the figure, the larger sample is less susceptible to errors. For the square the error is about 2% when the thickness is half the shortest side length. This is comparable to the error from the thickness measurement for 1 mm thick samples and hence provides a good rule for the maximum thickness. This is not a harsh requirement since the sample in most cases is much thinner than this. This requirement is similar to the rule for round samples, less than half the diameter, but it is not readily applicable to other sample geometries. Nonetheless, it may be a reasonable assumption that the general rule is either that the thickness should be less than half the shortest distance across a sample or between two contacts. Parallelogram shaped samples are used extensively in Chapter 4 and both of these suggested rules have been carefully followed with good margins in all cases.

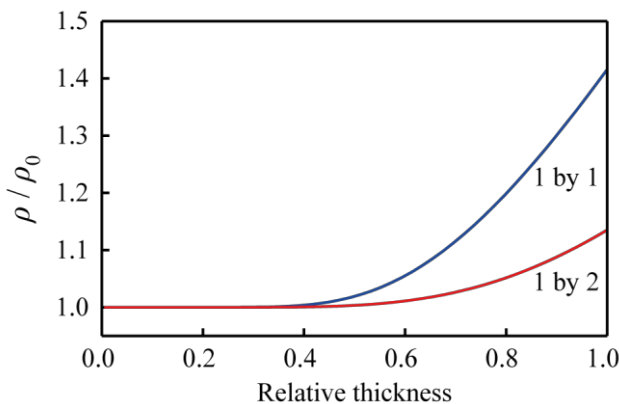


Figure 3-2: Measured relative to correct resistivity, ρ/ρ_0 for a square and rectangular sample. The thickness is relative to the shortest side length. The plots were made by calculating the two resistances used in the van der Pauw method, R_A and R_B , using the three-dimensional image pole method. The contacts were placed on the corners. The resistances were then used to extract the resistivity from the van der Pauw equation, Equation (3-1).

Electrical contacts are made to the sample with spring loaded pressure contacts. In transport property measurements it is common practice to attach leads with conductive adhesives or pastes. This can for instance be silver containing epoxies (or other adhesive), which is extensively used in the PPMS. At elevated temperatures this is not necessarily a feasible solution due to both reactivity of the conductive component and decomposition of the (organic) adhesive component. Silver, for instance, readily diffuses into many solids and reacts with many p-block elements. Additionally, adhesives and pastes can significantly increase the contact area which leads to errors in the van der Pauw method.

The contacts have to be made from a metal that does not react with the samples. Typically, Pt contacts are used due to the high inertness of platinum to oxidation. This is not a good choice for thermoelectrics at high temperatures since Pt readily reacts with many elements often found in thermoelectrics, including Sb, Te, Si, and Ge. For example, PtSb_2 has been investigated as a thermoelectric⁴⁶ and $\text{Ge}_x\text{Si}_{1-x}$ samples have been known to react with and dissolve Pt and Pt/Rh thermocouples. Instead, the refractory metals Nb, Mo, Ta, and W are good alternatives. These rarely participate in solid state reactions. Ta is also frequently used for reaction vessels at temperatures above 1200°C where quartz turns soft. In this setup, Mo has been chosen due to a combination of good elastic properties and inertness. Since springs often lose their elasticity at high temperatures it is difficult to spring load contacts this way. Instead, by pressing thin wire rods of an appropriate thickness against the sample with a screw, the good elastic properties of Mo will ensure the contact is still spring loaded at high temperatures. The design with posts, screws and wire rods is shown in Figure 3-3. Wire rods of 0.5 mm thickness are used and the screws are tightened until the rods starts bending plastically. This ensures an appropriate pressure independent of the relative thermal expansion: The rods will bend plastically or straighten elastically depending on need. If more force is desired, thicker rods can be used; however, 0.5 mm rods have been found to supply sufficient pressure for good contact but not break moderately fragile samples.

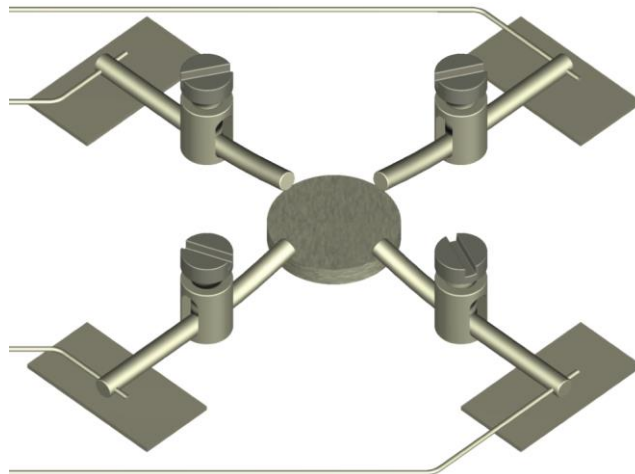


Figure 3-3: Post and screw design for the van der Pauw measurement. The sample is placed in the middle with four Mo wire rods pressed against the edge. The pressure is supplied by screws and posts fixed in the sample holder. The screws are made from stainless steel while the posts are also made from Mo. This ensures the screws and posts will not sinter together. Electrical contact is made to the wire rods by either attaching wires directly to the rods or through a metal pad below the rod.

To supply force, four posts are fixed to the sample holder. Screws are inserted in a hole in the top while the wire rod is inserted through a hole through the side. This allows the wire rod to be pressed downward by the screw. To prevent the screw and post to sinter together and becoming stuck they need to be made from different metals. Since stainless steel screws are cheap and readily available, these are used while the posts have been machined from Mo. Due to the high melting point of Mo it does not sinter at temperatures relevant for thermoelectric measurements. To make electrical contact, a wire is either attached to the wire

rod behind the post, to a metal pad below the post, or the rod is pressed against a spiral of wire. Alternatively, the wire can be attached to the post. Currently, a spiral of Mo wire is used with a thin Mo plate between the wire and wire rod. It was found that attaching the wire directly to the wire rod makes mounting the sample difficult while attaching the wire to a pad by crimping makes it more difficult to change the wiring.

In some cases a metal-semiconductor junction can behave rectifying due to the different energy levels of the conducting electrons in the two materials. This causes non-ohmic contacts. For thermoelectrics, which are heavily doped semiconductors, at high temperatures this is not expected to be a problem. To test this, I-V curves between two contacts can be measured. One contact will be in forward bias while the other will be in backward bias and hence a possible Schottky barrier can be detected. An example of this is shown in Figure 3-4. A Mg₂Si sample was mounted and the I-V curve between two contacts was measured, resulting in the red curve and the data in the insert. No nonlinearity is seen at low voltages indicating no appreciable Schottky barrier. The deviation from linearity (relative to the straight, blue reference line) at high currents and voltages is a result of Joule heating or the Peltier effect. To determine which effect is the cause, the curve can be measured for both increasing and decreasing voltage. If a large hysteresis is seen the primary cause is Joule heating since a temperature increase will cause the resistance to change until the sample has cooled down again. Inserting delays between individual resistance measurements can reduce Joule heating. When these delays have been increased sufficiently for the hysteresis to be gone the remaining non-linearity is most likely caused by the Peltier effect. Since the current density at the contacts is very high the Peltier effect is expected to affect the I-V measurement much more than in a van der Pauw measurement. The sample below would normally be measured with a current in the range 10-100 mA and the Peltier effect is not expected to affect the measurement.

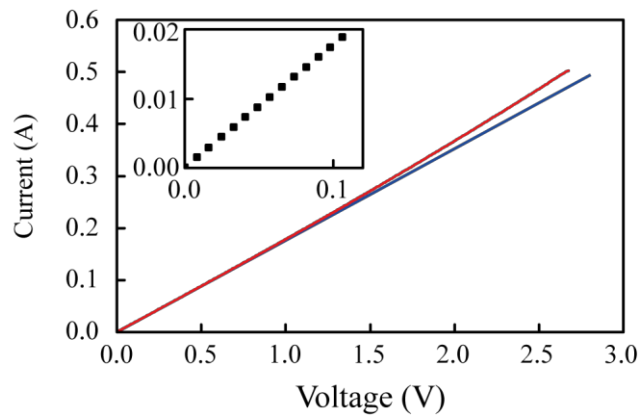


Figure 3-4: Example of I-V curve for Mo contacts. The red line as well as the black squares in the insert is the measured data. The straight, blue line serves as a guide to the eye. The sample is un-doped Mg₂Si with $n_H = -2.8 \cdot 10^{18} \text{ cm}^{-3}$.

Since full I-V curves is time consuming for characterizing the contact quality, two point measurements are used routinely during sample mounting instead. This is done by measuring the resistance from one contact to the three other (in parallel). This allows for identification of up to two bad contacts. If there are three bad contacts, the one good contact cannot be detected. This does not identify non-ohmic contacts but is a very convenient and quick way to check if there is contact to the sample during the mounting procedure.

3.1.2.2 Sample holder

Since the measurement needs to be conducted in a magnetic field the sample holder including heater and insulation has to fit between the poles of an electromagnet. This puts some restrictions on the possible designs and was one of the main reasons for choosing the post and screw design in Figure 3-3. To reduce the space required for the heater this is incorporated into the sample holder, which is shown as a computer rendered illustration in Figure 3-5 without wires and thermocouples. The sample holder is held in place by two Al_2O_3 rods and clamps. By loosening the clamps the sample holder slides freely along the rods to allow for accurate positioning in the electromagnet. The sample is placed in a groove in the middle of the sample holder. The posts are placed in holes in the groove and are held in place by washers on the back of the sample holder (not shown). Thermocouples are inserted in holes directly below the sample. Heaters are embedded in the sample holder between the groove and Al_2O_3 rod on both sides of the groove.

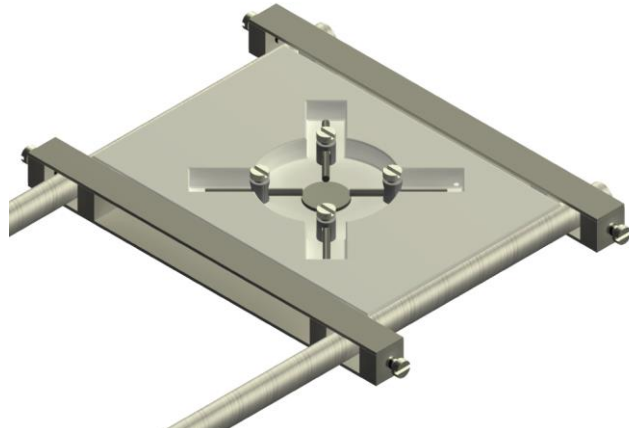


Figure 3-5: Illustration of the sample holder. The sample is mounted in the middle of the groove with the posts and rods. Heaters are embedded in the sample holder between the groove and the long rods on both sides. The rods are used to place the sample holder in the electromagnet. Two clamps hold the sample holder in place. Thermocouples are placed in holes directly under the sample.

The heater is a 1.5 m long 0.5 mm thick nichrome (80% nickel – 20% chromium alloy) wire. The wire is coiled in two sections that are placed along the Al_2O_3 rods. The straight section connects the two coils in the top of the sample holder. Electrical contact is made to the other end of both coils via stainless steel crimps. The crimps are made from small sections (~0.5-1 cm) of 1 mm Swagelok tubing. This design avoids inducing large magnetic fields on the sample. By using DC current instead of AC (or pulsed DC) the heater generates very little

noise in the measurement circuit. Pulsed 48 V DC current was used in the first design; however, this was observed to generate bad measurements. The relative number of bad resistance measurements was higher at high than low temperature, there were more on heating than cooling, and they were not present when the heater was off. By switching to regulated DC current this problem was removed. The magnetic field generated is believed to be much smaller than that from the electromagnet. Furthermore, the coils are perpendicular to the magnetic field and will hence not affect the apparent magnetic field in the Hall measurements.

The sample holder itself is cast in SiC cement (Rescor 770 Castable SiC by Cotronics Corp., New York, USA). A mold has been made from plastic which allows for easy casting of a new sample holder when the heater wire burns out. This has successfully been used to 800°C (higher temperatures have not been tested) but the lifetime of the heaters depends on the temperatures used. Typically, the sample holder needs changing every 6 months.

One problem that has become apparent is that the nicrome wire slowly evaporates when running at high temperatures. This causes the sample holder to become slightly conductive over time. This can cause errors in the resistance measurements but is generally only seen in poorly conducting samples when less than 1 mA is used. It can be identified by comparing equivalent resistance measurements: When interchanging the voltage and current contacts, the resistances are only identical if the circuit is unchanged. If they differ more than the noise level, the sample holder will need to be changed. An example of a perfect circuit is shown in Figure 3-6 (a). The wires are implied to have a resistance but these are not shown. Even if the wire resistances are not identical this causes no errors. In (b) an example of a circuit where current is lost in the leads is shown. Lead resistances are still implied but now one lead has been connected to ground through a large resistor. Usually $R_1 \gg R_2$ and hence this mainly affects high resistance samples. In this case, reversing the polarity of the current source will change the current flowing through the sample while interchanging current source and voltmeter will add an extra current contact. Identifying the bad contact from the raw data in (c) is not possible without further assumptions (the program provides these plots), even when only one contact is bad. When the current source polarity is reversed, it may or may not connect to the positive terminal or it may be a result of interaction with the heater current. The latter is easily tested by disconnecting the heater current, but the first cannot be determined.

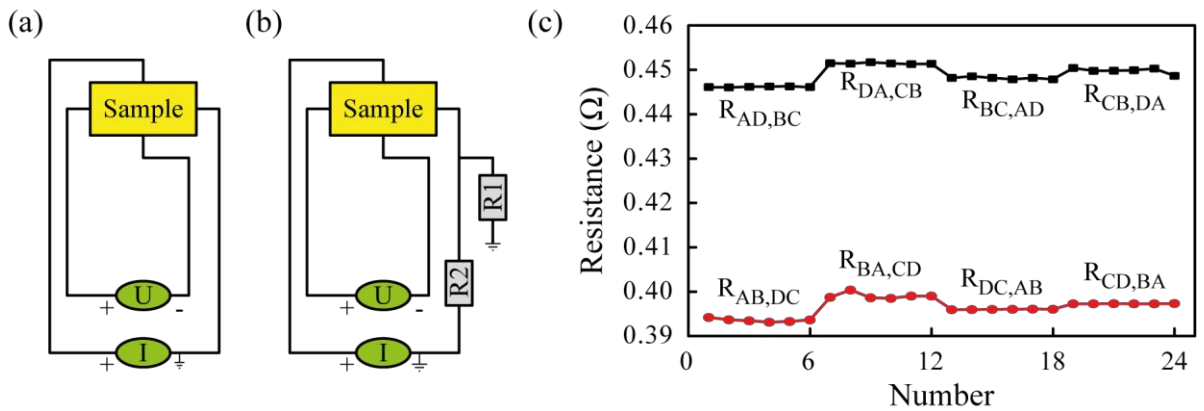


Figure 3-6:Schematics of the measurement circuit and an example of raw data from a high resistance sample. (a) shows a diagram for a perfect circuit; (b) for a circuit with current loss; (c) is an example of a measurement where current is lost. The data in (c) was measured on SnO_2 sample with $\rho = 457 \text{ m}\Omega \cdot \text{cm}$ at 523°C . The effect is present at all temperatures.

To avoid problems with the sample holder turning conductive two approaches are currently being considered. Firstly, casting thin cartridge heaters into the sample holder will be attempted. These are metal coated which may still cause evaporation. Additionally this can significantly decrease the mechanical strength since the cement will be thin where they are placed. A different approach is to machine it from Al_2O_3 and attach the cartridge heaters mechanically. Since machining alumina is difficult this is an expensive approach but will provide greater mechanical strength. Additionally, since it is not porous it does not absorb any evaporated metal as easily except for at the surface, which may be chemically cleaned with acids.

With the ‘hot plate’-like heater design, radiative heat loss from the sample may be a concern. Even with thermocouples imbedded in the sample holder only 2 mm below the sample this may still be a problem. Radiative heat loss follows $q_{rad} = \epsilon A \Delta T^4 \approx \epsilon A T^3 \Delta T$ where ϵ is the emissivity, A is the surface area, $\Delta T = T - T_{ext}$ is the temperature difference between the sample and surroundings, and T is the sample temperature. The second expression only holds for small ΔT (first order Taylor expansion around $\Delta T = 0$). To reduce this, the sample holder is wrapped in insulation. A cloth woven from alumina fibers is wrapped around the sample holder to electrically insulate it. Around this, 0.05 mm stainless steel foil is wrapped as a reflective heat shield. To improve the thermal contact between the sample and sample holder, the bottom of the sample groove is sprayed with boron nitride spray. This increases the contact area and hence increases the thermal transfer. Boron nitride has a high thermal conductivity even at high temperatures while being electrically insulating. To test these measures, a temperature reference has been made by casting a platinum resistance thermometer device (RTD) into SiC cement. Two large crimps are attached to each leg and extend outside the cement. This can be mounted similarly to a regular sample and used to monitor the actual sample temperature, see Figure 3-7.

Figure 3-7 shows a particularly bad example which was measured using a broken sample holder. From panel (b) three problems can be identified: From room temperature to about 350°C the sample temperature is underestimated; The curve has an upward curvature; and there appears to be a hysteresis. The measurement was conducted with a slightly broken sample holder that showed the problems with being conductive discussed above. Since the Pt1000 RTD has a resistance of just above 1000 Ω at room temperature (and almost double that at 500°C) this problem is expected to be significant. The hysteresis and underestimation of the temperature at low temperatures is most likely due to poor thermal contact between the thermocouples and sample holder. The radiation loss is probably the main cause of the upward curvature but since the resistance of the RTD almost doubles and the resistance of the sample holder probably decreases, this may also be a significant contribution. One problem with SiC is that it can be synthesized to be conductive. The data sheet for the SiC cement states no resistivity. It is possible that this problem has not become apparent until a recent upgrade of the current source (discussed later) that allows measurement of these highly resistive samples. Since the sample holder is gray after casting but turns black after a number of runs, the increased conductivity after a number of runs may also be due to the cement sintering and removing the white binder. To test this alumina cement with a resistivity of $>10^9$ Ohm-cm has been ordered and will be compared to the SiC cement.

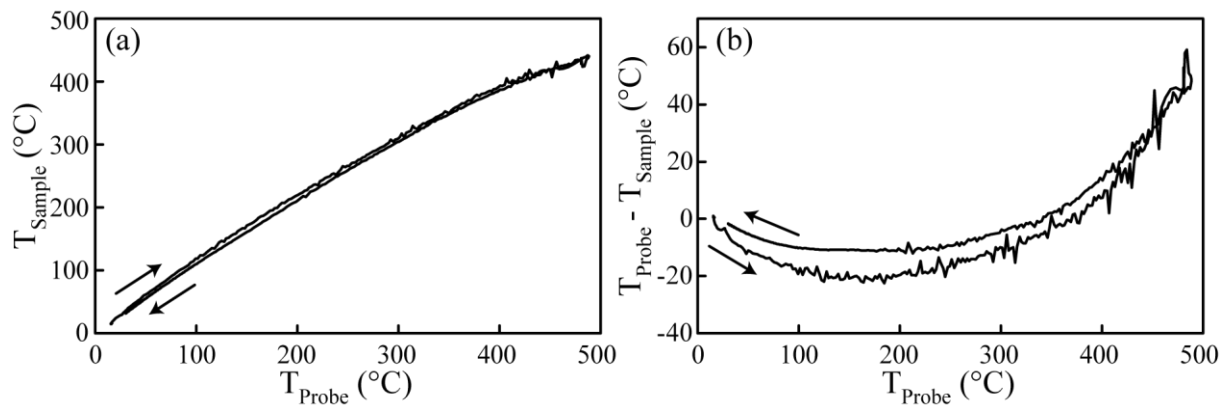


Figure 3-7: Results from measuring a Pt1000 RTD. (a) is the sample versus probe temperature and (b) is the temperature loss from the sample as function of probe temperature.

3.1.3 Sample chamber and magnet

Since the sample chamber has to fit between the poles of an electromagnet, there is very little space for insulation and chamber walls. Due to this constraint vacuum has been chosen as the atmosphere; however, non-oxidizing gasses can also be used with reduced maximum temperature (to prevent the chamber walls from overheating). The space requirement was also the primary reason for choosing this sample holder and contact design.

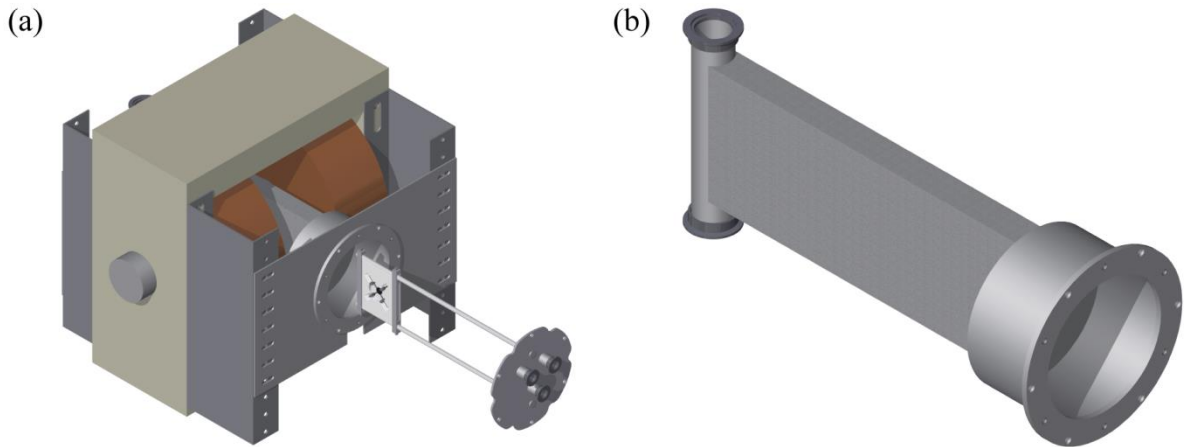


Figure 3-8: Computer rendered illustrations of the setup made from the technical drawings used for building the vacuum chamber. (a) shows the whole setup while (b) shows the main part of the vacuum chamber only. The vacuum chamber is attached to rails on the magnet which allows for vertical positioning and rotation. The sample holder is attached to the end flange which also holds the electrical feedthroughs. All wiring is attached to the end flange and does not need to be detached before the sample holder can be removed from the chamber.

The whole setup without instruments and wires is shown in Figure 3-8 (a). A flat chamber (shown isolated in (b)) is placed between the poles of the electromagnet. This is 30 mm wide and made from 3 mm stainless steel plate, leaving only 24 mm for the sample holder and insulation. Due to the post and screw design, the sample holder can be made as thin as 10 mm, leaving roughly 6 mm for insulation on both sides. If radiative furnace-style heating had been used this would leave even less space. In front of the magnet the chamber has a cylindrical section to accommodate the wires extending from the feedthroughs. The cylindrical section ends with a flange for closing the chamber. Behind the magnet a vertical tube with flanges in both ends. In the bottom a turbo pump is attached, and in the top a t-piece with a valve and pressure gauge is attached. The chamber is attached to support plates in front and back. These are attached to rails on the magnet. The rails can slide vertically on the magnet while the plates can slide sideways on the rail. This allows both rotation and vertical alignment of the chamber. The sample holder is attached to alumina rods as described above. These are attached to the end flange which also has three feedthroughs for heater power, measurement leads, and thermocouples. The end flange mounts on the flange on the cylindrical section of the chamber. Guides make sure the end flange cannot rotate more than 0.5° . This ensures the sample holder is always placed in the same position in the magnetic field.

Two thermocouples are inserted in the sample holder directly under the sample. This provides an estimate of the accuracy of the temperature measurement. They typically agree within 5 K. A third thermocouple is placed inside the chamber close to the feedthroughs. This monitors the temperature of the plastic connectors etc. used for electrical connection to ensure they do not overheat and melt. Two thermocouples are also attached to the outside of the chamber next to the sample holder to prevent the chamber from overheating. Stainless steel is only vacuum tight up to around 200°C where gasses start to diffuse through micro cracks.

The chamber is made from 3 and 6 mm stainless steel plates which are arc welded together. The vertical tube on the back of the chamber is stock 40 mm outer diameter stainless steel tube. This is normally not recommended for vacuum chambers since the cold processed steel and weld areas have micro cracks which can cause gas diffusion. However, the recommended alternative, to machine the chamber from one piece of metal, is excessively expensive. The chamber is air tight to less than 10^{-4} mbar, which is the lower limit of the pirani gauge. The flat sides of the rectangular cross section part are roughly 585 cm^2 which translates to roughly 585 kg of force on both sides. It is hence being squeezed by more than a ton of force. Since it is evenly spread over the entire surface it does not cause the sides to bend inwards visibly. However, it puts large stresses on the weld areas along the sides, which will eventually fail. The rectangular chamber was welded instead of bend in a hope that this would create fewer cracks and hence give a better vacuum. When the chamber fails a replacement is not expensive, only roughly \$1000.

The alignment of the sample holder in the magnetic field is an iterative procedure. First, a Hall probe is used to find the maximum field strength in the chamber between the poles. This serves as a target for further alignment. The probe is then mounted on the sample holder and placed in the chamber. Firstly the sample holder is centered in the magnetic field along the alumina rods. Then the height and rotation are adjusted to maximize the measured magnetic field. Then the sample holder is centered along the alumina rods again, followed by an adjustment of the height and rotation. Finally the sample holder is moved in small steps along the alumina rods to measure the field strength profile. This is shown in Figure 3-9. The posts are separated by 3 cm, which is the maximum sample size. Within this distance the field strength drops by 4% relative to the maximum. Most samples are 12.7 mm hot pressed discs which have a variation in field strength of less than 1% if properly centered. The maximum field strength is 1.24 T. Since the field strength is reversed between measurements the resolution is twice that, 2.48 T. The value used in the program is measured by measuring the change in field strength when the field is reversed. This value does not change between individual measurements and measurement of the field strength is not necessary as part of the measurement procedure.

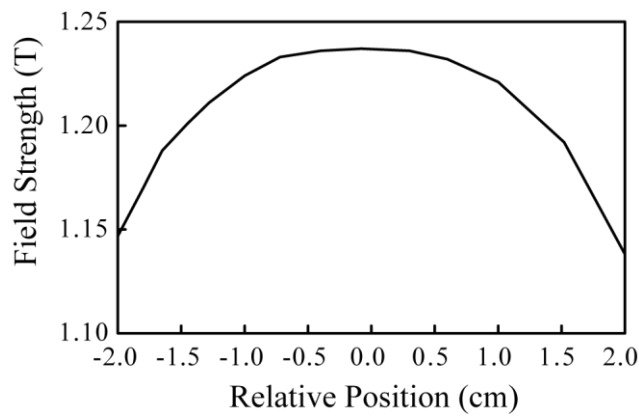


Figure 3-9: Field strength as a function of sample holder position. The position is relative to the maximum field strength, which is the center position.

3.1.4 Electronics and wiring

A block diagram of the whole setup with all instruments and connections is shown in Figure 3-10. All instruments except the vacuum system is controlled by a computer. The instruments connect to the computer through LAN cables. Not all instruments support LXI (LAN Extension for Instrumentation) and these are connected to the computer through appropriate converters, either from GPIB (nanovoltmeter) or RS 485 (Temperature controller). This is not shown in the figure. The polarity switch is controlled by a 12 V signal switch by the free channels on the matrix card. This is also not shown.

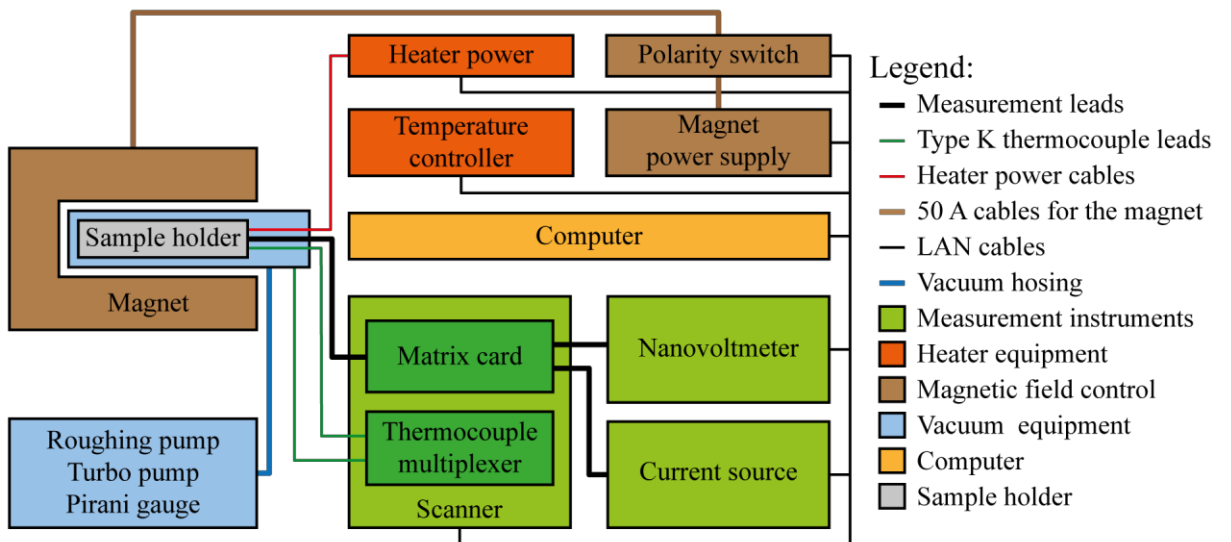


Figure 3-10: Block diagram of the setup. Instruments with related functions are shown in the same color. The scanner has two insertion cards shown in a darker green. The polarity switch for the electromagnet is controlled by a 12 V signal switched by the matrix card. The nanovoltmeter is connected to the computer by a GPIB → LAN converter and the Temperature controller is connected by a RS 485 → LAN converter. These circuits are not shown.

Since electrical contact to the sample is made by molybdenum rods, all measurement wiring inside the vacuum chamber is made from molybdenum. This avoids thermo-electromotive voltages arising from differences in Seebeck coefficient between different metals. These can affect the measurements accuracy. The electrical feedthrough is likewise made from molybdenum. Outside the chamber, the measurement leads are shielded (coaxial) copper wires with the outer lead connected to chassis ground. These are connected to the molybdenum feedthrough with crimp contacts encased in an insulating plastic. This reduces the temperature differences between the different junctions and limits the Seebeck voltage from the junctions. The shielding on the coaxial cables reduces the voltage noise induced by electromagnetic pickup. The extra shielding in a triax cable is as a rule of thumb necessary when less than 1 nA is used. In these cables, the same voltage is applied to the lead and inner shield (from separate sources) to eliminate creep currents. Since that low currents are never used (usually no less than 1 μ A) coaxial cables provide sufficient shielding.

Since any combination of two cables needs to be connected to both the current source and voltmeter, the four leads from the sample are connected to a matrix card which in turn is connected to the voltmeter and current source. This is shown in Figure 3-11. The matrix card has 4 rows by 8 columns and any number of rows and columns can be connected at one time. The voltmeter and current source are connected to the rows while the four leads from the sample are connected to the columns. Each row and column has both a high and low terminal. Since the matrix card provides no way to connect a high to a low terminal, only one set is used. While this is a source of noise, the impedance between the channels ($> 10 G\Omega$) is sufficient not to cause errors with currents of 1 μ A and above. Usually the output voltage from the current source is about 1 V, giving < 0.1 nA creep current between the channels. As discussed above, creep currents through the sample holder is the largest cause of error.

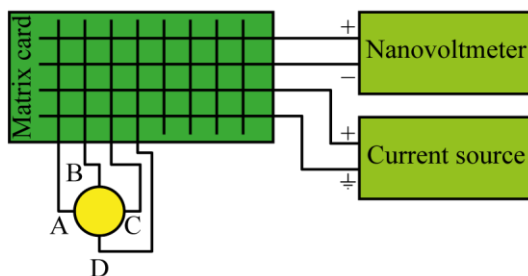


Figure 3-11: Schematic of the measurement circuit. The four sample leads are connected to the columns of a 4 by 8 matrix card while the current source and voltmeter are connected to the rows.

Agilent instruments have been chosen and the different model numbers are: Scanner, 34972A; Matrix, 34904A; Nanovoltmeter, 34420A; Current source, B2961A. The current source is a full four-quadrant source (can both output and dissipate power) with a resolution of 10 fA. This allows accurate programming and measurement of output current. Previously, an E3640A was used. This has a lower current limit of 1 mA, only one polarity and poor programming accuracy. At that time, the circuit in Figure 3-11 also had a section for

measuring the output current. This upgrade resulted in significantly improved performance (see section 3.1.5). The nanovoltmeter has an impedance of more than $10\text{ G}\Omega$ in the voltage range of interest. These impedances are all sufficiently high for measuring very high resistances. The main source of current loss is not in the instruments or wiring but rather the sample holder.

Temperature control is performed by a separate temperature controller. This simplifies software development and maintenance since programming PID (Proportional, Integral, Derivative) control and subsequent tuning is difficult. The PID controller has an auto-tune feature that can be used. The output power is read by the program as a percentage and used to set the output current from a DC current source. The current source and PID controller have no simple way of interfacing electrically and hence the communication is handled by the software. The PID controller is a CN7500 controller from Omega Engineering Ltd. These are cheap and allows for easy setup of temperature profiles. The DC current source is an Agilent N8740A with a maximum output of 120 V and 22 A. This has an excessively high output power but provides a large flexibility in testing and choosing heating methods. It was previously used for an electromagnet and not purchased specifically for the heater setup.

The electromagnet is powered by a Delta Elektronika SM3300 power supply with an output of 55 A and 66 V. This only has an unipolar output and hence a polarity switch is needed. This is made from two large electromechanical relays which are controlled by 240 V AC power. This in turn is controlled by a smaller relay which is controlled by a 12 V DC signal. This is controlled by vacant columns on the matrix card for easy computer control. Charging and discharging of the magnet is done slowly to prevent too high or negative output power. The current source has no power sink and negative output should hence be avoided. This is caused by the power stored in the magnetic field which results in a current in the opposite direction of that used for charging. By slowly discharging the magnet, this power is dissipated as Joule heating in the magnet coils instead of the power supply. When the magnet has been discharged, the relays are switched before it is charged with opposite polarity. This results in highly reproducible field strengths that do not need to be measured during each measurement. The field strength is only calibrated when changes are made to the setup. The output of any current source has a finite noise level. In the case of the magnet power supply this translates into a noise in the magnetic field. This is easily picked up in the measurement circuit and causes a small extra noise when the magnetic field is on. This can be lowered by inserting a large capacitor parallel to the power supply output. However, in this setup it is only detectable for high mobility samples where the general noise is very low.

3.1.5 Measurement procedure and data analysis

The measurement procedure needs to be designed to minimize noise and reduce the errors from the Peltier and Seebeck effect. This is difficult to achieve simultaneously since noise reduction generally require high currents and slow measurements while avoiding the Peltier effect requires the opposite. Hence, even with expensive, high quality instruments the measurement procedure is important to ensure accurate results. The measurement procedure includes everything from finding an appropriate current setting, characterizing the electrical contact to the sample, making individual resistance measurements, and putting all these together. The data analysis then takes the output from this and calculates the final result. This can give new input to the measurement procedure that needs to be taken into account. This can be the number of repetitions when measuring the resistances, integration time in voltage measurements, or a different current. Much of this is automated but some things require human intuition and experience, which is difficult to incorporate into a program. The program can supply an appropriate initial guess for settings that work well in most cases. Especially analyzing the results and changing settings based on this require operator experience and does not follow sufficiently explicit rules to be incorporated into the program. All this is discussed here, both the automation and human intervention.

3.1.5.1 Raw resistance measurements and the Peltier effect

The core of the measurement procedure is the resistance measurement. Each resistance is measured a predetermined number of times. Each measurement corresponds to measuring the voltage and current for both positive and negative output current. The resistance is the change in voltage divided by the change in current. Since the current source needs a finite time for stabilizing the current, a delay t_1 is needed between turning the current on and measuring the voltage and current. The current is measured explicitly to make sure the voltage limit is not reached, which happens when contact is lost or for highly resistive samples. Immediately after the measurement with positive current, the polarity is switched followed by another delay of t_1 and then the measurements. This is repeated in a loop until the desired number of measurements has been reached. This square wave-like current profile reduces the Peltier effect while still keeping it essentially DC (discussed below). The current source needs slightly longer time to estimate the resistance of the circuit and stabilize the current when turned on compared to switching polarity. To avoid bad measurements from this, a negative current is applied followed by a t_1 delay immediately before the actual measurement loop is started.

An alternative to the fixed number of resistance measurements used here is dynamic averaging. This is used in the setup at Caltech described in the joint publication in reference 56. In this method the resistance is measured continually until the standard deviation of the average is below some threshold or a predefined number of measurements have been performed. When this was tested no significant improvement was observed in either the scatter in the results or the measurement time. Instead it was chosen to use a fixed but user

defined number of repetitions. The standard settings in the program, which are almost always used, are 6 repetitions for each of the 8 resistances in the resistivity measurement and 50 repetitions for each of the 4 resistances per field direction in the Hall measurement. This results in a total of 48 resistances for resistivity (24 for each of R_A and R_B) and 400 for Hall effect (200 per field direction, 100 per diagonal per field direction). 50 repetitions are hardly needed for the Hall effect measurement but is chosen to give a large amount of data to make it easier to identify drift in offset resistances.

The resulting resistivity was not observed to change significantly compared to the statistical noise for values of t_1 ranging from 50 – 100 ms. This was tested on a bar shaped sample since the inline configuration of the current and voltage contacts causes a higher Peltier effect than in the van der Pauw method. Below 50 ms high noise levels were observed while the Peltier effect was observed from about 150 ms. The noise in the resulting resistivity was observed to decrease from 50 – 100 ms and hence $t_1 = 100$ ms was chosen. Data to support this is shown later in Figure 3-13. A slight change was observed when changing from unipolar to bipolar current source; especially in samples with high Seebeck coefficient where the Peltier effect is more pronounced. The integration time of the voltage measurement can help decrease the noise but the slower measurement may cause problems with the Peltier effect. The standard integration time in the program is 20 ms which corresponds to one power line cycle. This is always the recommended minimum integration time in DC measurements to suppress noise from the power line frequency. In some cases, especially in Hall effect measurements, the noise levels can be too high to get meaningful results. In this case it can sometimes be necessary to increase the integration time. This is not done automatically by the program and requires the user to inspect the data and make an appropriate compromise between noise rejection and errors from the Peltier effect.

Often it is recommended to use AC measurements to eliminate Peltier effects. With AC measurements an additional problem with wire capacitance arises which makes it difficult to choose a suitable frequency. At low frequencies the Peltier effect is present and the resistance is a function of frequency. At high frequencies the capacitance of the circuit (any measurement circuit can be described as a resistor and a capacitor in parallel) causes the measured resistance to be too low. At intermediate frequencies the resistance is expected to be correct and independent of frequency. However, with the low thermal diffusivity and high Seebeck and Peltier coefficients of thermoelectrics, the high and low frequency regions may overlap. An example is shown in Figure 3-12. The resistance of a bar shaped PbSe sample was measured as a function of frequency in the TTO option of a PPMS. The puck was then connected to the setup described here via the test station provided with the PPMS. This allows the same sample with the exact same attached leads to be connected to both setups and hence eliminates errors from the geometric factor.

For both measurements a current of 0.1 mA was chosen since this only caused minor heating when tested in the PPMS. This is important for accurate comparison of the two. The PPMS dewer was warm at the time this measurement was done and hence both measurements were done at room temperature without temperature control. The measurement at 1 Hz in the PPMS was repeated for 3 hours. This caused a slight increase in temperature (visible by a slight increase in resistance) in the beginning. This data was discarded and only the data measured after the temperature had stabilized is shown. The measurements from the custom setup showed no significant heating but fluctuations in resistance during the time of 90 measurements were visible (each measurement consists of a total of 48 resistance measurements). The sample was n-type PbSe with a room temperature Seebeck coefficient of $-80 \mu\text{V/K}$. Hence the Peltier effect should be sufficiently high to cause errors. Since the Peltier effect always increases the measured resistance,^{80, 81} the resistance is expected to decrease with frequency at low frequencies, become stable, and decrease again at higher frequencies. In Figure 3-12 the resistance is observed to decrease at all frequencies, which makes it difficult to choose an appropriate frequency. The PPMS used for this test is usually operated at a frequency of 89 Hz since this has low noise and usually is sufficient to suppress the Peltier effect. The Peltier effect would increase if the current is increased while the current loss due to wire capacitance would decrease.

In Denmark the power line frequency is 50 Hz. Hence there is a high noise level at 50 Hz as well as integer multiples and fractions of this. Especially odd multiples and fractions are bad since there is an odd number of wavelengths of the measurement signal for each wavelength of the power line voltage. This causes one wavelength of the measurement signal to be shared between the two half-waves of the power line frequency. This appears particularly bad as can be seen from Figure 3-12. There is low noise at 100 and 150 Hz while it is much lower at 100 Hz. Apart from 150 Hz no odd multiples or fractions of 50 Hz were measured.

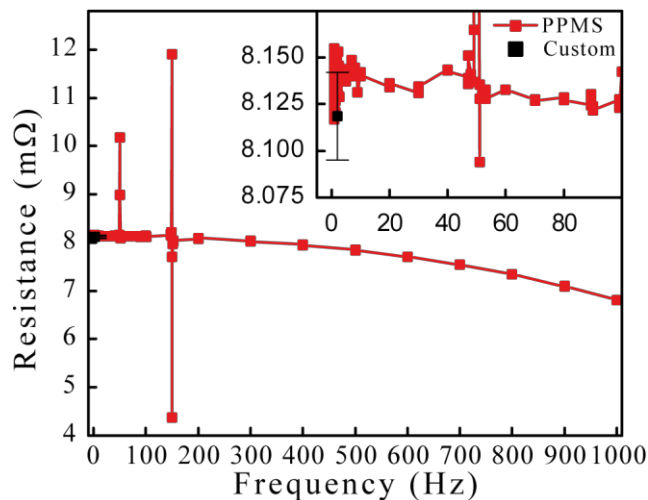


Figure 3-12: Frequency dependence (red) of the resistance of a bar shaped sample compared to pulsed DC measurements (black). The PbSe sample was mounted in a PPMS TTO puck. 0.1 mA was used for all measurements.

The results from the custom setup have been assigned a frequency 2 Hz in the figure. This was estimated from the measurement time but will vary depending on settings. The 90 measurements were averaged and the average with standard deviation is shown in the figure. In the insert it can be seen that the measurement from the custom setup is slightly lower than that from the PPMS at similar frequencies but they largely agree within the noise and standard deviation. The agreement with the 90 Hz measurements is good. Due to the t_1 delay discussed above, the measurement is not affected much by wire capacitances but the Peltier effect can instead be a problem. Since the Peltier effect always increases the measured resistance the Peltier effect can be ruled out as the cause of the lower resistance. To further test this, the resistance has been measured with different currents and t_1 delays. This is shown in Figure 3-13. The black lines were measured with different currents while the red and blue were measured with different delays. When the current or delay is increased the Peltier effect will become more pronounced and hence the resistance is expected to increase. For the current variation the change is less than the changes due to temperature fluctuations. When increasing the delay the resistance increases by about 0.6%. This is caused by the Peltier effect, indicating that $t_1 = 150$ ms is too high.

The resistance in Figure 3-13 is slightly lower than in Figure 3-12 even though they are from the exact same sample. The two measurements were carried out on different days. The temperature in the lab was approximately 25°C when the data in Figure 3-12 was measured, while it was approximately 19°C when the data in Figure 3-13 was measured. This corresponds to a temperature coefficient for the resistivity of about 0.5%/K which is reasonable (for comparison Pt resistance thermometers typically have a temperature coefficient of 0.385%/K). The temperature fluctuations in Figure 3-13 then translates to about 1 K, which is also reasonable.

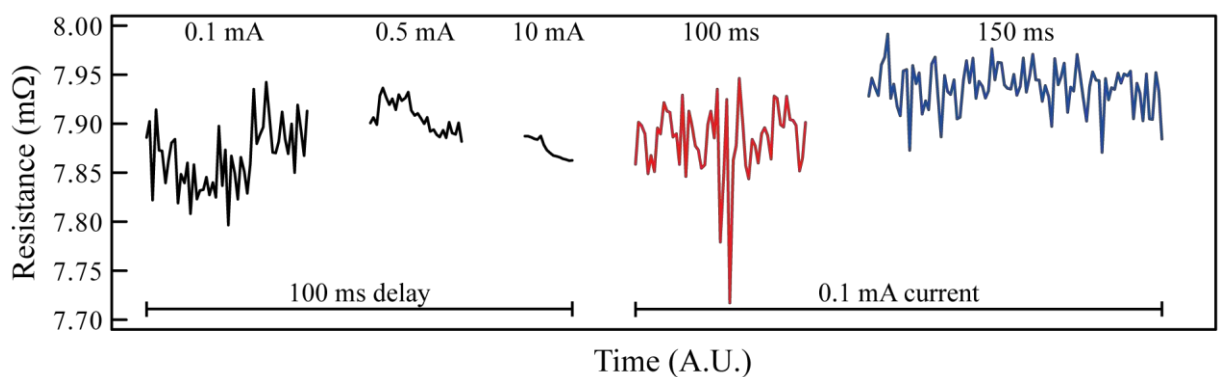


Figure 3-13: Resistance of the PbSe sample for different current and t_1 delay settings. The low changes indicate that the Peltier effect at the most causes minor errors. The gaps between the measurements are the time necessary to change to code and start a new measurement. These gaps are slightly exaggerated (factor 2-3) to better separate the different groups.

From the data comparison above it is concluded that the system provides reliable resistance measurements. The resistance has been compared instead of the resistivity and only one sample with the same leads has been used. This eliminates errors from the geometric factor. This error can be large, as discussed in Chapter 1 and reference 27. The resistivity and Hall effect measurements will be compared to other setups later to get an estimate of the overall accuracy.

A good and somewhat surprising example of the importance of proper use of the individual instruments when building setups is the matrix card. In the early period of operation it was observed that the first few resistance measurements in a series were always off compared to the later measurements. This systematic change could be reduced by inserting long delays after closing (connecting) the appropriate matrix points and commencing the repeated resistance measurements. It appeared similar to the discharge of a capacitor.

Several tests were done to improve this. The final solution was to always leave the sample leads connected to the instruments instead of opening (disconnecting) all matrix points. Between groups of repeated resistance measurements one row and one column of the matrix card is left closed. This shorts every instrument lead to all sample leads and all rows and columns of the matrix card and prevents capacitive buildup. Before the measurement starts, the additional needed matrix points are closed and then the unneeded ones opened. This is followed by a short delay of 250 ms before the resistance measurement is started. This eliminated the capacitive discharge completely and decreases the noise in the resistivity and Hall effect measurements substantially. This is illustrated in Figure 3-14. Both the scatter in the results and the error bars (discussed in section 3.1.5.4) are substantially decreased. Especially in the Hall effect measurement, illustrated by the Hall carrier concentration n_H , the noise reduction is substantial. The Hall resistance is much smaller than the resistances in the resistivity measurement and is hence more susceptible to the capacitive discharge. The current used caused a slight increase in temperature, as can be seen from the figure; however this only adds a slight error to the temperature of the measurement.

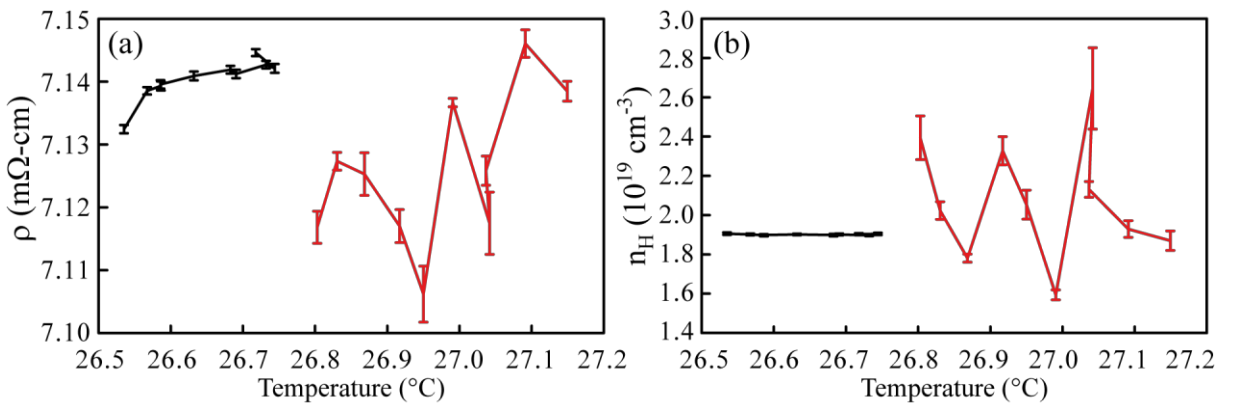


Figure 3-14: Reduction in measurement noise when changing the matrix card control. The black line was measured with suppression of the capacitive buildup while the red line was measured with all matrix points open between measurement of the different resistance groups. The same current was used for both measurements, 150 mA. The temperature is used as the x-axis since this appears to be slightly increasing during the test.

3.1.5.2 Lead resistance and current selection

Ensuring good electrical contact to the sample and selecting a current appropriate for the specific sample is very important to ensure good data quality. The system provides a help for both.

The contact quality is best checked with I-V curves, and the system can perform these measurements, but they are very time consuming. Instead the program performs two-point measurements by passing a current from one contact to the three others and measuring the voltage across the same circuit. With the usual terminology this corresponds to the resistances $R_{A(BCD),A(BCD)}$, $R_{B(ACD),B(ACD)}$, $R_{C(ABD),C(ABD)}$, and $R_{D(ABC),D(ABC)}$. In this way the system can easily and quickly identify up to 2 bad contacts. If there are 3 or 4 they will all appear bad. Generally, the aim is to make sure all four resistances are within the same order of magnitude and as low as possible. The value will depend on the resistance through the sample and should seem meaningful when compared to the measured resistivity. As part of this crude estimates of R_A and R_B are also measured by only measuring one resistance in each group three times. From this the ratio R_A/R_B is calculated. This has been termed the van der Pauw ratio since the solution to the van der Pauw equation can be shown to be R_A multiplied by some function of this ratio.⁵⁸ This is mainly used to ensure the contacts have been properly aligned: If it deviates from 1 the contacts are not entirely symmetric and there will be an offset in the Hall effect measurement from the resistance of the sample. This is most important when the resistivity is strongly dependent on temperature (intrinsic samples, phase transitions, etc.) since in this case the offset can change noticeably during a Hall effect measurement. It also helps to reduce the voltage level. Since the noise in a voltage measurement is a constant plus a percentage of the measurement, reducing the voltage levels can reduce the noise in the resistance. Even if the van der Pauw ratio only deviates slightly from 1, the offset due to the sample resistance can be much greater than the Hall resistance. If the van der Pauw ratio is greater than 1, R_A needs to be reduced. This can be done by moving the A and B or C and D contacts closer together, or further away if the ratio is smaller than 1.

When mounting the sample, the goal is then to get the lead resistances low and of equal magnitude while trying to get the van der Pauw ratio close to 1. This has proven to be a great help when mounting the sample. With experience, this can take as little as 10 minutes, including setting up the program to run a measurement.

Using the van der Pauw ratio to place the contacts is only possible when other considerations do not outweigh it. For example, for rectangular samples the contacts should always be placed on the corners to reduce errors.^{22, 57} In Chapter 4 methods for extracting information on anisotropic samples will be discussed. In this case the information of the anisotropy is contained in the relation between the sample geometry and van der Pauw ratio, which cannot be used for placing the contacts.

From the van der Pauw equation it is seen that the size of R_A and R_B only depends on the sample thickness and resistivity. The van der Pauw ratio, on the other hand, will depend on the sample shape and contact placement. Since the contacts are placed to give a van der Pauw ratio of 1 the thickness and resistivity determines the measured resistances completely. This is also true for two-point resistances (which corresponds to $R_A/R_B \rightarrow 0$ or ∞). The two point resistance between the current contacts together with the applied current determines the power dissipated in the sample. Since the goal is to maximize the signal level while minimizing the heating of the sample, the two-point resistance provides a way to select an appropriate current. Since this depends on the contact and lead resistance this is not easily measured accurately. Instead, since both the two and four point resistances depend only on the resistivity and sample thickness, the van der Pauw resistances R_A and R_B are used. These are measured and the current is iteratively adjusted to give a voltage reading of 1 mV (this can be adjusted by the user). This does not adjust the power dissipation in the sample directly but works surprisingly well for most samples. Since the power output is $P = R \cdot I^2$ but the current is selected linearly based on R , this will result in too high heating rates when high currents (typically above 500 mA) are selected. Likewise, higher currents can be used for high resistance samples without heating the sample significantly. In most cases, however, the current found from this works sufficiently well for thermoelectrics or at least provides a good starting point for further improvement. The user inspects the quality of the raw data for one or two measurements of both resistivity and Hall effect and adjusts from the automatically determined value afterwards. Especially the Hall effect data will sometimes need higher current to get sufficiently low noise levels.

This current adaption can also be done as part of the measurement procedure. When measuring intrinsic or lightly doped semiconductors, the resistivity can drop several orders of magnitude over the course of a measurement. In this case on-the-fly current adaption can significantly improve the data quality. For these samples the Hall effect data is rarely useful (or physically meaningful) and the current only needs to be adapted to give good resistivity data, which the adaption method is designed to do. For metallic samples (defined by the

resistivity increasing linearly with temperature) this is not necessary and usually the current is set to a fixed value. Since the carrier concentration is usually approximately independent of temperature in this kind of sample, a current giving good Hall effect data at room temperature will also work well at higher temperatures. Hence a fixed current works well unless the resistivity increases sufficiently to cause joule heating or the Peltier coefficient increases too much.

3.1.5.3 Full measurements

When starting the measurement it is the responsibility of the user that the sample holder has been inserted in the electromagnet in the correct orientation and that the chamber has been properly evacuated. No check is performed for any of this. When the measurement routine starts, firstly the matrix points are opened as described above. This is also done when the program connects to the instrument but is repeated to make sure the matrix is set up correctly. Afterwards the program is prepared to receive and plot the data and the temperature control is initiated, if necessary. Then a loop is entered where data points are continuously measured until the temperature profile has ended or the user chooses to abort. After each measurement the control thermocouples for the chamber described in section 3.1.3 are measured and if they have overheated the measurement is stopped and the temperature control is turned off. This safety feature can be turned on or off by the user if necessary.

Each measurement point consists of measuring the resistivity and then the Hall data. The data analysis is performed after each of these two measurements. The program has the ability to make a guess of an appropriate current based on the resistivity measurement. If the user chooses to use this a new current is calculated after the measurements. To make sure electrical contact to the sample has not been lost, the lead resistance is also measured after every few measurements. This is also discussed below.

The resistivity measurement starts by measuring the temperature of the sample holder after which the instrument setup takes place. This includes integration times and channel selection on the voltmeter and channel on the current source. After this a delay of $3 \cdot t_2$ (t_2 is a constant used in the program) is used to thermally equilibrate the sample. This is to remove thermal gradients established by the current. Then $R_{AB,DC}$ and $R_{BA,CD}$ are measured followed by a single t_2 delay to remove the thermal gradients. Then $R_{DC,AB}$ and $R_{CD,BA}$ are measured. These corresponds to all resistance measurements in R_A . After this another long $3 \cdot t_2$ delay is used to reduce thermal gradients. The longer $3 \cdot t_2$ delays are used when the pairing of contacts changes. In this case a former current contact is paired with a former voltage contact. Due to the much higher current density at the current contacts these may be locally warmer than the voltage contacts. To remove voltage drifts from this temperature difference decaying the longer delay is used. This is only necessary when the pairing changes; when the voltage and current contacts are interchanged a single t_2 delay is sufficient. No delay is needed when reversing the polarity. R_B is measured according to the same approach: $R_{AD,BC}$, $R_{DA,CB}$, single

t_2 delay, $R_{BC,AD}$, $R_{CB,DA}$. After these measurements the temperature is measured again and the data is treated to give the resistivity. The measurement is assigned the average of the two temperatures. The t_2 time is set in the program to be 5 s, but it can be changed by the user. Values of 0, 1, 2, 5, 10, and 15 s can be selected.

The Hall effect measurement follows that of the resistivity closely. First a temperature measurement, then the instruments are set up. Then the magnetic field is turned on in the positive direction followed by a 2 s delay to stabilize the field, which was found to give better data. This is sufficient delay to remove thermal gradients after the resistivity measurement. Then $R_{AC,BD}^+$ and $R_{CA,DB}^+$ are measured followed by a t_2 delay. Then the other diagonal is measured, $R_{BD,CA}^+$ and $R_{DB,AC}^+$. After this the field polarity is changed followed by another 2 s delay. Then the same four resistances are measured in the same way but with negative field: $R_{AC,BD}^-$, $R_{CA,DB}^-$, t_2 delay, $R_{BD,CA}^-$, $R_{DB,AC}^-$. Then the field is turned off followed by a 2 s delay, the temperature is measured and the data is analyzed. The resistivity and Hall effect measurements are seen as a single data point. They are both assigned the same temperature, the average of the four measured. The difference between the highest and lowest temperature is also recorded and is used to estimate the temperature drift during the measurement.

3.1.5.4 Data analysis

The output from the measurements is a large number of resistances. These need to be appropriately averaged and turned into the desired quantities and standard deviations of these. For resistivity, all resistances in all four groups comprising each of R_A and R_B are averaged together and the standard deviation is calculated. In the Hall effect measurement, the Hall resistance is the difference between $R_{MN,OP}^+$ and $R_{MN,OP}^-$, where M, N, O, and P are the A, B, C, or D contacts. This difference is calculated point wise and the average of these differences is calculated. This way only one average is calculated instead of calculating an average for each diagonal and both directions (4 in total) which then have to be averaged. After this the standard deviation is calculated.

Due to the sample holder turning slightly conductive, noise can enter from the heater circuit when the current is changed through this. If this change happens between the resistance measurement with positive and negative current the resistance will be wrong. This appears as spikes in the raw resistance plots. Since these do not constitute a Gaussian noise, they need to be removed from the raw data. In practice this is done by removing all data points further from the average than some threshold. If a threshold of two standard deviations is chosen, the resistivity was found to have few bad data points. If no spikes occur in the raw data, this threshold will not remove many data points. After these have been removed a new average is calculated but the standard deviation is not recalculated. This serves as an indication that this should be examined further. After this the resistivity, Hall coefficient, and Hall carrier concentration and mobility are calculated. The standard deviations of the resistance averages are used to calculate the standard deviation of each of these.

After the data has been analyzed the program provides the opportunity to plot the raw data. This is useful for inspecting the data and deciding whether the current suggested by the program is appropriate or there is something wrong with the measurement. It also displays the number of data points that have been removed from each group. This should correspond to the number of visibly bad data points.

3.1.6 Software

The software necessary to run the measurements consists of roughly 16,000 lines of code. Writing, testing, and debugging this amount of code is a slow and cumbersome task and it deserves a short discussion even though this is not the main focus. Much of this code has been rewritten or at least changed many times and it is estimated that 30-50,000 lines of code have been written in total. Due to previous personal programming experience, an object oriented type of Pascal was chosen as the language. Today, a better solution would be to use Python which is growing fast in the scientific community and is very easy to learn. The program is written for Linux which provides an excellent platform for both coding and running scientific equipment reliably.

Since the program is used to control the measurements, I/O operations is a large part of the program. To simplify the low level I/O programming, LAN connections were chosen for all instruments. Instead of programming specific protocols for GPIB or other serial communication, converters were bought for these. This allows easy I/O programming using Sockets over the TCP/IP protocols. This is a good choice since the LAN based LXI standard is continually becoming more wide spread. Even though USB connections are easy to use, the coding is difficult and is most useful when few instruments need to be connected to a computer. The LXI standard can in principle handle as many instruments as there are IP addresses with only one physical connection to the computer.

The main function of the program is I/O to instruments, which blocks the program while the operation takes place. This means the user interface cannot be used as long as a measurement is running. For this reason the program is split in two threads which run independently. One thread handles the user interface while the other handles instrument I/O, data treatment and writing data files. The two threads communicate through shared variables, which is safe in this implementation of Pascal. Data is stored in a large, shared data structure to allow on the go plotting of raw data. This has proven to work reasonably well but makes debugging the program difficult. For this reason it can be run as a single thread when debugging.

The program runs reliably now and rarely crashes unless something happens to an instrument that makes it loose connection. This probably happens in 1 in 50 measurement runs, which is acceptable. Other errors, such as loss of contact, happen more frequently. As a rule of thumb, there is one bug per 10 lines of code for phone apps, 1 in 100 for computer programs, 1 in 1000 in operating systems, and as little as 1 in 100000 in the code for space craft. This program is expected to underperform even compared to phone apps in this respect. The goal

is not correct code but a stable program that carries out the measurements reliably and does the calculations correctly. This goal has been achieved, the remaining few bugs per 10 lines of code are of little concern.

3.1.7 Comparison of results and conclusion

Figure 3-15 shows a comparison of measurement results for two samples. The PbSe sample (measured at Caltech and Aarhus) is an ‘easy’ high mobility, low carrier concentration sample while the Mg₂Si sample (Measured at DLR and Aarhus) is more difficult with lower mobility and a large change in Hall carrier concentration due to intrinsic excitation.

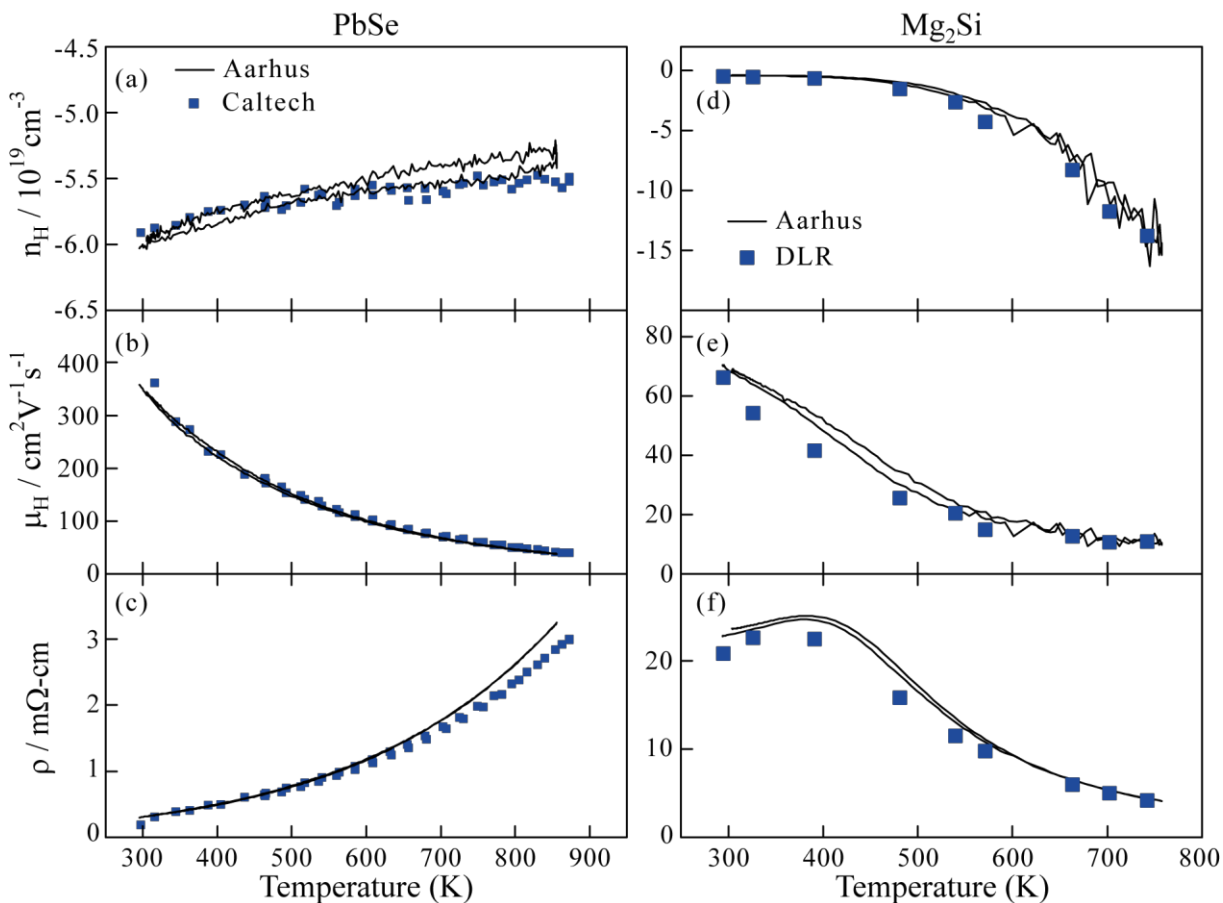


Figure 3-15: Comparison of results for two materials measured at Aarhus and either Caltech or DLR. The PbSe data are courtesy of Heng Wang from Jeff Snyder’s group at Caltech. The Mg₂Si data are courtesy of Johannes de Boor from Eckhard Müller’s group at the German Aerospace Centre, DLR.

The Caltech setup is in many aspects similar to the one described here: It uses the post-and-screw contact design with a ‘hot plate’-like heater and bipolar pulsed DC measurements. The measurement procedure, data analysis, and electronics are different. Furthermore, the heat shield is a single layer of aluminum. From panel (a) to (c) it is seen that the measurements agree reasonably well, especially at low temperatures. The Hall carrier concentration from Aarhus has a slight hysteresis. This is partially due to the change in resistivity with temperature affecting the measured Hall signal; however the hysteresis is very low and comparable to the noise level. The resistivity data has no hysteresis but deviates from that

from Caltech at higher temperatures. This can be caused either the Aarhus setup overestimating or the Caltech setup underestimating the temperature. Considering Figure 3-7 and accompanying discussion, the first seems unlikely while the latter is more likely with the difference in heat shielding. An alternative cause is the Peltier effect, which will be discussed below. The mobility is also shown since this is independent of sample thickness. This agrees between the two systems as expected when both resistivity and Hall carrier concentration agrees.

The DLR setup differs more from the Aarhus setup than does the one at Caltech. It is also a van der Pauw measurement, but it uses radiative heating and AC measurements. The temperature is stabilized before each measurement, contrary to the Aarhus setup which measures during ramping. Additionally, the Hall resistance is not extracted from two resistances with different field strengths but from many data points of resistance vs. temperature. The setup at DLR is still under development and initial testing and this comparison was done as a verification of the DLR setup. The Hall effect data agrees reasonably well. The deviation is more pronounced on logarithmic scale; while the measurement agrees at low and high temperatures the deviation is stronger at intermediate temperatures. The DLR Hall carrier concentration is always higher (note the negative scale corresponding to n-type samples) than that from Aarhus. The resistivity data also agrees at high and low temperatures while it deviates more at intermediate temperatures. It is always lower than the resistivity from the Aarhus setup. This could be due to the thickness (too low at DLR or too high at Aarhus); however the mobility does not agree any better and hence this is unlikely to be the main cause. Instead, the strongest deviation corresponds to the region with the highest Seebeck coefficient (just before the onset of bipolar conduction) and hence Peltier effect. The Peltier effect is not expected to affect the Hall measurements much since it is field independent; hence, the Peltier effect alone is unlikely to be the main cause.

Both comparisons in Figure 3-15 were done before the upgrade to the bipolar current source. This means that the resistance measurements were done by switching the current on and off repeatedly. This is expected to cause a larger error from the Peltier effect since the current is only passed in one direction, resulting in a temperature gradient along the sample. The Peltier effect always leads to an overestimated resistance with $\Delta R \propto TS^2$ (assuming the leads to have zero Seebeck coefficient).^{80, 81} This may also explain the deviation in resistivity in the comparison to the Caltech setup. The PbSe data has a linearly increasing Seebeck causing the Aarhus measurement to diverge from the Caltech measurements. For Mg₂Si the deviation is larger at temperatures below the onset of bipolar conduction where the Seebeck coefficient is highest; however, due to the deviation in Hall carrier concentration this is not expected to be the main cause. In the comparison with the Caltech setup the deviation is believed to be a combination of the Peltier effect and temperature error. The comparison with DLR needs to be further analyzed before a conclusion can be made. This is the target of a future publication.

From the discussion in this section it is concluded that the setup is reliable, especially after the current source upgrade. Reducing the Peltier effect was one of the main reasons for the upgrade to a bipolar current source. From the comparison to the PPMS the system is believed to remove the Peltier effect sufficiently. Since the upgrade was done recently no new comparison of overall results have yet been made. This will be done when the problem with the sample holder becoming conductive has been resolved.

3.2 Seebeck

This section describes the Seebeck setup. In the literature the main cause of error has been identified as the cold finger effect which is particularly pronounced when the thermal contact resistance between sample and thermocouple is high.^{47, 48, 52} The setup is constructed with the uniaxial 4-point geometry^{1, 54} which is intended to reduce the cold finger effect. Due to the importance of this effect, it is extensively discussed throughout this section. Seebeck measurements are continually developed and improved. To allow for upgrades as the measurements develop, the actual measurement setup can be easily changed. This also allows for construction of measurement setups to accommodate other sample types. For instance, a thin film setup has been developed which adapts some of the advantages of the uniaxial geometry while still measuring the Seebeck coefficient in-plane. Currently, an upgrade to the heaters is being implemented to remedy some of the problems which have been identified during operation. This will all be discussed in this section.

The thermal gradients in the setup, which are the cause of most of the errors, cannot easily be modelled using finite element methods. This is due to the combination of imperfect thermal contact and a combination of radiative and conductive thermal transfers. While the effect of one of these can be modelled, it is difficult to make an accurate model which quantifies the combined effect. Since all of these parameters change between measurements, such a model is never general. This is probably one of the main causes for the relatively slow development of Seebeck metrology: All effects will have to be studied experimentally. The lack of appropriate high temperature standard reference materials also makes it difficult to estimate absolute accuracy and hence to distinguish a good measurement from a bad measurement.

3.2.1 Instrument geometry

A diagram of the instrument is shown in Figure 3-16 (a). The sample is placed between two independently controlled heater blocks inside a vacuum chamber. A heat shield is placed around the heater blocks, illustrated by the two black lines. This is made from three layers of 0.05 mm stainless steel foil. The heaters are attached to a top and bottom base plate and are pressed against the sample by springs with adjustable force. The measurement thermocouples are inserted through holes through the center of the heater blocks and are also spring loaded. A considerably larger force can be used on the thermocouples without breaking, bending, or shifting the sample than can be used in the off-axis geometry, see section 1.2.3. This and the fact that they are inserted through the heaters are believed to be the main advantages. Two

type K thermocouples for temperature control are inserted in each heater (only one per heater block is shown in the figure for simplicity).

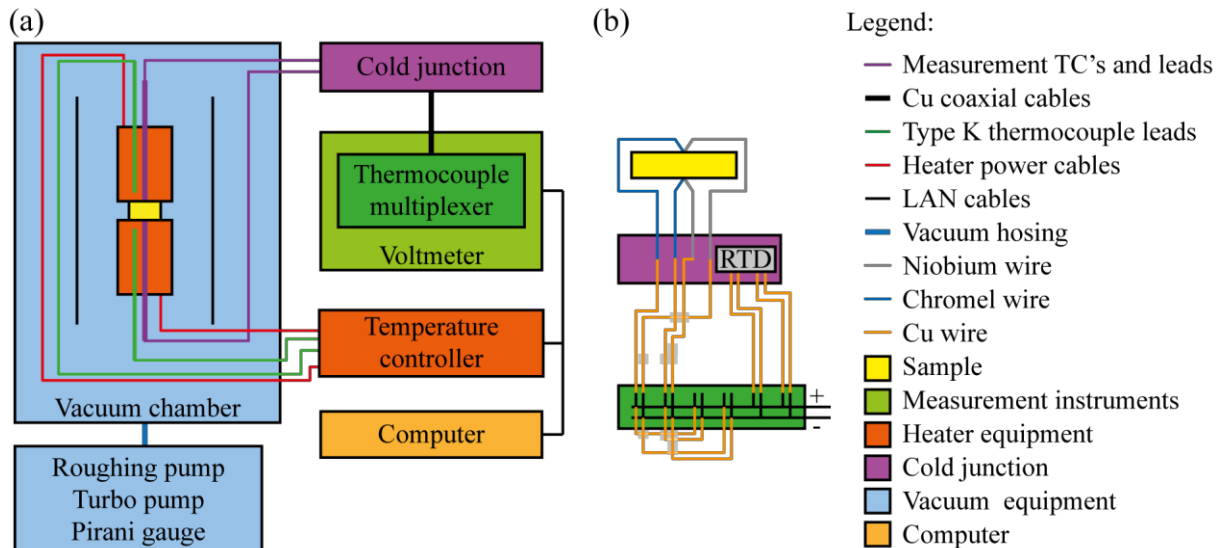


Figure 3-16: (a) Diagram of the whole instrument. The measurement is done in air or vacuum. (b) The measurement circuit is much simpler than in the resistivity and Hall effect system. Nonetheless, the measurement is prone to a higher number of errors which are harder to identify and quantify.

The control thermocouples are connected to the temperature controllers directly. The measurement thermocouples are attached to copper leads in a dedicated cold junction to improve the reference temperature precision; while the built in junction is sufficiently accurate for normal temperature monitoring it is too imprecise for sensitive measurements. After the cold junction coaxial copper wires are used for the signals to reduce the noise as much as possible. Before the cold junction the thermocouple leads are covered in a metallic sleeve to shield them. The cold junction temperature is measured with a Pt1000 RTD. The measurement circuit is shown in more detail in panel (b).

The vacuum chamber is constructed in a similar way to the one in the resistivity and Hall effect system. It consists of a cylinder made from 3 mm stainless steel with a 5 mm thick top. This has a flange on the bottom which seals against an O-ring in a groove on a ‘table’. The cylindrical top is 50 cm in diameter and 1 m high. The heater setup is made as an insert which can be placed inside this chamber. This gives a large flexibility and makes it easy to construct different setups for various sample types. All feedthroughs and the connection for the vacuum pumps are placed in the table. As with the resistivity and Hall effect system, the vacuum chamber can be evacuated to less than 10^{-4} mbar.

3.2.1.1 Heater design

An illustration of a single heater block is shown in Figure 3-17. Like with the resistivity and Hall effect setup, the heaters are made from silicon carbide cement. It is 6 cm in diameter and 5-6 cm high (varies). The heater coils are also made from the same 0.5 mm nichrome wire cast into the cement. Originally, cartridge heaters were inserted in the six large holes; however good thermal contact between the cartridges and heater block was difficult to ensure and resulted both low cartridge lifetimes and poor temperature control. The nichrome wire gives much better temperature control. To ensure a uniform temperature profile across the center of the bottom face (not shown) in contact with the sample, the heater coils are places in a circular pattern around the thermocouple in the center hole. The height of the heater ensures a reasonably good thermal coupling between the heater and the measurement thermocouple. This is hoped to reduce the cold finger effect. The center hole is widened at the top to allow insertion of an Al_2O_3 tube to mechanically protect the fragile thermocouple rod.

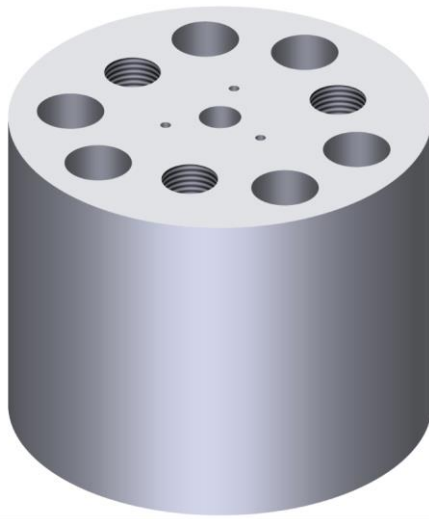


Figure 3-17: Computer rendered illustration of a single heater block. The six large holes marks the position of the heater coils, the three threaded holes marks the position of the support rods, the central hole is for the measurement thermocouple while the three small holes around the center are for the control thermocouples.

The control thermocouples are inserted in the small holes around the center hole. These end approximately 5 mm from the bottom; however, this may be adjusted when the block is cast. Good thermal contact to the control thermocouples is ensured by mechanical force: The thermocouple is slightly bent at multiple places close to the end. This causes the thermocouple to fit tightly in the hole and spring loads it against the sides.

Three alumina tubes are cast into the heater block and are used for structural support. These are attached to the base plates used to apply the spring force to the heaters. These draw away some heat from the heater. While this creates thermal gradients in the heater block, drawing away heat is necessary for the heaters to cool and thus allow accurate temperature control. This is important for accurate control of the temperature gradient across the sample.

An important advantage of this heater design is that the sample surface is approximately isothermal on the surfaces in contact with the thermocouples. This is expected to improve the accuracy of the temperature measurements compared to the 4-point off axis geometry where there is a gradient along the face where the temperature is measured.

3.2.1.2 Thermocouples

The measurement thermocouples are custom niobium/chromel thermocouples (abbreviated as Nb/CP – chromel is often called chromel P, hence the abbreviation CP). Niobium has a very low Seebeck coefficient (-1.5 to $+7 \mu\text{V/K}$) at all temperatures of interest.⁸² This is ideal for voltage measurements since even large relative errors in the niobium Seebeck coefficient results in low relative errors in the measured Seebeck of materials. Compared to a Type K thermocouple (alumel/chromel), the Nb/CP thermocouples only gives approximately half the voltage at the same temperature. While this is not ideal for routine measurements of temperature it is well within the sensitivity of modern voltmeters.

Nb/CP thermocouples have the advantage that niobium has a low Seebeck coefficient and is relatively unreactive. Often platinum is chosen for inertness to oxidation; however, it readily reacts with many elements frequently found in thermoelectrics. These include Si, Ge, Sb, and Te etc. Chromel (nickel + 10% chrome) is less reactive, even though nickel may be somewhat reactive. An alternative is Nb/W thermocouples, where both elements are inert to most elements, mainly due to kinetic effects. This thermocouple has roughly half the voltage as Nb/CP thermocouples but this is still well within the accuracy of modern voltmeters. A disadvantage is that the sensitivity is low at around room temperature (flat voltage vs. temperature curve). This is opposed to Nb/CP thermocouples which have reduced sensitivity from around 8-900°C, as can also be seen in Figure 3-19 (d).

The thermocouple wires are inserted in 4-bore alumina tubes. These are 2.35 mm outer diameter with 0.5 mm bores. According to the data sheet the thermal conductivity is 30 W/mK. This is quite high and may lead to enhanced cold finger effect. Alumina was originally chosen for its high mechanical strength which extends the lifetime significantly. Many commercial systems also use alumina thermocouples and these are often of higher cross sectional areas. Inserting the thermocouples through the heater blocks is hoped to remove or decrease the cold finger effect. Other materials with lower thermal conductivity can be chosen to decrease the cold finger effect further. Examples are various stabilized zirconia ceramics, mullite (mineral consisting of Al_2O_3 and SiO_2) or other electrically insulating ceramics with large compressive strength. The thermal contact, cold finger effect, and related error sources will be discussed further below.

The thermocouple wires are 0.125 mm thick and meet in a cross at one end of the rod with the ends of the wires extending from the other end of the rod. The wires are only kept in contact by mechanical force when pushed against the sample surface. This provides shorter lifetime than weld beads and after a number of runs (usually 10-20) one wire usually breaks.

While weld beads improve electrical contact between the wires and extend the life time, they also provide a thermal contact resistance between the sample and thermocouple junction. Furthermore, the voltage and temperature may not be measured at the same point in space. This can enhance the error from the cold finger effect. With the crossed wire geometry the temperature is measured at a well-defined point (where the wires meet) and the voltage is measured somewhere along the line contact between one wire and the sample surface. Since the surface is approximately isothermal, this will improve the accuracy of the temperature measurement compared to the off-axis 4-point geometry, especially compared to the situation where large weld beads are used on the thermocouples. A disadvantage of custom thermocouples is the need for custom vacuum feedthroughs, thermocouple connectors, and extension wires. The custom feedthroughs are expensive but provide much better measurements than using alternative feedthroughs with other metals. The extension wires are made from 0.5 mm niobium wire (high purity) and the chromel wire from type K extension wires, also 0.5 mm. The thermocouple connectors are made by changing the alumel legs in type K connectors. The custom feedthroughs, appropriate extension wires, and custom connectors are all important to avoid errors from changing thermo-electromotive forces when using dissimilar metals.

The cold junction built into the thermocouple multiplexer card is not accurate enough for the measurement thermocouples. To improve the accuracy and reduce the temperature fluctuations, a custom junction was made. This is simply a large copper block where each thermocouple wire is connected to copper wires in holes in the block. The wire junctions are carefully insulated with heat shrink and epoxy glue. A Pt1000 RTD is used to measure the temperature of the copper block. The high thermal conductivity and heat capacity of copper ensures low gradients in the junction. The block is covered in insulation and placed in a plastic bag to reduce convection and prevent air circulation through the insulation. This ensures a very stable cold junction temperature with variations only on the time scale of hours or longer. This is shown in Figure 3-18. The initial temperature increase is due to the roughing pump which is placed close to the instruments and cold junction. Since the temperature increase is over the course of a few hours it is essentially constant during each raw $U(\Delta T)$ measurement, where U is the voltage and ΔT is the temperature difference, and causes no error to the final results. The small fluctuations mostly visible from 6 to 18 hours are probably due to fluctuations in the voltmeter temperature. This cannot be reduced significantly. The larger fluctuations are due to temperature changes during the day (sun hitting the lab in the afternoon) while the source of the two sharp dips is unknown. One explanation could be that the window in the lab was opened.

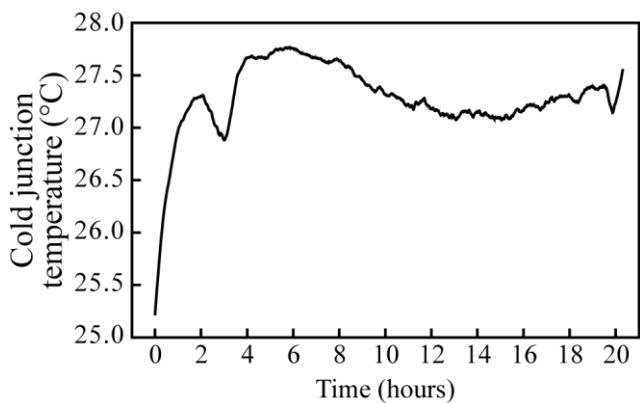


Figure 3-18: Cold junction temperature as a function of time. The initial increase in temperature is due to the roughing pump heating the junction.

Since the thermocouples are custom no standard calibration table exist. This can either be obtained from the calibration table for chromel (a standard thermocouple alloy) and literature values for the Seebeck coefficient of Niobium (see, for example, reference 82) or it can be obtained experimentally. The latter approach was chosen. Thermocouple calibration is not merely measuring the thermocouple voltage as a function of temperature. Also appropriate calibration for cold junction temperature is necessary thus rendering it essentially a 2D problem. This is somewhat simplified by the high thermal stability of the cold junction. This means the cold junction temperature can be regarded as constant during short time periods. The calibration is done against type K thermocouples. This is not optimal but provides sufficient accuracy for the needs of this setup. A better solution would be to use a resistance thermometer as a standard but this complicates the high temperature calibration since the vacuum chamber is not fitted with appropriate feedthroughs for RTD measurements.

The calibration is done in two rounds: One at low temperature which is used to correct for the cold junction temperature and one at high temperatures which gives the bulk of the reference table. The low temperature calibration is done by inserting a Nb/CP thermocouple in a hole in a copper block partially submerged in an ethanol/ice mixture. Two reference thermocouples are inserted in holes close to the hole with the Nb/CP thermocouple. This is cooled to slightly below 0°C before the calibration is started. Figure 3-19 (a) shows the temperature as a function of time for the two calibration rounds. The ethanol/ice bath is placed on a hot plate. When the calibration starts the hot plate is turned on at a low setting which causes the ice to melt and the temperature to slowly increase to slightly above 0°C. From approximately 5°C the hot plate power is turned up, causing the temperature to increase slightly faster. This is continued until the temperature is well above the reference junction temperature, usually 35-40°C. The Nb/CP thermocouple is then inserted in the system and prepared for high temperature calibration.

The high temperature calibration is done by placing a $25 \times 25 \times 10 \text{ mm}^3$ steel piece between the heaters. This has holes on the top and bottom faces which tightly fits the Nb/CP thermocouples. These meet at the middle and are separated with 0.1 mm steel. A small piece of graphite paper is placed in each hole. The Nb/CP thermocouples are extended through the heater blocks and placed in the holes. 1 – 3 kg of force is applied to each with springs. The same two reference thermocouples are inserted in two other holes from one side of the steel piece. These holes end close to the Nb/CP thermocouple ends to ensure a consistent temperature. The reference thermocouples are wrapped in aluminum foil to improve thermal contact. This melts at about 660°C fusing the thermocouples to the steel, which further improves the thermal contact. No sharp anomaly is seen in the calibration curves at this temperature (see Figure 3-19 (d)). The upwards curvature is due to the chromel Seebeck decreasing. Both heaters are set to the same temperature profile and heated to about 20 K above the desired maximum temperature of the system. The two reference temperatures, the two Nb/CP thermocouple voltages, and the cold junction temperature are recorded as a function of time during heating. The data is treated in several steps. Each of these is described in detail below using the latest calibration data as an example. The thermocouples do not need to be calibrated often but it is done every time changes affecting the thermocouples are made to the (changing feedthroughs, modifying the cold junction, changing extension wires, or purchasing a new batch of wire). The latest calibration was done on May 14th and 15th of 2012 after changing the thermocouple feedthrough and connectors.

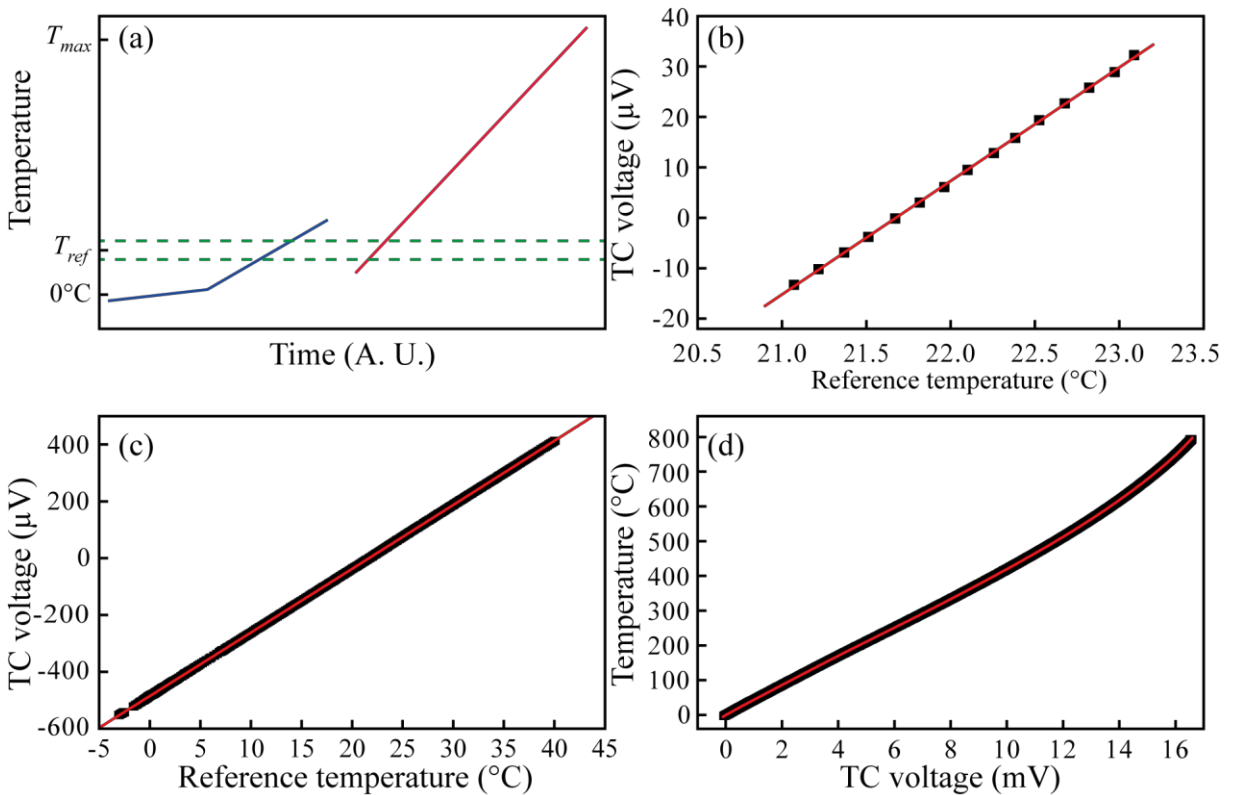


Figure 3-19: Example of thermocouple calibration. In (a) a sketch of the temperature profile is shown as a function of time for both the low (blue) and high (red) temperature calibration part. The dashed green lines indicate the band within which the cold junction temperature T_{ref} varies. In (b) the thermocouple (abbreviated TC) voltage is shown as a function of reference temperature in the region close to the cold junction temperature for the measurement represented by a blue line in (a). In (c) the thermocouple voltage for all measurement points for the blue line are shown with correction for variations in the cold junction temperature but without correction for the temperature itself. In (d) the temperature is shown as a function of the thermocouple voltage corrected for the cold junction temperature.

The first step of the data treatment is to correct the low temperature data for fluctuations in the cold junction temperature. First, the thermocouple voltage is approximated to be a linear function of temperature around the reference junction temperature. The low temperature data from 1 K below the lowest cold junction temperature to 1 K above the highest is used to fit a straight line. In this example the cold junction varies between 22.028°C and 22.103°C . The program does not accept the data if the variation in cold junction temperature is more than 1 K. This data with the fit is shown in Figure 3-19 (b) and the fit is seen to be good, thus validating the assumption. The slope of the fit is now used to correct all the low temperature data for the changes in cold junction temperature.

After the correction a second order polynomial is fitted to all the corrected low temperature data. This is shown in Figure 3-19 (c). This gives a polynomial which can be used for proper correction for the cold junction temperature. All the low and high temperature data is corrected for cold junction temperature using this polynomial. After this correction all thermocouple voltages are relative to a 0°C cold junction. This is the standard cold junction temperature when reporting thermocouple calibration tables. Finally, all corrected data from

both the low and high temperature part is used to fit a 10th order polynomial, this time with voltage as x-axis and temperature as y axis. This is shown in Figure 3-19 (d). The polynomial is stored in a calibration file and is used for future measurements.

The corrected thermocouple voltage at a given temperature is the integrated thermocouple Seebeck S_{TC} , defined as $S_{TC} = S_{CP} - S_{Nb}$, from 0°C to that temperature. Hence the thermocouple Seebeck is the slope of the voltage vs. temperature curve. This can also be calculated as the inverse of the derivative of the calibration polynomial (temperature as function of voltage) at the voltage corresponding to this temperature. The polynomial was obtained without assuming any known Seebeck coefficient. Hence, if literature values for the Nb Seebeck coefficient are used, the chromel Seebeck can be calculated from this and the calibration polynomial as $S_{CP} = S_{TC} + S_{Nb} = 1/\alpha + S_{Nb}$ where α is the slope of the calibration polynomial. To check the validity of the polynomial, the Seebeck coefficient can be measured with both the Nb and chromel leads and compared. The sample Seebeck is $S_{Sample} = -\frac{dU_{lead}}{d(\Delta T)} + S_{lead}(\bar{T})$ where S_{lead} is the Seebeck of the leads used for the voltage measurement. If the niobium Seebeck is wrong with the error δS_{Nb} , the sample Seebeck measured by the two leads will be $S_{Sample}^{Nb} = -\frac{dU_{Nb}}{d(\Delta T)} + S_{Nb} + \delta S_{Nb}$ and $S_{Sample}^{CP} = -\frac{dU_{CP}}{d(\Delta T)} + S_{TC} + S_{Nb} + \delta S_{Nb}$. The superscript marks the lead used for the measurement. Hence both Seebeck coefficients are affected equally and in the same direction. If, on the other hand, there is an error δS_{TC} the Seebeck coefficients will be $S_{Sample}^{Nb} = -\frac{dU_{Nb}}{d(\Delta T)} + S_{Nb}$ and $S_{Sample}^{CP} = -\frac{dU}{d(\Delta T)} + S_{TC} + S_{Nb} + \delta S_{TC}$. In this case only the Seebeck coefficient measured with the chromel leads is affected. ΔT has been assumed to be independent of δS_{TC} , which is correct for small errors.

If the thermocouple Seebeck is correct (meaning the TC calibration table is correct to within a constant), the two measured Seebeck coefficients will be identical. To do this comparison, the Nb Seebeck coefficient has been extracted from reference 82 and is used in the program. An example of the difference between the sample Seebeck coefficient measured with the niobium and chromel leads is shown in Figure 3-20. The Seebeck coefficient varies between 98 $\mu\text{V/K}$ and 165 $\mu\text{V/K}$ while the difference between the two Seebeck coefficients only varies between -50 and +50 nV/K , three orders of magnitude lower. Furthermore, the difference has no significant temperature dependence. As mentioned above this means the thermocouple calibration polynomial is correct to within a constant. This constant is unimportant since only temperature differences are important to the measurement. If any of the thermocouples in the calibration were affected significantly by the cold finger effect, the temperature dependence would be wrong, resulting in differences in the sample Seebeck coefficient. Hence it is concluded that this is not the case.

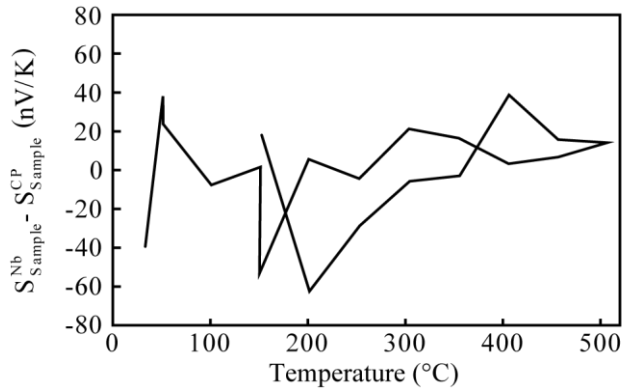


Figure 3-20: Difference between the sample Seebeck measured with niobium leads ($S_{\text{Sample}}^{\text{Nb}}$) and chromel leads ($S_{\text{Sample}}^{\text{CP}}$). The sample is a p-type $\text{Ge}_x\text{Si}_{1-x}$ doped with boron. The Seebeck coefficient is measured at 50 K intervals between 30°C and 500°C on both heating and cooling.

3.2.1.3 Thermal contact and cold finger effect

Martin^{47, 52} did a thorough study of the effect of the cold finger effect and thermal contact resistance between the sample and thermocouples. He compared the 2-point and off-axis 4-point geometries and concluded that the off-axis 4-point geometry would overestimate the Seebeck coefficient compared to the 2-point geometry due to the cold finger effect. He found that the difference between the Seebeck coefficients measured in the two geometries was proportional to the temperature difference between the sample and surroundings. This was supported by calculations. In these, the thermocouples were assumed to be infinitely long and radiatively coupled to the surroundings while the sample surface was assumed to be adiabatic.

Such a treatment is difficult for the uniaxial 4-point geometry. Instead, the thermocouples will be assumed to have a fixed temperature at the ends away from the sample while radiative losses will be neglected. Due to the thermal contact resistance there will be a temperature drop across the sample-thermocouple interface, with the sample being warmer. The contact resistance will be assumed to be identical for all thermocouple-sample interfaces and equal to R .

In the off-axis geometry in Figure 3-21 (a), which will be treated first, the temperature just inside the sample surface at the thermocouples are T_1 and T_2 . Since the thermocouples draw away the heat q_n , with n being 1 or 2 for the two thermocouples, there will be a temperature drop $\delta T_n = R \cdot q_n$. Neglecting radiative coupling to the surroundings the heat conducted away is $q_n = \kappa \cdot \frac{A}{l} \cdot (T_n - \delta T_n - T_0)$. κ is the thermal conductivity of the thermocouple, $\frac{A}{l}$ is cross sectional area over length, and T_0 is the temperature of the thermocouples where they are fixed to the furnace wall (always close to ambient temperature). From these two equations δT_n can be isolated

$$\delta T_n = \frac{1}{1 + \frac{l}{A \cdot R \cdot \kappa}} (T_n - T_0) = k(T_n - T_0). \quad (3-2)$$

k is a collection of all the constants. From this equation the thermocouples are seen underestimate the temperatures, with the difference being proportional to the temperature difference between the sample and surroundings.

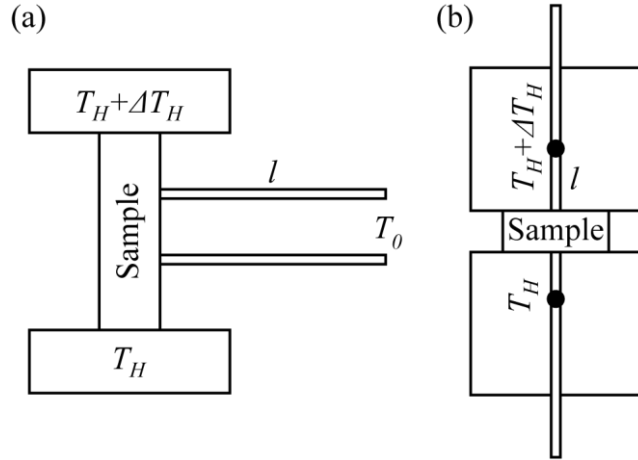


Figure 3-21: Schematic of the off-axis 4-point and uniaxial 4-point geometries used for estimating the error from the cold finger effect. In (a), the temperature of the thermocouples (long rods) is assumed to be fixed at ambient temperature T_0 in one end. In (b), the thermocouples are assumed to be fixed to the heater temperature at some point inside the heater. In both cases the thermal contact resistance is assumed to be identical for the two thermocouples.

The measured temperature difference ΔT^m and average temperature T^m can also be calculated

$$\Delta T^m = T_1^m - T_2^m = T_1 - k(T_1 - T_0) - \{T_2 - k(T_2 - T_0)\} = \Delta T - k\Delta T \quad (3-3.a)$$

$$T^m = \frac{T_1^m + T_2^m}{2} = T - k(T - T_0) \quad (3-3.b)$$

Since $T_1 - T_2$ is small, the correction in Equation (3-3.a) is a second order effect while that in (3-3.b) is the first order effect. The two effects together explain the linear deviation with temperature observed by Martin. If radiative loss is added the heat flow q will be higher thus effectively increasing k in the equations. This correction is difficult since the thermocouples extend from the hot part of the furnace to a region at ambient temperature. It is further complicated if IR furnaces are used, as is the case in the commercial ZEM systems. In this case the temperature is controlled with radiative coupling to tungsten filaments at several thousands of degrees. In this case the temperature depends on the emissivities of the different components. Hence, if the sample, thermocouples, and gradient heater is not shielded from the IR radiation bath there can be large temperature differences. This can potentially cause large errors in the Seebeck coefficient.

In the uniaxial geometry in Figure 3-21 (b) the thermocouples are assumed to be fixed to the heater temperature some distance l from the sample surface. The setup is assumed to be symmetric: l is the same in both heaters, the sample has the same average temperature as the two heaters, and the thermal contact resistances are again identical. Since the sample surface is not at the same temperature as the heaters there is again a temperature drop at the sample-thermocouple interfaces. In this case, however, one thermocouple will overestimate the temperature while the other will underestimate it. The measured temperature difference can be calculated the same way as above and gives

$$\Delta T^m = \Delta T - k(T_1 - T_2 - \Delta T_H) \quad (3-4)$$

Since the temperature difference between the heaters ΔT_H must be larger than the temperature difference across the sample ΔT , the measured temperature difference is larger than the actual difference $T_1 - T_2$. The average sample temperature has no correction. The effect of radiative coupling between thermocouples and heaters is again to increase the heat flow; however, this is much less than in the off-axis geometry since only a small temperature difference between the heaters and thermocouples is expected. If, on the other hand, the thermocouples are poorly coupled to the heaters, they will act as cold fingers and the thermopower (absolute of Seebeck coefficient) will be overestimated by the same argument as for the off-axis geometry.

Since $\frac{A}{l}$ is much larger in the uniaxial geometry the error in ΔT may be comparable for the two geometries. It is not obvious whether the thermocouple can be assumed to have the same temperature as the heater at some point within the heater. If the coupling to the heater is low, the cold finger effect from outside the heater may be dominant. To reduce the error in ΔT , the sample surface temperature should be close to the heater temperature. This can be improved in two ways: The sample thickness can be increased and the heater thermal conductivity should be high. The latter is a design optimization that should be addressed. How to do this in the off-axis geometry is less obvious. In this treatment using long, thin thermocouples is an improvement; however, this will depend on the radiative coupling and in some cases thicker thermocouples may be an advantage to decrease this radiative coupling relative to the thermal conduction. The main advantage of the uniaxial geometry is that the sample temperature is measured more accurate and that the heater thermal conductivity can be engineered to be high. This will be addressed later. In conclusion the uniaxial geometry is expected to be an improvement over the more traditional off-axis geometry.

3.2.2 Measurement procedure

The setup employs the quasi steady-state method with differential measurements. A temperature difference is stabilized around the desired temperature for the measurement as shown in Figure 3-22 (a). The temperature difference is then slowly inverted around the same average temperature while the two temperatures and voltages using both the niobium and

chromel leads are measured continuously. To remove the effect of linear drifts in temperatures and voltages the raw measurements are conducted symmetrically in time according to the delta method. That is, the measurements are performed in the order T_1^1 , T_2^1 , V_{Nb}^1 , V_{CP} , V_{Nb}^2 , T_2^2 , T_1^2 . The average of the two measurements is used saved. The measurements are performed with equal time steps. This removes linear changes when the average is used. If the time steps are not equal, linear interpolation using the time stamps of the measurements is necessary.⁴⁹ Only data from the grey regions in Figure 3-22 (a) is used for extracting the Seebeck coefficient. Between the two regions the curvature will be high (which is not removed in the delta method) and using the data before, after, and between the grey regions will bias the result for the measurements with high temperature difference.

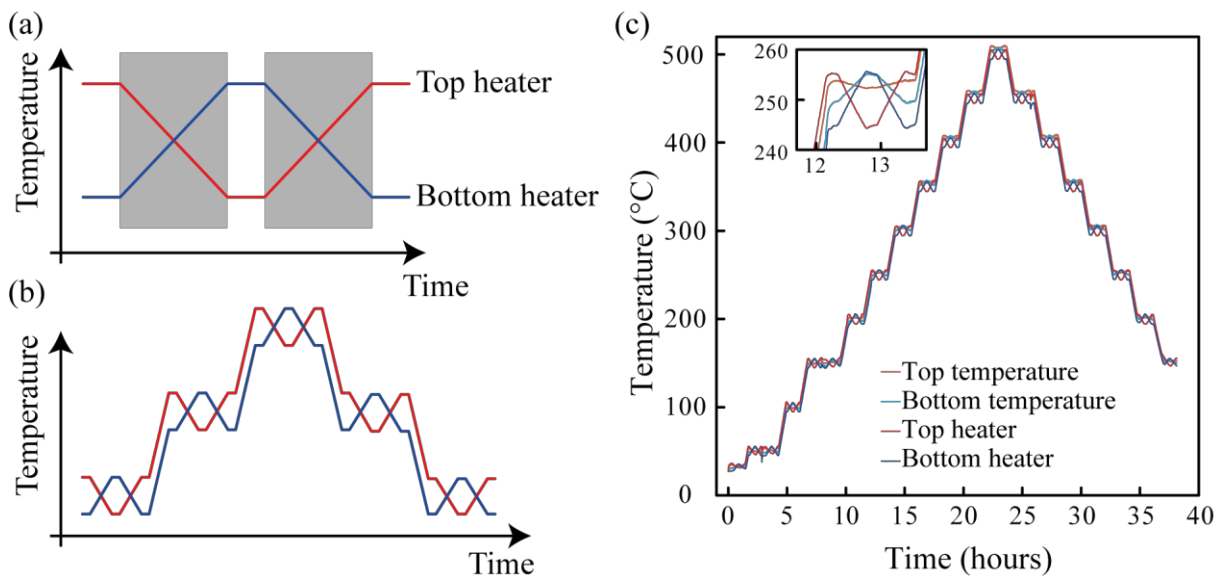


Figure 3-22: The temperature profile used for measuring the Seebeck coefficient in the quasi steady-state method. In (a) the temperature profile for one measurement of the Seebeck coefficient is shown. In (b) the overall profile is shown while (c) shows an example of an actual temperature profile from a measurement. Both the heater and sample surface temperatures are shown.

The temperature profile in Figure 3-22 (a) results in one data point. To measure the Seebeck coefficient as a function of temperature, these sections are put together as shown in panel (b). The Seebeck coefficient is usually measured every 50 K on both heating and cooling, but this can be changed by the user. Below about 150°C the heat loss from the heaters is too low to be able to control the temperature profile accurately in vacuum. Hence, from room temperature to 150°C the measurement is performed in air or an inert gas. From 150°C and up, the measurement is performed in vacuum. An example of an actual temperature profile is shown in Figure 3-22 (c). In the example the measurement at 150°C is performed both in air and vacuum. If the Seebeck coefficient changes when the chamber is evacuated it is most likely a sign that there is poor thermal contact between the thermocouples and sample. The insert shows a slight magnification of one Seebeck measurement. The temperature difference across the sample (illustrated by the orange and light blue lines) appears to be smaller than the temperature difference between the two heaters (illustrated by the red and blue lines).

Additionally, the thermal contact between the sample and bottom heater appears to be better than between the sample and top temperature. This can equally well be explained by bad thermal contact between the sample and top thermocouple; however, no other signs of bad thermal contact were observed in the particular experiment. These problems are likely due to the heaters having too low thermal conductivity. This will be addressed in section 3.2.3.

3.2.2.1 Data analysis

When the voltage is measured using both leads, the Seebeck coefficient S can be calculated in two ways

$$S = -\frac{U_{Nb}}{\Delta T} + S_{Nb} \quad (3-5.a)$$

$$S = -\frac{U_{CP}}{\Delta T} + S_{CP} \quad (3-5.b)$$

S_{Nb} and S_{CP} are the Seebeck coefficients of niobium and chromel, respectively, while U_{Nb} and U_{CP} are the voltages. ΔT is the measured temperature difference. This is known as the single point measurement method. Since the temperature difference is slowly varied the voltages are measured as a function of ΔT . This leads to the differential formulation,

$$S = -\frac{dU_n}{d(\Delta T)} + S_n \quad (3-6)$$

n is either Nb or CP. This is known as differential measurements. This has the advantage that constant offsets in U and ΔT are removed. These can be from the thermocouples ageing or voltages from reactions with the sample. In practice the $U(\Delta T)$ is fitted to a straight line and the slope used in Equation (3-6). The intercept of the fitted line is a dark offset voltage and can reach several hundreds of microvolts. If it is regarded as an offset along the x-axis instead it corresponds to a few Kelvin.

When the voltage is measured with both leads, Equation (3-5.a) and (3-5.b) can be rewritten to remove ΔT , as proposed by de Boor and Müller.⁴⁹ This gives

$$S = \frac{S_{TC}}{1 - \frac{U_{CP}}{U_{Nb}}} + S_{Nb} \quad (3-7.a)$$

$$S = \frac{-S_{TC}}{1 - \frac{U_{Nb}}{U_{CP}}} + S_{CP} \quad (3-7.b)$$

Again, $S_{TC} = S_{CP} - S_{Nb}$ is the thermocouple Seebeck obtained from the derivative of the calibration polynomial. These can also be rewritten to differential form by substituting $\frac{U_{CP}}{U_{Nb}} = \frac{dU_{CP}}{dU_{Nb}}$ and $\frac{U_{Nb}}{U_{CP}} = \frac{dU_{Nb}}{dU_{CP}}$. Equation (3-7.a) and (3-7.b) and their differential counterparts do not represent physically different measurements and will give the same result as Equation

(3-6). This method is still interesting since only two measurements (the two voltages) are necessary instead of three (two temperatures and a voltage) for the more traditional method. Additionally, since ΔT is the difference between two fairly large numbers with noise, the noise level in the U vs. ΔT curves is significantly larger than in the U_{Nb} vs. U_{CP} curves. An example of these curves are shown in Figure 3-23. It can clearly be seen that the voltage vs. temperature difference data is more noisy (lines are not smooth) than the chromel vs. niobium voltage data (smooth line).

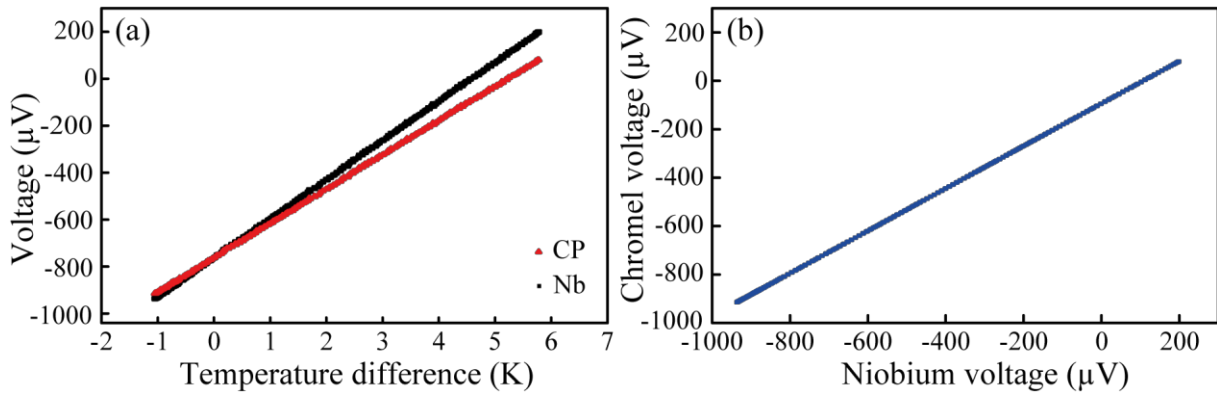


Figure 3-23: Examples of raw voltage vs. temperature difference data (a) and chromel vs. niobium voltage (b). This data corresponds to the 500°C data in Figure 3-22 (c). The difference in slope in (a) corresponds to the difference in Seebeck of niobium and chromel. In (b) the slope is caused by the difference in Seebeck of the sample and chromel.

The difference in noise levels is also illustrated by the correlation coefficients which are shown in Figure 3-24. The correlation coefficient is always larger for the fits of voltage vs. temperature difference. Additionally the correlation coefficient for Nb is slightly higher than the correlation coefficient for CP. This is because the Nb voltage is measured twice while the CP voltage is measured only once and is hence slightly less susceptible to non-linear changes in voltage. As mentioned above, this does not mean that the voltage only method is more accurate; just that the noise level is lower. The two measurements with significantly higher $1 - R^2$ had poor temperature control. This illustrates the importance of good temperature control to obtain accurate results.

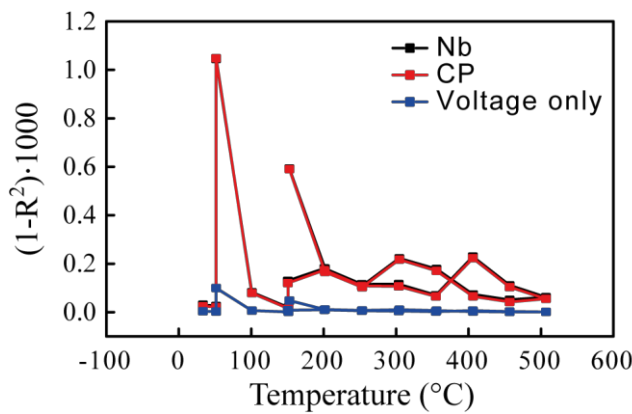


Figure 3-24: Correlation as a function of temperature for the three methods for extracting the Seebeck coefficient. This was obtained from the measurement shown in Figure 3-22 (c).

The program calculates the Seebeck coefficient, offset, and correlation coefficient from Equation (3-5.a), (3-5.b), and (3-7.a). All this is supplied in the output file. Normally the Seebeck coefficients calculated from the voltage only method are used since these have lower noise. The difference between all three Seebeck coefficients is usually less than $0.5 \mu\text{V/K}$.

3.2.2.2 Dark voltage and dark temperature

When fitting lines to the data shown in Figure 3-23 there is a constant offset. The origin of this dark offset voltage will be discussed here. Figure 3-25 (a) shows the dark voltage as a function of temperature for the three different ways of extracting the Seebeck coefficient. The dark voltage is almost identical for the measurements using the niobium and chromel leads while the voltage only method has a significantly lower offset. This indicates that the dark voltage is more a dark temperature (*i.e.* an error along the x-axis), which is plotted in Figure 3-25 (b). There is no temperature error in the voltage only method and hence the dark temperature is not shown in (b) for this method. Since there is still an offset voltage in the voltage only method the total offset is most likely a combination of a temperature and voltage offset. Pure voltage offsets can be caused by reactivity with sample, drift in thermocouples, inhomogeneous wires etc. Temperature difference offsets can be caused by non-equal drifts in thermocouples, inhomogeneous thermocouple wires, or non-equal cold finger effects. All explanations for both offsets except the reactivity with the sample and non-equal cold finger effect implies that the change in offset between successive runs is low. This is not the case, there can indeed be very large differences even at room temperature. The temperature dependence if the explanation was reactions with a sample also appears wrong. An Arrhenius-type activated behavior would generally be expected.

The effect of the offset on the measured Seebeck coefficient depends on the stability of the offset during one measurement. If the offset changes during one measurement the voltage vs. temperature curves will show hysteresis. If this is not the case the measurement is likely unaffected. It is possible, however, that the offset is proportional to the temperature of one thermocouple. From Figure 3-25 (b) this would cause on the order of 1% error in the temperature difference, which leads to a minor error in Seebeck.

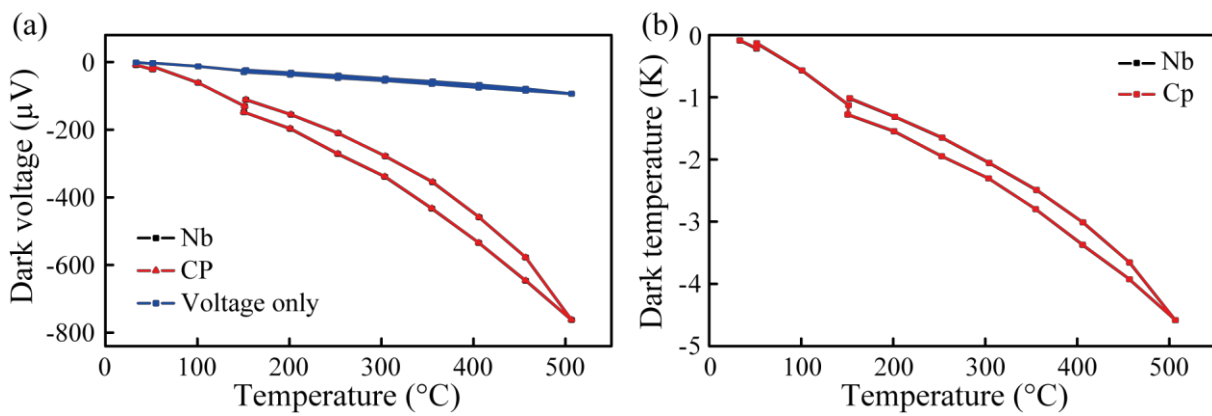


Figure 3-25: Dark offset voltage (a) and temperature (b) for a measurement.

A temperature offset from non-equal cold (or hot) finger effect is the most likely cause. This can be caused by two things: Difference in the thermal contact resistance to the sample or differences in the thermal coupling to the heater. To test this, three $\text{Ge}_x\text{Si}_{1-x}$ samples with x ranging from close to 1 to 2/3 were used. These have very different thermal conductivity. They were measured at 150°C in both air and vacuum and both with and without a piece of thin graphite paper on each side. Samples with higher thermal conductivity have a higher heat flow and are expected to cause a higher temperature drop across the sample-thermocouple interface. Without the graphite paper the thermal contact between both sample and thermocouple and thermocouple and heater can change when evacuating the chamber. Contrary, the sample-thermocouple contact resistance is expected not to change (or change less) with the graphite paper. Hence, comparing the change in Seebeck when evacuating the chamber can give an indication of where the thermal contact is bad and whether the thermocouples act as hot or cold fingers. This change is shown in Table 3-1.

Table 3-1: The effect of sample thermal conductivity and thermal contact resistance on the Seebeck coefficient when the chamber is evacuated. The samples were prepared and measured by Ellen Marie Jensen Hedegaard.

κ	Spacer	Change in Thermopower
Low (low x)	None	-0.15 $\mu\text{V/K}$
	Graphite	+13 $\mu\text{V/K}$
Medium	None	-1.3 $\mu\text{V/K}$
	Graphite	+28 $\mu\text{V/K}$
High (high x)	None	+2.0 $\mu\text{V/K}$
	Graphite	+70 $\mu\text{V/K}$

The graphite spacers will enhance the cold and hot finger effects. In the table the thermopower increases for all samples. Since the thermal contact between the sample and thermocouples is roughly constant during evacuation of the chamber when using the graphite paper, this can only be due to the thermal coupling between thermocouples and heaters. An increase in thermopower corresponds to a relative underestimation of ΔT and is then likely caused by the thermal contact between thermocouples and heater decreasing. The effect is expected to be enhanced by the sample thermal conductivity, which is also observed. Without the graphite paper spacer, there is only a small change in Seebeck. This indicates that the thermal contact to the sample is better and that the measurement is only slightly affected by the decreased coupling to the heaters. In all cases in air the thermopower is slightly lower with graphite paper than without.

Several things can be done to improve this. Firstly, the thermal coupling to the heaters can be increased to remove the cold finger effect. Secondly, the thermal conductivity of the thermocouple rods can be decreased to reduce the heat flowing across the sample-thermocouple interface. Lastly the thermal conductivity of the heaters can be increased to reduce the temperature difference between the sample surface and heater and reduce the temperature gradients in the heater. Both the alumina thermocouple rod and silicon carbide cement have a thermal conductivity at room temperature of 30 W/mK according to their respective data sheets. The actual thermal conductivity of the silicon carbide cement will vary depending on porosity. Hence, the heat flow across the thermocouple-sample interface can actually be quite high. Improving upon this is discussed in the next section.

3.2.3 Upgrade

To address the concerns discussed above a new heater has been designed but not yet implemented, the thermocouple rods will be changed to mullite (with a room temperature thermal conductivity of 2.4 W/mK), and the thermocouples will be better anchored to the new heater.

To increase the thermal conductivity of the heaters, they will be machined from molybdenum. This has a thermal conductivity of about 140 W/mK which is a significant improvement. This was chosen over tungsten, which has an even higher thermal conductivity, since it is more easily machined. The new design is shown in Figure 3-26. In the new design, the control thermocouples will be moved considerably closer to the measurement thermocouples (about 3-4 mm apart); this is expected to give a better temperature control of the sample surfaces. Finally, the nichrome heater wire will be changed to cartridge heaters. These will be clamped between two molybdenum blocks with graphite paper between the cartridge heaters and the molybdenum. This is hoped to give a good thermal contact and result in fast and accurate temperature control. When using metal heaters it is necessary to either electrically isolate the sample surfaces from the heaters or isolate the two heaters from each other. This is to prevent current from flowing through the sample and affect the

measured Seebeck coefficient (which is defined as the open circuit voltage). To ensure this, a wire will be attached to each heater and used for measuring the resistance between the two before mounting a sample.

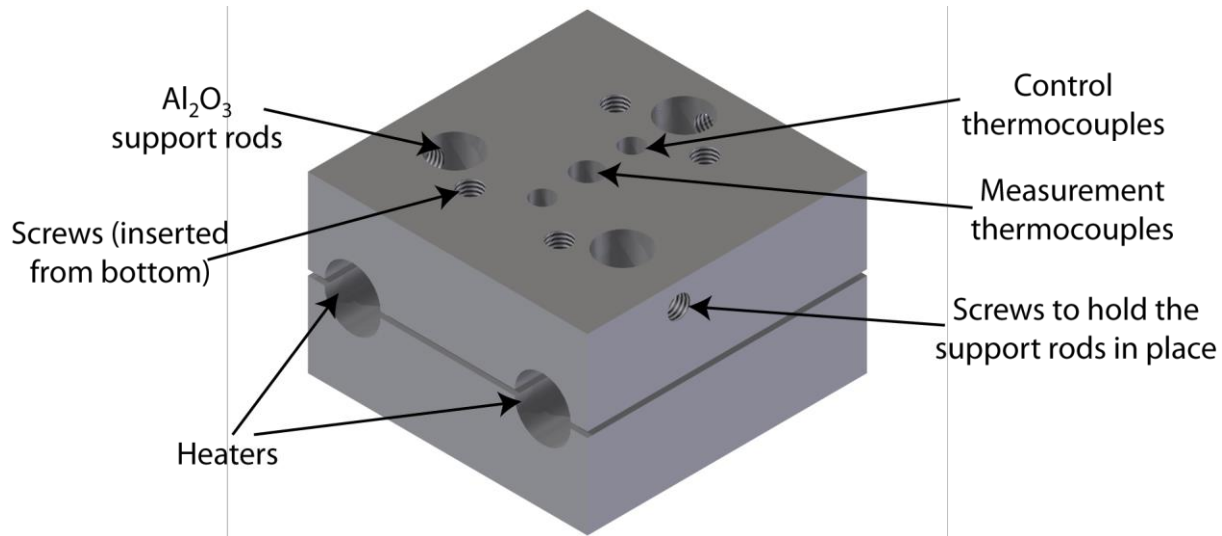


Figure 3-26: The new heater design. It has many of the same important characteristics as the design in Figure 3-17. Most importantly, it is still the uniaxial geometry but it is designed for better heat transfer to the sample and a smaller temperature gradient in the heater itself.

Each heater consists of two blocks with the cartridge heaters clamped in between. They are held together by stainless steel screws which are inserted through the bottom piece in the figure and screwed into the top piece. The four holes in the top are shown threaded. To avoid breaking the heater with thermal stress the cartridge heater will be wrapped in two layers on 0.25 mm graphite foil. This will function as both a stress absorber and enhance the thermal contact. The hole for the measurement thermocouple is too large in the top piece and fits the thermocouple tightly (0.1 mm clearance) in the bottom piece. The extra space in the top piece will be filled with graphite paper to couple the thermocouple rod to the heater. Additionally, an alumina tube will be inserted in this hole to protect the thermocouple rod. This tube will have a thermal gradient which reduces radiation loss from the thermocouple. Finally, a piece of 0.25 mm graphite paper will be placed between the two blocks to decrease the thermal contact resistance between the two and decrease thermal gradients.

3.2.3.1 Adaptation for thin films and bar shaped samples

Due to the strictly cross-plane measurements in the uniaxial geometry, thin films and other samples mounted on a substrate cannot be measured. It is also not optimal for bar shaped samples, and these can again only be measured across the length. Being able to measure bar shaped sample is interesting for several reasons. One fairly important reason is to be able to measure the direction dependence of the Seebeck coefficient in anisotropic samples. The direction is better defined in bar shaped samples. Measuring anisotropic samples in the van der Pauw geometry is addressed in Chapter 4 but can be solved using math. This is not as

easy for the uniaxial geometry for Seebeck measurements and hence a combined adaptation for thin films and bars is more convenient. This is designed as an insert that can easily be changed back and forth to the uniaxial setup.

Due to the problems with the off-axis geometry described by Martin^{47, 52} and discussed in section 3.2.1.3 it was decided not to use this geometry. Instead, a new measurement geometry in between the off-axis and uniaxial geometries was developed. The geometry is shown in Figure 3-27. The idea is to heat the two ends of the sample but have the thermocouples inserted through the heaters like in the uniaxial geometry. The heater will be made in two pieces which will be kept in thermal contact. The upper and lower pieces are clamped around the end of one sample with a spring force. This allows relatively uniform temperature of the end. The thermocouple is pressed against the sample from the bottom. Since the pressure is strictly uniaxial, large forces can still be used on the thermocouples without breaking or bending the sample. This is important to reduce the thermal contact resistance. Like in the uniaxial geometry the thermocouples are inserted through the heater to reduce the radiation loss and cold finger effect. The holes for the thermocouples will be placed close to the edge of the heaters. This allows them to be placed close together to allow measurement of short samples. The final dimensions are still uncertain but the minimum sample length is expected to be between 4 and 6 mm. While the drawings are ready and the parts have been ordered, the actual dimensions will also depend on practical experience.

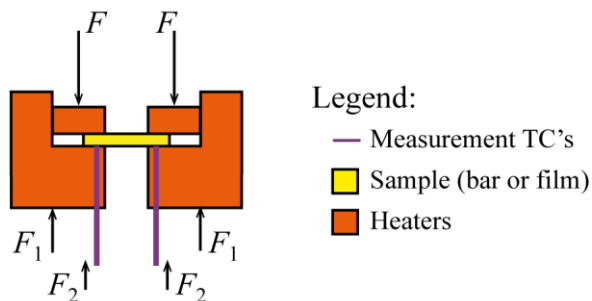


Figure 3-27: Schematic of the geometry for measuring thin films and bar shaped samples. The heaters are made in two pieces which will be clamped around the end of the sample. The measurement thermocouple is inserted through the bottom of the heater and pressed against the sample. To avoid stressing and possibly bending the sample, it is important that $F = F_1 + F_2$.

The setup can also accommodate disc shaped samples and can hence be sited to measure the in-plane Seebeck of these samples. This can be done for many rotations of the sample to get good directional resolution. Hence using the combination of the uniaxial geometry and the new thin film adaptation the Seebeck coefficient can be measured in all directions in the sample; however, the accuracy of the direction is low in the uniaxial geometry since the thermocouples have to be exactly across each other to avoid in-plane contributions.

3.2.4 Software

The software is designed from the same principals as the resistivity and Hall system software. It consists of roughly 10,000 lines of code, somewhat less than the resistivity and Hall system. This is mainly due to the lower number of instruments necessary, the somewhat simplified measurement procedure and simpler data structure necessary. The user interface is made to resemble that of the resistivity and Hall effect system as much as possible.

The program runs stably and it is estimated that less than 1 in 20 failed measurements is due to errors in the software. The program offers a few tools to help the user during sample mounting. These include a dialogue for measuring the two point resistance of all thermocouples and through the sample with both the niobium and chromel leads. The corresponding temperatures and voltages are also measured. This provides an easy way to identify broken thermocouples or poor electrical contact. The program also provides plots of the Seebeck coefficient from both niobium and chromel wires and the voltage only method. The corresponding single point measurements can also be plotted. To help identify bad measurements the dark voltage and temperature and correlation coefficient of the fits can also be plotted. All the voltage vs. temperature difference or chromel vs. niobium voltage plots with corresponding linear fits can also be plotted. This provides a fast way to identify bad measurements on the fly.

The input to the program is simply minimum and maximum temperature, number of Seebeck coefficient measurements (or temperature difference between points), desired temperature difference for the heaters, heating rates, and whether data should be measured on both heating or cooling or just heating.

3.2.5 Conclusion

Estimating the accuracy of the Seebeck measurements is difficult. On one side only one standard reference material exist for Seebeck coefficient measurements (NIST SRM 3451). This standard reference material is calibrated to only 390 K and is additionally not compatible with the geometry of this setup. On the other hand few systems exist which accept samples similar to the one discussed here. The setup at Caltech accepts the same samples but is too similar in design to be used for a critical comparison. These setups agree within 5% for all tested samples if good thermal contact is ensured in both setups.

When the adaptation for thin films is completed this provides a good system for comparison since it has the capability to accommodate disc shaped samples but measure them in-plane. The two setups are sufficiently dissimilar to provide good comparisons. Additionally, the comparison to and discussion of the setup by Martin⁴⁷ is intended to give a hint of the expected accuracy. Martin's setup gives upper and lower bounds of the Seebeck coefficient. The setup discussed here has been designed to reduce some of the errors from both the 2-point and off-axis 4-point geometries. It is hence expected to provide results within the

bounds provided by Martin's setup, provided these design features work as expected. It is hence expected that the accuracy is better than 10%, and it is hoped to be as low as 5%.

4 Anisotropic resistivity

4.1 Introduction

Experimentally, the most common method to extract the resistivity tensor is to simply measure the resistivity of bars cut in different orientations from a larger sample. This could be along the unit cell axes of a single crystal. This seems like the most straight forward approach but it is not necessarily the simplest method, the one giving the most information, or the most accurate. As discussed previously, the four-point method using bars has some inherent inaccuracies due to the geometric factor. In single crystals, an additional error arises from properly orienting the bar along the crystallographic direction of interest. Furthermore, all contacts have to be in a line along that direction to avoid contributions from off-diagonal tensor elements. This can partially be avoided by using plane samples. In methods such as the van der Pauw (vdP) method the geometric error can be reduced and with single crystals the error from orienting the bars can also be somewhat reduced. Furthermore, plane samples also allow extraction of off-diagonal tensor elements. This is especially useful for samples that are not single crystals.

This chapter is concerned with the development of theory for treating anisotropic samples in the vdP method. This has been studied to a limited degree in the literature previously; however, little work has been done on methods for extracting the full tensor using only standard vdP measurements. Either the tensor principal axes are assumed to be parallel to the sides of rectangular samples^{83, 84} or non-standard methods are developed⁸⁵⁻⁸⁹ to extract the full tensor. The most successful of the non-standard techniques uses 5 contacts on a rectangle (4 on corners, one placed on a side). This requires modification of both the instrument geometry and measurement procedure and is not readily applicable, especially with commercial setups. Here, the focus is on extracting information using only the standard vdP method on parallelogram shaped samples. Parallelograms is a relaxation of the requirements for the geometry compared to previous studies which all require rectangles. Since the problem is solved in a different way than that applied in the literature, both rectangular and parallelogram shaped samples are treated. This serves to verify the approach and compare to the few previously published results. For completeness, the 5-point vdP method is also adapted to allow for parallelogram shaped samples.

One advantage of this technique is from the fundamental similarity of conduction of heat and charge. All methods developed for electrical conduction can be used for heat conduction when the heat flow is used for current and temperature for electrostatic potential. The van der Pauw method has been extended to thermal conduction⁷⁰ and hence the theory developed in this Chapter is readily applicable to anisotropic conduction of heat.

This chapter has a very different appearance compared to the previous chapter. Describing equipment quickly turns into lengthy technical descriptions and discussions. This makes the text quite voluminous as is also apparent from the previous chapter. In contrary, this chapter is concerned with the development of a mathematical framework for analyzing data. This makes it much more compact and heavy. Even though this chapter is shorter, this still represents the main results in this thesis. When performing the work presented in this chapter a significant portion of the time was spent carrying out the necessary derivations. While this is important and time consuming, it can easily clutter the message if kept in the general text. For this reason all derivations which require more than a few lines of manipulation have been placed in the appendix. These derivations can be skipped if desired; only the main text is necessary to understand and apply the techniques.

4.1.1 Coordinate transformations

This section is intended as a short introduction to the tensor algebra used in the following sections. Knowledge of linear algebra is assumed and only the difference between tensors and matrices and specific applications to tensors are explained.

Let $\mathbf{A} = (a_{ij})$ be the matrix representing the coordinate transformation $H \rightarrow G$, where H has the basis $(\mathbf{x}_1, \mathbf{x}_2, \dots, \mathbf{x}_n)$ and G the basis $(\mathbf{u}_1, \mathbf{u}_2, \dots, \mathbf{u}_n)$. \mathbf{A} can be expressed in terms of the basis vectors as $\mathbf{A} = (\mathbf{x}_1^G, \mathbf{x}_2^G, \dots, \mathbf{x}_n^G)$ where \mathbf{x}_i^G is the i 'th basis vector for H expressed in the G coordinate system. That is $\mathbf{x}_i = a_{i1}\mathbf{u}_1 + a_{i2}\mathbf{u}_2 + \dots + a_{in}\mathbf{u}_n$ so that $\mathbf{x}_i^G = \begin{pmatrix} a_{i1} \\ \vdots \\ a_{in} \end{pmatrix}$ (or, for orthonormal bases, $a_{ij} = \mathbf{x}_i \cdot \mathbf{u}_j$). A vector \mathbf{z} , rank-2 tensor Ω , and matrix \mathbf{B} expressed in the H coordinate system can be transformed to the G system from

$$\mathbf{z}^G = \mathbf{A}^{-1}\mathbf{z}^H \quad (4-1.a)$$

$$\Omega^G = \mathbf{A}^T \Omega^H \mathbf{A} \quad (4-1.b)$$

$$\mathbf{B}^G = \mathbf{A}^{-1} \mathbf{B}^H \mathbf{A} \quad (4-1.c)$$

\mathbf{A}^T is the transpose of \mathbf{A} . The difference between (4-1.b) and (4-1.c) illustrates an important difference between matrices and tensors and that normal algebra for matrices is not always applicable to tensors. In fact, (4-1.b) is usually the definition for (rank-2) tensors. When only orthonormal bases are used, the distinction between (4-1.b) and (4-1.c) is not necessary since \mathbf{A} will be orthogonal ($\mathbf{A}^T \mathbf{A} = \mathbf{I}$) but transformations from Cartesian to oblique coordinate systems will occur later, and hence this distinction is necessary.

4.2 Extension of the theory

4.2.1 Change of coordinates

The goal is to calculate the electrostatic potential φ on a parallelogram-shaped sample with the current density \mathbf{j} . A change of coordinates defined by the matrix \mathbf{A} or $\mathbf{M} = \mathbf{A}^{-1}$ will be used to slightly rewrite the problem. \mathbf{A}^{-1} is non-singular (later \mathbf{M} is used; see below for an explanation). The standard transformation rule for vectors \mathbf{x} is $\mathbf{x}' = \mathbf{A}^{-1}\mathbf{x}$ (true for any non-singular \mathbf{A}). The prime is used to symbolize a transformed quantity.

The equation of continuity for the current density \mathbf{j} is (no net charge is entering or leaving the system)

$$\nabla \cdot \mathbf{j} = -\frac{\partial q}{\partial t} = 0 \quad (4-2)$$

$\nabla \cdot$ is the divergence operator. From the definition of conductivity σ (a rank-2 tensor)

$$\mathbf{j} = \boldsymbol{\sigma} \mathbf{E} = -\boldsymbol{\sigma} \nabla \varphi \quad (4-3)$$

\mathbf{E} is the electric field and ∇ is the gradient operator. In both cases $\nabla^T = \begin{pmatrix} \frac{\partial}{\partial x} & \frac{\partial}{\partial y} \end{pmatrix}$. Equation (4-2) and (4-3) together form the Laplace equation for an anisotropic medium

$$\nabla \cdot (\boldsymbol{\sigma} \mathbf{E}) = \nabla \cdot (\boldsymbol{\sigma} \nabla \varphi) = (\nabla^T \boldsymbol{\sigma} \nabla) \varphi = 0 \quad (4-4)$$

$\nabla^T \boldsymbol{\sigma} \nabla$ is the anisotropic Laplace operator and $\nabla \cdot = \nabla^T$ with the vector notation above.

Applying the change of coordinates to the Laplace operator gives

$$\nabla'^T \boldsymbol{\sigma}' \nabla' = (\mathbf{A}^{-1} \nabla)^T \boldsymbol{\sigma}' (\mathbf{A}^{-1} \nabla) = \nabla^T ((\mathbf{A}^{-1})^T \boldsymbol{\sigma}' \mathbf{A}^{-1}) \nabla \quad (4-5)$$

This is a change of coordinates and hence φ does not change itself: It is a physical quantity independent of the chosen basis. Applying the Laplace operator to it in any basis has to yield the same result. In other words, the Laplace operator has to be invariant under the change of coordinates, or

$$\boldsymbol{\sigma} = (\mathbf{A}^{-1})^T \boldsymbol{\sigma}' \mathbf{A}^{-1} = (\mathbf{A}^T)^{-1} \boldsymbol{\sigma}' \mathbf{A}^{-1} \quad (4-6)$$

And hence

$$\boldsymbol{\sigma}' = \mathbf{A}^T \boldsymbol{\sigma} \mathbf{A} \quad (4-7)$$

This is the standard transformation rule for tensors and expresses the conductivity tensor after the change of coordinates. In this thesis the resistivity is used and the transformation rule for this is then

$$\boldsymbol{\rho}' = (\boldsymbol{\sigma}')^{-1} = (\mathbf{A}^T \boldsymbol{\sigma} \mathbf{A})^{-1} = \mathbf{A}^{-1} \boldsymbol{\sigma}^{-1} (\mathbf{A}^T)^{-1} = \mathbf{A}^{-1} \boldsymbol{\rho} (\mathbf{A}^{-1})^T = \mathbf{M} \boldsymbol{\rho} \mathbf{M}^T \quad (4-8)$$

Hence the resistivity tensor transforms in a non-standard way. In terms of \mathbf{M} vectors transform as

$$\mathbf{x}' = \mathbf{M} \mathbf{x} \quad (4-9)$$

The last two equations are used below. The Laplace equation above does not represent the whole problem; The change of coordinates also has to be applied to the boundary conditions. These are:

- 1) Current cannot flow perpendicular to the sample circumference at the circumference.
- 2) Current can only enter and leave at two designated contacts and no net flux of charge into the sample is allowed ($\frac{\partial q}{\partial t} = 0$).

The circumference of the anisotropic sample is represented by two vectors along the AB and AD sides (See Figure 4-1 below for definitions). Boundary condition 1) is hence transformed by applying \mathbf{M} to these two vectors. By applying the transformation to the position vectors of the contacts 2) is also transformed.

In some cases it may be convenient to ‘rotate’ a tensor property inside a sample such as rotating the tensor from the principal axes system to the laboratory frame. In this case the transformation is not applied to the boundary conditions since these are already expressed in the lab frame. This can be done with the tensor \mathbf{R}^φ , which rotates in the positive direction

$$\mathbf{R}^\varphi = \begin{pmatrix} \cos(\varphi) & -\sin(\varphi) \\ \sin(\varphi) & \cos(\varphi) \end{pmatrix} \quad (4-10)$$

The inverse of a rotation in the positive direction is an equal rotation in the negative direction and hence

$$(\mathbf{R}^\varphi)^{-1} = \mathbf{R}^{-\varphi} = (\mathbf{R}^\varphi)^T \quad (4-11)$$

The magnitude of a tensor along a direction $\hat{\mathbf{x}}$ is $\hat{\mathbf{x}}^T \boldsymbol{\rho} \hat{\mathbf{x}}$. After rotating the tensor $\boldsymbol{\rho}$ to $\boldsymbol{\rho}'$, the magnitude along the rotated $\hat{\mathbf{x}}' = \mathbf{R}^\varphi \hat{\mathbf{x}}$ must be the same as along $\hat{\mathbf{x}}$ itself. Hence,

$$\hat{\mathbf{x}}'^T \boldsymbol{\rho}' \hat{\mathbf{x}}' = (\mathbf{R}^\varphi \hat{\mathbf{x}})^T \boldsymbol{\rho}' (\mathbf{R}^\varphi \hat{\mathbf{x}}) = \hat{\mathbf{x}}^T (\mathbf{R}^{-\varphi} \boldsymbol{\rho}' \mathbf{R}^\varphi) \hat{\mathbf{x}} = \hat{\mathbf{x}}^T \boldsymbol{\rho} \hat{\mathbf{x}} \quad (4-12)$$

From which

$$\boldsymbol{\rho}' = \mathbf{R}^\varphi \boldsymbol{\rho} \mathbf{R}^{-\varphi} = \mathbf{R}^\varphi \boldsymbol{\rho} (\mathbf{R}^\varphi)^T \quad (4-13)$$

This shows that the non-standard transformation rule also applies to this kind of transformations.

4.2.2 Isotropic equivalent sample

Consider the anisotropic sample in Figure 4-1 left. Its resistivity tensor has a principal axes with orthogonal unit vectors \mathbf{e}_1 and \mathbf{e}_2 which are assumed to be rotated at an angle φ in the negative direction relative to the sample frame spanned by x and y . The resistivity tensor expressed in the laboratory frame is then (a positive rotation)

$$\boldsymbol{\rho} = \mathbf{R}^\varphi \boldsymbol{\rho}_0 (\mathbf{R}^\varphi)^T = \begin{pmatrix} c^2 \rho_{11} + s^2 \rho_{22} & cs(\rho_{11} - \rho_{22}) \\ cs(\rho_{11} - \rho_{22}) & c^2 \rho_{22} + s^2 \rho_{11} \end{pmatrix} \equiv \begin{pmatrix} \rho_{xx} & \rho_{xy} \\ \rho_{xy} & \rho_{yy} \end{pmatrix} \quad (4-14)$$

Where $c = \cos(\varphi)$ and $s = \sin(\varphi)$. The form of the tensor at the right in Equation (4-14) is general, independent of the principal axis frame. ρ_{xx} and ρ_{yy} have to be positive while ρ_{xy} can have any sign. The tensor is always symmetric.⁹⁰

4.2.2.1 Anisotropic rectangles

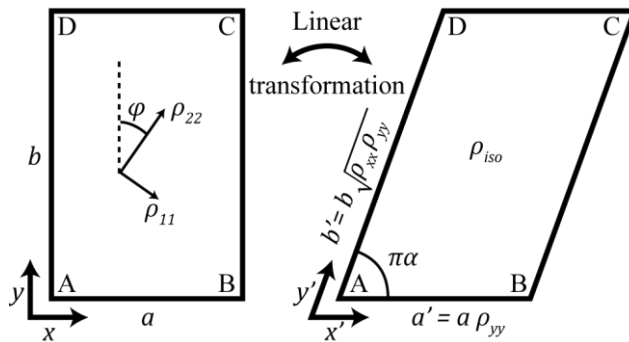


Figure 4-1: Illustration of the transformation of an anisotropic rectangle into an isotropic parallelogram. The transformation corresponds to a scaling and shearing.

Now, the change of coordinates, $x' = \rho_{yy}x - \rho_{xy}y$, $y' = \rho_{iso}y$ will be applied, as suggested by Kleiza *et al.*,⁸⁷ where the definition $\rho_{iso} = \sqrt{\det(\boldsymbol{\rho})} = \sqrt{\rho_{xx}\rho_{yy} - \rho_{xy}^2}$ is. The effect of the transformation is shown in Figure 4-1 above. The transformation is represented by the matrix $\mathbf{A} = \begin{pmatrix} \rho_{yy} & -\rho_{xy} \\ 0 & \rho_{iso} \end{pmatrix}$. Since $\det(\mathbf{A}) = \rho_{yy}\rho_{iso}$, this transformation does not conserve units of length, and the appropriate matrix to use is instead

$$\mathbf{M} = \frac{1}{\sqrt{\rho_{yy}\rho_{iso}}} \mathbf{A} = \frac{1}{\sqrt{\rho_{yy}\rho_{iso}}} \begin{pmatrix} \rho_{yy} & -\rho_{xy} \\ 0 & \rho_{iso} \end{pmatrix}. \quad (4-15)$$

Applying this to the resistivity tensor as outlined above gives

$$\boldsymbol{\rho} = \mathbf{M} \begin{pmatrix} \rho_{xx} & \rho_{xy} \\ \rho_{xy} & \rho_{yy} \end{pmatrix} \mathbf{M}^T = \begin{pmatrix} \rho_{iso} & 0 \\ 0 & \rho_{iso} \end{pmatrix} \quad (4-16)$$

This represents the tensor of an isotropic sample with resistivity ρ_{iso} . This transformation also needs to be applied to the boundary conditions, *i.e.* vectors spanning the sample, $\mathbf{a} = a \begin{pmatrix} 1 \\ 0 \end{pmatrix}$ and $\mathbf{b} = b \begin{pmatrix} 0 \\ 1 \end{pmatrix}$, as discussed in section 4.2.1. This gives $\mathbf{a}' = a\mathbf{M} \begin{pmatrix} 1 \\ 0 \end{pmatrix} = a \sqrt{\frac{\rho_{yy}}{\rho_{iso}}} \begin{pmatrix} 1 \\ 0 \end{pmatrix}$ and $\mathbf{b}' = b \sqrt{\frac{\rho_{xx}}{\rho_{yy}\rho_{iso}}} \begin{pmatrix} -\rho_{xy} \\ \rho_{iso} \end{pmatrix}$ which have lengths

$$a' = a \sqrt{\frac{\rho_{yy}}{\rho_{iso}}} \quad (4-17.a)$$

$$b' = b \sqrt{\frac{\rho_{xx}}{\rho_{iso}}} \quad (4-17.b)$$

The angle between the two sides can be calculated as

$$\cos(\pi\alpha) = \frac{\mathbf{a}' \cdot \mathbf{b}'}{a'b'} = -\frac{\rho_{xy}}{\sqrt{\rho_{xx}\rho_{yy}}} \quad (4-18)$$

Hence, after the transformation a parallelogram with isotropic resistivity is obtained. This will be called the isotropic equivalent sample since any resistance measurement performed on the anisotropic sample may equally be performed on the isotropic equivalent, provided the contact placement is correctly transformed by the matrix \mathbf{M} .

The orientation of the principal axis system of the tensor can be related to α by inserting the expressions for the tensor elements in terms of the principal system elements. After rewriting, the relation is $\cos(\pi\alpha) = \left(\frac{8\rho_{11}\rho_{22}}{(1-\cos(4\phi))(\rho_{11}-\rho_{22})^2} + 1 \right)^{-\frac{1}{2}}$. While this does not directly give α , it reduces the problem from three to two unknown parameters. This will be further explored in section 4.2.4.1 below.

The fact that the matrix \mathbf{A} defined above does not conserve length was not realized by Kleiza *et al.*^{87, 89} and Ašmontas *et al.*⁸⁸ in their papers, and hence their isotropic equivalent sample has wrong dimensions and resistivity. This is, however, not of importance to their final results since the absolute scaling is not of importance; only the aspect ratio is. It merely means that their isotropic equivalent sample cannot be constructed physically (its dimensions are in units of Ωm^2) and does not have resistivity ρ_{iso} as claimed. The original derivation is much more cumbersome than the one presented here and involves applying the change of coordinates in the explicit expressions for the 2D Laplace equation. The method using linear algebra presented here is much shorter and clearer.

4.2.2.2 Anisotropic parallelograms

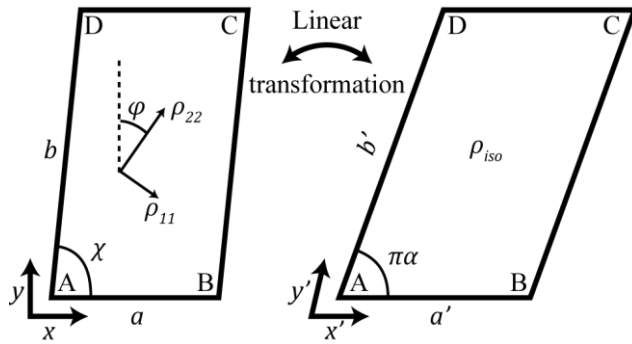


Figure 4-2: The transformation of an anisotropic to isotropic parallelogram. The transformation is the same as in Figure 4-1 but the resulting $\pi\alpha$ angle is different for the same orientation of the tensor principal axes relative to the lab frame (φ).

In the above derivation a rectangle was used. This is not strictly necessary: An anisotropic parallelogram is equally valid. See Figure 4-2. The sides of the sample are represented by the vectors $\mathbf{a} = a \begin{pmatrix} 1 \\ 0 \end{pmatrix}$ and $\mathbf{b} = b \begin{pmatrix} \cos(\chi) \\ \sin(\chi) \end{pmatrix}$, where χ is the angle of the A corner. Applying the transformation matrix from Equation (4-15) yields the vectors representing the sides of the isotropic equivalent, $\mathbf{a}' = a \sqrt{\frac{\rho_{yy}}{\rho_{iso}}} \begin{pmatrix} 1 \\ 0 \end{pmatrix}$ and $\mathbf{b}' = \frac{b}{\sqrt{\rho_{yy}\rho_{iso}}} \begin{pmatrix} \cos(\chi)\rho_{yy} - \sin(\chi)\rho_{xy} \\ \sin(\chi)\rho_{iso} \end{pmatrix}$. As above, the quantities of interest are the side lengths and angle between the sides of the isotropic equivalent sample. The derivation is slightly lengthy and not of general interest and is thus left for Appendix A.1. Here only the results are included. The side lengths are

$$a' = a \sqrt{\frac{\rho_{yy}}{\rho_{iso}}} \quad (4-19.a)$$

$$b' = b \sqrt{\cos^2(\chi) \frac{\rho_{yy}}{\rho_{iso}} + \sin^2(\chi) \frac{\rho_{xx}}{\rho_{iso}} - 2 \cos(\chi) \sin(\chi) \frac{\rho_{xy}}{\rho_{iso}}} \quad (4-19.b)$$

while the angle is

$$\cos(\pi\alpha) = \frac{1}{\sqrt{\rho_{yy}}} \frac{\cos(\chi)\rho_{yy} - \sin(\chi)\rho_{xy}}{\sqrt{\cos^2(\chi)\rho_{yy} + \sin^2(\chi)\rho_{xx} - 2 \cos(\chi) \sin(\chi) \frac{\rho_{xy}}{\rho_{iso}}}} \quad (4-20)$$

It should be noted that the results for the rectangular sample in Equations (4-17.a), (4-17.b), and (4-18) is reproduced when $\chi = 90^\circ$ is assumed ($\cos(\chi) = 0$ and $\sin(\chi) = 1$).

Both a rectangle and parallelogram will be used in the following for completeness. The math involved with a parallelogram is much more complicated than necessary to treat a rectangle and both are included to simplify treatment of data from rectangular samples. Since rectangles have been used in previous literature, this also provides a means for checking the procedure employed.

4.1.1 Conformal mapping from the complex half plane

When van der Pauw derived his equation, he used the mathematical technique of conformal mapping. A mapping is said to be conformal if angles are locally preserved. In his case it was enough to know that a conformal mapping from the upper complex half plane to any singly connected surface (*i.e.* without holes) in \mathbb{R}^2 . More mathematical requirements exist but these are not of physical interest. Since the mapping is conformal a solution to the Laplace equation on the half-plane will also map to a solution on the surface in \mathbb{R}^2 if the boundary conditions are also mapped. The real axis of the complex half plane will generally map to the circumference of the surface in \mathbb{R}^2 . By placing the contacts on the real axis they will also map to contacts on the circumference. The appropriate boundary condition in the complex half plane is that no current flows across the real axis and current may only enter and leave the sample at the contacts. This will result in no current leaving the surface in \mathbb{R}^2 other than at the contacts. These are the appropriate boundary conditions for calculating the resistances in the experiment. The fact that the distances between the contacts on the complex half plane are not of importance in the original derivation means that van der Pauw had to rely only on the existence of such a mapping. Now, an explicit expression for the mapping of the complex half plane to a certain shape, namely the isotropic equivalent sample (parallelogram) introduced above, will be used. The transformation is illustrated in Figure 4-3.

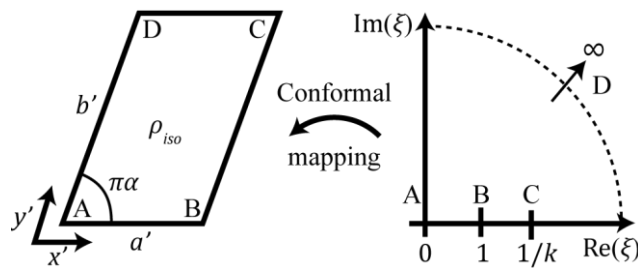


Figure 4-3: Illustration of the conformal mapping from the complex half plane to the isotropic equivalent. On the complex half plane, the corners A, B, and C correspond to 0, 1 and $1/k$ on the real axis while D corresponds to the limit of infinity on both the real and imaginary axes and anywhere in between. The real axis on the complex half plane maps to the circumference of the parallelogram.

A point $\xi = x + iy$ on the complex half plane is mapped to a point (x', y') (represented by $\xi' = x' + iy'$) via the function

$$\xi' = w(\xi) = \frac{a'}{A_{\alpha,k}} \int_0^\xi f_{\alpha,k}(z) dz \quad (4-21)$$

Where

$$A_{\alpha,k} = \int_0^1 f_{\alpha,k}(z) dz = \Gamma(\alpha)\Gamma(1-\alpha) {}_2F_1(\alpha, 1-\alpha; 1; k) \quad (4-22.a)$$

$$f_{\alpha,k}(z) = z^{\alpha-1} (1-z)^{-\alpha} (1-kz)^{\alpha-1} \quad (4-22.b)$$

$\Gamma(a)$ is the gamma function and ${}_2F_1(a, b; c; \mathbf{z})$ (a, b and c are real while \mathbf{z} is complex) is the Gaussian hypergeometric function. $a' = a\sqrt{\rho_{yy}/\rho_{iso}}$ is the AB side length of the isotropic equivalent sample along the x-axis and $a'/A_{\alpha, k}$ is a normalization factor. α and k are quantities to be determined experimentally and $0 < k, \alpha < 1$. The effect of this transformation is illustrated graphically in Figure 4-4. Lines on the complex half plane parallel (red) and perpendicular (blue) to the real axis are transformed via $w(\xi)$. On the parallelogram the red and blue lines always intercept at right angles, while lines of the same color never meet, as required for a conformal mapping. It is also noted that, strictly speaking, the transformation is only valid for $Im(\xi) > 0$, i.e. the real axis itself cannot be transformed since a straight line cannot be conformally mapped to sharp corners. This is of no physical significance but needs to be realized when making plots as in Figure 4-4.

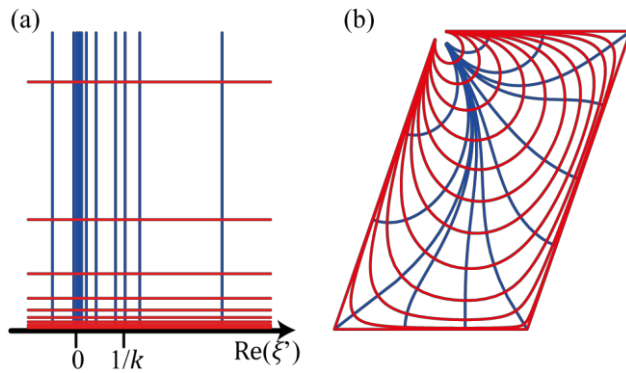


Figure 4-4: Illustration of the effect of the conformal mapping. Straight lines in the complex half plane in (a) are mapped onto lines on the parallelogram in (b). The full length of the lines used for the transformation is not shown in a), only the relative positions are correctly represented. Lines close to the real and imaginary axes are too close to properly resolve in a). For the mapping, $k = 0.1$ and $\alpha = 70/180$ was chosen to give a 70° corner in the isotropic equivalent sample.

4.2.2.3 Relating experiment to tensor elements

When passing current into an infinite plane conductor with resistivity ρ_{iso} and thickness d , the electric potential at a distance r from the contact is $U(r) = -\frac{I\rho_{iso}}{2\pi d} \ln(r)$, as derived in section 2.2.1 Equation (2-1). The boundary conditions in the complex half plane (no current flowing across the real axis) is reproduced by placing the contacts on the real. Hence, the simple case of an infinite plane can be used to calculate the potential on the half plane. The current entered into the contact is $2I$ to ensure a current of I flowing through the upper half plane. When passing a current from A to B in Figure 4-3 the electrical potential at C will be $U_C = \frac{I\rho_{iso}}{\pi d} (\ln(k^{-1} - 1) - \ln(k^{-1})) = \frac{I\rho_{iso}}{\pi d} \ln(1 - k)$. Similarly, the potential at D will be $U_D = \frac{I\rho_{iso}}{2\pi d} \lim_{r \rightarrow \infty} \ln\left(\frac{r-1}{r}\right) = 0$ and the resistance can be calculated. The resistances along the two edges and diagonal are thus

$$R_{AB,DC} = \frac{U_D - U_C}{I_{AB}} = \frac{-\rho_{iso}}{\pi d} \ln(1 - k) \quad (4-23.a)$$

$$R_{BC,AD} = \frac{-\rho_{iso}}{\pi d} \ln(k) \quad (4-23.b)$$

$$R_{AC,BD} = \frac{-\rho_{iso}}{\pi d} \ln(k^{-1} - 1) \quad (4-23.c)$$

By rearranging, taking the exponential, and adding the two first equations the VDP equation can easily be obtained. The third resistance corresponds to the diagonal resistance used for Hall effect measurements in the VDP geometry. The calculated resistance is the offset resistance due to contact misalignment.⁵⁶ It is noted that it has the correct limits: For $k = 0.5$ corresponding to $a' = b'$ the resistance vanishes; When k is close to 1 (0), corresponding to $a' \gg b'$ ($a' \ll b'$), $R_{AC,BD}$ approaches $R_{AB,DC}$ ($R_{BC,AD}$).

The three equations above are not independent. After solving the vdp equation only one of the measured resistances is necessary to extract k while no information about α can be obtained from resistance measurements in this geometry. How to obtain this is addressed later. From the VDP equation, ρ_{iso} is obtained,

$$\sqrt{\rho_{xx}\rho_{yy} - \rho_{xy}^2} = \rho_{iso} \quad (4-24)$$

By calculating the side length b' from the conformal mapping a further relation can be obtained

$$b' = b \sqrt{\frac{\rho_{xx}}{\rho_{iso}}} = \frac{a'}{A_{\alpha,k}} \int_1^{k^{-1}} |f_{\alpha,k}(z)| dz = \frac{a'}{A_{\alpha,k}} \int_0^1 |f_{\alpha,1-k}(z)| dz = \frac{a' A_{\alpha,1-k}}{A_{\alpha,k}} \quad (4-25)$$

The third equality represents a cyclic permutation of contact names ($A' = B$, $B' = C$ etc) so that $\alpha' = 1 - \alpha$, $k' = 1 - k$.

Or, introducing $B_{\alpha,k} = \frac{A_{\alpha,1-k}}{A_{\alpha,k}} = \frac{{}_2F_1(\alpha, 1-\alpha; 1-k)}{{}_2F_1(\alpha, 1-\alpha; k)}$,

$$\sqrt{\frac{\rho_{xx}}{\rho_{yy}}} = \frac{a}{b} B_{\alpha,k} \quad (4-26)$$

A third equation is obtained from the linear transformation,

$$\cos(\pi\alpha) = -\frac{\rho_{xy}}{\sqrt{\rho_{xx}\rho_{yy}}} \quad (4-27)$$

This gives three equations for the four parameters ρ_{xx} , ρ_{yy} , ρ_{xy} , and α , when k and ρ_{iso} has been determined from the experiment. All tensor elements can be expressed in terms of α (for the derivation see Appendix A.2):

$$\rho_{xx} = rB_{\alpha,k}\lambda_\alpha \quad (4-28.a)$$

$$\rho_{yy} = r^{-1}B_{\alpha,k}^{-1}\lambda_\alpha \quad (4-28.b)$$

$$\rho_{xy} = -\lambda_\alpha \cos(\pi\alpha) \quad (4-28.c)$$

Here $\lambda_\alpha = \rho_{iso}/\sin(\pi\alpha)$ and $r = a/b$. The remaining task now is to find ways to determine α . The simplest case, when the principal axes are parallel to the edges of the sample, simply corresponds to $\alpha = 0.5$ (only for rectangles, not general parallelograms). If the orientation of the principal axes are known but not parallel to the sides, sufficient information to solve the problem is provided, even though alpha cannot be calculated directly from this angle. How this can be used will be discussed later.

If no additional information about the tensor is known, assuming $\alpha = 0.5$ still yields important information. In Figure 4-5 (a) the tensor elements are calculated as a function of orientation when $\alpha = 0.5$ is assumed in Equation (4-28.a) and (4-28.b). As can be seen, the calculated anisotropy (defined as ρ_{11}/ρ_{22}) is never greater than the correct anisotropy (that is, further from unity), which is obtained for $\varphi = 0^\circ$ and $\varphi = 90^\circ$. Hence, this can be used as a quick test for anisotropy since a sample will never be less anisotropic than the estimate provided by this. Not observing anisotropy is not a guarantee that the sample is isotropic; however, it is highly unlikely that $\varphi = 45^\circ$ was obtained by accident. If no anisotropy is measured, cutting a new rectangle from the original with new orientation of the sides will give another estimate of the minimum anisotropy. If no anisotropy is obtained for the second rectangle, the sample must be isotropic, provided the rectangles are not related by a 90° rotation. This can in fact be used for obtaining the full tensor, as will be discussed later.

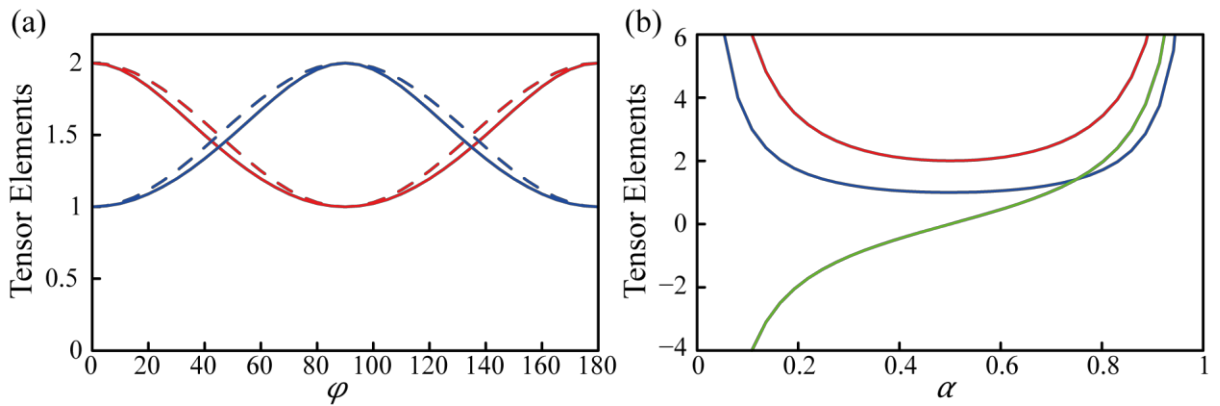


Figure 4-5: Calculated ρ_{xx} (red), ρ_{yy} (blue) and ρ_{xy} (green) as a function of (a) correct tensor orientation φ when $\alpha = 0.5$ is assumed and (b) α used in the calculation when $\varphi = 0^\circ$. The dashed lines in (a) represent the magnitude of the tensor along x and y calculated from the correct tensor. Hence the $\alpha = 0$ calculation is a good estimate of the resistivity along the two directions.

4.2.2.4 Anisotropic parallelogram

Equation (4-28.a) to (4-28.c) can be rewritten to accommodate the anisotropic parallelogram. The derivations are only sketched here since they are rather lengthy but can be found at full length in Appendix A.3. The definition of ρ_{iso} , equation (4-24), is still valid, while equation (4-26) and (4-27) are substituted by

$$rB_{\alpha,k} = \frac{\sqrt{\cos^2(\chi)\rho_{yy} + \sin^2(\chi)\rho_{xx} - \cos(\chi)\sin(\chi)\rho_{xy}}}{\sqrt{\rho_{yy}}} \quad (4-29.a)$$

$$\cos(\pi\alpha) = \frac{1}{\sqrt{\rho_{yy}}} \frac{\cos(\chi)\rho_{yy} - \sin(\chi)\rho_{xy}}{\sqrt{\cos^2(\chi)\rho_{yy} + \sin^2(\chi)\rho_{xx} - 2\cos(\chi)\sin(\chi)\rho_{xy}}} \quad (4-29.b)$$

Equation (4-29.a) is derived using equation (4-26) and the side lengths derived for the isotropic equivalent in section 4.2.2.2 which also contains the derivation of Equation (4-29.b). If $\chi = 90^\circ$ is used in these equations the equations for rectangular samples are obtained. From equation (4-24), (4-29.a), and (4-29.b) the tensor components can be expressed in terms of known parameters and α :

$$\rho_{xx} = \frac{1}{\sin(\chi)} rB_{\alpha,k} \lambda_\alpha + \frac{\cos(\chi)}{\sin(\chi)} \lambda_\alpha (\cos(\chi) r^{-1} B_{\alpha,k}^{-1} - 2 \cos(\pi\alpha)) \quad (4-30.a)$$

$$\rho_{yy} = \sin(\chi) r^{-1} B_{\alpha,k}^{-1} \lambda_\alpha \quad (4-30.b)$$

$$\rho_{xy} = \cos(\chi) r^{-1} B_{\alpha,k}^{-1} \lambda_\alpha - \lambda_\alpha \cos(\pi\alpha) \quad (4-30.c)$$

Once again, if $\chi = 90^\circ$ is used the expressions for the rectangular anisotropic sample in equation (4-28.a) to (4-28.c) are obtained. λ_α , r , and $B_{\alpha,k}$ has the same meaning as above.

4.2.3 Known methods

Few studies deal with anisotropic resistivity in plane samples and none extracts the full tensor from a standard vdp measurement or uses parallelogram shaped samples. The approach chosen in the early literature is to assume the tensor principal axes to be parallel to the sides of a rectangular sample. This is equivalent to only allowing $\alpha = 0.5$. This has been solved using both geometric considerations⁸⁴ and the method of image poles.⁸³ For the full tensor (general α) extended contacts along the full length of two sides of a rectangle and point contacts on the other sides has been extensively used.⁸⁵⁻⁸⁷ This is difficult to apply experimentally since extended contacts of uniform quality are difficult to achieve. The extended contacts are assumed to have a constant electrostatic potential. This means they have to be made from a much more conductive material than the sample and the contact resistance has to be low, preferably 0. Otherwise the electrostatic potential just inside the sample will not be constant. These types of measurements are not related to the vdp method but the theory is similar.

Two approaches have been suggested using a slightly modified vdp method. In one,⁸⁹ a third experiment is performed (with the same contacts) where a potential is applied along each diagonal in turn and the two resulting currents are measured. The ratio of the two currents can be used to extract α . This only requires a slight modification of the measurement procedure but no modification of the instrument itself (provided the contacts can be connected to the current source and voltmeter in the correct way). For this to work the contact and lead resistances have to all be zero. This is not experimentally realizable, especially for intrinsic semiconductors where Shottky barriers can be a significant problem. In the second method a fifth contact is added at a point along the AB side on a rectangular sample. The position of the fifth contact needs to be known. While this is possible experimentally, it may be difficult to measure with sufficient accuracy, especially on small samples. Nonetheless, this is the most promising approach and the only approach which does not pose any significant problems with the resistance measurements.

4.2.3.1 5-point method

The goal of this section is to extend the 5-point vdp method developed by Ašmontas *et al.*⁸⁸ to accommodate parallelogram shaped samples. The sample and contact placement is shown in Figure 4-6 (a) and the contact positions on the complex plane in (b) after mapping. The new E contact is placed at a distance a_2 along the AB side with total length a . E maps to the position $0 < m < 1$ on the real axis on the complex plane.

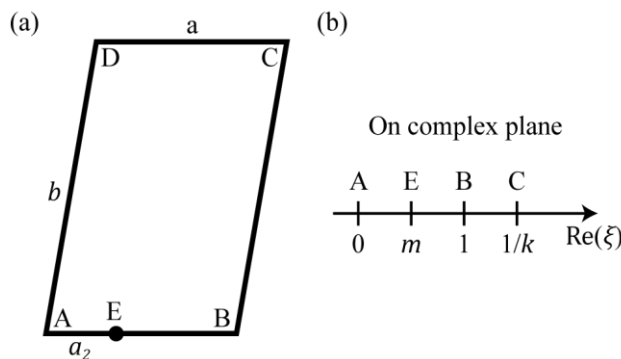


Figure 4-6: (a) Anisotropic sample with contact placement; (b) Images of the contacts on the real axis on the complex half plane. In (a) the length a_2 is between the A and E contacts while the sample itself still has side lengths a and b and angle χ (not shown). The E contact maps to the position $0 < m < 1$ on the complex plane while contacts A through E maintain their usual positions.

m can be determined from experiment like k . There are 4 ways to select 4 contacts that include contact E from the total of 5 contacts. For each group, two distinct resistances can be measured which have to fulfill the vdp equation. Here, one resistance from each group is calculated. These are obtained in the same way as Equation (4-23.a) to (4-23.c) and are shown below.

$$R_{DC,AE} = \frac{-\rho_{iso}}{\pi d} \ln \left(\frac{k^{-1}-m}{k^{-1}} \right) \quad (4-31.a)$$

$$R_{DC,EB} = \frac{-\rho_{iso}}{\pi d} \ln \left(\frac{k^{-1}-1}{k^{-1}-m} \right) \quad (4-31.b)$$

$$R_{BC,EA} = \frac{-\rho_{iso}}{\pi d} \ln \left(\frac{1-m}{1-mk} \right) \quad (4-31.c)$$

$$R_{AD,EB} = \frac{-\rho_{iso}}{\pi d} \ln(m) \quad (4-31.d)$$

Only the resistances giving distinct values are shown. Each one can be measured in a total of four different ways, corresponding to switching current direction, interchanging voltage and current contacts, and combining both. The 4 resistances in Equation (4-31.a) to (4-31.d) are related to the other resistance in the respective group by exchanging the term in the logarithm by 1 minus the same term. For instance, in Equation (4-31.d) $\ln(m)$ becomes $\ln(1 - m)$. This follows directly from the vdP equation. Any one of the total of 8 resistances can be used to obtain m .

In the isotropic equivalent sample, both contact B and E map to the AB side with a factor $\sqrt{\rho_{yy}/\rho_{iso}}$ on their positions, which are then $a' = a\sqrt{\rho_{yy}/\rho_{iso}}$ and $a'_2 = a_2\sqrt{\rho_{yy}/\rho_{iso}}$, respectively. From the complex plane they map via Equation (4-21). The two mapped distances have to be identical, giving the equation

$$\frac{a'_2}{a'} = \frac{\frac{a'}{A_{\alpha,k}} \int_0^m f_{\alpha,k}(z) dz}{\frac{a'}{A_{\alpha,k}} \int_0^1 f_{\alpha,k}(z) dz} = \frac{\int_0^m f_{\alpha,k}(z) dz}{A_{\alpha,k}} = \frac{a_2}{a} \equiv r_2 \quad (4-32)$$

The first equality is from equating the two mappings, the second follows from Equation (4-22.a), and third is due to the $\sqrt{\rho_{yy}/\rho_{iso}}$ factors cancelling. The last equation provides a means for extracting α since this is the only unknown parameter. It cannot be solved explicitly but can be solved numerically. A MATLAB™ is provided in Appendix B.12. Equation (4-32) can be rewritten as $(\int_0^m f_{\alpha,k}(z) dz / A_{\alpha,k}) - r_2 = 0$. The left hand side of this is plotted in Figure 4-7 as a function of α for various input parameters (m , α , and k extracted from various sample geometries and tensors). Due to the $\Gamma(\alpha)\Gamma(1 - \alpha)$ factor (see Equation (4-22.a)), $A_{\alpha,k}$ approaches infinity as α approaches 0 or 1. The left hand side of the equation will then approach $-r_2$ in both cases since the integral stays finite. Hence, the equation will always have two solutions (unless the maximum corresponds to the zero point), as is also seen in Figure 4-7. No comments were made on this in the original publication by Ašmontas *et al.*⁸⁸ In all cases in Figure 4-7 the correct solution is the right most one, unfortunately this is not always so. For very low α the leftmost solution is in some cases the correct one (can be explored by generating more of these plots). No simple tests can be made to determine which solution is correct and hence it will have to be done theoretically. Before

this is solved the 5-point method is only strictly useable when additional information or an estimate of α is available.

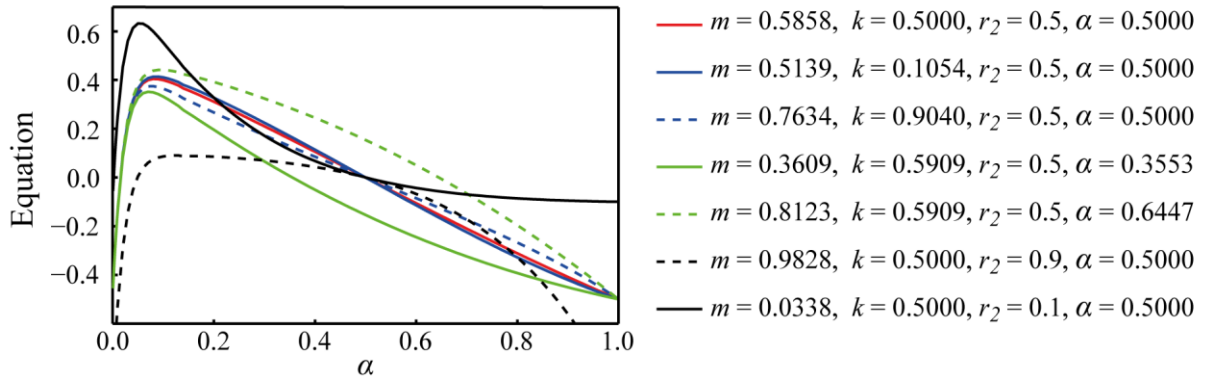


Figure 4-7: Plots of the equation which determines α from a 5-point measurement. Different input parameters have been used to plot the lines to illustrate the effect of the different parameters. Red is the parent line. Blue is different k (made by changing ρ_{11}/ρ_{22}). Green is different α (calculated by changing φ compared to the dashed blue line). Black is for different r_2 . All parameters have been varied by changing either assumed input tensor elements or sample geometry; hence more than one parameter is sometimes changed at a time.

It may be tempting to simply use the resistance in (4-31.d) for extracting m . This is not always the optimal choice since uncertainties in the E contact position affects the measured m more if the voltage contacts are at positions with high current density. High current density also means large spatial variation in the electrostatic potential and hence uncertainty in the measured resistance. It is hence best to keep current and voltage contacts well separated. Since the current distribution is affected by the resistivity tensor this criteria needs to be applied to the isotropic equivalent sample. This makes choosing an appropriate resistance difficult before all measurements have been performed and the equations solved. One possibility is to use an initial measurement to solve the equations, do an error analysis on all possible resistances (8 in total), measure the one with lowest errors, and use a refined m to solve the equations again. Additionally, there are two possible orientations for the sample. Giving strict guidelines for which one to choose is not easy as it depends on several parameters. This can also be solved by an error analysis after an initial measurement when an approximate tensor is known. How to do this error analysis will be discussed later.

The equations above only depend on the AB side of the anisotropic and isotropic samples. These are not affected when going from rectangular to parallelogram shaped samples and hence the method is directly applicable to both provided the correct set of equations is used to calculate the tensor after α has been obtained.

4.2.4 New methods

4.2.4.1 Principal axes in crystals

When the orientation of the tensor is known, as indicated in Figure 4-1, the tensor elements can be expressed in terms of the elements along the principal axes and the orientation from Equation (4-14) and (4-28.a) to (4-28.c):

$$\rho_{xx} = \cos^2(\varphi) \rho_{11} + \sin^2(\varphi) \rho_{22} = rB_{\alpha,k}\lambda_\alpha \quad (4-33.a)$$

$$\rho_{yy} = \sin^2(\varphi) \rho_{11} + \cos^2(\varphi) \rho_{22} = r^{-1}B_{\alpha,k}^{-1}\lambda_\alpha \quad (4-33.b)$$

$$\rho_{xy} = \cos(\varphi) \sin(\varphi) (\rho_{11} - \rho_{22}) = -\lambda_\alpha \cos(\pi\alpha) \quad (4-33.c)$$

This can be rewritten into an equation for α which needs to be solved numerically. The derivation is easily done by taking the difference of the first two equations, multiplying by $\cos(\varphi) \sin(\varphi)$ and simplifying using the third equation. This gives

$$0 = (\tan(\varphi) - \tan(\varphi)^{-1}) \cos(\pi\alpha) - rB_{\alpha,k} + r^{-1}B_{\alpha,k}^{-1} \quad (4-34)$$

Once k has been obtained from the experiment this equation relates α to φ and the full tensor can be obtained. This is readily applicable to single crystals, since knowledge of the orientation of the unit cell axes also gives the principal axis system for all crystal classes except triclinic, which are rarely encountered as semiconductors or metals.

In the case of single crystals it may be particularly advantageous to use samples shaped as parallelograms since the available sample area is small. The equations derived above can also be derived using Equation (4-30.a) to (4-30.c) for parallelograms. The derivation is slightly more involved but follows the same procedure. It can be found in Appendix A.4 and the result is

$$0 = (\tan(\varphi)^{-1} - \tan(\varphi) - \tan(\chi)^{-1})(\cos(\chi) r^{-1}B_{\alpha,k}^{-1} - \cos(\pi\alpha)) - \frac{1}{\sin(\chi)} rB_{\alpha,k} + \sin(\chi) r^{-1}B_{\alpha,k}^{-1} + \tan(\chi)^{-1} \cos(\pi\alpha) \quad (4-35)$$

This equation is not valid for $\varphi = n\pi/2$. This corresponds to the tensor principal axes and laboratory axes being identical and this can hence be solved by other means (redoing the derivation with $\varphi = n\pi/2$ gives a simple expression). Additionally, it is not strictly defined for $\chi = 90$ but the limit exists and reproduces Equation (4-34). Equation (4-35) can easily be solved for α numerically using the Newton-Raphson method. However, depending on the φ , χ , and k , there can be one or two solutions. Naming the right hand side of the equation $f(\alpha)$ the problem is to solve $f(\alpha) = 0$ in the interval $0 < \alpha < 1$. $f(\alpha)$ will in most cases have an extremum (but never more than 1), and the solution will be on either or both sides of this. By finding the extremum (solving $f'(\alpha) = 0$, f' being the derivative with respect to α) helps

finding an appropriate starting guess. If α_e is the solution to $f'(\alpha) = 0$, $f(\alpha) = 0$ will have a solution between α_e and 1 if $f(\alpha)$ and $f(1)$ have opposite signs, and similarly for 0 and α_e . Both solutions can be used to construct a tensor from equation (4-30.a) to (4-30.c); however, only one of these will be diagonal when rotated φ in the negative direction (see Figure 4-2). This can be used to determine which solution is correct. Since only one solution is appropriate, the relation between the two solutions has not been studied analytically.

The full process of solving $f(\alpha) = 0$ is then

- If $f'(0)$ and $f'(1)$ have opposite signs there is an extremum. Find this using the Newton-Raphson method (starting guess $\alpha = 0.5$). The solution will be called α_e .
- Depending on the signs of $f(\alpha_e)$, $f(1)$ and $f(0)$ find the solutions on both sides of α_e . Appropriate starting guesses are $1 + \alpha_e/2$ and $\alpha_e/2$.
- If there are two solutions, rotate the tensors corresponding to both solutions φ in the negative direction and keep only the solution giving a diagonal tensor.

This is illustrated in Figure 4-8. A tensor of $\begin{pmatrix} 1 & 0 \\ 0 & 2 \end{pmatrix}$ in the principal axis system was assumed (arbitrary units) with a rotation of $\varphi = 20^\circ$ or 40° relative to the sample frame. $\chi = 90^\circ$ was used corresponding to a rectangular sample. From this, both ρ_{iso} and k can be calculated, thus simulating the output from an experiment. By solving Equation (4-35) for this input and comparing to the assumed starting tensor, the validity of the approach can be verified. In the case of $\varphi = 20^\circ$ only one solution was found and this reproduced the correct tensor. For the case of $\varphi = 40^\circ$ two solutions were found, $\alpha_1 = 0.208$ and $\alpha_2 = 0.607$. After calculating the corresponding tensor and rotating by 40° in the negative direction, the two tensors $\rho_1 = \begin{pmatrix} 1.97 & 0.171 \\ 0.171 & 1.03 \end{pmatrix}$ and $\rho_2 = \begin{pmatrix} 1 & 0 \\ 0 & 2 \end{pmatrix}$ was obtained. Clearly, only α_2 yields a diagonal tensor as expected in the principal axis system and α_1 is rejected. A MATLABTM script for solving this equation is found in Appendix B.10.

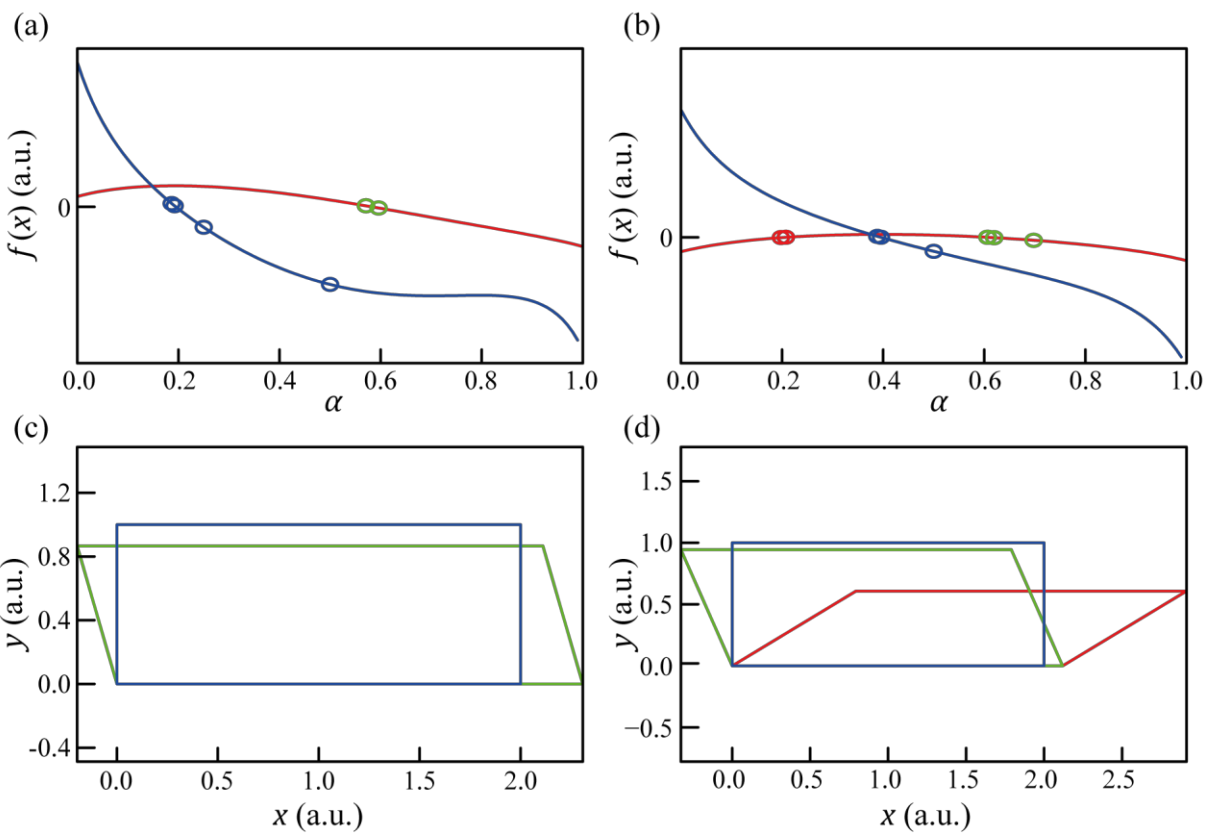


Figure 4-8: Illustration of the solution to Equation (4-35). In (a) and (b) the right side of the equation is shown (red) with its derivative (blue). Circles mark the iterative improvement of the zero-points. In (b) the equation has two solutions marked with green and red circles. In (c) and (d) the corresponding geometries of the anisotropic sample (blue) and isotropic equivalent samples are shown. In (c) there is only one solution (green), while in d) there are two (correct green, wrong red). See the text for details on the used parameters.

The symmetry of the crystal determines the possible tensors since the symmetry of a physical property can never be lower than the symmetry of the crystal (Neumann's principle). It is sufficient to consider the crystal class since these determine the symmetry of the unit cell and hence tensor. In Table 4-1 below the defining symmetry elements and resulting tensor in the unit cell axes frame are summarized.

Table 4-1: Possible tensors in the unit cell axes frame. The c-axis is the unique axis in all cases to simplify the tensor. This is non-standard for the monoclinic class where the b-axis is normally chosen to be unique.

Crystal class	Defining symmetry	Axes and angles	Possible tensor
Triclinic	None.	$a \neq b \neq c$ $\alpha, \beta, \gamma \neq 90^\circ$	$\begin{pmatrix} \rho_{11} & \rho_{12} & \rho_{13} \\ \rho_{12} & \rho_{22} & \rho_{23} \\ \rho_{13} & \rho_{23} & \rho_{33} \end{pmatrix}$
Monoclinic	1 2-fold axis or 1 mirror plane.	$a \neq b \neq c$ $\alpha, \beta = 90^\circ, \gamma \neq 90^\circ$	$\begin{pmatrix} \rho_{11} & \rho_{12} & 0 \\ \rho_{12} & \rho_{22} & 0 \\ 0 & 0 & \rho_{33} \end{pmatrix}$
Orthorhombic	3 2-fold axes or 1 2-fold axis and 2 mirror planes.	$a \neq b \neq c$ $\alpha = \beta = \gamma = 90^\circ$	$\begin{pmatrix} \rho_1 & 0 & 0 \\ 0 & \rho_2 & 0 \\ 0 & 0 & \rho_3 \end{pmatrix}$
Hexagonal	1 3- or 6-fold axis.	$a = b \neq c$ $\alpha, \beta = 90^\circ, \gamma = 120^\circ$	$\begin{pmatrix} \rho_1 & 0 & 0 \\ 0 & \rho_1 & 0 \\ 0 & 0 & \rho_2 \end{pmatrix}$
Tetragonal	1 4-fold axis.	$a = b \neq c$ $\alpha = \beta = \gamma = 90^\circ$	$\begin{pmatrix} \rho_1 & 0 & 0 \\ 0 & \rho_1 & 0 \\ 0 & 0 & \rho_2 \end{pmatrix}$
Cubic	4 3-fold axes.	$a = b = c$ $\alpha = \beta = \gamma = 90^\circ$	$\begin{pmatrix} \rho & 0 & 0 \\ 0 & \rho & 0 \\ 0 & 0 & \rho \end{pmatrix}$

4.2.4.2 Changing tensor orientation

In this section a method for extracting the tensor from large samples where the tensor orientation is not known is discussed. The first part is concerned with rectangles since the math is much more tractable for this case and allows explicit expressions. For parallelograms the expressions become excessively long and provide no additional insight. The principle is to reshape the sample to gain additional information that allows the extraction of the full tensor from two measurements with four probes.

For rectangles, cutting a smaller rectangle with a known orientation from the original one is used. This is illustrated in Figure 4-9. The two rectangles need not have the same aspect ratios, that is $a_A/b_A = a_B/b_B$ is not required where A and B are the two rectangles. It is important to pay attention to the sign of θ : The rotation of the second rectangle relative to the first has the opposite sign of the rotation of the tensor principal axes.

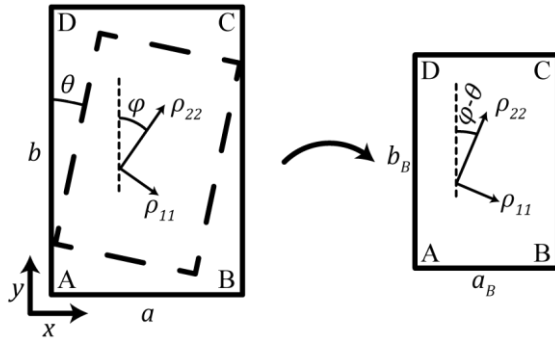


Figure 4-9: Reshaping a sample with a known angle can be used to calculate the tensor elements. The aspect ratio of the two samples is not required to be identical. The angle θ needs to be accurately determined and the sign is important. In this example θ is positive.

For sample A the set of equations (4-28.a) to (4-28.c) must be fulfilled with both $k = k_A$ and ρ_{iso} known from the experiment and an unknown α . The same is true for B with the same ρ_{iso} but different $k = k_B$ and α , now called β to more easily distinguish. The two tensors only differ by a rotation by θ in the negative direction (from B to A) and hence $\boldsymbol{\rho}_A = (\mathbf{R}^\theta)' \boldsymbol{\rho}_B \mathbf{R}^\theta$. Or, using the abbreviations $c = \cos \theta$ and $s = \sin \theta$ and equation (4-28.a) to (4-28.c) for sample A and B

$$\rho_{xx} = r_A B_{\alpha, k_A} \lambda_\alpha = c^2 \{r_B B_{\beta, k_B} \lambda_\beta\} + s^2 \{r_B^{-1} B_{\beta, k_B}^{-1} \lambda_\beta\} + 2cs \{\lambda_\beta \cos(\pi\beta)\} \quad (4-36.a)$$

$$\rho_{yy} = r_A^{-1} B_{\alpha, k_A}^{-1} \lambda_\alpha = c^2 \{r_B^{-1} B_{\beta, k_B}^{-1} \lambda_\beta\} + s^2 \{r_B B_{\beta, k_B} \lambda_\beta\} - 2cs \{\lambda_\beta \cos(\pi\beta)\} \quad (4-36.b)$$

$$\rho_{xy} = \lambda_\alpha \cos(\pi\alpha) = (1 - 2s^2) \{\lambda_\beta \cos(\pi\beta)\} + cs \{r_B^{-1} B_{\beta, k_B}^{-1} \lambda_\beta - r_B B_{\beta, k_B} \lambda_\beta\} \quad (4-36.c)$$

While this seems intractable the right hand side simply provides a set of parametric equations in the two parameters α and β . Each line defines a 2D surface on (α, β) . Define the vector:

$$\mathbf{d} = \begin{pmatrix} [c^2 \{r_B B_{\beta, k_B} \lambda_\beta\} + s^2 \{r_B^{-1} B_{\beta, k_B}^{-1} \lambda_\beta\} + 2cs \{\lambda_\beta \cos(\pi\beta)\}] - r_A B_{\alpha, k_A} \lambda_\alpha \\ [c^2 \{r_B^{-1} B_{\beta, k_B}^{-1} \lambda_\beta\} + s^2 \{r_B B_{\beta, k_B} \lambda_\beta\} - 2cs \{\lambda_\beta \cos(\pi\beta)\}] - r_A^{-1} B_{\alpha, k_A}^{-1} \lambda_\alpha \\ [(1 - 2s^2) \{\lambda_\beta \cos(\pi\beta)\} + cs \{r_B^{-1} B_{\beta, k_B}^{-1} \lambda_\beta - r_B B_{\beta, k_B} \lambda_\beta\}] - \lambda_\alpha \cos(\pi\alpha) \end{pmatrix} \quad (4-37)$$

The Equations (4-36.a) to (4-36.c) now corresponds to $\mathbf{d} = 0$.

The same can be done for parallelograms but here the equations become excessively lengthy and will not be shown. There are also many more possibilities for reshaping the sample. Two possibilities are shown in Figure 4-10 where the central sample is changed in two ways. Now, θ can be 0; both the sign and size is still important. It is somewhat simplified since θ is in the cases below related to the change in the χ angle, which can be much more easily determined than θ itself.

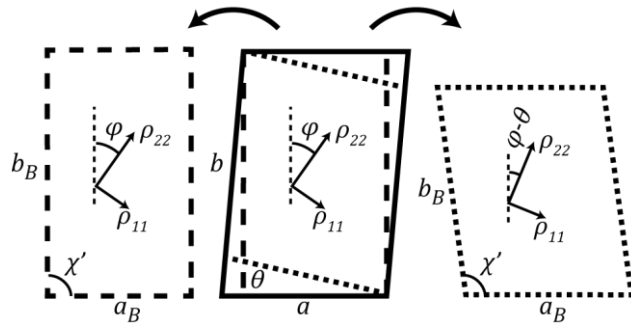


Figure 4-10: Reshaping a parallelogram shaped sample. Many more possibilities exist for this, two of which are shown here starting from the central sample. Going left, only χ is changed. Going right, both χ and φ are changed and now become $\chi' = \chi + \theta$ and $\varphi' = \varphi - \theta$.

The problem is in both cases is to solve $\mathbf{d} = 0$. This can be done in several ways, either by considering it as three equations that needs to be solved simultaneously or by solving $|\mathbf{d}| = 0$ or $\mathbf{d}^2 = 0$. The latter two reduces the problem to finding the zero-point of one surface. The zero point will also be a minimum. This can be solved using standard mathematical software and numerical methods, either the method of steepest descent or Newton's method. Since \mathbf{d}^2 is approximately quadratic close to the solution, Newton's method is a good candidate for solving this. It is necessary to calculate both the gradient vector and Hessian matrix in each iteration. This extends the time necessary for the calculation but makes the algorithm more stable and reduces the number of steps necessary. Typically, on the order of 20 iterations are needed which takes about 30 seconds (depending on processor speed). A script for solving this equation is found in Appendix B.11.

An example of solving this is given in Figure 4-11. A simulated case has been successfully solved using Newton's method. Referring to Figure 4-10, the input parameters for sample A were $\chi_A = 70^\circ$, $\rho_0 = \begin{pmatrix} 1 & 0 \\ 0 & 2 \end{pmatrix}$, $\varphi = 40^\circ$, and $r_A = 2$. For B, which was rotated with $\theta = 30^\circ$, the parameters used were $\chi_B = 100^\circ$, $r_B = 1.8$ was used. This approximately resembles going from the middle to the right sample in Figure 4-10. From this ρ in both samples was calculated together with the dimensions of the isotropic equivalent which in turn was used for extracting k . This simulates an experiment by providing both ρ_{iso} and k , which are determined by experiment. α and β were found by solving $\mathbf{d}^2 = 0$ for parallelogram shaped samples, which correctly reproduced $\alpha = 0.30$ and $\beta = 0.54$. The starting guess was $\alpha = \beta = 0.5$. As can be seen in Figure 4-8, Newton's method doesn't follow the path of steepest descent but converges faster since the quadrature is used. The below example used 20 steps to get a relative tolerance better than 10^{-6} . The exact criterion was $\mathbf{d}^2 < 10^{-12} \cdot \rho_{iso}^2$.

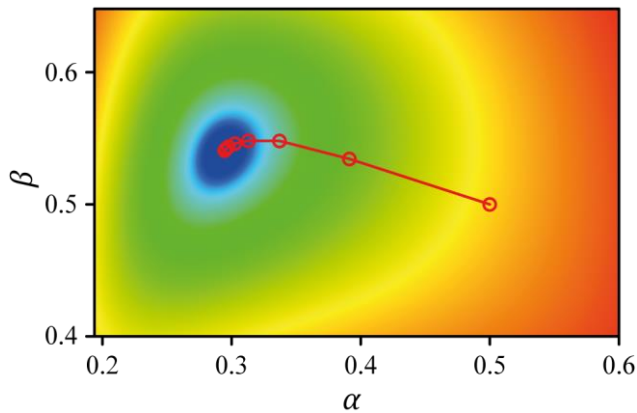


Figure 4-11: d^2 as a function of α and β . Red corresponds to high d^2 while blue is low. The color scale is logarithmic. The function has only one zero-point corresponding to its global minimum, which has been located using Newton's method. The red line and circles illustrate the iterative improvement of the starting guess $\alpha = \beta = 0.5$.

4.2.5 Verification

This section provides numerical and experimental tests for the different parts of the theory. Above, simulations were used to ensure the rigidity of the theoretical framework. It was demonstrated that the methods intended for treatment of experimental data would reach the same results as those reached from complete knowledge of the problem, namely tensors, their orientations and sample geometries of both the anisotropic and isotropic equivalent samples. This ensures both that the theory is internally consistent and that the numerical methods for data treatment have been correctly applied. Here, different sources of errors are explored numerically and experimentally, and the methods are tested experimentally. In the end, measurements of a real system will be shown and discussed.

4.2.6 Numerical error analysis

Deriving explicit, even approximate, expressions for most errors is difficult at best and provide relatively little insight. Instead they can easily be simulated numerically. The error simulations are done using MATLAB and the scripts are available in the appendices. Two important errors are from contact misplacement (when they are not placed exactly in the corner) and from measuring the sample dimensions and angle. The sample dimensions appear in the expressions for the tensor elements as the r factor. The advantage of this is that systematic errors cancel and only random variations propagate to the tensor elements. The error from this is hence believed to be small, in most cases below 2%. As for the normal vdP method, small errors are expected to be additive to first order.^{57, 58} In the following we will consider only one type of error at a time and for only one contact. The size of the errors will also depend on how anisotropic the sample is, that is the ratio of the highest to the lowest principal axis element (ρ_{11} and ρ_{22}).

The error from the angle has two contributions: Error in χ and deviations from a parallelogram, *e.g.* towards a trapezoid. The first can easily be simulated while the later has to be tested experimentally since the conformal mapping is only valid for parallelograms. Errors in χ can be simulated by assuming a sample geometry and tensor, calculating correct α and k , and using an erroneous χ with the correct α and k for calculating the tensor elements. Since ρ_{iso} sets the scale for the tensor elements the changes from the correct elements are calculated as a percentage of this. This avoids exaggerating the error in small tensor elements. A tensor with principal elements $\rho_{11} = 1$, $\rho_{22} = 2$ (arbitrary units) and rotation $\varphi = 40^\circ$ and sample geometry defined by $r = 1$ and $\chi = 60^\circ$ is used as an example. The error can be calculated for both the 60° and 120° corners by rotating the sample and tensor 120° . The results are shown in Figure 4-12. The script used to produce this plot is found in Appendix B.2.

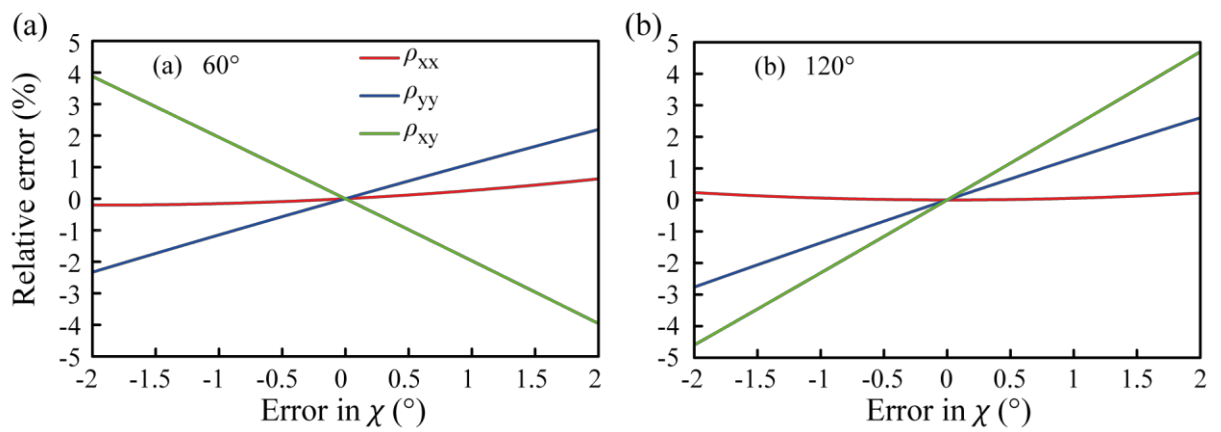


Figure 4-12: Error from the measured χ . A tensor and sample geometry is assumed from which α and k are extracted. The tensor elements are then calculated from this plus an error in χ . The change from the elements without error are calculated as a percentage of ρ_{iso} .

The x-axis in panel (b) appear inverted relative to (a) since a positive error in the 60° corner corresponds to a negative error in the 120° corner. As a result, panel (a) and (b) are almost mirror images of each other. If (b) is inverted, the errors are very similar but not identical. This is because the laboratory frame which is used as the basis for the tensor is defined by the AB side of the sample. The calculations were done by placing the A contact on the corner of interest and calculating the error. Hence, the tensor elements are not identical but related by a 120° basis rotation. Since the error in the angle is the same for all corners only one such plot is necessary to characterize the error in each sample. Both corners are shown here to illustrate that the error will depend on the sample orientation even though they are similar. The angle can be measured using optical microscopes with good precision. While absolute lengths are prone to large errors from this technique, relative lengths and angles are highly accurate. The error in χ is believed to not exceed 0.5° with this technique and hence the error is usually below 1-2%.

An analysis similar to the one for χ can be made for the contact placement. The script can be found in Appendix B.3. The same sample and tensor as above is used. Errors for both corners are shown again. The error was calculated by extracting α and k from the correct sample geometry and contact placement. This is used for the conformal mapping. Then the A contact was moved away from 0 on the complex half plane. From the new position the $R_{AB,DC}$ resistance was calculated and Equation (4-23.a) was used to calculate an erroneous k . This simulates an experiment where the contact is misplaced. The true position of contact A was then mapped to the sample using first the conformal mapping and then the linear transformation. This allows the tensor elements to be calculated (from erroneous k) and plotted against the true contact position (mapped using the correct k). The results are shown in Figure 4-13 as a function of the relative contact displacement along the AB side. The error is again given as a function of ρ_{iso} . For the two corners, the errors from displacement along the two sides are not identical; however, only one direction is used for each corner in Figure 4-13. The script can be found in Appendix B.3.

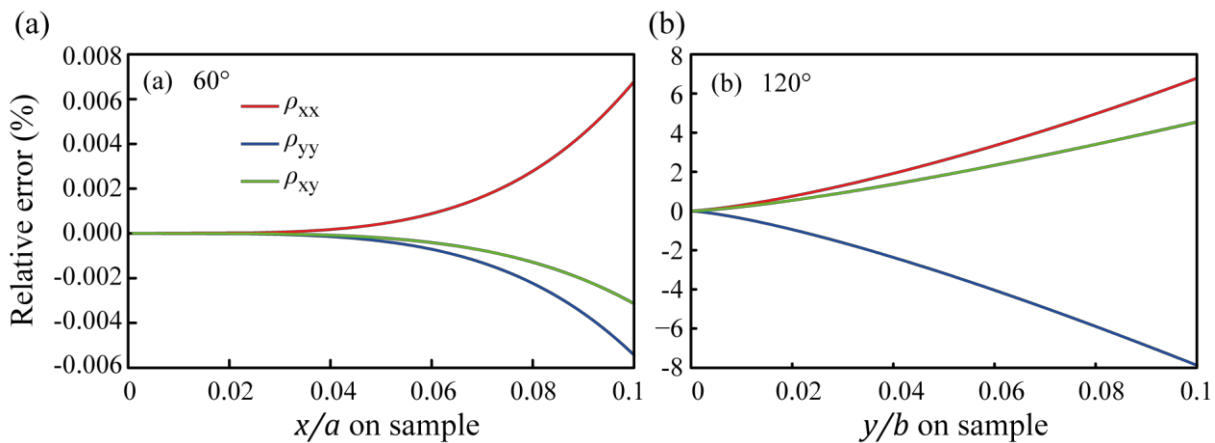


Figure 4-13: Error from contact displacement when keeping α constant. This was calculated by displacing the contact on the complex half-plane and calculating a corresponding k . The displaced contact was then mapped to the anisotropic sample.

From Figure 4-13 it can be seen that the error in the 60° corner is much lower than in the 120° corner – by a factor of 1000. Assuming the current to be passed between the two 60° corners, displacements of the contact in the 120° corner will be along the current path. This significantly affects the measured resistance and hence k . The errors shown in Figure 4-13 depends strongly on the tensor and sample geometry. Generally, the error from misplacement in the acute corner is lower than in the obtuse corner of a sample; However, the anisotropy makes it difficult to generalize. A better criterion is for the isotropic equivalent: To reduce the error α should be close to 0.5. This is more general than a requirement for χ since the current paths will depend on both the tensor and sample geometry for the anisotropic sample. In Figure 4-13 the error reaches 8% at 10% displacement. With care the contacts can be placed much more accurate than this and hence the error from misplaced contacts is expected not to exceed 5%. After a measurement, the possible error can be estimated numerically using the

script. If high errors are found for small displacements or errors in χ , the results should be used with care.

Errors enter the methods for single and polycrystalline samples in Section 4.2.4 in more ways. For single crystals, Section 4.2.4.2, errors from both the tensor orientation and contact misplacement or χ will affect the extracted α . Above α was kept constant and only the error in χ or k was used. The same tensor and sample as previously is used to simulate the errors in measurements on single crystals. Errors from the tensor orientation φ , angle in parallelogram χ , and contact misplacement in both corners are included. The result is shown in Figure 4-14. The error from wrong χ in panel (a) is approximately the same as with constant α . The Error from bad measurements of φ , panel (b), is significantly larger. It is hence very important to determine the orientation of the principal axes carefully. This is more difficult than determining the angle of the parallelogram and a larger error is expected, as high as 5 – 10%. The error from misplaced contacts is significantly enhanced compared to constant α as seen in panels (c) and (d). The sample used here has $\alpha \approx 0.25$ which was chosen since it gives large errors. If $\chi = 90^\circ$ is used instead, $\alpha \approx 0.40$ is obtained. This reduces the error in panel (d) to a maximum of 12% while that in panel (c) is increased to 1.5%. This is much more tolerable. It is, however, still important to determine φ accurately. $\chi = 107.25^\circ$ gives $\alpha = 0.500$ and in this case the limits for the errors are (a) 3%, (b) 6%, (c) 2.5%, and (d) 1.5%. The errors in (c) and (d) are still not identical since the isotropic equivalent is not square but has $a'/b' \approx 1.17$. These errors are much more tolerable and show the importance of having α close to 0.5 when possible. The script used to produce this is found in 0.

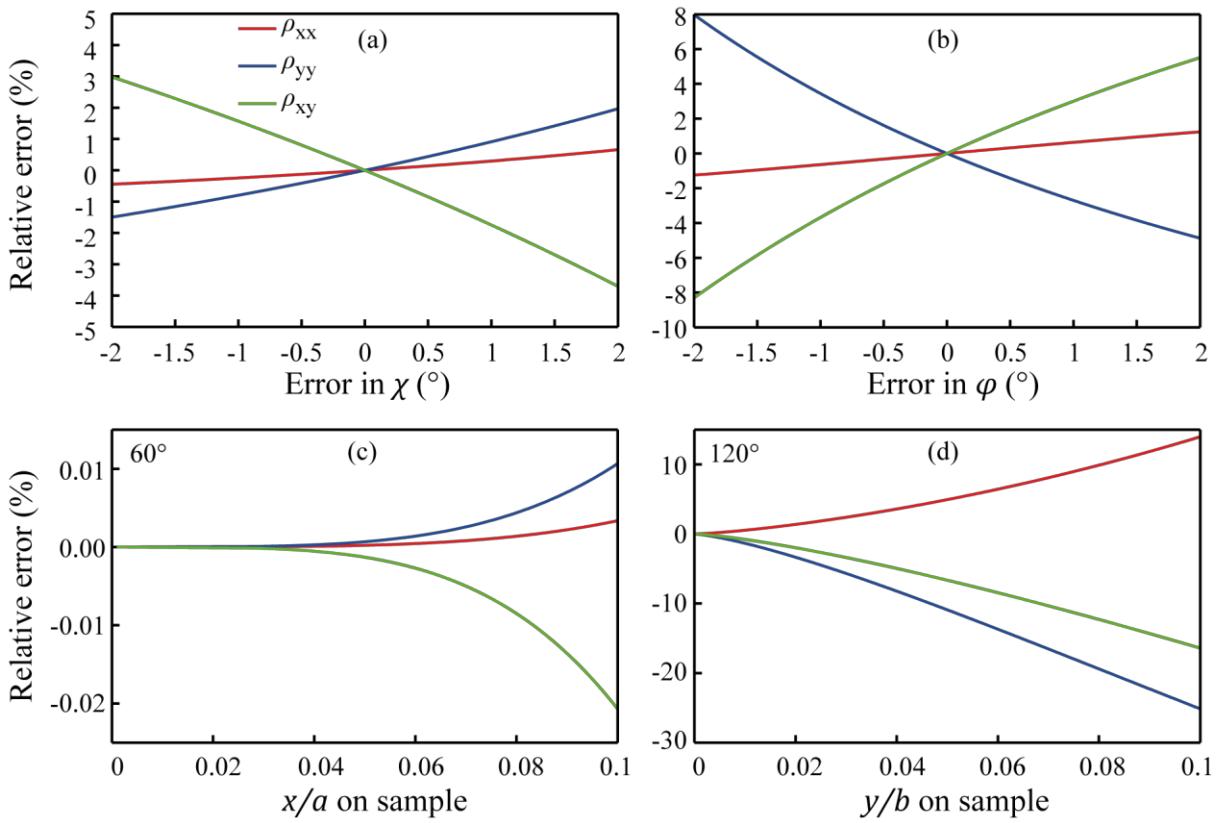


Figure 4-14: Errors relative to ρ_{iso} from different sources when treating single crystals. (a) Error from χ ; (b) Error from measuring the tensor orientation; (c) and (d) error from misplaced contacts in the two corners. $\chi = 60^{\circ}$ and $r=1$ was used as input for the sample while the tensor was defined as $\rho_{11} = 1$, $\rho_{22} = 2$, $\varphi = 40^{\circ}$.

An analysis similar to the one in Figure 4-14 can be done for the method of reshaping the sample. The same input parameters as in Figure 4-11 are used. To simplify the analysis errors will only be applied to the A sample which has the highest deviation from $\alpha = 0.5$. Errors in θ are correlated to errors in χ in this case. This is not always so (such as when cutting a rectangle from another rectangle) and here they are applied independently. The results are shown in Figure 4-15. The errors are significantly reduced compared to the treatment of single crystals. More information is used to extract α in this case which suppresses the error. In this method 8 contacts and 3 angles (can be reduced to 2) contribute to the total error in this case, compared to 4 contacts and 2 angles for single crystals. The total error is still believed to be reduced, however.

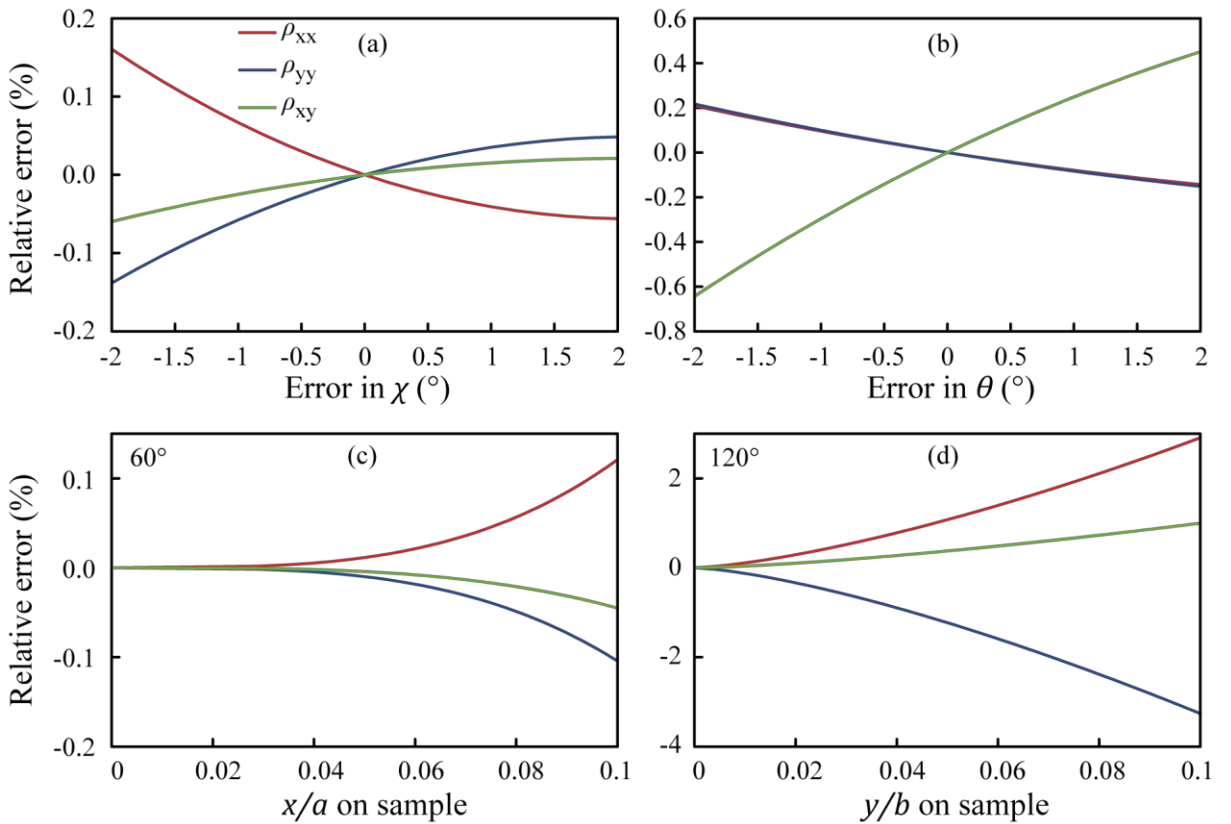


Figure 4-15: Errors relative to ρ_{iso} when treating samples measured in several orientations. (a) Error from measuring χ ; (b) error from determining θ ; (c) and (d) error from contact placement in the two corners. The error is only applied to the A sample since this has the highest deviation from $\alpha = 0.5$. The input parameters are identical to the ones used in Figure 4-11.

Finally, an analysis of the error in the 5-point method is included for completeness. Only the error from misplaced A and E contacts are calculated. The result is shown in Figure 4-16. The same sample and tensor as above is used but only the error from the 60° corner is shown. In (a) the error from a misplaced A contact is shown. The error is quite low as usual for this corner; however, it is slightly higher than in the other methods. In the 120° corner (not shown) the error increases to a maximum of 20% for 10% displacement, comparable to the single crystal method. This error was calculated as previously. The error from the E contact was calculated by adding an error to r_2 and then calculating the m that would be measured assuming a correct k and α . This was then used together with the wrong r_2 (fixed at 0.5) and correct k to extract α from Equation (4-32). This error is quite high, as much as 30% of ρ_{iso} for a displacement of 10% of a . To have an error below 10% the E contact has to be displaced less than 4%, which is difficult. This makes the 5-point method the least accurate method discussed in this Chapter. One way to reduce this and circumvent the problem with two solutions to Equation (4-32) is to first extract α from the method of reshaping the sample. This can then be used to improve the value for r_2 and determine which solution to Equation (4-32) is correct. An advantage of this method is that it is more readily useable for temperature resolved measurements, where the tensor orientation may not stay constant (e.g.

through phase transitions etc.). The other methods cannot be used without further assumptions, such as constant φ or α .

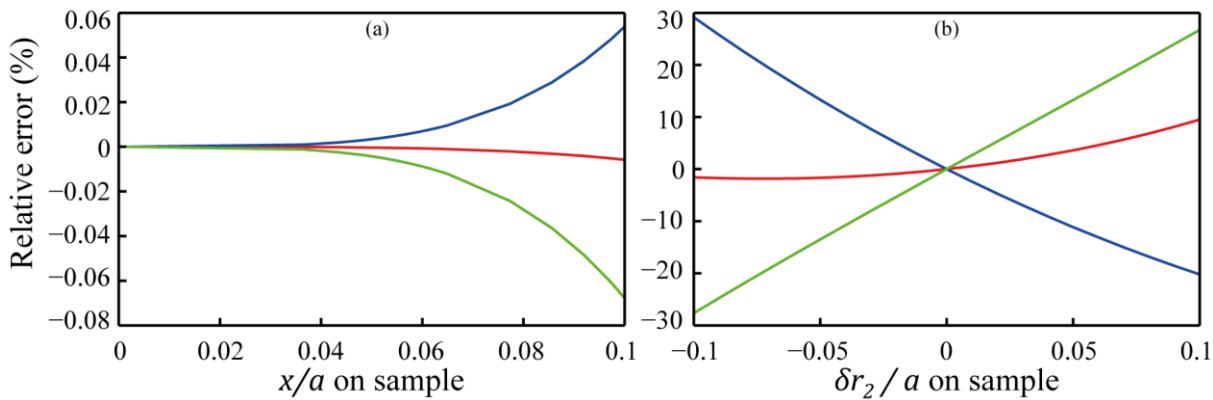


Figure 4-16: Estimation of errors in the 5-point method: (a) Error from displacing the A contact; (b) error from displacing the E contact. The error from χ is expected to be comparable to the other methods. $\chi = 60^\circ$ and $r=1$ was used as input for the sample while the tensor was defined as $\rho_{11} = 1$, $\rho_{22} = 2$, $\varphi = 40^\circ$.

4.2.7 Experimental tests

To test the consistency of the theory as well as experimental noise levels, a pseudo-anisotropic sample was prepared. An isotropic graphite sample was shaped as the isotropic equivalent of an imagined anisotropic sample. This approach is theoretically valid since the linear transformation means that any measurement performed on an anisotropic sample could have been performed on its isotropic equivalent with the same result. Hence, using the measured resistivity as ρ_{iso} and assuming the aspect ratio to be $r = 1$ and angle $\chi = 90^\circ$ for the anisotropic sample, the tensor of the anisotropic sample can be calculated both from the geometry of the isotropic equivalent sample and the measured resistances. Since the experiment provides no information about α , this was extracted from the angle of the isotropic sample. Tests for the methods for extracting α will be presented below.

Two slabs of graphite were used for the test, one shaped as a rectangle and one as a parallelogram. After the measurements, each sample was shortened as indicated in Figure 4-17 and a measurement on the new sample was performed after determining its geometry. This procedure was repeated and resulted in 12 measurements with aspect ratios ranging from 0.5 to 1.45 for the rectangle and 15 measurements with aspect ratios from 0.45 to 1.45 for the parallelogram.

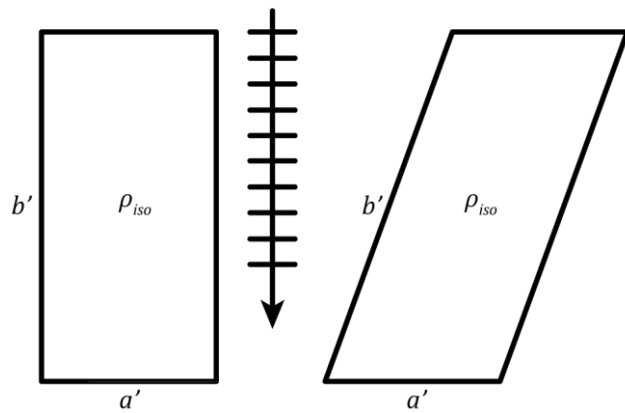


Figure 4-17: The isotropic samples used to test the linear transformation, reproducibility, and effects of measurement noise. A rectangle and parallelogram were cut from graphite and used for the test. The aspect ratio of both samples were changed in small steps indicated by the arrow and lines. The geometry was determined for each sample and a measurement was performed.

Using the resistivity, k extracted from the experiment and α from the sample geometry, the tensor elements for each sample of both geometries can likewise be calculated from equation (4-30.a) to (4-30.c). For each of the two geometries, this can be compared to the tensor elements calculated from the average resistivity from all measurements and α and k calculated as a function of aspect ratio ($r' = a'/b'$). In comparing the two methods, different errors can be examined: the consistency of the theory, experimental errors from extracting k (mostly from reproducibility of contact placement), and error from resistivity measurement. These errors will have distinct effects on the data. If the theory is inconsistent, there will be different dependences of the aspect ratio r' ; Errors in extracting k will change the observed anisotropy and hence shift ρ_{xx} and ρ_{yy} in opposite directions while leaving ρ_{xy} unaffected; Errors in ρ_{iso} will shift ρ_{xx} , ρ_{yy} and ρ_{xy} in the same direction since this is a constant scaling. The results of the test measurements on graphite samples are shown in Figure 4-18 for both the rectangular and parallelogram shaped sample. The two methods have the same dependence as a function on aspect ratio with the experimental points scattered in a narrow band around the semi-theoretical lines, indicating the theory is internally consistent. This verifies the applicability of the methods developed in this chapter and indicates that the experimental errors are small. From the reproducibility plots, the two different kinds of shifts are both visible, however; the antiparallel shift is much higher. This indicates that errors from extracting k are dominant. This is most likely due to errors from contact placement as will be further discussed below and discussed theoretically above.

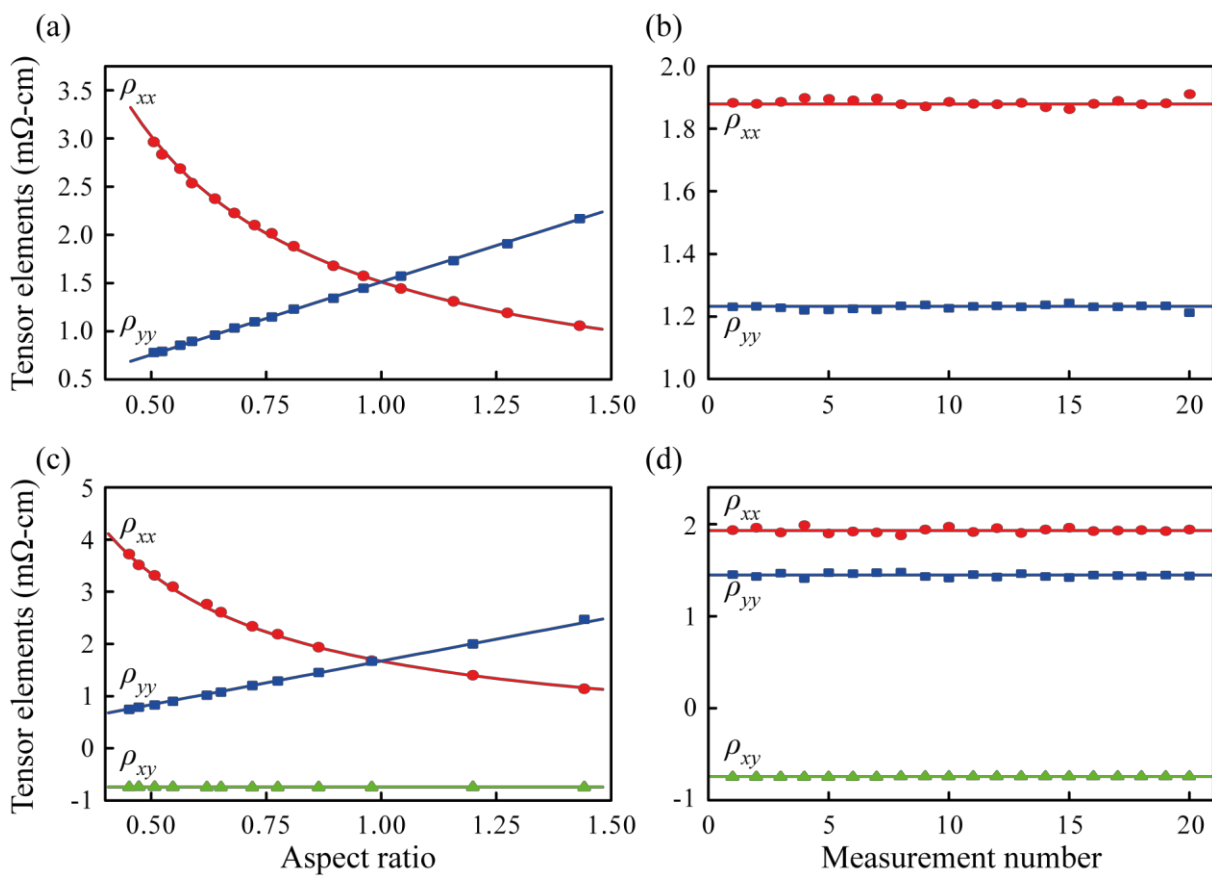


Figure 4-18: Experimental measurements of graphite samples shaped as the isotropic equivalent of an imaginary anisotropic sample. Lines represent the tensor elements obtained from the relation between the anisotropic and isotropic sample geometries. Points represent tensor elements from experimental ρ_{iso} and k with α from the sample geometry. (a) and (b) are tensor elements as a function of aspect ratio and reproducibility for one aspect ratio, respectively, for a rectangular isotropic sample. (c) and d) are the corresponding measurements for a parallelogram.

To experimentally verify the error analysis in the previous section, a series of measurements were carried out with continuously worse contact placement. The results are shown in Figure 4-19. The first measurement was carried out with the best achievable contact placement after which the A contact was slowly moved towards the B contact in small, approximately equidistant steps. This was stopped when the contact had been moved 1/4-1/3 of the way. This was carried out on the same rectangular graphite sample as was used in the reproducibility test in Figure 4-18 (b). Determining the actual displacement proved difficult and is hence omitted in the plot. The deviation in ρ_{xx} and ρ_{yy} has the same shape as expected from the previous section and the deviation is of the same magnitude. The sample used here is rectangular and hence equal errors with opposite signs are expected for the ρ_{xx} and ρ_{yy} .

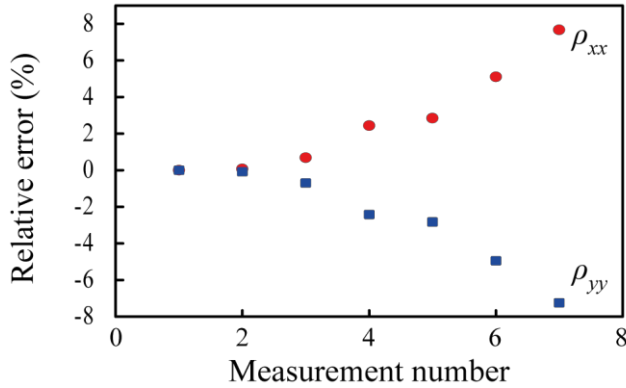


Figure 4-19: Experimental error from contact placement. 7 measurements were carried out where the A contact was slowly moved away from the corner in small steps. The 7th measurement corresponds to the A contact being roughly 1/3 of the way along AB. No specific displacements are given since these could not be determined with sufficient accuracy. The position of the fourth point is poorly represented; in reality it is much closer to the fifth.

An important source of error which cannot be studied by simulation is deviations from parallelograms. The simplest such deviation is towards a trapezoid, *i.e.* two opposing sides are slightly non-parallel while the remaining two are still parallel. An example of the effect of this error on a rectangle is shown in Figure 4-20. The relative error is relatively small for all ω , which is the deviation angle. Since it is easy to cut parallelograms with high accuracy using *e.g.* a diamond saw, the actual effect of this kind of error is believed to be small. Making parallel sides is not expected to be difficult, while ensuring corners of 90° is much more difficult. This is, however, accounted for in the theory.

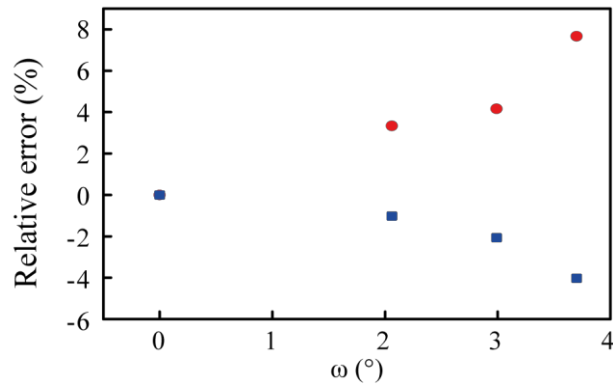


Figure 4-20: Error from deviation from parallelogram. The angle of the deviation is called ω . This was done by filing one edge of a graphite rectangle to become increasingly trapezoidal.

From the tests using graphite here it is concluded that the method can be applied with sufficient accuracy to extract information on the anisotropic tensor with high accuracy. The measurements are found to be highly repeatable with repeated mounting and measurement and the error sources have been analyzed and ways to reduce these have been suggested. Generally, the measurements are most accurate when the isotropic equivalent is close to a rectangle. The last remaining challenge is to test the methods proposed for extracting α .

The method of changing the tensor orientation from section 4.2.4.2 can also be easily tested using isotropic graphite. In this case $\rho_{iso} = \rho_{xx} = \rho_{yy}$ and $\rho_{xy} = 0$, which is easy to test. The test was done starting from a rectangle as in Figure 4-10 and changing the angle corresponding to going from the middle to the right. This was done in small steps. Five measurements were carried out with a total change in χ of 18.7° . The second through fifth measurement were compared to the first measurement, resulting in four estimates of the tensor elements. These are plotted as a function of θ (change in χ) in Figure 4-21. The results seem to be consistent; however, the value for ρ_{xx} appears to be systematically higher than that for ρ_{yy} . The difference is approximately 2%, which is not more than can be expected. ρ_{xy} , which is not shown, is in all cases on the order of $0.01\text{ m}\Omega\text{-cm}$. Since the error is within that expected for a graphite sample the method is concluded to be working.

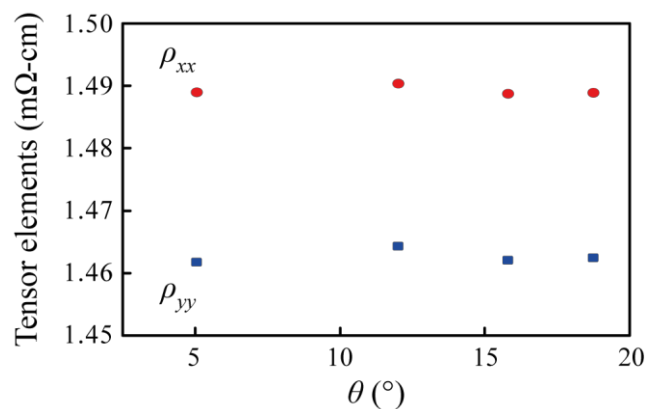


Figure 4-21: Experimental test of the rotating tensor method. A rectangle was shaped towards a parallelogram in small steps and van der Pauw measurements were performed on all shapes. The tensor elements are extracted by comparing the measurement on the first (rectangular) sample to each of the following.

All results in Figure 4-21 are in agreement; however, it is generally expected that the accuracy is higher when θ is high. In this case the error in θ is relatively smaller than for small θ . In section 4.2.4.2, θ is defined as the positive rotation of the tensor when reshaping the sample. The tensor does not have to rotate for the method to work. Changing χ without rotating the tensor gives the same amount of information and the same considerations apply to the error. In both cases a change in angle of $15\text{--}20^\circ$ is expected to give the desired accuracy.

The last method left to check is the single crystal method. This requires the knowledge of the orientation of the principal axis system. This cannot be tested using graphite samples but requires an actual sample with a known orientation of the tensor. To this end a RuSb_2 single crystal has been synthesized using the self-flux method. This material was chosen since sufficiently large single crystals can relatively easily be grown. A good alternative would be FeSb_2 since this material is more thoroughly studied; however, growing large crystals of this material is somewhat more difficult. The RuSb_2 crystal was cut into a parallelogram in the crystallographic ab-plane. The crystallographic directions were identified by indexing all

facets using X-Ray diffraction. The ab-plane was chosen since it would give the largest surface area sample. Referring to Figure 4-2, the sample had $\chi = 96.2^\circ$, $a = 2.83$ mm, $b = 4.01$ mm, and the tensor orientation was given by $\varphi = 44.38^\circ$. The fact that χ differs from 90° serves as a motivation for extending the theory to accommodate parallelograms. The resulting tensor is plotted in Figure 4-22 in both the lab and principal axes frames. Since the sample cooled down somewhat during the 11 repeated measurements, temperature is used as the x-axis. The material is undoped and is hence expected to behave as an intrinsic semiconductor, *i.e.* resistivity decreasing with temperature. This is also observed experimentally. The observed anisotropy (defined as ρ_{aa}/ρ_{bb}) at room temperature of 2.3 is slightly higher than that in FeSb_2 ,⁹¹ however, it is still within the expected range. The resistivity tensor of RuSb_2 has not been reported in the literature and the experiment can hence not be compared to this. Since the band gap is higher, the resistivity is also higher at room temperature. Hence, when comparing the two materials this should not be done at the same temperature but with similar ρ_{iso} .

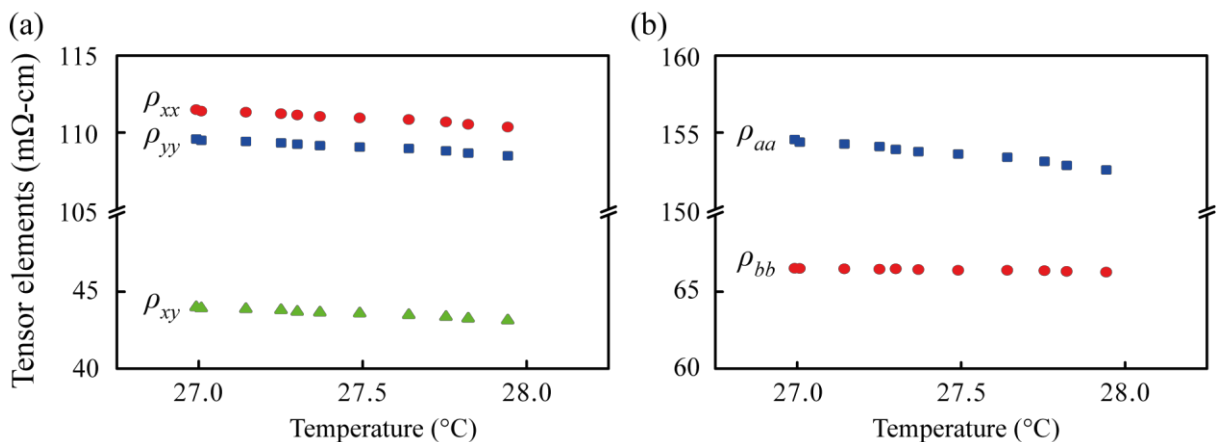


Figure 4-22: Resistivity tensor of RuSb_2 extracted from a van der Pauw measurement using the known tensor orientation. The tensor is shown in both the lab frame (a) and principal axes system (b). Temperature is used as the x-axis since the sample cooled down slightly during the measurements.

The accuracy of the tensor in Figure 4-22 depends on a number of things. Most importantly the error from the tensor orientation, as discussed in connection with Figure 4-14, can be quite high. In this particular case the angle φ is close to 45° , which increases the sensitivity to this error. Performing the same numerical error analysis as above reveals that the error can be as high as 15% of ρ_{iso} for 2° error in φ .

4.3 Conclusion

In this chapter the theory behind van der Pauw measurements has been extended to be able to extract the resistivity tensor from parallelogram shaped samples. Several methods have been outlined and their application has been discussed. The errors from various sources have been analyzed numerically for all methods and their importance has been estimated. Experimental tests have likewise been performed. Most of these are based on graphite samples since this is easy to cut in various sizes and shapes and is expected to be highly isotropic. This provides a

good foundation for many tests. The method of reshaping the sample was able to reproduce the isotropy of the graphite satisfactorily. The method of known tensor orientation gave a resistivity tensor for RuSb₂ within the expected range; however, other measurements are necessary for rigid verification. In conclusion the theory is seen to work and provide reasonable results. Before the widespread application more experience with the techniques is necessary; however, they are deemed to be sufficiently mature for application to materials science problems.

5 Studies utilizing the instruments (and other projects)

This last, short chapter is intended to give a few examples of studies utilizing the instruments discussed in Chapter 3. In all cases my involvement has been through aiding other group members characterizing and analyzing their materials. This is a natural extension of the main project and has taken up considerable amounts of time.

Three examples of studies using the two systems have been chosen. They have all been or are about to be published and the papers or manuscripts are found in the appendices. They share some similarities but are nonetheless quite different. The first is a graded $\text{Ge}_x\text{Si}_{1-x}$ ingot which was grown using the Czochralski technique. The second is a more traditional study of the thermoelectric material system $\text{Mg}_2\text{Si}_x\text{Sn}_{1-x}$. The last is within a completely different field, namely topological insulators. In the end is a short description of further projects which have not been discussed in detail in this thesis. Some of these projects are still ongoing while others have been published. They have not been included in detail either because they are not sufficiently mature to include, or because they are too far from the main project and hence do not fit in this thesis.

5.1 Graded $\text{Ge}_x\text{Si}_{1-x}$

$\text{Ge}_x\text{Si}_{1-x}$ solid solutions have been thoroughly studied as thermoelectric materials.⁹² This makes it a good model system since the properties are known with high precision for all compositions and doping levels. In this project, mainly carried out by Ellen Marie Jensen Hedegaard, an ingot of boron doped $\text{Ge}_{1-x}\text{Si}_x$ was synthesized with a twofold grading along the length: Both the composition (x) and the concentration of boron, *i.e.* the doping level. The manuscript can be found in Appendix C.4.

In thermoelectric materials, zT usually peaks at a temperature just before bipolar conduction sets in. Bipolar conduction is a result of charge carriers being excited across the band gap. This lowers the Seebeck coefficient and increases the thermal conductivity. Even though the resistivity decreases, the overall effect is to decrease zT . Hence, by increasing the band gap the bipolar conduction is suppressed and the peak in zT moves to higher temperatures. The same effect is observed by increasing the doping level as this increases the effective band gap. This has been suggested utilized in thermoelectric modules by grading the materials in such a way, that zT is at its peak value at all temperatures through the material.⁹³ This is expected to enhance the efficiency compared to homogenous materials.

In $\text{Ge}_x\text{Si}_{1-x}$ the band gap is known to be a function of composition,⁹⁴ while boron is known to preferentially incorporate in the solid instead of remaining in the liquid upon solidification. Hence by directional solidification the dopant concentration can be made to vary through the material, with the part first solidified having the highest dopant concentration. From the Ge-Si phase diagram in Figure 5-1 it is seen that the Si content in the newly solidified material

will decrease as slow solidification progresses. The starting composition of the melt is Ge: Si: B = 95: 5: 0.1. Due to the low slope of the solidus, this results in the solid containing roughly 25% Si upon initial solidification. Note that the phase diagram in Figure 5-1 is only a sketch and cannot be used quantitatively. With further solidification the Si content decreases and in the end almost pure Ge is solidified. Since the band gap decreases with decreasing Si content both the band gap and doping level decreases as solidification progresses. Hence the effects of the two gradients enhance each other.

Gradients in both composition and carrier concentration have been demonstrated previously; however, this is the first time double grading has been demonstrated experimentally. As examples, compositional grading of $\text{Ba}_8\text{Ga}_{16}(\text{Ge}_x\text{Si}_{1-x})_{30}$ clathrates has been reported⁹⁵ while carrier concentration gradients has been reported in *e.g.* Bi_2Te_3 .⁹⁶ To verify that the ingot is graded in composition, energy dispersive X-ray spectroscopy (EDX) was used. This was further supported by the unit cell sizes extracted from X-ray diffraction. See Figure 2 a) in the manuscript in Appendix C.4 for further details.

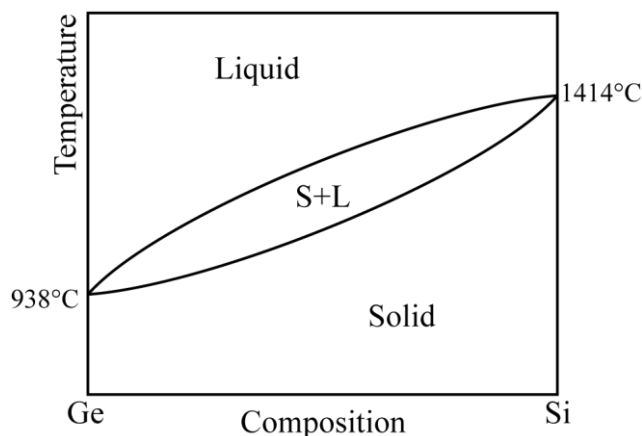


Figure 5-1: The Ge-Si phase diagram showing complete solid miscibility. This makes it a good system for compositional grading. The slope of the solidus curve also indicates that the Si content in the solid decreases as slow solidification progresses.

This study is a prime example of using the equipment. The synthesis method produces an ingot that has to be characterized in slices along its length. This results in discs of varying shape and size, which can all easily be measured using the equipment. Since the ingot had too low diameter to be used for flash diffusivity measurements (the ingot was below $\frac{1}{2}$ inch in diameter, which is the only accepted sample size in the LFA in Aarhus) this flexibility was further utilized by cleaving the ingot along its length. The surface thus created on the larger half was used for making a scanning Seebeck map. This is shown in Figure 5-2. After this map was measured three discs were cut from the ingot in order to measure the properties at higher temperatures. The three discs were cut from the top, middle and bottom sections of the ingot and contains roughly 17%, 5%, and 1 % silicon, respectively.

From Figure 5-2 a) the Seebeck coefficient is seen to change approximately linearly through the ingot. Since the Seebeck coefficient is strongly dependent on the carrier concentration this is an indication that the sample is also graded in doping level. The Seebeck coefficient also depends on the band gap, however, and it is difficult to separate the two contributions from each other. The linear change in Seebeck differs from the change in band gap, which is strongest in the left part (the top of the ingot) and fairly constant in the right part. It is thus concluded that the sample has been successfully graded in both band gap and doping level.

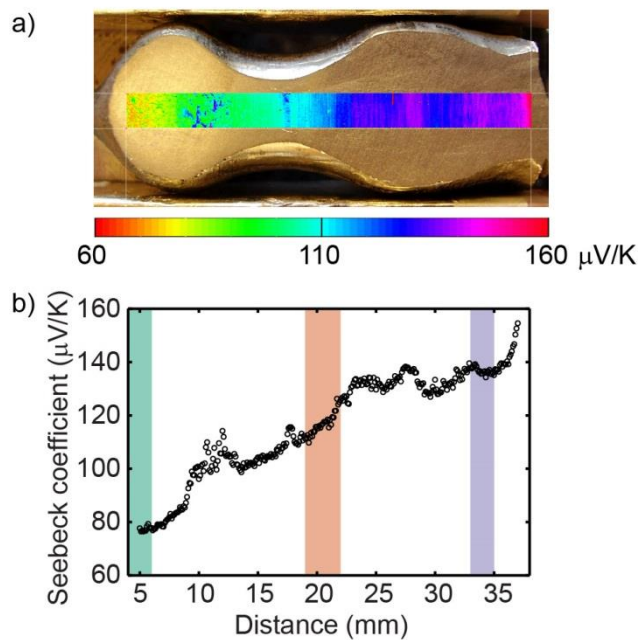


Figure 5-2: a) Photograph of the surface of the ingot after cleaving with a scanning Seebeck map superimposed. b) Vertical average of the Seebeck coefficient showing the Seebeck coefficient of the ingot as a function of position along its length. The three colored regions in b) indicates the discs that were used for high temperature measurements. Reproduced from the manuscript in Appendix C.4.

The high temperature properties of the discs are shown in Figure 5-3. The resistivity and Hall carrier concentration of the three discs is consistent with the expected gradient in doping level. The Seebeck coefficient differs from that in Figure 5-2; however, the scanning Seebeck measurement is not quantitative and the two methods differ substantially so this discrepancy is expected. In the resistivity, Seebeck coefficient, and Hall carrier concentration the onset of bipolar conduction occurs first in the bottom sample, then the middle and lastly in the top. This is consistent with a gradient in effective band gap. Usually the bipolar conduction is visible in the Seebeck coefficient at lower temperatures than it is in resistivity and Hall carrier concentration. This is also the case here. In the bottom sample, the Hall carrier concentration changes sign (goes from majority p- to n-type) at roughly 675 K. At this temperature the Seebeck coefficient is still positive and hence the two have opposite signs. This is usually not expected; however, the two properties measures different parts of the band structure and hence this is possible in complicated band structures and multiband systems.

Since the discs were not compatible with LFA in Aarhus, the thermal conductivity has not been measured and zT cannot be calculated. Instead, the purely electronic $zT_e = \frac{S^2}{\kappa_e \rho} T$ is calculated. κ_e is the electronic part of the thermal conductivity. This provides a means to compare with theoretical calculations (see the manuscript in Appendix C.4 for details) but is a poor indication of the actual zT . In Figure 5-3 the high temperature thermoelectric properties of three slices of the ingot are shown. These slices correspond to the colored regions in Figure 5-2 (b). It appears that the bottom sample is better at almost all temperatures. This sample has a silicon content of only about 1% and hence has a much higher lattice thermal conductivity than the middle (5%) and top (17%) samples. Hence the actual zT is smaller and may bring the maxima to roughly the same value. The manuscript has been through the first review cycle and one of the changes being made is to include literature values for the lattice thermal conductivity to calculate zT .

One final remark is that the sample has in no way been optimized; it is only a proof of principle. Several properties have the be optimized: The overall doping level, compositional range, and the actual gradients. The gradients are determined by thermodynamics; however, they can be affected by the growth rate which can change the conditions from quasi equilibrium to non-equilibrium. This may substantially alter the gradients. This sample was grown at 4 mm/hr which likely gives quasi equilibrium growth conditions. This is also supported by the gradient in composition. The overall doping level and compositional range can be changed by altering the initial composition of the melt. Alternate growth methods (Bridgman, Stockbarger, floating zone etc.) can change the gradients. Post processing, such as zone refining can also be used to alter the gradients in the sample.

Another example of a study of a graded ingot is the paper on graded PtSb₂ in Appendix C.5. This material is interesting as an analogue to FeSb₂, which has a record high thermopower at low temperatures.⁹¹ In this study, a PtSb₂ single crystal was grown using the Stockbarger technique. The resulting crystal was observed to have a gradient in Seebeck coefficient measured by scanning Seebeck measurements. The gradient in Seebeck coefficient was found to arise from a gradient in charge carrier concentration. This was measured on 11 discs cut from the ingot. The charge carrier concentration gradient results from a gradient in the Pt:Sb ratio through the crystal, making it increasingly antimony deficient as the growth progressed. This was concluded to be due to antimony evaporating. This study also benefited from the easy characterization of discs.

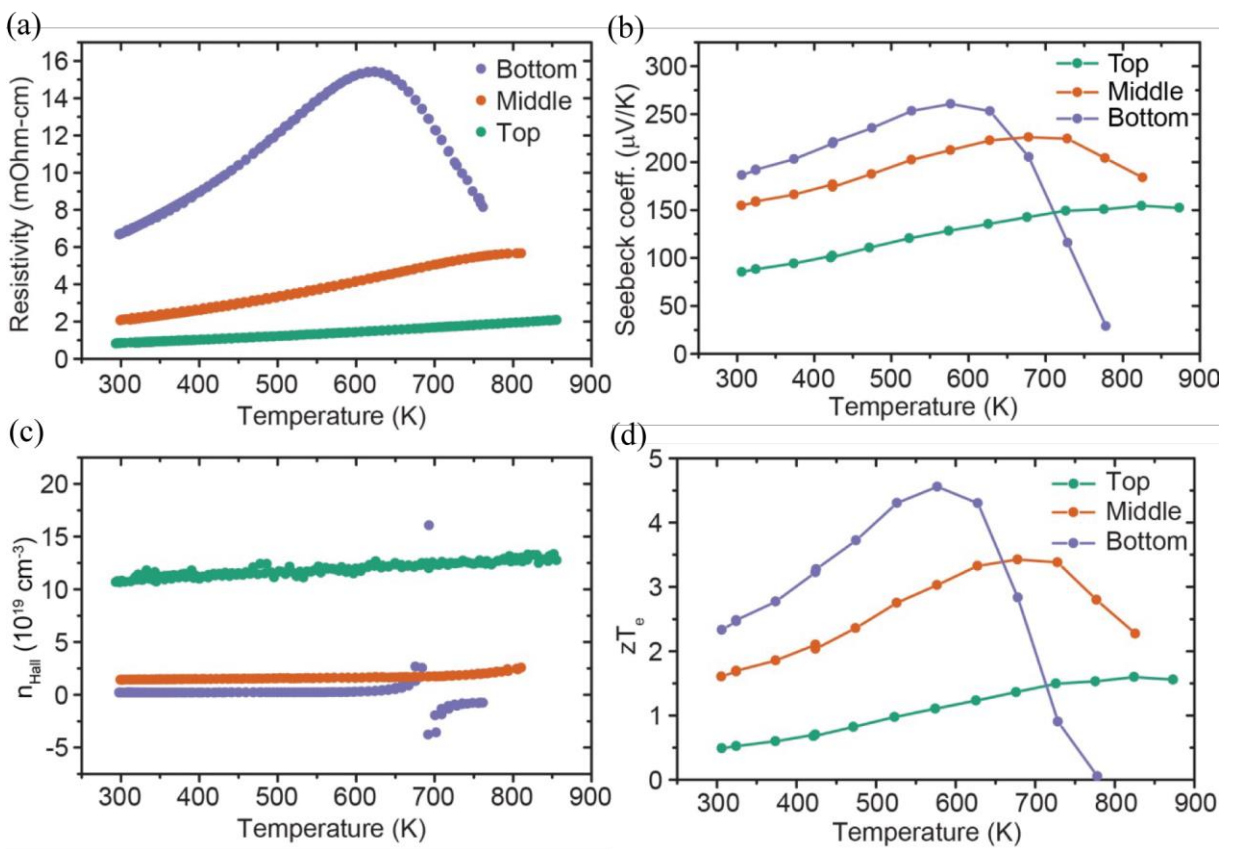


Figure 5-3: High temperature properties of the three slices. (a) Resistivity, (b) Seebeck coefficient, (c) Hall carrier concentration, and (d) figure of merit disregarding the lattice thermal conductivity. All properties were measured using the equipment described in Chapter 3. Reproduced from the manuscript in Appendix C.4.

5.2 The $\text{Mg}_2\text{Si}_{1-x}\text{Sn}_x$ system

The $\text{Mg}_2\text{Si}_{1-x}\text{Sn}_x$ system is interesting for thermoelectric applications due to the low cost of the materials and relatively high zT . At zT of 1.3 near 700 K was reported for the $x=0.7$ compound.¹⁷ This was attributed to a combination of convergence of the two lowest conduction bands at this composition, low lattice thermal conductivity due to alloy scattering, and low deformation and alloy scattering potentials.⁶⁶ The convergence of the conduction bands increases the Seebeck coefficient as it is now arising from two bands with low doping level. This has also been observed in *e.g.* PbTe.¹⁶ The deformation potential measures the shift in band edge energy as the lattice parameters are varied. Hence it is a measure of the electron-phonon coupling.⁹⁷ If the band energy does not change much when the lattice spacing is changed, such as when a phonon passes, the electrons are unlikely to be scattered by the phonon. The alloy scattering potential is analogous to this; it measures the change in energy with atomic level disorder.⁹⁸

Martin Søndergaard led the three studies discussed here. One study characterized the entire composition range,⁹⁹ one focused on the effects of spark plasma sintering (SPS) on the materials,³⁶ while the last focused on the thermal stability.³⁷ The three published papers can be found in Appendix C.6, Appendix C.7, and Appendix C.8, respectively. The focus was on

understanding the effects of different processing steps to prepare the material for use in thermoelectric modules.

5.2.1 Transport properties as function of composition

In the study of the entire composition range, samples ranging from $x = 0$ to $x = 1$ were synthesized in steps of $x = 0.1$. All samples were found to be homogenous and were successfully compacted to dense pellets. All samples were doped with the same amount of antimony and the Hall carrier concentration was in the range $0.8 - 1.8 \cdot 10^{20} \text{ cm}^{-3}$ for all samples. This is shown in Figure 5-4. This is considered fairly constant for thermoelectrics and hence the differences in sample properties are not due to the carrier concentration. Since the band structure changes with x , the Hall factor might affect the Hall carrier concentration differently. However, no systematic variation of the Hall carrier concentration with x was observed, as seen in Figure 5-4. Both the Hall mobility and resistivity were found to be fairly constant in the range $x = 0.2 - 0.8$. Compositions closer to pure Mg_2Si and Mg_2Sn have higher mobility due to decreased alloy scattering of the electrons. In contrast, the Seebeck coefficient was observed to give a peak at $x = 0.7$. This is consistent with the suggested convergence of the conduction bands. The electronic properties, Hall carrier concentration, Hall mobility, resistivity, and Seebeck coefficient are all consistent with the results by Liu *et al.*⁶⁶ while the thermal conductivity is slightly higher. This results in a maximum zT of 0.9 for $x = 0.7$ which is lower than the 1.3 reported by Liu *et al.* Several things may cause this, including difference in microstructure and hence phonon scattering or measurement error. The heat capacity was estimated relative to a standard in the LFA, which has been known to sometimes give errors.^{23, 31}

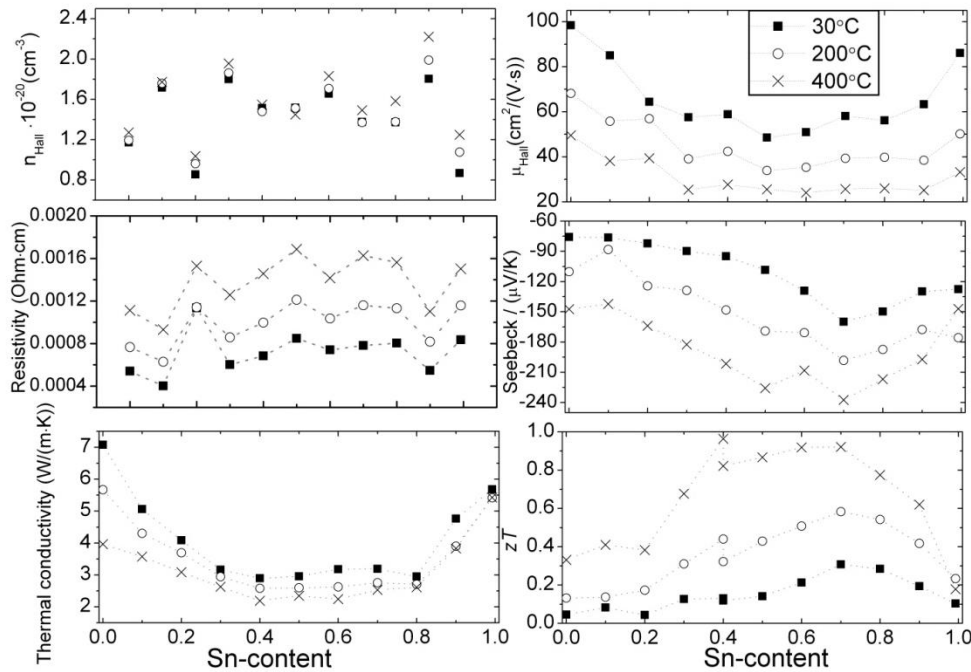


Figure 5-4: Thermoelectric properties of the entire composition range in $\text{Mg}_2\text{Si}_{1-x}\text{Sn}_x$ as a function of x . Reproduced from reference 99.

5.2.2 Effect of spark plasma sintering

After spark plasma sintering, some samples visually appeared different on the two sides.³⁶ To investigate this further, five samples were prepared of each of the compositions $x = 0.6$ and $x = 0.4$. The average Seebeck coefficients of the two sides (top and bottom side during SPS) were measured using scanning Seebeck measurements. In all samples a difference of 20-30 $\mu\text{V/K}$ was observed, with the bottom side being the most negative. A corresponding difference was also observed in the lattice parameter of the two sides, with the bottom side having the largest unit cell. In all samples, both sides were found to be the correct $\text{Mg}_2\text{Si}_{1-x}\text{Sn}_x$ phase but some samples were found to contain small Zn or ZnO impurities. From Figure 5-4 it is seen that the Sn rich samples have a higher Seebeck coefficient than the Si rich ones. Hence, both the lattice parameter and difference in Seebeck coefficient indicates that the bottom side is richer on Sn than the top side. This was further confirmed by EDX measurements on the two sides of a sample.

Some samples were cut along the diagonal and scanning Seebeck measurements were performed on the cross sectional surface. An example of this is shown in Figure 5-5. The overall charge carrier concentration is the same as in Figure 5-4 and hence the Seebeck coefficient measurements are comparable. In the middle of the sample in Figure 5-5 the average Seebeck coefficient of 120 $\mu\text{V/K}$ matches well with the $x = 0.6$ sample in Figure 5-4. On the bottom surface the average Seebeck coefficient is closer to the $x = 0.7$ sample while the top surface is closer to the $x = 0.5$ sample. The match is not perfect but the Scanning Seebeck system has on several occasions shown to underestimate the thermopower (absolute of Seebeck coefficient).

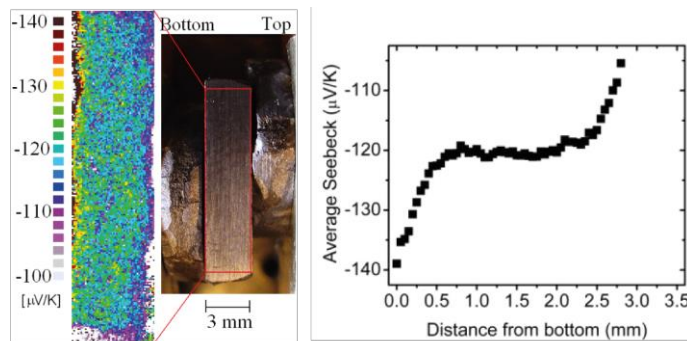


Figure 5-5: Example of gravity induced gradient in an $\text{Mg}_2\text{Si}_{0.4}\text{Sn}_{0.6}$ sample. Reproduced from reference 36.

The profile of the Seebeck coefficient matches well with diffusion of two species in opposite direction when the process is limited by diffusion.¹⁰⁰ If the material is sintered for a longer time the middle plateau is expected to decrease, making the gradient less steep. With long sintering time, two plateaus in the two ends are expected with an increasingly sharp transition zone in between. Hence, by optimizing the sintering time this provides a way to produce graded materials during SPS.

Since the Sn and Si are expected to have the same ion charges the electric field in the SPS is not expected to be the cause of this diffusion. Instead, since there is a significant difference in density of Mg₂Sn (3.59 g/cm³) and Mg₂Si (1.88 g/cm³) gravity may be the cause. This is not expected to affect solid solutions much; however, the Mg₂Si_{1-x}Sn_x system has previously been reported to contain a miscibility gap which provides the necessary mechanism for phase splitting.¹⁰¹ Many parameters can be used to optimize this gradient. These include sintering time, pressure, temperature, starting composition etc. Additionally, stacking powders of different compositions in the SPS die may help develop a specific gradient or reduce the necessary sintering time and hence processing cost. An unfortunate implication of this is that the material may develop this gradient unintended upon continued use at high temperature with constant orientation of the module.

A problem with the gradient is that characterization of thermoelectric properties becomes inaccurate. In the setups discussed in Chapter 3 the Seebeck coefficient is measured cross plane while the resistivity is measured in plane. Flash diffusivity is also cross plane. Since the material has a cubic crystal structure, the samples are expected to be isotropic except for the discussed gradient. Since resistivity is the only property being measured in plane the effect can be estimated by measuring the resistivity with both the top and bottom face turned up. Since the electrical contacts are made to the top surface, the two measurements are expected to differ if the gradient affects the measurements. Since the gradient is continuous and there are no contact resistances, as there would be in segmented materials, the gradient is expected to affect the in plane and cross plane resistivity measurements equally. No change in resistivity was observed for the two orientations, and hence the gradient is not expected to cause significant errors in the transport property measurements.

5.2.3 Thermal stability

The thermal stability is very important to application in modules. Since the modules will most likely be operating in air, it is important to know the stability of the materials towards oxidation. To test this, high temperature powder X-Ray diffraction (PXRD) was performed on ball milled powder, powdered pieces of pellets compacted by SPS, and on the surface of the pellets.³⁷ The transport properties were also measured at high temperatures to compare with the PXRD results. A Mg₂Si_{0.4}Sn_{0.6} and a Mg₂Si_{0.6}Sn_{0.4} sample was used for the study.

The powdered samples were observed to gradually decompose into a Sn rich Mg₂Si_{1-x}Sn_x phase and MgO. The reaction is not balanced for Si which indicates the Si is contained in an amorphous phase such as SiO. The Mg₂Si_{0.4}Sn_{0.6} sample was observed to evolve more of the Sn rich phase than the Mg₂Si_{0.6}Sn_{0.4} sample, which may simply be due to the higher initial Sn content. The SPS processed samples evolved significantly more of the Sn rich phase (15-25%) than the ball milled samples (3-12%). This indicated that SPS processing somehow destabilizes the samples; however, the mechanism is unknown. One explanation could be that micro cracks or defects generated by the stress during the SPS increases the reaction rate. The

reaction is likely diffusion limited as oxygen has to diffuse toward the centers of the individual grains. The pellets were not found to decompose upon heating. This is likely due to the much lower surface area and longer diffusion paths. Instead of decomposing, the main phase peaks were found to sharpen slightly, indicating an increased grain size.

To compare the microstructural changes in the pellets observed in PXRD, the resistivity was measured during repeated thermal cycling to 400°C. Since the resistivity is a very precise measurement (low scatter on repeated measurement; not to be confused with accuracy) it provides an excellent property for this comparison. This data is shown in Figure 5-6. The sample has a low charge carrier concentration and shows a behavior intermittent of an intrinsic and heavily doped semiconductor. The resistivity is lowest at the beginning of the first cycle but increases drastically from approximately 50-275° after which it shows intrinsic behavior again. After the first cycle the resistivity has increased somewhat but decreases upon continued thermal cycling. One explanation for this behavior could be that residual stresses from the SPS processing are released during the first cycle. This could be from formation of micro cracks or other microstructural change. At high temperatures the grains grow (as also hinted by PXRD) and the material sinters to slowly reverse the effect of the first cycle. This fits well with the PXRD data where powder from SPS processed pellets was observed to be more unstable than the ball milled material while the bulk pellets were stable.

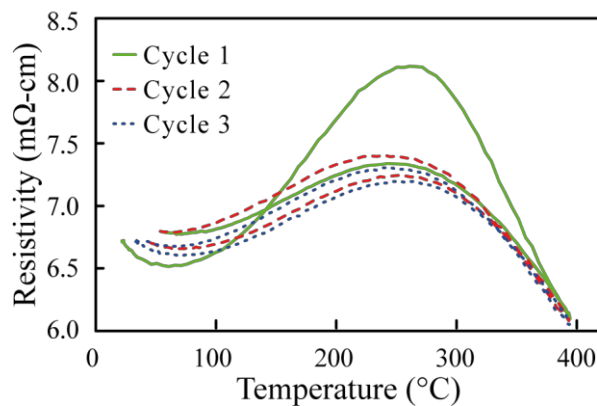


Figure 5-6: Resistivity measured with repeated thermal cycling of $\text{Mg}_2\text{Si}_{0.4}\text{Sn}_{0.6}$.

All high temperature thermoelectric properties of the two samples are shown in Figure 5-7. Both samples show a decrease in thermal conductivity with thermal cycling. This also point towards some microstructural changes; however the change is within the error of the LFA method when the heat capacity is measured relative to a standard. It is likewise difficult to draw conclusions from the Hall effect data due to the noise level; however, the mobility of $\text{Mg}_2\text{Si}_{0.4}\text{Sn}_{0.6}$ does appear to increase slightly. The charge carrier concentration appears constant within the noise for both samples. The charge carrier concentration and mobility was measured simultaneously with the resistivity and the data for the Sn rich sample was measured during cycle 1 in Figure 5-6. The resistivity from the first cycle is also shown in Figure 5-7. The Seebeck coefficient does not change much. A small hysteresis appears in

Seebeck for the Sn rich sample. Apart from this the observed change is within the precision of the measurement. This and the charge carrier concentration indicates that the electronic properties, both doping level and band structure, are unchanged. This again indicates that the observed changes are due to microstructural changes. The zT is also shown for comparison; it is lower by a factor of 2 compared to what was previously measured. This is due to the much lower charge carrier concentration.

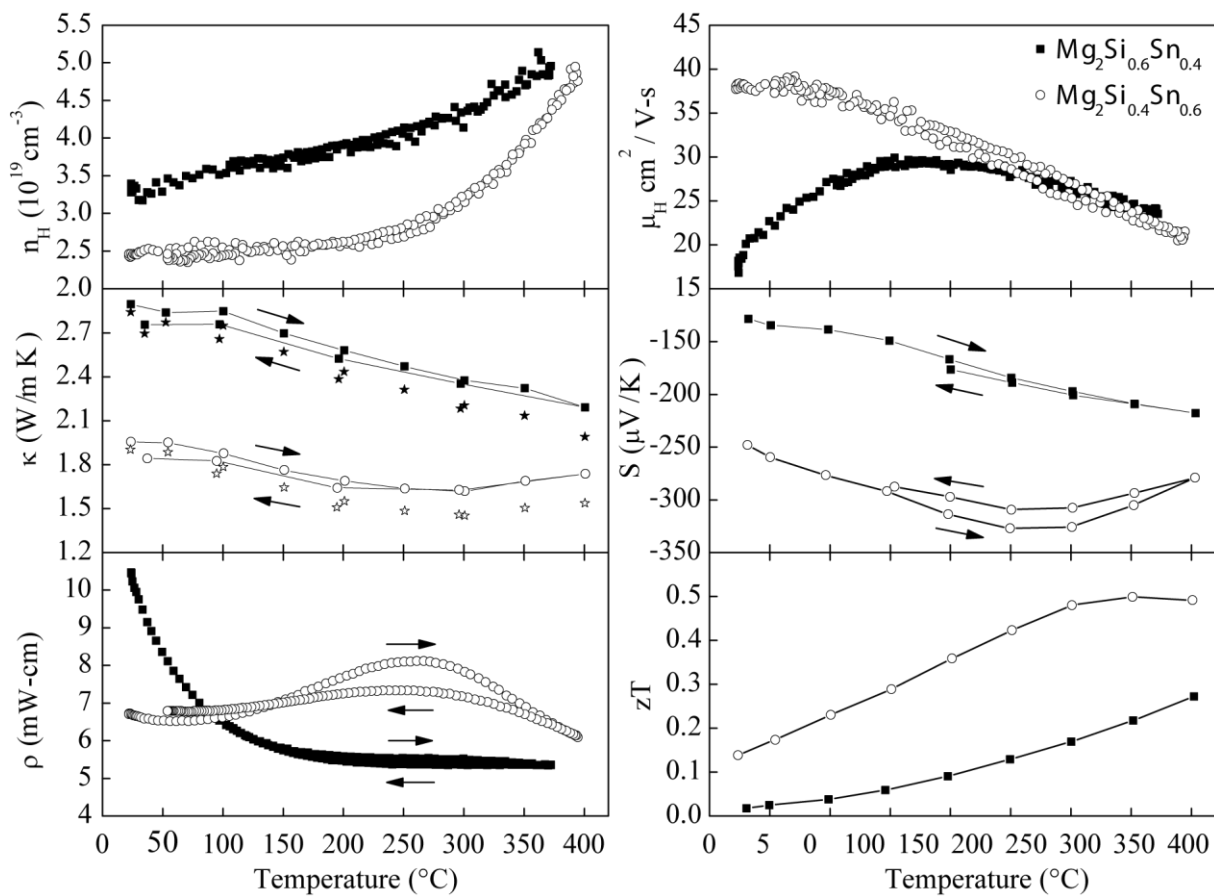


Figure 5-7: High temperature thermoelectric properties of $Mg_2Si_{0.6}Sn_{0.4}$ and $Mg_2Si_{0.4}Sn_{0.6}$. Resistivity and Hall effect data were measured first, then Seebeck and last the thermal conductivity.

The stability when heating in an oxygen containing atmosphere was found to be good for bulk pellets while powders were found to decompose. Powders from SPS processed pellets were more unstable than the ball milled powder, which was used for the SPS processing. Whether the stability of the bulk material is also good when heated for a prolonged time is unknown; however, the reactivity towards oxygen is low. This is important as easily oxidized materials will need to be encapsulated in an oxygen blocking coating. For the $Mg_2Si_{1-x}Sn_x$ series, a moderate protection from oxygen is necessary at most. The charge carrier concentration of the samples employed here were lower than in the other study; this may influence the sensitivity to sintering etc. Nonetheless, long sintering times appear to be necessary to get stable properties. If small grains are desired (such as in attempts to lower the thermal conductivity), grain growth will need to be hindered.

5.3 Bi₂Te₂Se topological insulators

The last example which will be discussed in some detail is not focused on thermoelectric properties but rather topological insulators (TIs). 3D TIs (to which Bi₂Te₂Se belongs) are insulating in the bulk but have topologically protected metallic surface states. They are typically non-cubic heavy insulators with a bulk band gap created by the spin orbit coupling and contains an odd number of band inversions.¹⁰² Other classes of topological insulators exist but discussing these is outside the scope of this section. Bi₂Te₂Se is predicted to be a TI but growing bulk insulating crystals is difficult due to the intrinsic defect chemistry. The dominant defect types are Bi vacancies or Bi_{Te} antisite (Bi on a Te site) defects (both making the material p-type) and Te vacancies or Te_{Bi} antisite defects (both making the material n-type).¹⁰³ In an attempt to grow a bulk insulating crystal, the Stockbarger method was used. This resulted in a graded crystal with several phases with different compositions and physical properties. This was published in reference 104 and the paper can be found in Appendix C.9. Most of the project was carried out by Jian-Li Mi.

The Bi₂Te_xSe_y sample was grown by the Stockbarger method with a starting composition of Bi₂Te₂Se. Along the 40 mm long rod four different phases were identified, numbered I-IV by order of solidification during the growth. Phase I, the phase first solidified, was found by inductively coupled plasma atomic emission spectroscopy (ICP) to have an approximate stoichiometry of Bi₂Te_{1.5}Se_{1.5} but with x + y slightly less than 3. This comprised the first ~20 mm of the rod (note that due to the 20 mm long pointed tip the volume fraction is less than 0.5 and closer to 0.17). Phase II was found from ~20 to ~32 mm and had a composition close to Bi₂Te_{1.7}Se_{1.2}, closer to the ideal 2:2:1 stoichiometry. Phase III was found from ~32 to ~38 mm and was found to have a stoichiometry of Bi₂Te_{2.32}Se_{0.43}. Phase IV was a mixture of Bi₂Te_xSe_x and Te. All Bi₂Te_xSe_y phases grew with x + y < 3 and an average Te: Se < 2 and hence there is an excess of Te at the end of solidification.

Scanning Seebeck measurements were used to characterize the conduction type in the rod. Phase I was found to be n type. The Seebeck coefficient decreased along the rod, indicating decreasing carrier concentration, until it reached a maximum. Then increased smoothly through 0 in phase II and reached a maximum in phase III, after which it decreased again. This indicates that the electron concentration was continuously decreasing while the hole concentration was continuously increasing. The minimum and maximum corresponds to regions where one carrier type is still dominant but the other type starts to become significant. This is the expected behavior when the Fermi level is continuously lowered from inside the conduction band to inside the valence band in a narrow gap semiconductor. Hence there is a transition in defect chemistry (Te_{Bi} to Se_{Bi} and Te to Se vacancies). Since Se_{Te} antisite defects have a negative formation energy¹⁰³ they are always present and may explain the difficulty in growing bulk insulating Bi₂Te₂Se crystals. They turn out to be a mixture of phase I and II possibly with excess Te which is not insulating in the bulk.

The further characterize the different phases high temperature resistivity and Hall effect data was measured on pieces of phase I, II, and III. These were all single crystals. The structure is layered and can be described by the space group $R\bar{3}m$, which belongs to the hexagonal crystal class. Hence, it has one unique axis which is expected to have a different resistivity than the isotropic plane perpendicular to this. This is a good example of an application of the theory in Section 4.2.4.1; however this was not yet developed at the time. The unique axis is perpendicular to the layers in the structure. Since the crystal was cleaved from the ingot, the measured resistivity is in the isotropic plane. Knowledge of both the in-plane and cross-plane resistivities would be useful when measuring the surface properties of the cleaved crystals.

The high temperature properties are shown in Figure 5-8. Phase I shows properties of a heavily doped semiconductor, phase II behaves like an intrinsic semiconductor, while phase III behaves like a lightly doped semiconductor. Phase I and II are n-type with Hall carrier concentrations in the 10^{18} cm^{-3} range, consistent with the sign and magnitude of the Seebeck coefficient. Phase III is initially p-type but as thermal carriers are excited it turns n-type. Assuming the defect chemistry is not substantially altered this indicates that the conduction band has a higher mobility than the valence band, as confirmed by the measured room temperature Hall mobilities of phase I and III. Phase II has both carrier types and hence the Hall mobility is lower since the carrier concentration is overestimated. The increase in mobility of phase III after 375 K is an artifact of the change in dominant carrier type. Hence, a method for growing bulk insulating $\text{Bi}_2\text{Te}_x\text{Se}_y$ samples has been demonstrated. Angle resolved photoemission spectroscopy (ARPES) measurements of phase I and II are shown in Figure 2 the paper in Appendix C.9. These confirm that the bulk conduction band is unoccupied in phase II while it is occupied in phase I. The band gaps are also found to be close to the estimates from resistivity measurements.

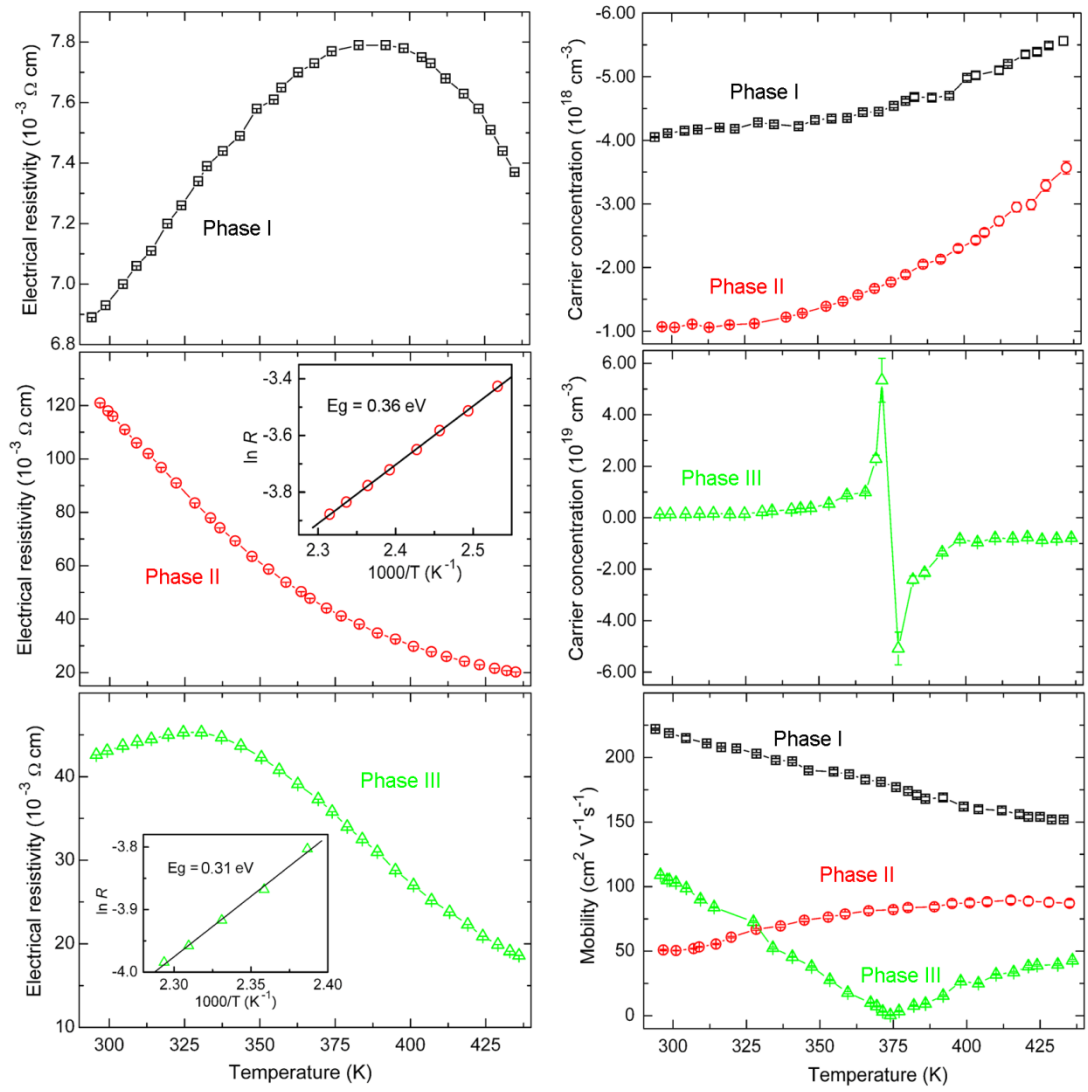


Figure 5-8: High temperature resistivity and Hall effect of $\text{Bi}_2\text{Te}_x\text{Se}_y$ phases. All measurements are performed in the isotropic ab crystallographic plane. No measurements were performed along the unique b axis.

The band gap is of high importance to topological insulators. This can be extracted from the resistivity since in the intrinsic region $\rho = A \cdot \exp(E_g/2k_B T)$ where E_g is the band gap, k_B is the Boltzmann constant, T is the absolute temperature and A is a constant. Hence when plotting $\ln(\rho)$ versus $1/T$, the slope is $E_g/2k_B$. Using the data above 400 K the band gap for phase II and III were found to be 0.36 eV and 0.31 eV, respectively. The data and fits are shown as inserts in Figure 5-8. This indicates that the band gap decreases with increasing Te content. The band gap of phase I cannot be estimated since it has not completely transitioned to the intrinsic region.

This study is a good example of applications of the resistivity and Hall effect setup to another field. This shows that measurements can be carried out on a wide range of samples and the results can be used for many purposes, including estimating band gaps. This is also a prime example of a study where the theory for extracting anisotropic resistivity from van der Pauw measurements could prove useful.

5.4 Further projects not included in this thesis

This last section contains a short summary of other published and ongoing projects which have not been included in this thesis. These are no more or less important but were not included since they are only remotely related to the main project or are not sufficiently mature to include yet. They are all within the field of thermoelectrics but deal with a wide range of topics.

The first study is related to the work on $Mg_2Si_{1-x}Sn_x$ discussed in section 5.2. In this study the thermal conductivity of Mg_2Si was attempted lowered by inclusion of TiO_2 nanoparticle inclusion. This was mainly carried out by Daniel Cederkrantz from Anders Palmqvist's group at Chalmers University of Technology, Gothenburg, Sweden. The paper can be found in reference 105. Samples containing 0-3% by volume of TiO_2 was made from a batch of undoped Mg_2Si . TiO_2 nanoparticles (average size 15 nm) were added to small portions of the Mg_2Si powder to the desired volume fractions and the mixture was then ball milled to ensure good mixing. The powder mixtures were then compacted by SPS. By PXRD it was found that the TiO_2 nanoparticles had been reduced during SPS to form $TiSi_2$ and MgO and possibly traces of Ti metal. This is consistent with a reaction between Mg_2Si and TiO_2 . The addition of the nanoparticles was not found to decrease the thermal conductivity; instead, the Seebeck coefficient and resistivity were found to decrease while the Hall carrier concentration increased with increased TiO_2 content. The Seebeck coefficient was found to systematically decrease with increased nominal TiO_2 content. This is consistent with the formation of metallic Ti inclusions and possibly changes in the average Mg_2Si matrix composition from the reaction. An explanation for the lack of thermal conductivity reduction could be the small grain sizes obtained by ball milling and the existence of MgO in the parent compound. In a related study by the same group (not including any contributions from Aarhus University) the thermal conductivity of $Ba_8Ga_{16}Ge_{30}$ was successfully lowered by TiO_2 inclusion; however, the resistivity was also significantly increased resulting in only minor effects on the zT .¹⁰⁶

In a related study carried out by Hao Yin the addition of TiO_2 was used to thermally stabilize Zn_4Sb_3 . This work can be found in reference 107. Even as little as 0.5% by weight of TiO_2 was found to greatly enhance the thermal stability of Zn_4Sb_3 . Unfortunately, the resistivity and thermal conductivity was greatly increased compared to the pure compound resulting in the zT being lowered from 0.7 in the pure compound to ~0.3 for the TiO_2 containing compounds. This was mainly ascribed to problems with controlling the charge carrier

concentration. Decomposition or reaction of TiO_2 may be part of the explanation but was not observed in PXRD.

Oxides are receiving much attention for high temperature thermoelectric applications. Since they are oxides they are expected to be stable when heated in an oxygen atmosphere. In reality this is found to not always be the case as the transport properties are highly dependent on the actual oxygen content and may thus deteriorate when operating at high temperatures, both in air and vacuum.¹⁰⁸ The most promising thermoelectric oxide is ZnO which can reach $zT = 0.65$ at 1247 K with dual Al and Ge doping.¹⁰⁹ This makes it important to understand the effect of different processing conditions on the thermoelectric properties. In a study led by Martin Søndergaard, the microstructure and thermal diffusivity was investigated as a function of processing conditions. This is published in reference 110. The studied parameters include grain size, sintering temperature during SPS and duration of a post compaction anneal at 800°C in air. Both doped and undoped samples were investigated. Both increased sintering temperature during SPS (780°C, 850°C, and 900°C) and post compaction annealing time (0,1, and 2 weeks) was found to increase the thermal diffusivity. The difference from SPS temperature became smaller with increased annealing time. This is consistent with an increased grain size observed by PXRD. Interestingly higher SPS sintering temperature was also found to increase the carrier concentration in the Al doped samples. The mechanism behind this is not known. The main result was that the Al doping seems to stabilize the particle size, causing less growth during annealing. This results in more stable thermoelectric properties and makes Al doped ZnO a promising material for high temperature applications.

In another study doubly doped CaMnO_3 was characterized, led by Le Thanh Hung from Nini Pryds' group at the Technical University of Denmark. This work is published in reference 111. CaMnO_3 is a promising oxide thermoelectric material but difficulties in controlling the carrier concentration reduce the efficiency.^{112, 113} In order to increase the efficiency, doping on both the Ca and Mn sites was attempted to give the material $\text{Ca}_{0.9}\text{Y}_{0.1}\text{Mn}_{1-x}\text{Fe}_x\text{O}_3$. It was found that the $x = 0.05$ compound increased the zT by 20% to 0.11. This is due to a too low carrier concentration. Attempts to measure this failed since the material had a high resistivity (order of 1 $\Omega\text{-cm}$ at room temperature) and a low mobility. This is the most difficult combination of properties for Hall effect measurements since it results in high noise levels. An additional complication of intrinsic samples is the strong temperature dependence of the resistivity. This causes even very small fluctuations in temperature (from e.g. Joule heating or the Peltier effect) to cause large errors and noise in the small Hall signal.

Cu_2Se and $\text{Cu}_{1.97}\text{Ag}_{0.03}\text{Se}$ were extensively studied in the 1960'es by NASA JPL, 3M Corporation and other affiliated companies.¹¹⁴ The materials were eventually abandoned due to severe problems with loss of Se and reactions with the contact materials. Nonetheless, these materials are receiving much interest as thermoelectric materials today. The materials are super-ionic conductors at temperatures above their super-ionic phase transition at

approximately 410 K.¹¹⁵ In Cu₂Se this has been suggested to lead to a lowered thermal conductivity since the Cu ions behave as a liquid and can hence not transport transverse phonons.¹¹⁶ Even though the materials have been extensively studied some 40-50 years ago, revisiting old materials can sometimes lead to important new discoveries. A prime example is PbSe which was abandoned as a thermoelectric material due to its high thermal conductivity; when this was reevaluated using modern methods the thermal conductivity was found to have been overestimated.^{29, 30} In a joint project with David Brown and Tristan Day from Jeff Snyder's group at Caltech the mechanisms behind the good thermoelectric performance are being investigated. This includes both the thermoelectric properties across the super-ionic phase transitions in Cu₂Se and Ag₂Se and the high temperature properties of Cu₂Se and Cu_{1.97}Ag_{0.03}Se.

Super-ionic conductors can be classified as type I or type II depending on the order of their super-ionic transition. Type I have a first order (discontinuous) transition while type II have a second order (continuous) transition. An intermittent type is also possibly known as a disrupted second order transition, where a first order transition disrupts a second order transition. Cu₂Se was found to be purely type II with a continuous transition in structure as well as all thermoelectric properties. This work is found in reference 10. The transition is characterized by a critical temperature. As this temperature is approached all thermodynamic and transport parameters follow a power law with a critical exponent. A peak is observed in Seebeck coefficient, heat capacity, and resistivity while a dip is observed in thermal diffusivity. The overall effect is to give a peak in zT . A decrease in Hall carrier concentration and mobility are also observed. The fact that both the mobility and thermal diffusivity have a dip indicates that there are some critical scattering processes taking place.¹¹ This could be due to the gradual structural transition which scatters the phonons. The Hall mobility decrease can likely be explained by the static and dynamic disorder during the transition. A rigid band model (single parabolic band in the degenerate limit) of the Seebeck coefficient together with the measured Hall carrier concentration fits the experimental data well both before and after the transition, indicating only minor changes to the band structure occurs. During the transition there is an extra increase in Seebeck coefficient which cannot be explained by this model.

To understand the enhanced Seebeck coefficient and peak in zT Cu₂Se has been compared to Ag₂Se, which is also super-ionic but with purely first order transition. This has not yet been published but will be submitted soon. In this material a sharp drop in Seebeck at the transition temperature was observed. This was accompanied by a sharp drop in thermal diffusivity and sharp increase in mobility while a peak in electrical conductivity was observed before the transition and a sharp drop at the transition. The Hall carrier concentration was found to only change slightly and smoothly across the transition. A peak was also observed in heat capacity; however, this is not a steady state property and hence does not contribute to the thermal conductivity. Instead the values before and after the peak were interpolated and used

for calculating the thermal conductivity. The combined effect was almost no change in zT . The difference between the two compounds lies in the gradual transition and disordering of the ions in Cu₂Se. Since the Seebeck coefficient is closely related to entropy (it can be expressed as entropy transported per carrier) the entropy of the ion disordering is a natural place to look for the mechanism. If the ions and electrons are coupled, the structural entropy is also coupled to the electrons and can thus enhance the Seebeck coefficient. This can be treated rigorously using Onsager equations and including either ion or entropy fluxes. This was found to lead to a mechanism for enhancing the Seebeck coefficient; however, it was also found to not be transparent and useful. Instead different approaches using classical thermodynamics are being examined. This is the last work before the paper will be submitted.

In the literature there has been some debate about which heat capacity to use for the second order transition in Cu₂Se. Since the heat capacity associated with a second order transition is a steady state property it is expected to contribute to the thermal conductivity. This was also done in reference 10. However, Liu *et al.*¹¹ used the much lower Dulong-Petit value across the transition. Even though the contribution to the heat capacity from the structural transition is a steady state property, this energy may not be accessible by the phonons as excitations. In reality, the phonon heat capacity is most likely intermittent of the two. In another study by Liu *et al.*¹¹⁶ the heat capacity was found to decrease at high temperature. Values almost as low as $2k_B T$ were reached which is in violation of the Dulong-Petit law. This was explained by the liquid like behavior of Cu ions. In a liquid the heat capacity can theoretically reach values as low as $2k_B T$. This is not always the case, however, which is clearly shown by water which has a heat capacity of 4.18 J/gK, slightly above the Dulong-Petit value of 4.16 J/gK. The heat capacity is an expression of the number of modes available for excitation where the Dulong-Petit law corresponds to all modes being available. It seems unlikely that a material which is initially above its Debye temperature would lose excitational modes as the temperature is increased. The liquid like Cu ions still vibrate in a 3D potential and hence still have three vibrational modes. To elucidate this and the discussion of the heat capacity contributing to thermal conduction across the phase transition, several properties relevant to thermal conductivity are being measured in an ongoing project. These include direct thermal conductivity measurements as well as different indirect measurements and the micro- and macroscopic thermal expansion coefficient (from PXRD and dilatometry, respectively). This will be compared to phonon heat capacities extracted from neutron diffraction experiments. To this end, a method for growing large single crystals of Cu₂Se with various Cu deficiencies has been developed.

While Cu_{1.97}Ag_{0.03}Se was thoroughly studied in the 1960's the transport properties were never thoroughly analyzed. To remedy this, the single parabolic model was applied and found to describe the transport properties well. These results are found in reference 117. The most important result is that the material appears to be overly doped and the thermoelectric performance can be improved if the carrier concentration is lowered. The material (like

Cu_2Se) is intrinsically p-type due to Cu vacancies. The material is always Cu deficient and reducing the carrier concentration is difficult without producing metallic Cu impurities. One method which was found to successfully reduce the carrier concentration was by annealing the material on top of a clean Cu surface at 500°C. This was tested on a piece of single crystalline Cu_2Se and was found to successfully reduce the carrier concentration from $7.0 \cdot 10^{21} \text{ cm}^{-3}$ to $1.17 \cdot 10^{20} \text{ cm}^{-3}$. This is lower than for any of the materials in the studies discussed above.

This section has summarized all larger projects not included in the thesis. Several minor projects have been or are being carried out. These include an article in a Danish popular science journal about thermoelectrics (aimed at high school level chemistry and physics), a study of the thermal stability of $\text{Ba}_8\text{Ga}_{16}\text{Ge}_{30}$ using PXRD and transport property measurements, and crystal growth work which was intended for applying the methods for anisotropic resistivity in Chapter 4 as well as Cu_2Se for neutron diffraction and transport property measurements.

6 Conclusion

In this dissertation two extensive experimental setups have been described. One measures the Seebeck coefficient and one measures the resistivity and Hall effect data. Both are operational and can measure the properties from room temperature to 800°C. This temperature can be further extended but this has not yet proved necessary. The setups have been discussed in relation to published literature and other state of the art instruments. They are found to be accurate but several possible improvements to both have been pointed out. The initial construction took about two years. After the commission of the instruments several issues and improvements were identified and continued work on them was necessary. This is not expected to change, and this is of high importance to accurate thermoelectric measurements. It is my hope that future generations of Ph.D students will continue this work to keep the setups operational and of the highest quality. Most of this work was done under the supervision of Dr. G. Jeffrey Snyder at Caltech and in a close collaboration with his group.

After the setups were put in use the main project was the work on the extension of the van der Pauw method to anisotropic samples. The theory has successfully been worked out and two new methods have been presented. Additionally, the requirements for the sample geometry has been relaxed compared to the sparse previous literature (from rectangular to parallelogram shaped samples). These methods are believed to be accurate ways to determine the anisotropic resistivity. MATLAB™ scripts have been developed both for data analysis and error estimation. The initial tests proved the methods to be useful and accurate. The results are currently being prepared for publication. This will be submitted once a more suitable test system than the RuSb₂ has been found and all scripts have been thoroughly tested and corrected. These scripts will also be part of the publication, as supplemental material, to ease the implementation in other labs.

Several materials science projects were discussed where the setups have contributed. These include both the fields of thermoelectrics and topological insulators, proving the systems to be of wide applicability. One of these projects, namely on the Bi₂Te₂Se topological insulator, is furthermore a prime example of a study where the methods for treating anisotropic resistivity would have been of help. This is also applicable to many other studies, including the study of the Cu₂Se phase transition. Many interesting properties have been found of this transition and the anisotropy of single crystals may also be of interest.

7 References

1. M. Trakalo, C. J. Moore, J. D. Leslie and D. E. Brodie, *Rev. Sci. Instrum.*, 1984, **55**, 754-760.
2. T. M. Tritt and M. A. Subramanian, *MRS Bull.*, 2006, **31**, 188-194.
3. F. J. DiSalvo, *Science*, 1999, **285**, 703-706.
4. J. H. Yang and T. Caillat, *MRS Bull.*, 2006, **31**, 224-229.
5. D. Samson, M. Kluge, T. Becker and U. Schmid, *Sensor. Actuat. A*, 2011, **172**, 240-244.
6. A. Dewan, S. U. Ay, M. N. Karim and H. Beyenal, *J. Power Sources*, 2014, **245**, 129-143.
7. L. E. Bell, *Science*, 2008, **321**, 1457-1461.
8. T. C. Harman, J. H. Cahn and M. J. Logan, *J. Appl. Phys.*, 1959, **30**, 1351-1359.
9. X. Y. Ao, J. de Boor and V. Schmidt, *Adv. Energy Mater.*, 2011, **1**, 1007-1011.
10. D. R. Brown, T. Day, K. A. Borup, S. Christensen, B. B. Iversen and G. J. Snyder, *APL Mater.*, 2013, **1**, 52107.
11. H. Liu, X. Yuan, P. Lu, X. Shi, F. Xu, Y. He, Y. Tang, S. Bai, W. Zhang, L. Chen, Y. Lin, L. Shi, H. Lin, X. Gao, X. Zhang, H. Chi and C. Uher, *Adv. Mater.*, 2013, **25**, 6607-6612.
12. G. J. Snyder and E. S. Toberer, *Nat. Mater.*, 2008, **7**, 105-114.
13. M. Cutler and N. F. Mott, *Phys. Rev.*, 1969, **181**, 1336-1340.
14. J. P. Heremans, B. Wiendlocha and A. M. Chamoire, *Energ. Environ. Sci.*, 2012, **5**, 5510-5530.
15. V. I. Fistul, *Heavily doped semiconductors*, Plenum Press, New York, 1969.
16. Y. Z. Pei, X. Y. Shi, A. LaLonde, H. Wang, L. D. Chen and G. J. Snyder, *Nature*, 2011, **473**, 66-69.
17. W. Liu, X. J. Tan, K. Yin, H. J. Liu, X. F. Tang, J. Shi, Q. J. Zhang and C. Uher, *Phys. Rev. Lett.*, 2012, **108**, 166601.
18. S. Wang and N. Mingo, *Phys. Rev. B*, 2009, **79**.
19. J. M. Ziman, *Electrons and phonons: the theory of transport phenomena in solids*, Oxford University Press, Oxford, 2007.
20. N. W. Ashcroft and N. D. Mermin, *Solid state physics*, CBS Publishing, Philadelphia, 1988.
21. P. Hofmann, *Solid state physics: an introduction*, Wiley-VCH, Weinheim, 2008.
22. C. J. Vineis, T. C. Harman, S. D. Calawa, M. P. Walsh, R. E. Reeder, R. Singh and A. Shakouri, *Phys. Rev. B*, 2008, **77**, 235202.
23. A. F. May, E. S. Toberer, A. Saramat and G. J. Snyder, *Phys. Rev. B*, 2009, **80**, 125205.
24. A. F. May and G. J. Snyder, in *Materials, Preparation, and Characterization in Thermoelectrics*, CRC Press, 2012, pp. 1-18.
25. E. H. Putley, *The Hall effect and related phenomena*, Butterworths, London, 1960.
26. A. Matthiessen and C. Vogt, *Philos. Trans. R. Soc. London*, 1864, **154**, 167-200.
27. H. Wang, W. Porter, H. Böttner, J. König, L. Chen, S. Bai, T. Tritt, A. Mayolet, J. Senawiratne, C. Smith, F. Harris, P. Gilbert, J. Sharp, J. Lo, H. Kleinke and L. Kiss, *J. Electron. Mater.*, 2013, **42**, 654-664.
28. H. Wang, W. Porter, H. Böttner, J. König, L. Chen, S. Bai, T. Tritt, A. Mayolet, J. Senawiratne, C. Smith, F. Harris, P. Gilbert, J. Sharp, J. Lo, H. Kleinke and L. Kiss, *J. Electron. Mater.*, 2013, **42**, 1073-1084.
29. H. Wang, Y. Pei, A. D. LaLonde and G. J. Snyder, *Adv. Mater.*, 2011, **23**, 1366-1370.
30. H. Wang, Y. Pei, A. D. LaLonde and G. J. Snyder, *P. Natl. Acad. Sci. USA*, 2012, **109**, 9705-9709.
31. E. S. Toberer, M. Christensen, B. B. Iversen and G. J. Snyder, *Phys. Rev. B*, 2008, **77**, 075203.
32. S. M. Kauzlarich, *Chemistry, structure, and bonding of Zintl phases and ions*, VCH New York, 1996.
33. S. C. Sevov, in *Intermetallic Compounds - Principles and Practice*, John Wiley & Sons, Ltd, 2002, pp. 113-132.
34. S. M. Kauzlarich, S. R. Brown and G. Jeffrey Snyder, *Dalton Trans.*, 2007, 2099-2107.
35. E. S. Toberer, A. F. May and G. J. Snyder, *Chem. Mater.*, 2009, **22**, 624-634.
36. M. Søndergaard, M. Christensen, K. A. Borup, H. Yin and B. B. Iversen, *Acta Mater.*, 2012, **60**, 5745-5751.
37. M. Søndergaard, M. Christensen, K. Borup, H. Yin and B. Iversen, *J. Mater. Sci.*, 2013, **48**, 2002-2008.
38. H. Yin, M. Christensen, N. Lock and B. B. Iversen, *Appl. Phys. Lett.*, 2012, **101**, 043901.
39. T. Dasgupta, C. Stiewe, A. Sesselmann, H. Yin, B. Iversen and E. Mueller, *J. Appl. Phys.*, 2013, **113**, 103708.

40. M. Beekman, M. Baitinger, H. Borrmann, W. Schnelle, K. Meier, G. S. Nolas and Y. Grin, *J. Am. Chem. Soc.*, 2009, **131**, 9642-9643.
41. N. Chen, F. Gascoin, G. J. Snyder, E. Müller, G. Karpinski and C. Stiewe, *Appl. Phys. Lett.*, 2005, **87**, 171903.
42. D. Platzek, G. Karpinski, C. Stiewe, P. Ziolkowski, C. Drasar and E. Muller, Potential-Seebeck-microprobe (PSM): measuring the spatial resolution of the Seebeck coefficient and the electric potential, Clemson, South Carolina, USA, 2005.
43. H. L. Ni, X. B. Zhao, G. Karpinski and E. Müller, *J. Mater. Sci.*, 2005, **40**, 605-608.
44. S. Iwanaga and G. J. Snyder, *J. Electron. Mater.*, 2012, **41**, 1667-1674.
45. A. F. May, J.-P. Fleurial and G. J. Snyder, *Phys. Rev. B*, 2008, **78**, 125205.
46. M. Sondergaard, M. Christensen, L. Bjerg, K. A. Borup, P. Sun, F. Steglich and B. B. Iversen, *Dalton Trans.*, 2012, **41**, 1278-1283.
47. J. Martin, *Meas. Sci. Technol.*, 2013, **24**, 085601.
48. J. Martin, T. Tritt and C. Uher, *J. Appl. Phys.*, 2010, **108**, 121101.
49. J. de Boor and E. Muller, *Rev. Sci. Instrum.*, 2013, **84**, 065102.
50. P. H. M. Bottger, E. Flage-Larsen, O. B. Karlsen and T. G. Finstad, *Rev. Sci. Instrum.*, 2012, **83**, 025101.
51. R. L. Kallaher, C. A. Latham and F. Sharifi, *Rev. Sci. Instrum.*, 2013, **84**, 013907.
52. J. Martin, *Rev. Sci. Instrum.*, 2012, **83**, 065101-065109.
53. C. Wood, D. Zoltan and G. Stauffer, *Rev. Sci. Instrum.*, 1985, **56**, 719-722.
54. S. Iwanaga, E. S. Toberer, A. LaLonde and G. J. Snyder, *Rev. Sci. Instrum.*, 2011, **82**, 063905.
55. A. Guan, H. Wang, H. Jin, W. Chu, Y. Guo and G. Lu, *Rev. Sci. Instrum.*, 2013, **84**, 043903.
56. K. A. Borup, E. S. Toberer, L. D. Zoltan, G. Nakatsukasa, M. Errico, J.-P. Fleurial, B. B. Iversen and G. J. Snyder, *Rev. Sci. Instrum.*, 2012, **83**, 123902.
57. L. J. van der Pauw, *Philips Res. Rep.*, 1958, **13**, 1.
58. L. J. van der Pauw, *Philips Tech. Rev.*, 1958, **20**, 220.
59. A. T. Burkov, A. Heinrich, P. P. Konstantinov, T. Nakama and K. Yagasaki, *Meas. Sci. Technol.*, 2001, **12**, 264.
60. V. Ponnambalam, S. Lindsey, N. S. Hickman and T. M. Tritt, *Rev. Sci. Instrum.*, 2006, **77**, 073904.
61. B. Céline, B. David and D. Nita, *Meas. Sci. Technol.*, 2012, **23**, 035603.
62. D. M. Rowe, *Thermoelectrics Handbook: Macro to Nano*, CRC press, 2006.
63. D. M. Rowe, *CRC handbook of thermoelectrics*, CRC press, 2010.
64. L.-D. Zhao, J. He, S. Hao, C.-I. Wu, T. P. Hogan, C. Wolverton, V. P. Dravid and M. G. Kanatzidis, *J. Am. Chem. Soc.*, 2012, **134**, 16327-16336.
65. H. Wang, A. D. LaLonde, Y. Pei and G. J. Snyder, *Adv. Func. Meter.*, 2013, **23**, 1586-1596.
66. X. Liu, T. Zhu, H. Wang, L. Hu, H. Xie, G. Jiang, G. J. Snyder and X. Zhao, *Adv. Energy Mater.*, 2013, **3**, 1238-1244.
67. J. W. Vandersande, A. Zoltan and C. Wood, *Int. J. Thermophys.*, 1989, **10**, 251-257.
68. C. B. Vining, A. Zoltan and J. W. Vandersande, *Int. J. Thermophys.*, 1989, **10**, 259-268.
69. W. J. Parker, R. J. Jenkins, C. P. Butler and G. L. Abbott, *J. Appl. Phys.*, 1961, **32**, 1679-1684.
70. J. de Boor and V. Schmidt, *Adv. Mater.*, 2010, **22**, 4303-4307.
71. A. L. Pope, B. Zawilski and T. M. Tritt, *Cryogenics*, 2001, **41**, 725-731.
72. T. M. Tritt, *Thermal conductivity: theory, properties, and applications*, Springer, 2004.
73. V. K. Zaitsev, M. I. Fedorov, E. A. Gurieva, I. S. Eremin, P. P. Konstantinov, A. Y. Samunin and M. V. Vedernikov, *Phys. Rev. B*, 2006, **74**, 045207.
74. G. T. Alekseeva, E. A. Gurieva, P. P. Konstantinov, L. V. Prokofeva and M. I. Fedorov, *Semiconductors*, 1996, **30**, 1125-1127.
75. R. D. Cowan, *J. Appl. Phys.*, 1963, **34**, 926-927.
76. L. M. Clark III and R. E. Taylor, *J. Appl. Phys.*, 1975, **46**, 714-719.
77. J. A. Cape and G. W. Lehman, *J. Appl. Phys.*, 1963, **34**, 1909-1913.
78. J. S. Hwang, K. J. Lin and C. Tien, *Rev. Sci. Instrum.*, 1997, **68**, 94-101.
79. C. Kasl and M. J. R. Hoch, *Rev. Sci. Instrum.*, 2005, **76**, 033907.
80. C. G. M. Kirby and M. J. Laubitz, *Metrologia*, 1973, **9**, 103.
81. M. V. Cheremisin, Peltier effect induced correction to ohmic resistance, Washington, DC, USA, 2001.
82. H. Brodowsky, Q. Y. Chen, Z. L. Xiao and Z. L. Yin, *J. Electron. Mater.*, 2011, **40**, 1984-1989.
83. W. L. V. Price, *Solid-State Electron.*, 1973, **16**, 753-762.
84. O. Bierwagen, R. Pomraenke, S. Eilers and W. T. Masselink, *Phys. Rev. B*, 2004, **70**, 165307.

85. J. Kleiza and V. Kleiza, *Electron. Electr. Eng.*, 2005, **59**, 51-54.
86. J. Kleiza and V. Kleiza, *Lith. J. Phys.*, 2005, **45**, 333-338.
87. J. Kleiza, M. Sapagovas and V. Kleiza, *Informatica*, 2007, **18**, 253-266.
88. S. Ašmontas, V. Kleiza and J. Kleiza, *Acta Phys. Pol. A*, 2008, **113**, 1559-1569.
89. J. Kleiza and V. Kleiza, *Acta Phys. Pol. A*, 2011, **119**, 148-150.
90. J. F. Nye, *Physical Properties of Crystals: Their Representation by Tensors and Matrices*, Clarendon Press, 1985.
91. A. Bentien, S. Johnsen, G. K. H. Madsen, B. B. Iversen and F. Steglich, *Europhys. Lett.*, 2007, **80**, 17008.
92. C. B. Vining, W. Laskow, J. O. Hanson, R. R. Van der Beck and P. D. Gorsuch, *J. Appl. Phys.*, 1991, **69**, 4333-4340.
93. E. Müller, Č. Drašar, J. Schilz and W. A. Kayser, *Mater. Sci. Eng.*, 2003, **362**, 17-39.
94. R. Braunstein, A. R. Moore and F. Herman, *Phys. Rev.*, 1958, **109**, 695-710.
95. M. Christensen, S. Johnsen, M. Søndergaard, J. Overgaard, H. Birkedal and B. B. Iversen, *Chem. Mater.*, 2008, **21**, 122-127.
96. V. Kuznetsov, in *CRC Handbook of Thermoelectrics: Macro to Nano*, ed. D. M. Rowe, CRC press, 2006.
97. J. Bardeen and W. Shockley, *Phys. Rev.*, 1950, **80**, 72-80.
98. S. Krishnamurthy, A. Sher and A. B. Chen, *Appl. Phys. Lett.*, 1985, **47**, 160-162.
99. M. Søndergaard, M. Christensen, K. A. Borup, H. Yin and B. B. Iversen, *J. Electron. Mater.*, 2013, **42**, 1417-1421.
100. D. A. Porter and K. E. Easterling, *Phase Transformations in Metals and Alloys*, CRC press, 1992.
101. I.-H. Jung, D.-H. Kang, W.-J. Park, N. J. Kim and S. Ahn, *Calphad*, 2007, **31**, 192-200.
102. L. Müchler, H. Zhang, S. Chadov, B. Yan, F. Casper, J. Kübler, S.-C. Zhang and C. Felser, *Angew. Chem. Int. Ed.*, 2012, **124**, 7333-7337.
103. D. O. Scanlon, P. D. C. King, R. P. Singh, A. de la Torre, S. M. Walker, G. Balakrishnan, F. Baumberger and C. R. A. Catlow, *Adv. Mater.*, 2012, **24**, 2154-2158.
104. J. L. Mi, M. Bremholm, M. Bianchi, K. Borup, S. Johnsen, M. Søndergaard, D. Guan, R. C. Hatch, P. Hofmann and B. B. Iversen, *Adv. Mater.*, 2012, **25**, 889-893.
105. D. Cederkrantz, N. Farahi, K. A. Borup, B. B. Iversen, M. Nygren and A. Palmqvist, *J. Appl. Phys.*, 2012, **111**, 023701.
106. R. Heijl, D. Cederkrantz, M. Nygren and A. Palmqvist, *J. Appl. Phys.*, 2012, **112**, 044313.
107. H. Yin, S. Johnsen, K. A. Borup, K. Kato, M. Takata and B. B. Iversen, *Chem. Commun.*, 2013, **49**, 6540-6542.
108. D. Bérardan, C. Byl and N. Dragoe, *J. Am. Ceram. Soc.*, 2010, **93**, 2352-2358.
109. M. Ohtaki, K. Araki and K. Yamamoto, *J. Electron. Mater.*, 2009, **38**, 1234-1238.
110. M. Søndergaard, E. D. Bøjesen, K. A. Borup, S. Christensen, M. Christensen and B. B. Iversen, *Acta Mater.*, 2013, **61**, 3314-3323.
111. L. T. Hung, N. V. Nong, L. Han, D. L. Minh, K. A. Borup, B. B. Iversen, N. Pryds and S. Linderoth, *J. Mater. Sci.*, 2013, **48**, 2817-2822.
112. D. Flahaut, T. Mihara, R. Funahashi, N. Nabeshima, K. Lee, H. Ohta and K. Koumoto, *J. Appl. Phys.*, 2006, **100**, 084911.
113. Y. Wang, Y. Sui and W. Su, *J. Appl. Phys.*, 2008, **104**, 093703.
114. D. Brown, T. Day, T. Caillat and G. J. Snyder, *J. Electron. Mater.*, 2013, **42**, 2014-2019.
115. M. Horvatić and Z. Vučić, *Solid State Ionics*, 1984, **13**, 117-125.
116. H. Liu, X. Shi, F. Xu, L. Zhang, W. Zhang, L. Chen, Q. Li, C. Uher, T. Day and G. J. Snyder, *Nat. Mater.*, 2012, **11**, 422-425.
117. T. Day, K. Borup, T. Zhang, F. Drymiotis, D. Brown, X. Shi, L. Chen, B. Iversen and G. J. Snyder, *Mater. Renew. Sustain. Energy*, 2014, **3**, 23.

8 Appendices

Appendix A Derivations from Chapter 4

Appendix A.1 Anisotropic parallelogram side lengths and angle

From the linear transformation, the vectors representing the sides of the isotropic sample are obtained:

$$\begin{aligned}\mathbf{a}' &= a \sqrt{\frac{\rho_{yy}}{\rho_{iso}}} \begin{pmatrix} 1 \\ 0 \end{pmatrix} \\ \mathbf{b}' &= \frac{b}{\sqrt{\rho_{yy}\rho_{iso}}} \begin{pmatrix} \cos(\chi) \rho_{yy} - \sin(\chi) \rho_{xy} \\ \sin(\chi) \rho_{iso} \end{pmatrix}\end{aligned}$$

Their lengths are

$$\begin{aligned}a' &= |\mathbf{a}'| = a \sqrt{\frac{\rho_{yy}}{\rho_{iso}}} \\ b' &= |\mathbf{b}'| = \left(\left(\frac{b}{\sqrt{\rho_{yy}\rho_{iso}}} \right)^2 \begin{pmatrix} \cos(\chi) \rho_{yy} - \sin(\chi) \rho_{xy} \\ \sin(\chi) \rho_{iso} \end{pmatrix} \cdot \begin{pmatrix} \cos(\chi) \rho_{yy} - \sin(\chi) \rho_{xy} \\ \sin(\chi) \rho_{iso} \end{pmatrix} \right)^{\frac{1}{2}} \\ &= \frac{b}{\sqrt{\rho_{yy}\rho_{iso}}} \sqrt{\cos(\chi)^2 \rho_{yy}^2 + \sin(\chi)^2 \rho_{xy}^2 - 2 \cos(\chi) \sin(\chi) \rho_{yy} \rho_{xy} + \sin(\chi)^2 \rho_{iso}^2} \\ &= b \sqrt{\cos(\chi)^2 \frac{\rho_{yy}}{\rho_{iso}} + \sin(\chi)^2 \frac{\rho_{xy}^2 + \rho_{iso}^2}{\rho_{yy}\rho_{iso}} - 2 \cos(\chi) \sin(\chi) \frac{\rho_{xy}}{\rho_{iso}}}\end{aligned}$$

The angle between the vectors, $\pi\alpha$, is calculated by

$$\cos(\pi\alpha) = \frac{\mathbf{a}' \cdot \mathbf{b}'}{a'b'}$$

That is, the dot product divided by the product of the lengths. The dot product is

$$\begin{aligned}\mathbf{a}' \cdot \mathbf{b}' &= \frac{ab}{\rho_{iso}} \begin{pmatrix} 1 \\ 0 \end{pmatrix} \cdot \begin{pmatrix} \cos(\chi) \rho_{yy} - \sin(\chi) \rho_{xy} \\ \sin(\chi) \rho_{iso} \end{pmatrix} \\ &= \frac{ab}{\rho_{iso}} (\cos(\chi) \rho_{yy} - \sin(\chi) \rho_{xy})\end{aligned}$$

And the product of the lengths

$$\begin{aligned} a'b' &= ab \sqrt{\frac{\rho_{yy}}{\rho_{iso}}} \sqrt{\cos(\chi)^2 \frac{\rho_{yy}}{\rho_{iso}} + \sin(\chi)^2 \frac{\rho_{xy}^2 + \rho_{iso}^2}{\rho_{yy}\rho_{iso}} - 2 \cos(\chi) \sin(\chi) \frac{\rho_{xy}}{\rho_{iso}}} \\ &= ab \sqrt{\cos(\chi)^2 \left(\frac{\rho_{yy}}{\rho_{iso}} \right)^2 + \sin(\chi)^2 \frac{\rho_{xy}^2 + \rho_{iso}^2}{\rho_{iso}^2} - 2 \cos(\chi) \sin(\chi) \frac{\rho_{yy}\rho_{xy}}{\rho_{iso}^2}} \end{aligned}$$

And the angle is obtained as

$$\begin{aligned} \cos(\pi\alpha) &= \frac{\frac{ab}{\rho_{iso}} (\cos(\chi) \rho_{yy} - \sin(\chi) \rho_{xy})}{ab \sqrt{\cos(\chi)^2 \left(\frac{\rho_{yy}}{\rho_{iso}} \right)^2 + \sin(\chi)^2 \frac{\rho_{xy}^2 + \rho_{iso}^2}{\rho_{iso}^2} - 2 \cos(\chi) \sin(\chi) \frac{\rho_{yy}\rho_{xy}}{\rho_{iso}^2}}} \\ &= \frac{\cos(\chi) \rho_{yy} - \sin(\chi) \rho_{xy}}{\sqrt{\cos(\chi)^2 \rho_{yy}^2 + \sin(\chi)^2 (\rho_{xy}^2 + \rho_{iso}^2) - 2 \cos(\chi) \sin(\chi) \rho_{yy}\rho_{xy}}} \\ &= \frac{\cos(\chi) \rho_{yy} - \sin(\chi) \rho_{xy}}{\sqrt{\cos(\chi)^2 \rho_{yy}^2 + \sin(\chi)^2 \rho_{xx}\rho_{yy} - 2 \cos(\chi) \sin(\chi) \rho_{yy}\rho_{xy}}} \\ &= \frac{1}{\sqrt{\rho_{yy}}} \frac{\cos(\chi) \rho_{yy} - \sin(\chi) \rho_{xy}}{\sqrt{\cos(\chi)^2 \rho_{yy} + \sin(\chi)^2 \rho_{xx} - 2 \cos(\chi) \sin(\chi) \rho_{xy}}} \end{aligned}$$

Further simplification is not possible since the nominator can be both positive and negative, depending on χ .

Appendix A.2 Resistivity tensor elements for an anisotropic rectangle

From section 4.2.2.1 we have the equations, which need to be solved for ρ_{xx} , ρ_{yy} , and ρ_{xy}

$$\rho_{iso} = \sqrt{\rho_{xx}\rho_{yy} - \rho_{xy}^2}$$

$$\frac{a}{b} B_{\alpha,k} = \sqrt{\frac{\rho_{xx}}{\rho_{yy}}}$$

$$\cos(\pi\alpha) = -\frac{\rho_{xy}}{\sqrt{\rho_{xx}\rho_{yy}}}$$

Multiplication of the last two equations gives

$$\frac{a}{b} B_{\alpha,k} \cos(\pi\alpha) = -\sqrt{\frac{\rho_{xx}}{\rho_{yy}}} \frac{\rho_{xy}}{\sqrt{\rho_{xx}\rho_{yy}}} = -\frac{\rho_{xy}}{\rho_{yy}}$$

$$\rho_{yy} = -\frac{b}{a} B_{\alpha,k}^{-1} \frac{\rho_{xy}}{\cos(\pi\alpha)}$$

Squaring the second equation and using the above

$$\rho_{xx} = \rho_{yy} \frac{a^2}{b^2} B_{\alpha,k}^2 = -\frac{a}{b} B_{\alpha,k} \frac{\rho_{xy}}{\cos(\pi\alpha)}$$

Squaring the expression for ρ_{iso} and substituting the expressions for ρ_{xx} and ρ_{yy}

$$\rho_{iso}^2 = \rho_{xx}\rho_{yy} - \rho_{xy}^2 = \frac{a}{b} B_{\alpha,k} \frac{\rho_{xy}}{\cos(\pi\alpha)} \frac{b}{a} B_{\alpha,k}^{-1} \frac{\rho_{xy}}{\cos(\pi\alpha)} - \rho_{xy}^2 = \rho_{xy}^2 \left(\frac{1}{\cos^2(\pi\alpha)} - 1 \right)$$

$$= \rho_{xy}^2 \frac{\sin^2(\pi\alpha)}{\cos^2(\pi\alpha)}$$

$$\rho_{xy} = -\cos(\pi\alpha) \frac{\rho_{iso}}{\sin(\pi\alpha)}$$

When taking the square root above the negative sign has been chosen since otherwise ρ_{xx} and ρ_{yy} would be negative when this is inserted in the equations above. Finally, ρ_{xx} and ρ_{yy} are obtained

$$\rho_{xx} = \frac{a}{b} B_{\alpha,k} \frac{\rho_{iso}}{\sin(\pi\alpha)}$$

$$\rho_{yy} = \frac{b}{a} B_{\alpha,k}^{-1} \frac{\rho_{iso}}{\sin(\pi\alpha)}$$

Appendix A.3 Resistivity tensor elements for the anisotropic parallelogram

Here the equations presented in section 4.2.2.4 will be derived. From section 4.2.2.2 we have

$$\cos(\pi\alpha) = \frac{1}{\sqrt{\rho_{yy}}} \frac{c\rho_{yy} - s\rho_{xy}}{\sqrt{c^2\rho_{yy} + s^2\rho_{xx} - cs\rho_{xy}}}$$

And from equation (4-26) in section 4.2.2.3 we have

$$B_{\alpha,k} = \frac{b'}{a'}$$

And the definition of $\rho_{iso} = \sqrt{\rho_{xx}\rho_{yy} - \rho_{xy}^2}$ is still valid and provided by experiment.

Inserting the expressions derived for a' and b' in Appendix A.1 the following is obtained

$$\begin{aligned}
B_{\alpha,k} &= \frac{b \sqrt{c^2 \frac{\rho_{yy}}{\rho_{iso}} + s^2 \frac{\rho_{xy}^2 + \rho_{iso}^2}{\rho_{yy}\rho_{iso}} - 2cs \frac{\rho_{xy}}{\rho_{iso}}}}{a \sqrt{\frac{\rho_{yy}}{\rho_{iso}}}} = \frac{b}{a} \sqrt{c^2 + s^2 \frac{\rho_{xy}^2 + \rho_{iso}^2}{\rho_{iso}^2} - 2cs \frac{\rho_{xy}}{\rho_{yy}}} \\
&= \frac{b}{a} \sqrt{c^2 + s^2 \frac{\rho_{xx}\rho_{yy}}{\rho_{yy}^2} - 2cs \frac{\rho_{xy}}{\rho_{yy}}} = \frac{b}{a} \frac{1}{\sqrt{\rho_{yy}}} \sqrt{c^2\rho_{yy} + s^2\rho_{xx} - 2cs\rho_{xy}}
\end{aligned}$$

In the third equality the definition of ρ_{iso} has been used. Multiplying by $\cos(\pi\alpha)$

$$\begin{aligned}
B_{\alpha,k} \cos(\pi\alpha) &= \frac{b}{a} \frac{1}{\sqrt{\rho_{yy}}} \sqrt{c^2\rho_{yy} + s^2\rho_{xx} - 2cs\rho_{xy}} \frac{1}{\sqrt{\rho_{yy}}} \frac{c\rho_{yy} - s\rho_{xy}}{\sqrt{c^2\rho_{yy} + s^2\rho_{xx} - cs\rho_{xy}}} \\
&= \frac{b}{a} \frac{1}{\rho_{yy}} (c\rho_{yy} - s\rho_{xy})
\end{aligned}$$

Or, isolating ρ_{xy}

$$\rho_{xy} = \frac{\rho_{yy}}{s} \left(c - \frac{a}{b} B_{\alpha,k} \cos(\pi\alpha) \right)$$

From the definition of ρ_{iso}

$$\rho_{xx} = \frac{\rho_{iso}^2 + \rho_{xy}^2}{\rho_{yy}}$$

Rewriting one of the expressions for $B_{\alpha,k}$

$$\begin{aligned}
B_{\alpha,k} &= \frac{b}{a} \frac{1}{\sqrt{\rho_{yy}}} \sqrt{c^2\rho_{yy} + s^2\rho_{xx} - 2cs\rho_{xy}} = \frac{b}{a} \frac{1}{\sqrt{\rho_{yy}}} \sqrt{c^2\rho_{yy} + s^2 \frac{\rho_{iso}^2 + \rho_{xy}^2}{\rho_{yy}} - 2cs\rho_{xy}} \\
&= \frac{b}{a} \frac{1}{\sqrt{\rho_{yy}}} \sqrt{c^2\rho_{yy} + s^2 \frac{\rho_{iso}^2}{\rho_{yy}} + s^2 \frac{\rho_{xy}^2}{\rho_{yy}} - 2cs\rho_{xy}} = \frac{b}{a} \frac{1}{\rho_{yy}} \sqrt{c^2\rho_{yy}^2 + s^2\rho_{iso}^2 + s^2\rho_{xy}^2 - 2cs\rho_{xy}\rho_{yy}} \\
&= \frac{b}{a} \frac{1}{\rho_{yy}} \sqrt{c^2\rho_{yy}^2 + s^2\rho_{iso}^2 + s^2 \frac{\rho_{yy}^2}{s^2} \left(c - \frac{a}{b} B_{\alpha,k} \cos(\pi\alpha) \right)^2 - 2cs\rho_{yy} \frac{\rho_{yy}}{s} \left(c - \frac{a}{b} B_{\alpha,k} \cos(\pi\alpha) \right)} \\
&= \frac{b}{a} \frac{1}{\rho_{yy}} \sqrt{2c^2\rho_{yy}^2 + s^2\rho_{iso}^2 + \rho_{yy}^2 \frac{a^2}{b^2} B_{\alpha,k}^2 \cos^2(\pi\alpha) - 2c\rho_{yy}^2 \frac{a}{b} B_{\alpha,k} \cos(\pi\alpha) - 2c^2\rho_{yy}^2 + 2c\rho_{yy}^2 \frac{a}{b} B_{\alpha,k} \cos(\pi\alpha)} \\
&= \frac{b}{a} \frac{1}{\rho_{yy}} \sqrt{s^2\rho_{iso}^2 + \frac{a^2}{b^2} \rho_{yy}^2 B_{\alpha,k}^2 \cos^2(\pi\alpha)}
\end{aligned}$$

And isolating ρ_{yy}

$$\frac{a^2}{b^2} \rho_{yy}^2 B_{\alpha,k}^2 = s^2 \rho_{iso}^2 + \frac{a^2}{b^2} \rho_{yy}^2 B_{\alpha,k}^2 \cos^2(\pi\alpha)$$

$$\rho_{yy}^2 \frac{a^2}{b^2} B_{\alpha,k}^2 (1 - \cos^2(\pi\alpha)) = s^2 \rho_{iso}^2$$

$$\rho_{yy}^2 \frac{a^2}{b^2} B_{\alpha,k}^2 \sin^2(\pi\alpha) = s^2 \rho_{iso}^2$$

$$\rho_{yy} = s \frac{b}{a} B_{\alpha,k}^{-1} \frac{\rho_{iso}}{\sin(\pi\alpha)}$$

From this ρ_{xy} is easily obtained

$$\begin{aligned} \rho_{xy} &= \frac{\rho_{yy}}{s} \left(c - \frac{a}{b} B_{\alpha,k} \cos(\pi\alpha) \right) \\ &= c \frac{b}{a} B_{\alpha,k}^{-1} \frac{\rho_{iso}}{\sin(\pi\alpha)} - \frac{\rho_{iso}}{\sin(\pi\alpha)} \cos(\pi\alpha) \end{aligned}$$

Finally, ρ_{xx} can be calculated from $\rho_{xx} = \frac{\rho_{iso}^2 + \rho_{xy}^2}{\rho_{yy}}$

$$\rho_{xy}^2 = c^2 \frac{b^2}{a^2} B_{\alpha,k}^{-2} \frac{\rho_{iso}^2}{\sin^2(\pi\alpha)} + \frac{\rho_{iso}^2}{\sin^2(\pi\alpha)} \cos^2(\pi\alpha) - 2c \frac{b}{a} B_{\alpha,k}^{-1} \frac{\rho_{iso}^2}{\sin^2(\pi\alpha)} \cos(\pi\alpha)$$

$$\frac{\rho_{xy}^2}{\rho_{yy}} = \frac{c^2 b}{s a} B_{\alpha,k}^{-1} \frac{\rho_{iso}}{\sin(\pi\alpha)} + \frac{1}{s} \frac{a}{b} B_{\alpha,k} \frac{\rho_{iso}}{\sin(\pi\alpha)} \cos^2(\pi\alpha) - 2 \frac{c}{s} \frac{\rho_{iso}}{\sin(\pi\alpha)} \cos(\pi\alpha)$$

$$\frac{\rho_{iso}^2}{\rho_{yy}} = \frac{1}{s} \frac{a}{b} B_{\alpha,k} \rho_{iso} \sin(\pi\alpha)$$

$$\begin{aligned} \rho_{xx} &= \frac{\rho_{xy}^2}{\rho_{yy}} + \frac{\rho_{iso}^2}{\rho_{yy}} \\ &= \frac{c^2 b}{s a} B_{\alpha,k}^{-1} \frac{\rho_{iso}}{\sin(\pi\alpha)} + \frac{1}{s} \frac{a}{b} B_{\alpha,k} \frac{\rho_{iso}}{\sin(\pi\alpha)} \cos^2(\pi\alpha) - 2 \frac{c}{s} \frac{\rho_{iso}}{\sin(\pi\alpha)} \cos(\pi\alpha) \\ &\quad + \frac{1}{s} \frac{a}{b} B_{\alpha,k} \rho_{iso} \sin(\pi\alpha) \\ &= \frac{1}{s} \rho_{iso} \frac{a}{b} B_{\alpha,k} \left(\sin(\pi\alpha) + \frac{\cos^2(\pi\alpha)}{\sin(\pi\alpha)} \right) + \frac{c^2 b}{s a} B_{\alpha,k}^{-1} \frac{\rho_{iso}}{\sin(\pi\alpha)} - 2 \frac{c}{s} \frac{\rho_{iso}}{\sin(\pi\alpha)} \cos(\pi\alpha) \\ &= \frac{1}{s} \rho_{iso} \frac{a}{b} B_{\alpha,k} \left(\frac{\sin^2(\pi\alpha)}{\sin(\pi\alpha)} + \frac{\cos^2(\pi\alpha)}{\sin(\pi\alpha)} \right) + \frac{c}{s} \frac{\rho_{iso}}{\sin(\pi\alpha)} \left(c \frac{b}{a} B_{\alpha,k}^{-1} - 2 \cos(\pi\alpha) \right) \\ &= \frac{1}{s} \frac{a}{b} B_{\alpha,k} \frac{\rho_{iso}}{\sin(\pi\alpha)} + \frac{c}{s} \frac{\rho_{iso}}{\sin(\pi\alpha)} \left(c \frac{b}{a} B_{\alpha,k}^{-1} - 2 \cos(\pi\alpha) \right) \end{aligned}$$

Now, ρ_{xx} , ρ_{yy} , ρ_{xy} has been expressed in terms of known parameters and α . If $\lambda_\alpha = \rho_{iso}/\sin(\pi\alpha)$ and $r = a/b$ is used to rewrite these expressions, the form used in equations (4-30.a) to (4-30.c) in section 4.2.2.4 is obtained.

Appendix A.4 Tensor orientation in parallelogram-shaped single crystals

Here, the relation between the tensor orientation in a parallelogram and α is derived. The exact same procedure can be followed for rectangular samples; however, this is much simpler and is not done explicitly. The equivalent to equation (4-28.a) to (4-28.c) for a parallelogram are

$$\begin{aligned}\rho_{xx} &= \cos^2(\varphi)\rho_{11} + \sin^2(\varphi)\rho_{22} \\ &= \frac{1}{\sin(\chi)}rB_{\alpha,k}\lambda_\alpha + \frac{\cos(\chi)}{\sin(\chi)}\lambda_\alpha(\cos(\chi)r^{-1}B_{\alpha,k}^{-1} - 2\cos(\pi\alpha)) \\ \rho_{yy} &= \sin^2(\varphi)\rho_{11} + \cos^2(\varphi)\rho_{22} = \sin(\chi)r^{-1}B_{\alpha,k}^{-1}\lambda_\alpha \\ \rho_{xy} &= \cos(\varphi)\sin(\varphi)(\rho_{11} - \rho_{22}) = \cos(\chi)r^{-1}B_{\alpha,k}^{-1}\lambda_\alpha - \lambda_\alpha\cos(\pi\alpha)\end{aligned}$$

First, the difference between the two first equations is taken and then rewritten using the third equation

$$\begin{aligned}&\cos^2(\varphi)(\rho_{11} - \rho_{22}) + \sin^2(\varphi)(\rho_{22} - \rho_{11}) \\ &= \frac{1}{\sin(\chi)}rB_{\alpha,k}\lambda_\alpha - \sin(\chi)r^{-1}B_{\alpha,k}^{-1}\lambda_\alpha + \frac{\cos(\chi)}{\sin(\chi)}\lambda_\alpha(\cos(\chi)r^{-1}B_{\alpha,k}^{-1} - 2\cos(\pi\alpha)) \\ &(\cos^2(\varphi) - \sin^2(\varphi))(\cos(\chi)r^{-1}B_{\alpha,k}^{-1}\lambda_\alpha - \lambda_\alpha\cos(\pi\alpha))\frac{1}{\cos(\varphi)\sin(\varphi)} \\ &= \frac{1}{\sin(\chi)}rB_{\alpha,k}\lambda_\alpha - \sin(\chi)r^{-1}B_{\alpha,k}^{-1}\lambda_\alpha + \frac{\cos(\chi)}{\sin(\chi)}\lambda_\alpha(\cos(\chi)r^{-1}B_{\alpha,k}^{-1} - 2\cos(\pi\alpha)) \\ 0 &= (\tan(\varphi)^{-1} - \tan(\varphi))(\cos(\chi)r^{-1}B_{\alpha,k}^{-1} - \cos(\pi\alpha)) - \frac{1}{\sin(\chi)}rB_{\alpha,k} + \sin(\chi)r^{-1}B_{\alpha,k}^{-1} \\ &- \frac{\cos(\chi)}{\sin(\chi)}(\cos(\chi)r^{-1}B_{\alpha,k}^{-1} - 2\cos(\pi\alpha)) \\ 0 &= \left(\tan(\varphi)^{-1} - \tan(\varphi) - \frac{\cos(\chi)}{\sin(\chi)}\right)(\cos(\chi)r^{-1}B_{\alpha,k}^{-1} - \cos(\pi\alpha)) + \frac{\cos(\chi)}{\sin(\chi)}\cos(\pi\alpha) \\ &- \frac{1}{\sin(\chi)}rB_{\alpha,k} + \sin(\chi)r^{-1}B_{\alpha,k}^{-1} \\ 0 &= (\tan(\varphi)^{-1} - \tan(\varphi) - \tan(\chi)^{-1})(\cos(\chi)r^{-1}B_{\alpha,k}^{-1} - \cos(\pi\alpha)) - \frac{1}{\sin(\chi)}rB_{\alpha,k} \\ &+ \sin(\chi)r^{-1}B_{\alpha,k}^{-1} + \tan(\chi)^{-1}\cos(\pi\alpha)\end{aligned}$$

While this is not defined for $\chi = 90^\circ$, the limit when approaching this angle gives an equation for rectangular samples (this can also be derived independently),

$$0 = (\tan(\varphi) - \tan(\varphi)^{-1}) \cos(\pi\alpha) - rB_{\alpha,k} + r^{-1}B_{\alpha,k}^{-1}$$

Appendix B MATLAB™ scripts from Chapter 4

All scripts in this can be copied to .m files in MATLAB. They have been tested on MATLAB R2012a without extra packages.

Appendix B.1 setup.m: General settings and definitions

This script is used in most scripts below. It contains general definitions and equations that are more easily maintained if kept in one place. This needs to be put in a “setup.m” file placed in the same folder as the scripts below. More custom functions are necessary; these are found from Appendix B.7 and onward.

```
%Contains common settings and definitions for anisotropic resistivity.
%Is used as part of other scripts and functions.

%% User input
%Output from functions
PlotSolutions=false; %Graphic representation of numerical solutions?
R_Resolution=25; %Resolution for the plots. WARNING: High numbers will
                  %result in excessively long execution times!

R_gamma=1; %Gamma from Newton's method. Calculated change is multiplied by
            %this before it is applied. Should be <=1 !!
R_tolerance=1e-12; %Max square deviation in units of rhoiso
useNewton=true; %Use Newtons method? If not, use method of steepest descent
MaxIterations=250;

%% Definitions - don't change!
%General functions
rot = @(theta) [cos(theta) -sin(theta); sin(theta) cos(theta)];
matnorm = @(A) (A(1,1)^2+A(2,2)^2+A(1,2)*A(2,1));
%From conformal mapping
Aalphak = @(al,k) hypergeom([1-al al],1,k)*gamma(al)*gamma(1-al);
Balphak = @(al,k) hypergeom([1-al al],1,1-k)/hypergeom([1-al al],1,k);

rhoxx = @(al,k,r,chi,rhoiso) r*Balphak(al,k)*rhoiso/sin(pi*al)/sin(chi) ...
        +cos(chi)/sin(chi)*rhoiso/sin(pi*al)*(cos(chi)*r^-1 ...
        *Balphak(al,k)^-1-2*cos(pi*al));
rhoyy = @(al,k,r,chi,rhoiso) sin(chi)*r^-1*Balphak(al,k)^-1 ...
        *rhoiso/sin(pi*al);
rhoxy = @(al,k,r,chi,rhoiso) cos(chi)*r^-1*Balphak(al,k)^-1 ...
        *rhoiso/sin(pi*al)-rhoiso/sin(pi*al)*cos(pi*al);
rho    = @(al,k,r,chi,rhoiso) [rhoxx(al,k,r,chi,rhoiso) ...
```

```

rhoxy(al,k,r,chi,rhoiso); rhoxy(al,k,r,chi,rhoiso) ...
rhoyy(al,k,r,chi,rhoiso)];
rhovec = @(al,k,r,chi,rhoiso) [rhoxx(al,k,r,chi,rhoiso); ...
rhoyy(al,k,r,chi,rhoiso); rhoxy(al,k,r,chi,rhoiso)];

%Equations for single crystal measurements
    %Equation to solve to get alpha from tensor orientation
SC_eq = @(al,k,r,chi,phi) (tan(phi)^-1-tan(phi)-tan(chi)^-1) ...
* (cos(chi)*r^-1*Balphak(al,k)^-1-cos(pi*al))-1/sin(chi) ...
*r*Balphak(al,k)+sin(chi)*r^-1*Balphak(al,k)^-1 ...
+cos(chi)/sin(chi)*cos(pi*al);

    %Derivative and double derivative
SC_deqdalp = @(al,k,r,chi,phi) (SC_eq(al,k,r,chi,phi) ...
-SC_eq(al+(1-al)*0.001,k,r,chi,phi))/((al-1)*0.001);
SC_d2eqdalp2 = @(al,k,r,chi,phi) (SC_deqdalp(al,k,r,chi,phi) ...
-SC_deqdalp(al+(1-al)*0.001,k,r,chi,phi))/((al-1)*0.001);

%Equations from rotating tensor in sample
    %Equation to solve
R_eq = @(al,be,ka,kb,ra,rb,chia,chib,theta,rhoiso) ...
matnorm(rho(al,ka,ra,chia,rhoiso)-rot(theta) ...
*rho(be,kb,rb,chib,rhoiso)*rot(theta)');

    %Derivative (vector) and Hessian
R_deqdalbe = @(al,be,ka,kb,ra,rb,chia,chib,theta,rhoiso) ...
[(R_eq(al,be,ka,kb,ra,rb,chia,chib,theta,rhoiso) ...
-R_eq(al+(1-al)*0.01*R_tolerance,be,ka,kb,ra,rb, ...
chia,chib,theta,rhoiso))/((al-1)*0.01*R_tolerance); ...
(R_eq(al,be,ka,kb,ra,rb,chia,chib,theta,rhoiso) ...
-R_eq(al,be+(1-be)*0.01*R_tolerance,ka,kb,ra,rb, ...
chia,chib,theta,rhoiso))/((be-1)*0.01*R_tolerance)];
R_d2eqdalbe2 = @(al,be,ka,kb,ra,rb,chia,chib,theta,rhoiso) ...
[(R_deqdalbe(al,be,ka,kb,ra,rb,chia,chib,theta,rhoiso) ...
-R_deqdalbe(al+(1-al)*0.01*R_tolerance,be,ka,kb,ra,rb, ...
chia,chib,theta,rhoiso))/((al-1)*0.01*R_tolerance) ...
(R_deqdalbe(al,be,ka,kb,ra,rb,chia,chib,theta,rhoiso) ...
-R_deqdalbe(al,be+(1-be)*0.01*R_tolerance,ka,kb,ra,rb, ...
chia,chib,theta,rhoiso))/((be-1)*0.01*R_tolerance)];

```

Appendix B.2 Error from χ

Script that calculates the error in the tensor elements from errors in χ shown in Figure 4-12. The settings used to produce panel (a) are shown.

```
clear all; close all; clc;
tic

%-----User input-----
r=1; %(a/b) of anisotropic sample
phi=40*pi/180; %Angle between tensor principal axes and sample x-axis
                %Use negative rotation
chi=60*pi/180; %Angle of parallelogram
rhomat=[1 0; 0 2]; %Tensor in principal axis system
chi_error=-2:0.01:2; %Error in chi
%----End user input-----

setup

%Calculate anisotropic and isotropic sample properties
rhoiso=sqrt(det(rhomat)); %isotropic equivalent resistivity
rhomat=rot(phi)*rhomat*rot(phi)'; %Tensor in lab frame
alpha=acos(1/sqrt(rhomat(2,2)))*(cos(chi)*rhomat(2,2)-
sin(chi)*rhomat(1,2))...
    /sqrt(cos(chi)^2*rhomat(2,2)+sin(chi)^2*rhomat(1,1)-2*cos(chi)...
        *sin(chi)*rhomat(1,2))/pi; %Angle/pi of isotropic parallelogram

app=r*sqrt(rhomat(2,2)/rhoiso); %Isotropic a'
bpp=sqrt((cos(chi)^2*rhomat(2,2)+sin(chi)^2*rhomat(1,1)...
    -2*cos(chi)*sin(chi)*rhomat(1,2))/rhoiso); %b'

%Calculate correct k
k=getk(app,bpp,alpha*180);

%Calculates tensor from erroneous chi and correct alpha
for i=1:length(chi_error)
    rhoxxcalc(i)=rhoxx(alpha,k,r,chi+chi_error(i)*pi/180,rhoiso);
    rhooyycalc(i)=rhooyy(alpha,k,r,chi+chi_error(i)*pi/180,rhoiso);
    rhoxyccalc(i)=rhoxy(alpha,k,r,chi+chi_error(i)*pi/180,rhoiso);
end

figure
clf
title('Change / \rho_{iso}')
xlabel('Error in \chi (\circ)')
ylabel('Change / \rho_{iso} (%)');
hold on
plot(chi_error, (rhoxxcalc-rhomat(1,1))/rhoiso*100, 'r')%
```

```

plot(chi_error,(rhoYYcalc-rhomat(2,2))/rhoiso*100,'b')%
plot(chi_error,(rhoXXcalc-rhomat(1,1))/rhoiso*100,'green')%
legend('rho_xx','rho_yy','rho_xy');
ylim([-5 5])

figure
clf
title('Wrong / correct elements')
xlabel('Error in \chi (\circ)')
ylabel('Relative elements');
hold on
plot(chi_error,(rhoXXcalc/rhomat(1,1)), 'r')%
plot(chi_error,(rhoYYcalc/rhomat(2,2)), 'b')%
plot(chi_error,(rhoXYcalc/rhomat(1,2)), 'green')%
legend('rho_xx','rho_yy','rho_xy');

```

Appendix B.3 Error from contact placement

Script that calculates the error from band contact placement as shown in Figure 4-13. The settings from panel (a) are shown.

```

clear all; close all; clc;
tic

-----User input-----
r=1; %(a/b) of anisotropic sample
phi=40*pi/180; %Angle between tensor principal axes and sample x-axis
                %Use negative rotation
chi=60*pi/180; %Angle of parallelogram
rhomat=[1 0; 0 2]; %Tensor in principal axis system
x=0.0:0.001:0.3; %x-space for test on the complex half plane
-----End user input-----


setup

%Calculate anisotropic and isotropic sample properties
rhoiso=sqrt(det(rhomat)); %isotropic equivalent resistivity
rhomat=rot(phi)*rhomat*rot(phi)'; %Tensor in lab frame
alpha=acos(1/sqrt(rhomat(2,2)))*(cos(chi)*rhomat(2,2)-
sin(chi)*rhomat(1,2))...
    /sqrt(cos(chi)^2*rhomat(2,2)+sin(chi)^2*rhomat(1,1)-2*cos(chi)...
        *sin(chi)*rhomat(1,2)))/pi; %Angle of isotropic parallelogram
app=r*sqrt(rhomat(2,2)/rhoiso); %Isotropic a'
bpp=sqrt((cos(chi)^2*rhomat(2,2)+sin(chi)^2*rhomat(1,1)...
    -2*cos(chi)*sin(chi)*rhomat(1,2))/rhoiso); %b'

%Calculate correct k
k=getk(app,bpp,alpha*180);

```

```

%Calculates M matrix for linear transformation-takes anisotropic to
isotropic
M=1/sqrt(rhomat(2,2)*rhoiso)*[rhomat(2,2) -rhomat(1,2); 0 rhoiso];

invM=M^-1; %Inverse of M, takes isotropic -> anisotropic

%Calculates the measured resistances and k
y=1E-10; %y=0 doesn't work (ABCD corners can't be conformally mapped from
           %a straight line), but we just need to be close
Rplane = @(rp,rn) -rhoiso/pi*log(rp./rn); %Electrostatic potential at a
point
                                         %with distance rp to positive contact and rn
to
                                         %negative (normalized by current and
thickness)

RA=-Rplane(k^-1-x,k^-1-1); %Current A->B
RB=Rplane(1-x,k^-1-x); %Current B->C

kmeas = 1-exp(-RA*pi/rhoiso); %Measured k

%Calculates tensor from erroneous k and correct alpha
for i=1:length(kmeas)
    rhoxxmeas(i)=rhoxx(alpha,kmeas(i),r,chi,rhoiso);
    rhooyymeas(i)=rhooyy(alpha,kmeas(i),r,chi,rhoiso);
    rhoxyymeas(i)=rhoxy(alpha,kmeas(i),r,chi,rhoiso);
end

%Maps the x-space in the half plane to the anisotropic sample AB side

for i=1:length(x)
    xiso(i)=transf(x(i),y,alpha,k)*[1;0]; %Half plane -> isotropic; Correct
                                              %k is used in transformation to map to the
sample
    xanis(i)=[1      0]*invM*[xiso(i);0]; %Isotropic -> Anisotropic
parallelogram
end

figure
clf
title('Change / \rho_{iso}')
xlabel('x/a on sample')
ylabel('Change / \rho_{iso}');
hold on
plot(xanis,(rhoxxmeas-rhomat(1,1))/rhoiso,'r')
plot(xanis,(rhooyymeas-rhomat(2,2))/rhoiso,'b')

```

```

plot(xanis,(rhoxy(meas-rhomat(1,2))/rhoiso,'green')
legend('\rho_{xx}', '\rho_{yy}', '\rho_{xy}');
xlim([0 0.1])

figure
clf
title('Wrong / correct elements')
xlabel('x/a on sample')
ylabel('Relative elements');
hold on
plot(xanis,rhoxx(meas/rhomat(1,1), 'r')
plot(xanis,rhoyy(meas/rhomat(2,2), 'b')
plot(xanis,rhoxy(meas/rhomat(1,2), 'green')
legend('\rho_{xx}', '\rho_{yy}', '\rho_{xy}');
xlim([0 0.1])

```

Appendix B.4 Errors from single crystal measurements

Error when treating single crystals. This script reproduces Figure 4-14.

```

clear all; close all; clc;
tic

%-----User input-----
r=1; %(=a/b) of anisotropic sample
phi=40*pi/180; %Angle between tensor principal axes and sample x-axis
chi=60*pi/180; %Angle of parallelogram
rhomat=[1 0; 0 2]; %Tensor in principal axis system

chi_error=-2:0.5:2; %Error in chi
phi_error=-2:0.5:2; %Error in phi
xA=0.0:0.00001:0.0003; %x-space for test on the complex half plane
xB=0.0:0.003:0.3; %x-space for test on the complex half plane
%----End user input-----

%% General setup and common definitions
setup

%Calculate anisotropic and isotropic sample properties
rhoiso=sqrt(det(rhomat)); %isotropic equivalent resistivity
rhomat=rot(phi)*rhomat*rot(phi)'; %Tensor in lab frame
alpha=acos(1/sqrt(rhomat(2,2)))*(cos(chi)*rhomat(2,2)-
sin(chi)*rhomat(1,2))...
/sqrt(cos(chi)^2*rhomat(2,2)+sin(chi)^2*rhomat(1,1)-2*cos(chi)...
*sin(chi)*rhomat(1,2))/pi; %Angle/pi of isotropic parallelogram
app=r*sqrt(rhomat(2,2)/rhoiso); %Isotropic a'
bpp=sqrt((cos(chi)^2*rhomat(2,2)+sin(chi)^2*rhomat(1,1)...
-2*cos(chi)*sin(chi)*rhomat(1,2))/rhoiso); %b'

```

```

%Calculate correct k
k=getk(app,bpp,alpha*180);

%% Error from chi
%Calculates and plots tensor from erroneous chi and alpha
al=[];
for i=1:length(chi_error)
    al=SC_getalpha(k,r,chi+chi_error(i)*pi/180,phi);
    rhoxxcalc(i)=rhoxx(al,k,r,chi+chi_error(i)*pi/180,rhoiso);
    rhooyycalc(i)=rhooyy(al,k,r,chi+chi_error(i)*pi/180,rhoiso);
    rhooxycalc(i)=rhoxy(al,k,r,chi+chi_error(i)*pi/180,rhoiso);
end

figure
clf
title('Change / \rho_{iso}')
xlabel('Error in \chi (\circ)')
ylabel('Change / \rho_{iso} (%)');
hold on
plot(chi_error,(rhoxxcalc-rhomat(1,1))/rhoiso*100,'r')%
plot(chi_error,(rhooyycalc-rhomat(2,2))/rhoiso*100,'b')%
plot(chi_error,(rhooxycalc-rhomat(1,2))/rhoiso*100,'green')%
legend('\rho_{xx}', '\rho_{yy}', '\rho_{xy}');
ylim([-5 5])

%% Error from phi
%Calculates and plots tensor from erroneous phi and alpha
al=[];
for i=1:length(phi_error)
    al=SC_getalpha(k,r,chi,phi+phi_error(i)*pi/180);
    rhoxxcalc(i)=rhoxx(al,k,r,chi,rhoiso);
    rhooyycalc(i)=rhooyy(al,k,r,chi,rhoiso);
    rhooxycalc(i)=rhoxy(al,k,r,chi,rhoiso);
end

figure
clf
title('Change / \rho_{iso}')
xlabel('Error in \phi (\circ)')
ylabel('Change / \rho_{iso} (%)');
hold on
plot(chi_error,(rhoxxcalc-rhomat(1,1))/rhoiso*100,'r')%
plot(chi_error,(rhooyycalc-rhomat(2,2))/rhoiso*100,'b')%
plot(chi_error,(rhooxycalc-rhomat(1,2))/rhoiso*100,'green')%
legend('\rho_{xx}', '\rho_{yy}', '\rho_{xy}');

%% Error from contacts - A corner

```

```

%Calculates M matrix for linear transformation-Takes anisotropic to
isotropic
M=1/sqrt(rhomat(2,2)*rhoiso)*[rhomat(2,2) -rhomat(1,2); 0 rhoiso];
invM=M^-1; %Inverse of M, takes isotropic -> anisotropic

%Calculates the measured resistances and k
y=1E-10; %y=0 doesn't work (ABCD corners can't be conformally mapped from a
           %straight line), but we just need to be close
Rplane = @(rp,rn) -rhoiso/pi*log(rp./rn); %Electrostatic potential at a
point
                                         %with distance rp to positive contact and rn
to
                                         %negative (normalized by current and
thickness)

RA=-Rplane(k^-1-xA,k^-1-1); %Current A->B
RB=Rplane(1-xA,k^-1-xA); %Current B->C

kmeas = 1-exp(-RA*pi/rhoiso); %Measured k

%Calculates tensor from erroneous k and correct alpha
al=[];
for i=1:length(kmeas)
    al=SC_getalpha(kmeas(i),r,chi,phi);
    rhoxxmeas(i)=rhoxx(al,kmeas(i),r,chi,rhoiso);
    rhoyymeas(i)=rhoyy(al,kmeas(i),r,chi,rhoiso);
    rhoxymeas(i)=rhoxy(al,kmeas(i),r,chi,rhoiso);
end

%Maps the x-space in the half plane to the anisotropic sample AB side

for i=1:length(xA)
    xiso(i)=transf(xA(i),y,alpha,k)*[1;0]; %Half plane -> isotropic;
Correct
                                         %k+alpha is used in
transformation
                                         %to map to the sample
    xanis(i)=[1      0]*(invM*[xiso(i);0]); %Isotropic -> Anisotropic
paralellogram
end

figure
clf
title('Change / \rho_{iso}')
xlabel('x/a on sample')
ylabel('Change / \rho_{iso}');

```

```

hold on
plot(xanis,(rhoxxmeas-rhomat(1,1))/rhoiso*100,'r')
plot(xanis,(rhooyymeas-rhomat(2,2))/rhoiso*100,'b')
plot(xanis,(rhoxyymeas-rhomat(1,2))/rhoiso*100,'green')
legend('\rho_{xx}', '\rho_{yy}', '\rho_{xy}');
xlim([0 0.1])

%% Error from contacts - B corner
%Calculate anisotropic and isotropic sample properties
r=r^-1;
chi=pi-chi; %Angle of B corner
phi=phi+chi;
rhomat=rot(chi)*rhomat*rot(chi)'; %Tensor in new lab frame
alpha=acos(1/sqrt(rhomat(2,2)))*(cos(chi)*rhomat(2,2)-
sin(chi)*rhomat(1,2))...
/sqrt(cos(chi)^2*rhomat(2,2)+sin(chi)^2*rhomat(1,1)-2*cos(chi)...
*sin(chi)*rhomat(1,2))/pi; %Angle/pi of isotropic parallelogram
app=r*sqrt(rhomat(2,2)/rhoiso); %Isotropic a'
bpp=sqrt((cos(chi)^2*rhomat(2,2)+sin(chi)^2*rhomat(1,1)-2*cos(chi)...
*sin(chi)*rhomat(1,2))/rhoiso); %b'

%Calculate correct k
k=getk(app,bpp,alpha*180);

%Calculates M matrix for linear transformation-Takes anisotropic to
isotropic
M=1/sqrt(rhomat(2,2)*rhoiso)*[rhomat(2,2) -rhomat(1,2); 0 rhoiso];
invM=M^-1; %Inverse of M, takes isotropic -> anisotropic

%Calculates the measured resistances and k
y=1E-10; %y=0 doesn't work (ABCD corners can't be conformally mapped from a
%straight line), but we just need to be close
Rplane = @(rp,rn) -rhoiso/pi*log(rp./rn); %Electrostatic potential at a
point
                                         %with distance rp to positive contact and rn
to
                                         %negative (normalized by current and
thickness)

RA=-Rplane(k^-1-xB,k^-1-1); %Current A->B
RB=Rplane(1-xB,k^-1-xB); %Current B->C

kmeas = 1-exp(-RA*pi/rhoiso); %Measured k

%Calculates tensor from erroneous k and correct alpha
rhoxxmeas=[];
rhooyymeas=[];

```

```

rhoxymeas=[];
al=[];
for i=1:length(kmeas)
    al=SC_getalpha(kmeas(i),r,chi,phi);
    rhoxxmeas(i)=rhoxx(al,kmeas(i),r,chi,rhoiso);
    rhoyymeas(i)=rhoyy(al,kmeas(i),r,chi,rhoiso);
    rhoxymeas(i)=rhoxy(al,kmeas(i),r,chi,rhoiso);
end

%Maps the x-space in the half plane to the anisotropic sample AB side
xiso=[];
xanis=[];
for i=1:length(xB)
    xiso(i)=transf(xB(i),y,alpha,k)*[1;0]; %Half plane -> isotropic;
Correct
                                %k+alpha is used in
transformation
                                %to map to the sample
    xanis(i)=[1      0]*(invM*[xiso(i);0]);%Isotropic -> Anisotropic
paralellogram
end

figure
clf
title('Change / \rho_{iso}')
xlabel('x/a on sample')
ylabel('Change / \rho_{iso}');
hold on
plot(xanis,(rhoxxmeas-rhomat(1,1))/rhoiso*100,'r')
plot(xanis,(rhoyymeas-rhomat(2,2))/rhoiso*100,'b')
plot(xanis,(rhoxymeas-rhomat(1,2))/rhoiso*100,'green')
legend('\rho_{xx}', '\rho_{yy}', '\rho_{xy}')
xlim([0 0.1])

```

Appendix B.5 Errors in the method of changing tensor orientation

This script gives the errors from the rotating tensor method. The script reproduces Figure 4-15.

```

clear all; close all;
tic

-----User input-----
ra=2; %(a/b) of anisotropic sample A
rb=1.8; %(a/b) of anisotropic sample B
phi=40*pi/180; %Angle between tensor principal axes and sample x-axis in A
chia=70*pi/180; %Angle of parallelogram A
chib=100*pi/180; %Angle of parallelogram B

```

```

theta=30*pi/180; %Angle from A to B
rh=[1 0; 0 2]; %Tensor in principal axis system

chi_error=(-2:0.2:2)*pi/180; %Error in chi
theta_error=(-2:0.04:2)*pi/180; %Error in phi
xA=0.0:0.0001:0.01; %x-space for test on the complex half plane
xB=0.0:0.002:0.2; %x-space for test on the complex half plane
%-----End user input-----

%% General setup and calculations
setup;

R=rot(phi);
Rab=rot(theta);

rhoiso=sqrt(det(rh));

rhoa=R*rh*R'; %Positive rotation
rhob=Rab'*rhoa*Rab; %Negative rotation

alphaa=acos(1/sqrt(rhoa(2,2))*(cos(chia)*rhoa(2,2)-sin(chia)*rhoa(1,2))...
    /sqrt(cos(chia)^2*rhoa(2,2)+sin(chia)^2*rhoa(1,1)-2*cos(chia)...
    *sin(chia)*rhoa(1,2)))/pi; %Angle of isotropic parallelogram A
alphab=acos(1/sqrt(rhob(2,2))*(cos(chib)*rhob(2,2)-sin(chib)*rhob(1,2))...
    /sqrt(cos(chib)^2*rhob(2,2)+sin(chib)^2*rhob(1,1)-2*cos(chib)...
    *sin(chib)*rhob(1,2)))/pi; %Angle of isotropic parallelogram B

aa=ra*sqrt(rhoa(2,2)/rhoiso); %Isotropic a' for A
ba=sqrt((cos(chia)^2*rhoa(2,2)+sin(chia)^2*rhoa(1,1)-2*cos(chia)...
    *sin(chia)*rhoa(1,2))/rhoiso); %b' for A
ab=rb*sqrt(rhob(2,2)/rhoiso); %Isotropic a' for B
bb=sqrt((cos(chib)^2*rhob(2,2)+sin(chib)^2*rhob(1,1)-2*cos(chib)...
    *sin(chib)*rhob(1,2))/rhoiso); %b' for B

ka=getk(aa,ba,alphaa*180);
kb=getk(ab,bb,alphab*180);

%% Error from Chi (applied to A)
%Calculates and plots tensor from erroneous chi and alpha
albe=[];
toc
for i=1:length(chi_error)
    albe=R_getalbe(ka,kb,ra,rb,chia+chi_error(i),chib,theta,rhoiso);
    rhoxxcalc(i)=rhoxx(albe(1),ka,ra,chia+chi_error(i),rhoiso);
    rhoyycalc(i)=rhoyy(albe(1),ka,ra,chia+chi_error(i),rhoiso);
    rhoxyccalc(i)=rhoxy(albe(1),ka,ra,chia+chi_error(i),rhoiso);
    toc
end

```

```

end

figure
clf
title('Change / \rho_{iso}')
xlabel('Error in \chi (\circ)')
ylabel('Change / \rho_{iso} (%)');
hold on
plot(chi_error*180/pi,(rhoxxcalc-rhoa(1,1))/rhoiso*100,'r')%
plot(chi_error*180/pi,(rhoyycalc-rhoa(2,2))/rhoiso*100,'b')%
plot(chi_error*180/pi,(rhoxycalc-rhoa(1,2))/rhoiso*100,'green')%
legend('\rho_{xx}', '\rho_{yy}', '\rho_{xy}');
ylim([-0.2 0.2])

%% Error from theta
%Calculates and plots tensor from erroneous chi and alpha
toc
rhoxxcalc=[];
rhoyycalc=[];
rhoxycalc=[];
albe=[];
for i=1:length(theta_error)
    albe=R_getalbe(ka,kb,ra,rb,chia,chib,theta+theta_error(i),rhoiso);
    rhoxxcalc(i)=rhoxx(albe(1),ka,ra,chia,rhoiso);
    rhoyycalc(i)=rhoyy(albe(1),ka,ra,chia,rhoiso);
    rhoxycalc(i)=rhoxy(albe(1),ka,ra,chia,rhoiso);
    toc
end

figure
clf
title('Change / \rho_{iso}')
xlabel('Error in \theta (\circ)')
ylabel('Change / \rho_{iso} (%)');
hold on
plot(theta_error*180/pi,(rhoxxcalc-rhoa(1,1))/rhoiso*100,'r')%
plot(theta_error*180/pi,(rhoyycalc-rhoa(2,2))/rhoiso*100,'b')%
plot(theta_error*180/pi,(rhoxycalc-rhoa(1,2))/rhoiso*100,'green')%
legend('\rho_{xx}', '\rho_{yy}', '\rho_{xy}');
ylim([-0.5 0.5])

%% Error from contacts - A corner
%Calculates M matrix for linear transformation-Takes anisotropic to
isotropic
M=1/sqrt(rhoa(2,2)*rhoiso)*[rhoa(2,2) -rhoa(1,2); 0 rhoiso];
invM=M^-1; %Inverse of M, takes isotropic -> anisotropic

%Calculates the measured resistances and k

```

```

y=1E-10; %y=0 doesn't work (ABCD corners can't be conformally mapped from
          %a straight line), but we just need to be close
Rplane = @(rp,rn) -rhoiso/pi*log(rp./rn); %Electrostatic potential at a
point
                                         %with distance rp to positive contact and rn
to
                                         %negative      (normalized      by      current      and
thickness)

RA=-Rplane(ka^-1-xA,ka^-1-1); %Current A->B
RB=Rplane(1-xA,ka^-1-xA); %Current B->C

kmeas = 1-exp(-RA*pi/rhoiso); %Measured k

%Calculates tensor from erroneous k and alpha
rhoxxmeas=[];
rhoyymeas=[];
rhoxymeas=[];
albe=[];
for i=1:length(kmeas)
    albe=R_getalbe(kmeas(i),kb,ra,rb,chia,chib,theta,rhoiso);
    rhoxxmeas(i)=rhoxx(albe(1),kmeas(i),ra,chia,rhoiso);
    rhoyymeas(i)=rhoyy(albe(1),kmeas(i),ra,chia,rhoiso);
    rhoxymeas(i)=rhoxy(albe(1),kmeas(i),ra,chia,rhoiso);
end

%Maps the x-space in the half plane to the anisotropic sample AB side
xiso=[];
xanis=[];
for i=1:length(xA)
    xiso(i)=transf(xA(i),y,alphaa,ka)*[1;0];%Half plane -> isotropic;
Correct
                                         %k+alpha           is           used
intransformation
                                         %to map to the sample
    xanis(i)=[1      0]* (invM*[xiso(i);0]);%Isotropic      ->      Anisotropic
parallellogram
end

rho(albe(1),ka,ra,chia,rhoiso)
rho(albe(2),kb,rb,chib,rhoiso)

figure
clf
title('Change / \rho_{iso}')
xlabel('x/a on sample A')
ylabel('Change / \rho_{iso}');
hold on

```

```

plot(xanis,(rhoxxmeas-rhoa(1,1))/rhoiso*100,'r')
plot(xanis,(rhoyymeas-rhoa(2,2))/rhoiso*100,'b')
plot(xanis,(rhoxymeas-rhoa(1,2))/rhoiso*100,'green')
legend('\rho_{xx}', '\rho_{yy}', '\rho_{xy}');
xlim([0 0.1])

%% Error from contacts - B corner
%Calculate anisotropic and isotropic sample properties
ra=ra^-1; %(=a/b) of anisotropic sample A
chia=pi-chia; %Angle of parallelogram A
phi=phi+chia; %Angle between tensor principal axes and sample x-axis in A
theta=theta+chia; %Angle from A to B

rhoa=rot(chia)*rhoa*rot(chia)'; %Tensor in new lab frame
alphaaa=acos(1/sqrt(rho(a(2,2)))*(cos(chia)*rhoa(2,2)-sin(chia)*rhoa(1,2))...
    /sqrt(cos(chia)^2*rhoa(2,2)+sin(chia)^2*rhoa(1,1)-2*cos(chia)...
    *sin(chia)*rhoa(1,2)))/pi; %Angle of isotropic parallelogram A
aa=ra*sqrt(rho(a(2,2)/rhoiso); %Isotropic a' for A
ba=sqrt((cos(chia)^2*rhoa(2,2)+sin(chia)^2*rhoa(1,1)-2*cos(chia)...
    *sin(chia)*rhoa(1,2))/rhoiso); %b' for A

%Calculate correct k
ka=getk(aa,ba,alphaaa*180);

%Calculates M matrix for linear transformation-Takes anisotropic to
isotropic
M=1/sqrt(rho(a(2,2)*rhoiso)*[rhoa(2,2) -rhoa(1,2); 0 rhoiso];
invM=M^-1; %Inverse of M, takes isotropic -> anisotropic

%Calculates the measured resistances and k
y=1E-10; %y=0 doesn't work (ABCD corners can't be conformally mapped from
    %a straight line), but we just need to be close
Rplane = @(rp,rn) -rhoiso/pi*log(rp./rn); %Electrostatic potential at a
point
    %with distance rp to positive contact and rn
to
    %negative (normalized by current and
thickness)

RA=-Rplane(ka^-1-xB,ka^-1-1); %Current A->B
RB=Rplane(1-xB,ka^-1-xB); %Current B->C

kmeas = 1-exp(-RA*pi/rhoiso); %Measured k

%Calculates tensor from erroneous k and alpha
rhoxxmeas=[];
rhoyymeas=[];

```

```

rhoxymeas=[];
albe=[];
for i=1:length(kmeas)
    albe=R_getalbe(kmeas(i),kb,ra,rb,chia,chib,theta,rhoiso);
    rhoxxymeas(i)=rhoxx(albe(1),kmeas(i),ra,chia,rhoiso);
    rhooyymeas(i)=rhooyy(albe(1),kmeas(i),ra,chia,rhoiso);
    rhoxyymeas(i)=rhoxy(albe(1),kmeas(i),ra,chia,rhoiso);
    toc
end

%Maps the x-space in the half plane to the anisotropic sample AB side
xiso=[];
xanis=[];
for i=1:length(xB)
    xiso(i)=transf(xB(i),y,alphaa,ka)*[1;0];%Half plane -> Isotropic;
    %Correct
    %k+alpha is used in transformation
    %to map to the sample
    xanis(i)=[1 0]*(invM*[xiso(i);0]);%Isotropic -> Anisotropic
parallellogram
end

figure
clf
title('Change / \rho_{iso}')
xlabel('y/b on sample A')
ylabel('Change / \rho_{iso}');
hold on
plot(xanis,(rhoxxymeas-rhoa(1,1))/rhoiso*100,'r')
plot(xanis,(rhooyymeas-rhoa(2,2))/rhoiso*100,'b')
plot(xanis,(rhoxyymeas-rhoa(1,2))/rhoiso*100,'green')
legend('\rho_{xx}', '\rho_{yy}', '\rho_{xy}');
xlim([0 0.1])

```

Appendix B.6 Error in 5-point method

This script calculates the errors specific to the method using 5 points. This reproduces Figure 4-16.

```

clear all; close all; clc;
tic

%-----User input-----
r=1; %(a/b) of anisotropic sample
r2=0.5; %Position of contact E along AB
phi=40*pi/180; %Angle between tensor principal axes and sample x-axis
chi=60*pi/180; %Angle of parallelogram

```

```

rhomat=[1 0; 0 2]; %Tensor in principal axis system
r2_error=-0.1:0.01:0.1;
x=[0:0.000005:0.000045 0.00005:0.00005:0.0005];
%-----End user input-----

setup

%Calculate anisotropic and isotropic sample properties
rhoiso=sqrt(det(rhomat)); %isotropic equivalent resistivity
rhomat=rot(phi)*rhomat*rot(phi)'; %Tensor in lab frame
alpha=acos(1/sqrt(rhomat(2,2)))*(cos(chi)*rhomat(2,2)-
sin(chi)*rhomat(1,2))...
/sqrt(cos(chi)^2*rhomat(2,2)+sin(chi)^2*rhomat(1,1)-2*cos(chi)...
*sin(chi)*rhomat(1,2))/pi; %Angle/pi of isotropic parallelogram
app=r*sqrt(rhomat(2,2)/rhoiso); %Isotropic a'
bpp=sqrt((cos(chi)^2*rhomat(2,2)+sin(chi)^2*rhomat(1,1)-2*cos(chi)...
*sin(chi)*rhomat(1,2))/rhoiso); %b'

%Calculate correct k and m
k=getk(app,bpp,alpha*180);
m=getm(r2,k,alpha);

%% Error from E contact
for i=1:length(r2_error)
    merr=getm(r2+r2_error(i),k,alpha); %Measured m with wrong placement
    al= getalpha_5pt(r2,k,merr); %Alpha calculated with measured m
    rhoxx_calc(i)=rhoxx(al,k,r,chi,rhoiso);
    rhoyy_calc(i)=rhoyy(al,k,r,chi,rhoiso);
    rhoxy_calc(i)=rhoxy(al,k,r,chi,rhoiso);
    toc
end

figure
hold on
plot(r2_error,(rhoxx_calc-rhomat(1,1))/rhoiso*100,'r');
plot(r2_error,(rhoyy_calc-rhomat(2,2))/rhoiso*100,'b');
plot(r2_error,(rhoxy_calc-rhomat(1,2))/rhoiso*100,'green');
legend('\rho_{xx}', '\rho_{yy}', '\rho_{xy}');
toc

%% Error from A contact
%Calculates M matrix for linear transformation-Takes anisotropic to
isotropic
Mmat=1/sqrt(rhomat(2,2)*rhoiso)*[rhomat(2,2) -rhomat(1,2); 0 rhoiso]; %
invM=Mmat^-1; %Inverse of M, takes isotropic -> anisotropic

```

```

%Calculates the measured resistances and k
y=1E-10; %y=0 doesn't work (ABCD corners can't be conformally mapped from
          %a straight line), but we just need to be close
Rplane = @(rp,rn) log(rp./rn); %Electrostatic potential at a point with
                                  %distance rp to positive contact and rn to
                                  %negative (normalized by current and
thickness)

RA=Rplane(k^-1-x,k^-1-1); %Current A->B (gets k)
RB=Rplane(m-x,1-x); %Current A->D (gets m)

kmeas = 1-exp(RA); %Measured k
mmeas = exp(RB);

%Calculates tensor from erroneous k and correct alpha
for i=1:length(kmeas)
    al=getalpha_5pt(r2,kmeas(i),mmeas(i));
    rhoxxmeas(i)=rhoxx(al,kmeas(i),r,chi,rhoiso);
    rhoyymeas(i)=rhoyy(al,kmeas(i),r,chi,rhoiso);
    rhoxy(meas(i))=rhoxy(al,kmeas(i),r,chi,rhoiso);
end

%Maps the x-space in the half plane to the anisotropic sample AB side

for i=1:length(x)
    xiso(i)=transf(x(i),y,alpha,k)*[1;0]; %Half plane -> isotropic; Correct
                                              %k is used in transformation to
                                              %map to the sample
    xanis(i)=[1      0]*invM*[xiso(i);0]; %Isotropic      ->      Anisotropic
parallellogram
end

figure
clf
title('Change / \rho_{iso}')
xlabel('x/a on sample')
ylabel('Change / \rho_{iso}');
hold on
plot(xanis,(rhoxxmeas-rhomat(1,1))/rhoiso*100,'r')
plot(xanis,(rhoyymeas-rhomat(2,2))/rhoiso*100,'b')
plot(xanis,(rhoxy(meas)-rhomat(1,2))/rhoiso*100,'green')
legend('\rho_{xx}', '\rho_{yy}', '\rho_{xy}');
xlim([0 0.1])

```

Appendix B.7 getk.m: Extracting k from isotropic equivalent sample geometry

This function extracts k from isotropic equivalent sample geometry. This function needs to be placed in the same folder as setup.m.

```
function k = getk( a, b, theta )
%GETK Finds k from angle and side lengths
%   a, b are side lengths of the isotropic equivalent sample. Theta is
%   angle in degrees.

setup;
alpha=theta/180; %Angle as radians divided by pi
k=0.5;

l2 = @(x) a*Balphak(alpha,x);

%Solves l2(k)=b using binary search
i=3;
k1=1/(i+0.1);
k2=1-1/(i+0.2);

%Expands search space to include the solution
while sign(b-l2(k1))==sign(b-l2(k2))
    i=i*10;
    k1=1/(i+0.1);
    k2=1-1/(i+0.2);
end;

%Finds the solution
k3=(k1+k2)/2;

while (l2(k1)-l2(k2))/b>1e-10
    if sign(b-l2(k1))==sign(b-l2(k3))
        k1=k3;
    else
        k2=k3;
    end
    k3=(k1+k2)/2;
end
k=(k1+k2)/2;

end
```

Appendix B.8 getm.m: Extracting m in the 5-point method from sample geometry

Function for extracting m in the 5-point method using the isotropic equivalent sample geometry and k . This function needs to be placed in the same folder as setup.m.

```
function m = getm(r2, k, alpha )
%GETM Finds m from isotropic equivalent geometry and k
%   r2 is a/b from side lengths of the isotropic equivalent sample. Theta
is
%   angle in degrees.

setup;
m=0.5;

l2 = @(x) transf(x,0,alpha,k);

%Solves l2(k)=b using binary search
i=3;
m1=1/(i+0.1);
m2=1-1/(i+0.2);

while sign(r2-l2(m1))==sign(r2-l2(m2))
    i=i*10;
    m1=1/(i+0.1);
    m2=1-1/(i+0.2);
end;

k3=(m1+m2)/2;

while abs(m1-m2)>1e-10
    if sign(r2-l2(m1))==sign(r2-l2(k3))
        m1=k3;
    else
        m2=k3;
    end
    k3=(m1+m2)/2;
end
m=(m1+m2)/2;

end
```

Appendix B.9 transf.m: Function to calculate the conformal mapping

The conformal mapping $w(\xi)$ from the complex half plane to the isotropic equivalent sample. This function needs to be placed in the same folder as setup.m.

```
function w = transf(x,y,alpha,k)
%TRANSF Conformal mapping of (x,y) in complex half-plane to parallelogram.

t=x+1i*y;
setup

w=intf(alpha,k,t)/Aalphak(alpha,k);
w=[real(w) imag(w)];
end

function f=falphakq(alpha,k,q)
%f, q complex number; 0<alpha<1, 0<k<1 real
f=q.^ (alpha-1).* (1-q).^ (-alpha).* (1-k.*q).^ (alpha-1);
end

function intf = intf(alpha,k,t)
%quad works better than quadl and quadgk. Singularity in f for Re(t)=0,1
%and 1/k. More powerful integration that takes proper care of
%singularities may be necessary for accurate transformations. This is OK
%for making rough sketches of the transformation.
intf=quad(@(x) falphakq(alpha,k,x),0, t);
end
```

Appendix B.10 SC_getalpha.m: Solve the single crystal equation

This function solves Equation (4-35) for single crystals to give alpha. After this the tensor can be calculated with rho(al,k,r,chi,rhoiso) from setup.m. This function needs to be in the same folder as setup.m.

```
function alpha = SC_getalpha( k,r,chi,phi)
%SC_GETALPHA Gets alpha from chi, phi, k and sample aspect ratio.

%% Runs setup to get common functions
setup
alpha=[];
%There is one extremum in the interval from 0 to 1. If the two ends have
%the same sign there must be two zero-points.

%% Plot functions
%Plot function, derivative, and iterative improvements og guess
if PlotSolutions
    al=0:0.01:1;
    for i=1:length(al);
        f(i)=SC_eq(al(i),k,r,chi,phi); %Solev SC_eq=0
        d(i)=SC_deqdalpa
```

```

        %c(i)=SC_d2eqdalp2(al(i),k,r,chi,phi); %Second derivative
    end;
    figure
    hold on
    plot(al,f,'r')
    plot(al,c,'green');
    plot(al,d,'b')
    set(gca,'box','on');
    axis([0 1 -4 4])
end

%% Find extremum of SC_eq
alpha_guess=0.5; %Initial guess
alpha_extremum=0.5;
plotGuess=[];

if sign(SC_eq(1,k,r,chi,phi))==sign(SC_eq(0,k,r,chi,phi))%=>two
solutions
    if PlotSolutions
        plot(alpha_guess,SC_deqdalp2(alpha_guess,k,r,chi,phi),...
              'blueo','LineWidth',1,'MarkerSize',10);
    end
    while abs(SC_deqdalp2(alpha_guess,k,r,chi,phi))>1e-8
        delta_alpha=-SC_deqdalp2(alpha_guess,k,r,chi,phi)/...
                    SC_d2eqdalp2(alpha_guess,k,r,chi,phi);
        if (alpha_guess+delta_alpha)>=1
            alpha_guess=(alpha_guess+1)/2;
        elseif (alpha_guess+delta_alpha)<=0
            alpha_guess=(alpha_guess+0)/2;
        else
            alpha_guess=alpha_guess+delta_alpha;
        end

        %Plot current guess
        if PlotSolutions
            plot(alpha_guess,SC_deqdalp2(alpha_guess,k,r,chi,phi)...
                  , 'bo','LineWidth',1,'MarkerSize',10);
        end

        alpha_extremum=alpha_guess;
    end
end

%% Solve actual equation - there may be two solutions
%Is there a solution to the left of the extremum?
if sign(SC_eq(alpha_extremum,k,r,chi,phi))==-sign(SC_eq(0,k,r,chi,phi))
    % Solution is between 0 and extremum
    alpha_guess=(0+alpha_extremum)/2; %Initial guess

```

```

% Plot starting guess
if PlotSolutions
    plot(alpha_guess,SC_eq(alpha_guess,k,r,chi,phi),...
          'ro','LineWidth',1,'MarkerSize',10);
end

%Iteratively improve guess, using Newton-Raphson
while abs(SC_eq(alpha_guess,k,r,chi,phi))>1e-8
    delta_alpha=-SC_eq(alpha_guess,k,r,chi,phi)/...
        SC_deqdalpha(alpha_guess,k,r,chi,phi);
    if (alpha_guess+delta_alpha)>=1
        alpha_guess=(alpha_guess+1)/2;
    elseif (alpha_guess+delta_alpha)<=0
        alpha_guess=(alpha_guess+0)/2;
    else
        alpha_guess=alpha_guess+delta_alpha;
    end
    if PlotSolutions
        plot(alpha_guess,SC_eq(alpha_guess,k,r,chi,phi),...
              'ro','LineWidth',1,'MarkerSize',10);
    end
end
alpha=alpha_guess;
end

%Is there a solution to the right of the extremum?
if sign(SC_eq(alpha_extremum,k,r,chi,phi))==-sign(SC_eq(1,k,r,chi,phi))
    % Solution is between 1 and extremum
    alpha_guess=(1+alpha_extremum)/2; %Initial guess

    % Plot starting guess
    if PlotSolutions
        plot(alpha_guess,SC_eq(alpha_guess,k,r,chi,phi),...
              'go','LineWidth',1,'MarkerSize',10);
    end

    %Iteratively improve guess, using Newton-Raphson
    while abs(SC_eq(alpha_guess,k,r,chi,phi))>1e-8
        delta_alpha=-SC_eq(alpha_guess,k,r,chi,phi)/...
            SC_deqdalpha(alpha_guess,k,r,chi,phi);
        if (alpha_guess+delta_alpha)>=1
            alpha_guess=(alpha_guess+1)/2;
        elseif (alpha_guess+delta_alpha)<=0
            alpha_guess=(alpha_guess+0)/2;
        else
            alpha_guess=alpha_guess+delta_alpha;
        end
        if PlotSolutions

```

```

        plot(alpha_guess,SC_eq(alpha_guess,k,r,chi,phi),...
              'go','LineWidth',1,'MarkerSize',10);
    end
end
alpha=[alpha alpha_guess];
end
end

```

Appendix B.11 R_getalbe.m: Solve the rotating tensor equation

This function solves $d^2 = 0$ from Equation (4-37) with the modification for parallelogram shaped samples. The result is α and β for the two samples. The tensor in both samples can be calculated using rho(al,k,r,chi,rhoiso) from setup.m. This function needs to be in the same folder as setup.m.

```

function albe = R_getalbe(ka,kb,ra,rb,chia,chib,theta,rhoiso)
%R_GETALBE Finds alpha and beta from data on samples with rotated tensor.
% The minimum in R_eq is found via Newton's method for two variables -
% alpha and beta.

%% Runs setup to get common functions
setup

%% Solves the equation
% We want the gradient along both alpha and beta to be very close to
zero
% which the condition below ensures. Tolerance and gamma from Newton's
% methos is set in setup.
albeg=[0.5;0.5]; %Initial guess which is improved upon
oldLen=0;

%Initiate matrix for plotting iterative improvements
if PlotSolutions
    albeg_plot=[albeg; R_eq(albeg(1),albeg(2),ka,kb,ra,rb,chia,chib, ...
                           theta,rhoiso)];
end
I=0;
if useNewton
    while
R_eq(albeg(1),albeg(2),ka,kb,ra,rb,chia,chib,theta,rhoiso)/...
      rhoiso^2>R_tolerance && (I<MaxIterations)
    I=I+1;

    albedelta=-R_gamma*(R_d2eqdalbe2(albeg(1),albeg(2),ka,kb,ra, ...
                           rb,chia,chib,theta,rhoiso)\R_deqdalbe(albeg(1),albeg(2), ...
                           ka,kb,ra,rb,chia,chib,theta,rhoiso));
end

```

```

%Make sure we stay within 0<alpha,beta<1
if (albeg(1)+albedelta(1))>1
    albeg(1)=(albeg(1)+1)/2;
elseif (albeg(1)+albedelta(1))<0
    albeg(1)=(albeg(1)+0)/2;
else
    albeg(1)=albeg(1)+albedelta(1);
end
if (albeg(2)+albedelta(2))>1
    albeg(2)=(albeg(2)+1)/2;
elseif (albeg(2)+albedelta(2))<0
    albeg(2)=(albeg(2)+0)/2;
else
    albeg(2)=albeg(2)+albedelta(2);
end

%Add next iteration to array
if PlotSolutions
    albeg_plot=[albeg_plot [albeg; R_eq(albeg(1),albeg(2),ka, ...
kb,ra,rb,chia,chib,theta,rhoiso)]];
```

end

```

else %Steepest descent
while
(R_eq(albeg(1),albeg(2),ka,kb,ra,rb,chia,chib,theta,rhoiso)/...
rhoiso^2>R_tolerance) && (I<MaxIterations)
I=I+1;

slope=R_deqdalbe(albeg(1),albeg(2),ka,kb,ra,rb,chia,chib, ...
theta,rhoiso);
albedelta=-R_gamma*(R_eq(albeg(1),albeg(2),ka,kb,ra,rb,chia, ...
chib,theta,rhoiso)/(slope'*slope)*slope);

%Make sure we stay within 0<alpha,beta<1
if (albeg(1)+albedelta(1))>1
    albeg(1)=(albeg(1)+1)/2;
elseif (albeg(1)+albedelta(1))<0
    albeg(1)=(albeg(1)+0)/2;
else
    albeg(1)=albeg(1)+albedelta(1);
end
if (albeg(2)+albedelta(2))>1
    albeg(2)=(albeg(2)+1)/2;
elseif (albeg(2)+albedelta(2))<0
    albeg(2)=(albeg(2)+0)/2;
else

```

```

        albeg(2)=albeg(2)+albedelta(2);
    end

        %Add next iteration to array
    if PlotSolutions
        albeg_plot=[albeg_plot albeg; R_eq(albeg(1),albeg(2),ka, ...
kb,ra,rb,chia,chib,theta,rhoiso)]];
    end
end
I
%% Plot function
if PlotSolutions
    toc; tic
    al=linspace(max(0.1,min(albeg_plot(1,:))-0.1),min(0.9, ...
max(albeg_plot(1,:))+0.1),R_Resolution);% 0.05:0.05:0.95;
    be=linspace(max(0.1,min(albeg_plot(2,:))-0.1),...
min(0.9,max(albeg_plot(2,:))+0.1),R_Resolution);%
0.05:0.05:0.95;
    fid=fopen('C:\Users\Kaspe_000\Desktop\plot.csv','w');
    fprintf(fid,'alpha, beta, eq\n');
    for i=1:length(al)
        for j=1:length(be)

f(i,j)=R_eq(al(i),be(j),ka,kb,ra,rb,chia,chib,theta,rhoiso);
            alpha(i,j)=al(i);
            beta(i,j)=be(j);
            fprintf(fid,[num2str(al(i)) ', ' num2str(be(j)) ', '...
                           num2str(f(i,j)) '\n']);
        end

        if abs(mod(i,R_Resolution/100))<0.5001
            [num2str(i/R_Resolution*100) '%']
            toc
        end
    end

    for i=1:size(albeg_plot,2)
        fprintf(fid,[num2str(albeg_plot(1,i)) ', ' ...
                           num2str(albeg_plot(2,i)) '\n']);
    end
    fclose(fid);
    figure
    hold on
    surf(alpha,beta,f)
    colormap(jet(256));
    %caxis([0 max(albeg_plot(3,:))*1.1])

```

```

shading flat
plot3(albeg_plot(1,:),albeg_plot(2,:),albeg_plot(3,:)+10, ...
        'ro-','LineWidth',2,'MarkerSize',14);
axis square
axis tight
xlabel('\alpha')
ylabel('\beta')
end
albe=albeg';
end

```

Appendix B.12 getalpha_5pt.m: Solves the equation for the 5 point method

This function solves (4-32) using k and m from experiment and the position of contact E defined by Equation 4-32. The tensor can be calculated from rho(al,k,r,chi,rhoiso) from setup.m. This function needs to be in the same folder as setup.m.

```

function alpha = getalpha_5pt( r2, k, m )
%Getalpha_5pt Finds alpha from measured k and m
%   a, b are side lengths of the isotropic equivalent sample. Theta is
%   angle in degrees.

setup;
alpha=0.5;

l2 = @(x) transf(m,0,x,k);

% Solves l2(k)=r2 using binary search
i=3;
a1=1/(i+0.1);
a2=1-1/(i+0.2);

while sign(r2-l2(a1))==sign(r2-l2(a2))
    i=i*10;
    a1=1/(i+0.1);
    a2=1-1/(i+0.2);
end;

a3=(a1+a2)/2;

while abs(a1-a2)>1e-10
    if sign(r2-l2(a1))==sign(r2-l2(a3))
        a1=a3;
    else
        a2=a3;
    end
    a3=(a1+a2)/2;
end

```

```
end  
alpha=(a1+a2)/2;  
  
end
```

Appendix C Attached papers

The appendix contains papers that form part of this dissertation. Nine papers are included out of the total of 13 published papers as of the date of submission. The remaining papers published can be found in the publication list after the preface.

Appendix C.1 Measurement of the Electrical Resistivity and Hall Coefficient at High Temperatures

Reproduced with permission from Review of Scientific Instruments, Copyright 2012 American Institute of Physics.

Measurement of the electrical resistivity and Hall coefficient at high temperatures

Kasper A. Borup,¹ Eric S. Toberer,² Leslie D. Zoltan,³ George Nakatsukasa,³ Michael Errico,³ Jean-Pierre Fleurial,³ Bo B. Iversen,¹ and G. Jeffrey Snyder^{4,a)}

¹Center for Materials Crystallography, Department of Chemistry and iNANO, Aarhus University, Aarhus DK-8000, Denmark

²Department of Physics, Colorado School of Mines, Golden, Colorado 80401, USA

³Jet Propulsion Laboratory/California Institute of Technology, 4800 Oak Grove Drive, Pasadena, California 91109, USA

⁴Materials Science, California Institute of Technology, Pasadena, California 91125, USA

(Received 25 June 2012; accepted 21 November 2012; published online 14 December 2012)

The implementation of the van der Pauw (VDP) technique for combined high temperature measurement of the electrical resistivity and Hall coefficient is described. The VDP method is convenient for use since it accepts sample geometries compatible with other measurements. The technique is simple to use and can be used with samples showing a broad range of shapes and physical properties, from near insulators to metals. Three instruments utilizing the VDP method for measurement of heavily doped semiconductors, such as thermoelectrics, are discussed. © 2012 American Institute of Physics. [http://dx.doi.org/10.1063/1.4770124]

I. INTRODUCTION

The electrical resistivity and Hall coefficient are important materials properties. They play an important role in any field of research concerned with the electronic transport properties of materials such as semiconductors and metals. From the Hall coefficient, the charge carrier concentration can be directly calculated. By simultaneous measurement of the resistivity, the carrier mobility can also be inferred. The temperature dependence and magnitude of the carrier mobility makes it possible to extract information about the scattering mechanisms.¹ This cannot be done with separated measurements of the resistivity and Hall coefficient.

With the traditional bar shaped samples, six contacts are needed for simultaneous measurement of the resistivity and Hall coefficient. Additionally, all dimensions of the sample and the distance between the contacts for resistance measurement need to be known. With the van der Pauw (VDP) technique, only four contacts are needed and only the sample thickness is necessary to calculate the resistivity.² The sample geometry is also suitable for other transport measurements such as flash diffusivity.

Few systems implement the VDP technique for combined high temperature resistivity and Hall coefficient measurements.^{3–5} A number of reports exist on systems utilizing other methods and sample geometries for both direct current (dc)^{6–8} and alternating current (ac)^{9–15} measurements. In this paper, we describe some of the challenges encountered when designing a high temperature resistivity and Hall effect apparatus based on the VDP geometry and outline general solutions that greatly facilitate the use of this method at high temperatures. Specific implementation of these solutions is assessed for three high temperature systems at NASA-JPL,

Caltech, and Aarhus University. All of these systems were designed for thermoelectric research; nevertheless, the general design rules are expected to hold regardless of application.

II. MEASUREMENT BACKGROUND

Traditional measurements of the electrical resistivity utilize a four-point bar geometry (Figure 1(a)), where an electrical current is applied at or near the ends and the voltage is measured between two points where the current is uniform. Here, the distance between the contacts and cross-sectional area are critical geometric parameters in converting the measured resistance to resistivity. As virtually no current flow through the voltage contacts when such a four-point method is used, there is normally no error due to contact resistance.

A. Van der Pauw method

Alternatively, van der Pauw showed that the resistivity of an isotropic, homogeneous flat sample could be determined from four probes located arbitrarily around the edge through conformal mapping mathematics.^{2,16} Here, the specific probe location is less critical to reliable measurements, but the sample thickness remains important. Instead of measuring the distance between the contacts, the in-plane geometric factor is determined by switching the probes used for current and voltage.

When measuring the resistivity using the van der Pauw approach, current between two adjacent probes on the sample edge induces a voltage between two additional probes on the edge of the sample. This is shown in panel (c), a current is passed from contact *p* to *o*, while the voltage is measured between contacts *m* and *n* resulting in a resistance $R_{po,mn} = V_{mn}/I_{po}$. Due to symmetry, reversing the polarity of both the voltmeter and current source or interchanging the voltmeter and current source results in the same resistance.

^{a)}Author to whom correspondence should be addressed. Electronic mail: jsnyder@caltech.edu.

This resistance is called R_A . Measuring all four resistances and using the average reduces the effect of imperfect contacts and inhomogeneous samples but is not strictly necessary.^{17,18} Likewise, using the contact arrangement in panel (d), $R_B = R_{no,np}$ and its three analogs can be measured. R_B is in general different from R_A . The two resistances fulfill the VDP relationship,²

$$\exp\left(-\frac{\pi d R_A}{\rho}\right) + \exp\left(-\frac{\pi d R_B}{\rho}\right) = 1. \quad (1)$$

Here, ρ is the sample resistivity and d its thickness. The VDP relationship cannot be solved analytically for ρ except for the special case where R_A and R_B are identical. Instead, a standard numerical method such as binary search or the Newton-Raphson method is used.

B. Hall coefficient

In an isotropic material, the Hall coefficient is a measure of the induced voltage orthogonal to both an electric current and magnetic field.¹⁹ The typical four-point bar geometry is shown in Figure 1(b), with the magnetic field normal to the sample surface. Thus, in a traditional bar geometry, five or six leads are required to measure both the resistivity and Hall coefficient. The ratio of the induced transverse voltage to the current can be described as a resistance $R_{mn,qr} = V_{qr}/I_{mn}$. The Hall coefficient is generally described as $R_H = R_{mn,qr}d/B$ where d is the sample thickness (in direction of magnetic induction B); however, care must be taken to avoid Ohmic voltage signal and the magnetic response may not be linear in B (both discussed below).

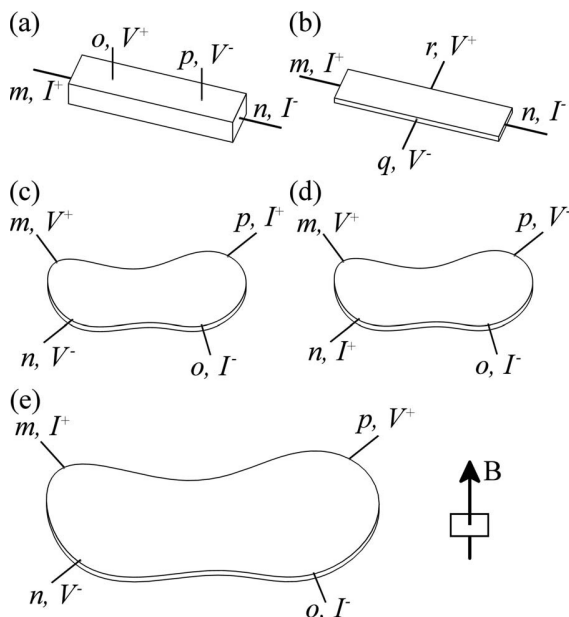


FIG. 1. Common sample geometries. (a) Preferred geometry for four-probe resistivity measurements, (b) common geometry for a Hall effect measurement, resistance measurements, (c) and (d) arbitrarily shaped lamella for VDP measurements showing contact arrangements for two resistance measurements, and (e) contact arrangement for a Hall effect measurement with the VDP method. The arrow in the bottom right corner indicates the positive direction of the magnetic field in panels (b) and (e).

With the van der Pauw geometry, the Hall coefficient can be obtained from the same four contacts used in the resistivity measurement. A current is passed diagonally across the sample, which is in a magnetic field perpendicular to the sample plane. For example, $R_H = R_{mo,np}d/B$ (Figure 1(e)) is used for Hall effect measurement. Four identical measurements can be made with the current in both directions along both diagonals. The measurements are repeated for at least two field strengths, such as positive and negative fields to subtract the Ohmic voltage signal.

III. INSTRUMENT SETUP AND MEASUREMENT PROCEDURES

A. Instrument geometry

A high temperature van der Pauw system requires a sample stage, heater, magnet, and associated electronics. However, the geometry and high temperature material selection can pose a challenge. This is further exacerbated when the sample must be kept under vacuum or a controlled environment via an enclosure. The following describes general design requirements for each of these components and the specific implementations which have been chosen in the three systems reviewed here.

1. Magnet

The magnet can be either a cryostat magnet or an electromagnet. A cryostat magnet usually has a narrow, cylindrical sample space within the superconducting coil where the magnetic field is directed along this cylindrical axis. This gives very limited space in the sample plane perpendicular to the magnetic field and limits space for contacts, which is unsuitable for large samples. In an electromagnet, there is more space perpendicular to the magnetic field but the pole gap should be small to allow for a high magnetic field, and hence restricts the space perpendicular to the sample plane. The electromagnet has the advantage that the direction of the field is more easily changed and the total accessible volume for the sample holder can be made larger.

The Caltech and JPL magnets are nearly identical electromagnets with different pole caps. The pole caps on the JPL magnet have much space between them (7.5 cm) to accommodate the sample stage, heater, and vacuum enclosure but do not focus the magnetic flux down as much as the Caltech magnet (2.5 cm between pole caps). The larger distance between the pole caps on the JPL magnet decreases the maximum field (approximately 1.0 T for JPL vs 2.0 T for Caltech). The Aarhus setup uses a different electromagnet with a 3.0 cm pole gap. This gives a 1.2 T field when the pole shoes are adjusted to give a homogeneous area (change less than 1.5%) of 3.0 cm in diameter.

2. Controlled atmosphere vessel

In order to prevent sample oxidation and sublimation, a controlled atmosphere vessel is needed. The atmosphere can either be vacuum or an inert cover gas. At high temperatures,

thermally insulating the heater from the walls of the vessel is necessary to maintain the vessel's mechanical strength and stabilize the sample temperature. Choice of atmosphere (vacuum or an inert cover gas) is a critical decision. In a vacuum there is no convection, which facilitates insulating the vessel from the heaters. However, compared to a cover gas, the vacuum can increase evaporation from high vapor pressure samples. To counteract this, a layer of boron nitride spray can be applied after mounting the sample. A final consideration is the gap between the electromagnet pole caps. In both cases, the vessel and associated insulation will significantly decrease the available spaces between the pole caps.

In the systems described here, all three use vacuum atmosphere within the vessel. Radiation shielding is employed to minimize heat flow from the sample to the vessel.

3. Heating

There are in general three different strategies to heating the sample and probe: embedded heaters in the sample holder, radiative heating of the holder from inside the vessel, or heating the controlled atmosphere vessel from the outside. Heating from the outside is less efficient, requiring higher heater temperatures and requires more space for insulation. If outside heating is chosen, an inert gas atmosphere allows for better heat transfer to the sample than a vacuum.

When using resistance heaters, the field generated from the current should be reduced around the sample. If heating coils are used, a double helix with antiparallel current can be used to cancel out the generated field. A low current dc source is preferred since this minimizes the magnetic field in the heaters. An ac source will generate oscillating magnetic moments, which can cause vibrations when interacting with the field from the electromagnet. These vibrations can both damage the sample holder and increase the measurement noise due to changing capacitances of the leads and voltages induced by the oscillating magnetic field.

When using embedded heaters, it is particularly important to avoid temperature errors associated with radiative losses from the stage/sample. A thin metal sheet or foil (without electrically contacting the sample or electrical wiring) or equivalent insulation efficiently inhibits radiation from the sample and reduces the heat loss. In Figure 2(a), the heat shield around the stage is represented as a box with one end open. Several layers may be needed to improve the insulation, especially at high temperatures. If the innermost layer is in good thermal contact with the stage, the shielding will be close to the stage temperature and further stabilize the sample temperature.

The wider pole gap of the NASA-JPL system permits radiative heaters to surround the sample and a maximum temperature of 1000 °C. The heaters are simple resistive heaters. In contrast, the Caltech and Aarhus systems use heaters directly embedded into the sample stage. The Aarhus design uses a heater wire embedded into a ceramic binder within the stage while the Caltech heater is the size of a commercial cartridge heater and replaceable. Both systems exhibit a maximum temperature of 600 °C; this value is expected to increase with improved radiation shielding.

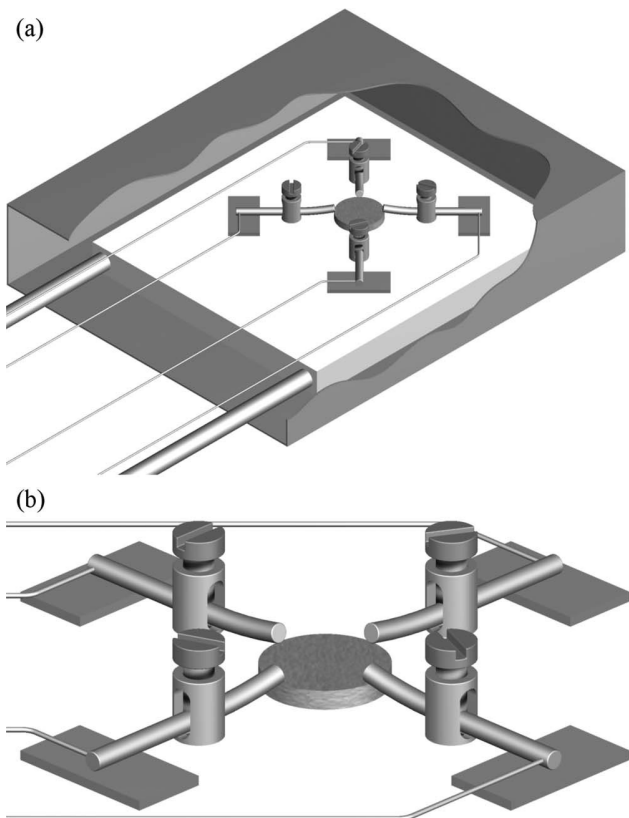


FIG. 2. Illustration of the sample holder. (a) The sample is mounted on a heated plate inside a heat shield. Two rods can be used to fix the sample holder between the poles of the electromagnet (not shown). (b) Zoom on the post-and-screw design. When the metal rods are pressed against the sample they bend elastically. This ensures good electrical contact during thermal expansion. The other end of the rods are either pressed against metal pads or connected directly to wires, in which case the pads are unnecessary. Both methods are shown for comparison.

4. Thermocouples

Thermocouples are critical for both controlling the heater response and for accurately measuring the sample temperature while data are being collected. Thermocouples (not shown) can be embedded in the sample holder below the sample. The thermocouple wires cannot be in direct contact with the sample since this interferes with the measurements.

In the Caltech and Aarhus systems, both the thermocouple and heaters are embedded in the stage. As the stage is a good thermal conductor, the heater PID control is quite good for these systems. The NASA-JPL system uses a thermocouple next to the sample that is attached to the stage. Thus, the thermocouple is radiatively coupled with the heaters, much like the sample.

5. Sample holder

The sample holder can be made from any electrically insulating material that can sustain the desired maximum temperature. It should also have sufficiently high thermal conductivity to reduce temperature gradients across the sample holder. Possible materials are ceramics such as boron nitride, alumina, and silicon carbide. Boron nitride is easily machin-

able and has a high thermal conductivity but a low mechanical strength. Alumina and silicon carbide are hard to machine but can be purchased as cements, which can be cast to the desired shape. Figure 2(a) shows the principal components of a sample holder with embedded heaters for use in an electromagnet. The same general design can be used with radiated heaters in which case the heat shield is replaced by the heaters. The sample holder is rigidly mounted to fix the sample holder between the poles of the electromagnet.

Different approaches to the sample holder have been chosen. At Caltech, boron nitride is used for its machinability although it is expensive and the low mechanical strength has led to it requiring replacement after about 1000 uses. Holes bored into the boron nitride are used to contain custom cartridge heaters. The sample holder is rigidly attached by means of two rods. In Aarhus, the sample holder is cast from silicon carbide cement. Since silicon carbide cement is inexpensive, the heating coils are cast directly into the sample holder. This gives good heat transfer and eases temperature control but they cannot be changed if they break. To prolong the lifetime, thicker heating wire and higher currents are used to keep the wire temperature low. The wires are spatially separated from the sample to minimize the magnetic field and the coils are kept parallel to the sample plane. At JPL, refractory metal bolts are used to hold thick alumina plates together. The initial fabrication is not trivial, as the alumina requires a multitude of holes, but the stage is quite robust.

The stage can be designed to hold a sample on each side. In practice, the temperature control is typically the source of increased measurement time and a dual sample stage can double system throughput. If designed well, this will only increase the probe thickness slightly. The two sample design is best implemented in systems where the time required for a single measurement is low to keep the number of measurements high. Such a dual-stage has been implemented at NASA-JPL.

6. Electrical contacts to sample

The connections to the sample are made with four pressure contacts¹⁹ as seen in Figure 2(b). Screws and posts are used to press metal rods against the top edge of the sample making electrical contact and keeping the sample in place. This geometry allows for many sample sizes to be used, from a few millimeters in diameter to almost the diameter of the post arrangement as well as from thin films to ~ 3 mm in thickness. This eliminates the need for contact glue or paste, thus decreasing the contact area. Contact glues and pastes can additionally react with or diffuse into the sample at high temperatures, leading to offset voltages and bad measurements. The post and screw design is additionally attractive, as it does not significantly increase stage thickness.

Errors arise in the measurements if the contacts have large areas or are far from the periphery.²⁰ The use of cylindrical metal wires at an angle to the sample plane can help to form point contacts just on the sample edge. Here, the top surface of the sample is higher than the contact pads surrounding the sample. The sample height can be adjusted with alumina plates to ensure the wires have the right angle. Alternatively,

line contacts can be used on the side of the sample.³ Such contacts will limit the flexibility when placing the contacts and gives higher restrictions on the sample geometry.

In the Hall effect measurement, when the contacts are not placed exactly opposite of each other with respect to the current direction, the sample resistance will contribute to the measured voltage. While in principle this effect is subtracted it should be avoided as much as possible to reduce the measurement uncertainty and noise. Errors also arise if the distance between two contacts becomes comparable to the sample thickness. For square and rectangular samples, the contacts should be made to the corners rather than the sides.²¹ The measurement error is expected to be proportional to sample thickness over diameter.

The correct choice of material for the metal contacts is crucial for obtaining high accuracy measurements.¹⁹ The metal should be inert, maintain good mechanical and electrical properties in the used temperature range, and have a low Seebeck coefficient (low thermopower). Typically used metals such as silver and copper, and even nickel and platinum, can give reactions with many materials. Additionally, nickel is ferromagnetic and not preferred for Hall effect measurements. Instead metals with high melting points that are inert to most materials should be used. Some possible choices are niobium, molybdenum, tantalum, and tungsten. For the contacts to remain good during thermal expansion, the metal rods should be flexible and act as springs. This means that they cannot be too thin or thick, and should keep their mechanical strength and elasticity in the used temperature range. When the screws are tightened the rods should bend before the sample breaks.

If the pressure screws and posts are made from the same material, they will fuse during high temperature operation. Possible materials are inert and non-magnetic metals including stainless steel and the above mentioned elements, among others. Since screws of stainless steel are cheap and easy to replace another material can be chosen for the posts.

We have found 1.0–1.5 mm molybdenum or tungsten wire have good electrical and mechanical properties and works well for thermoelectric measurements. It is strong and flexible and maintains its strength to very high temperatures, allowing for thin rods to be used. This minimizes the contact area.

The usual procedures for electrical wiring, insulation, and shielding should be used to reduce noise and stray voltages to acceptable levels.

B. Measurement strategy

For accurate measurement of the resistivity and Hall coefficient, a number of measurement offsets need to be removed. In the resistivity measurement, these include zero point offsets in the voltage versus current curve due to thermal voltages from the sample, measurement leads, and electronics. In a Hall coefficient measurement, offsets resulting from the sample resistance additionally arise when the contacts are not perfectly aligned.

When using dc measurements, the offset from thermal voltages can be removed by measuring the offset voltage before and after the resistance measurement, with the current turned off. By measuring it twice and using the average off-

set, linear changes in the voltage offset are taken into account. The average offset voltage is subtracted from the voltage measurement before calculating the resistance.

If the current source has the ability to reverse the direction of the current, the delta method can be used instead. Here, the current is turned on in the positive direction, switched to negative and then back to positive. In each step, the current and voltage are measured as V_1^+ and I_1^+ for positive current, V^- and I^- for negative current, and finally V_2^+ and I_2^+ for positive current. The resistance is then calculated as $R = (V_1^+ + V_2^+ - 2V^-)/(I_1^+ + I_2^+ - 2I^-)$. These both removes the offset voltage and combines one resistance measurement with its equivalent with reversed polarity of the current source and voltmeter. It is important to note that the circuit has to be the same for the measurements with positive and negative current for the offset voltage to be constant. Hence, the current should be reversed in the current source and not by switching a matrix card or other instruments between the current source and sample. Thermal offsets are removed automatically when using ac measurements, provided an appropriate frequency is chosen.

If R_H changes linearly with B , the resistive offset in the Hall effect measurement can be removed by measuring the Hall voltage for several magnetic field strengths and subtracting the offset at $B = 0$. This increases the measurement time significantly, and often it is more convenient and sufficiently accurate to use only two field strengths. Reversing the field direction is preferred over turning the field on and off since it doubles the measured Hall resistance and removes magnetoresistance effects (voltages proportional to even powers of B) but still appropriate when the Hall effect is nonlinear (Hall voltages proportional to odd powers of B). Using thinner samples results in higher effective resistances which improves resolution, especially for low-mobility samples. Both the relative effect of noise proportional to the current and current independent thermal noise are lowered, resulting in a larger signal-to-noise ratio.

To reduce the measurement uncertainty, the contacts should be Ohmic and there should be no Shottky barrier. This is generally the case for high charge carrier concentrations as in heavily doped semiconductors and metals, especially at room temperature and above. For very low carrier concentration, the contacts may not be Ohmic, and measuring the I-V curve is necessary.

C. Other considerations

When making temperature varying measurements the temperature can either be continually ramped or increased in steps. Although increasing the temperature in steps makes the measurements more accurate, it also increases the measurement time considerably. If the temperature is ramped continually, the rate should be adjusted so the temperature does not change enough during measurements to substantially change the sample resistivity.

The measured resistivity is not affected much if the temperature changes slightly during the measurement; however, fine features in the resistivity versus temperature curve might be lost. If the contacts are slightly misaligned, the resistive

offset in the Hall measurement will be very large and the Hall resistance can reduce to only a few percent of the measured value. If the temperature changes considerably between measuring with positive and negative fields, the resistance of the sample also changes and the resistive offset may not be subtracted off correctly.

Both ac and dc measurements can be used with the method described here. Alternating current measurements are often considered to give more precise measurements but are also harder to implement as shielding and capacitance considerations are different. An ac magnetic field with an ac test current through the sample^{13–15} can also be used for measurement of the Hall effect.

IV. MEASUREMENT EXAMPLE

Figure 3 shows a two-point (current and voltage across the same two contacts) I-V curve for a material with a charge carrier concentration of $2.8 \times 10^{18} \text{ cm}^{-3}$. The current range typically used is covered, 0–500 mA. The voltage is measured across a contact-sample-contact double junction and is hence antisymmetric when reversing the current direction. Therefore, only positive currents are shown. No Schottky anomaly is visible. The sample is a Mg₂Si intrinsic semiconductor and a slight decrease in resistance ($\sim 5\%$ corresponding to $\sim 2 \text{ K}$ temperature increase) can be ascribed to Joule heating at high currents (more than 1 W of Joule heating at the maximum current). Because this is a two-point measurement the resistance is a sum of the resistances of the leads, contacts, and the sample.

An example of a high temperature measurement is shown in Figure 4. A PbS sample was heated to $\sim 600 \text{ }^{\circ}\text{C}$ and cooled to room temperature at a rate of 100 K/hr while continually measuring the resistivity and Hall coefficient. The measurement was performed on both the Caltech (squares) and Aarhus (line) setups. The measurements agree quite well at room temperature. The slight disagreement in resistivity and Hall carrier concentration is most likely due to errors in the temperature measurement. The hysteresis in the Hall carrier

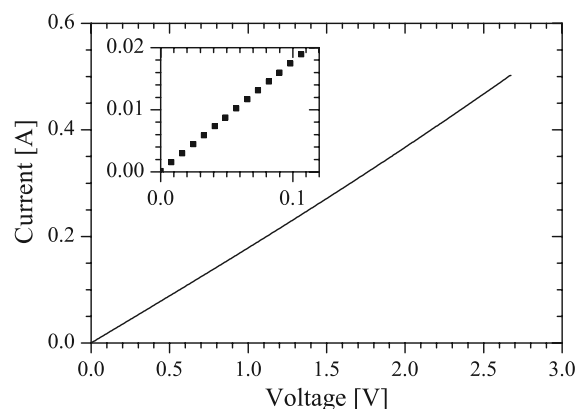


FIG. 3. I-V curve for metal contacts showing no Shottky anomaly. The current range, 0–500 mA, covers the currents typically used. The inset shows a zoom on the low current data to emphasize the absence of a Shottky anomaly. The sample used is n-type intrinsic Mg₂Si with $n \sim 2.8 \times 10^{18} \text{ cm}^{-3}$. Molybdenum has been chosen for the contacts.

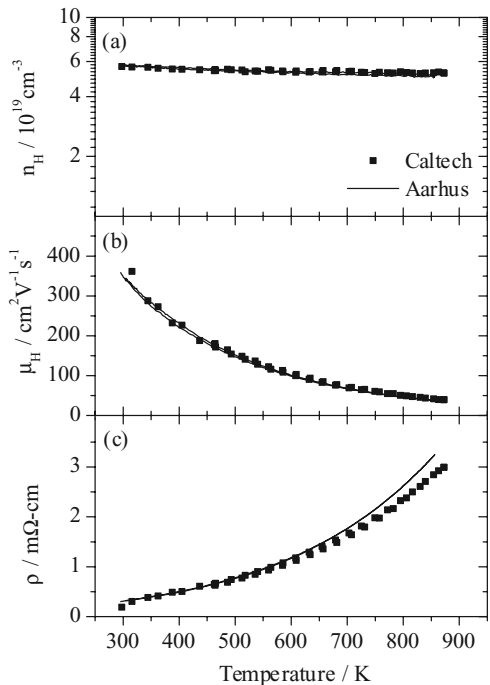


FIG. 4. Example of a measurement of (a) Hall carrier concentration, (b) Hall mobility and (c) electrical resistivity. The data were measured during heating and cooling to 600 °C on both the Caltech (squares) and Aarhus (line) setups. The sample is doped PbS.

concentration, most visible in the Aarhus data, is due to the sample resistivity changing during the measurement, as discussed above. The single parabolic band model is quite accurate for PbS and hence the change in Hall carrier concentration with temperature is small. With the method described herein the uncertainty in the resistivity and Hall coefficient is believed to be less than 5% for uniform samples. However, in the Hall effect measurement the noise can often exceed this, especially for low mobility or low carrier concentration samples. Additionally, bad alignment of the sample contacts or high heating rates may give systematic deviations in excess of this, as discussed in detail above. The error in the temperature measurements depends on the exact thermocouple placement, thermal resistance between sample and thermocouple and heat loss from the sample. In the apparatus described here, the error in temperature measurements is believed to be less than 15 °C, including the thermocouple precision.

V. DISCUSSION

A. Measurement approach

1. Bar method

The most frequently used sample geometry for both resistivity and Hall effect measurements is the bar shape (Figs. 1(a) and 1(b)). For the measured resistivity to be accurate, the contacts *o* and *p* should be sufficiently far from contacts *m* and *n* to ensure parallel current paths. A primary source of uncertainty in these measurements is the ability to measure the geometric factors, namely, the distance *l* between contacts *o* and *p* as well as the cross-sectional area *A* of the

bar. Often the contacts are attached with an electrical conducting adhesive, paste or solder, thus increasing the contact areas and making measurement of the distance between the contacts, *l*, ambiguous, leading to a primary source of inaccuracy. Additional contacts are needed for simultaneous resistivity and Hall measurements where large contacts *r*, *q*, may alter the current path for resistance measurements.

2. VDP method

In the VDP technique, explicit knowledge of the current paths is not needed, allowing for the resistivity and Hall coefficient to be measured on the same sample using the same contacts. The sample must be isotropic within the plane and of uniform thickness, may not contain any holes, and the contact areas have to be small compared to the surface area and ideally should be along the entire thickness at the edge. Like the traditional geometry, the sample is assumed to be homogeneous and without cracks. The sample can be polished to an even thickness, which can be measured sufficiently accurately not to lower the accuracy of the method significantly.

Like the traditional method, finite size of the contacts in the VDP leads to sources of error in the measurement. For a circular disc of diameter *D*, the error from a line contact extending a distance *l* along the sample periphery, away from the periphery, or a point contact placed away from the periphery, scales as $\Delta\rho/\rho \propto l^2/D^2$ and $\Delta R_H/R_H \propto l/D$. If $l/D \ll 1$, the errors are to a first approximation additive¹⁶ and the error from a contact of finite area scales according to the same relationships. Tests have shown that the sample thickness should not exceed half the diameter for the technique to remain accurate.¹⁷

3. Hall effect

Inspired by the free electron model, the Hall carrier concentration can be defined from the Hall coefficient as $n_H = -1/eR_H$ for electrons or $p_H = 1/eR_H$ for holes where *e* is the electron charge. For materials with more complex band structures, *n_H* simply becomes a measure of the Hall coefficient in units related to carrier concentration that can be negative or positive. Together with the resistivity, the Hall mobility can also be defined as $\mu_H = 1/n_H e \rho$ or $\mu_H = 1/p_H e \rho$ for electrons and holes, respectively. For complicated systems, we define $\mu_H = 1/n_H e \rho = R_H/\rho$ as simply a measure of the Hall effect in units of mobility that would be negative for electrons and positive for holes. For materials where a simple single band model does not apply, the results should be used with care since they can be quite far from the real charge carrier concentrations and mobilities. This is frequently apparent when more than one carrier type is present. In this case, the Hall voltages of the two species partially cancel leading to low values of *R_H* and *μ_H* or high *n_H* where the magnitude and sign of the values depend in a complicated way on the transport parameters of the individual species.¹⁹

B. Application in thermoelectrics

In thermoelectrics, the electronic properties strongly affect the material performance. The efficiency of a

thermoelectric material is to first order proportional to the thermoelectric figure of merit given by $zT = S^2 T / k \rho$, where S is the Seebeck coefficient, κ is the thermal conductivity, ρ is the electrical resistivity, and T is the temperature. The Seebeck coefficient, electrical resistivity, and the electronic contribution to the thermal conductivity depend on the charge carrier concentration.²² Hence, the charge carrier concentration, being calculated from the Hall coefficient, is also important for full characterization of the material. Additionally, charge carrier scattering impacts both the electronic mobility (and thus resistivity) and the Seebeck coefficient. The temperature dependence of the mobility is one way to identify the dominant charge carrier scattering mechanism.

Within thermoelectrics, one of the experimental challenges is to accurately measure properties contributing to the figure of merit at high temperatures. Measuring individual properties on different samples can reduce the accuracy due to variations between the samples. Cutting a single sample between individual measurements can give the same problem due to sample inhomogeneities. The development of techniques utilizing the same sample geometry can hence increase the accuracy of the figure of merit substantially.

Thermoelectric materials are often prepared as pressed pellets or as ingots made by the Bridgman-Stockbarger or Czochralski techniques. Polycrystalline pressed pellets of cubic materials are usually isotropic.²³ Polycrystalline pressed pellets of weakly anisotropic materials are often isotropic within experimental uncertainty.²⁴ Strongly anisotropic crystalline materials such as Bi_2Te_3 can be expected to be isotropic within the plane perpendicular to the pressing direction but can have very different transport properties along the pressing direction.²⁵ The properties of melt-grown ingots may have properties that change along the length of the ingot, and each slice may make a different study.

In all these cases, these circular disks are frequently used directly for measuring the thermal diffusivity in the laser flash technique²⁶ and can also be used for measuring the Seebeck coefficient^{27,28} along the same direction (parallel to the pressing direction). The same sample geometry can be used for measuring the resistivity and Hall coefficient in the VDP method but the measurements are performed in the plane of the disk. Hence, a complete characterization of a material can be obtained from the same sample without shaping it between individual measurements, provided the properties are isotropic.

These benefits reveal why the three thermoelectric research groups discussed herein have adopted the VDP method for high temperature measurements.

VI. SUMMARY

We have discussed general design guidelines for successfully implementing the VDP geometry in combined measurements of the resistivity and Hall coefficient at high temperature. Three instruments that were specifically designed for

thermoelectric measurements are discussed in detail. The approach is convenient for measurements on thermoelectrics due to the compatibility of the sample geometry with other measurements. Several overarching design principles and guidelines discussed herein are also equally applicable to traditional bar measurements at high temperature.

ACKNOWLEDGMENTS

We gratefully acknowledge the assistance of the NASA-JPL thermoelectrics group for design, initial development, and testing, as well as funding for this project. The work was supported by the Danish National Research Foundation (Center for Materials Crystallography) and the Danish Strategic Research Council (Center for Energy Materials). E.S.T. acknowledges support from the U.S. National Science Foundation (NSF) MRSEC program—REMRSEC Center, Grant No. DMR-0820518. G.J.S acknowledges support of Fred Harris and others at BSST/Amerigon during the fabrication of the Caltech system.

- ¹V. I. Fistul, *Heavily Doped Semiconductors* (Plenum, New York, 1969).
- ²L. J. van der Pauw, Philips Res. Rep. **13**, 1 (1958).
- ³C. Wood, A. Lockwood, A. Chmielewski, J. Parker, and A. Zoltan, Rev. Sci. Instrum. **55**, 110 (1984).
- ⁴J. A. McCormac and J.-P. Fleurial, in *Modern Perspectives on Thermoelectrics and Related Materials Symposium* (Materials Research Society, Anaheim, CA, 1991), p. 135.
- ⁵M. Morvic, in *Proceedings of the Modern Perspectives on Thermoelectrics and Related Materials Symposium, Smolenice Castle, Slovakia, 2000* (IEEE, 2000), p. 327.
- ⁶T. M. Dauphinee and E. Mooser, Rev. Sci. Instrum. **26**, 660 (1955).
- ⁷C. M. Hurd, J. Sci. Instrum. **42**, 465 (1965).
- ⁸D. M. Rowe and R. W. Bunce, J. Phys. E **4**, 902 (1971).
- ⁹G. L. Guthrie, Rev. Sci. Instrum. **36**, 1177 (1965).
- ¹⁰J. M. Lavine, Rev. Sci. Instrum. **29**, 970 (1958).
- ¹¹E. E. Olson and J. E. Wertz, Rev. Sci. Instrum. **41**, 419 (1970).
- ¹²E. M. Pell and R. L. Sproull, Rev. Sci. Instrum. **23**, 548 (1952).
- ¹³T. Kaneda, S. Kobayash, and K. Shimoda, Jpn. J. Appl. Phys. **12**, 1335 (1973).
- ¹⁴N. Z. Lupu, N. M. Tallan, and D. S. Tannhaus, Rev. Sci. Instrum. **38**, 1658 (1967).
- ¹⁵B. R. Russell and C. Wahlig, Rev. Sci. Instrum. **21**, 1028 (1950).
- ¹⁶L. J. van der Pauw, Philips Tech. Rev. **20**, 220 (1958).
- ¹⁷C. Kasl and M. J. R. Hoch, Rev. Sci. Instrum. **76**, 033907 (2005).
- ¹⁸D. W. Koon and C. J. Knickerbocker, Rev. Sci. Instrum. **63**, 207 (1992).
- ¹⁹E. H. Putley, *The Hall Effect and Related Phenomena* (Butterworths, London, 1960).
- ²⁰C. J. Vineis, T. C. Harman, S. D. Calawa, M. P. Walsh, R. E. Reeder, R. Singh, and A. Shakouri, Phys. Rev. B **77**, 235202 (2008).
- ²¹D. W. Koon and C. J. Knickerbocker, Rev. Sci. Instrum. **64**, 510 (1993).
- ²²G. J. Snyder and E. S. Toberer, Nature Mater. **7**, 105 (2008).
- ²³H. Wang, Y. Pei, A. D. LaLonde, and G. J. Snyder, Proc. Natl. Acad. Sci. U.S.A. **109**, 9705 (2012).
- ²⁴A. Zevalkink, W. Zeier, G. Pomrehn, E. Schechtel, W. Tremel, and G. J. Snyder, Energy Environ. Sci. **5**, 9121 (2012).
- ²⁵L. P. Hu, X. H. Liu, H. H. Xie, J. J. Shen, T. J. Zhu, and X. B. Zhao, Acta Mater. **60**, 4431 (2012).
- ²⁶C. B. Vining, A. Zoltan, and J. W. Vandersande, Int. J. Thermophys. **10**, 259 (1989).
- ²⁷C. Wood, D. Zoltan, and G. Stapfer, Rev. Sci. Instrum. **56**, 719 (1985).
- ²⁸S. Iwanaga, E. S. Toberer, A. LaLonde, and G. J. Snyder, Rev. Sci. Instrum. **82**, 063905 (2011).

Appendix C.2 Review of Thermoelectric Measurement Techniques
Reproduced by permission of The Royal Society of Chemistry

Measuring Thermoelectric Transport Properties of Materials

Kasper A. Borup^a, Johannes de Boor^b, Heng Wang^c, Franck Gascoin^d, Xun Shi^e, Lidong Chen^e, Mikhail I. Fedorov^f, Eckhard Müller^{b,g}, Bo B. Iversen^a, G. Jeffrey Snyder^{*c,h}

Received (in XXX, XXX) Xth XXXXXXXXX 20XX, Accepted Xth XXXXXXXXX 20XX

DOI: 10.1039/b000000x

In this review we discuss considerations regarding the common techniques used for measuring thermoelectric transport properties necessary for calculating the thermoelectric figure of merit, zT . Advice for improving the data quality in Seebeck coefficient, electrical resistivity, and thermal conductivity (from flash diffusivity and heat capacity) measurements are given together with methods for identifying possible erroneous data. Measurement of the Hall coefficient and calculation of the charge carrier concentration and mobility is also included due to its importance for understanding materials. It is not intended to be a complete record or comparison of all the different techniques employed in thermoelectrics. Rather, by providing an overview of common techniques and their inherent difficulties it is an aid to new researchers or students in the field. The focus is mainly on high temperature measurements but low temperature measurements are also briefly discussed.

Introduction

Thermoelectric materials are a group of electronic materials which can interconvert gradients in electrical potential and temperature.¹ Thermoelectrics can be used for both cooling and power generation.^{2,3} The first is widely used for cooling delicate optoelectronics, detectors, and small scale refrigeration. The latter has successfully been used for power generation in deep space missions⁴ but is now proposed for waste heat recovery, *e.g.* in vehicles,⁵ or for wireless remote sensing such as in aircraft.^{6,7} While the impact on global energy consumption may not necessarily be large,⁸ niche applications abound as materials are improved and novel materials commercialized. Since thermoelectric devices are solid state and contain no moving parts, they find application because they are easily scalable and require little maintenance even though they are inferior in efficiency compared to traditional dynamic heat engine/refrigeration methods.^{2,3,5}

The physics of thermoelectrics are governed by three thermodynamic effects, the Seebeck, Peltier, and Thomson effects. These have a common physical origin and are related through the Seebeck coefficient. The Seebeck effect generates an electrical potential gradient when a temperature gradient is applied (used for power generation), while the Peltier effect pumps reversible heat and can thus establish a temperature gradient when a current is passed through the material (used for cooling). Thomson heat is released or absorbed internally in a material if the Seebeck coefficient depends on temperature,

balancing for the flowing Peltier heat. All effects are related to heat being transported by the charge carriers.
While the effects were discovered in metals, modern thermoelectric materials are heavily doped semiconductors. Both n- and p-type materials are used and both are needed in a device.

The maximum efficiency of a thermoelectric material (whether in cooling or power generation) is depending upon the thermoelectric figure of merit, zT ,

$$zT = \frac{S^2}{\rho\kappa} T. \quad (1)$$

S is the Seebeck coefficient, ρ is the electrical resistivity, κ is thermal conductivity, and T is absolute temperature. The device efficiency is given by the Carnot efficiency, $(T_h - T_c)/T_h$, multiplied by a complicated function of the properties and geometry of the materials and device. This function generally increases monotonously with the average of zT of the two materials across the temperature range used.^{9,10}

With the continued growing interest in the development of better materials, where even a 20% improvement over state-of-the-art would make significant commercial impact, measurement accuracy is of critical importance. For example, excessively large electrical contacts in resistivity and Hall effect measurements lead to misinterpretation of the transport properties and inaccurate reports of Seebeck enhancement in PbTe-based quantum dot superlattices.¹¹⁻¹³ Conversely, early measurements and estimates of the high temperature thermal conductivity of the lead chalcogenides

are some 30% higher than the values obtained today resulting in an underestimation of zT for decades.^{14, 15} Such discrepancies are to be expected even today as absolute accuracy in thermoelectric measurements is still not possible; even published results on standards should be periodically reevaluated. The Seebeck coefficient is particularly difficult as it is inherently a relative measurement. While instruments with identical geometries often give similar values, estimating the relative accuracy of different geometries is more difficult. In one study, the off-axis 4-point geometry was found to overestimate the Seebeck coefficient relative to the 2-point geometry due to cold finger effects. The overestimation was found to be proportional to the temperature difference between the sample and surroundings, reaching 14% at 900 K.^{16, 17}

While there are many recent studies and prior reviews on thermoelectric measurements and instrumentation, data treatment, and developing new methods¹⁶⁻²³ this is often highly specialized work and may not be readily accessible or seem overwhelming to new researchers or research groups in the field. We here present a review of the most common techniques used for measuring the transport properties necessary to characterize a bulk thermoelectric material. The main focus is on techniques for characterization at room temperature and above, but some low temperature techniques are also briefly included. Common problems encountered when using each technique are discussed as well as their advantages, disadvantages, and limitations. The effects of various user or instrument errors on the results are discussed to aid the researcher in identifying erroneous data early in the characterization process.

General Considerations

In order to direct material development, high precision measurement of zT as well as good estimates of the error is necessary. Due to the lack of appropriate standard reference materials, especially at high temperatures, true measurement accuracy is not known. Propagation of the statistical uncertainties of the individual measurements does not give a good estimate for the accuracy, but instead gives an estimate of the data quality. In a recent round-robin by Hsin Wang *et al.*,²⁴ the in zT when comparing data on the same material measured at several laboratories was estimated to be 12% at 300 K, increasing to 21% at 475 K; above this temperature higher variation can be expected. The scatter is defined as the maximum spread in data divided by the average.

Before characterization of a bulk sample, its density needs to be evaluated. The theoretical density can be calculated from the unit cell size and contents, and from this the relative density can be calculated. This is usually greater than 98% for dense samples. The measured zT usually deviates from that of a dense sample when the relative

density is less than 90% and suspect when less than 97%.²⁵

55 Internal standards

Commercial standards with properties close to typical values for thermoelectrics are not available for all measurements. Hence it is recommended that laboratories develop internal standards. These can be materials the group has some experience working with and that are stable in the desired temperature range and with repeated thermal cycling. Elements with high vapor pressure, easily oxidized materials, or materials which can potentially react with thermocouples or contacts should be avoided. While such laboratory standards do not provide an estimate of apparatus accuracy, they are useful for identifying instrument drift and other errors. For example, thermocouple drift at elevated temperatures can be well in excess of 10 K due to thermocouple ageing or reactivity with samples or environment. This can potentially cause large systematic errors in Seebeck measurements.

Even with apparently trivial measurements, skill and experience can be required to obtain high quality measurements. Hence, when training new researchers or students, having them repeatedly mount and measure an internal standard until consistent and accurate results are obtained ensures proper instrument use. Especially when both good electrical and thermal contact is required at multiple points, inexperience can lead to erroneous measurements. This may not always be obvious from the measurement itself, and hence using a standard is recommended.

Sample homogeneity

There are two different types of inhomogeneity worth distinguishing: multi-phase inhomogeneity and charge carrier concentration (dopant) fluctuations. The first is normally detected by powder X-ray diffraction (PXRD) when large amounts ($> 2 - 5\%$) of impurities are present. Small amounts of impurities or amorphous phases are more easily detected by microscopy (e.g. scanning electron microscopy (SEM)).^{26, 27} The effect of secondary phases is strongly linked to the shape of inclusions. While a few volume percent of dispersed compact impurities normally do not affect the transport properties (especially Seebeck coefficient), insulating or metallic phases or cracks along grain boundaries may significantly influence the electrical and thermal conductivities. The presence of impurities may change the dopant content and hence charge carrier concentration of the main phase. For materials where the charge carrier concentration can be estimated from simple charge counting (e.g. using the Zintl principle)²⁸⁻³² comparison of stoichiometry (nominal and e.g. Electron Microprobe Analysis) with the measured Hall effect charge carrier concentration can be used to check for this. A sample falling outside the general trend calls for further examination.

Post synthesis processing, e.g. ball milling, hot pressing, spark plasma sintering (SPS), annealing, etc. may develop secondary phases or otherwise change the material, particularly in SPS where large DC currents may drive mobile species.^{33–37} Again while scanning PXRD and SEM are powerful tools for investigating purity, they may completely miss dopant variations.³⁸ Instead, spatially resolved scanning Seebeck coefficient measurements^{38–41} (e.g. PSM from Panco GmbH, Germany) can detect these variations and thus provide an important complementary technique for establishing homogeneity and quality control of bulk materials.

Even materials (both single crystals and polycrystalline materials) believed to melt congruently will in general produce doping inhomogeneity during solidification from the melt.⁴² Figure 1a shows a scanning Seebeck map of melt solidified Ba₃Ga₁₆Si₃₀ displaying a solidification microstructure not seen in PXRD or SEM. Such dopant gradients can also be observed and controlled in Bridgman grown single crystals of PtSb₂ (Figure 1b) which clearly demonstrates that single crystals are not necessarily homogeneous.⁴³

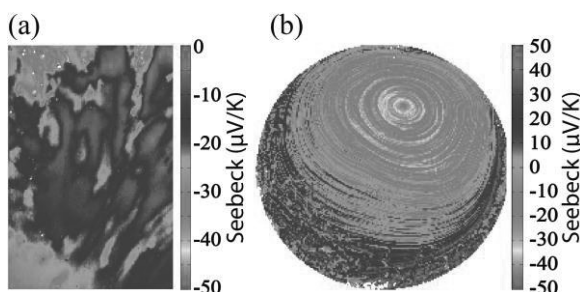


Fig 1. Scanning Seebeck plots of a Ba₃Ga₁₆Si₃₀ raw synthesis product (a) and a Bridgman grown PtSb₂ single crystal (b). In (a), the scan is 3.275×4.85 mm² with a resolution of 0.025 mm and in (b) 9 mm in diameter with 0.05 mm resolution.

Powdered, hot pressed, and solid-state annealed samples are typically better to ensure homogeneous charge carrier concentration on the macroscopic and microscopic level.^{42–44} Inhomogeneities can potentially cause large errors in zT if all properties are measured on different samples or in some cases along different directions.

Seebeck coefficient

A variation of about 5% in measured Seebeck coefficient at 500 K can generally be expected at room temperature.^{45–47} This will, however, also depend on the method employed.¹⁷ The differences between the methods and possible ways to improve the results are discussed below. The accuracy of Seebeck coefficient measurements is unknown since it can only be relatively between two materials. A standard reference material (NIST SRM 3451) is available in the temperature range 10–390 K. At higher temperatures no appropriate standard reference materials are available.

Constantan, chromel, and other thermocouple alloys have well determined Seebeck coefficients; however, the values fall outside the range of interest for thermoelectrics.

Measurements and data extraction

The Seebeck coefficient is the ratio of a resulting electric field gradient to an applied temperature gradient. While the Seebeck coefficient is conceptually simple, in reality it can be difficult to measure accurately. A recent review addresses some of the instrument design challenges,⁴⁸ while another studies data analysis.⁴⁹ In a typical measurement, the temperature is varied around a constant average temperature and the slope of the voltage (V) vs. temperature difference (ΔT) curve gives the Seebeck coefficient (the slope method) or just $V/\Delta T$ is measured (single point measurement). Either a specific temperature difference is stabilized before each measurement (steady-state), which takes longer,^{16, 50, 51} or measurements are conducted continuously while the temperature difference is varied slowly (quasi-steady-state).^{16, 19, 52, 53} In a recent study,¹⁷ little difference was found between steady-state and quasi-steady-state measurements when good thermal and electrical contact is ensured.

The employed temperature difference should be kept small, but too small will lead to decreased accuracy. Usually 4–20 K (or $\pm 2 - \pm 10$ K) is appropriate for the full temperature span. When using the quasi-steady-state method, all voltages and temperatures should ideally be measured simultaneously^{16, 48} or timed using the “delta measurement” technique (individual voltage measurements performed symmetrically in time) or with time stamps to compensate for a linear drift.^{19, 49}

In the slope method the measured raw data is corrected for constant offset voltages by using the slope of several ($\Delta T, V$) points for extracting the Seebeck coefficient.^{16, 19, 48, 49} The offset voltages can reach several hundred microvolts increasing at elevated temperatures and can be caused by several effects, including differences in thermocouple wires, reactive samples, and the cold finger effect (heat being drawn away from the sample through the thermocouple, causing a temperature drop between the sample and thermocouple tip due to the thermal contact resistance). It is an open circuit voltage and is not usable for power generation since a heat engine cannot output power without a heat flow. The single point method is unable to separate this from the actual Seebeck coefficient. The slope method, in contrary, is designed to extract only the usable part of the voltage, provided the offset is constant during one measurement. Most commercial systems (including the ZEM series by ULVAC-Rico) use the slope method to extract the Seebeck coefficient from steady-state measurements.

Instrument geometries

The contact arrangement is also of importance. Generally

three different geometries exist:^{19, 48} 2-point (Figure 2a), off-axis 4-point (Figure 2b), and uniaxial 4-point (Figure 2c). It is important to minimize electrical and thermal contact resistances and make sure the temperature and voltage are measured at the same point in space. This is not realized in the 2-point geometry, where thermocouple and voltage leads are generally imbedded in metallic contact pads in the heaters, however, the error may be small when good thermal and electrical contact is made to the sample (e.g. by soldering or using pads of high thermal conductivity metals such as tungsten).¹⁷ The 2-point geometry is also often used where other considerations than accuracy are important, such as in scanning systems.³⁹

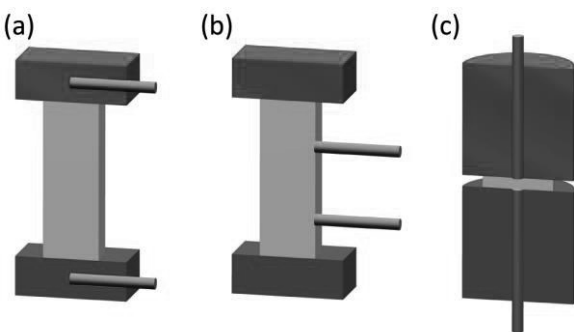


Fig. 2 The three common geometries for Seebeck coefficient measurements in cross sectional view: 2-point (a), off-axis 4-point (b) and uniaxial 4-point (c). The upper and lower heaters are shown in red and blue, the sample in between the two heaters in yellow, and the thin thermocouple rods in green. The thermal gradient can be applied in both directions.

In the off-axis 4-point geometry the thermocouples and voltage leads are pressed against the sides of the sample thus allowing concurrent measurement of Seebeck and resistivity during one measurement run. This method is used in the most popular commercial instruments (e.g. by ULVAC-Rico or Linseis). Here the thermocouples are in direct contact with the sample, reducing the distance between the electrical and thermal contacts. Since only low force can be used on the thermocouples to avoid bending (some materials may turn soft at high temperatures), breaking or shifting the sample, the thermal and electrical contact resistance may actually be large. High thermal conductivity alumina sheathed thermocouples extend to outside the heated zone to a chamber near room temperature. They may thus act as cold fingers and create a temperature gradient across the thermocouple tip-sample interface. The thermocouples would then underestimate each temperature and also the resulting ΔT , leading to an overestimated thermopower (absolute value of Seebeck coefficient).^{17, 19} The analysis of the cold finger effect by Martin¹⁷ further implies that the average temperature of the two thermocouples (which is used as the sample temperature) underestimates the true average temperature of the sample. This effect is expected to be a linear function

of the temperature difference between the sample and surroundings and will compress the temperature interval of the measured Seebeck coefficient. If the Seebeck coefficient has strong temperature dependence this can affect the accuracy significantly. A large deviation between the temperatures of the gradient heaters in direct contact with the sample and average sample temperature can be an indication that cold finger effects are affecting the measurement accuracy.

In a recent study by Martin¹⁷ the results from the 2-point and off-axis 4-point geometries were compared. The off-axis 4-point geometry was observed to yield thermopower values higher than the 2-point geometry, with the difference being proportional to the temperature difference between the sample and surroundings. With a thorough analysis of the thermal resistances the study concludes that the cold finger effect is responsible for the higher thermopower values and that the 2-point geometry is preferable.

The uniaxial 4-point geometry was developed to remedy these problems. The cold finger effect is reduced by inserting the thermocouples through the heaters, while the thermal contact resistance is kept low by having the thermocouples in direct contact with the sample with independent, constant pressure. The thermocouples may act as both cold and hot fingers in this geometry, depending on the strength of the thermal coupling to the heaters. Due to the heaters, the cold finger effect will be reduced compared to the 4-point off-axis geometry and since the temperature difference between the heater and sample is small, the hot finger effect is also believed to be small. With bad thermal contact in this setup, the thermocouples can both over- and underestimate the temperature and ΔT , depending on whether they act as cold or hot fingers; however, the error is believed to be smaller than for the 4-point off-axis geometry. The thin sample geometry with high cross sectional area leads to a high heat flux compared to the off-axis geometry and may increase the temperature drop across the heater-sample and thermocouple-sample interfaces. If each sample-heater and sample-thermocouple interface is not of approximately equal quality, it can be difficult to keep the average sample temperature constant during a ΔT sweep.

At low temperatures, the Quantum Design, Physical Property Measurement System (PPMS) has been extensively used. In the Thermal Transport Option (TTO), four copper leads are attached to a bar sample with conductive adhesive and a heater, two resistance thermometers and a heat sink are mechanically attached to these (corresponding to the off-axis 4-point geometry but without the thermocouples in direct contact with the sample). Hence, the temperature and voltage are measured far from each other and the cold-finger effect may be large. This geometry is further discussed in the section on thermal conductivity.

Thermal and electrical contact

If possible, points should be measured for both increasing and decreasing ΔT and the data checked for hysteresis, such as in Figure 3b. Hysteresis can be an indication of poor thermal contact between sample and thermocouples or heaters. In Figure 3a measurements with good and bad thermal contact are shown. Thermal voltages resulting from temperature changes in the wiring can also lead to

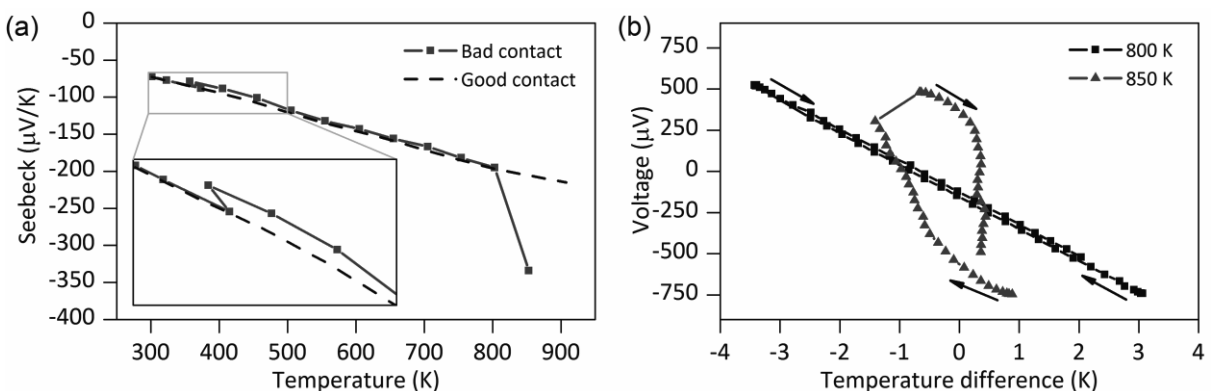
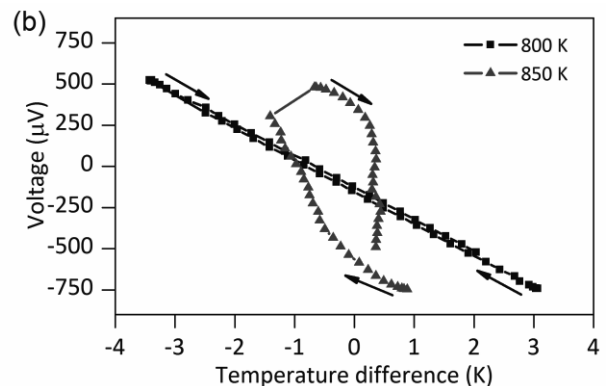


Fig. 3 Example of the effect of bad thermal contact in Seebeck coefficient measurements. (a) A sample was measured from 300 K to 900 K both with good (dashed black line) and bad thermal contact between the sample and thermocouples (solid blue line and square symbols). (b) The raw voltage vs. temperature difference plots at 800 K (squares) and 850 K (triangles) for the measurement with bad thermal contact.

Since the thermocouples are exposed to many reactive materials, monitoring the ageing is important. This can be monitored by comparing the sample temperature to the furnace or gradient heater temperatures. After a number of measurement runs, the temperature difference will change indicating ageing of the thermocouples. Platinum, for example, is frequently used due to its high inertness to oxygen and many oxides but it reacts readily with Pb, Te, Sb, Si and other elements often found in thermoelectric materials. During a measurement run and sample mounting, poor electrical or thermal contact and other instrument errors can be identified by examining the voltage vs. temperature difference curves for hysteresis. For non-reactive samples, the heating and cooling curves of the Seebeck coefficient should be identical, and the same is true for repeated measurement (if the first cooling and second heating curves agree but the rest do not, the sample properties are most likely changing). During sample mounting, 2-point I-V curves or resistances between two electrical contacts, including current contacts in combined Seebeck and resistivity systems, can help identify bad electrical contacts.

As with hysteresis, if the Seebeck coefficient depends on the heating rate and size or direction of the temperature difference employed there is likely bad thermal contact between the sample and thermocouples. When measuring in inert gas atmospheres (or air), the Seebeck coefficient should not depend on the gas pressure as this is an indication of bad thermal contact between the sample and thermocouples. This is also visible in Figure 3a where data

hysteresis. The later can be checked by heating local areas around the sample stage with a heat gun or soldering tip. Using higher pressure on the thermocouples or inserting a thin piece of graphite foil may help improving thermal contact. When combining resistivity and Seebeck measurements, the graphite may significantly increase the contact size and hence affect the resistivity measurement and should be used with care.



below 400 K are measured in air. For the measurement with bad thermal contact a change in the measurement is observed when the chamber is evacuated. In air the two measurements agree since the air improves the thermal contact. This is an early indication of bad thermal contact and the data quality is expected to be bad. In some instruments inert gasses are used to improve thermal contact.

Electrical resistivity

Even though resistivity measurements are often regarded as routine, they are still prone to large errors. The most widely used method is the linear 4-point method with bar-shaped samples as shown in Figure 4a. Current is passed from one end to the other while the voltage is being measured at two intermediate points. The voltage contacts should be placed sufficiently far from the ends to ensure a uniform current distribution in the bar at and between the voltage contacts (usually placed at 1/3 and 2/3 of the sample length). The resistivity is $\rho = R \cdot A/l$ where R is the measured 4-point resistance, A is the cross sectional area, and l is the separation of the voltage contacts. The resistivity is therefore highly sensitive to errors in the geometric factor A/l which can easily be in excess of 5%. If the sample is not a parallelepiped, appropriate geometric factors need to be found, either analytically or numerically, e.g. from finite element methods. The voltage contacts should be narrow along the length of the sample to avoid uncertainty in l . This can be a problem when resistivity and Seebeck

coefficient measurements are combined since the thermocouple tip often has a significant size.

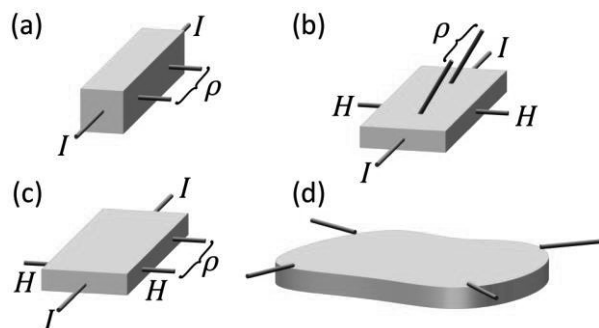


Fig. 4 Four different samples and contact arrangements for resistivity and Hall effect measurements: (a) Contact arrangement and optimal sample geometry for only resistivity measurements on bar samples; (b) 6-point and (c) 5-point for combined resistivity and Hall effect measurements with sample geometry optimized for Hall effect measurements; (d) For combined resistivity and Hall effect measurement with the van der Pauw method. In (a)-(c), contacts for the applied current are marked with an *I*, contacts for resistivity measurements with ρ , and contacts for Hall effect with *H*. In (d), resistivity measurements are performed by applying current between adjacent contacts while Hall effect measurements are performed with current along a diagonal. This is further discussed in Reference 18.

Other techniques exist that may be less sensitive to errors in geometric factors. The most widely used of these in thermoelectrics is the van der Pauw technique, Figure 4d.⁵⁴ In this technique, the resistivity is obtained from a flat sample of arbitrary shape but uniform thickness with point contacts along its circumference. Since flat samples can be polished to have a uniform thickness (preferably with a variation of 0.005 mm or less, depending on thickness) that can be measured accurately using a micrometer, the error from the geometric factor may be reduced. In this method, the resistivity can be measured directly from hot pressed samples or slices of Bridgman, Stockbarger, or Czochralski grown ingots. The sample geometry is compatible with measurements of all thermoelectric transport properties, and zT can hence be obtained using only one sample.¹⁸

The variation in electrical resistivity when using the 4-point bar method can be as high as 10% at 500 K,⁴⁵ twice that in Seebeck coefficient. The reason for the high scatter is mainly errors in determining the geometric factor,⁵⁶⁻⁵⁸ indicating that this is indeed important in obtaining accurate resistivities. In the PPMS several options exist for measuring the electrical resistivity. Leads are attached with conducting adhesive, such as silver containing epoxy, which can lead to excessively large contact areas that reduce the accuracy.

Errors can also be caused by inaccurate temperature determination, which can be caused by poor thermal contact between the sample and the mass the thermocouple is attached to. Additionally, the thermocouples can act as

85 cold or hot fingers. The first should be avoided especially in systems that heat the sample with heater blocks in direct contact with the sample. Other systems have a furnace-like heating zone where the sample is radiatively heated. In this case, caution is also needed as high temperature measurements are usually done under vacuum, which means the temperature profile inside the furnace might not be uniform without convection. The commercial ZEM system uses a furnace together with partial back-filled helium so the temperature profile could be quite uniform. However, as long bars are used for the voltage contacts and it is common to apply only a minimum amount of pressure against the sample, this makes temperature reading likely to be either lower or higher than the real sample temperature due to the cold and hot finger effects.

Even a subtle change in measurement procedure can significantly change results. For example Figure 5 shows the resistivity of n type PbTe and PbSe from [citation] that was significantly underestimated (the gray dots) due to an underestimation of the sample temperature. A substrate was inserted between the sample and the heater block to protect the sample which resulted in poor thermal contact with the thermocouple.¹⁸ The error is much higher at high temperature where radiative cooling is strongest and the change in resistivity with temperature is high. This error can be detected and avoided two ways: one is by using an insulation shield that reduces the radiation loss from the surface of the sample to the cold chamber wall, shown by blue dots in (a), the other is by directly attaching the thermocouple to the sample, yellow open squares in (a). Designing the system to avoid excessive radiation loss from sample surfaces is preferable as thermocouple attachment adds complication, possibility of chemical reaction, and user variability. Insulating the sample space using either a radiation shield made of aluminum with ceramic coating (green open triangles in (b)) or 2mm thick glass wool (yellow open squares in (b)) makes the sample temperature measurement sufficiently accurate.

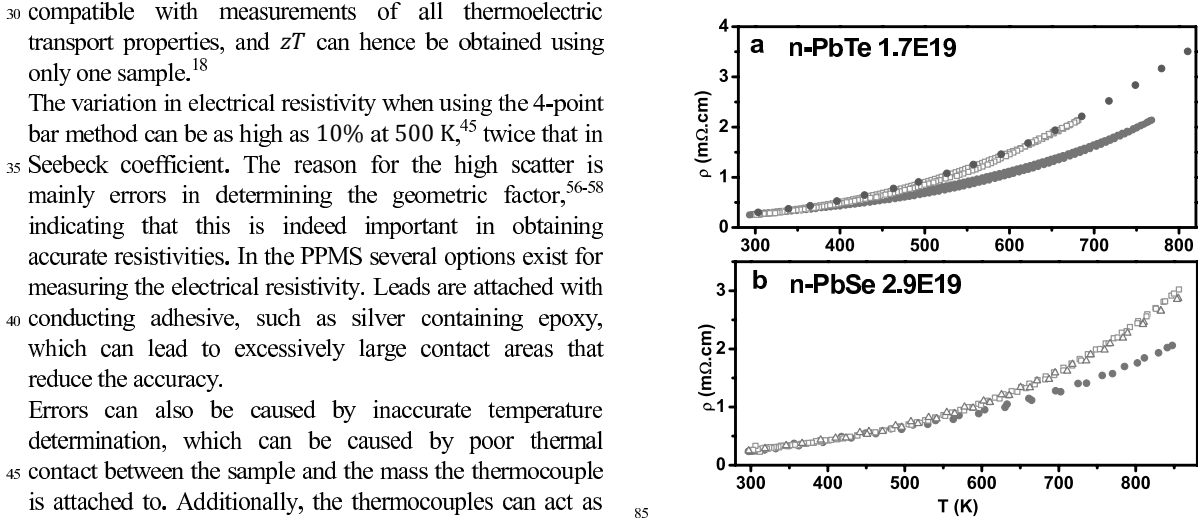


Fig. 5 resistivity measurement of (a) n type PbTe and (b) n type PbSe using a Van de Pauw setup as described in ref. 18. Results shown in gray dots are underestimated due to inaccurate temperature determination as a result of poor thermal contact between sample and the heater block. Two effective ways to mitigate this is by either applying insulation/radiation shielding around the sample, shown by blue dots in (a), and yellow open squares and green triangles in (b), or by making direct contact between thermocouple and sample, shown by yellow open squares in (a).

- There are a number of offsets that have to be accounted for in resistance measurements. There are constant or slowly varying voltage offsets which mainly arise from the Seebeck effect when temperature gradients are present.
These may arise both in the sample, leads, and at junctions between dissimilar metals, such as vacuum feedthroughs and other connectors. These are removed by measuring the voltage as a function of applied current instead of simply measuring the voltage under constant applied current.
- In all resistivity measurements, a current sufficiently low to avoid significant Joule heating should be used. In thermoelectrics, there is a further complication due to the high Peltier effect.⁹ Heat is transported by the current from one contact to the other creating a temperature gradient, which in turn leads to Seebeck voltages.¹⁰ This causes an overestimation of the resistance for both positive and negative Seebeck coefficients.^{59, 60} To reduce these errors either AC or pulsed DC measurements, where the voltage is measured before and after turning the current on, are used. This also removes constant offset voltages from the Seebeck effect. Carefully heat sinking the sample can further help reduce the errors from the Peltier effect. In DC measurements, switching the current direction can help minimizing the temperature gradient established.
- A simple experimental criterion is that repeated raw resistance measurements should not show a systematic change, which is usually caused by the Peltier effect. Changes in resistivity in repeated full measurements are often due to Joule heating of the sample. The quality of the contacts is best tested with 2-point I-V curves: Nonlinearity at low voltage indicates poor electrical contact while a curvature at higher currents is most likely caused by the Peltier effect or Joule heating. If I-V sweeps are not possible, 2-point resistance measurements can be used.
- If AC measurements are used, the frequency should be chosen sufficiently high to suppress the Peltier effect, usually some tens of hertz. A thermal time constant can be estimated as $\tau = l^2/D_T$, where l is the distance between the voltage contacts and D_T is the thermal diffusivity. The error from the Peltier effect is low for frequencies significantly greater than τ^{-1} . Since the measurement leads have a finite capacitance, low currents and high frequencies lead to current loss in the wires. This current is deposited as charge in the wires and does not contribute to the measured signal, causing a too low resistance. Generally, all circuits can be described as a capacitor and a resistor in parallel,

Additionally, to avoid noise in frequency sensitive measurements, the base frequency should be chosen different from the power line frequency and integer multiples or fractions of this.

Charge carrier concentration and mobility

Even though the charge carrier concentration is not necessary for calculating zT , it is still very important since all transport properties depend strongly upon it. It provides an important reference frame for characterizing and identifying the cause of changes in transport properties. In heavily doped semiconductors such as thermoelectrics, the charge carrier concentration is usually calculated from the Hall coefficient measured on a flat sample in a magnetic field. The Hall voltage V_H is the voltage arising perpendicular to both the field and current direction. The Hall resistance is $R_\perp = V_H/I$ and Hall coefficient $R_H = R_\perp d/B$. d is the sample thickness and B is the perpendicular field strength. Since the current distribution does not have to be uniform, flat and wide samples are usually preferred to samples with square cross sectional area of the same size since these allow the same current and give a high R_\perp due to the low thickness.⁶¹ The traditional 5 and 6-point measurement geometries for combined Hall effect and resistivity measurements are shown in Figure 4c and b. A flat sample is less appropriate for resistivity measurements than one with square cross section since the current distribution is less uniform. Combining Hall effect measurements with van der Pauw resistivity reduces this problem and allows a simpler setup with 4 contacts instead of the 5 and 6-point geometries.^{18, 54, 55} In addition, the van der Pauw configuration can be used to avoid the need for switching the magnetic field.

Inspired by the free electron model, the Hall carrier concentration is calculated as $n_H = 1/eR_H$ and will be positive for holes and negative for electrons.⁶¹ e is the elementary charge. If the resistivity ρ is also known, the Hall mobility can be calculated as $\mu_H = R_H/\rho$. The Hall carrier concentration is related to the true carrier concentration n by $n = r_H n_H$. r_H is the Hall factor which is generally only equal or close to 1 in the free electron model and the limit of high doping levels in a single parabolic band.⁶² In other cases, either appropriate modelling using single or multi band models^{15, 31, 63-66} or *ab initio* calculations are necessary for estimating the true carrier concentration.⁶⁷ In complex band structures or for bipolar samples, r_H can deviate strongly from 1. Despite the ambiguity, the Hall carrier concentration is an excellent way to compare relative carrier concentrations within the same materials system (with similar band structure).

The challenges associated with measuring the Hall coefficient are generally the same as for resistivity measurements. In addition, there is also a resistive offset when the voltage contacts are not placed directly across

from each other but are displaced slightly along the current path. The Hall signal is usually very low ($R_{\perp} \approx 63 \mu\Omega$ for $n_H = 10^{20} \text{ cm}^{-3}$, $B = 1 \text{ T}$, and $d = 1 \text{ mm}$) and can be orders of magnitude lower than the voltage offset. For this reason at least two magnetic fields (e.g., on/off or with opposite directions) are necessary to remove all offsets. Especially for metals (or semiconductors with very high doping levels) and intrinsic or bipolar semiconductors the Hall signal can be very low. In intrinsic semiconductors, the resistivity changes rapidly with temperature and hence Joule heating can strongly affect the offset resistance, making Hall effect measurements difficult.

For high mobility samples there is also an offset from the magneto resistance; however, this does not depend on the field orientation and can be subtracted by reversing the field direction rather than switching it on and off.¹⁸ Alternatively, several points on a $V(B)$ curve including both positive and negative B can be used. In such a curve, magneto resistance would lead to a parabolic curve shape while the Hall effect is primarily linear, allowing separation of the two.

Due to the low signal level, accurate nanovoltmeters and shielded cables are necessary for measuring the Hall coefficient.¹⁸ All measurement leads should be mechanically fixed to reduce errors from wires due to magnetic induction forces. In sensitive measurements, the signal can be overlaid by an induced voltage arising from leads vibrating in the magnetic field. If this coincides with the frequency in AC measurements, this voltage cannot be eliminated by lock-in techniques.

Thermal conductivity

Many methods exist for measuring thermal conductivity, κ . While the most frequently used method today is flash diffusivity,^{68–70} (see Figure 5a) traditionally direct methods were employed (Figure 5b). Since flash diffusivity also requires measurement of the heat capacity and density these are also covered in this section.

Other methods also exist. One example is the thermal van der Pauw method,⁷¹ which illustrates the fundamental analogy between thermal and electrical conduction. The Harman method^{72, 73} for directly measuring zT is also frequently used. In this method, zT is calculated from the difference in resistance with very low frequency (with Peltier effect) and high frequency (only resistive part). Both methods fundamentally have the same difficulties as direct thermal conductivity measurements and are hence not discussed individually.

While most of the techniques for measuring resistivity and Seebeck coefficient also work for thin films, thermal conductivity needs to be measured with specialized techniques. The most widely used of these are the 3ω ^{74, 75} and time domain thermoreflectance (TDTR) techniques.⁷⁶

78

Direct measurements

Before the development of the flash diffusivity method,⁷⁰ methods directly using the Fourier equation, $q = -\kappa A \nabla T$, were most common. Here q is the heat flow along the sample, A is the cross sectional area, and ∇T is the temperature gradient. The heat flow needs to be corrected for loss through heater and thermometer wires and radiation. While this works well at low temperatures (below approximately 200 K), the difficulty in accurately correcting for radiation loss limits the accuracy at higher temperatures.⁷⁹ In these methods the sample needs to be in good thermal contact with the heater, heat sink, and thermocouples while being thermally insulated from the surroundings. For small temperature differences between the sample and surroundings, the heat loss due to radiation is $q_{rad} = \epsilon A \Delta T T^3$, where ϵ is the emissivity, A is the surface area, T is the temperature, and ΔT the temperature difference between sample and surroundings.²⁰ Hence, accurate radiation correction becomes much more important at high temperatures

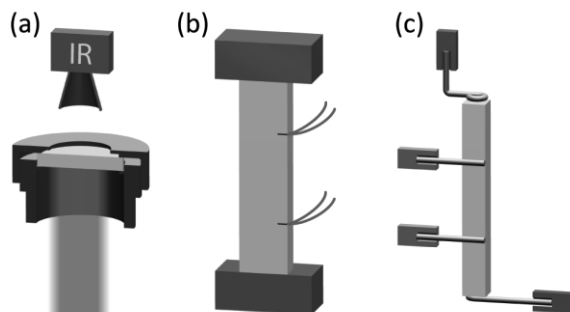


Fig. 6 Geometries for measuring thermal diffusivity with the laser flash method, (a), thermal conductivity with the steady-state method, (b), and in the PPMS TTO, (c). In (a), a short laser pulse is applied to the bottom of a sample (shown in a sample holder) and the resulting temperature rise on the top is monitored with an IR camera. In (b), a constant power is applied to a heater at the top of a sample (red) while the temperature is monitored along its length with thermocouples inserted in small holes (green wires). The thermal conductivity is calculated when steady-state has been reached. In (c), a heat pulse is applied to a heater shoe (red) at the top of a sample while the temperature response is monitored with thermometers (green) along its length and the thermal conductivity is calculated from the transient. This sample and contact arrangement is also used for Seebeck and resistivity measurements. In (b) and (c) the sample is heat sunk at the bottom (blue). Samples are shown in yellow.

A steady-state setup described by Zaitsev *et al.*⁸⁰ uses a radiation shield thermally anchored to both the heater and heat sink to establish a temperature gradient similar to the gradient in the sample. The space between sample and heat shield is filled with thermally insulating powder (alumina or silicate based ceramics) to further reduce the radiation loss, whereas heat loss due to conduction through the powder was calibrated. Alekseeva *et al.*⁸¹ reported thermal conductivity of n-type PbSe using this setup and the result

is consistent with the laser flash method around room temperature. However, it is noticeably higher at high temperatures, as seen in figure 7. Nonetheless, comparing an improved steady-state setup with the laser flash method, the results are fairly consistent up to 700 K for n-type PbSe, suggesting the steady-state method as implemented by the Ioffe Institute could be as accurate in this temperature range. This will be thoroughly described in a future publication which will also include a more detailed comparison to results from flash diffusivity. Figure 7 shows a comparison of results from the same PbSe sample including low temperature data obtained from a PPMS, together with Alekseeva's result from a sample with very similar electrical properties.

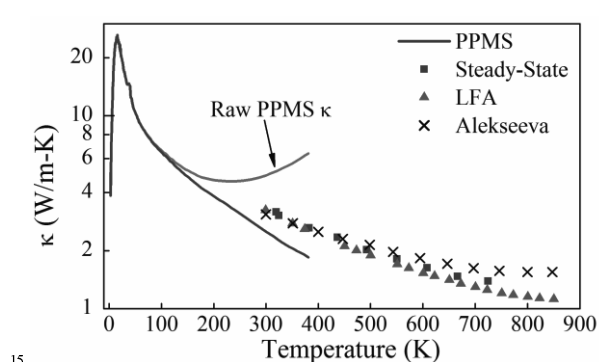


Fig. 7 Comparison of thermal conductivity between the PPMS (blue line), laser flash method (green triangles), Ioffe Institute steady-state method (blue squares) and published data from Reference 81 (black crosses). The same PbSe sample with $n_H = 2.0 \cdot 10^{19} \text{ cm}^{-3}$ are used for all measurements except the crosses. The grey line marked as "Raw PPMS κ " is the measured thermal conductivity before correction for radiation loss.

In the PPMS the thermal conductivity is measured by a direct transient method where the increase and decrease in temperature between two thermometers is modeled when a square wave heat pulse is applied. The geometry is shown in figure 6c. The heat loss through the electrical wires is accounted for through the calibration, while the radiation loss is calculated from the sample surface area and emissivity and is subtracted from the measured thermal conductivity. The latter is difficult since the emissivity is usually not known and the surface area is difficult to calculate since leads are attached with thermally conductive adhesive to the surface of the sample, as shown in Figure 6c (without the adhesive). This difficulty is clearly visible from Figure 7, where the radiation loss is clearly overestimated. The radiation correction is visible from about 100 K and becomes a significant fraction of the thermal conductivity at approximately 200 K. The emissivity was set to 1 (an overestimate) while the sample surface area without attached leads was used (an underestimate). These errors oppose each other and the resulting correction in this case is an overestimate resulting in an underestimated thermal conductivity. A more

comprehensive comparison between the PPMS and LFA can be found in reference 82, including a thorough discussion of the radiation correction and problems with choosing an appropriate emissivity.

Flash diffusivity

In the flash diffusivity method, the thermal conductivity is calculated as $\kappa = D_T d C_p$ where D_T is thermal diffusivity, d is density, and C_p is the constant pressure heat capacity. In this method, a short heat pulse (often by laser flash) is applied to one side of a thin sample, while the temperature of the other side is monitored continuously. The temperature will rise to a maximum, after which it will decay. In the original method, which makes an excellent check for the data, the time for the temperature to increase to half-maximum, $T_{1/2}$, is used to calculate the thermal diffusivity $D_T = 1.38d^2/\pi T_{1/2}$ where d is the thickness.⁷⁰ This is derived assuming only axial flow of heat and no heat loss, and hence the sample thickness should be much smaller than the diameter and $T_{1/2}$ should be kept in the range from a millisecond to no more than a few seconds, but always much larger than the pulse duration.

A correction was proposed by Cowan⁸³ to account for heat losses on the sample faces, still assuming axial flow. He used the temperature at $T_{1/2}$ and 5 or 10 times $T_{1/2}$ to also estimate the heat loss terms occurring in his revised expression for α . Alternatively, Clark and Taylor⁸⁴ proposed a method only using the heating section of the transient. This method also accounts for heat loss at the sides of the sample and finite heat pulse duration. These two methods are usually recommended²⁴ but another method by Cape and Lehman⁸⁵ is also frequently used. In the modern implementation of these methods, the expressions are fitted to the entire transient to obtain better estimates of the heat loss terms and corrections for the pulse width and shape can also be applied.

In the comparison to the steady-state method and PPMS data in Figure 7, the laser flash data is believed to be more accurate since it is less susceptible to errors from radiation loss corrections. However, the Ioffe Institute steady-state method does seem to produce good results below 700 K (the highest reported temperature) and may provide a useful method for measuring thermal conductivity, especially when the heat capacity is not easily obtained, such as across phase transitions etc.^{86,87}

The scatter in thermal diffusivity between different laboratories can be as high as 5% at room temperature and almost 10% at 500 K.²⁴ Much of this can be ascribed to variations in measured thickness. This indicates that a constant and accurately measured thickness is as important for diffusivity measurements as the geometric factor is for resistivity measurements. Another possible source of error is the graphite coating often employed in diffusivity measurements. While this ensures a high emissivity and hence good absorption of the laser pulse and maximum

detector signal, too thick coatings or poor adhesion to the sample can cause significant errors, especially for thin samples.

Heat capacity

When using flash diffusivity, measurement of the heat capacity is also necessary to obtain thermal conductivity. While some commercial flash diffusivity systems can estimate the heat capacity relative to a standard, this is often inaccurate and can lead to underestimates of thermal conductivity. Instead, drop calorimetry provides the best accuracy (especially at high temperatures) but today differential scanning calorimetry (DSC) is more frequently used. As an example, Toberer *et al.*²⁵ measured a room temperature C_p on Ba₈Ga₁₆Ge₃₀ of 0.23 J/gK using a laser flash analysis (LFA) setup. This was later corrected by the same group to 0.30 J/gK using DSC, much closer to the Dulong-Petit value of 0.307 J/gK (see below).³¹ In a DSC, the heat capacity is measured relative to a standard, usually sapphire. First a baseline is measured with empty sample holders, then the sample and reference is measured. Often, the baseline is measured again after measuring the sample to check for changes in baseline during the measurement.²⁴ The reference should be chosen to give a signal close to the measured sample to reduce errors. In the PPMS heat capacity option the heat capacity is measured without a reference. First a baseline is measured with only thermal grease in the sample holder, then the sample is added and measured. The heat capacity is calculated from the heating and cooling transient when applying a heat pulse from the two-tau method.⁸⁸

A scatter in heat capacity of 15% has been observed.²⁴ The primary sources of error are operator error or inexperience, baseline shift and inappropriate reference sample. Heat capacity is the measurement most sensitive to operator error and inexperience.²⁴ Above the Debye temperature and in the absence of phase transitions, C_p normally increases slightly with temperature. The best data quality check is comparison to the Dulong-Petit law which states that the constant volume heat capacity above the Debye temperature is approximately $3k_B$ per atom, or $C_V^{DP} = 3N_A k_B/M$. C_V^{DP} is the Dulong-Petit heat capacity, k_B the Boltzmann constant, N_A Avogadro's number, and M is the molar mass. C_V is related to C_p by $C_p = C_V^{DP} + 9\alpha^2 T/\beta_T D$. α is linear coefficient of thermal expansion, β_T isothermal compressibility, and D density. The measured C_p above the Debye temperature should be close to or slightly higher than the Dulong-Petit value and increase slowly with temperature. When the correction is applied, the measured and calculated heat capacities usually agree within 2%. When the values disagree more than about 5%, extra verification is recommended before using the measured values. If no DSC is available or measured values are unexplainable, the authors recommend using the corrected Dulong-Petit value.

In the example with Ba₈Ga₁₆Ge₃₀, both LFA and DSC resulted in a heat capacity that was increasing linearly with temperature. However, the C_p estimated from LFA was lower than the $C_V^{DP} = 0.307 \text{ J/gK}$ for all temperatures while the DSC values crossed C_V^{DP} slightly above the Debye temperature of approximately 300 K as expected. This is a clear indication that the LFA estimate was unreliable, which the authors also commented upon.

Density and thermal expansion

The last property necessary for calculating thermal conductivity is the density. The geometric density is measured by calculating the volume from the geometry and dimension of the sample which works well for regularly shaped samples. Density measured using Archimedes' principle (by immersion in a liquid) can overestimate the density relevant for $\kappa = D_T d C_p$ if the liquid is absorbed in the pores. This can be checked by measuring the weight in air both before and after the measurement in the liquid. These measurements are fairly accurate at room temperature and the density is usually assumed to be independent of temperature.²⁴

The density as well as resistivity, diffusivity, and thermal conductivity are dependent on the sample dimensions and hence thermal expansion. An analysis by Toberer *et al.*²⁵ shows that while each property is affected by thermal expansion, both $\rho\kappa$, Seebeck and zT are unaffected by this. This was derived assuming a temperature independent coefficient of linear thermal expansion; however, it can be extended to any temperature dependence of thermal expansion. If the sample has anisotropic thermal expansion and all properties are not measured along the same direction, this is no longer true.

Some commercial LFA software has the capability to correct for thermal expansion. While this can increase the accuracy of the thermal diffusivity and conductivity, it can decrease the accuracy of zT unless the same expansion correction is applied to all the properties affected by thermal expansion (density, resistivity and thermal diffusivity). Since the software form different companies applies this differently, it is important to understand how this is done to avoid introducing errors from the correction.

Conclusion

We have described the most common methods and issues related to measurement of thermoelectric properties of bulk samples. Due to the vast number of different methods employed for measuring the individual properties, no strict guidelines have been given for conducting measurements. Instead, different effects leading to errors have been discussed and signatures of erroneous data and remediation methods have been reviewed. It is hoped that this will aid new researchers as well as young students in the field of thermoelectrics to better understand and appreciate the

challenge of conducting high quality measurements. Even for routinely conducted measurements by experienced groups, differences can be 20% as found by Hsin Wang *et al.*²⁴ and uncertainty increases with temperature. The heat capacity is the largest contribution to the error in thermal conductivity which can be significantly reduced by comparison to the Dulong-Petit value. In addition systematic differences due to different techniques in measuring Seebeck coefficient can add on the order of 5% uncertainty, which also increases strongly with temperature. As methodologies change and evolve in the future as they have in the past, this issue will need to be critically revisited.

Acknowledgements

The authors are thankful to Hsin Wang, Terry Tritt, Atsushi Yamamoto, and Joshua Martin for advice and sharing personal experiences. The work was supported by the Danish National Research Foundation (Center for Materials Crystallography). J. de Boor acknowledges endorsement by the Helmholtz Association.

Notes and references

* Corresponding author

^a Center for Materials Crystallography, Department of Chemistry and iNANO, Aarhus University, DK-8000 Aarhus, Denmark.

^b Institute of Materials Research, German Aerospace Center, Linder Höhe, D-51147 Cologne, Germany

^c Materials Science, California Institute of Technology, Pasadena, California 91125, USA. E-mail.: jsnyder@caltech.edu

^d Laboratoire CRISMAT UMR 6508 CNRS ENSICAEN, 14050 Caen Cedex 04, France

^e State Key Laboratory of High Performance Ceramics and Superfine Microstructure, Shanghai Institute of Ceramics, Chinese Academy of Sciences, Shanghai 200050, China

^f Justus Liebig University Giessen, Institute of Inorganic and Analytical Chemistry, D-35392 Giessen, Germany

^g ITMO University, Saint Petersburg, Russia.

1. G. J. Snyder and E. S. Toberer, *Nat. Mater.*, 2008, **7**, 105-114.
2. L. E. Bell, *Science*, 2008, **321**, 1457-1461.
3. F. J. DiSalvo, *Science*, 1999, **285**, 703-706.
4. A. D. LaLonde, Y. Pei, H. Wang and G. Jeffrey Snyder, *Materials Today*, 2011, **14**, 526-532.
5. J. H. Yang and T. Caillat, *MRS Bull.*, 2006, **31**, 224-229.
6. D. Samson, M. Kluge, T. Becker and U. Schmid, *Sensor. Actuat. A*, 2011, **172**, 240-244.
7. A. Dewan, S. U. Ay, M. N. Karim and H. Beyenal, *J. Power Sources*, 2014, **245**, 129-143.
8. C. B. Vining, *Nat. Mater.*, 2009, **8**, 83-85.
9. D. M. Rowe, *Thermoelectrics handbook: macro to nano*, CRC press, 2006.
10. D. M. Rowe, *CRC handbook of thermoelectrics*, CRC press, 2010.
11. T. C. Harman, D. L. Spears and M. P. Walsh, *J.*

- 55 *Electron. Mater.*, 1999, **28**, L1-L5.
12. T. C. Harman, P. J. Taylor, D. L. Spears and M. P. Walsh, *J. Electron. Mater.*, 2000, **29**, L1-L2.
13. C. J. Vineis, T. C. Harman, S. D. Calawa, M. P. Walsh, R. E. Reeder, R. Singh and A. Shakouri, *Phys. Rev. B*, 2008, **77**, 235202.
60 14. H. Wang, Y. Pei, A. D. LaLonde and G. J. Snyder, *Adv. Mater.*, 2011, **23**, 1366-1370.
15. H. Wang, Y. Pei, A. D. LaLonde and G. J. Snyder, *P. Natl. Acad. Sci. USA*, 2012, **109**, 9705-9709.
65 16. J. Martin, *Rev. Sci. Instrum.*, 2012, **83**, 065101-065109.
17. J. Martin, *Meas. Sci. Technol.*, 2013, **24**, 085601.
18. K. A. Borup, E. S. Toberer, L. D. Zoltan, G. Nakatsukasa, M. Errico, J.-P. Fleurial, B. B. Iversen and G. J. Snyder, *Rev. Sci. Instrum.*, 2012, **83**, 123902-123907.
70 19. S. Iwanaga, E. S. Toberer, A. LaLonde and G. J. Snyder, *Rev. Sci. Instrum.*, 2011, **82**, 063905.
20. T. M. Tritt, *Thermal conductivity: theory, properties, and applications*, Springer, 2004.
75 21. R. P. Tye, *Thermal conductivity*, Academic Press London, 1969.
22. J. Parrott and A. Stuckes, *Thermal Conductivity of Solids*, 1975.
23. E. S. Toberer, L. L. Baranowski and C. Dames, *Annu. Rev. Mater. Sci.*, 2012, **42**, 179-209.
80 24. H. Wang, W. Porter, H. Böttner, J. König, L. Chen, S. Bai, T. Tritt, A. Mayolet, J. Senawiratne, C. Smith, F. Harris, P. Gilbert, J. Sharp, J. Lo, H. Kleinke and L. Kiss, *J. Electron. Mater.*, 2013, **42**, 1073-1084.
25. E. S. Toberer, M. Christensen, B. B. Iversen and G. J. Snyder, *Phys. Rev. B*, 2008, **77**, 075203.
26. J. He, J. Androulakis, M. G. Kanatzidis and V. P. Dravid, *Nano Lett.*, 2012, **12**, 343-347.
27. M. Ohta, K. Biswas, S. H. Lo, J. He, D. Y. Chung, V. P. Dravid and M. G. Kanatzidis, *Adv. Energy Mater.*, 2012, **2**, 1117-1123.
90 28. S. M. Kauzlarich, *Chemistry, structure, and bonding of Zintl phases and ions*, VCH New York, 1996.
29. S. C. Sevov, in *Intermetallic Compounds - Principles and Practice*, John Wiley & Sons, Ltd, 2002, pp. 113-132.
95 30. S. M. Kauzlarich, S. R. Brown and G. Jeffrey Snyder, *Dalton Trans.*, 2007, 2099-2107.
31. A. F. May, E. S. Toberer, A. Saramat and G. J. Snyder, *Phys. Rev. B*, 2009, **80**, 125205.
100 32. E. S. Toberer, A. F. May and G. J. Snyder, *Chem. Mater.*, 2009, **22**, 624-634.
33. M. Søndergaard, M. Christensen, K. A. Borup, H. Yin and B. B. Iversen, *Acta Mater.*, 2012, **60**, 5745-5751.
105 34. M. Søndergaard, M. Christensen, K. Borup, H. Yin and B. Iversen, *J. Mater. Sci.*, 2013, **48**, 2002-2008.

35. H. Yin, M. Christensen, N. Lock and B. B. Iversen, *Appl. Phys. Lett.*, 2012, **101**, 043901-043903.
36. T. Dasgupta, C. Stiewe, A. Sesselmann, H. Yin, B. Iversen and E. Mueller, *J. Appl. Phys.*, 2013, **113**, 103708-103709.
5 37. M. Beekman, M. Baitinger, H. Borrmann, W. Schnelle, K. Meier, G. S. Nolas and Y. Grin, *J. Am. Chem. Soc.*, 2009, **131**, 9642-9643.
10 38. N. Chen, F. Gascoin, G. J. Snyder, E. Müller, G. Karpinski and C. Stiewe, *Appl. Phys. Lett.*, 2005, **87**, 171903.
15 39. D. Platzek, G. Karpinski, C. Stiewe, P. Ziolkowski, C. Drasar and E. Muller, Potential-Seebeck-microprobe (PSM): measuring the spatial resolution of the Seebeck coefficient and the electric potential, Clemson, South Carolina, USA, 2005.
40. H. L. Ni, X. B. Zhao, G. Karpinski and E. Müller, *J. Mater. Sci.*, 2005, **40**, 605-608.
41. S. Iwanaga and G. J. Snyder, *J. Electron. Mater.*, 2012, 20 **41**, 1667-1674.
42. A. F. May, J.-P. Fleurial and G. J. Snyder, *Phys. Rev. B*, 2008, **78**, 125205.
43. M. Sondergaard, M. Christensen, L. Bjerg, K. A. Borup, P. Sun, F. Steglich and B. B. Iversen, *Dalton Trans.*, 2012, **41**, 1278-1283.
25 44. M. Christensen, S. Johnsen, M. Sondergaard, J. Overgaard, H. Birkedal and B. B. Iversen, *Chem. Mater.*, 2008, **21**, 122-127.
45. H. Wang, W. Porter, H. Böttner, J. König, L. Chen, S. Bai, T. Tritt, A. Mayolet, J. Senawiratne, C. Smith, F. Harris, P. Gilbert, J. Sharp, J. Lo, H. Kleinke and L. Kiss, *J. Electron. Mater.*, 2013, **42**, 654-664.
30 46. N. D. Lowhorn, W. Wong-Ng, W. Zhang, Z. Q. Lu, M. Otani, E. Thomas, M. Green, T. N. Tran, N. Dilley, S. Ghamaty, N. Elsner, T. Hogan, A. D. Downey, Q. Jie, Q. Li, H. Obara, J. Sharp, C. Caylor, R. Venkatasubramanian, R. Willigan, J. Yang, J. Martin, G. Nolas, B. Edwards and T. Tritt, *Appl. Phys. A*, 2009, **94**, 231-234.
40 47. Z. Lu, N. D. Lowhorn, W. Wong-Ng, W. Zhang, M. Otani, E. E. Thomas, M. L. Green and T. N. Tran, *J. Res. Natl. Inst. Stand. Technol.*, 2009, **114**, 37-55.
48. J. Martin, T. Tritt and C. Uher, *J. Appl. Phys.*, 2010, **108**, 121101.
45 49. J. de Boor and E. Muller, *Rev. Sci. Instrum.*, 2013, **84**, 065102-065109.
50. P. H. M. Bottger, E. Flage-Larsen, O. B. Karlsen and T. G. Finstad, *Rev. Sci. Instrum.*, 2012, **83**, 025101-025106.
51. R. L. Kallaher, C. A. Latham and F. Sharifi, *Rev. Sci. Instrum.*, 2013, **84**, 013907-013907.
52. C. Wood, D. Zoltan and G. Stapfer, *Rev. Sci. Instrum.*, 1985, **56**, 719-722.
53. A. Guan, H. Wang, H. Jin, W. Chu, Y. Guo and G. Lu, *Rev. Sci. Instrum.*, 2013, **84**, 043903-043905.
55 54. L. J. van der Pauw, *Philips Res. Rep.*, 1958, **13**, 1.
55. L. J. van der Pauw, *Philips Tech. Rev.*, 1958, **20**, 220.
56. A. T. Burkov, A. Heinrich, P. P. Konstantinov, T. Nakama and K. Yagasaki, *Meas. Sci. Technol.*, 2001, **12**, 264.
60 57. V. Ponnambalam, S. Lindsey, N. S. Hickman and T. M. Tritt, *Rev. Sci. Instrum.*, 2006, **77**, 073904-073905.
58. B. Céline, B. David and D. Nita, *Meas. Sci. Technol.*, 2012, **23**, 035603.
65 59. C. G. M. Kirby and M. J. Laubitz, *Metrologia*, 1973, **9**, 103.
60. M. V. Cheremisin, Peltier effect induced correction to ohmic resistance, 2001.
61. E. H. Putley, *The Hall effect and related phenomena*, Butterworths, London, 1960.
70 62. V. I. Fistul, *Heavily doped semiconductors*, Plenum Press, New York, 1969.
63. Y. Z. Pei, X. Y. Shi, A. LaLonde, H. Wang, L. D. Chen and G. J. Snyder, *Nature*, 2011, **473**, 66-69.
64. L.-D. Zhao, J. He, S. Hao, C.-I. Wu, T. P. Hogan, C. Wolverton, V. P. Dravid and M. G. Kanatzidis, *J. Am. Chem. Soc.*, 2012, **134**, 16327-16336.
65. H. Wang, A. D. LaLonde, Y. Pei and G. J. Snyder, *Adv. Func. Meter.*, 2013, **23**, 1586-1596.
80 66. X. Liu, T. Zhu, H. Wang, L. Hu, H. Xie, G. Jiang, G. J. Snyder and X. Zhao, *Adv. Energy Mater.*, 2013, 1238-1244.
67. N. W. Ashcroft and N. D. Mermin, *Solid state physics*, CBS Publishing ASIA, Philadelphia, 1988.
68. J. W. Vandersande, A. Zoltan and C. Wood, *Int. J. Thermophys.*, 1989, **10**, 251-257.
69. C. B. Vining, A. Zoltan and J. W. Vandersande, *Int. J. Thermophys.*, 1989, **10**, 259-268.
70. W. J. Parker, R. J. Jenkins, C. P. Butler and G. L. Abbott, *J. Appl. Phys.*, 1961, **32**, 1679-1684.
90 71. J. de Boor and V. Schmidt, *Adv. Mater.*, 2010, **22**, 4303-4307.
72. T. C. Harman, J. H. Cahn and M. J. Logan, *J. Appl. Phys.*, 1959, **30**, 1351-1359.
73. X. Y. Ao, J. de Boor and V. Schmidt, *Adv. Energy Mater.*, 2011, **1**, 1007-1011.
74. D. G. Cahill and R. O. Pohl, *Phys. Rev. B*, 1987, **35**, 4067-4073.
75. T. Tong and A. Majumdar, *Rev. Sci. Instrum.*, 2006, **77**, -.
100 76. C. A. Paddock and G. L. Eesley, *J. Appl. Phys.*, 1986, **60**, 285-290.
77. D. G. Cahill, *Rev. Sci. Instrum.*, 2004, **75**, 5119-5122.
78. Y. K. Koh, S. L. Singer, W. Kim, J. M. O. Zide, H. Lu,

-
- D. G. Cahill, A. Majumdar and A. C. Gossard, *J. Appl. Phys.*, 2009, **105**, -.
79. A. L. Pope, B. Zawilski and T. M. Tritt, *Cryogenics*, 2001, **41**, 725–731.
80. V. K. Zaitsev, M. I. Fedorov, E. A. Gurieva, I. S. Eremin, P. P. Konstantinov, A. Y. Samunin and M. V. Vedernikov, *Phys. Rev. B*, 2006, **74**, 045207.
81. G. T. Alekseeva, E. A. Gurieva, P. P. Konstantinov, L. V. Prokof'eva and M. I. Fedorov, *Semiconductors*, 1996, **30**, 1125–1127.
82. E. Müller, C. Stiewe, D. Rowe and S. Williams, in *Thermoelectrics Handbook: Macro to nano*, 2005, pp. 26-21 – 26-30.
83. R. D. Cowan, *J. Appl. Phys.*, 1963, **34**, 926–927.
84. L. M. Clark III and R. E. Taylor, *J. Appl. Phys.*, 1975, **46**, 714–719.
85. J. A. Cape and G. W. Lehman, *J. Appl. Phys.*, 1963, **34**, 1909–1913.
86. D. R. Brown, T. Day, K. A. Borup, S. Christensen, B. B. Iversen and G. J. Snyder, *APL Mater.*, 2013, **1**, 52107.
87. H. Liu, X. Yuan, P. Lu, X. Shi, F. Xu, Y. He, Y. Tang, S. Bai, W. Zhang, L. Chen, Y. Lin, L. Shi, H. Lin, X. Gao, X. Zhang, H. Chi and C. Uher, *Adv. Mater.*, 2013, **25**, 6607–6612.
88. J. S. Hwang, K. J. Lin and C. Tien, *Rev. Sci. Instrum.*, 1997, **68**, 94–101.

Appendix C.3 Extracting Anisotropic Resistivity from van der Pauw Measurements

This is a crude manuscript which is not yet ready for publication. A journal has not yet been decided upon.

Extracting Anisotropic Resistivity from van der Pauw Measurements

Kasper A. Borup, Karl F. F. Fischer, David R. Brown, G. Jeffrey Snyder, Bo B. Iversen

I. INTRODUCTION

II. THEORY

The purpose of this section is to relate the measured resistances to the tensor elements. A parallelogram will be used as the sample which is a relaxation of the geometrical requirements used previously in the literature. Since calculating the measured resistances directly on an anisotropic parallelogram is difficult at best, two transformations will be used to simplify the calculations: Firstly the anisotropy will be ‘removed’ by a change of variables which will result in an isotropic parallelogram; secondly the geometry will be simplified to an infinite half plane. Using the infinite half plane, the resistances can be calculated from the sample geometry and tensor elements. This allows extraction of more information from the measurements.

A. Isotropic equivalent sample

Here we consider a parallelogram shaped sample with angle χ , side lengths a and b , and resistivity tensor $\rho = \begin{pmatrix} \rho_{xx} & \rho_{xy} \\ \rho_{xy} & \rho_{yy} \end{pmatrix}$. The resistivity tensor is always symmetric and hence this represents the most general case. The principal axes system of the tensor is rotated by φ in the negative direction relative to the laboratory frame. This is illustrated in the left of Figure 1. If the orientation is known the tensor in the laboratory frame can be written in terms of its components ρ_{11} and ρ_{22} along the principal axes e_1 and e_2 . This will be further explored later.

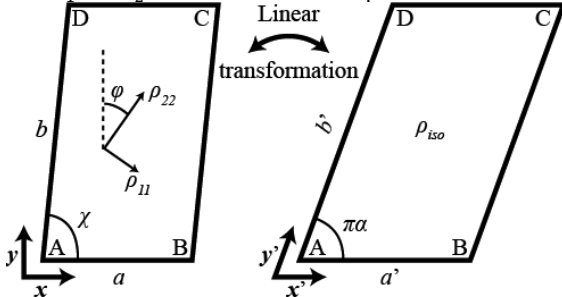


FIG. 1. Illustration of the effect of the change of coordinates on the sample geometry and tensor. Before the transformation the sample is anisotropic while it is isotropic after. φ is the angle between the tensor principal axes system and the laboratory axes. Before the transformation the laboratory axes are defined with x along the AB side and y perpendicular to this in the AD direction. χ is the angle in the anisotropic parallelogram while $\pi\alpha$ is the angle in the isotropic parallelogram.

The problem is to solve the Laplace equation for the anisotropic parallelogram when a current is passed between two points. To simplify the problem we make a change of variables according to the matrix

$$\mathbf{M} = \frac{1}{\sqrt{\rho_{yy}\rho_{iso}}} \begin{pmatrix} \rho_{yy} & -\rho_{xy} \\ 0 & \rho_{iso} \end{pmatrix}. \quad (1)$$

The definition $\rho_{iso} = \sqrt{\det \rho} = \sqrt{\rho_{xx}\rho_{yy} - \rho_{xy}^2}$ has been used. In this case, the transformation rule $\rho' = \mathbf{M}\rho\mathbf{M}^T$ applies to the resistivity tensor and results in $\rho' = \begin{pmatrix} \rho_{iso} & 0 \\ 0 & \rho_{iso} \end{pmatrix}$. That is, the change of variables results in an isotropic sample with resistivity ρ_{iso} . The sample geometry is transformed by transforming the vectors representing the sample \mathbf{a} and \mathbf{b} sides according to $\mathbf{a}' = \mathbf{M}\mathbf{a}$ and similarly for \mathbf{b} . These are both non-standard transformation rules which result from the change of variables in the Laplace equation (see supporting information). After the transformation, the new side lengths are

$$a' = a \sqrt{\frac{\rho_{yy}}{\rho_{iso}}}, \quad (2)$$

$$b' = b \sqrt{c(\chi)^2 \frac{\rho_{yy}}{\rho_{iso}} + s(\chi)^2 \frac{\rho_{xx}}{\rho_{iso}} - 2 c(\chi) s(\chi) \frac{\rho_{xy}}{\rho_{iso}}}, \quad (3)$$

and the angle between them is calculated from

$$\cos(\pi\alpha) = \frac{1}{\sqrt{\rho_{yy}}} \frac{c(\chi)\rho_{yy} - s(\chi)\rho_{xy}}{\sqrt{c(\chi)^2\rho_{yy} + s(\chi)^2\rho_{xx} - c(\chi)s(\chi)\rho_{xy}}}. \quad (4)$$

In Equation 3 and 4, $s(\chi)$ and $c(\chi)$ has been used as short hand for sine and cosine, respectively. Since the change of variables was applied to the Laplace equation, either sample can be used to calculate or measure the electrostatic potential. Any measurement performed on one sample would give the same result if performed on the other, provided the contact placement is also transformed correctly. Here, the contacts will be assumed placed at the corners A , B , C , and D . This means that the resistivity obtained from a van der Pauw measurement performed on an anisotropic sample will give the square root of the determinant of the resistivity tensor.

B. Conformal mapping

The change of coordinates somewhat simplifies the problem but it is still not straight forward to calculate the electrostatic potential. In the original derivation of the van der Pauw equation,^{1, 2} the existence of a conformal mapping between some 2D areas and an infinite half plane was used. The criterion of physical interest is that the outline of the area has to be singly connected, which is to say there can be no isolated holes in the area. A conformal mapping is any mapping that locally preserves angles while distances are not necessarily conserved. Van der Pauw did not need an explicit expression for the mapping since the contact placement on the infinite half plane vanishes from the van der Pauw equation. Here, an explicit expression is necessary since the information contained in the sample geometry is needed to extract more information from the measured resistances.

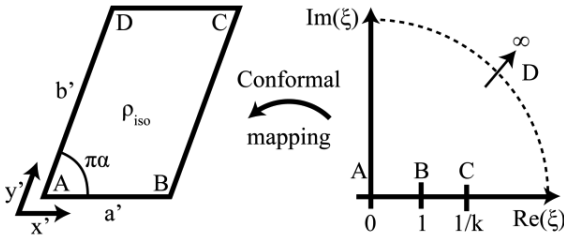


FIG. 2. Illustration of the conformal mapping with contact placements. Contact D corresponds to infinity in any direction on the upper complex half plane. k is in the range $0 < k < 1$ for contact C to be placed between contact B and D .

Figure 2 illustrates the conformal mapping defined by the equation^{3,4}

$$\xi' = \frac{a'}{A_{\alpha,k}} \int_0^\xi f_{\alpha,k}(z) dz, \quad (5)$$

where

$$f_{\alpha,k}(z) = z^{\alpha-1} (1-z)^{-\alpha} (1-kz)^{\alpha-1} \quad (6)$$

and

$$A_{\alpha,k} = \int_0^1 |f_{\alpha,k}(z)| dz \\ = \Gamma(\alpha)\Gamma(1-\alpha) {}_2F_1(\alpha, 1-\alpha; 1; k). \quad (7)$$

This takes a point $\xi = x + iy$ on the half plane and maps it to a point (x', y') $\xi' = x' + iy'$ in the isotropic parallelogram. α is the angle in the parallelogram, k^{-1} is the position of contact C on the half plane. Γ and ${}_2F_1$ are the Gamma function and Gaussian hypergeometric function, respectively.

k can be related to the geometry of the isotropic equivalent sample by considering the length of the mapped BC side. This can be calculated from the conformal mapping as^{5,6}

$$b' = \frac{a'}{A_{\alpha,k}} \int_0^{k^{-1}} |f_{\alpha,k}(z)| dz = \frac{a' A_{\alpha,1-k}}{A_{\alpha,k}} \quad (8)$$

$A_{\alpha,k}$ is a normalization constant and in the following only ratios such as in Equation 8 will appear. Hence it is convenient to define

$$B_{\alpha,k} = \frac{A_{\alpha,1-k}}{A_{\alpha,k}} = \frac{{}_2F_1(\alpha, 1-\alpha; 1; k)}{{}_2F_1(\alpha, 1-\alpha; 1; k)} \quad (9)$$

This can easily be calculated using standard mathematical software such as MATLAB.

The infinite (complex) half plane provides a system that allows easy calculation of the electrostatic potential differences between the contacts when a current is passed through the sample. As no scaling is performed the resistivity of the infinite half plane sample is still ρ_{iso} . $R_{AB,DC}$ denotes the ratio of the voltage between contact D and C when a current is passed from A to B . In a vdp including Hall effect measurement three such resistances are measured:

$$R_{AB,DC} = \frac{U_D - U_C}{I_{AB}} = \frac{-\rho_{iso}}{\pi d} \ln(1-k), \quad (10)$$

$$R_{BC,AD} = \frac{-\rho_{iso}}{\pi d} \ln(k), \quad (11)$$

$$R_{AC,BD} = \frac{-\rho_{iso}}{\pi d} \ln(k^{-1} - 1). \quad (12)$$

The derivation can be found in the supporting information. d is the sample thickness. These are not independent and one measurement is enough to determine k while α cannot be obtained from these resistance measurements. The resistance in Equation 12 corresponds to the Hall effect measurement and is a resistive offset to the Hall signal. Both resistances in Equation 10 and 11 are necessary for

the vdp measurement and are used to calculate ρ_{iso} from the vdp equation.

C. Calculating the tensor elements

After the measurement ρ_{iso} and k are known but no information on α is obtained. This will be the focus of the following sections. Using the definition for ρ_{iso} together with Equation 2-4 and 8 the tensor elements can be expressed in terms of α and known parameters

$$\rho_{xx} = \frac{1}{\sin(\chi)} r B_{\alpha,k} \lambda_\alpha + \quad (13)$$

$$\frac{\cos(\chi)}{\sin(\chi)} \lambda_\alpha (\cos(\chi) r^{-1} B_{\alpha,k}^{-1} - 2 \cos(\pi\alpha)) \quad (14)$$

$$\rho_{yy} = \sin(\chi) r^{-1} B_{\alpha,k}^{-1} \lambda_\alpha, \quad (15)$$

$$\rho_{xy} = \cos(\chi) r^{-1} B_{\alpha,k}^{-1} \lambda_\alpha - \lambda_\alpha \cos(\pi\alpha). \quad (15)$$

$r = a/b$ is the ratio of the anisotropic sample a and b sides and $\lambda_\alpha = \rho_{iso}/\sin(\pi\alpha)$. The derivation is quite lengthy and can be found in the supporting information.

Even with no more information simply assuming $\alpha = \chi/180^\circ$ provides useful information. The assumption is equivalent to assuming the principal axis system to be identical to the lab frame. The estimated anisotropy (difference between ρ_{11} and ρ_{22}) from this will never exceed the true anisotropy and can hence be used as a lower limit. If the sample is anisotropic it is still possible but unlikely that the sample will be found to be isotropic. This will only happen for $\varphi = 45^\circ$. This may happen in single crystals but it is otherwise highly unlikely.

D. Single crystals

In single crystals the orientation of the crystallographic axes can easily be determined. In all crystal classes except triclinic (see supporting information for a discussion) this also implies knowledge of the principal axes orientation and hence φ is known. The tensor can then be expressed in terms of the elements along the principal axes and the orientation

$$\rho = R^\varphi \rho_0 (R^\varphi)^T =$$

$$\begin{pmatrix} c^2(\varphi) \rho_{11} + s^2(\varphi) \rho_{22} & c(\varphi) s(\varphi) (\rho_{11} - \rho_{22}) \\ c(\varphi) s(\varphi) (\rho_{11} - \rho_{22}) & c^2(\varphi) \rho_{22} + s^2(\varphi) \rho_{11} \end{pmatrix} \quad (16)$$

R^φ is the matrix rotating vectors φ in the positive direction and $s(\varphi)$ and $c(\varphi)$ has been used for sine and cosine, respectively (see Transformation Rules section of supporting information). Now only two tensor elements need to be determined. This can be combined with Equation 13-15 to give an equation relating α to measured parameters.

$$0 = (\tan(\varphi)^{-1} - \tan(\varphi) - \tan(\chi)^{-1}) \cdot \\ (\cos(\chi) r^{-1} B_{\alpha,k}^{-1} - \cos(\pi\alpha)) \quad (17)$$

$$- \frac{1}{\sin(\chi)} r B_{\alpha,k} + \sin(\chi) r^{-1} B_{\alpha,k}^{-1} + \tan(\chi)^{-1} \cos(\pi\alpha)$$

This equation needs to be solved numerically. Once α has been obtained the tensor in the laboratory frame can be calculated from Equation 13-15 and the principal elements can be obtained by a rotation of this. Equation 17 can in some cases have two solutions, however, only one of these gives a tensor that is diagonal in the principal axis frame. This is the only valid solution.

An algorithm for solving Equation 17 is found in the supporting information and a MATLAB function for solving this is also supplied. It can be solved using the

Newton-Raphson method. The MATLAB function automatically determines whether there is one or two solutions and finds both. The procedure is shown in Figure 3, which can be reproduced with the supplied MATLAB function (see supporting information). $f(\alpha)$ is the right hand side of Equation 17 and $f'(\alpha)$ is its derivative with respect to α .

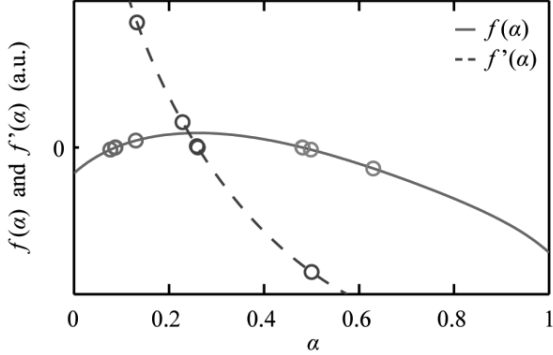


FIG. 3. The procedure for solving Equation 17. The dashed blue line is $f'(\alpha)$ while the solid red is $f(\alpha)$. First $f'(\alpha) = 0$ is solved to find the extremum in $f(\alpha)$. Then, the solutions to $f(\alpha) = 0$ on both sides of the extremum are found. Circles represent iterative improvements of the initial guess for the three solutions.

E. Polycrystalline materials

If the orientation of the tensor elements is not known more information needs to be obtained by other means. It is possible to perform a 5-point analogue to the vDP measurement,⁶ however, this requires modification of the measurement system. This is not easily done with commercial systems such as the Quantum Design Physical Properties Measurement System (PPMS) or MMR Technologies Hall Measurement System. Custom setups may be more easily adapted to accommodate a fifth contact.⁷

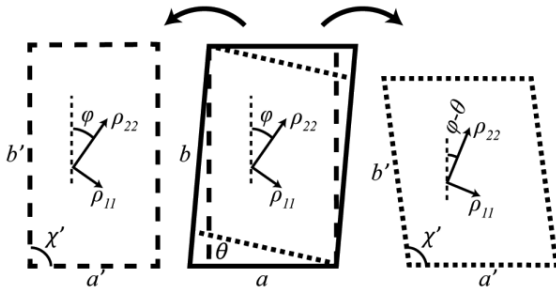


FIG. 4. Reshaping the sample between two measurements can provide enough information to determine α . After the first measurement the middle sample is cut along either the dotted or dashed lines. In the right sample with the dotted line the tensor principal axes has been rotated relative to the lab frame, indicated by the angle θ . In the left sample, the sample geometry has changed but the tensor principal axes have the same orientation. The sample can be reshaped in many more ways which will give the right result provided attention is paid to the rotation of the tensor principal axes. If such modification is not feasible extra information can be obtained by modifying the sample, as indicated in Figure 4.

An initial measurement is performed (middle sample), the sample geometry is changed and a second measurement is performed (such as on the left or right samples). Provided the sample is homogenous the tensor in the two measurements is identical (if ρ_{iso} changes more than 1-2% the sample is most likely inhomogeneous or other errors have been made). After the first measurement r , k , χ , and ρ_{iso} are known and the tensor can be calculated as a function of only alpha, $\rho(\alpha)$. In the second measurement these are different but known and the tensor $\rho'(\beta, \theta)$ can also be calculated as a function of the new α , called β to better distinguish the two, and θ . Hence, rotating the tensor in the second sample θ in the negative direction gives the equation

$$\rho(\alpha) = \rho'(\beta, \theta) = (R^\theta)^T \rho(\beta) R^\theta. \quad (18)$$

θ may or may not be 0. This gives three equations, one for each of the tensor elements. To solve this, the vector

$$d(\alpha, \beta) = \begin{pmatrix} \rho_{xx}(\alpha) \\ \rho_{yy}(\alpha) \\ \rho_{xy}(\alpha) \end{pmatrix} - \begin{pmatrix} \rho_{xx}(\beta, \theta) \\ \rho_{yy}(\beta, \theta) \\ \rho_{xy}(\beta, \theta) \end{pmatrix} \quad (19)$$

is used to reduce the system of equations to one equation. Equation 18 can be solved by finding the minimum in $d^2(\alpha, \beta)$. This corresponds to a least squares optimization. This equation can be solved using Newton's method and a MATLAB function for this is supplied and a description is found in the supporting information.

F. Error analysis

The requirements for the vDP method still apply: The sample has to be flat and of uniform thickness and there can be no holes. For round samples it has been found that samples can be considered flat if the thickness is less than the radius.⁸ Extending this to other geometries is not simple; however, keeping the thickness well below the shortest distance across a sample and between any two contacts should provide a reasonable rule of thumb. If a more accurate estimate is needed, an experimental test is required. The contacts also need to have a low area. This is particularly important if high accuracy of the individual elements is required.

Another source of error is the contact placement. If the contacts are not placed exactly on the corners errors in the tensor elements are expected while ρ_{iso} is not expected to change. Finding an analytic expression for the error from misplaced contacts is difficult and provides little insight. Instead, it can easily be simulated numerically by moving the A contact on the complex half plane away from the origin and mapping this to the sample using the two transformations. For small errors, the errors from several misplaced contacts are expected to be additive as with the normal vDP method.^{1,2}

In a parallelogram there are two different corners which will give different errors. An example of an error simulation is shown in Figure 5. The MATLAB script used to obtain this is supplied in the supplemental material. After the tensor has been obtained, this script can be used to check the error from misplaced contacts. In most cases the error on the resistivity tensor elements is lower than the error on the contact placement. For corners with high angle the error is significantly larger than for low angle corners and hence these should be avoided. The best criterion is to

keep $\pi\alpha$ close to 90° . This is a more general requirement than can be made for the anisotropic sample itself since the current paths will depend strongly on the tensor. Keeping the error in contact placement less than a few percent is possible even for small samples and the total error from this source are expected to be less than 3-5% of ρ_{iso} if care is taken.

For the calculations a tensor with principal axis elements $\rho_{11} = 1$ and $\rho_{22} = 2$ and orientation $\varphi = 30^\circ$ was used for both corners (not the same sample). In Figure 5 the change in tensor elements was divided by ρ_{iso} since this sets the scale for the tensor elements. If the change is calculated relative to the individual elements errors in elements with low values are overemphasized. This is further discussed in the supporting information.

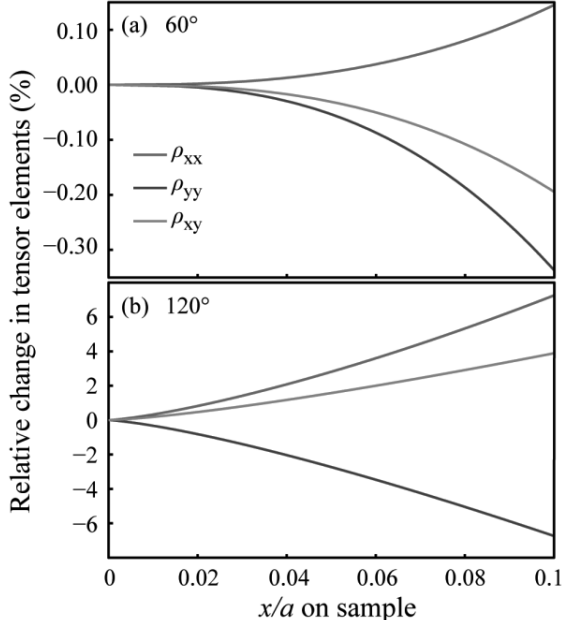


FIG. 5. Tensor elements relative to correct contact placement as a function of the A contact placement (x) on the AB side. The simulation was done using $\chi = 60^\circ$ (a) and $\chi = 120^\circ$ (b) with the same tensor. The 120° corner is more susceptible to error since the contact displacement is along the current path. The change from the correct tensor was calculated relative to ρ_{iso} .

Another source of error is from the angles in the parallelogram, either errors in χ or deviations from a parallelogram towards a trapezoid. The first can easily be simulated numerically while the later has to be tested experimentally since the conformal mapping no longer holds (another expression is needed).

A simulation of the error as a function of the error in the χ is shown in Figure 6. Contrary to the error from misplaced contacts, the error from measuring χ is almost independent on the angle of the parallelogram. The angle of the sample can be measured with high accuracy with a digital microscope or equivalent and will usually not exceed 0.5° . Hence, the error from measuring the angle is expected not to exceed 1-2% of ρ_{iso} .

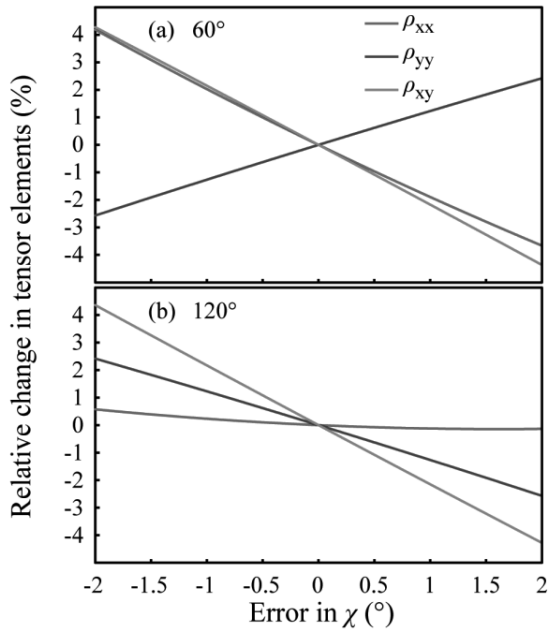


FIG. 6. Relative change in tensor elements as a function of error in χ . The simulation was again done using $\chi = 60^\circ$ (a) and $\chi = 120^\circ$ (b), the same tensor as in Figure 5, and normalized with ρ_{iso} . The error from measuring the angle is less dependent on the corner angle than the error from contact placement.

III. EXPERIMENTAL TEST

Several test systems were employed to test the rigidity of the theory and assess experimental noise. All geometry parameters were measured ten times, where the sample was moved between every measurement to minimize artifacts. Angles were measured with a digital microscope and dimensions were measured with a micrometer screw with $10\mu\text{m}$ delimitation. The standard deviation from the mean never exceeded 0.5° and $40\mu\text{m}$ but was generally below 0.15° and $10\mu\text{m}$. To ensure that all samples could be considered flat, the thickness of any sample never exceeded a third of the shortest side length and was generally less than a fifth.

A. Conformal mapping

Pseudo-anisotropic samples were prepared from isotropic polycrystalline graphite shaped as the isotropic equivalent of an imagined square anisotropic sample; the tensor was then calculated from the measured resistances and the geometry of the graphite. The aspect ratio of the graphite was progressively increased while angles were kept fixed to change the tensor of the imagined anisotropic sample. As shown in Figure 7 there is a good agreement between the tensor elements calculated from the aspect ratio and the ones derived from the measurements.

The reproducibility of a single measurement was tested by remounting and rotating a sample twenty times, from which two types of errors can be calculated: a parallel shift from the calculated value corresponds to an error in ρ_{iso} while an antiparallel shift corresponds to an error in geometry most

likely the contact placement. The relative errors scaled to ρ_{iso} can be seen in Figure 8.

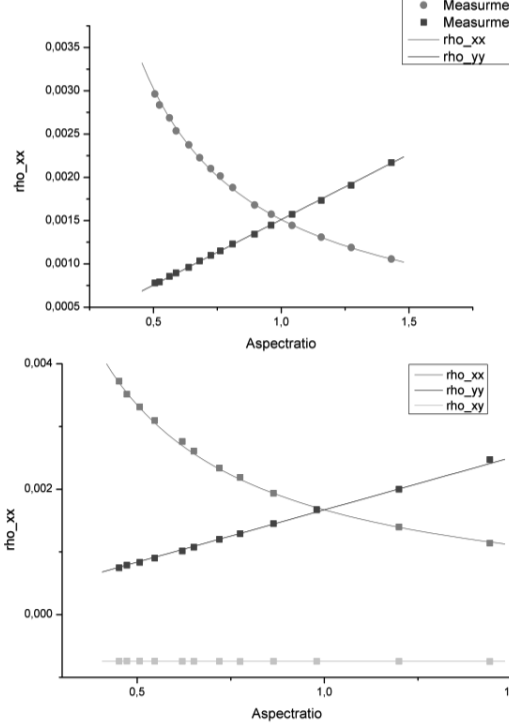


FIG. 7. Tensor elements with respect to aspect ratio of the isotropic equivalent, the points are from the measured resistances and the lines are the calculated tensor elements from the aspect ratio. The graphite was shaped as a rectangle in (a) and as a parallelogram with $\pi\alpha = 63.55^\circ$ in (b).

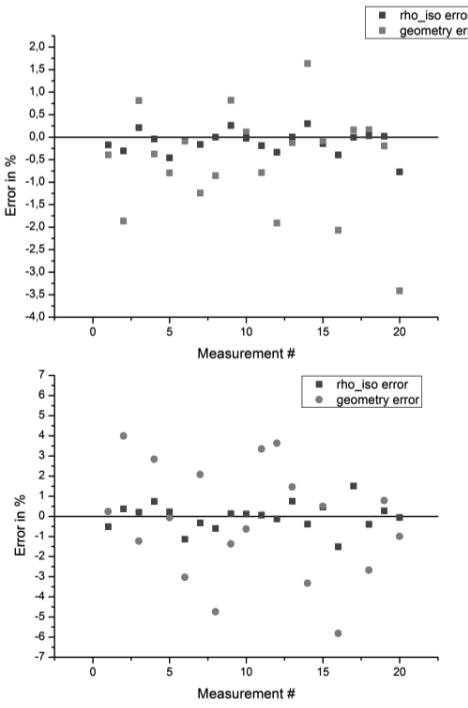


FIG. 8. Relative errors in tensor elements scaled to ρ_{iso} resulting from different experimental factors for the twenty reproducibility measurements. The graphite was shaped as a rectangle in (a) and as a parallelogram with $\pi\alpha = 63.55^\circ$ in (b).

The errors are three times larger for the parallelogram than the rectangle. This is mainly due to $\pi\alpha$ being far from 90° and to a lesser extent due to the fact that parallelograms are slightly harder to mount correctly.

B. Polycrystalline materials

The graphite used to test the conformal mapping was also employed to test the extraction of α with equation 19, because polycrystalline graphite is never perfectly isotropic. A rectangular piece of graphite was gradually cut into a progressively more skewed parallelogram and all unique combinations of the five measurements were used to find α and calculate the tensor elements, the results of which can be seen in Figure 9.

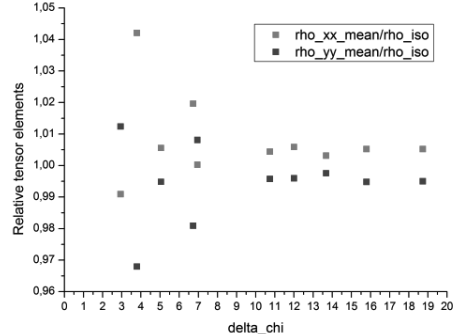


FIG. 9 Tensor elements divided by the isotropic resistance with respect to the change in χ in the parallelogram.

If the two samples are very similar, equation 19 will be very flat and many iterations will be needed to reach convergence. This results in experimental noise having a significant impact on the result. Establishing a minimum change in χ required to minimize the effect of experimental noise is not straightforward: the further $\pi\alpha$ and $\pi\beta$ are from 90° and r from 1 the larger a change is needed. However a minimum change of 15° should suffice for any case.

IV. REAL SAMPLES

An approximately 20 mm^3 single crystal of RuSb₂ was grown by antimony flux from which a piece in the a, b -plane was cut. This piece was then reshaped so α could be calculated from the orientation of the crystallographic axes and from the rotational relationship between the two samples. The geometries of the two samples were $r = 0.71$; $\chi = 96.2$; $\phi = 45.7$ and $r = 0.96$; $\chi = 79.6$; $\phi = 62.3$ respectively. The first geometry is problematic, because it is very close to an area where equation 17 has no solutions. This can be seen by the abrupt end of the error analysis plots in Figure 10. The resistivity results for the first geometry by itself are not reliable, because of the error-prone geometry. The best test is ensuring that $\tan(\varphi)^{-1} - \tan(\varphi) - \tan(\chi)^{-1}$ is larger than 0.1. The

results from the second geometry and the relation between the two are in decent agreement giving the tensors $\begin{bmatrix} 0.0980 & 0 \\ 0 & 0.1522 \end{bmatrix}_2$ and $\begin{bmatrix} 0.0808 & 0 \\ 0 & 0.1553 \end{bmatrix}_{1 \rightarrow 2}$.

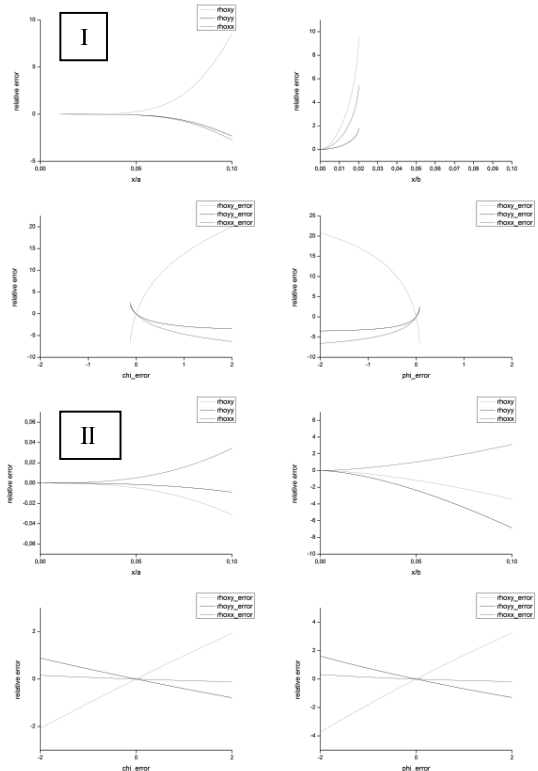


FIG. 10. Tensor elements for the first geometry (I) and second geometry (II) relative to different errors, contact placement along the AB side in (a) and along the BC side in (b), chi in (c) and phi in (d). The change from the correct tensor was calculated relative to ρ_{iso} .

V. REFERENCES

- 1 L. J. van der Pauw, Philips Res. Rep. **13**, 1 (1958).
- 2 L. J. van der Pauw, Philips Tech. Rev. **20**, 220 (1958).
- 3 J. Kleiza and V. Kleiza, Electronics and Electrical Engineering **59** (2005).
- 4 J. Kleiza, M. Sapagovas, and V. Kleiza, Informatica **18**, 253 (2007).
- 5 J. Kleiza and V. Kleiza, Lith Math J **38**, 232 (1998).
- 6 S. Ašmontas, V. Kleiza, and J. Kleiza, Acta Phys. Pol. A **113**, 1559 (2008).
- 7 K. A. Borup, E. S. Toberer, L. D. Zoltan, G. Nakatsukasa, M. Errico, J.-P. Fleurial, B. B. Iversen, and G. J. Snyder, Rev. Sci. Instrum. **83**, 123902 (2012).
- 8 C. Kasl and M. J. R. Hoch, Rev. Sci. Instrum. **76** (2005).

Appendix C.4 Functionally Graded $\text{Ge}_{1-x}\text{Si}_x$ Thermoelectrics by Simultaneous Band Gap and Carrier Density Engineering

Reproduced with permission from Chemistry of Materials, submitted for publication.
Unpublished work copyright 2014 American Chemical Society

Functionally graded $\text{Ge}_{1-x}\text{Si}_x$ thermoelectrics by simultaneous band gap and carrier density engineering

Ellen M. J. Hedegaard, Simon Johnsen, Lasse Bjerg, Kasper A. Borup, and Bo B. Iversen*

Center for Materials Crystallography, Dept. of Chemistry, Aarhus University, Langelandsgade 140, DK-8000 Aarhus C, Denmark.

KEYWORDS Thermoelectricity, Czochralski method, functionally graded materials

ABSTRACT: Exploiting the material gradients inherent to crystal growth techniques, boron doped $\text{Ge}_{1-x}\text{Si}_x$ ($x=0$ to ~ 0.25) samples graded in both band gap and carrier concentration have been prepared by the Czochralski method. Along the length of the $\text{Ge}_{1-x}\text{Si}_x$ samples x changes continuously giving rise to changes in the band gap from 0.87 eV to 0.65 eV. Similarly, gradients in the boron content results in continuous carrier density changes along the sample. This results in samples graded in all material parameters relevant to thermoelectric performance. The present study thereby demonstrates a one-step method for preparing thermoelectrics graded in both carrier concentration and band gap. By careful matching of dopant and material system, it is demonstrated how the gradient in dopant and band gap can work in synergy and mutually enhance the thermoelectric performance over the individual contributions.

INTRODUCTION

Thermoelectricity, directly interconverting thermal and electrical energy by solid state materials, has long been suggested as one of the answers to the worlds rising energy demand.¹ Conversion of waste heat into electricity would result in a better utilization of currently available energy sources and new sources may be exploited. However, development of new materials as well as optimization of known materials is needed before cost-efficiency allows for the widespread consumer use which has long been strived for.

The performance of a thermoelectric material increases monotonically with its figure of merit, zT .¹⁻²

$$zT = \frac{\alpha^2 \sigma}{\kappa} T \quad (1)$$

α is the Seebeck coefficient, σ the electrical conductivity, T is the absolute temperature, and κ the thermal conductivity given by $\kappa = \kappa_e + \kappa_l$ where e and l specify the electrical and lattice contributions respectively, and $\kappa_e = L\sigma T$, L being the Lorentz number.

For a homogeneous material zT peaks in a narrow temperature range.¹ However, in a module application the material is often subjected to a large temperature gradient.³ By grading the properties determining zT through the sample, the peak zT position along the length of the sample can be shifted to match the local operating temperature and

consequently improve the efficiency of the thermoelectric device. This idea was first introduced by Ioffe in 1949.³⁻⁴ It has later been proven that an exact match between parameters and temperature profile is not a necessity to enhance the exploitation of the temperature gradient. This is an important result as achieving a predetermined property profile through a material is a complex task.³

Generally speaking, the onset of bipolar conduction and the decrease in zT is coupled.⁵ Therefore the larger the band gap the higher the optimal working temperature, i.e. the peak in zT . This is illustrated by the “ $10k_bT$ rule”, which states that a material should have a band gap of roughly $10k_bT$, with T being the optimal operating temperature.⁶ Similarly, the carrier concentration shifts the peak in zT , such that the higher the dopant concentration, the higher the peak temperature in zT .³

Grading of the band gap along the sample can be done by grading the sample composition by ensuring overall directional solidification through bulk crystal growth techniques such as Bridgman-Stockbarger or Czochralski. Suitable materials systems are therefore (pseudo-) binary with full or partial miscibility, see figure XX. For this to result in a grading of the band gap this must change between the values of the end members.

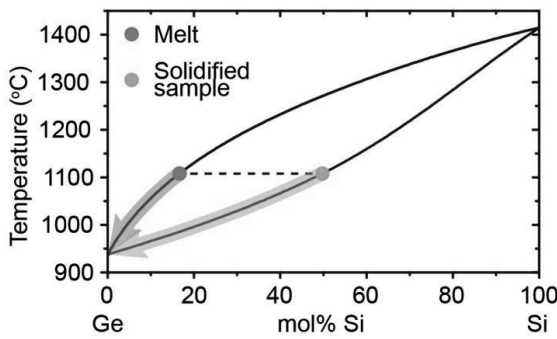


Figure XX: The phase diagram of the Ge-Si solid solution showing how, for a given composition of the melt, the composition of the resulting solidified sample can be found by drawing a line at constant temperature. The development in composition as crystallization proceeds is indicated by the arrows. Phase diagram reproduced from⁷

Furthermore, assuming complete equilibrium in the system, grading of the dopant concentration along a Czochralski or Bridgman-Stockbarger grown crystal is given as:⁸

$$C = kC_0(1 - g)^{k-1} \quad (2)$$

C is the dopant concentration at the crystal-liquid interface at a given time during solidification, k is the equilibrium segregation coefficient, C_0 is the original dopant concentration in the melt, and g is the fraction of the melt solidified at the given time. The value of k thereby determines the development in dopant concentration, i.e. whether it decreases ($k>1$) or increases ($k<1$) as solidification proceeds. In reality, k depends on the synthesis conditions such as pulling speed, and effective segregation coefficients closer to unity are obtained.

Previously, Czochralski pulled samples of the thermoelectric clathrate $\text{Ba}_8\text{Ga}_{16}(\text{Si}_x\text{Ge}_{1-x})_{30}$ with continuously varying composition have shown that thermoelectric performance can be engineered by a band gap gradient in a bulk synthesized sample.⁹ Similarly samples graded in dopant concentration (for example Bi_3Te_3) have been prepared by bulk crystal growth in several studies.³

However, little is known about the possibilities of simultaneously grading band gap and dopant concentration to make the two contributions enhance each other. Consequently, we chose to investigate double-graded boron doped Czochralski pulled $\text{Ge}_{1-x}\text{Si}_x$ as a proof of principle system.

The Ge-Si solid solution is a well-established thermoelectric system showing full miscibility in the entire composition range, with a high tendency for alloy segregation, see figure XX.¹⁰ From literature,¹¹

the band gap is known to increase with increasing Si content, with the increase being steeper with composition below 15 mol% Si than above. By inspection of the phase diagram,⁷ it is seen that a Czochralski pulled $\text{Ge}_{1-x}\text{Si}_x$ sample will have decreasing Si content as solidification proceeds, leading to decreasing band gap. By choosing a low concentration of Si the highest effect from band gap grading is expected. A decreasing dopant concentration, i.e. a segregation coefficient above one, is therefore needed to enhance the effect on the properties from band gap grading. The most commonly used p-type dopant in germanium-silicon alloys is boron. Bridgers *et al.*¹² report the equilibrium segregation coefficient of B in Ge to be 17.4 although other values have also been reported.¹³ However, all of these are significantly above one, making boron a suitable proof of principle dopant in germanium and germanium-rich GeSi alloys.

Whereas many studies in recent years have focused on improving the thermal contributions to zT , the present study focuses on manipulating the electronic contributions to the thermoelectric figure of merit and therefore these have been isolated from the zT equation:

$$zT_e = \frac{\alpha^2 \sigma}{\kappa_e} T = \frac{\alpha^2 \sigma}{L \sigma T} T = \frac{\alpha^2}{L} \quad (3)$$

where L is the Lorenz factor, which is dependent of carrier density, scattering mechanism and band structure. Focusing on acoustic phonon scattering in a single parabolic band L assumes values from $1.49 \cdot 10^{-8} \text{ W}\Omega\text{K}^{-2}$ to $2.44 \cdot 10^{-8} \text{ W}\Omega\text{K}^{-2}$.¹⁴

The thermal conductivity of silicon-germanium alloys is relatively high compared to other state of the art thermoelectric materials.¹⁵ Hence, high zT materials are not expected in this study. Rather, the objective is to demonstrate the feasibility of a one-step synthesis route to achieve functionally graded samples free of the problems inherent to functionally segmented samples.^{4, 16} Several recent studies deal with the efforts of raising the value of zT , and the considerations of material choice for this purpose.¹⁷

Hence, this work is a proof of principle of the double doping principle as a method for optimizing materials to function in the temperature gradient experienced by a thermoelectric module.

EXPERIMENTAL SECTION

Sample Preparation

The sample was prepared in an Arthur D. Little induction furnace under He pressure. Elemental Ge, Si and B were mixed in the molar ratio 95:50:1 in a glassy carbon crucible within a graphite susceptor,

and heated above the melting point of the overall composition to ensure full mixing. Czochralski pulling was performed at a pulling rate of 4.4 mm/h using a sharpened tip of Mo wire as seed.

The prepared sample was cut in halves along the pulling direction and half-circle shaped samples were cut from one of the halves at three positions along the pulling direction, see figure 1.

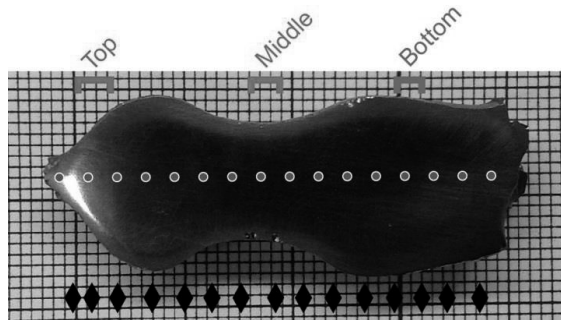


Figure 1: A cut though the Czochralski pulled sample. The sample is shown on mm grid, with the part first solidified shown to the left. The positions along the pulling direction where PXRD was measured are marked by diamonds and the positions for EDX on the surface by circles. Furthermore, the positions of the slices used for high temperature characterization are marked at the top of the figure.

Experimental methods

Powder X-ray diffraction (PXRD) was done on a STOE STADI P in-house transmission diffractometer equipped with a Cu-source and a Ge(111) single crystal monochromator which selects the Cu K_α line ($\lambda=1.54056 \text{ \AA}$). The diffracted X-rays were collected at room temperature in the 2θ range of $2.05\text{--}126.92^\circ$ with a position sensitive image plate detector. This was done for 15 positions along the pulling direction, see figure 1. These data were analyzed by Rietveld refinement in FullProf,¹⁸ refining data in the 2θ range $20\text{--}80^\circ$ assuming full occupancy and only refining the Lorentz contributions to the peak profile. To further characterize the composition along the sample energy dispersive X-ray spectroscopy (EDX) was performed on a Nova NanoSEM with an EDAX detector for 16 points along the pulling direction of the sample, as marked on figure 1.

High temperature characterization was done on two custom made setups. Resistivity and Hall coefficients were measured on a setup as described by Borup *et al.*¹⁹ from room temperature to temperatures of 856 K, 811 K and 762 K for the three samples top, middle and bottom, respectively. Seebeck coefficients

were measured on an instrument as described by Iwanega *et al.*²⁰ and extracted as described by de Boor and Müller.²¹ These measurements were performed at 306 K and then in steps of 50 K from 324 K to 873 K, 826 K and 778 K for top, middle and bottom, respectively. Furthermore, the grown sample was characterized for room temperature Seebeck coefficients along the entire sample length by Potential Seebeck Microprobe (PSM by Panco GmbH) scans as described by Platzek *et al.*²² with grid point spacings of 0.100 and 0.050 mm.

As reference the electronic band structure of Germanium was calculated using the DFT program WIEN2k²³ with the PBE functional²⁴ and an $RK_{\max}=7$ on a $62\times 62\times 62$ k grid. From the band structure, the electronic properties were calculated using BoltzTraP.²⁵ The band gap was varied to match the experimentally measured values of $\text{Ge}_{1-x}\text{Si}_x$ with x varying from 0 to 0.2.

RESULTS AND DISCUSSION

In the following, the characterization of the parameters relevant for thermoelectric performance is presented. The room temperature parameters are summarized in table 1.

Sample	Si content (Mol%)	Seebeck coefficient ($\mu\text{V/K}$)	Resistivity (mOhm-cm)	n_{Hall} (10^{19} cm^{-3})
Top	17(2)	85.49(3)	0.855(2)	10.69(3)
Middle	3.8(5)	154.59(7)	2.13(1)	1.422(3)
Bottom	0.47(2)	186.3(2)	6.91(3)	0.2021(1)

Table 1: Room temperature parameters for the three samples used for high temperature characterization

Unit cell parameters and composition.

The composition along the Czochralski pulled sample as found by EDX is shown in figure 2a. Furthermore, the unit cell parameters were obtained from PXRD. The grading in composition was calculated from a known relation between unit cell parameters and composition²⁶ and is shown alongside the EDX data in figure 2a. It is seen that the agreement between PXRD and EDX is good. Inspecting the phase diagram,⁷ the expected composition at the top of the sample is 23 mol% Si. Starting compositions of 22.23 mol% silicon from PXRD and 24.28 mol% silicon from EDX are therefore in good agreement with expected values.

From polynomial fits to published data of the correlation between Si content and band gap,¹¹ the band gaps along the sample have been estimated, see figure 2b. The band gap is found to be approximately 0.87 eV in the part of the sample first solidified and then decrease through the sample to the value of pure Ge as solidification proceeds.

At silicon concentrations above ~15 mol%, the development in band gap is dominated by the <100> silicon-like conduction band giving a slow decrease with decreasing silicon concentration. At lower silicon concentrations, the <111> germanium-like band dominates the development, causing a steeper decrease. From this development in band gap with composition, it is expected that even a sample with a uniformly varying composition will have a band gap variation which is not perfectly smooth. However, a good grading of properties should still be possible.

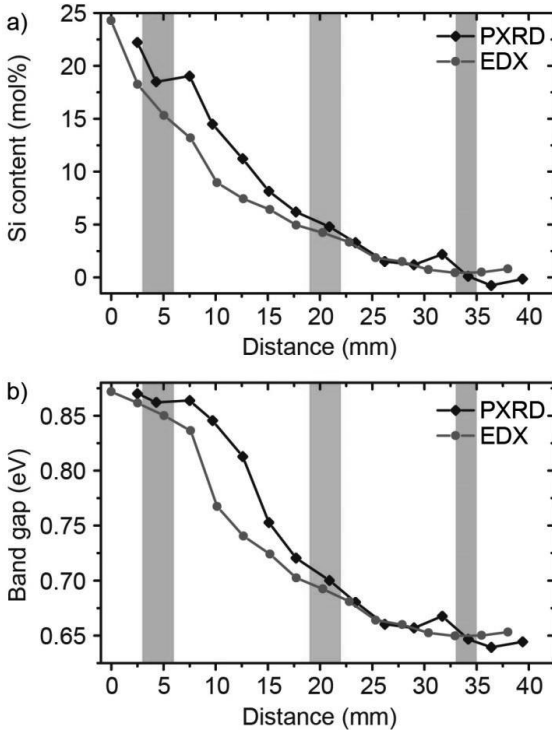


Figure 2: a) The variation in Si content through the sample as found by PXRD and EDX. b) Band gap as calculated from Si content through the sample. The shaded areas in both a) and b) mark the sections of the sample used for high temperature characterization.

Seebeck coefficient

Spatially resolved room temperature Seebeck coefficient along the sample has been determined by PSM (figure 3a). These data were averaged

perpendicular to the pulling direction, see figure 3b. Overall, a clear grading is seen along the sample. The Seebeck coefficient depends on the carrier concentration as n^r (r being positive).^{6b} This indicates that the carrier concentration does indeed decrease in a continuous manner along the length of the sample, as expected.

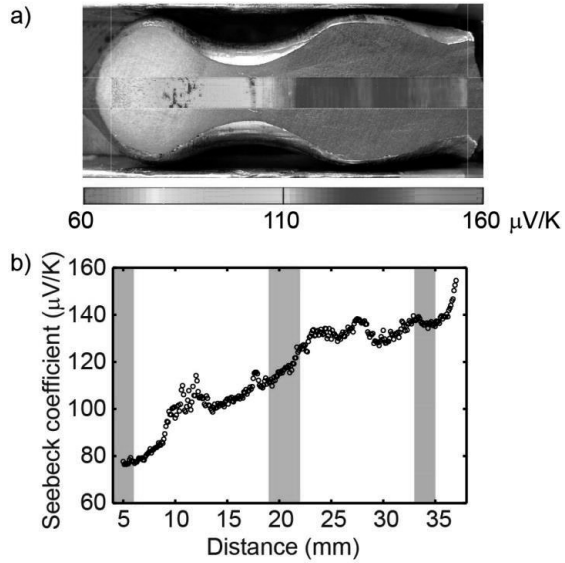


Figure 3: a) Potential Seebeck microprobe scan along the pulling direction of the sample. b) Data averaged perpendicular to the pulling direction showing the development in Seebeck coefficient as the band gap and carrier concentration changes. Besides from small deviations at the positions of slight instability in growth conditions, a continuous development is seen. The shaded areas correspond to the position of the samples used for high temperature characterization.

The temperature dependency of the Seebeck coefficient has been determined for three samples cut at positions marked "top", "middle" and "bottom", see figure 4. These correspond to Si concentrations of 17(2) mol%, 3.8(5) mol% and 0.47(2) mol%, respectively, as found by EDX (see figure 2a). At room temperature all three samples show the expected p-type behavior. The bars "top" and "middle" continue this behavior over the entire temperature range, but at high temperatures the sample "middle" show a turnover in the development of the Seebeck coefficient as bipolar conduction becomes significant. The "bottom" sample, being the lowest doped sample, shows a complete shift to bipolar behavior at around 750 K. Thereby it is shown that the position of the peak in the Seebeck coefficient does indeed shift as

wanted along the sample, with the top end having the peak at higher temperature than the bottom.

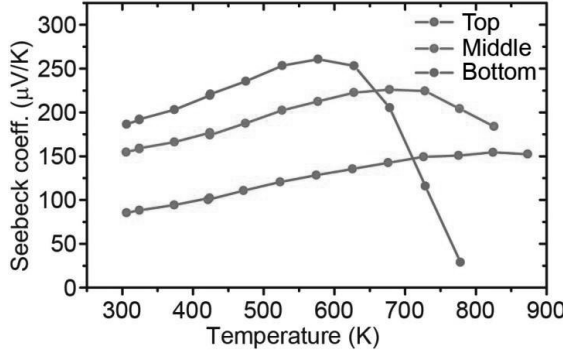


Figure 4: High temperature behavior of the Seebeck coefficient at three positions along the synthesized sample.

Resistivity and Hall Coefficient

The same samples used for measuring the high temperature Seebeck coefficients were also investigated for high temperature resistivity and Hall coefficients.¹⁹ The resistivity data are shown in figure 5a. As expected from equation (2) and measured Seebeck coefficients the resistivity increases along the length of the sample. Once again the clear difference between “top” and “middle” (having an extrinsic semiconductor behavior over the entire temperature range), and “bottom”, (changing from extrinsic to bipolar behavior at around 600 K) is seen.

The Hall carrier concentrations have been calculated from the Hall coefficients. As anticipated the carrier concentration decreases along the sample as the segregation coefficient would suggest. Besides sample “bottom”, where the change to bipolar conduction is observed, the samples show a slight increase in carrier concentration over the entire temperature range, indicating the extrinsic range of a doped semiconductor as expected. The relative higher decrease in carrier concentration from “top” to “middle” than from “middle” to “bottom” fits well with the power law behavior of equation (2) describing the development in carrier concentration along a Czochralski synthesized sample. Fitting to this equation gives an effective segregation coefficient of 6.2(3) as can be seen from table S1-2 and figure S2.

Inspecting figure 5a it is found that if the present sample was placed in a temperature gradient from 300 K to 900 K, with the “top” end at highest temperatures, the resistivity would vary in a non-ideal manner along the sample, since the cold part of the sample would have a higher resistivity than the

hot part (compare “bottom” at 300 K and “top” at 900 K). This means that if a leg for a thermoelectric module was made out of the current material the leg cross section would have to be varied through the leg. To circumvent this, the effective segregation coefficient could be lowered by a higher pulling rate. This would flatten out the gradient in dopant through the sample.

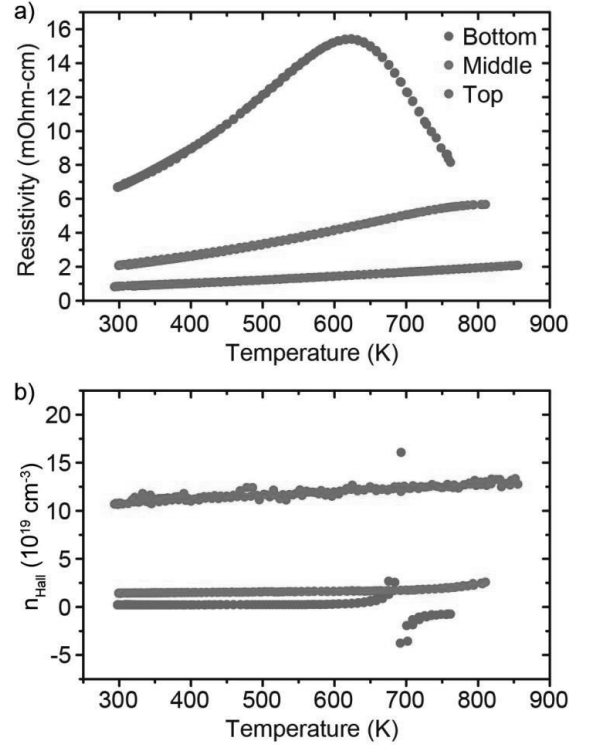


Figure 5: a) Resistivity at high temperatures for samples from three positions along the Czochralski pulled germanium silicon ingot. b) Hall carrier concentrations for the same three samples as in a).

$$zT_e$$

To investigate the expected effect of the grading of the properties on the thermoelectric performance, zT_e has been calculated from the Seebeck coefficients shown in figure 4 using a Lorenz factor of $1.49 \cdot 10^{-8}$ WΩK⁻² (For justification of this see figure S3). These are plotted in figure 6. To enhance the thermoelectric performance of the material through functionally grading of the electronic properties, the position of the zT_e peak should preferably shift to lower temperatures along the sample. Figure 6 shows a clear shift in the peak position of zT_e to higher temperatures with increasing x and boron concentration. As the lattice thermal conductivity usually scales with T^x ,²⁷ the difference in the zT

values at the peaks can be expected to be smaller than the difference in zT_e . In this way it has been shown that by bulk crystal growth the temperature of optimal efficiency can be made to span a temperature interval comparably to the temperature intervals experienced by a thermoelectric module.

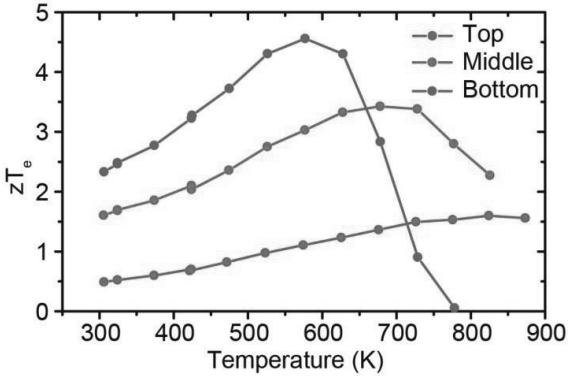


Figure 6: Experimentally found zT_e values at three positions along the Czochralski pulled sample.

Theoretical calculations

To support the evaluation of the achieved gradient in thermoelectric performance, zT_e has been calculated for Ge/Si ratios and doping levels corresponding to the synthesized sample. A model using the band structure of germanium has been applied and the band gap has been adjusted to match relevant sample compositions. The resulting values are shown in figure 7.

The indirect band gap of Ge decrease with increasing temperature from 0 K to 300 K²⁸. Theoretical calculations furthermore predict the band gap to continuously decrease up to temperatures as high as 1000 K.²⁹ This temperature dependency will cause the positions of the peaks in both figure 7a and figure 7b to move to lower temperatures and be spaced closer together in accordance with the smaller band gap at the temperatures of the peaks.

Figure 7a shows the dependency on carrier concentration at the lowest band gap value in the composition range. Due to the temperature dependency of the band gap the exact positions of the peaks cannot be expected to match the experimental data. However, a good qualitative agreement is seen between the experimental (figure 6) and the calculated (figure 7a) curves.

The dependency on band gap only is shown in figure 7b. The peak in zT_e can be seen in the calculated temperature interval for all three

compositions. A clear dependency on the band gap size is seen in the positions of the peaks in zT_e . Again, the temperature dependency of the band gap should shift the peaks to lower temperatures and closer together.

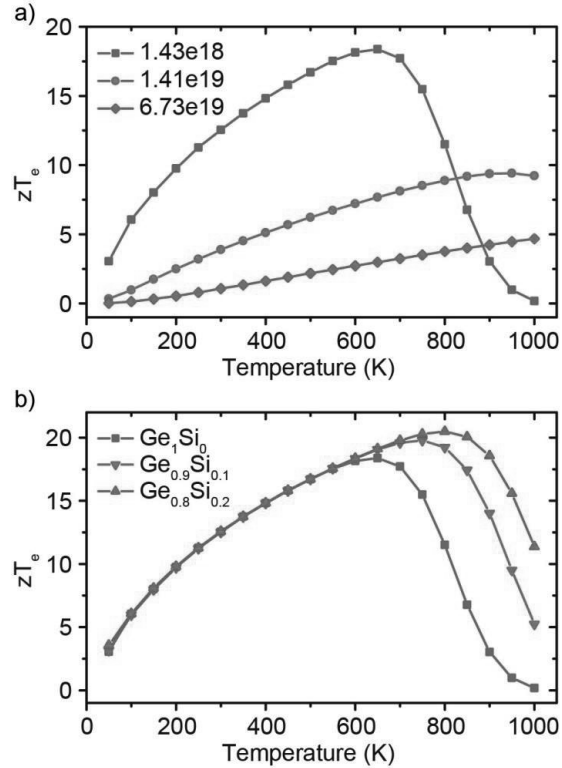


Figure 7: a) Calculated zT_e values for pure germanium with varying carrier concentration. b) Calculated zT_e for varying composition at a carrier concentration of $1.43 \times 10^{18} \text{ cm}^{-3}$.

CONCLUSIONS

In summary, we have presented a one-step synthesis of a thermoelectric material graded in both carrier concentration and band gap. This allows for screening of properties in materials graded in both band gap and carrier concentration.

It has been shown that by bulk crystal growth, the electronic part of the thermoelectric figure of merit can be engineered to fit the temperature gradients experienced by a functional thermoelectric module. This is done by simultaneously tuning of the band gap and the carrier concentration along the sample through a stoichiometry control dictated by thermodynamic principles of the sample growth process. These stoichiometric gradings would provide the necessary functional grading of a material

engineered for better exploitation of the heat gradients experienced in thermoelectric generator applications.

Hence, with suitably choice of dopant other thermoelectric systems such as PbTe could be expected to be optimized for the temperature gradient they experience when operating in a generating mode. In general, a broader view of optimizing thermoelectric materials is needed. Not only looking at the homogeneous materials properties but also on the conditions under which the material will be operating.

ASSOCIATED CONTENT

Supporting information

Following information is available as supporting material

- Schematic of the experimental setup for sample synthesis
- PSM and EDX data investigating the radial distribution of the composition

- Parameters and refinement used for determining the effective segregation coefficient

- Calculated Lorenz values

This material is available free of charge via the Internet at <http://pubs.acs.org>

AUTHOR INFORMATION

Corresponding Author

*: bo@chem.au.dk

Notes

The authors declare no competing financial interest.

ACKNOWLEDGMENT

The work was kindly supported by the Danish National Research Foundation (Center for Materials Crystallography, DNRF93).

References

1. Snyder, G. J.; Toberer, E. S., *Nat. Mater.* **2008**, *7* (2), 105-114.
2. Sootsman, J. R.; Chung, D. Y.; Kanatzidis, M. G., *Angew. Chem. Int. Edit.* **2009**, *48* (46), 8616-8639.
3. Kuznetsov, V., Functionally Graded Materials for Thermoelectric Applications. In *Thermoelectrics handbook : macro to nano*, Rowe, D. M., Ed. CRC/Taylor & Francis: Boca Raton, 2006.
4. Muller, E.; Drasar, C.; Schilz, J.; Kaysser, W. A., *Mat. Sci. Eng. a-Struct.* **2003**, *362* (1-2), 17-39.
5. Slack, G. A.; Hussain, M. A., *J. Appl. Phys.* **1991**, *70* (5), 2694-2718.
6. (a) Sofo, J. O.; Mahan, G. D., *Phys. Rev. B* **1994**, *49* (7), 4565-4570; (b) Mahan, G. D., *Solid State Phys* **1998**, *51*, 81-157.
7. Olesinski, R. W.; Abbaschian, G. J., Ge-Si (Germanium-Silicon). In *Binary alloy phase diagrams*, 2nd; Massalski, T. B.; Okamoto, H.; ASM International., Eds. ASM International: Materials Park, Ohio, 1990.
8. Pamplin, B. R., *Crystal Growth*, 1st; Pergamon Press: Oxford, New York,, 1975; p 672.
9. Christensen, M.; Johnsen, S.; Søndergaard, M.; Overgaard, J.; Birkedal, H.; Iversen, B. B., *Chem. Mater.* **2009**, *21* (1), 122-127.
10. Vining, C. B., Silicon Germanium. In *CRC handbook of thermoelectrics*, Rowe, D. M., Ed. CRC Press: Boca Raton, FL, 1995; p 701.
11. Braunstein, R.; Moore, A. R.; Herman, F., *Phys. Rev.* **1958**, *109* (3), 695-710.
12. Bridgers, H. E.; Kolb, E. D., *J. Chem. Phys.* **1956**, *25* (4), 648-650.
13. Taishi, T.; Ohno, Y.; Yonenaga, I., *Thin Solid Films* **2010**, *518* (9), 2409-2412.
14. Fistul', V. I., *Heavily doped semiconductors*, Plenum Press: New York,, 1969; p 418.
15. Rowe, D. M., *J. Power Sources* **1987**, *19* (4), 247-259.
16. (a) Snyder, J., Thermoelectric Power Generation: Efficiency and Compatibility. In *Thermoelectrics handbook : macro to nano*, Rowe, D. M., Ed. CRC/Taylor & Francis: Boca Raton, 2006; (b) Schilz, J.; Helmers, L.; Muller, W. E.; Niino, M., *J. Appl. Phys.* **1998**, *83* (2), 1150-1152.
17. (a) Zhao, L. D.; Dravid, V. P.; Kanatzidis, M. G., *Energ Environ Sci* **2014**, *7* (1), 251-268; (b) Gaultois, M. W.; Sparks, T. D.; Borg, C. K. H.; Seshadri, R.; Bonificio, W. D.; Clarke, D. R., *Chem. Mater.* **2013**, *25* (15), 2911-2920.
18. Rodriguez-Carvajal, J., *Physica B* **1993**, *192* (1-2), 55-69.
19. Borup, K. A.; Toberer, E. S.; Zoltan, L. D.; Nakatsukasa, G.; Errico, M.; Fleurial, J. P.; Iversen, B. B.; Snyder, G. J., *Rev. Sci. Instrum.* **2012**, *83* (12), 123902.
20. Iwanaga, S.; Toberer, E. S.; LaLonde, A.; Snyder, G. J., *Rev. Sci. Instrum.* **2011**, *82* (6), 063905.
21. de Boor, J.; Muller, E., *Rev. Sci. Instrum.* **2013**, *84* (6), 065102.
22. Platzek, D.; Karpinski, G.; Stiewe, C.; Ziolkowski, P.; Drasar, C.; Muller, E., *ICT: 2005 24th International Conference on Thermoelectrics* **2005**, 13-16.
23. Schwarz, K.; Blaha, P.; Madsen, G. K. H., *Comput. Phys. Commun.* **2002**, *147* (1-2), 71-76.
24. Perdew, J. P.; Burke, K.; Ernzerhof, M., *Phys. Rev. Lett.* **1996**, *77* (18), 3865-3868.
25. Madsen, G. K. H.; Singh, D. J., *Comput. Phys. Commun.* **2006**, *175* (1), 67-71.
26. Dismukes, J. P.; Paff, R. J.; Ekstrom, L., *J. Phys. Chem.-Us* **1964**, *68* (10), 3021-3027.
27. Ashcroft, N. W.; Mermin, N. D., *Solid state physics*, Holt: New York,, 1976; p 826.
28. Macfarlane, G. G.; McLean, T. P.; Quarrington, J. E.; Roberts, V., *Phys. Rev.* **1957**, *108* (6), 1377-1383.
29. Lautenschlager, P.; Allen, P. B.; Cardona, M., *Phys. Rev. B* **1985**, *31* (4), 2163-2171.

Appendix C.5 Investigation of the Correlation Between Stoichiometry and Thermoelectric Properties in a PtSb₂ Single Crystal

Reproduced by permission of The Royal Society of Chemistry.

Cite this: *Dalton Trans.*, 2012, **41**, 1278

www.rsc.org/dalton

PAPER

Investigation of the correlation between stoichiometry and thermoelectric properties in a PtSb₂ single crystal

Martin Søndergaard,^a Mogens Christensen,^a Lasse Bjerg,^a Kasper A. Borup,^a Peijie Sun,^b Frank Steglich^b and Bo B. Iversen^{*a}

Received 12th August 2011, Accepted 26th October 2011

DOI: 10.1039/c1dt11523e

The thermoelectric properties of a PtSb₂ single crystal containing a stoichiometric gradient were investigated. The gradient was produced by employing a Stockbarger synthesis technique. The gradient was observed through the use of spatial resolved Seebeck coefficient measurements and verified utilizing X-Ray Diffraction and Energy Dispersive X-Ray Spectroscopy. The correlation between Pt/Sb ratio and physical property parameters – Seebeck coefficient, mobility, resistivity and charge carrier concentration – was studied. Elemental analysis by Energy Dispersive X-Ray Spectroscopy, X-Ray Fluorescence and Inductively Coupled Plasma revealed Sb deficiency in the crystal, which explains the observed high charge carrier concentration and metallic properties. The transport properties were measured in the temperature range $T = 20\text{--}300\text{ K}$ on a polycrystalline sample. Furthermore, *ab initio* theoretical calculations have been conducted to support the interpretation of the measurements.

Introduction

Efficient thermoelectric materials for cryogenic applications ($T < 100\text{ K}$) are currently a significant challenge for material scientists. The efficiency of a thermoelectric material is determined by the figure of merit $zT = S^2 T / (\rho \kappa)$, where S is the Seebeck coefficient, κ is the thermal conductivity, ρ is the electrical resistivity and T is the absolute temperature. Some of the highest zT values reported at low temperatures are: $zT \approx 0.1$ at 100 K for Fe_{0.96}Ir_{0.04}Si,^{1,2} and $zT = 0.23$ at 200 K for CePd₃.³ The narrow band-gap ($\sim 6\text{--}10\text{ meV}$) compound FeSb₂ exhibits a record high Seebeck coefficient (approximately $-45\,000\text{ }\mu\text{V K}^{-1}$ at about 10 K) and a record high power factor ($\approx 2300\text{ }\mu\text{W cm}^{-1}\text{ K}^{-2}$), due to strong electron–electron correlation.^{4–6} However, the lattice thermal conductivity is too high for the compound to have a high zT value. Extensive efforts have been carried out to lower κ_L by grain boundary scattering in thin films, however, optimizing the carrier concentration has been problematic.^{7,8} Normally, a thermoelectric material should have a band gap of approximately $10 k_B T$,⁹ where T is the operating temperature. This value corresponds to a narrow band gap in the order of tens of meV for cryogenic applications.

PtSb₂ crystallizes in the pyrite structure ($a = 6.4423\text{ \AA}$)¹⁰ and has a measured band gap of $E_g = 110\text{ meV}$ at $T \approx 10\text{ K}$,¹¹ while calculations show 80 meV at 0 K .¹² This band gap is comparable

to the state of the art thermoelectric at low temperature, FeSi $E_g \approx 100\text{ meV}$.¹³ Single crystals of PtSb₂ have been reported with both metallic and semiconducting behaviour due to deviations of ideal stoichiometry.¹⁴ Semiconducting samples reach $S \approx -800\text{ }\mu\text{V K}^{-1}$ at $T \approx 30\text{ K}$,¹⁵ and rare-earth doped PtSb₂ single crystals exhibit superconductivity below 2 K .¹⁶ Undoped PtSb₂ single crystals can be n- or p-type with charge carrier concentrations extending several orders of magnitude ($10^{16}\text{--}10^{20}\text{ cm}^{-3}$) due to differences in synthesis methods and parameters.^{11,14–20} Samples of various charge carrier concentrations have been produced using synthesis methods with and without B₂O₃ liquid encapsulation.¹⁷ PtSb₂ has a high mobility due to the small Pauling electronegativity difference between Pt (2.28) and Sb (2.05).²¹ Although κ is too high for PtSb₂ to have a high zT at low temperatures, studying the material can give valuable insight into the properties of narrow band gap materials and their possible thermoelectric applications.

In the present study, the correlations between Sb/Pt content and important thermoelectric parameters such as Seebeck coefficient, mobility, resistivity and charge carrier concentration, are investigated in a large single crystal with a stoichiometric gradient. A similar approach has previously been used to study quaternary clathrate systems synthesized with elemental gradients by Czochralski pulling, where a clear correlation between stoichiometry and properties was established.²² Furthermore, the thermal transport properties have been measured at $20\text{--}300\text{ K}$ on a polycrystalline PtSb₂ sample. DFT calculations have been performed for comparison with the obtained physical properties measurements.

^aCentre for Materials Crystallography, Department of Chemistry and iNANO, University of Aarhus, DK-8000, Aarhus C, Denmark. E-mail: bo@chem.au.dk

^bMax Planck Institute for Chemical Physics of Solids, D-01187, Dresden, Germany

Experimental

Synthesis

Stoichiometric amounts of elemental Pt and Sb having a total mass of 11 g were placed in a glassy carbon crucible. Pieces of B_2O_3 were added on top of the elements as a liquid encapsulant during the synthesis. The crucible was placed in a graphite susceptor and heated to a temperature of $\sim 1400\text{ }^\circ\text{C}$ using an induction furnace. From the resulting polycrystalline ingot, a bar shaped sample was cut for thermal transport measurements. Subsequently, the ingot was crushed and placed in another glassy carbon crucible with an inner diameter of 10 mm and a pointed tip. Pieces of B_2O_3 were used as a lid. The pointy crucible was heated in the induction furnace with the temperature of the susceptor being $\sim 1400\text{ }^\circ\text{C}$. The susceptor and crucible were pulled out of the induction coil with a speed of 1 mm h^{-1} .

Spatially resolved Seebeck coefficient

A Potential Seebeck Microprobe (PSM) was employed to investigate the spatial values of the Seebeck coefficient on a polished side of the crystal.²³ Measurements were conducted at room temperature over an area of $7.8 \times 2.0\text{ mm}$ with a spacing of 0.05 mm between each measurement point.

X-Ray Diffraction

In order to determine phase purity, powder samples were filed from the top and bottom of the crystal and Powder X-Ray Diffraction (PXRD) patterns were collected on a STOE STADI P diffractometer equipped with an Imaging Plate Position Sensitive Detector and using a Cu $K_{\alpha 1}$ source in transmission geometry.

Spatially Resolved X-Ray Diffraction (XRD) was performed on a polished surface of the crystal using a Rigaku Smartlab diffractometer configured with a Cu source, parallel beam and a Ge(220) double bunch monochromator. Single peak scans of the (200) reflection were collected in steps of 0.5 mm along the pulling direction for a total length of 9 mm . The lattice parameter at each position was extracted through single peak fitting using Winplotr in the Fullprof software package.²⁴

Elemental analysis

A polished surface along the pulling direction of the crystal was investigated using Energy Dispersive X-Ray Spectroscopy (EDX) on a Nova 600 Nano SEM from FEI for quantification of the relative amounts of Pt and Sb in the crystal. An accelerating voltage of 25 keV was used and each spectrum was recorded for 100 s . The resolution was $\sim 10\text{ }\mu\text{m}$. Furthermore a small piece of the crystal was investigated with X-Ray Fluorescence (XRF) on a SPECTRO XEPOS and by Inductively Coupled Plasma (ICP) on a SPECTRO ARCOS to confirm purity and stoichiometry. Prior to the ICP measurement, the $PtSb_2$ material was crushed and dissolved in hot aqua regia.

Hall measurements

Nine slices were cut orthogonally to the pulling direction of the crystal with thicknesses of approximately 1 mm . These slices were used for measurements of specific resistivity, Hall coefficient,

charge carrier concentration and mobility at room temperature. The samples were measured on an in-house system employing the van der Pauw method in a 1.25 T magnetic field and optimized for doped semiconductors and high resistivity metals.²⁵

Physical properties

The transport properties were measured in a Quantum Design Physical Properties Measurement System (PPMS) from $20\text{--}300\text{ K}$ on a sample from the polycrystalline ingot. Conducting epoxy was used for mounting Cu-wires onto the samples. Resistivity, thermal conductivity and Seebeck coefficient were measured using a 4-point probe technique under quasi steady-state conditions employed by the thermal transport option (TTO) for the PPMS.²⁶

Theoretical calculations

The electronic band structure of $PtSb_2$ was calculated using the Density Functional Theory (DFT) package WIEN2k with the Engel-Vosko functional.^{27,28} RK_{\max} was set to 7.5 and self consistency was achieved on $10 \times 10 \times 10 k$ -grid. The band structure was then calculated on a $33 \times 33 \times 33 k$ -grid, and from the band structure, the Seebeck coefficient was calculated for different charge carrier concentrations using a rigid band approach and Boltzmann's transport equations. The program BoltzTraP was used for these calculations.²⁹

Results and discussion

X-Ray Diffraction

Powder X-Ray Diffraction patterns collected from samples taken from the top and bottom of the crystal revealed only the $PtSb_2$ phase (see Fig. 1). The spatially resolved X-Ray Diffraction measurements from the polished surface revealed only the (200)-reflection at $2\theta \approx 27.69^\circ$, which supports the sample being a single crystal. The reflection was displaced in 2θ along the pulling direction from $27.477(8)^\circ$ in the bottom to $27.762(2)^\circ$ in the top. The calculated lattice parameter, a , as function of distance to the top, is shown in Fig. 2 and decreases almost linearly from $6.487(3)\text{ \AA}$ in the top to $6.422(1)\text{ \AA}$ in the bottom. The inset shows the data

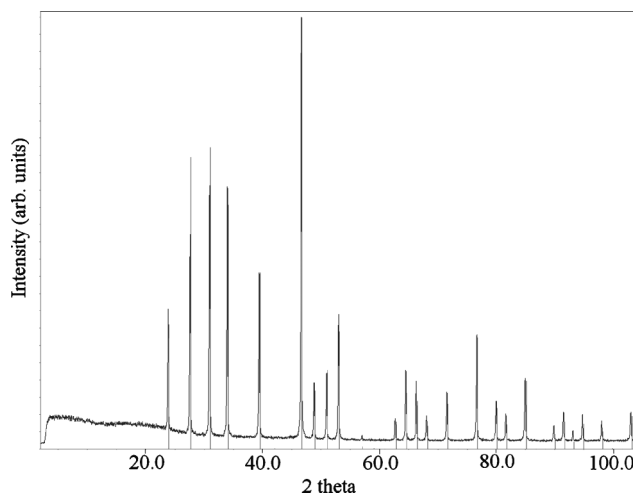


Fig. 1 Powder X-Ray Diffraction pattern of a powdered sample from the crystal. The vertical lines are from the ICSD.

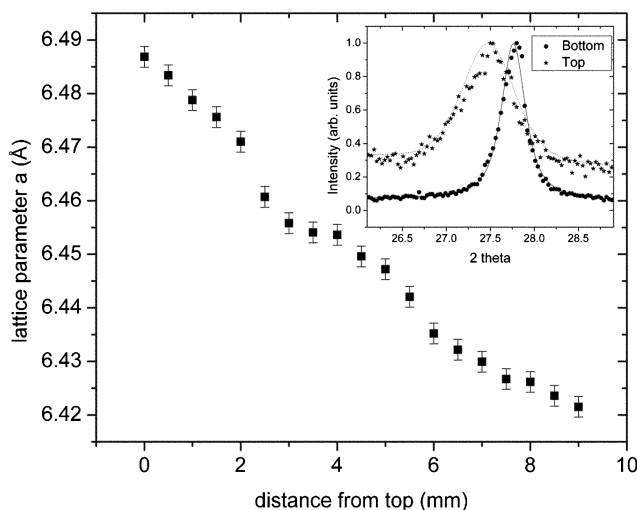


Fig. 2 Lattice parameter *versus* distance from the top of the PtSb_2 single crystal.

and fitted curves to the two extreme points in the top and bottom of the crystal. The relative change in lattice parameter over the distance of 9 mm corresponds to approximately 1%. For a normal solid solution following Vegard's law,³⁰ this is roughly equal to a change in the stoichiometric ratio of ~1 atomic%. The literature values on the lattice parameter are $a = 6.44 \text{ \AA}$.^{10,31,32} As Sb is larger than Pt, the decreasing unit cell size from the top towards the bottom implies an increase in Pt/Sb ratio from top to bottom.

Elemental analysis

The results on the Energy Dispersive X-Ray Spectroscopy measurements along the pulling directions are shown in Fig. 3. The relative amount of Sb is virtually identical from the top (64.9(3)% to the bottom (63.9(3)%). At the pointed tip in the very bottom, the sample did not look homogeneous and EDX measurements revealed Sb contents close to the ideal stoichiometry (66.6%), and even slightly above (up to 67.5(3)%). However, the main part of the sample studied here was Sb-deficient compared with the stoichiometry of PtSb_2 . This implies that some Sb has evaporated during the synthesis, or Sb-rich areas are found in the top or

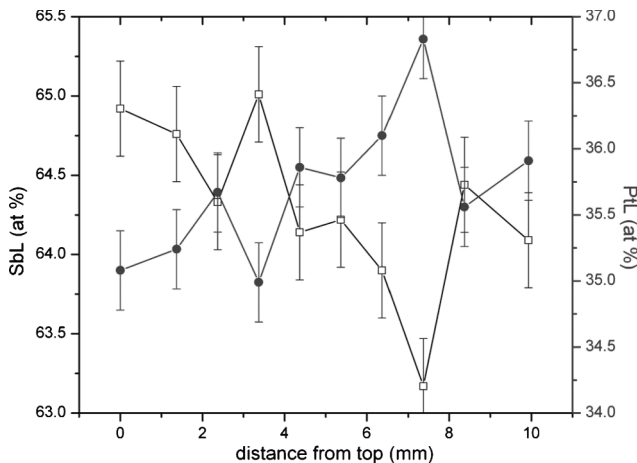


Fig. 3 Results from EDX measurements from the top towards the bottom of the crystal. The hollow circles are SbL, while the filled are PtL.

bottom parts of the crystal, which have not been measured. Estimates of the uncertainties are based on probing on various spots at the same distance from the top. Large fluctuations in the apparent trend are observed. This could be due to the fact that the area probed is rather small compared to the XRD data and the EDX measurements are therefore more sensitive to local variations in the atomic contents.

XRF and ICP measurements on a sample approximately 2 mm from the top revealed no significant amounts (<3 ppm) of other elements than Pt and Sb. The Sb-content was determined by XRF and ICP to be 62.5(3)% compared with the 64.5(3)% determined by the EDX measurement. This will be commented on later in the PSM results section. All three techniques agree on the Sb-deficiency compared with the ideal stoichiometry of 66.6 atomic%. This could be due to an extended phase width of PtSb_2 . The most recent phase diagram describes PtSb_2 as a line phase.³³ In other studies, typical growth rates of single PtSb_2 single crystals have been 5–50 mm h⁻¹,^{17–19,34} while the crystal produced in this work was grown at a rate of 1 mm h⁻¹. Additionally, the Stockbarger method in a vertical setup is more influenced by gravity than the Czochralski method, as more of the heavy Pt atoms go to the bottom of the melt. This could give rise to a more Pt-rich phase crystallizing first.

Potential Seebeck microprobe

In PSM measurements on the edge of the crystal, the Seebeck coefficient changes gradually from ~10 $\mu\text{V K}^{-1}$ in the bottom of the crystal to approximately -50 $\mu\text{V K}^{-1}$ at a distance of 4 mm from the top of the crystal (see Fig. 4). This is in accordance with the suspected more metallic behavior of a Pt-rich sample in the bottom. The majority charge carriers change from electrons to holes when going from top to bottom of the crystal. Observations of local inhomogeneities on the micrometer scale are in accordance with the observed stoichiometry values extracted from EDX measurements. Subsequent to cutting the crystal in slices for the

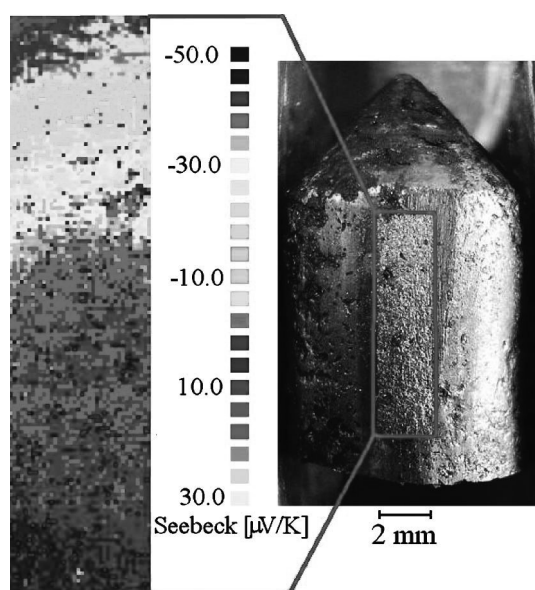


Fig. 4 Potential Seebeck microprobe measurements along the pulling direction of the crystal.

Hall measurements, PSM measurements were conducted on the slices orthogonal to the pulling direction. These measurements revealed a gradient from the edge towards the centre of the crystal. Two examples are shown in Fig. 5 for a slice from the bottom (right) and one approximately 5 mm from the top (left). The Seebeck coefficient changes gradually from $-44 \mu\text{V K}^{-1}$ at the edge to $-60 \mu\text{V K}^{-1}$ in the centre of the rod. In the bottom sample the changes are larger, with a gradient from $50 \mu\text{V K}^{-1}$ at the edge to $-40 \mu\text{V K}^{-1}$ in the centre. This is an indication of gradual crystallization from the edges towards the centre of the melt during the pulling. The inhomogeneities in the cross section could explain the discrepancy between EDX, XRF and ICP measurements, as the EDX-measurements are from the edge of the crystal, while XRF was on the cross section of a crystal slice and the ICP was from a small piece near the centre of a slice.

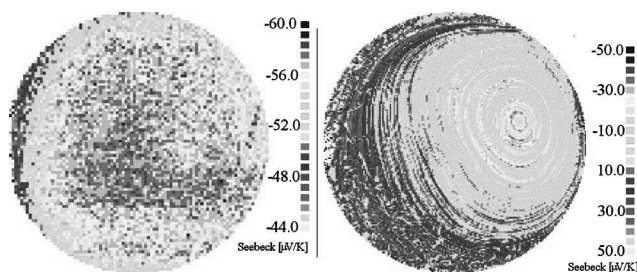


Fig. 5 PSM scans orthogonal to the pulling direction of the crystal. To the left a sample from the middle section (resolution 0.1 mm), to the right a sample from the bottom of the crystal (resolution 0.05 mm).

Hall measurements

The results from the Hall measurements on the slices with varying distance from the top are shown in Fig. 6–8. The measured charge carrier concentration decreases from the top of the crystal ($1.16 \times 10^{20} \text{ cm}^{-3}$) towards the bottom ($\sim 7.3 \times 10^{19} \text{ cm}^{-3}$). This heavy doping is most likely due to Sb-vacancies as the elemental analysis techniques revealed no presence of impurity dopants. The sign of the Hall coefficient was negative for all samples, indicating electrons as the main charge carriers. This is in accordance with expectations for an Sb-deficient sample.¹⁶ The trend of decreasing

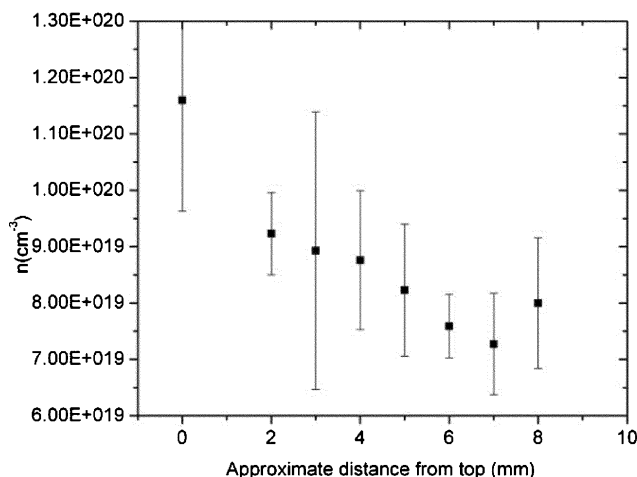


Fig. 6 Charge carrier concentration versus approximate distance from the top.

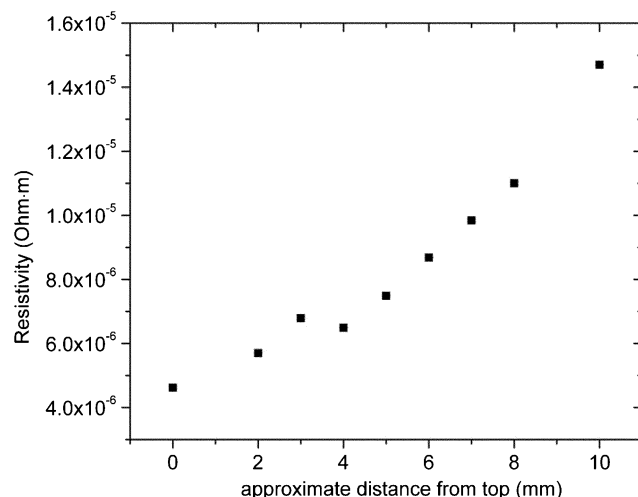


Fig. 7 Electrical resistivity versus approximate distance from the top.

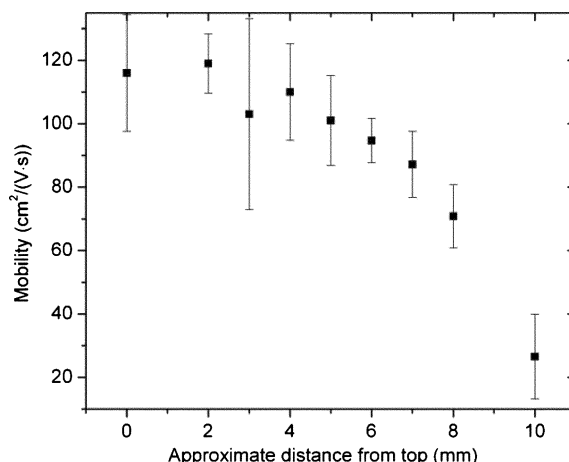


Fig. 8 Electron mobility versus approximate distance from the top.

charge carrier concentration towards the bottom is in accordance with the increase of the Seebeck coefficient measured by PSM. The resistivity of the samples (Fig. 7) increases with the decreasing carrier concentration from $4.62 \times 10^{-6} \Omega\text{m}$ in the top to $14.70 \times 10^{-6} \Omega\text{m}$ in the bottom. These values are comparable to literature values.^{11,15,16,18} Additionally, the mobility is seen to decrease from $119 \text{ cm}^2 \text{ V}^{-1} \text{ s}^{-1}$ in the top to $27 \text{ cm}^2 \text{ V}^{-1} \text{ s}^{-1}$ in the bottom. These values are also comparable to literature values, considering the large charge carrier concentration. The electron mobility is lower than the electron-hole mobility and for low charge carrier concentrations (10^{16} – 10^{17} cm^{-3}) an electron mobility of $\sim 3000 \text{ cm}^2 \text{ V}^{-1} \text{ s}^{-1}$ at 77 K is reported,¹⁵ while the hole mobility can reach $c. 6000 \text{ cm}^2 \text{ V}^{-1} \text{ s}^{-1}$ at 77 K.¹¹ At room temperature the electron mobility is reported to be from one to a few hundred $\text{cm}^2 \text{ V}^{-1} \text{ s}^{-1}$.^{15,18}

The calculated band structure is shown in Fig. 9. Qualitative agreement was found with a band structure previously calculated using a tight-binding approach.¹² However, the material was predicted to be a semimetal. Calculations of the Seebeck coefficient from DFT and Boltzmann's transport equations, resulted in values ranging from $S = -70 \mu\text{V K}^{-1}$ for $n = 10^{20} \text{ cm}^{-3}$ to $S = -60 \mu\text{V K}^{-1}$ for $n = 7 \times 10^{19} \text{ cm}^{-3}$ at 300 K (see Fig. 10). The values and the trend correspond well to the measured values of S and n , however,

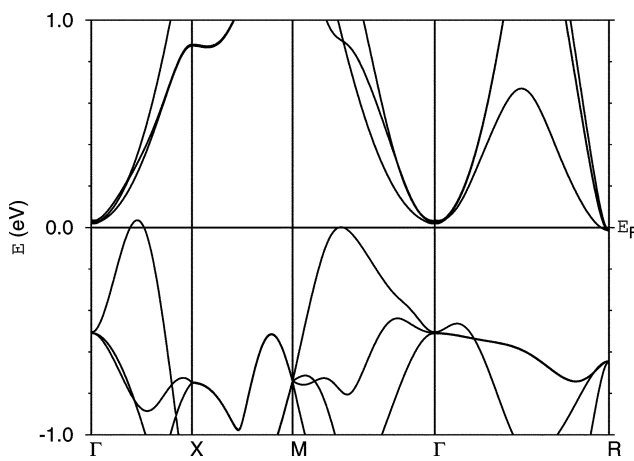


Fig. 9 Calculated band structure of PtSb_2 .

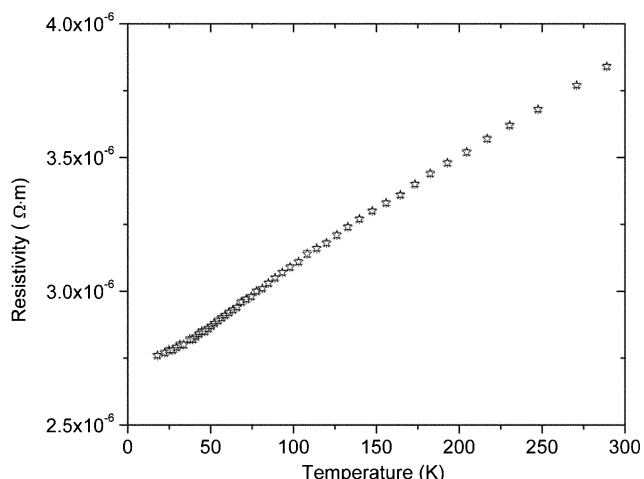


Fig. 11 Resistivity *versus* temperature for a polycrystalline sample.

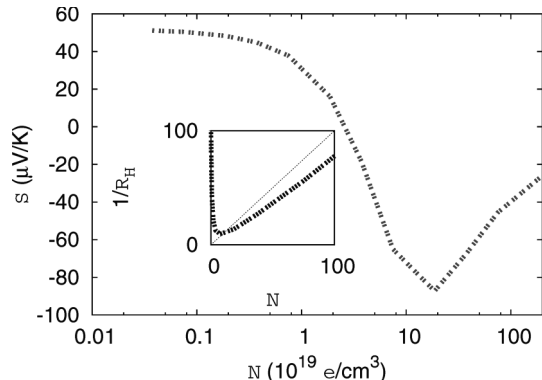


Fig. 10 Calculated Seebeck coefficient *versus* charge carrier concentration.

it is important to keep in mind the inhomogeneity of the slices with respect to the Seebeck coefficient.

Thermal transport

The results of the thermal transport measurements on the sample from the polycrystalline ingot are shown in Fig. 11–13. The sample showed metallic behavior, as the resistivity increased with increasing temperature. The Seebeck coefficient is $-68 \mu\text{V K}^{-1}$ at 300 K, and does not reach high absolute values at low temperatures. The relatively low numerical value of the Seebeck coefficient compared with the value reported by Dargys and Kundrotas¹⁵ is in agreement with the larger carrier concentration. Large changes in the Seebeck coefficient are also observed in FeSb_2 , when the carrier concentration is varied.^{7,8} The thermal conductivity has a peak at low temperature characteristic for metallic samples and it is significantly lower than the values reported by Abdullaev *et al.* ($39 \text{ W K}^{-1} \text{ m}^{-1}$ at 300 K),²⁰ which can be explained by the deviating stoichiometry of our sample. The value of the thermal conductivity measured here is $20 \text{ W K}^{-1} \text{ m}^{-1}$ at room temperature. This gives a rather low figure of merit, $zT \approx 0.001$ at 80 K, which can be compared with the value of 0.007 for undoped FeSi at 60 K.²

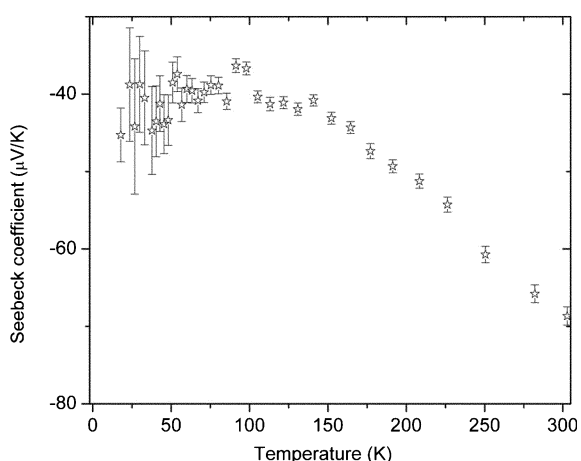


Fig. 12 Seebeck coefficient *versus* temperature for a polycrystalline sample.

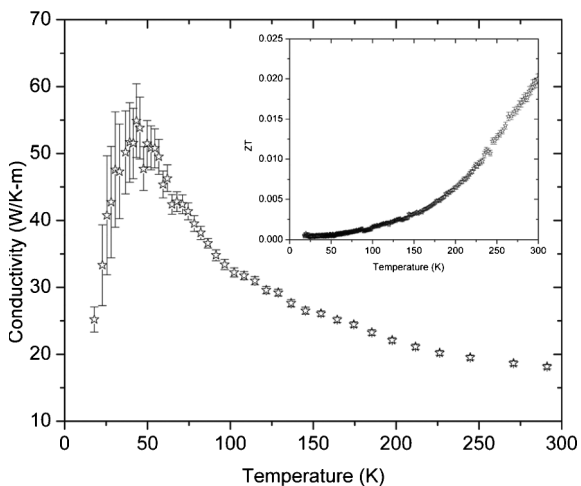


Fig. 13 Thermal conductivity and zT (inset) for a polycrystalline sample.

Conclusions

A large PtSb_2 single crystal was grown by the Stockbarger method. The crystal contained a stoichiometric gradient along the pulling direction. Elemental analysis determined the crystal to be

Sb-deficient and combined X-Ray Diffraction and Energy Dispersive X-Ray Spectroscopy suggested the Sb-content decreased by ≈ 1 at% from 65% in the top to 64% in the bottom. The gradient in Pt/Sb ratio was reflected in the physical properties: due to increasing Sb-vacancies from the top towards the bottom of the crystal, the charge carrier concentration decreased along with the mobility, while the resistivity and Seebeck coefficient increased. Thermal transport measurements of a polycrystalline sample was measured from 20–300 K and revealed metallic properties of the samples. The zT -value is below 0.03 in the entire temperature range due to a high thermal conductivity.

Acknowledgements

This work was supported by the Danish National Research Foundation (Center for Materials Crystallography), and the Danish Strategic Research Council (Center for Energy Materials).

References

- B. C. Sales, E. C. Jones, B. C. Chakoumakos, J. A. Fernandezbaca, H. E. Harmon, J. W. Sharp and E. H. Volckmann, *Phys. Rev. B: Condens. Matter*, 1994, **50**, 8207.
- B. C. Sales, O. Delaire, M. A. McGuire and A. F. May, *Phys. Rev. B*, 2011, **83**, 7.
- G. D. Mahan, B. C. Sales and J. Sharp, *Phys. Today*, 1997, **50**, 42.
- A. Bentien, S. Johnsen, G. K. H. Madsen, B. B. Iversen and F. Steglich, *Europhys. Lett.*, 2007, **80**, 17008.
- P. Sun, M. Sondergaard, Y. Sun, S. Johnsen, B. B. Iversen and F. Steglich, *Appl. Phys. Lett.*, 2011, **98**, 072105.
- P. Sun, N. Oeschler, S. Johnsen, B. B. Iversen and F. Steglich, *Dalton Trans.*, 2010, **39**, 1012.
- Y. Sun, S. Johnsen, P. Eklund, M. Sillassen, J. Bottiger, N. Oeschler, P. Sun, F. Steglich and B. B. Iversen, *J. Appl. Phys.*, 2009, **106**, 4.
- Y. Sun, E. Zhang, S. Johnsen, M. Sillassen, P. Sun, F. Steglich, J. Bottiger and B. B. Iversen, *J. Phys. D-Appl. Phys.*, 2010, **43**, 5.
- J. O. Sofo and G. D. Mahan, *Phys. Rev. B: Condens. Matter*, 1994, **49**, 4565.
- N. E. Brese and H. G. von Schnering, *Z. Anorg. Allg. Chem.*, 1994, **620**, 393.
- R. A. Reynolds, M. J. Brau and R. A. Chapman, *J. Phys. Chem. Solids*, 1968, **29**, 755.
- P. R. Emtage, *Phys. Rev.*, 1965, **138**, A246.
- O. Delaire, K. Marty, M. B. Stone, P. R. C. Kent, M. S. Lucas, D. L. Abernathy, D. Mandrus and B. C. Sales, *Proc. Natl. Acad. Sci. U. S. A.*, 2011, **108**, 4725.
- D. H. Damon, R. C. Miller and P. R. Emtage, *Phys. Rev. B: Solid State*, 1972, **5**, 2175.
- A. Dargys and J. Kundrotas, *J. Phys. Chem. Solids*, 1983, **44**, 261.
- M. C. Bennett, M. C. Aronson, D. A. Sokolov, C. Henderson and Z. Fisk, *J. Alloys Compd.*, 2005, **400**, 2.
- R. A. Laudise, W. A. Sunder, R. L. Barns, G. W. Kammlott, A. F. Witt and D. J. Carlson, *J. Cryst. Growth*, 1990, **102**, 21.
- C. T. Elliott and S. E. R. Hiscocks, *J. Mater. Sci.*, 1968, **3**, 174.
- P. M. Nikolic, S. S. Vujatovic, D. M. Todorovic, M. B. Miletic, A. Golubovic, A. I. Bojicic, F. Kermendi, S. Duric, K. T. Radulovic and J. Lazar, *Jpn. J. Appl. Phys.*, 1997, **36**(Part 1, No. 3A), 1006.
- A. A. Abdullaev, L. A. Angelova, V. K. Kuznetsov, A. B. Ormont and Y. I. Pashintsev, *Phys. Status Solidi A*, 1974, **21**, 339.
- G. A. Slack, in, DM Rowe (ed.) *CRC Handbook of Thermoelectrics*, CRC Press, Boca Raton, FL, 1995, pp. 407.
- M. Christensen, S. Johnsen, M. Sondergaard, J. Overgaard, H. Birkedal and B. B. Iversen, *Chem. Mater.*, 2009, **21**, 122.
- D. Platzek, G. Karpinski, C. Stiewe, P. Ziolkowski, C. Drasar and E. Muller, in Potential-Seebeck-microprobe (PSM): measuring the spatial resolution of the Seebeck coefficient and the electric potential, IEEE, Piscataway, NJ 08855-1331, USA, 2005, p.13.
- T. Roisnel and J. Rodriguez-Carvajal, *Mater. Sci. Forum*, 2001, **378–381**, 118.
- L. J. v. d. Pauw, *Philips Research Reports*, 1958, **13**, 1.
- O. Maldonado, *Cryogenics*, 1992, **32**, 908.
- P. Blaha, K. Schwarz, G. K. H. Madsen, D. Kvasnicka and J. Luitz, in, *An augmented plane wave plus local orbitals program for calculating crystal properties*, Vienna University of Technology, Austria, 2001.
- E. Engel and S. H. Vosko, *Phys. Rev. B: Condens. Matter*, 1993, **47**, 13164.
- G. K. H. Madsen and D. J. Singh, *Comput. Phys. Commun.*, 2006, **175**, 67.
- A. R. Denton and N. W. Ashcroft, *Phys. Rev. A: At., Mol., Opt. Phys.*, 1991, **43**, 3161.
- S. Furuseth, K. Selte and A. Kjekshus, *Acta Chem. Scand.*, 1965, **19**, 735.
- L. Thomassen, *Z. Phys. Chem. B-Chem. E.*, 1929, **2**, 349.
- V. P. Itkin and C. B. Alcock, *J. Phase Equilib.*, 1996, **17**, 356.
- R. C. Miller, D. H. Damon and A. Sagar, *J. Appl. Phys.*, 1964, **35**, 3582.

**Appendix C.6 Thermoelectric Properties of the Entire Composition Range in
 $Mg_2Si_{0.9925-x}Sn_xSb_{0.0075}$**

Reproduced with permission from Springer.

Thermoelectric Properties of the Entire Composition Range in $Mg_2Si_{0.9925-x}Sn_xSb_{0.0075}$

M. SØNDERGAARD,¹ M. CHRISTENSEN,^{1,2} K.A. BORUP,¹ H. YIN,¹ and B.B. IVERSEN¹

1.—Department of Chemistry and iNANO, Centre for Materials Crystallography and Centre for Energy Materials, Aarhus University, 8000 Aarhus C, Denmark. 2.—e-mail: mch@chem.au.dk

Eleven samples of nominal composition $Mg_{2.2}Si_{0.9925-x}Sn_xSb_{0.0075}$ with $x = 0, 0.1, 0.2, 0.3, 0.4, 0.5, 0.6, 0.7, 0.8, 0.9, 0.9925$ were prepared by induction melting, ball milling, and spark plasma sintering. Hall effect, resistivity, Seebeck coefficient, and thermal conductivity measurements were conducted from room temperature to 400°C. Six of the samples were investigated for thermal stability by measuring powder x-ray diffraction while heating to 400°C. All samples were stable in air during the ~12-h-long data collection, except for $Mg_{2.2}Sn_{0.9925}Sb_{0.0075}$, which showed development of an elemental Sn phase after heating. The lattice parameter of each sample was extracted through Rietveld refinement and revealed a linear dependency on nominal composition. Measurement of top and bottom of the pellets exhibited systematic differences in lattice parameter and Seebeck coefficient, indicating that stoichiometry gradients are created during sintering.

Key words: Thermoelectric, $Mg_2Si_{1-x}Sn_x$, thermal stability, functionally graded materials

INTRODUCTION

The efficiency of thermoelectric materials depends on material-specific parameters summarized in the dimensionless figure of merit, zT :

$$zT = \frac{S^2}{\kappa\rho}T,$$

where S is the Seebeck coefficient, κ is the thermal conductivity, T is the absolute temperature, and ρ is the electrical resistivity. For commercial interest, a zT of unity or above is desired over an extended temperature range.^{1–3} In recent years the $Mg_2Si_{1-x}Sn_x$ compounds have been investigated intensively for potential mid-temperature (300°C to 550°C) thermoelectric energy conversion.^{4–12} In contrast to state-of-the-art thermoelectrics in this temperature range, the $Mg_2Si_{1-x}Sn_x$ compounds consist of earth-abundant and environmentally benign elements. The best compounds reported have Sn contents between

$x = 0.3$ to 0.7 and are n -doped with Sb to reach charge carrier concentrations of $1 \times 10^{20} \text{ cm}^{-3}$ to $3 \times 10^{20} \text{ cm}^{-3}$. These compounds reach zT values of 1 and above from 250°C to 530°C.¹¹ Zaitsev et al.^{4,5} reported on the end-members of the solid solution, Mg_2Si and Mg_2Sn , having both light and heavy conduction bands with the light being the lowest for Mg_2Si and vice versa for the Mg_2Sn , and the possibility for band convergence in the solid solutions. Recently, Liu et al.¹¹ reported on the convergence of the conduction bands for Sn contents in the range 0.65 to 0.7. This convergence was reflected in the higher numerical Seebeck coefficient of the samples. The method of fabrication can result in large deviations of the performance of the materials; e.g., Liu et al.¹³ investigated the importance of excess Mg content. Due to the large difference in melting points between the constituent elements and the high vapor pressure of Mg, the stoichiometry can be challenging to control. Therefore, several synthesis methods have been suggested, including liquid encapsulation,⁸ solid-state reaction,⁹ direct spark plasma sintering synthesis,¹⁴ and mechanical alloying.¹⁵ The solid solution of $Mg_2Si_{1-x}Sn_x$ has been reported to contain

a miscibility gap in the phase diagram;¹⁶ however, as the splitting of the phases is a slow process, several reports on the compounds inside the immiscibility region exists.^{8,11,17} In another recent study we investigated the influence of SPS processing on gravity-induced stoichiometric gradients in $x = 0.6$ and 0.4 compounds.¹⁸ A more Mg_2Sn -rich $Mg_2Si_{1-x}Sn_x$ -phase was systematically present in the bottom of the pellets, while the top contained a more Mg_2Si -rich $Mg_2Si_{1-x}Sn_x$ -phase. This splitting was attributed to the tendency of the system to phase separate and the relatively large difference in density between the phases. In the present study the straightforward processing method of induction melting followed by ball milling and spark plasma sintering was employed to obtain the entire composition range $Mg_2Si_{1-x}Sn_x$ with nominal doping of 7500 ppm Sb. Measurements of thermoelectric properties were conducted from room temperature to 400°C, and thermal stability was investigated by employing powder x-ray diffraction during heating to 400°C. Furthermore, Rietveld refinement is employed to extract the thermal expansion coefficients.

EXPERIMENTAL PROCEDURES

Synthesis and Processing

The pure elements (Mg, 99.98%; Si, 99.9+%; Sn, 99.97%; Sb, 99.5%) were mixed according to the stoichiometry $Mg_{2.2}Si_{0.9925-x}Sn_xSb_{0.0075}$ with $x = 0, 0.1, 0.2, 0.3, 0.4, 0.5, 0.6, 0.7, 0.8, 0.9, 0.9925$ in Al_2O_3 crucibles, covered by lids, and reacted in an induction furnace under He pressure of 100 psi. The susceptor temperature was measured by pyrometer to ca. 1400°C. The total heating time was less than 15 min. The ingots were processed by ball milling followed by spark plasma sintering (SPS). To obtain dense and stable pellets with thickness ~3 mm the following procedure was employed: An initial pressure of 75 MPa was applied at room temperature. The sample was heated in 15 min to 650°C to 750°C (higher temperatures for higher Si contents). The temperature was held for 10 min; in the last 4 min the SPS pressure was reduced to 20 MPa to release strain. Finally, the sample was cooled to 200°C in 10 min, before the power was switched off. To protect the graphite matrix and punches, graphite paper was used inside the die and on the ends of the punches. The graphite paper was removed and the surfaces of the pellets polished prior to physical and structural characterization.

Structural Properties

Powder x-ray diffraction (PXRD) was conducted on both sides of all pellets utilizing a Rigaku Smartlab diffractometer configured with a Cu source and parallel beam optics. The lattice parameter of the main phase in each sample was extracted through Rietveld refinement employing the FullProf software package.¹⁹ For the high-temperature measurements,

the equipment and samples were shielded by a graphite dome and measured in air. Data were collected at intervals of 50°C from room temperature to 400°C and again at room temperature after the heating. At each temperature three datasets of ca. 23 min per diffraction pattern were collected to test if the pellet was stable over time at each temperature.

Physical Properties

Physical properties were measured on all samples from room temperature to 400°C. Measurements of the electrical resistivity, Hall carrier concentration and mobility were conducted on an in-house system employing the van der Pauw method²⁰ in a magnetic field of 1.25 T. The thermal conductivity values were calculated from the thermal diffusivity and the specific heat measured on a Netzsch LFA 457 laser flash apparatus and the density (measured by the Archimedes method). A standard pyroceram 9606 sample was employed as reference for calculations of the specific heat capacity. The Seebeck coefficient was measured using an in-house system, similar to the one reported by Iwanaga et al.²¹ Spatially resolved Seebeck coefficient measurements were performed at room temperature utilizing a potential Seebeck microprobe (PSM).²² The top and bottom surfaces of all pellets were scanned by PSM.

RESULTS AND DISCUSSION

Structural Properties

Diffractograms from the top and bottom of all pellets are depicted in Fig. 1. Some of the samples contained minute amounts of a MgO impurity, and the samples with $x = 0.1$ to 0.5 had several peaks indicating multiple phases. Furthermore, the most Sn-rich samples ($x = 0.9$ and $x = 0.9925$) showed Sn impurities on both sides of the pellets. Through the series a broadening of the peaks between $x = 0.3$ and 0.7 is observed, probably due to the presence of several phases. This range corresponds well to the miscibility gap reported by Jung et al.¹⁶ The lattice parameters of the main phases of all samples were extracted through Rietveld refinement of the data and are shown in Fig. 2. The error on each data point is on the order of 10^{-4} Å. Refinement results from the bottom side of the pellets are presented in Table I. The lattice parameters are seen to obey Vegard's law for all compositions. As previously reported for compounds with $x = 0.4$ and 0.6 ,¹⁸ SPS processing results in the top of the pellets being more Mg_2Si rich and the bottom being more Mg_2Sn rich. The lattice parameter for $x = 0.9925$ is identical to the value reported by Zaitsev et al.⁴ (6.765 Å), while the value for the $x = 0$ compound concurs with the previously reported 6.352 Å.^{4,23} The discrepancy in the lattice parameter between the top and bottom is reflected in the discrepancy of the Seebeck coefficient between the top and bottom of most of the

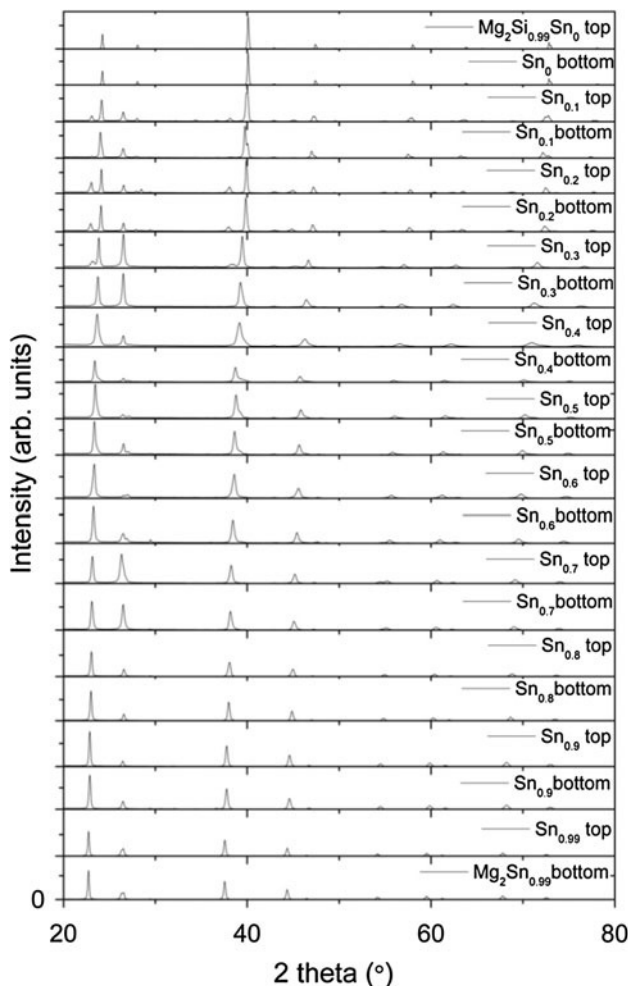


Fig. 1. Powder x-ray diffractograms for top and bottom of all $Mg_2Si_{1-x}Sn_x$ samples. The intense peak for $x = 0.7$ and 0.3 at 26.5° is from graphite paper not completely removed from the pellets prior to diffraction characterization.

samples. The errors on the Seebeck coefficient measurements are on the order of $1 \mu\text{V/K}$. The differences in Seebeck coefficient between top and bottom are approximately $10 \mu\text{V/K}$ to $20 \mu\text{V/K}$, in accordance with previous observations.¹⁸ However, the Sn-rich samples ($x = 0.9$ and 0.9925) do not show significant splitting of the lattice parameter, yet the Seebeck coefficient is different from top to bottom. This could be due to differences in the amount of Sn impurities observed in these samples. The Si-rich samples with $x = 0$ and 0.2 show almost no difference in lattice parameter and Seebeck coefficient between the top and bottom of the pellets. The relative difference between the densities of Mg_2Si (1.88 g/cm^3) and Mg_2Sn (3.59 g/cm^3) and the tendency of the system to phase separate are the most probable reasons for the observed trend of the top and bottom of the pellets. The ability to create a compositional gradient in these materials could be useful to produce functionally graded thermoelectric materials. If the materials are to be

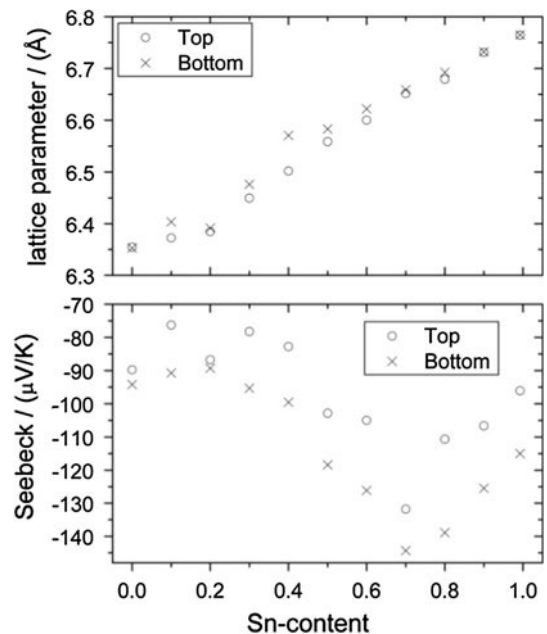


Fig. 2. Top: Extracted lattice parameters for the top and bottom sides of all pellets. Bottom: Average Seebeck coefficients on top and bottom surfaces of all pellets.

utilized in thermoelectric modules for energy harvesting, it will be important to turn the more Si-rich side of the pellet towards the hot end due to its higher performance and durability at higher temperatures. Furthermore, if the hot side is below the cold side in an operating module, the Sn could in time diffuse to the bottom and thus degrade the performance and durability of the module.

The PXRD measurements at elevated temperatures of the pellets with compositions $x = 0, 0.2, 0.4, 0.6, 0.8$, and 0.9925 revealed thermal stability of all pellets for several hours up to 400°C , except for $x = 0.9925$, for which an increasing amount of Sn impurity was observed. Furthermore, after several weeks at ambient conditions, the pellet had cracked and some of it turned into a black powder. The $x = 0.4$ and 0.6 compositions were studied in pellet and powder form for thermal stability in a recent report, revealing significant difference between the thermal stability of powder and pellets of the same material.²⁴ The $x = 0.4$ sample showed a tiny shoulder to the main phase at a lower angle after heating; however, it was too small to be quantified by Rietveld refinement. The remainder of the samples only exhibited a thermal shift of the peaks with no evolution of other phases. From Rietveld refinement of the diffractograms at each temperature step, the thermal expansion coefficients at 300 K were calculated (Table I). The Si-rich samples had thermal expansion coefficients around $1.6 \times 10^{-5}/\text{K}$ while the Sn-rich samples have larger coefficients of approximately $1.8 \times 10^{-5}/\text{K}$. The thermal expansion coefficient of pure Si is $0.3 \times 10^{-5}/\text{K}$ and that for Sn is $2.3 \times 10^{-5}/\text{K}$. Due to the relatively small

Table I. Density, linear thermal expansion coefficient at 300 K, unit cell, and reliability factors extracted from Rietveld refinement of the bottom of the pellets

Sn content	0	0.1	0.2	0.3	0.4	0.5	0.6	0.7	0.8	0.9	0.9925
ρ (g/cm ³)	1.82(10)	2.20(10)	2.30(10)	2.64(10)	2.79(10)	2.80(10)	3.01(10)	3.17(10)	3.18(10)	3.35(10)	3.56(10)
α_{300K} (10 ⁻⁵ K ⁻¹)	1.64(2)	—	1.64(2)	—	1.60(2)	—	1.76(2)	—	1.88(2)	—	1.79(2)
Unit cell (Å)	6.3546(2)	6.4037(2)	6.3915(3)	6.4761(2)	6.5705(3)	6.5831(2)	6.6218(3)	6.6590(1)	6.6927(1)	6.7311(1)	6.7644(1)
R_F (%)/ R_p (%)	5.5/8.6	7.3/28.1	24.8/27.4	8.1/16.4	7.8/25.2	5.7/16.2	6.5/19.5	4.4/14.1	4.3/7.9	3.5/8.9	3.0/8.0

All data contained 22 Bragg reflections and 12 parameters, were used in the refinements.

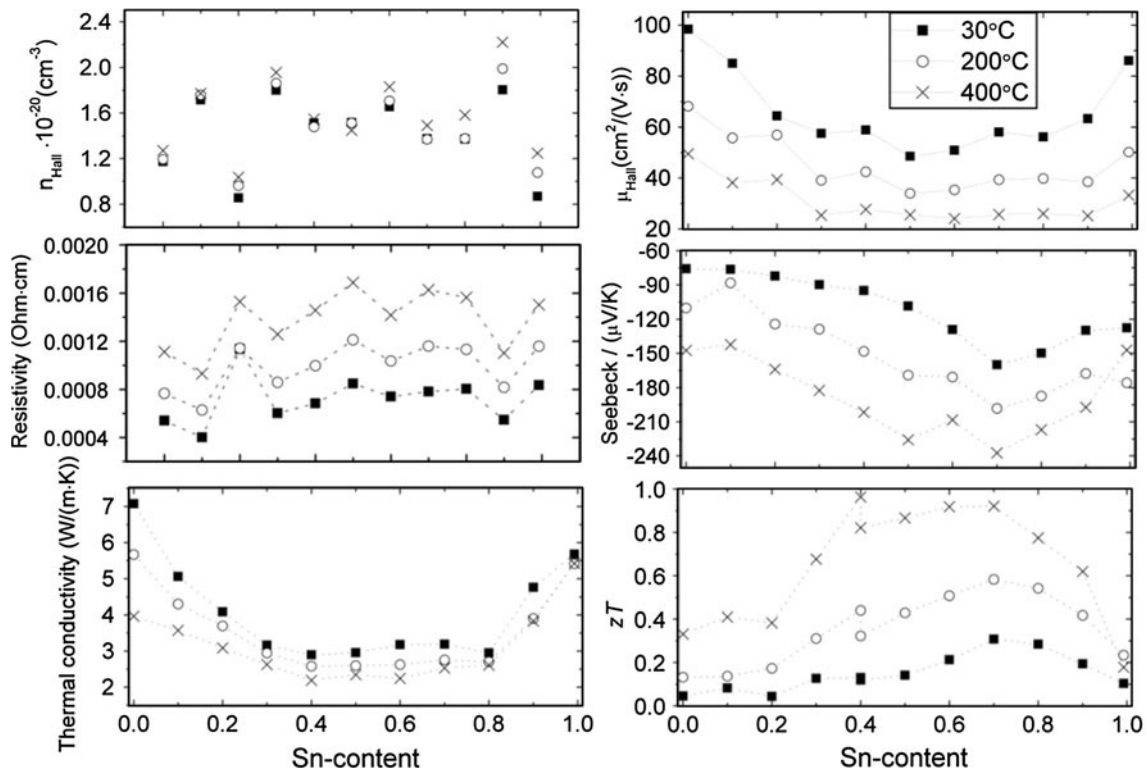


Fig. 3. Transport properties of all samples from room temperature to 400°C. Top left: Hall charge carrier concentration. Top right: Hall mobility. Middle left: Electrical resistivity. Middle right: Seebeck coefficient. Bottom left: Thermal conductivity. Bottom right: Thermoelectric figure of merit.

difference between the lattice parameters at the top and bottom of the pellets, the thermal expansion coefficients should not differ significantly between the top and bottom of the pellets.

Physical Properties

The densities of all samples were close to the theoretical value, increasing approximately linearly with increasing Sn content (Table I). Figure 3 depicts selected isotherms at 30°C, 200°C, and 400°C of all the physical properties as functions of Sn content. The Hall charge carrier concentrations differ significantly between the samples. While most samples have values from ca. $1.4 \times 10^{20} \text{ cm}^{-3}$ to $1.8 \times 10^{20} \text{ cm}^{-3}$, the compositions $x = 0.2$ and 0.9925 reach values as low as $0.8 \times 10^{20} \text{ cm}^{-3}$ at 30°C. A charge

carrier density of ca. $1.8 \times 10^{20} \text{ cm}^{-3}$ should be the optimal.¹¹ These variations in the Hall carrier concentration demonstrate the problems of reproducing results in this system with the method used in this work. The discrepancies are probably due to Sb evaporation during synthesis. The difference in Hall measurements on a sample when turned upside down was less than the standard uncertainty. The error on each measurement is ca. 10%. For most samples the Hall carrier concentration increases when the temperature reaches 400°C, however for $x = 0.1, 0.4$, and 0.5 the values are constant within the uncertainties. For all samples the Hall mobility decreased with temperature due to enhanced electron–phonon scattering. A minimum in the mobilities is observed in the composition range $x = 0.3$ to 0.9 due to alloy scattering in the isoelectronic solid

solutions. The values concur with results reported in the literature.^{4,11,12}

All samples exhibit metallic behavior with approximately linear increase in resistivity with temperature. However, the sample with $x = 0.2$ showed semiconducting behavior from room temperature to 140°C, in agreement with the low Hall carrier concentration of this sample. At room temperature the minimum resistivity is ~ 0.4 mΩ cm for $x = 0.1$, and at 400°C the maximum is ~ 1.7 mΩ cm for $x = 0.5$. The error on each data point is ca. 5%. The dependency of the Seebeck coefficients of all samples on temperature is approximately linear, in accordance with the Mott formula. For all samples the numerical Seebeck coefficient increases from room temperature to 400°C, except for the sample without Si, where the value decreases from 200°C to 400°C. The room-temperature values are seen to compare well to the values from the Seebeck microprobe. The error on each measurement is ca. 10%. The values compare well to data from the literature.^{9,11,25} The Seebeck coefficient reaches maximum absolute values for compositions $x = 0.4$ to 0.9 with the peak at $x = 0.7$. This is in accordance with the convergence of conduction bands and similar to the results reported by Liu et al.¹¹ The thermal conductivity is seen to reach minimum values for $x = 0.3$ to 0.8 compositions due to alloy scattering. The values correspond well to the values reported in the literature.⁵ The error on each measurement is ca. 10%. The dimensionless figure of merit reaches maximum values of 0.8 to 1.0 at 400°C for compositions 0.4 to 0.7 due to the low thermal conductivity and high Seebeck coefficient of these samples. This is in perfect agreement with previously reported values for identical compounds;^{4,6,9,25} according to those results the zT values will increase further at higher temperatures to ca. 1.1 at 600°C for the $Mg_{2.2}Si_{0.5925}Sn_{0.4}Sb_{0.0075}$ composition. The additional zT -value at $x = 0.4$ is from our recent study¹⁸ and further underlines the issues with reproducibility and uncertainties in calculations of zT .

CONCLUSIONS

The entire composition range of the system $Mg_2Si_{1-x}Sn_x$ has been investigated for thermoelectric properties. A splitting of phases in the SPS-processed pellets was observed for most compositions with a slightly more Mg_2Sn -rich bottom and Mg_2Si -rich top. This is probably due to the large difference in densities and the tendency of the system to phase separate. Good thermal stability while heating to 400°C in air was found for most of the compositions; however, the $Mg_{2.2}Sn_{0.9925}Sb_{0.0075}$ sample exhibited

thermal instability and furthermore degraded over time.

ACKNOWLEDGEMENTS

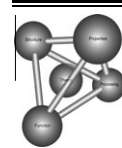
This work was supported by the Danish National Research Foundation (Center for Materials Crystallography) and the Danish Strategic Research Council (Center for Energy Materials).

REFERENCES

- A.J. Minnich, M.S. Dresselhaus, Z.F. Ren, and G. Chen, *Energy Environ. Sci.* 2, 466 (2009).
- G.J. Snyder and E.S. Toberer, *Nat. Mater.* 7, 105 (2008).
- J.R. Sootsman, D.Y. Chung, and M.G. Kanatzidis, *Angew. Chem. Int. Ed. Engl.* 48, 8616 (2009).
- V.K. Zaitsev, M.I. Fedorov, E.A. Gurieva, I.S. Eremin, P.P. Konstantinov, A.Y. Samunin, and M.V. Vedernikov, *Phys. Rev. B* 74, 045207 (2006).
- V.K. Zaitsev, M.I. Fedorov, I.S. Eremin, E.A. Gurieva, *Thermoelectric Handbook, Macro to Nano*, ed. D.M. Rowe (Boca Raton, FL: CRC Taylor & Francis, 2006), Chapter 29.
- Q. Zhang, J. He, T.J. Zhu, S.N. Zhang, X.B. Zhao, and T.M. Tritt, *Appl. Phys. Lett.* 93, 102109 (2008).
- Q. Zhang, X.B. Zhao, S.N. Zhang, T.J. Zhu, H. Yin, J. He, T.M. Tritt, *J. Phys. D Appl. Phys.* 41 (2008).
- H. Gao, T. Zhu, X. Liu, L. Chen, and X. Zhao, *J. Mater. Chem.* 21, 5933 (2011).
- W. Liu, X. Tang, and J. Sharp, *J. Phys. D Appl. Phys.* 43, 085406 (2010).
- W. Liu, Q. Zhang, X. Tang, H. Li, and J. Sharp, *J. Electron. Mater.* 40, 1062 (2011).
- W. Liu, X. Tan, K. Yin, H. Liu, X. Tang, J. Shi, Q. Zhang, and C. Uher, *Phys. Rev. Lett.* 108, 166601 (2012).
- W. Liu, X. Tang, H. Li, K. Yin, J. Sharp, X. Zhou, and C. Uher, *J. Mater. Chem.* 22, 13653 (2012).
- W. Liu, X. Tang, H. Li, J. Sharp, X. Zhou, and C. Uher, *Chem. Mater.* 23, 5256 (2011).
- J.-i. Tani and H. Kido, *J. Alloys. Compd.* 466, 335 (2008).
- R.B. Song, T. Aizawa, and J.Q. Sun, *Mater. Sci. Eng. B Solid* 136, 111 (2007).
- I.-H. Jung, D.-H. Kang, W.-J. Park, N.J. Kim, and S. Ahn, *Calphad* 31, 192 (2007).
- Y. Isoda, T. Nagai, H. Fujiu, Y. Imai, Y. Shinohara, *26th International Conference on Thermoelectrics (ICT 2007)*, 251 (2007).
- M. Sondergaard, M. Christensen, K.A. Borup, H. Yin, and B.B. Iversen, *Acta Mater.* 60, 5745 (2012).
- J. Rodriguezcarvajal, *Phys. B* 192, 55 (1993).
- L.J.v.d. Pauw, *Philips Res. Rep.* 13, 1 (1958).
- S. Iwanaga, E.S. Toberer, A. LaLonde, and G.J. Snyder, *Rev. Sci. Instrum.* 82, 063905 (2011).
- D. Platzek, G. Karpinski, C. Stiewe, P. Ziolkowski, C. Drasar, E. Muller, *ICT 2005. 24th International Conference on Thermoelectrics* (2005), pp. 13–16.
- D. Boudemagh, D. Fruchart, R. Haettel, E.K. Hlil, A. Lacoste, L. Ortega, N. Skryabina, J. Tobola, and P. Wolfers, *Diffus. Defect Data B* 170, 253 (2011).
- M. Søndergaard, M. Christensen, K.A. Borup, H. Yin, B.B. Iversen, *Submitted to J. Mater. Sci.* (2012).
- V.K. Zaitsev, M.I. Fedorov, E.A. Gurieva, I.S. Eremin, P.P. Konstantinov, A.Y. Samunin, M.V. Vedernikov, *2005 24th International Conference on Thermoelectrics (ICT) (IEEE Cat. No.05TH8854C)* (2005).

Appendix C.7 Gravity-Induced Gradients in Thermoelectric $\text{Mg}_2\text{Si}_{0.9925-x}\text{Sn}_x\text{Sb}_{0.0075}$

Reproduced with permission from Elsevier.



Gravity-induced gradients in thermoelectric $Mg_2Si_{0.9925-x}Sn_xSb_{0.0075}$

M. Søndergaard, M. Christensen ^{*}, K.A. Borup, H. Yin, B.B. Iversen

*Center for Materials Crystallography and Center for Energy Materials, Department of Chemistry and iNANO,
Aarhus University, DK-8000 Aarhus C, Denmark*

Received 8 June 2012; received in revised form 26 June 2012; accepted 27 June 2012

Available online 23 August 2012

Abstract

Ten samples of high-efficiency thermoelectric materials with nominal compositions $Mg_{2.2}Si_{0.3925}Sn_{0.6}Sb_{0.0075}$ and $Mg_{2.2}Si_{0.5925}Sn_{0.4}Sb_{0.0075}$ were prepared by induction melting, ball milling and spark plasma sintering (SPS). After SPS processing, all pellets were investigated for a potential compositional gradient in Si/Sn content by employing spatially resolved Seebeck coefficient measurements and X-ray powder diffraction including subsequent Rietveld refinement. The samples have gradients, with the Mg_2Sn -rich phase being consistently in the bottom of all samples. Energy dispersive X-ray spectroscopy confirmed the results. The large difference in densities between the Mg_2Sn -rich and the Mg_2Si -rich phases is responsible for the creation of the gradient. The results propose a new way to utilize SPS processing in fabrication of functionally graded materials. Additionally, the Seebeck coefficient, thermal conductivity, electrical resistivity, and Hall carrier concentration are measured on two samples from each batch from room temperature to 400 °C.

© 2012 Acta Materialia Inc. Published by Elsevier Ltd. All rights reserved.

Keywords: Functionally graded materials; SPS; Thermoelectric; $Mg_2Si_{1-x}Sn_x$; X-ray diffraction

1. Introduction

Thermoelectric materials are able to interconvert heat and electricity and are expected to play an important role in future green energy technology [1–4]. However, low efficiencies have so far limited the use of thermoelectric materials to niche applications. The efficiency scales with the dimensionless figure of merit, zT :

$$zT = \frac{S^2}{\kappa\rho} T \quad (1)$$

where S is the Seebeck coefficient, κ the thermal conductivity, T the absolute temperature and ρ the electrical resistivity. Alloys and materials with low dimensional nanostructures are well demonstrated to improve the figure of merit by reducing the thermal conductivity

through enhanced phonon scattering on defects and grain boundaries [5–9]. The reduction of the thermal conductivity should preferably be achieved without altering the electronic properties. Even greater efficiencies could potentially be realized by enhancing the power factor, S^2/ρ , through, for example, electron filtering or quantum confinement [10,11]. In several reports the system of $Mg_2Si_{1-x}Sn_x$ exhibit promising thermoelectric properties in the mid-temperature range of 300–550 °C [12–33]. Compared with other *n*-type thermoelectric materials in this temperature range the $Mg_2Si_{1-x-y}Sn_xSb_y$ materials have the advantage of consisting of abundant, cheap and non-toxic elements (for *p*-type materials, e.g. Zn_4Sb_3 materials, have the same advantages) [34–36]. However, a key issue of $Mg_2Si_{1-x}Sn_x$ -based thermoelectric materials is their method of preparation. The large difference in melting point between the elements, along with the relatively high vapor pressure of Mg at temperatures below the reaction temperature,

* Corresponding author. Tel.: +45 87155339.
E-mail address: mch@chem.au.dk (M. Christensen).

makes it difficult to produce homogeneous and stoichiometric products. Liu et al. [27] recently showed the importance of excess Mg for controlling the optimal thermoelectric performance. In this context, several low temperature synthesis routes have been proposed to minimize Mg losses during preparation, thereby gaining control of the stoichiometry. These include B_2O_3 liquid encapsulation synthesis [23], mechanical alloying [31], solid state reaction [37], and direct spark plasma sintering synthesis [25] (for low Sn content). The pseudo-binary part of the Mg_2Si – Mg_2Sn system is reported to possess an immiscibility region [38]. The discrepancies in the range of the gap reported in the literature are attributed to the kinetics of the separation: due to the splitting of the two phases being a relatively slow process at ambient conditions, most of the compositions within the miscibility gap can be synthesized in samples with meta-stable phases.

In the present study, we report on the systematic splitting of phases in the Mg – Si – Sn –system into Mg_2Si -rich and Mg_2Sn -rich areas from the top to the bottom of spark plasma sintering (SPS)-processed pellets. A similar gradient is not observed in a pellet from a comparative system, $Pb_{0.9-x}Sn_{0.1}Ge_xTe$, that has a similar immiscibility region [39]. The pattern created in the $Mg_2Si_{1-x}Sn_x$ pellets is ascribed to high atomic diffusivity and large difference in density. The Sn/Si ratio has previously been demonstrated to affect the peak thermoelectric efficiency temperature [16], thus the phenomenon could be applied in the fabrication of functionally graded materials [40–42]. The utilization of $Mg_2Si_{1-x}Sn_x$ has previously been attempted in a segmented sample by Müller et al. [43]. Additionally, functionally graded materials have been fabricated by SPS by stacking powders of various compositions in the pressing dies [44,45]. However, a smoother gradient in a functionally graded material that is presented here could avoid problems with differences in thermal expansion and furthermore minimize contact resistances between separate layers.

The SPS process has been applied extensively for the processing and syntheses of thermoelectric materials [46]. Traditionally, it is the fast heating rate of the SPS technique that is highlighted as being beneficial for fast processing and for achieving high densities while preserving nanograins in the samples. However, the large current applied during SPS has been suggested to alter the chemistry of the samples [46–50]. In the synthesis of the clathrate $Na_{24}Si_{136}$ the electrical field reduces/oxidizes the precursor elements [48], while the ion conducting ability of Zn in Zn_4Sb_3 with the high current results in interesting electromigration behavior [49,50]. Conversely, in the present study it is believed to be gravity, and the large difference in densities between the phases, which causes the gradients in the samples. This demonstrates a potential application of the SPS method and other hot-pressing methods to create functionally graded materials in systems containing immiscibility regions.

2. Experimental

2.1. Synthesis and processing

The pure elements (Mg 99.98%; Si 99.9+%; Sn 99.97%; Sb 99.5%) were mixed according to the stoichiometry $Mg_{2.2}Si_{0.9925-x}Sn_xSb_{0.0075}$ with $x = 0.4; 0.6$ in Al_2O_3 crucibles with lids and reacted in an induction furnace under a He pressure of 0.7 MPa. The carbon susceptor temperature was measured using a pyrometer to ~ 1400 °C. The total heating time was less than 15 min. The products were ball milled in a Fritsch Pulverisette 4 Vario-planetary Mill for 30 min utilizing WC vials and balls. The powder had grain sizes in a wide range from a few nm up to a few μm . Subsequently, the powder was densified by SPS. The following procedure was employed to obtain dense and stable pellets. An initial pressure of 75 MPa was applied at room temperature. The sample was heated in 15 min to 700 °C. The temperature was held for 10 min, the last 4 min the SPS pressure was reduced to 20 MPa to release strain. Finally, the sample was cooled to 200 °C in 10 min, before the power was switched off. Graphite paper was used inside the graphite die and on the ends of the punches for protection. The graphite paper was subsequently removed and the surfaces of the pellets polished prior to further characterization. Bottom and top were marked on all pellets; in the SPS, the current runs from the bottom to the top. To ensure reproducibility of the observed gradient, five pellets were prepared from each batch. From the $Mg_{2.2}Si_{0.5925}Sn_{0.4}Sb_{0.0075}$ batch a sample was made with increased sintering time (25 min at maximum temperature compared to 10 min, hereafter named sample 1.2) and one with larger thickness (5 mm compared to 3 mm, hereafter named sample 1.3). Several samples were cut with a wire saw in order to investigate the Seebeck coefficient gradient in the cross-sections. The $Pb_{0.3}Sn_{0.1}Ge_{0.6}Te$ sample was prepared by heating stoichiometric ratios of the pure elements in an evacuated carbon coated quartz ampoule at 850 °C for 1 h before quenching in salt water. The ingot was ball milled and the resulting powder sintered in SPS by the following procedure: an initial pressure of 75 MPa was applied followed by heating to 550 °C in 9 min. That temperature was held for 11 min, with release of the pressure to 20 MPa after 7 min. Note that too high mass load (>1.8 g) resulted in breaking of the die on several attempts by this method, possibly due to differences in thermal expansion between the graphite and the chalcogenides.

2.2. Structural properties

Powder X-ray diffraction (PXRD) was performed on both sides of all pellets on a Rigaku Smartlab diffractometer configured with a rotating anode Cu source and parallel beam optics. The lattice parameter of the main phase in each sample was extracted through Rietveld refinement of the PXRD data employing the Fullprof software package [51]. Chemical analysis was conducted on one sample

(sample 2.2) using energy-dispersive X-ray spectroscopy (EDX) on a Nova 600 Nano SEM from FEI equipped with an EDAX detector.

2.3. Physical properties

Physical properties were measured on selected samples, two from each batch named 1.4, 1.5 from the $Mg_{2.2}Si_{0.5925}Sn_{0.4}Sb_{0.0075}$ batch and 2.1 and 2.3 from the $Mg_{2.2}Si_{0.3925}Sn_{0.6}Sb_{0.0075}$ batch. The thermal conductivity values from room temperature to 400 °C were calculated from the thermal diffusivity and the specific heat measured on a Netzsch LFA 457 laser flash apparatus and the density (measured by the Archimedes method). A standard pyroceram 9606 sample was used as reference for calculations of the specific heat capacity. Measurements of the electrical resistivity, Hall carrier concentration and mobility were conducted from room temperature to 400 °C. The samples were measured on an in-house system employing the Van der Pauw method [52] in a magnetic field of 1.25 T [53]. The Seebeck coefficient was measured from room temperature to 400 °C on an in-house system, similar to the one reported by Iwanaga et al. [54]. Spatially resolved Seebeck coefficient measurements were performed at room temperature utilizing a potential seebeck microprobe (PSM) [55]. The top and bottom surfaces of all pellets were measured. A minimum of several hundreds of points were collected for each surface for good statistics. Additionally, several pellets were cut in two half-circles with a wire saw and the cross-sections were polished and measured with spacing of 50 µm between the points.

3. Results and discussion

3.1. Structural properties

Diffractograms measured on the top and bottom of all pellets are available in Supporting information (SI). Some of the samples contained minute amounts of Mg and MgO impurity (0–4 wt.%) and/or weak peaks indicating multiple $Mg_2Si_{1-x}Sn_x$ phases. When present, the Mg impurity was located in the top of the samples. A zoom on the Bragg peaks (220) and (311) for $Mg_2Si_{0.5925}Sn_{0.4}Sb_{0.0075}$ is shown in Fig. 1 and the lattice parameters from Rietveld refinement are in Fig. 2, top. A clear consistent shift in lattice parameters is observed. The shift of the lattice parameter appears to be larger for the Si-rich samples: 6.50–6.57 Å for $Mg_2Si_{0.5925}Sn_{0.4}Sb_{0.0075}$ and 6.60–6.62 Å for $Mg_{2.2}Si_{0.3925}Sn_{0.6}Sb_{0.0075}$ (Fig. 3, top). The error on the lattice parameter is on the order of 10^{-4} Å. The shifts towards larger lattice parameters are an indication of the bottom sides having relatively higher amounts of Sn atoms. Additionally, all refined occupancies of the correlated Si/Sn ratios showed a larger amount of Sn on the bottom side. The EDX measurements on a sample of nominal composition $Mg_{2.2}Si_{0.3925}Sn_{0.6}Sb_{0.0075}$ probed at four points on the top and four points on the bottom resulted in average

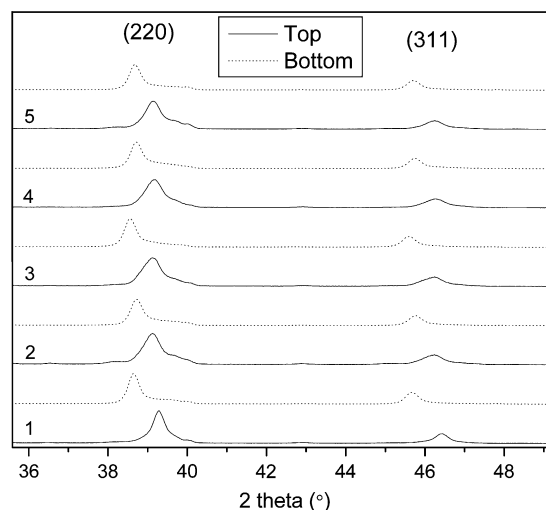


Fig. 1. Powder X-ray diffraction zoom of the Bragg peaks (220) and (311) of the top and bottom of the five $Mg_{2.2}Si_{0.5925}Sn_{0.4}Sb_{0.0075}$ samples. The sample sintered for extended time is number 2 and the sample sintered to larger thickness is number 3.

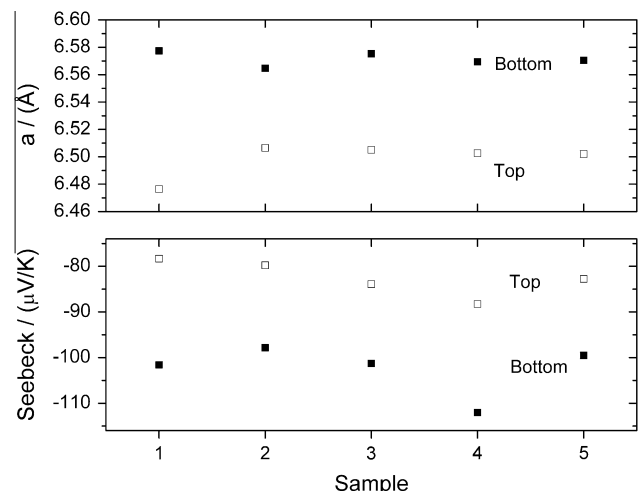


Fig. 2. Top: extracted lattice parameters for the top and bottom sides of the five $Mg_{2.2}Si_{0.5925}Sn_{0.4}Sb_{0.0075}$ samples. Bottom: average Seebeck coefficients on top and bottom surfaces of the five $Mg_{2.2}Si_{0.5925}Sn_{0.4}Sb_{0.0075}$ pellets.

ratios of $Si_{0.39}Sn_{0.61}$ on the bottom side and $Si_{0.47}Sn_{0.53}$ in the top. Thus the EDX measurement confirmed the results from PXRD.

3.2. Spatially resolved Seebeck coefficient

Fig. 2, bottom shows the variations of Seebeck coefficient on the top and bottom of the $Mg_{2.2}Si_{0.5925}Sn_{0.4}Sb_{0.0075}$ pellets. Similar to the lattice parameters, clear systematic variations from the top to the bottom of the samples are observed. All the $Mg_{2.2}Si_{0.5925}Sn_{0.4}Sb_{0.0075}$ samples show Seebeck coefficients on the bottom in the range -98 to $-112 \mu V K^{-1}$ and in the range -78 to $-88 \mu V K^{-1}$ for the top. Similarly, all of the Seebeck coefficients of $Mg_{2.2}Si_{0.3925}Sn_{0.6}Sb_{0.0075}$ samples are between

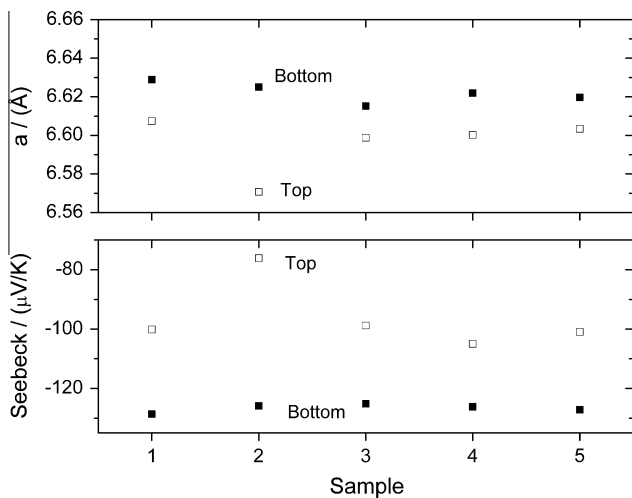


Fig. 3. Top: Extracted lattice parameters for the top and bottom sides of the five $\text{Mg}_{2.2}\text{Si}_{0.3925}\text{Sn}_{0.6}\text{Sb}_{0.0075}$ samples. Bottom: average Seebeck coefficients on top and bottom surfaces of the five $\text{Mg}_{2.2}\text{Si}_{0.3925}\text{Sn}_{0.6}\text{Sb}_{0.0075}$ pellets.

–125 and –129 $\mu\text{V K}^{-1}$ on the bottom side and in the range –99 to –105 $\mu\text{V K}^{-1}$ on the top side (except for one sample having –76 $\mu\text{V K}^{-1}$; see Fig. 3, bottom). The lower absolute values of the Seebeck coefficients on the

top sides of all ten samples are consistent with the structural data, due to the more Si-rich phases of $\text{Mg}_2\text{Si}_{1-x}\text{Sn}_x$ having lower absolute Seebeck coefficients at room temperature [15,29]. In the Seebeck microprobe scans on the cross-sections of two different pellets of composition $\text{Mg}_{2.2}\text{Si}_{0.3925}\text{Sn}_{0.6}\text{Sb}_{0.0075}$ shown in Fig. 4, a clear gradual change from $S = -140 \mu\text{V K}^{-1}$ in the bottom of the pellets to $S = -100 \mu\text{V K}^{-1}$ in the top of the pellets is observed. The gradients are seen to have a curvature towards the edges of the pellets. Note that in the close vicinity ($<10 \mu\text{m}$) of the edges of the samples the approximations that allow this technique to be used breaks down, thus the data point at the very edge is unreliable. The average Seebeck values as a function of distance to the bottom are seen below the color plots in Fig. 4. The gradient is seen to be steeper closer to the ends where it is changing 5–10 $\mu\text{V K}^{-1}$ over 0.5 mm. For the $\text{Mg}_{2.2}\text{Si}_{0.5925}\text{Sn}_{0.4}\text{Sb}_{0.0075}$ similar gradients were observed in the cross-sections (see SI). The sample that was sintered for a longer time showed a steeper gradient towards the end in the Seebeck coefficient. The sample with extra thickness showed no significant difference in the gradient.

The pseudo-ternary system of PbTe–SnTe–GeTe has been reported to contain an immiscibility region similar

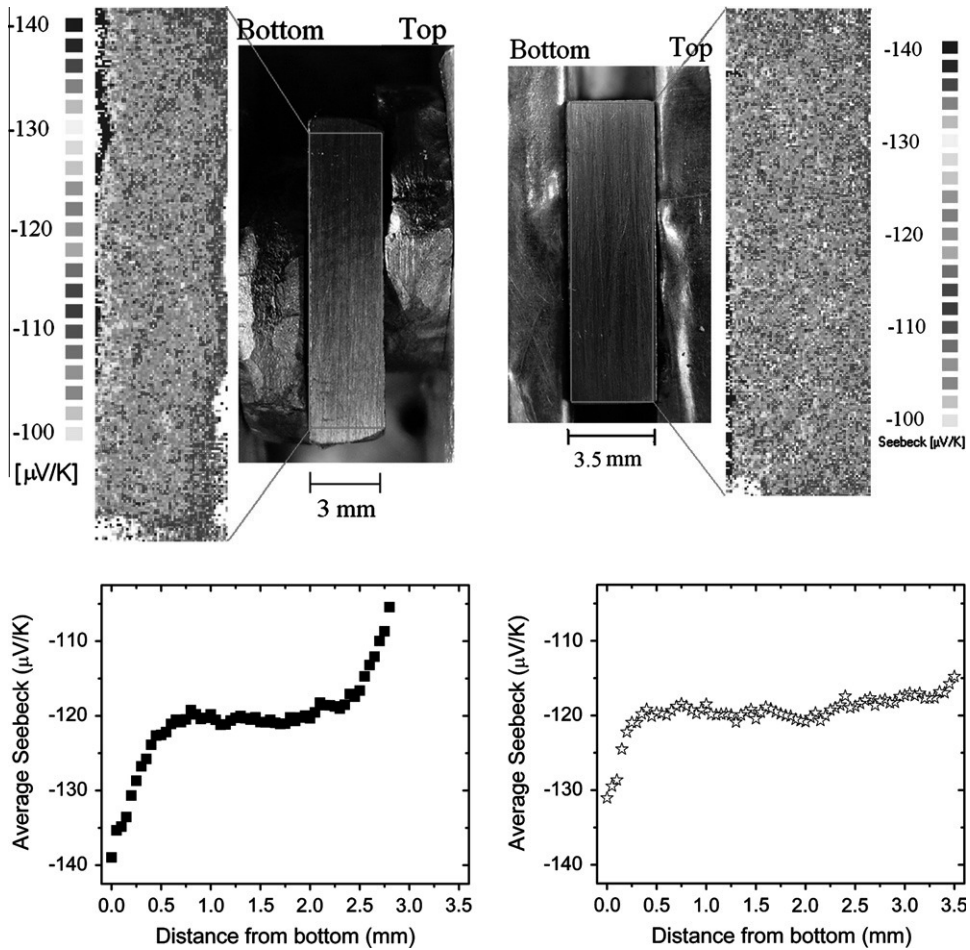


Fig. 4. Top: potential Seebeck microprobe scans on the cross-sections of two $\text{Mg}_{2.2}\text{Si}_{0.3925}\text{Sn}_{0.6}\text{Sb}_{0.0075}$ samples. Bottom: the average values across each column in the scans.

to the one in the Mg₂Si–Mg₂Sn system due to the large size difference between the cations [39,56,57]. However, powder X-ray diffraction and PSM measurements on both sides of a pellet of composition Pb_{0.3}Sn_{0.1}Ge_{0.6}Te revealed no difference between the two sides within the uncertainties (see SI). The relative difference between the densities of the end members PbTe (8.16 g cm⁻³) and GeTe (6.14 g cm⁻³) is much smaller than the relative difference between the densities of Mg₂Si (1.88 g cm⁻³) and Mg₂Sn (3.59 g cm⁻³). Furthermore, the sintering temperature in the SPS process of the Pb_{0.3}Sn_{0.1}Ge_{0.6}Te sample was much lower ($T_{\max} = 550$ °C) than in the sintering of the Mg_{2.2}Si_{1-x}Sn_x samples ($T_{\max} = 700$ °C). If the electric field or the high current during SPS causes diffusion, silicon and tin are expected to diffuse in the same direction. It is difficult to explain exactly what happens during SPS; however, investigations of hot-pressed or induction-pressed pellets could render further insights into the mechanism behind the creation of the gradient. It seems most probable that the Si/Sn gradients created during sintering are due to gravity and the tendency of the system to phase-separate.

The observation of the gradient in Mg₂Si_{1-x}Sn_x materials is important if the material is to be employed in modules for thermoelectric energy harvesting, as it will be important to know which side of the pellet to turn toward the hot and cold ends. Furthermore, for an operating module it could have an effect if the hot side is placed below the cold side. In time, gravity could make the Sn diffuse to the bottom side and thus lead to a decrease of the thermoelectric performance at both sides. As indicated in this study and reported by others [15,16,21]. The Sn-rich samples have higher zT at lower temperatures and Si-rich samples have higher zT at higher temperatures so they should be placed accordingly in a thermal gradient for optimal performance.

3.3. Physical properties

All Mg_{2.2}Si_{0.5925}Sn_{0.4}Sb_{0.0075} samples had overall densities of 2.64(3) g cm⁻³ and all Mg_{2.2}Si_{0.3925}Sn_{0.6}Sb_{0.0075} samples had densities of 3.01(3) g cm⁻³ close to the theoretical values of 2.66 and 3.04 g cm⁻³, respectively. The measurements of thermoelectric properties from room temperature to 400 °C are shown in Figs. 5–9. Resistivity and Hall measurements were conducted in-plane, while thermal conductivity and the Seebeck coefficient were measured through-plane. Due to the cubic crystal structure it should not matter; however, the local phase differences found in the PSM scans could cause minor discrepancies.

The Hall carrier concentrations of the four samples were extracted from Hall effect measurements from room temperature to 400 °C. The data are shown in Fig. 5. The Hall carrier concentration for the Si-rich samples is almost invariant with temperature: increases of (sample 1.4) 1.54–1.55 × 10²⁰ cm⁻³ and (sample 1.5) 1.65–1.66 × 10²⁰ cm⁻³ from room temperature to 400 °C are observed. The increases for the Sn-rich samples were more

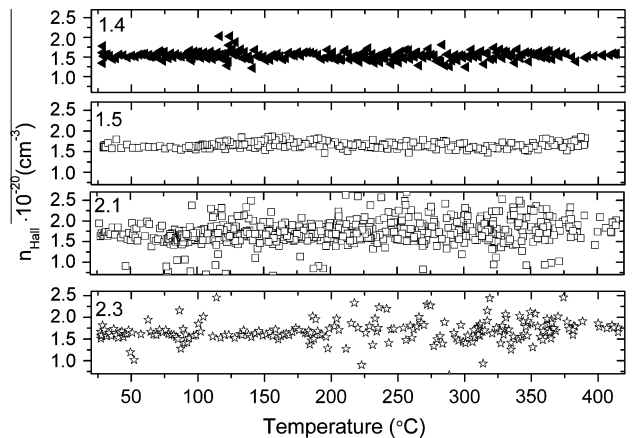


Fig. 5. The Hall carrier concentrations from Hall measurements from room temperature to 400 °C for two samples from the Mg_{2.2}Si_{0.5925}Sn_{0.4}Sb_{0.0075} batch (top) and Mg_{2.2}Si_{0.3925}Sn_{0.6}Sb_{0.0075} batch (bottom).

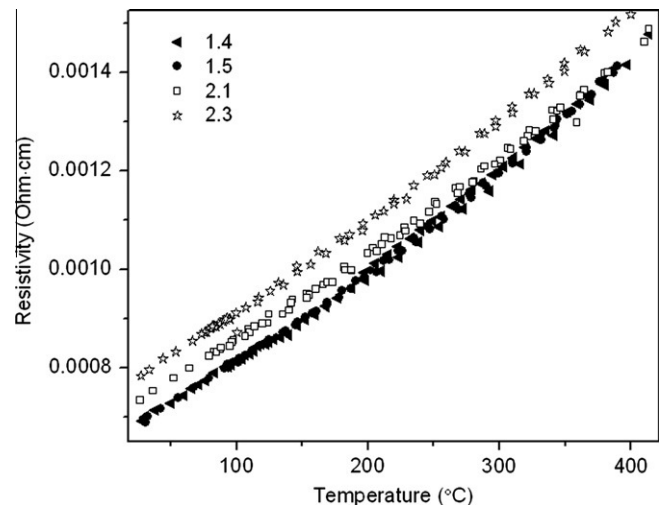


Fig. 6. Resistivity from room temperature to 400 °C for two samples from the Mg_{2.2}Si_{0.5925}Sn_{0.4}Sb_{0.0075} batch (1.4 and 1.5) and the Mg_{2.2}Si_{0.3925}Sn_{0.6}Sb_{0.0075} batch (2.1 and 2.3).

significant: (sample 2.1) 1.63–1.87 × 10²⁰ cm⁻³ and (sample 2.3) 1.56–1.80 × 10²⁰ cm⁻³. The band gaps are ~0.6–0.7 eV and hence we do not expect the changes in Hall carrier concentrations to be due to thermal excitations at or below 400 °C. The Hall carrier concentration is calculated from the Hall coefficient as $n_H = -\frac{R_H}{e}$, where R_H is the Hall coefficient and e is the electronic charge. This relation is derived using the free electron or single parabolic band models. In other systems the relation between the true carrier concentration and the Hall carrier concentration can be described as $n = n_H r_H$ [58], where n is the true carrier concentration and r_H is the so-called Hall factor. To explain the temperature dependence of the Hall carrier concentrations we consider this Hall factor, which is temperature-dependent when the structure is described by a multiband model. Mg₂Si and Mg₂Sn have two conduction bands offset in energy. The energy minima of the two bands converge in

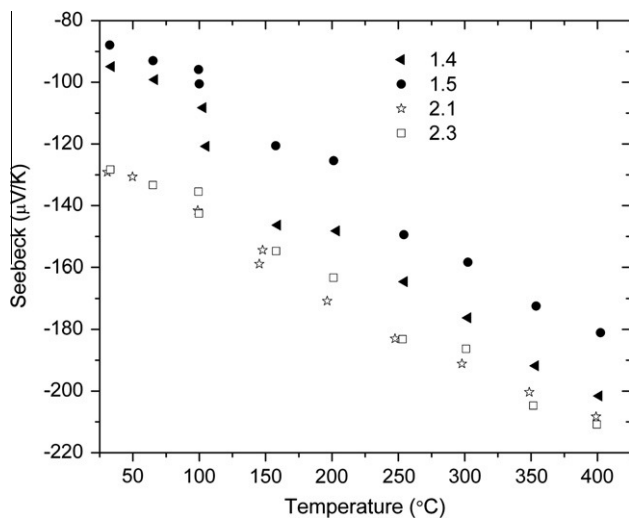


Fig. 7. Seebeck coefficient from room temperature to 400 °C for two samples from the $\text{Mg}_{2.2}\text{Si}_{0.5925}\text{Sn}_{0.4}\text{Sb}_{0.0075}$ batch (1.4 and 1.5) and the $\text{Mg}_{2.2}\text{Si}_{0.3925}\text{Sn}_{0.6}\text{Sb}_{0.0075}$ batch (2.1 and 2.3).

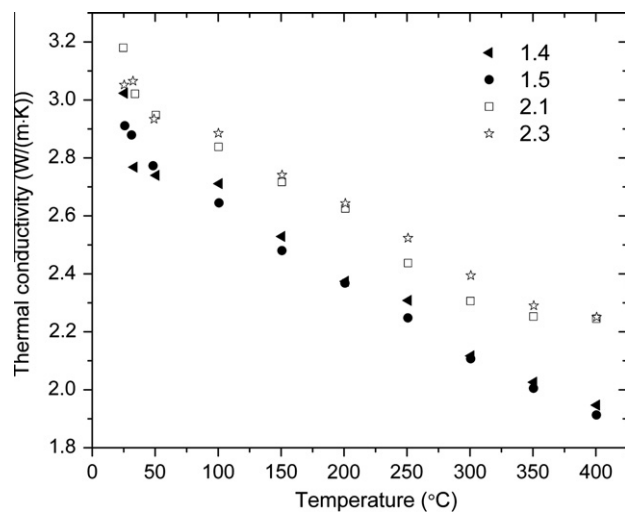


Fig. 8. Thermal conductivity from room temperature to 400 °C for two samples from the $\text{Mg}_{2.2}\text{Si}_{0.5925}\text{Sn}_{0.4}\text{Sb}_{0.0075}$ batch (1.4 and 1.5) and the $\text{Mg}_{2.2}\text{Si}_{0.3925}\text{Sn}_{0.6}\text{Sb}_{0.0075}$ batch (2.1 and 2.3).

the solid solution $\text{Mg}_2\text{Si}_{1-x}\text{Sn}_x$ for $x = 0.7$ [29]. Therefore, the two conduction band minima are relatively close for $x = 0.6$ compared with $x = 0.4$. Consequently, the sample with $x = 0.6$ cannot be described with a single parabolic band model and a temperature-dependent Hall carrier concentration is observed experimentally.

The resistivities of all samples exhibit metallic behavior with an approximately linear increase with temperature from $\sim 0.7 \text{ m}\Omega \text{ cm}$ at room temperature to $\sim 1.5 \text{ m}\Omega \text{ cm}$ at 400 °C. A relatively small difference is observed between the samples from each batch in accordance with the small differences in the Hall carrier concentrations. The error is $\sim 5\%$ on each data point. The temperature dependence of the Seebeck coefficients of all samples is approximately linear in accordance with the Mott formula,

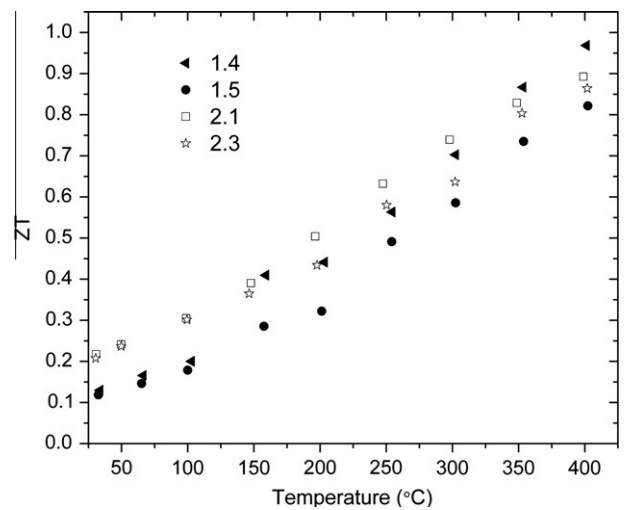


Fig. 9. Figure of merit, zT , from room temperature to 400 °C for two samples from the $\text{Mg}_{2.2}\text{Si}_{0.5925}\text{Sn}_{0.4}\text{Sb}_{0.0075}$ batch (1.4 and 1.5) and the $\text{Mg}_{2.2}\text{Si}_{0.3925}\text{Sn}_{0.6}\text{Sb}_{0.0075}$ batch (2.1 and 2.3).

$S = \frac{\pi^2}{3} \left(\frac{\kappa_B^2 T}{e} \right) \left[\frac{d \ln \sigma}{d E} \right]_{E=E_F}$ [59]. The values compare well to data from the literature [15,29,37]. The Sn-rich samples show numerically larger Seebeck coefficients at room temperature and good reproducibility between the two samples, while the Si-rich samples showed some discrepancy. The room temperature values are seen to compare well with the values from the Seebeck microprobe. The error on each measurement is $\sim 10\%$. For the thermal conductivity measurements the Sn-rich compounds show slightly higher thermal conductivities (~ 2.2 – $3.2 \text{ W m}^{-1} \text{ K}^{-1}$) than the Si-rich ones (~ 1.9 – $2.9 \text{ W m}^{-1} \text{ K}^{-1}$) due to the higher densities of the Sn-rich compounds. The values are comparable to data from the literature [15,20,37]. The error on each measurement is $\sim 10\%$. The dimensionless figure of merit reaches maxima of 0.8–1.0 at 400 °C. This is in perfect agreement with previously reported values for identical compounds [15,16,20,37]; according to those results the zT values will increase further at higher temperatures to ~ 1.1 at 600 °C for the $\text{Mg}_{2.2}\text{Si}_{0.5925}\text{Sn}_{0.4}\text{Sb}_{0.0075}$ compositions.

4. Conclusion

In summary, the system of $\text{Mg}_2\text{Si}_{1-x}\text{Sn}_x$ has a natural tendency to phase-separate into Mg_2Si -rich and Mg_2Sn -rich areas. Processing samples by ball milling yields small grain sizes, and this in turn leads to a higher grain boundary diffusion coefficient when processed by SPS. This is utilized to create gradients in pellets with Mg_2Si -rich areas in the top going gradually to Mg_2Sn -rich areas in the bottom of the pellets. Thus a new way of creating functionally graded materials in systems containing miscibility gaps is demonstrated. Actual tests of the thermoelectric efficiency of the produced functionally graded pellets in a real module turning the top side or bottom side towards the hot end in a temperature gradient would be of great interest.

Acknowledgements

This work was supported by the Danish National Research Foundation (Center for Materials Crystallography), and the Danish Strategic Research Council (Center for Energy Materials).

Appendix A. Supplementary material

Supplementary data associated with this article can be found, in the online version, at <http://dx.doi.org/10.1016/j.actamat.2012.06.050>.

References

- [1] Snyder GJ, Toberer ES. Nat Mater 2008;7:105.
- [2] Sootsman JR, Chung DY, Kanatzidis MG. Angew Chem Int Ed Engl 2009;48:8616.
- [3] Christensen M, Johnsen S, Iversen BB. Dalton Trans 2010;39:978.
- [4] Rowe DM. Thermoelectrics handbook: macro to nano. Boca Raton, FL: CRC/Taylor & Francis; 2006.
- [5] Vineis CJ, Shakouri A, Majumdar A, Kanatzidis MG. Adv Mater 2010;22:3970.
- [6] Dresselhaus MS, Chen G, Tang MY, Yang RG, Lee H, Wang DZ, et al. Adv Mater 2007;19:1043.
- [7] Poudel B, Hao Q, Ma Y, Lan Y, Minnich A, Yu B, et al. Science 2008;320:634.
- [8] Harman TC, Taylor PJ, Walsh MP, LaForge BE. Science 2002;297:2229.
- [9] Harman T, Walsh M, Laforgue B, Turner G. J Electron Mater 2005;34:19.
- [10] Zide JMO, Vashaee D, Bian ZX, Zeng G, Bowers JE, Shakouri A, et al. Phys Rev B 2006;74:205335.
- [11] Ohta H, Kim S, Mune Y, Mizoguchi T, Nomura K, Ohta S, et al. Nat Mater 2007;6:129.
- [12] Zaitsev VK, Fedorov MI, Burkov AT, Gurieva EA, Eremin IS, Konstantinov PP, et al. In: 21st International conference on thermoelectrics, proceedings ICT'02: IEEE; 2002. p. 151.
- [13] Fedorov MI, Pshenay-Severin DA, Zaitsev VK, Sano S, Vedernikov MV. In: Proceedings ICT'03. 22nd International conference on thermoelectrics (IEEE cat. no. 03TH8726); 2003.
- [14] Fedorov MI, Zaitsev VK, Eremin IS, Gurieva EA, Burkov AT, Konstantinov PP, et al. Proceedings ICT'03. 22nd International conference on thermoelectrics (IEEE cat. no. 03TH8726); 2003.
- [15] Zaitsev VK, Fedorov MI, Gurieva EA, Eremin IS, Konstantinov PP, Samunin AY, et al. In: 2005 24th International conference on thermoelectrics (ICT) (IEEE cat. no. 05TH8854C); 2005.
- [16] Zaitsev VK, Fedorov MI, Gurieva EA, Eremin IS, Konstantinov PP, Samunin AY, et al. Phys Rev B 2006;74:045207.
- [17] Fedorov MI, Zaitsev VK, Eremin IS, Gurieva EA, Burkov AT, Konstantinov PP, et al. Phys Solid State+ 2006;48:1486.
- [18] Isachenko GN, Zaitsev VK, Fedorov MI, Gurieva EA, Eremin IS, Konstantinov PP, et al. 2007 26th International conference on thermoelectrics (ICT 2007); 2007.
- [19] Fedorov MI, Zaitsev VK, Isachenko GN. Diffus De B 2011;170:286.
- [20] Zhang Q, He J, Zhu TJ, Zhang SN, Zhao XB, Tritt TM. Appl Phys Lett 2008;93:102109.
- [21] Zhang Q, Zhu TJ, Zhou AJ, Yin H, Zhao XB. Phys Scripta 2007;T129:123.
- [22] Zhang Q, Zhao XB, Zhang SN, Zhu TJ, Yin H, He J, et al. J Phys D Appl Phys 2008;41.
- [23] Gao H, Zhu T, Liu X, Chen L, Zhao X. J Mater Chem 2011;21:5933.
- [24] Zhang X, Lu Q-M, Wang L, Zhang F-P, Zhang J-X. J Electron Mater 2010;39:1413.
- [25] Tani J-I, Kido H. J Alloy Compd 2008;466:335.
- [26] Gao HL, Liu XX, Zhu TJ, Yang SH, Zhao XB. J Electron Mater 2011;40:830.
- [27] Liu W, Tang X, Li H, Sharp J, Zhou X, Uher C. Chem Mater 2011;23:5256.
- [28] Liu W, Zhang Q, Tang X, Li H, Sharp J. J Electron Mater 2011;40:1062.
- [29] Liu W, Tan X, Yin K, Liu H, Tang X, Shi J, et al. Phys Rev Lett 2012;108:166601.
- [30] Luo W, Yang M, Chen F, Shen Q, Jiang H, Zhang L. Mater Trans 2010;51:288.
- [31] Song RB, Aizawa T, Sun JQ. Mater Sci Eng B – Solid 2007;136:111.
- [32] Aizawa T, Song R, Yamamoto A. Mater Trans 2006;47:1058.
- [33] Chen L, Jiang G, Chen Y, Du Z, Zhao X, Zhu T, et al. J Mater Res 2011;26:3038.
- [34] Caillat T, Fleuriol JP, Borshchevsky A. J Phys Chem Solids 1997;58:1119.
- [35] Pedersen BL, Birkedal H, Nishibori E, Bentien A, Sakata M, Nygren M, et al. Chem Mater 2007;19:6304.
- [36] Sun Y, Christensen M, Johnsen S, Nong NV, Ma Y, Sillassen M, et al. Adv Mater 2012;24:1693.
- [37] Liu W, Tang X, Sharp J. J Phys D – Appl Phys 2010;43:085406.
- [38] Jung I-H, Kang D-H, Park W-J, Kim NJ, Ahn S. CALPHAD 2007;31:192.
- [39] Yashina LV, Leute V, Shtanov VI, Schmidtke HM, Neudachina VS. J Alloy Compd 2006;413:133.
- [40] Kuznetsov V. Functionally graded materials for thermoelectric applications. Thermoelectrics handbook. Boca Raton, FL: CRC Press; 2005. p. 38.
- [41] Christensen M, Johnsen S, Sondergaard M, Overgaard J, Birkedal H, Iversen BB. Chem Mater 2009;21:122.
- [42] Watanabe R, Nishida T, Hirai T. Metal Mater Int 2003;9:513.
- [43] Müller E, Drašar Č, Schilz J, Kaysser WA. Mater Sci Eng A – Struct 2003;362:17.
- [44] Heian EM, Gibeling JC, Munir ZA. Mater Sci Eng A – Struct Mater Prop Microstruct Process 2004;368:168.
- [45] Luo YM, Wei P, Li SQ, Wang RG, Li JQ. Mater Sci Eng A – Struct Mater Prop Microstruct Process 2003;345:99.
- [46] Munir ZA, Anselmi-Tamburini U, Ohyanagi M. J Mater Sci 2006;41:763.
- [47] LaLonde AD, Ikeda T, Snyder GJ. Rev Sci Instrum 2011;82:025104.
- [48] Beekman M, Baitinger M, Borrman H, Schnelle W, Meier K, Nolas GS, et al. J Am Chem Soc 2009;131:9642.
- [49] Dasgupta T, Stiewe C, Boettcher L, Yin H, Iversen BB, Mueller E. MRS proceedings; 2011. p. 1325.
- [50] Yin H, Christensen M, Lock N, Iversen BB. Appl Phys Lett 2012;101:4390.
- [51] Rodriguezcarvajal J. Physica B 1993;192:55.
- [52] Pauw LJVD. Philips Res Rep 1958;13:1.
- [53] Borup KA, Toberer ES, Fleuriol JP, Snyder GJ, Iversen BB. Rev Sci Instrum 2012; submitted for Publication.
- [54] Iwanaga S, Toberer ES, LaLonde A, Snyder GJ. Rev Sci Instrum 2011;82:063905.
- [55] Platzek D, Karpinski G, Stiewe C, Ziolkowski P, Drasar C, Muller E. ICT 2005. 24th International conference on thermoelectrics; 2005. p. 13.
- [56] Gelbstein Y, Dado B, Ben-Yehuda O, Sadia Y, Dashevsky Z, Dariel MP. Chem Mater 2009;22:1054.
- [57] Søndergaard M, Christensen M, Johnsen S, Stiewe C, Dasgupta T, Mueller E, et al. J Solid State Chem 2011;184:1172.
- [58] Fistul VI. Heavily doped semiconductors. New York: Plenum; 1969.
- [59] Cutler M, Mott NF. Phys Rev 1969;181:1336.

Appendix C.8 Thermal Stability and Thermoelectric Properties of $\text{Mg}_2\text{Si}_{0.4}\text{Sn}_{0.6}$ and $\text{Mg}_2\text{Si}_{0.6}\text{Sn}_{0.4}$

Reproduced with permission from Springer.

Thermal stability and thermoelectric properties of $\text{Mg}_2\text{Si}_{0.4}\text{Sn}_{0.6}$ and $\text{Mg}_2\text{Si}_{0.6}\text{Sn}_{0.4}$

Martin Søndergaard · Mogens Christensen ·
Kasper A. Borup · Hao Yin · Bo B. Iversen

Received: 27 July 2012 / Accepted: 15 October 2012 / Published online: 26 October 2012
© Springer Science+Business Media New York 2012

Abstract Compounds of $\text{Mg}_2\text{Si}_{1-x}\text{Sn}_x$ are environmentally friendly, inexpensive and high-efficiency thermoelectric materials for energy conversion in the temperature range 300–550 °C. In this study, the thermal stability is investigated of fine powders and sintered pellets of the compounds $\text{Mg}_2\text{Si}_{0.4}\text{Sn}_{0.6}$ and $\text{Mg}_2\text{Si}_{0.6}\text{Sn}_{0.4}$ by heating the samples from room temperature to ~400 °C in air, while measuring powder X-ray diffraction patterns. The diffractograms of the pellets show no significant changes upon heating for several hours, while the powder samples show increasing emergence of a Mg_2Sn -rich, $\text{Mg}_2\text{Si}_{1-x}\text{Sn}_x$ phase, and other impurities upon heating for only several minutes. This is attributed to the larger amount of surface area in the powder samples. The appearance of the Mg_2Sn -rich phase is most pronounced for the Sn-rich composition. In addition, the thermal expansion coefficients were extracted from the powder diffraction patterns. All materials have been synthesized by induction-melting followed by ball milling and spark plasma sintering. The thermal conductivity, Seebeck coefficient, electrical resistivity and Hall carrier concentrations have been measured from room temperature to 400 °C on the pellets.

Introduction

Compounds of $\text{Mg}_2\text{Si}_{1-x}\text{Sn}_x$ have attracted much attention due to their non-toxicity and promising thermoelectric properties [1–4]. The efficiency of thermoelectric materials scales with the dimensionless thermoelectric figure of merit, $zT = \frac{S^2}{\kappa\rho}T$, where S is the Seebeck coefficient, κ the thermal conductivity, T the absolute temperature and ρ the electrical resistivity [5–7]. For $\text{Mg}_2\text{Si}_{1-x}\text{Sn}_x$, the zT reaches values of unity and above for compositions of the compounds with $x = 0.4–0.7$ in the temperature range 300–500 °C [8–11]. The pseudo-binary Mg_2Si – Mg_2Sn -system is reported to possess an immiscibility region [12]. The composition range of the immiscibility region differs in the literature and these deviations are attributed to the kinetics of the separation. The splitting of the two phases is a relatively slow process at ambient conditions, therefore most of the compositions within the miscibility gap can be synthesized and the samples remain stable. Recently, we reported on the systematic splitting of $\text{Mg}_2\text{Si}_{1-x}\text{Sn}_x$ into Mg_2Si -rich phases in the top and Mg_2Sn -rich phases in the bottom of sintered pellets due to gravity and high thermal diffusivity during spark plasma sintering (SPS) [13, 14]. The main focus in the $\text{Mg}_2\text{Si}_{1-x}\text{Sn}_x$ -system has been on the thermoelectric properties, however, for long-term application in thermoelectric modules the structural stability is of paramount importance. In this study, two of the promising compounds of $\text{Mg}_2\text{Si}_{0.4}\text{Sn}_{0.6}$ and $\text{Mg}_2\text{Si}_{0.6}\text{Sn}_{0.4}$ have been prepared and investigated for structural thermal stability by measuring powder X-ray diffraction (PXRD) data, while heating the samples. The sintered pellets, powders from the ball milling and powders filed of the sintered pellets have been studied. The powders were heated for approximately 1 h, while the pellets were heated for significantly longer time, i.e. several hours. The pellets appear stable (only tiny

Electronic supplementary material The online version of this article (doi:10.1007/s10853-012-6967-0) contains supplementary material, which is available to authorized users.

M. Søndergaard · M. Christensen (✉) · K. A. Borup ·
H. Yin · B. B. Iversen
Department of Chemistry and iNANO, Centre
for Materials Crystallography, University of Aarhus, 8000,
Aarhus C, Denmark
e-mail: mch@chem.au.dk

phase changes are observed in one of the pellets), while the powder samples showed clear changes upon heating. The lattice parameters of the pellets were used to determine the thermal expansion coefficients of the materials. In addition, the thermoelectric transport properties are measured from room temperature to 400 °C on the pellets. Due to a relatively low charge carrier concentration, the maximum zT reaches ~ 0.5 at 350 °C.

Experimental

Synthesis and processing

The pure elements (Mg 99.98 %; Si 99.9+ %; Sn 99.97 %; Sb 99.5 %) were weighted according to the stoichiometry $Mg_{2.2}Si_{0.9925-x}Sn_xSb_{0.0075}$, with $x = 0.4$ and 0.6. The elements were mixed in Al_2O_3 -crucibles and reacted in an induction furnace under a He pressure of 100 Psi. Two batches of each composition were prepared. The lumps were processed in a Fritsch Pulverisette 4 Vario-planetary Mill utilizing WC vials and balls. The speed of the main disc was set to 370 rpm and the speed of the planets was 832 rpm rotating in the opposite direction. The milling time was 30 min and the powder had grain sizes in a wide range from a nm size up to a few μm (See SEM-images in supporting information). Subsequently, the powder was densified by spark plasma sintering. To obtain dense and stable pellets the following procedure was employed: An initial pressure of 75 MPa was applied at room temperature. The sample was heated in 15 min to 700 °C. The temperature was held for 10 min, and the last 4 min the pressure was reduced to 20 MPa to release strain. Finally, the sample was cooled to 200 °C in 10 min, before the power was switched off. Graphite paper was used inside the graphite die and on the ends of the punches for protection of the equipment. Afterwards, the graphite paper was removed and the surfaces of the pellets polished before measurements.

Structural properties

Synchrotron measurements have been conducted on powders from four different batches. Two batches of induction-melted ball-milled powders of compositions $Mg_2Si_{0.3925}Sn_{0.6}Sb_{0.0075}$ and $Mg_2Si_{0.5925}Sn_{0.4}Sb_{0.0075}$ and two batches of the same nominal compositions of powders filed of the pellets from induction-melting ball milling and spark plasma sintering. The measurements were performed at the SPring-8 synchrotron facility in Japan at beamline BL44B2 refitted with a Debye–Scherrer camera image plate setup [15]. The wavelength was calibrated to $\lambda = 0.500105(1)$ Å

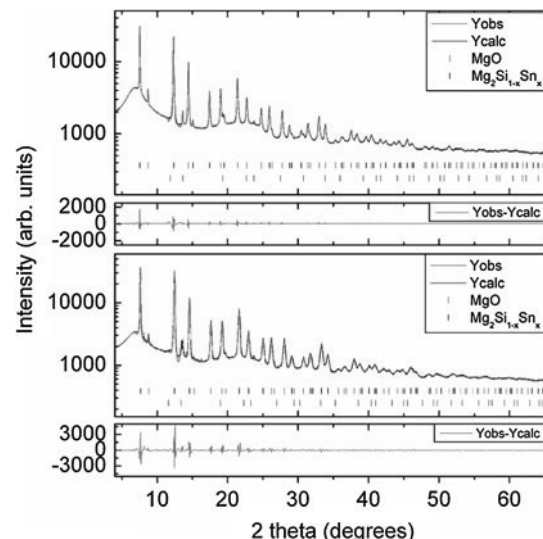


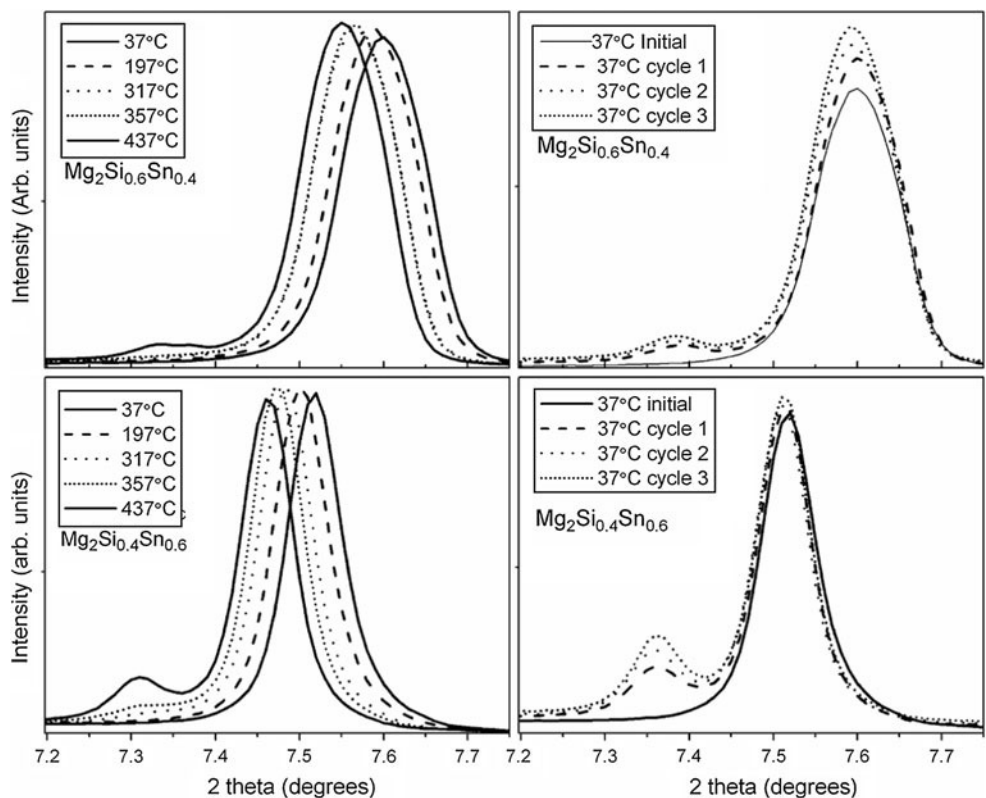
Fig. 1 The observed and calculated diffraction patterns for ball-milled powders of *top* $Mg_2Si_{0.4}Sn_{0.6}$ and *bottom* $Mg_2Si_{0.6}Sn_{0.4}$. The intensity is shown on a log scale to emphasize the weak diffraction peaks at high angle

using a CeO_2 standard. PXRD was conducted while heating the samples sealed in quartz capillaries in an air atmosphere. Data were collected in temperature steps of 40–50 °C from 27 to 437 °C for the first cycle and at the maximum temperature and room temperature for one to two subsequent heating cycles. A jet of hot air was used to heat the sample and the heating time was approximately 5 min for each temperature step of 40–50 °C and the data collection time was approximately 5 min at each step. The entire sintered pellets were heated in air in a Rigaku Smartlab diffractometer configured with a $Cu K\alpha$ source and parallel beam optics. The samples were placed in an Anton-Paar DHS-1100 furnace setup on the diffractometer and the data were collected using a Rigaku D/tex detector. Data were collected at intervals of 50 °C from room temperature to 400 °C and again at room temperature after the heating. At each temperature three identical data collections of ~ 23 min were carried out to observe possible changes during the data collection. The total heating time was ~ 12 h. The diffractograms were Rietveld refined employing the FullProf software package [16]. The ball-milled powder and the sintered pellet of sample $Mg_2Si_{0.4}Sn_{0.6}$ were investigated by scanning electron microscopy (SEM) and energy dispersive X-ray spectroscopy (EDX) on a Nova 600 Nano SEM from FEI equipped with an EDAX detector.

Transport properties

Transport properties were measured on the pellets of both samples from room temperature to 400 °C in vacuum.

Fig. 2 PXRD zoom on the (111)-reflection on ball-milled powders of $Mg_2Si_{0.4}Sn_{0.6}$ and $Mg_2Si_{0.6}Sn_{0.4}$. Top left PXRD at chosen temperatures on $Mg_2Si_{0.6}Sn_{0.4}$. Top right PXRD at 37 °C on $Mg_2Si_{0.6}Sn_{0.4}$ heated to 437 °C three times. Bottom left PXRD on $Mg_2Si_{0.4}Sn_{0.6}$ at chosen temperatures in the first heating cycle. Bottom right PXRD at 37 °C on $Mg_2Si_{0.4}Sn_{0.6}$ heated to 437 °C three times. The shift in the unit cell in the left side figures are due to thermal expansion



Measurements of the electrical resistivity and Hall carrier concentration were conducted on an in-house system employing the van der Pauw method [17] in a magnetic field of 1.25 T [18]. The thermal conductivity values were calculated from the thermal diffusivity and the specific heat capacity, measured on a Netzsch LFA 457 laser flash apparatus, and the density, measured by Archimedes method. A Pyroceram 9606 standard reference sample was employed for calculations of the specific heat capacity. The Seebeck coefficient was measured on an in-house system, similar to the one reported by Iwanaga et al. [19].

Results and discussion

Structural properties of powders

Initially, the synchrotron data revealed that both ball-milled powder samples had a single antifluorite structure as the major phase and a minor MgO impurity phase. Figure 1 shows the observed and refined diffractograms at room temperature. During heating, the emergence of a Mg_2Sn -rich $Mg_2Si_{1-x}Sn_x$ phase was observed from ~277 and ~397 °C for the ball-milled samples of $Mg_2Si_{0.4}Sn_{0.6}$ and $Mg_2Si_{0.6}Sn_{0.4}$, respectively. Figure 2 shows a zoom on the (111)-reflection for both samples during the first heating

cycle (left) and at room temperature between the heating cycles (right). The amount of the Mg_2Sn -rich phase increased as the temperature was increased to 437 °C and increased further for additional heating cycles. This trend is depicted in Fig. 3 with the refined weight fractions at the successive temperature steps. The weight fractions of the Mg_2Sn -rich phase are seen to be significantly larger in the powder samples of the sintered pellets where it reaches 15 and 25 % for $Mg_2Si_{0.6}Sn_{0.4}$ and $Mg_2Si_{0.4}Sn_{0.6}$, respectively, compared with only 3 and 12 % for the ball-milled samples of $Mg_2Si_{0.6}Sn_{0.4}$ and $Mg_2Si_{0.4}Sn_{0.6}$, respectively. However, for both batches more of the Mg_2Sn -rich phase is observed in the compound with the higher nominal Sn-content. Although the emergence of more of the Mg_2Sn -rich phase in $Mg_2Si_{0.4}Sn_{0.6}$ in the powdered samples is in accordance with the higher nominal Sn-content in this sample compared with the $Mg_2Si_{0.6}Sn_{0.4}$ sample, it has previously been shown that the Mg_2Sn solubility is decreased in the more Mg_2Si -rich region of the $Mg_2Si_{1-x}Sn_x$ phase diagram [12, 20]. The weight fractions and other key refined parameters can be seen for the ball-milled $Mg_2Si_{0.6}Sn_{0.4}$ in Table 1 and for the three other samples measured at the synchrotron in Supporting Information. Impurities of Sn and Si were observed in the samples after the first heating cycle, but the amounts were too small to be quantified. For the powdered samples of the sintered pellets

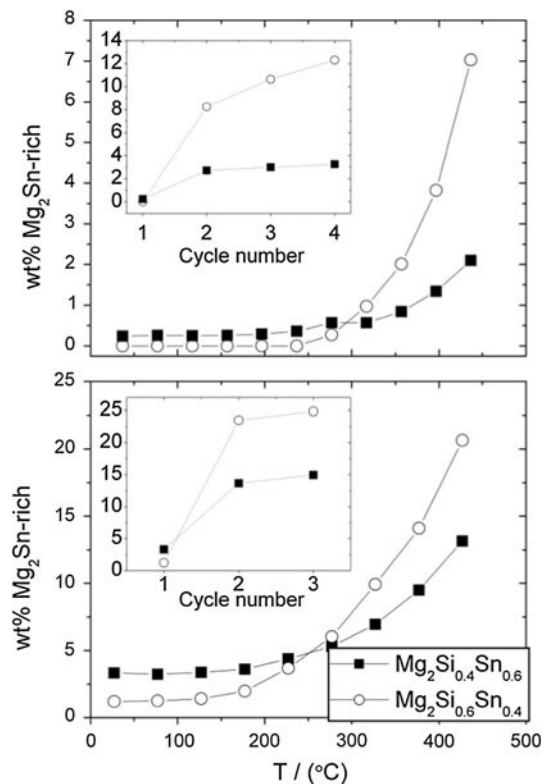


Table 1 Parameters extracted from the Rietveld refinements of the ball-milled powder of $\text{Mg}_2\text{Si}_{0.6}\text{Sn}_{0.4}$: Weight percent of the Mg_2Sn -rich $\text{Mg}_2\text{Si}_{1-x}\text{Sn}_x$ phase and the MgO phase unit cell and reliability factors

Temperature (°C)	37	117	197	317	357	437	37	437	37	437	37
Wt% Mg_2Sn -rich	0.24(3)	0.25(3)	0.29(3)	0.57(4)	0.84(4)	2.10(4)	2.72(5)	2.49(4)	3.01(5)	2.74(5)	3.26(5)
Wt% MgO	10.6(2)	10.3(2)	10.2(2)	9.8(2)	9.7(2)	10.0(2)	10.5(2)	10.6(2)	10.9(3)	11.1(2)	11.4(3)
Unit cell (Å)	6.5282(2)	6.5363(2)	6.5422(2)	6.5552(1)	6.5591(1)	6.5696(2)	6.5296(1)	6.5706(1)	6.5301(1)	6.5709(1)	6.5303(1)
R_p (%)	9.42	9.88	10.1	10.7	10.9	11	10.8	10.9	10.7	11.0	10.9
1 R_F (%)	1.09	1.24	1.42	1.34	1.41	1.42	1.63	1.56	1.84	1.84	2.10
2 R_F (%)	0.87	1.18	1.45	1.80	1.84	2.02	1.68	2.01	1.56	2.24	1.78
3 R_F (%)	2.76	3.66	4.11	4.32	4.20	4.02	3.24	3.58	3.28	4.27	3.40

All data contained 181–191 Bragg reflections and 12 parameters, were used in the refinements. The three R_F parameters are for the three phases: (1) the main $\text{Mg}_2\text{Si}_{1-x}\text{Sn}_x$ phase, (2) MgO and (3) the Mg_2Sn -rich $\text{Mg}_2\text{Si}_{1-x}\text{Sn}_x$ phase

concentration increased from approximately $2.4 \times 10^{19} \text{ cm}^{-3}$ at room temperature to $4.9 \times 10^{19} \text{ cm}^{-3}$ at 400 °C for $\text{Mg}_2\text{Si}_{0.4}\text{Sn}_{0.6}$ and from c. $3.6 \times 10^{19} \text{ cm}^{-3}$ at room temperature to $5.1 \times 10^{19} \text{ cm}^{-3}$ at 400 °C for $\text{Mg}_2\text{Si}_{0.6}\text{Sn}_{0.4}$. The increases in the Hall carrier concentrations with temperature are due to thermal excitations of charge carriers and an increase in the Hall factor [21]. The Hall carrier concentration was relatively low, considering the nominal 7,500 ppm of Sb-doping, and this could be due to Sb evaporation during the synthesis. The Hall mobilities of the samples decreased at elevated temperatures due to the increased electron–phonon scattering. The values were significantly lower compared with those reported in the literature due to the lower charge carrier concentration and the MgO impurities [1, 8]. Both samples exhibited semi-conducting behaviour at room temperature with a decrease in resistivity. However, for the $\text{Mg}_2\text{Si}_{0.4}\text{Sn}_{0.6}$ sample an increase in resistivity was seen from ~60 to ~260 °C and slight deviations were observed between the heating and the cooling cycle. The results of three heating/cooling cycles are depicted in Fig. 6. A gradual decrease in resistivity after each cycle was observed. The changes could be attributed to sintering of the sample during the measurement underlining the importance of annealing in the processing of these compounds. A powder diffraction pattern collected after the heating cycles revealed no structural transformations, only a tendency for sharper Bragg peaks corroborated with sintering of the sample. The thermal conductivity for the $\text{Mg}_2\text{Si}_{0.6}\text{Sn}_{0.4}$ sample compares well with data from the literature [1, 11, 22]. Due to the relatively low Hall carrier concentration, the electronic contribution to the thermal conductivity is small. The Lorenz number was calculated using the single parabolic band model and assuming that acoustic phonon scattering limits the electronic mobility [21]. For a more accurate treatment, a three band model with the two conduction bands and the valence band is needed. This is especially important for the $\text{Mg}_2\text{Si}_{0.4}\text{Sn}_{0.6}$, where the two conduction band minima are almost at the same energy. The absolute value of the Seebeck coefficient is the largest for the $\text{Mg}_2\text{Si}_{0.4}\text{Sn}_{0.6}$ sample, and the values are in agreement with the ones reported by Zaitsev et al. [1, 11, 22] considering the Hall carrier concentration. In addition, the larger absolute Seebeck coefficient value of the $\text{Mg}_2\text{Si}_{0.4}\text{Sn}_{0.6}$ sample concurs with the larger density of states when the two conduction band minima are close in energy [8]. The error bars on the Seebeck coefficient and thermal conductivity are estimated to be 10 % and the errors on the resistivity 5 %. The zT values reached a maximum of ~0.27 for $\text{Mg}_2\text{Si}_{0.6}\text{Sn}_{0.4}$ and 0.50 for $\text{Mg}_2\text{Si}_{0.4}\text{Sn}_{0.6}$ at ~400 °C. These values are in agreement with the low Hall carrier concentration of the samples. For calculations of zT of the $\text{Mg}_2\text{Si}_{0.4}\text{Sn}_{0.6}$ sample, the data from the first heating cycle resistivity measurements were utilized.

Fig. 4 The PXRD zoom of the (111)-reflection of the pellets at temperatures from 30 to 400 °C for left $\text{Mg}_2\text{Si}_{0.6}\text{Sn}_{0.4}$ and right $\text{Mg}_2\text{Si}_{0.4}\text{Sn}_{0.6}$

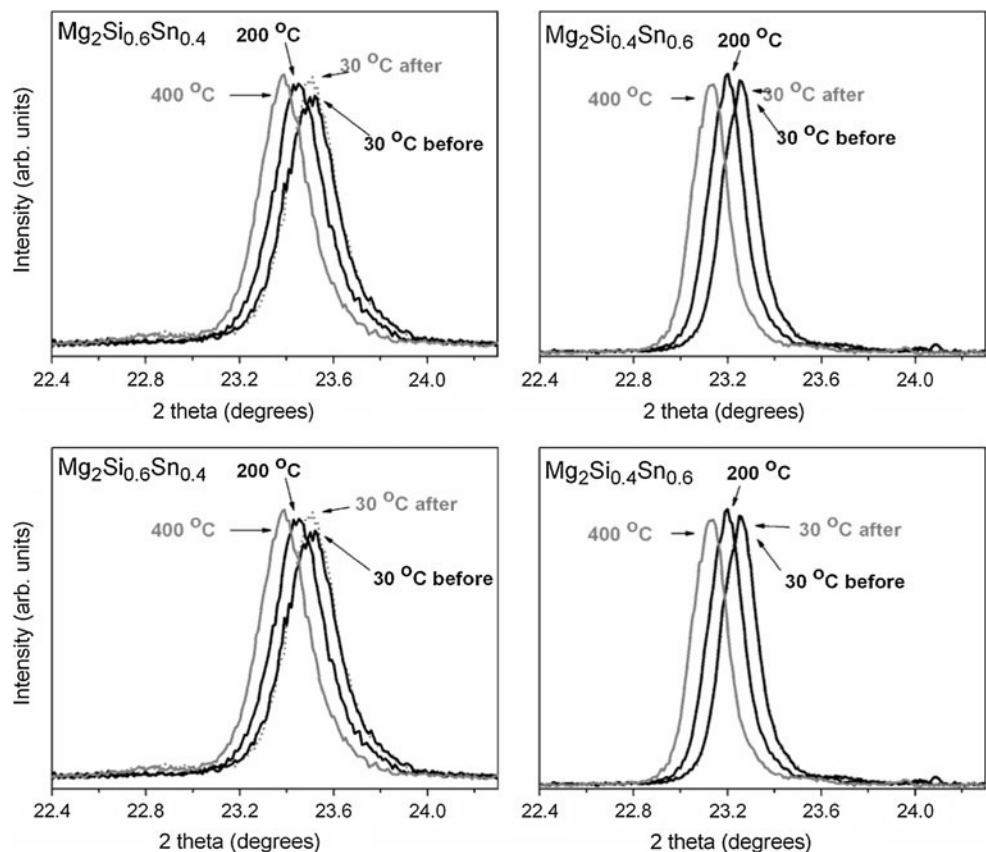
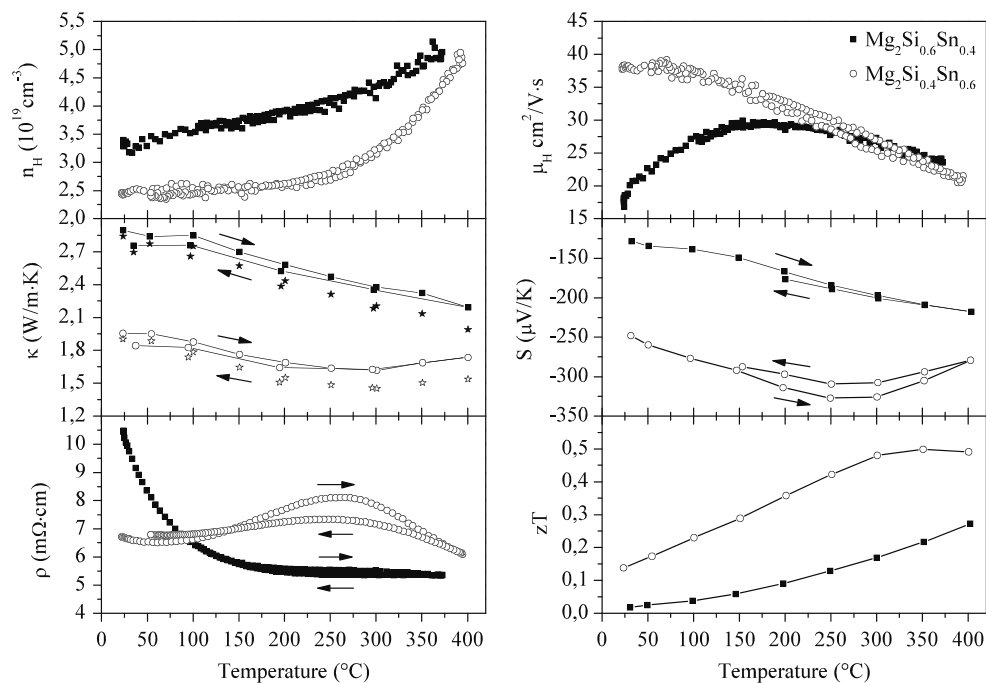


Fig. 5 Transport properties of both samples from room temperature to 400 °C. Top left hall charge carrier concentration. Top right hall mobility. Middle left thermal conductivity. The star-symbols show the lattice thermal conductivity. Middle right seebeck coefficient. Bottom left electrical resistivity. Bottom right thermoelectric figure of merit. The arrows on the figures indicate the heating going right and cooling going left



Conclusion

This study has shown the difference in thermal stability of powdered $\text{Mg}_2\text{Si}_{1-x}\text{Sn}_x$ samples and sintered pellets of $\text{Mg}_2\text{Si}_{1-x}\text{Sn}_x$ samples. The powders show the emergence

of a Sn-rich $\text{Mg}_2\text{Si}_{1-x}\text{Sn}_x$ phase when heated in air, while the pellets seem significantly more stable. The thermal expansion coefficients differ for the different compositions and suggest an option for optimizing module thermal stability by matching the $\text{Mg}_2\text{Si}_{1-x}\text{Sn}_x$ leg to the expansion of

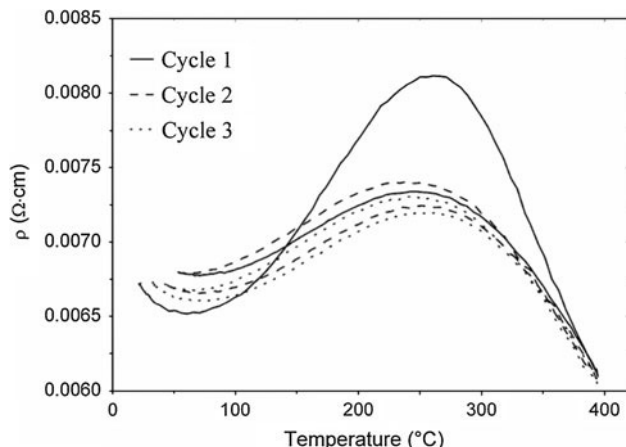


Fig. 6 The resistivity of the $\text{Mg}_2\text{Si}_{0.4}\text{Sn}_{0.6}$ sample measured in three heating cycles from room temperature to 400 °C

the *p*-type material. The transport properties at elevated temperatures yielded relatively low zT values due to the relatively low-charge carrier concentrations of the samples.

Acknowledgements This study was supported by the Danish National Research Foundation (Center for Materials Crystallography), and the Danish Strategic Research Council (Center for Energy Materials). The authors wish to thank the Riken beamline BL44B2 at Spring8 for allocation of beamtime.

References

- Zaitsev VK, Fedorov MI, Gurieva EA, Eremin IS, Konstantinov PP, Samunin AY, Vedernikov MV (2006) Phys Rev B 74:045207
- Zaitsev VK, Fedorov MI, Eremin IS, Gurieva EA (2006) In: Rowe DM (ed) Thermoelectric handbook, macro to nano. CRC Taylor & Francis, Boca Raton, p 29
- Isoda Y, Nagai T, Fujii H, Imai Y, Shinohara Y (2007) In: 26th International Conference on Thermoelectrics (ICT 2007), p 251
- Gao H, Zhu T, Liu X, Chen L, Zhao X (2011) J Mater Chem 21:5933
- Rowe DM (2006) Thermoelectrics handbook : macro to nano. CRC/Taylor & Francis, Boca Raton
- Snyder GJ, Toberer ES (2008) Nat Mater 7:105
- Vineis CJ, Shakouri A, Majumdar A, Kanatzidis MG (2010) Adv Mater 22:3970
- Liu W, Tan X, Yin K, Liu H, Tang X, Shi J, Zhang Q, Uher C (2012) Phys Rev Lett 108:166601
- Liu W, Tang X, Li H, Sharp J, Zhou X, Uher C (2011) Chem Mater 23:5256
- Zhang Q, He J, Zhu TJ, Zhang SN, Zhao XB, Trittm TM (2008) Appl Phys Lett 93:102109
- Zaitsev VK, Fedorov MI, Gurieva EA, Eremin IS, Konstantinov PP, Samunin AY, Vedernikov MV (2005) In: 24th International Conference on Thermoelectrics (ICT) (IEEE Cat. No. 05TH8854C)
- Jung I-H, Kang D-H, Park W-J, Kim NJ, Ahn S (2007) Calphad 31:192
- Søndergaard M, Christensen M, Borup KA, Yin H, Iversen BB (2012) Acta Mater 60:5745
- Søndergaard M, Christensen M, Borup KA, Yin H, Iversen BB (2012) J Electron Mater
- Adachi S, Oguchi T, Tanida H, Park SY, Shimizu H, Miyatake H, Kamiya N, Shiro Y, Inoue Y, Ueki T, Iizuka T (2001) Nucl Instrum Method A Part 1 711:467–468
- Rodriguezcarvajal J (1993) Phys B 192:55
- van der Pauw LJ (1958) Philips Res Rep 13:1–9
- Borup KA, Toberer ES, Fleurial JP, Snyder GJ, Iversen BB (2012) Rev Sci Instrum (submitted)
- Iwanaga S, Toberer ES, LaLonde A, Snyder GJ (2011) Rev Sci Instrum 82:063905
- Boudemagh D, Fruchart D, Haettel R, Hlil EK, Lacoste A, Ortega L, Skryabina N, Tobola J, Wolfers P (2011) Diffus Defect B 170:253
- Fistul VI (1969) Heavily doped semiconductors. Plenum Press, New York
- Fedorov MI, Zaitsev VK, Vedernikov MV (2006) In: 25th International Conference on Thermoelectrics (IEEE Cat No. 06TH8931C)

**Appendix C.9 Phase Separation and Bulk p-n Transition in Single Crystals of
Bi₂Te₂Se Topological Insulator**

Reproduced with permission from John Wiley and Sons.

Phase Separation and Bulk p-n Transition in Single Crystals of Bi₂Te₂Se Topological Insulator

Jian-Li Mi, Martin Bremholm, Marco Bianchi, Kasper Borup, Simon Johnsen, Martin Søndergaard, Dandan Guan, Richard C. Hatch, Philip Hofmann, and Bo B. Iversen*

Bismuth chalcogenide (Bi₂Ch₃) alloys are among the most extensively studied and commonly used thermoelectric materials.^[1] They are also currently of great interest in condensed-matter physics as prototypical three-dimensional topological insulators (TIs), due to the existence of stable and topologically protected Dirac like states on the surface.^[2,3] Shubnikov-de Haas and weak-field Hall anomalies show a substantially enhanced surface current and mobility of the surface states over bulk Bi₂Te₃ values.^[4] However, it is challenging to investigate the charge-transport characteristics of the surface states directly, as the charge transport is dominated by the bulk properties.^[3–5] Most studies of TIs in the Bi₂Ch₃ family have focused on binary Bi₂Se₃ and Bi₂Te₃ systems. Both compounds are semiconductors, but they display high bulk conductivities due to intrinsic defects.^[4–6] A conversion from n- to p-type conduction in Bi₂Te₃ thin films is observed when the growth condition changes.^[5b] Recently, the ternary compound Bi₂Te₂Se has been suggested to be the best material for studies of the surface transport due to its large bulk resistivity.^[3,6–8] However, controlling the bulk conductivity is difficult, even for Bi₂Te₂Se, due to unintentional doping by crystal defects.^[6,8] Here we show that the difficulty of making high-quality Bi₂Te₂Se single crystals originates from the internal features of the specific solid-state composition and phase separation in Bi₂Te₂Se. Bi₂Ch₃ has the tetradymite-type rhombohedral structure, which can be described by the R-3m space group. The lattice can be regarded as a hexagonal layered structure in which the layers stack in the sequence of Ch¹-Bi-Ch²-Bi-Ch¹, where Ch is Te or Se in the present study. Each unit cell consists of three of these five-layer groups, which are connected by bonds with a high degree of van der Waals character between the Ch¹-Ch¹ layers. Early phase-diagram studies showed that Bi₂Te_xSe_y ($x + y = 3$) compounds form continuous solid solutions at temperatures above 500 °C; however, the crystal structures tend to be ordered at

lower temperatures, where the Se atoms tend to occupy the Ch² sites.^[9,10] In equilibrium, the solubility limits were found to be Bi₂Te_{2.6}Se_{0.4} and Bi₂Te_{1.6}Se_{1.4}, and in between these two compositions there is a two-phase region. It is due to the two-phase region that it is difficult to make single-phase Bi₂Te₂Se. Some studies have suggested the presence of a unique Bi₂Te₂Se phase,^[9,11] and, by thermal quenching from high temperature, it is possible to produce single-phase Bi₂Te₂Se crystals with the disordered structure preserved.^[9] Other studies indicate that the Bi₂Te₂Se “phase” may in reality be a mixture of phases, as indicated by the broadening of powder X-ray diffraction (PXRD) peaks of Bi₂Te₂Se, compared with those of Bi₂Te₃.^[12] Due to the importance of Bi₂Te₂Se in both the thermoelectric and TI fields, we have undertaken a thorough characterization of the Bi₂Te₂Se single crystals grown by the Stockbarger method, to obtain a clear understanding of the composition, structure, defects, and properties. The present study shows that a large deviation from the nominal composition occurs in Stockbarger grown Bi₂Te₂Se crystals, and that high-quality crystals indeed can be produced for experimental studies of the surface-transport properties in TIs.

Figure 1a shows the ordered structure of Bi₂Te₂Se. By comparing the simulated PXRD patterns for ordered and disordered Bi₂Te₂Se structures, it is seen that the reflections (107), (0012), (027), and (1112) will have increased intensity in the ordered structure (Supporting Information, Figure S1). Similar features can be obtained in the ordered structures for other Bi₂Te_xSe_y ($x + y = 3$) compounds as long as the Ch² layer is occupied by Se atoms. A Stockbarger grown crystal rod is shown in Figure 1b, in which the symbols O, A, B, C, D, E, and F represent different positions of the crystal rod. The distance of each position from the growth starting point O is listed in Table 1. Figure 1c shows experimental PXRD patterns of samples A, C, E, and F taken from the different positions of the crystal rod. The sharp and symmetric peak shapes of the diffraction patterns A, C, and E suggest that these samples are single phase. The diffraction peaks are shifted progressively to lower 2θ angles from position A to C, E, and F, indicating that the composition and/or defects are not homogenous along the crystal rod. From the (107) and (0012) peaks, it is seen that samples A and C have ordered Se² layers, while samples E and F are disordered. Sample F from the top of the crystal rod consists of a mixture of the disordered Bi₂Ch₃ phase and elemental Te. Since the crystal was grown from a stoichiometric starting composition, Bi₂Te₂Se, the presence of elemental Te indicates a deficiency of the chalcogenide elements in the other parts of the crystal rod. This will result in a large amount of intrinsic defects which affect the bulk transport properties, as will be further discussed.

Dr. J.-L. Mi, Dr. M. Bremholm, K. Borup,
Dr. S. Johnsen, M. Søndergaard, Prof. B. B. Iversen
Center for Materials Crystallography
Department of Chemistry and iNANO
Aarhus University
8000 Aarhus C, Denmark
E-mail: Bo@chem.au.dk

M. Bianchi, Dr. D. Guan, Dr. R. C. Hatch, Prof. P. Hofmann
Department of Physics and Astronomy, and iNANO
Aarhus University
8000 Aarhus C, Denmark

DOI: 10.1002/adma.201203542



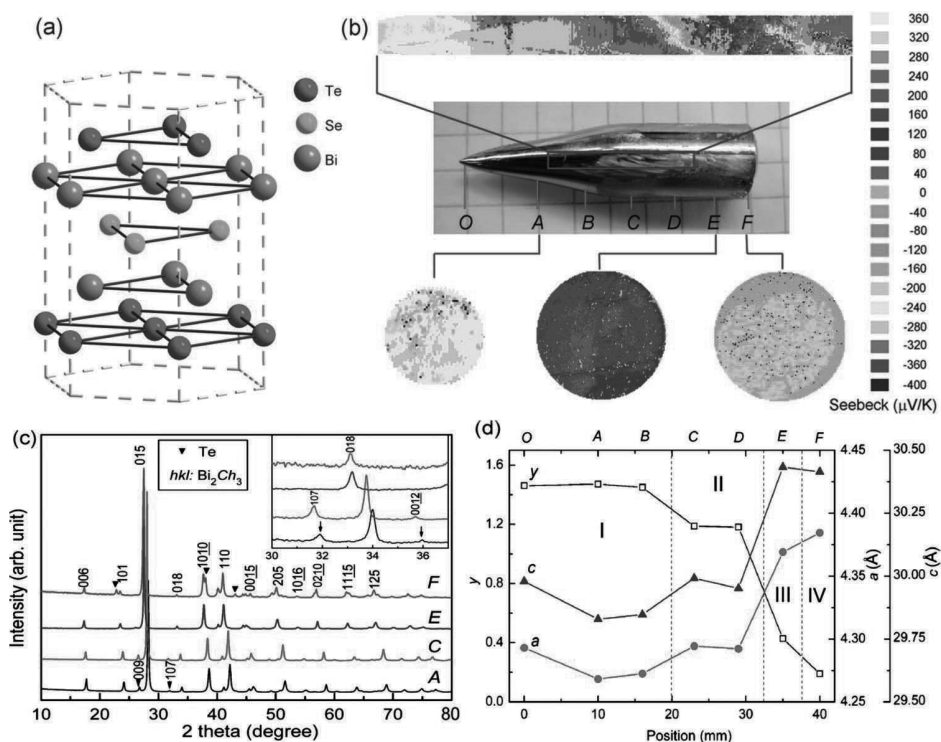


Figure 1. a) Schematic structure of ordered $\text{Bi}_2\text{Te}_2\text{Se}$. b) Potential Seebeck microprobe measurements of the cross sections A, E and F, and of the longitudinal section of the crystal rod. c) Experimental PXRD patterns of the samples A, C, E, and F obtained from different parts of the crystal rod. The inset shows the details of the (107) and (0012) peaks. d) Position dependences of the Se content y in the formula $\text{Bi}_2\text{Te}_x\text{Se}_y$, as well as the cell parameters a and c .

Inductively coupled plasma atomic-emission spectroscopy (ICP-AES) results indicate that the chemical composition varies along the crystal rod. Figure 1d demonstrates the position dependences of the Se content y in the formula $\text{Bi}_2\text{Te}_x\text{Se}_y$, as well as the cell parameters a and c , calculated from the PXRD patterns. Specific values are listed in Table 1. The composition is fairly uniform and the cell parameters are quite constant in different regions but then change abruptly at specific points along the crystal rod. Based on the results of composition and structure determination, phase separation is found along the crystal rod, which can be divided into four parts. At the part from position O to about 20 mm, we suggest an ordered phase

“I” with a composition close to $\text{Bi}_2\text{Te}_{1.5}\text{Se}_{1.5}$. Note that the crystal-growth starting point O has a composition close to stoichiometric Bi_2Ch_3 with $x + y$ of about 3. The cell parameters at position O are larger than those at A and B, and this could be due to a low concentration of vacancy defects at O. At positions from 20 mm to about 32 mm, another phase “II” with a composition close to the fully ordered structure of $\text{Bi}_2\text{Te}_2\text{Se}$ exists. However, it seems that a full replacement of Se^1 with Te^1 will never occur (i.e., Se_{Te} antisite defects are native to $\text{Bi}_2\text{Te}_2\text{Se}$). This can be understood from calculations of formation energies of defects in $\text{Bi}_2\text{Te}_2\text{Se}$ that show that the Se_{Te} antisite has a negative formation energy.^[8] As a result, phase II has a composition

Table 1. Elemental composition (ICP-AES) of $\text{Bi}_2\text{Te}_x\text{Se}_y$ at different positions, and the cell parameters determined from PXRD.

Position	Distance [mm]	x	y	$x + y$	a [Å]	c [Å]
O	0	1.5502	1.4609	3.0111	4.2930(1)	29.9793(1)
A	10	1.4506	1.4715	2.9221	4.2682(1)	29.8286(1)
B	16	1.4478	1.4496	2.8974	4.2725(1)	29.8471(1)
C	23	1.7488	1.1874	2.9362	4.2943(1)	29.9915(1)
D	29	1.6785	1.1814	2.8599	4.2922(1)	29.9512(1)
E	35	2.3292	0.4282	2.7574	4.3692(1)	30.4332(1)
F	40	3.6523	0.1905	3.8428	4.3844(1)	30.4144(1)

of $\text{Bi}_2\text{Te}_x\text{Se}_y$ with x of about 1.6–1.8 and y of about 1.2. Phase III around the E position corresponds to the other composition limit for the disordered phase with a composition close to $\text{Bi}_2\text{Te}_{2.5}\text{Se}_{0.5}$. Phase III has a disordered structure because there are not enough Se atoms to occupy the Ch^2 layers fully. Region IV has two phases, Bi_2Ch_3 and Te. The content of elemental Te of 25 mol% was calculated from the PXRD patterns. This is consistent with the ICP measurements, which, after subtracting the Te content in Bi_2Ch_3 , give about 22 mol% excess elemental Te at position F . It is well-known that temperature gradients during the crystal growth can also result in composition differences along the crystal rod, but such composition changes usually are very small. For example, in a Stockbarger grown $\text{Bi}_2\text{Te}_{2.4}\text{Se}_{0.6}$ crystal rod, no composition difference is evident and only a single phase is found along the crystal rod indicating that $\text{Bi}_2\text{Te}_{2.4}\text{Se}_{0.6}$ is already outside the phase-separation region (data not shown). As a result, the composition difference along the $\text{Bi}_2\text{Te}_2\text{Se}$ crystal rod is mainly due to the internal feature of phase separation in $\text{Bi}_2\text{Te}_2\text{Se}$.

The crystal quality is crucial for experimental detection of the surface states. In the present study, it is found that crystals grown by direct solidification with a very slow cooling rate ($2 \text{ }^\circ\text{C h}^{-1}$) have much-worse crystal quality than Stockbarger grown crystals. Indeed PXRD patterns (Supporting Information, Figure S2) indicate that the direct-solidification-grown sample has much broader diffraction peaks. By simulating the PXRD pattern, the experimental PXRD pattern of direct-solidification-grown samples can be well described by a mixture of phase I and phase II. Thus, we have not been able to separate phase I and II when using the direct-solidification method, and this method results in a relatively poor crystal quality.

Potential Seebeck microprobe (PSM) measurements (Figure 1b) show the spatially resolved room-temperature Seebeck coefficient. A negative Seebeck coefficient of about $-240 \mu\text{V K}^{-1}$ is obtained at position A , while a positive Seebeck coefficient of about $160 \mu\text{V K}^{-1}$ is obtained at position E . The Seebeck coefficient then becomes negative again at position F with a value of around $-160 \mu\text{V K}^{-1}$. There are a number of spots with Seebeck coefficients close to $0 \mu\text{V K}^{-1}$ distributed on the cross section of F , and these originate from the Te phase. A continuous change in the Seebeck coefficient along the crystal rod can be seen by the PSM measurement on the longitudinal section from the

position of 12 to 32 mm and a p-n transition occurs in the CD region. Thus, in the present crystal, a bulk p-n junction is created naturally by self-assembly. In addition, the Stockbarger synthesis method provides an effective way of growing functionally graded materials for thermoelectric energy-conversion applications.

It has been found that the conduction type changes from p- to n-type in the $\text{Bi}_2\text{Te}_3\text{-Bi}_2\text{Se}_3$ system when the Bi_2Se_3 content is above ≈ 20 mol% in the sample.^[11] Therefore, it should be possible to find an alloy composition between Bi_2Te_3 and Bi_2Se_3 that minimizes the carrier concentration and thereby achieves an intrinsic TI. Above, we have shown that the crystals of the ordered phase II in the CD region with the presence of a p-n transition can actually meet these requirements. According to ICP measurements, the chemical composition of most parts of the crystal rod deviate from the stoichiometric composition of Bi_2Ch_3 . Therefore, the intrinsic insulating CD region in our study is not due to the suppression of the formation of defects as suggested in earlier studies,^[3] but due to the counteracting effect of these defects. Scanlon et al.^[8] calculated the formation energies for defects in the $\text{Bi}_2\text{Te}_2\text{Se}$ system, and it was suggested that the preferred p-type defects are a Bi vacancy or a Bi_{Te} antisite, while the dominant n-type defects are a Te vacancy or a Te_{Bi} antisite, depending on the growth conditions. The defect mechanisms at different parts of the Stockbarger grown $\text{Bi}_2\text{Te}_2\text{Se}$ crystal rod are discussed in the following section. Except for the two ends, all of the other parts of the crystal rod have a Bi-rich composition. Consequently, the n-type conduction between O and C is likely due to Te vacancies and the p-type conduction between D and E is probably due to Bi_{Te} antisite defects. At the position between C and D , the two types of defects counteract each other resulting in a p-n transition. Thus, phase I is likely to be n-type and phase III is p-type, while for phase II, it is possible to realize bulk insulators. At the F position, the rod becomes n-type because of Te_{Bi} antisite defects, owing to the Te-rich condition.

Figure 2 shows the angle-resolved photoemission spectroscopy (ARPES) measurements on the crystals obtained from the phase I and phase II regions. The sharp V-like feature with Dirac-like dispersion of the topological surface state band (SSB) was observed for both samples. The Fermi surfaces (FSs) of the SSB are hexagonally warped. The ARPES measurements show that

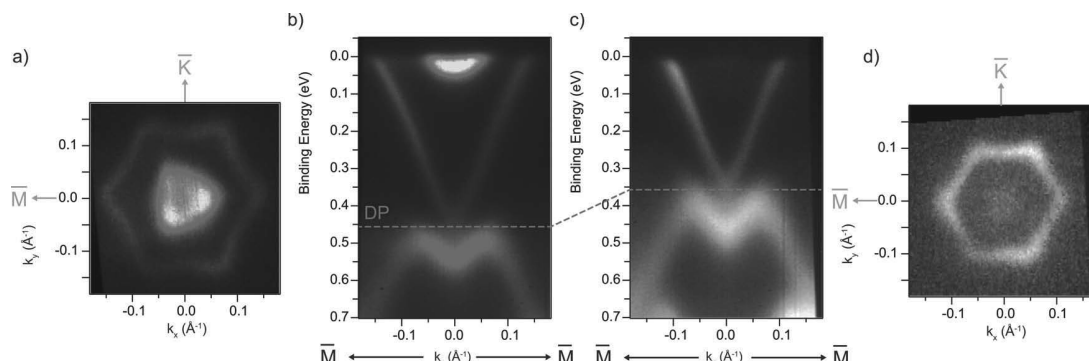


Figure 2. ARPES measurements showing the band characteristics of phase I (a,b) and phase II (c,d). The Dirac point is significantly higher in phase II than in phase I.

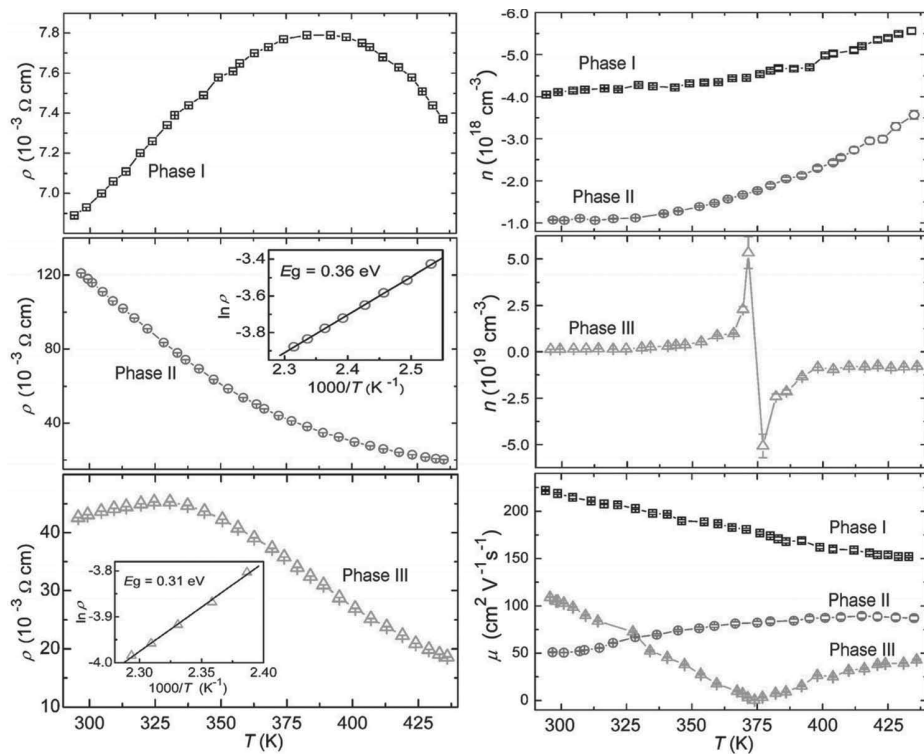


Figure 3. Electrical conductivity, Hall carrier concentration and mobility of the single crystals derived from phase I, II, and III, respectively. The Hall carrier concentrations are shown with the sign of the charge of the carriers to emphasize the dominant carrier type.

the Dirac point is significantly closer to the Fermi level in phase II than in phase I. In phase I, the intensity from another state at the Fermi level shows that the bottom of the bulk conduction band (BCB) is occupied. The sample of phase II is readily depleted of electrons in BCB states, and even more intrinsic crystals are observed in this region. Thus, phase II from the $\text{Bi}_2\text{Te}_2\text{Se}$ crystal rod is actually a more-ideal TI. To date, only very few reports have been published on ARPES measurements of $\text{Bi}_2\text{Te}_2\text{Se}$. For example, Scanlon et al. have shown depleted carriers in the BCB for $\text{Bi}_2\text{Te}_2\text{Se}$, while earlier results showed occupation of a small amount of BCB states.^[8] These contradictory results may be explained if the crystals that were studied belonged to different phases.

Bulk electrical-transport properties were measured from room temperature to 435 K on single crystals taken from the phase I, II, and III regions, as shown in Figure 3. Phase I shows an increase of the Hall carrier concentration and a decrease of the Hall mobility with increasing temperature, which are the typical transport characteristics of a heavily doped n-type semiconductor with a single carrier type. At higher temperatures, there is a decrease in resistivity and a steeper increase in the Hall carrier concentration, suggesting the onset of thermal excitation of charge carriers. Phase II has a much larger resistivity. The room-temperature resistivity of about $0.12 \Omega \text{ cm}$ is ≈ 18 times larger in magnitude than in phase I, and it is also 10 times higher than previously reported results^[3] (possibly due to mixed phases of I and II in the previous studies). As

discussed above, phase I shows n-type conduction due to Te vacancies, while phase III has a p-type conduction due to the Bi_{Te} antisite defects. These two types of defect coexist in phase II and counteract each other, resulting in a high resistivity. The two types of defect are confirmed by the bulk transport measurements since an increase in Hall mobility with temperature is observed up to 400 K in phase II. A transition from p-type to n-type conduction is observed at 375 K for phase III, which is due to the enhancement of the electron concentration by thermal excitation at high temperatures. The change in intrinsic resistivity of phase II and phase III allows for an estimation of the bandgaps, and they are found to be 0.36 and 0.31 eV, respectively, showing a decrease in the bandgap with increasing Te content in $\text{Bi}_2\text{Te}_x\text{Se}_y$ ($x + y \approx 3$).

In conclusion, we have shown composition and phase separation in $\text{Bi}_2\text{Te}_2\text{Se}$ single crystals grown by the Stockbarger method. Three different Bi_2Ch_3 phases have been identified in the crystal rod. Phase I shows n-type conduction, and phase III shows p-type conduction, while the mediate phase II is likely to realize bulk insulators due to the opposing effects of different types of defects. It might be possible to control the appearance of Phase II or III further by adjusting the starting composition and the growth conditions or by developing other growth methods. This could lead to control over the defect type and density, band structure, and finally the properties of $\text{Bi}_2\text{Te}_2\text{Se}$, which would be crucial for further design and realization of new TI devices.

Experimental Section

$\text{Bi}_2\text{Te}_2\text{Se}$ single crystals were grown by the Stockbarger method. 5N-purity elemental Bi, Te, and Se with stoichiometric ratios of 2:2:1 were loaded in a quartz ampoule with a pointed bottom and sealed in a vacuum of 1×10^{-4} mbar. The ampoule was placed vertically in a carbon crucible in an induction furnace. The carbon crucible with the ampoule inside was heated to above 800 °C. The ampoule with about 15 g of molten material was then lowered out of the induction coil at a constant speed of 1.1 mm h⁻¹. A potential Seebeck microprobe^[13] was employed to investigate the spatially resolved room-temperature Seebeck coefficient. Powders were filed from different parts of the crystal rod and characterized by powder X-ray diffraction on an STOE powder diffractometer using Cu K_{α1} radiation in transmission geometry. The chemical-composition determination was conducted by inductively coupled plasma atomic-emission spectroscopy on a SPECTRO ARCOS instrument. Angle-resolved photoemission spectroscopy measurements were performed at the SGM-3 beamline of the Aarhus Storage Ring in Denmark (ASTRID) synchrotron radiation facility in Aarhus.^[14] The samples were cleaved in ultrahigh vacuum at room temperature and ARPES data were taken at around 60 K. Electrical transport properties were measured on a high-temperature in-house system using the van der Pauw method^[15] along the crystal growth direction for different parts of the crystal rod.

Supporting Information

Supporting Information is available from the Wiley Online Library or from the author.

Acknowledgements

This work was supported by the Danish National Research Foundation (Center for Materials Crystallography), the Danish Strategic Research Council (Center for Energy Materials), and the Lundbeck Foundation. Peter Hald is gratefully acknowledged for assistance with ICP-AES, and Mogens Christensen is thanked for fruitful discussions.

Received: August 24, 2012

Revised: September 26, 2012

Published online: November 1, 2012

- [1] a) D.-Y. Chung, T. Hogan, P. Brazis, M. Rocci-Lane, C. Kannewurf, M. Bastea, C. Uher, M. G. Kanatzidis, *Science* **2000**, 287, 1024–1027; b) R. Venkatasubramanian, E. Siivola, T. Colpitts, B. O’Quinn, *Nature* **2001**, 413, 597–602; c) J. L. Mi, N. Lock, T. Sun,

- M. Christensen, M. Søndergaard, P. Hald, H. H. Hng, J. Ma, B. B. Iversen, *ACS Nano* **2010**, 4, 2523–2530.
- [2] a) H. Zhang, C. X. Liu, X. L. Qi, X. Dai, Z. Fang, S. C. Zhang, *Nat. Physics* **2009**, 5, 438–442; b) Y. Xia, D. Qian, D. Hsieh, L. Wray, A. Pal, H. Lin, A. Bansil, D. Grauer, Y. S. Hor, R. J. Cava, M. Z. Hasan, *Nat. Physics* **2009**, 5, 398–402; c) D. Hsieh, Y. Xia, L. Wray, D. Qian, A. Pal, J. H. Dil, J. Osterwalder, F. Meier, G. Bihlmayer, C. L. Kane, Y. S. Hor, R. J. Cava, M. Z. Hasan, *Science* **2009**, 323, 919–922; d) H. J. Noh, H. Koh, S. J. Oh, J. H. Park, H. D. Kim, J. D. Rameau, T. Valla, T. E. Kidd, P. D. Johnson, Y. Hu, Q. Li, *Europhys. Lett.* **2008**, 81, 57006; e) Y. L. Chen, J. G. Analytis, J. H. Chu, Z. K. Liu, S. K. Mo, X. L. Qi, H. J. Zhang, D. H. Lu, X. Dai, Z. Fang, S. C. Zhang, I. R. Fisher, Z. Hussain, Z. X. Shen, *Science* **2009**, 325, 178–181; f) M. Bianchi, D. Guan, S. Bao, J. Mi, B. B. Iversen, P. D. C. King, P. Hofmann, *Nat. Commun.* **2010**, 1, 128; g) P. D. King, R. C. Hatch, M. Bianchi, R. Ovsyannikov, C. Lupulescu, D. Guan, J. L. Mi, E. D. L. Rienks, J. Fink, A. Lindblad, S. Svensson, S. Bao, B. B. Iversen, W. Eberhardt, F. Baumberger, P. Hofmann, *Phys. Rev. Lett.* **2011**, 107, 096802.
- [3] Z. Ren, A. A. Taskin, S. Sasaki, K. Segawa, Y. Ando, *Phys. Rev. B* **2010**, 82, 241306(R).
- [4] D. X. Qu, Y. S. Hor, J. Xiong, R. J. Cava, N. P. Ong, *Science* **2010**, 329, 821–824.
- [5] a) N. P. Butch, K. Kirshenbaum, P. Syers, A. B. Sushkov, G. S. Jenkins, H. D. Drew, J. Paglione, *Phys. Rev. B* **2010**, 81, 241301(R); b) G. Wang, X. G. Zhu, Y. Y. Sun, Y. Y. Li, T. Zhang, J. Wen, X. Chen, K. He, L. L. Wang, X. C. Ma, J. F. Jia, S. B. Zhang, Q. K. Xue, *Adv. Mater.* **2011**, 23, 2929–2932.
- [6] S. Jia, H. Ji, E. Climent-Pascual, M. K. Fuccillo, M. E. Charles, J. Xiong, N. P. Ong, R. J. Cava, *Phys. Rev. B* **2011**, 84, 235206.
- [7] J. Xiong, A. C. Petersen, D. Qu, Y. S. Hor, R. J. Cava, N. P. Ong, *Physica E* **2012**, 44, 917–920.
- [8] D. O. Scanlon, P. D. C. King, R. P. Singh, A. de la Torre, S. M. Walker, *Adv. Mater.* **2012**, 24, 2154–2158.
- [9] H. G. Bouanani, D. Eddike, B. Liatard, G. Brun, *Mater. Res. Bull.* **1996**, 31, 177–187.
- [10] J. F. Dumas, G. Brun, B. Liatard, J. C. Tedenac, M. Maurin, *Thermochim. Acta* **1987**, 122, 135–141.
- [11] O. B. Sokolov, S. Y. Skiparov, N. I. Duvankov, G. G. Shabunina, *J. Cryst. Growth* **2004**, 262, 442–448.
- [12] A. Hruban, A. Materna, W. Dalecki, G. Strzelecka, M. Piersa, E. Jurkiewicz-Wegner, R. Diduszko, M. Romaniec, W. Orlowski, *Acta Phys. Pol. A* **2011**, 120, 950–953.
- [13] D. Platzek, G. Karpinski, C. Stiewe, P. Ziolkowski, C. Drasar, E. Muller, in *24th International Conference on Thermoelectrics, 2005 (ICT 2005)*, IEEE, Piscataway, NJ, USA **2005**, p.13.
- [14] M. Bianchi, M. R. C. Hatch, D. Guan, T. Planke, J. L. Mi, B. B. Iversen, P. Hofmann, *Semicond. Sci. Technol.* **2012**, in press.
- [15] L. J. van der Pauw, *Philips Res. Rep.* **1958**, 13, 1–9.

This dissertation was handed in to Aarhus University for evaluation in July 2014 by Kasper Andersen Borup. The dissertation is centered around two main projects. The first project is the construction of two setups for measuring the Seebeck coefficient and resistivity, respectively. The resistivity setup is also able to measure the Hall coefficient for calculation of the charge carrier concentration and mobility. These setups are described in detail. The second project is the extension of the van der Pauw method to treat anisotropic samples, especially single crystals. The van der Pauw method is utilized in the resistivity setup and hence this theory is directly linked to the first project. Two new methods for extracting the resistivity tensor has been developed and are ready for implementation. Several materials science projects utilizing the setups in thermoelectrics and topological insulators are also discussed.

Ph.D. dissertation

Kasper Andersen Borup

July 2014